energies

Special Issue Reprint

Advances in Bio-Energy

Biofuel and Other Value-Added Bioproducts, Production Technology, and Environmental Impact Systems Components

Edited by
Carlos Saul Osorio-González and Antonio Avalos Ramirez

mdpi.com/journal/energies

MDPI

Advances in Bio-Energy: Biofuel and Other Value-Added Bioproducts, Production Technology, and Environmental Impact
Systems Components

Advances in Bio-Energy: Biofuel and Other Value-Added Bioproducts, Production Technology, and Environmental Impact Systems Components

Guest Editors

Carlos Saul Osorio-González
Antonio Avalos Ramirez

MDPI

Basel • Beijing • Wuhan • Barcelona • Belgrade • Novi Sad • Cluj • Manchester

Guest Editors

Carlos Saul Osorio-González
Soil and Agri-Food
Engineering Department
Laval University
Quebec
Canada

Antonio Avalos Ramirez
Centre National en
Électrochimie et en
Technologies
Environnementales
Shawinigan
Canada

Editorial Office
MDPI AG
Grosspeteranlage 5
4052 Basel, Switzerland

This is a reprint of the Special Issue, published open access by the journal *Energies* (ISSN 1996-1073), freely accessible at: https://www.mdpi.com/journal/energies/special_issues/618WFY5COH.

For citation purposes, cite each article independently as indicated on the article page online and as indicated below:

Lastname, A.A.; Lastname, B.B. Article Title. *Journal Name* **Year**, *Volume Number*, Page Range.

ISBN 978-3-7258-9261-7 (Hbk)
ISBN 978-3-7258-9262-4 (PDF)
https://doi.org/10.3390/books978-3-7258-9262-4

© 2026 by the authors. Articles in this reprint are Open Access and distributed under the Creative Commons Attribution (CC BY) license. The reprint as a whole is distributed by MDPI under the terms and conditions of the Creative Commons Attribution-NonCommercial-NoDerivs (CC BY-NC-ND) license (https://creativecommons.org/licenses/by-nc-nd/4.0/).

Contents

About the Editors . . . . . **vii**

Preface . . . . . **ix**

Aneta Sienkiewicz, Małgorzata Kowczyk-Sadowy, Paweł Cwalina, Sławomir Obidziński, Małgorzata Krasowska, Alicja Piotrowska-Niczyporuk, et al.
Fruit-Vegetable Food Industry Waste as Biocomponents of Liquid Fuels
Reprinted from: *Energies* **2026**, *19*, 1685, https://doi.org/10.3390/en19071685 . . . . . **1**

Sławomir Obidziński, Paweł Cwalina, Małgorzata Kowczyk-Sadowy, Aneta Sienkiewicz, Jacek Mazur and Paweł Braun
The Effect of Cherry Stone Addition to Sawdust on the Pelletization Process and Fuel Pellet Quality
Reprinted from: *Energies* **2025**, *18*, 5356, https://doi.org/10.3390/en18205356 . . . . . **18**

Justyna Czerwinska, Szymon Szufa, Hilal Unyay and Grzegorz Wielgosinski
Emission of Total Volatile Organic Compounds from the Torrefaction Process: Meadow Hay, Rye, and Oat Straw as Renewable Fuels
Reprinted from: *Energies* **2025**, *18*, 4154, https://doi.org/10.3390/en18154154 . . . . . **39**

Krzysztof Mudryk, Jarosław Frączek, Joanna Leszczyńska and Mateusz Krotowski
Technology for the Production of Energy Briquettes from Bean Stalks
Reprinted from: *Energies* **2025**, *18*, 4009, https://doi.org/10.3390/en18154009 . . . . . **69**

Jovanny Rafael Duque, Fabio Bermejo-Altamar, Jorge Duarte-Forero and Brando Hernández-Comas
Performance and Environmental Assessment of Palm Oil–Coffee Husk Biodiesel Blends in a Dual-Fuel Diesel Engine Operating with Hydroxy
Reprinted from: *Energies* **2025**, *18*, 3914, https://doi.org/10.3390/en18153914 . . . . . **93**

Aravind Ganesan, Simon Barnabé, Younès Bareha, Simon Langlois, Olivier Rezazgui and Cyrine Boussabbeh
Turning Construction, Renovation, and Demolition (CRD) Wood Waste into Biochar: A Scalable and Sustainable Solution for Energy and Environmental Applications
Reprinted from: *Energies* **2025**, *18*, 3902, https://doi.org/10.3390/en18153902 . . . . . **121**

João Pedro Silva, Senhorinha Teixeira and José Carlos Teixeira
Thermogravimetric Assessment and Kinetic Analysis of Forestry Residues Combustion
Reprinted from: *Energies* **2025**, *18*, 3299, https://doi.org/10.3390/en18133299 . . . . . **160**

Admore Samuel Chiumia, Betchani Tchereni, Hope Baxter Chamdimba, Benjamin L. Robinson and Mike Clifford
Diagnosis of Socio-Economic Prospects and Constraints for Household Biogas Adoption: A Case of Lizulu Market in Ntcheu District of Malawi
Reprinted from: *Energies* **2025**, *18*, 2636, https://doi.org/10.3390/en18102636 . . . . . **185**

Aravind Ganesan, Simon Barnabé, Younès Bareha, Simon Langlois, Olivier Rezazgui and Cyrine Boussabbeh
Kinetic Analysis of Construction, Renovation, and Demolition (CRD) Wood Pyrolysis Using Model-Fitting and Model-Free Methods via Thermogravimetric Analysis
Reprinted from: *Energies* **2025**, *18*, 2496, https://doi.org/10.3390/en18102496 . . . . . **207**

About the Editors

Carlos Saul Osorio-González

Carlos Saul Osorio-González is an Assistant Professor at Université Laval, specializing in fermentation technology, bioprocess development, and sustainable resource recovery. His research focuses on valorizing agro-industrial residues, bioenergy production, and circular economy approaches. He has led and contributed to projects on bioactive compounds, bioremediation and bioenergy. A recipient of multiple awards, he has published extensively in leading journals. He actively serves on editorial boards and contributes to international scientific conferences and research initiatives.

Antonio Avalos Ramirez

Antonio Avalos Ramirez is a chemical engineer from the Universidad Nacional Autonoma de Mexico with a Ph.D. from the Universite de Sherbrooke. Dr. Avalos Ramirez is a researcher in environmental and bioprocesses engineering in the "Centre national en electrochimie et en technologies environnementales (CNETE)". He is a specialist with 25 years of experience in the treatment of air polluted with volatile organic compounds and greenhouse gases using biological and photocatalyic processes. He also works on anaerobic digestion, wastewater treatment, integration and simulation of chemical and biological processes, and biological and thermochemical valorisation of biomasses in biofuels and bioproducts.

Preface

"Advances in Bio-Energy: Biofuel and Other Value-Added Bioproducts, Production Technology, and Environmental Impact Systems Components" brings together emerging research at the intersection of sustainable energy, biotechnology, and environmental systems analysis. Its subject centers on innovative pathways for producing biofuels and high-value bioproducts, while its scope spans feedstock development, conversion technologies, process optimization, and lifecycle environmental assessment. The aim of this collection is to highlight cutting-edge scientific and engineering advances that improve efficiency, scalability, and sustainability across bio-energy systems. Particular emphasis is placed on integrated approaches that link production technologies with environmental impact evaluation, enabling a systems-level understanding of bio-based solutions. This issue is motivated by the urgent global need to transition away from fossil-based resources toward renewable, low-carbon alternatives. Scientific progress in this field is essential not only for energy security but also for climate change mitigation and circular bioeconomy development. It is addressed to researchers, engineers, industry practitioners, and policymakers seeking to deepen their understanding of bio-energy innovations and their broader environmental implications. By fostering interdisciplinary dialogue, the main aim is to support informed decision-making and accelerate the deployment of sustainable bio-based technologies.

Carlos Saul Osorio-González and Antonio Avalos Ramirez
Guest Editors

energies

MDPI

Article

Fruit-Vegetable Food Industry Waste as Biocomponents of Liquid Fuels

Aneta Sienkiewicz [1,*], Małgorzata Kowczyk-Sadowy [1], Paweł Cwalina [1], Sławomir Obidziński [1], Małgorzata Krasowska [1], Alicja Piotrowska-Niczyporuk [2] and Andrzej Bajguz [2]

[1] Department of Agri-Food Engineering and Environmental Management, Bialystok University of Technology, Wiejska 45E, 15-351 Bialystok, Poland; m.kowczyk@pb.edu.pl (M.K.-S.); s.obidzinski@pb.edu.pl (S.O.)
[2] Department of Plant Biology and Ecology, Faculty of Biology, University of Bialystok, Ciolkowskiego 1J, 15-245 Bialystok, Poland; alicjap@uwb.edu.pl (A.P.-N.); abajguz@uwb.edu.pl (A.B.)
* Correspondence: a.sienkiewicz@pb.edu.pl

Abstract

This study explores the potential of seeds from fruit and vegetable processing waste as feedstocks for biodiesel biocomponent production. Fatty acid methyl esters (FAMEs), obtained through a transesterification reaction, were extracted using ultrasound-assisted extraction and identified by gas chromatography–mass spectrometry (GC–MS) in selected ion monitoring (SIM) mode. A total of 31 to 34 individual FAME compounds were identified across all samples. The fatty acid profiles varied both quantitatively and qualitatively depending on the raw material; however, unsaturated FAMEs predominated over saturated ones in all cases. The highest proportions were observed for γ-linolenic acid (C18:3n6), particularly in apple, melon, lemon, and pumpkin seeds. Substantial contributions of oleic acid (C18:1n9c) were found in apple, quince, cherry, and melon seeds, while linolelaidic acid (C18:2n6t) dominated in melon, pumpkin, quince, and cherry seeds. The highest total FAME contents were recorded for apple, melon, lemon, and pumpkin seeds, while the lowest values were observed in apricot and pepper seeds. Among the materials studied, grape seeds proved to be the most promising feedstock, exhibiting a favorable cetane number and a beneficial fatty acid profile characterized by high monounsaturated fatty acid (MUFA) content, low polyunsaturated fatty acid (PUFA) content, and a moderate fraction of saturated fatty acids (SFAs). Plum and peach seeds also showed significant potential, but their higher PUFA levels may compromise oxidative stability and could require antioxidant supplementation or blending with MUFA-rich feedstocks.

Keywords: postproduction seed waste; transesterification; FAME; cetane number; biodiesel

1. Introduction

In the face of escalating challenges associated with the depletion of fossil fuel resources and the urgent need to mitigate greenhouse gas emissions, the transformation of the energy sector toward renewable sources has become a cornerstone of global climate and energy policy. Consequently, the search for renewable, low-emission energy carriers has emerged as one of the most critical areas of contemporary scientific and technological research. Among alternative fuels, biodiesel—defined as fatty acid methyl esters (FAMEs)—represents one of the most promising liquid biofuels capable of partially substituting conventional diesel fuel. Biodiesel offers several advantages, including biodegradability and reduced emissions of sulfur oxides and particulate matter, thereby contributing to the mitigation of greenhouse gas emissions [1,2].

Conventional biodiesel production relies predominantly on first-generation feedstocks (e.g., vegetable oils) and second-generation feedstocks (e.g., waste oils and animal fats). However, large-scale commercialization remains constrained by economic challenges, particularly those associated with feedstock availability and cost [3]. In response, increasing attention has been directed toward the utilization of agri-food industry residues—including waste cooking oils, residual fats, and other organic fractions—as low-cost substrates for liquid biofuel production, in alignment with circular economy principles [4].

Lipids derived from food waste and used cooking oils have demonstrated considerable potential as substrates for biodiesel production. Karmee et al. [5] reported that lipids extracted from food waste could be efficiently transesterified to FAMEs with yields approaching 100% using an alkaline catalyst (KOH), while biocatalytic systems employing the lipase Novozyme 435 achieved conversion efficiencies of approximately 90%. Comparable results have been reported for used cooking oils, where methyl ester contents of approximately 95.3% and overall process yields of about 92% were achieved, confirming the feasibility of large-scale biodiesel production from such waste streams [6]. Although the quality of used frying fats is highly variable, detailed analyses have demonstrated that FAME composition and polymeric degradation products can be effectively characterized, which is essential for evaluating their industrial applicability [7].

Biodiesel research focuses not only on traditional sources, such as used cooking oils, but also on unconventional waste streams like sewage sludge and dairy industry residues. Lipids extracted from sewage sludge generated during dairy wastewater treatment have been successfully recovered using solvent extraction methods and converted into biodiesel, while studies using green solvents for lipid extraction showed high recovery efficiency and effective FAME production, maintaining the biodegradability of the residual sludge [8,9]. Seasonal variations also affect lipid extraction efficiency and biodiesel yield, which is an important aspect in designing large-scale processes [10].

Expanding research to microbial lipid sources, the potential of microorganisms and microalgae cultivated in wastewater treatment systems as biodiesel feedstocks has been demonstrated. Although lipid yields from these sources may be lower than those from conventional waste oils, they still represent a promising alternative [11]. Oleaginous microorganisms, such as *Rhodosporidium toruloides*, can utilize food waste hydrolysates for lipid accumulation. Chen et al. [12] demonstrated that microbial lipids obtained through this method, after transesterification, comply with BS EN 14214 [13] and ASTM D6751 [14] biodiesel standards, confirming their suitability for biodiesel production. The fatty acid profile analyses of microalgae show the predominance of palmitic acid (C16:0), oleic acid (C18:1), and linoleic acid (C18:2) [15].

In addition to conventional catalytic transesterification, innovative conversion methods such as biocatalysis are being explored, where enzymes or microorganisms catalyze transesterification reactions, which can improve process efficiency and selectivity while reducing the need for traditional catalysts [16].

Specific agri-food waste streams, such as herbal processing residues, have also become an interesting source of lipids for biodiesel production. Studies have shown that the fatty acid profiles of FAMEs from these residues meet established biodiesel quality standards, supporting their role in sustainable biofuel systems [17].

Comprehensive valorization of agri-food residues is essential for assessing their suitability for biofuel conversion processes. Mukherjee and Gupta [18] demonstrated that converting agri-food waste into biodiesel and bioethanol can simultaneously address waste management challenges, enhance energy security, and support the development of a circular economy. Numerous studies further confirm that food waste can serve as a versatile feedstock for the production of biofuels and biochemicals, thereby contributing to envi-

ronmental protection and resource efficiency [19]. The conversion of these residues into liquid biofuel components aligns with the principles of a circular economy, zero-waste bioeconomy, and sustainable resource management, while reducing landfill disposal, lowering greenhouse gas emissions, and enabling the development of local, cost-effective biofuel sources [20,21].

Despite extensive research on biodiesel production from food processing residues, a knowledge gap remains regarding the comprehensive evaluation of diverse waste fractions—such as peels, pulp, seeds, and pomace—with respect to their fatty acid composition, transesterification susceptibility, and compliance of the resulting FAMEs with applicable fuel standards. Among these fractions, seeds and pomace are of particular interest, as they represent lipid-rich materials with significant potential for the production of high-quality biofuel components.

For instance, previous studies have shown that seeds of fruits such as watermelon (*Citrullus lanatus*) and honeydew melon (*Cucumis melo*) contain substantial amounts of oil that can be converted via transesterification into biodiesel exhibiting fuel properties comparable to those specified in the ASTM D6751 standard [14,22]. Furthermore, analyses of seed oils from nine industrial fruit species—including sea buckthorn (*Hippophae rhamnoides*), red currant (*Ribes rubrum*), pomegranate (*Punica granatum*), Japanese quince (*Chaenomeles japonica*), grape (*Vitis vinifera*), gooseberry (*Ribes uva-crispa*), and apple (*Malus domestica*)—have reported lipid contents ranging from approximately 11.8% to 28.5%. The fatty acid profiles of these oils, characterized by high proportions of unsaturated fatty acids, indicate their promising potential as alternative feedstocks for FAME production [23].

These findings suggest that fruit seed fractions generated by the fruit and vegetable processing industry represent valuable and underutilized feedstocks for biodiesel production. At the same time, they highlight the need for detailed valorization studies and comprehensive evaluation of the fuel properties of the resulting FAMEs to fully assess their industrial applicability and compliance with established quality standards.

Accordingly, the aim of the present study was to quantitatively determine the FAME content of seeds derived from selected fruit and vegetable processing residues, identify the dominant fatty acids, estimate the cetane number, and compare their composition with literature data for other plant-based feedstocks, in order to evaluate their suitability as biofuel components for biodiesel production.

2. Materials and Methods

2.1. Seed Materials

Samples of sixteen seed materials derived from fruits and vegetables—sour cherry (*Prunus cerasus*), European plum (*Prunus domestica*), common quince (*Cydonia oblonga*), common pumpkin (*Cucurbita pepo*), peach (*Prunus persica*), melon (*Cucumis melo*), grape (*Vitis vinifera*), watermelon (*Citrullus lanatus*), common apricot (*Prunus armeniaca*), common lemon (*Citrus limon*), avocado (*Persea americana*), apple (*Malus domestica*), common pear (*Pyrus communis*), bell pepper (*Capsicum annuum*), sweet cherry (*Prunus avium*), and sweet orange (*Citrus sinensis*)—were obtained from food-processing companies located in the Podlaskie Voivodeship, Poland.

2.2. Fatty Acid Methyl Ester (FAME) Analysis

All reactants used in the transesterification reaction were purchased from Avantor Performance Materials (Gliwice, Poland). Solvents for gas chromatography–mass spectrometry (GC–MS) analysis, as well as the Supelco 37 Component FAME Mix standard, were obtained from Merck (Darmstadt, Germany) (Table 1).

https://doi.org/10.3390/en19071685

Table 1. FAMEs standards used in the GC-MS analysis of seed samples.

Type of FAME	Systematic Name	The Common Name of FAME	Abbreviation
MUFA	Myristoleic acid methyl ester	Myristoleic acid	C14:1
	cis-10-Pentadecanoic acid methyl ester	Pentadecanoic acid	C15:1
	9-Hexadecenoic acid methyl ester	Palmitoleic acid	C16:1
	cis-10-Heptadecenoic acid methyl ester	Heptadecenoic acid	C17:1
	trans-9-Octadecenoic acid methyl ester (Z)	Elaidic acid	C18:1n9t
	9-Octadecenoic acid methyl ester (E)	Oleic acid	C18:1n9c
	cis-11-Eicosenoic acid methyl ester	Gondoic acid	C20:1
	13-Docosenoic acid methyl ester (Z)	Erucic acid	C22:1n9
	15-Tetracosenoic acid methyl ester (Z)	Nervonic acid	C24:1n9
PUFA	9,12-Octadecadienoic acid methyl ester (E, E)	Linolelaidic acid	C18:2n6t
	9,12-Octadecadienoic acid methyl ester (Z, Z)	Linoleic acid	C18:2n6c
	all-cis-6,9,12-Octadecatrienoic acid	γ-Linolenic acid	C18:3n6
	9,12,15-Octadecatrienoic acid methyl ester (Z, Z, Z)	Linolenic acid	C18:3n3
	cis-11,14-Eicosadienoic acid methyl ester	Eicosadienoic acid	C20:2
	cis-11,14,17-Eicosatrienoic acid methyl ester	Eicosatrienoic acid	C20:3n3
	cis-8,11,14-Eicosatrienoic acid methyl ester	Dihomo-γ-linolenic acid	C20:3n6
	5,8,11,14-Eicosatetraenoic acid methyl ester (all-Z)	Arachidonic acid	C20:4n6
	cis-5,8,11,14,17-Eicosapentaenoic acid methyl ester	Eicosapentaenoic acid	C20:5n3
	cis-13,16-Docasadienoic acid methyl ester	Docosadienoic acid	C22:2n6
	4,7,10,13,16,19-Docosahexaenoic acid methyl ester (all-Z)	Cervonic acid	C22:6n3
SFA	Butyric acid methyl ester	Butyric acid	C4:0
	Hexanoic acid methyl ester	Caproic acid	C6:0
	Octanoic acid methyl ester	Caprylic acid	C8:0
	Decanoic acid methyl ester	Capric acid	C10:0
	Undecanoic acid methyl ester	Undecylic acid	C11:0
	Dodecanoic acid methyl ester	Lauric acid	C12:0
	Tridecanoic acid methyl ester	Tridecylic acid	C13:0
	Tetradecanoic acid methyl ester	Myristic acid	C14:0
	Pentadecanoic acid methyl ester	Pentadecylic acid	C15:0
	Hexadecanoic acid methyl ester	Palmitic acid	C16:0
	Heptadecanoic acid methyl ester	Margaric acid	C17:0
	Octadecanoic acid methyl ester	Stearic acid	C18:0
	Eicosanoic acid methyl ester	Arachidic acid	C20:0
	Heneicosanoic acid methyl ester	Heneicosylic acid	C21:0
	Docosanoic acid methyl ester	Behenic acid	C22:0
	Tricosanoic acid methyl ester	Tricosylic acid	C23:0
	Tetracosanoic acid methyl ester	Lignoceric acid	C24:0

MUFA—monounsaturated fatty acid, PUFA—polyunsaturated fatty acid, SFA—saturated fatty acid.

For FAME analysis, a 0.5 g seed sample was subjected to extraction with hexane in the presence of a methanol–potassium hydroxide (KOH) solution acting as a catalyst. The reaction mixture was prepared by adding hexane to initiate the transesterification process. A detailed description of the transesterification procedure, including optimized extraction conditions and analytical parameters, is provided in the study by Sienkiewicz et al. [17].

2.3. Statistical Analysis

All results are expressed as mean values ± standard deviations (SDs) calculated from four independent replicates. Differences between mean values were evaluated using Tukey's honest significant difference (HSD) post hoc test at a significance level of $p < 0.05$.

Hierarchical cluster analysis (HCA) was applied to classify the samples and visualize similarities among them in the form of a dendrogram. Clustering was performed using

Euclidean distance as the measure of dissimilarity and Ward's method as the agglomerative criterion. The optimal number of clusters was determined using Sneath's criterion at 66% of the maximum linkage distance.

Subsequently, principal component analysis (PCA) was employed to explore the relationships among the analyzed variables. The first fifteen principal components were initially considered in the biplot analysis. The final biplot was constructed using the first two principal components (PC1 and PC2), which together accounted for 52.86% of the total variance in the dataset.

All statistical analyses were conducted using Statistica 13.3 software (TIBCO Software Inc., Palo Alto, CA, USA).

2.4. Cetane Number Prediction

To estimate the approximate cetane number (CN) of biodiesel derived from seed wastes based on their FAME compositions, a multiple linear regression model equation, proposed by Gopinath et al. [24], was applied:

$$\begin{aligned} CN = 62.2 + 0.017 \times PC_{12:0} + 0.074 \times PC_{14:0} + 0.115 \times PC_{16:0} + 0.177 \times PC_{18:0} \\ -0.103 \times PC_{18:1n9c} - 0.279 \times PC_{18:2n6c} - 0.366 \times PC_{18:3n3}, \end{aligned} \quad (1)$$

where Pn represents the weight percentage of the corresponding FAME component n.

It is important to note that Equation (1) can be used to predict the CN of both pure FAMEs and biodiesel blends. Additionally, the approximated error in the CN was calculated using the transformed relative error Equation (2):

$$CN_{\varepsilon} = \frac{CN}{1 \pm \varepsilon}, \quad (2)$$

where ε represents the assumed percentage error, for instance, 8%, which is the maximum relative estimation error of the model developed by Gopinath et al. [24].

3. Results and Discussion

Identification and Composition of Fatty Acid Methyl Esters

Analysis of the fatty acid composition isolated from seeds constituting waste from the fruit and vegetable processing industry, performed using gas chromatography coupled with mass spectrometry operating in selected ion monitoring mode (GC–MS/SIM), revealed the presence of 34 out of the 37 targeted fatty acid methyl esters (FAMEs). The detected compounds comprised 15 saturated fatty acids (SFAs), 9 monounsaturated fatty acids (MUFAs), and 10 polyunsaturated fatty acids (PUFAs).

The monounsaturated fatty acid content of the investigated seeds exhibited pronounced species-dependent variability (Table 2). Oleic acid (C18:1n9c) was the dominant MUFA in most samples, with the highest concentrations observed in apple (97.99 mg g^{-1}dry weight, dw), quince (39.04 mg g^{-1}dw), cherry (32.93 mg g^{-1}dw), and melon (21.51 mg g^{-1}dw) seeds. A high proportion of oleic acid is particularly advantageous for biodiesel production, as it enhances both the cetane number and oxidative stability of the resulting methyl esters. Notably, significant amounts of the trans isomer C18:1n9t were detected in cherry (28.70 mg g^{-1}dw), plum (24.22 mg g^{-1}dw), and melon (13.46 mg g^{-1}dw) seeds, suggesting species-specific lipid metabolism pathways.

Table 2. The content of monounsaturated fatty acids (MUFA) (mean ± SD, n = 4) in fruit and vegetable waste seeds. Means with the same letters are not significantly different ($p \geq 0.05$) according to Tukey's post hoc test.

Fruit and Vegetable Waste Seeds	[μg g^{-1}dw]								
	C14:1	**C15:1**	**C16:1**	**C17:1**	**C18:1n9t**	**C18:1n9c**	**C20:1**	**C22:1n9**	**C24:1n9**
Cherry	37.89 ± 0.39 e	1611.34 ± 27.34 c	23.82 ± 0.88 gh	146.28 ± 2.01 e	28,701.90 ± 522.90 a	32,927.03 ± 547.85 c	49.22 ± 0.93 g	21.07 ± 0.90 c	46.01 ± 8.33 b
Plum	34.98 ± 0.25 ef	763.44 ± 9.09 f	191.60 ± 3.14 d	18.97 ± 0.14 hi	24,216.43 ± 328.01 b	10,399.22 ± 130.82 g	34.37 ± 0.62 g	4.60 ± 5.88 ef	36.49 ± 2.38 bc
Quince	34.89 ± 0.34 ef	864.42 ± 3.56 f	14.15 ± 4.79 h	157.41 ± 1.79 de	8131.43 ± 218.41 f	39,037.22 ± 167.14 b	49.27 ± 8.71 g	91.81 ± 2.66 b	16.94 ± 0.40 ef
Pumpkin	33.53 ± 0.05 f	1145.81 ± 12.09 e	65.83 ± 1.59 f	538.60 ± 24.29 b	9063.43 ± 87.76 e	14,439.76 ± 31.39 f	2531.67 ± 48.16 c	11.97 ± 1.55 de	16.18 ± 0.76 ef
Peach	42.08 ± 0.21 d	828.30 ± 15.61 f	8.77 ± 0.27 h	249.52 ± 5.53 d	2759.78 ± 50.91 h	4460.79 ± 83.09 h	61.29 ± 0.82 g	10.36 ± 1.35 de	16.98 ± 0.39 ef
Melon	37.91 ± 0.35 e	3505.51 ± 36.76 b	55.40 ± 1.86 f	1330.54 ± 13.79 a	13,455.68 ± 312.83 d	21,508.22 ± 208.66 d	143.88 ± 7.41 f	16.05 ± 4.17 cd	25.24 ± 0.30 de
Grape	59.39 ± 0.24 c	268.28 ± 2.96 g	13.57 ± 0.16 h	134.08 ± 1.78 e	1675.45 ± 9.28 i	2734.63 ± 18.86 i	416.41 ± 12.12 e	14.58 ± 1.09 cd	27.50 ± 0.06 cd
Watermelon	35.23 ± 0.07 ef	2935.51 ± 209.64 b	5.27 ± 0.24 h	11.63 ± 0.54 i	3403.56 ± 0.54 g	3265.34 ± 40.65 hi	50,612.58 ± 579.99 a	2.79 ± 0.03 f	57.68 ± 9.41 a
Apricot	ND	3.63 ± 0.08 h	2.54 ± 0.73 h	0.70 ± 0.06 i	7.10 ± 0.43 j	35.81 ± 5.56 k	123.93 ± 0.94 f	1.74 ± 0.88 f	14.10 ± 0.41 f
Lemon	217.86 ± 3.64 b	4016.31 ± 305.33 a	3611.56 ± 66.27 b	16.85 ± 0.37 hi	9914.07 ± 82.26 e	15,991.39 ± 120.02 e	5241.87 ± 38.61 b	21.39 ± 0.87 c	30.64 ± 2.60 cd
Avocado	1666.77 ± 14.12 a	249.09 ± 11.21 g	289.20 ± 10.22 c	3239.54 ± 292.68 a	84.71 ± 0.52 j	370.57 ± 1.23 k	2684.01 ± 15.20 c	161.54 ± 1.57 a	31.20 ± 0.46 cd
Apple	176.65 ± 0.20 b	29.50 ± 0.29 h	6592.61 ± 66.12 a	78.13 ± 0.51 fg	1054.36 ± 7.39 i	97,987.14 ± 336.12 a	13,604.24 ± 33.78 b	106.37 ± 1.17 b	114.57 ± 0.80 a
Pear	86.95 ± 1.11 c	ND	360.32 ± 9.41 c	50.48 ± 3.26 gh	29.79 ± 2.57 j	1544.62 ± 14.46 j	599.45 ± 36.45 e	8.53 ± 0.32 ef	34.77 ± 0.18 bc
Pepper	36.47 ± 1.22 ef	9.11 ± 1.98 h	165.44 ± 5.99 d	4.64 ± 0.25 i	32.48 ± 9.41 j	613.61 ± 22.09 jk	353.83 ± 13.88 e	3.19 ± 0.40 f	13.31 ± 0.02 f
Sweet cherry	211.32 ± 1.06 b	8.13 ± 0.18 h	2791.15 ± 29.12 b	8.09 ± 0.61 i	39.07 ± 6.23 j	14,002.33 ± 400.95 f	4543.25 ± 64.06 b	14.95 ± 0.22 cd	14.14 ± 0.47 f
Orange	35.41 ± 0.15 ef	79.24 ± 3.36 h	233.35 ± 13.52 cd	48.25 ± 1.44 gh	14.03 ± 0.56 j	1264.73 ± 40.10 j	848.96 ± 30.33 d	4.24 ± 0.20 ef	13.70 ± 3.05 f

ND, not detected.

Long-chain MUFAs (C20:1, C22:1, and C24:1) were generally present at low levels; however, exceptionally high concentrations of C20:1 were recorded in watermelon seeds (50.61 mg g^{-1}dw), which may positively influence the cetane number of biodiesel. In contrast, apricot and pepper seeds exhibited the lowest total MUFA contents, indicating their limited suitability as feedstocks for producing oxidatively stable biofuel components.

The PUFA fraction was dominated by linoleic (C18:2n6) and linolenic (C18:3) acids (Table 3). The highest total PUFA concentrations were found in apple (540.36 mg g^{-1}dw), melon (356.76 mg g^{-1}dw), lemon (241.11 mg g^{-1}dw), and pumpkin (205.79 mg g^{-1}dw) seeds. Elevated PUFA levels are associated with improved low-temperature properties of biodiesel; however, they also imply reduced oxidative stability, in accordance with the relationships defined in the BS EN 14214 standard [13]. Particularly high concentrations of γ-linolenic acid (C18:3n6) were observed in apple, melon, lemon, and pumpkin seeds, indicating the predominance of PUFA biosynthesis pathways typical of oilseed plants.

In contrast, grape seeds were characterized by a low total PUFA content; the value of 641.02 μg g^{-1}dw refers exclusively to C18:3n6. Although the cumulative PUFA content was higher, it remained substantially lower than that observed in most other seeds, suggesting improved oxidative stability of the resulting fuel. Long-chain PUFAs (C20–C22) were detected only in trace amounts in all samples and therefore did not significantly affect fuel properties, although elevated concentrations of these compounds are known to adversely influence oxidative stability [25].

Table 3. The content of polyunsaturated fatty acids (PUFA) (mean ± SD, n = 4) in fruit and vegetable waste seeds. Means with the same letters are not significantly different ($p \geq 0.05$) according to Tukey's post hoc test.

Fruit and Vegetable Waste Seeds	[μg g^{-1}dw]									
	C18:2n6t	C18:2n6c	C18:3n6	C18:3n3	C20:2	C20:3n6	C20:4n6	C20:5n3	C22:2n6	C22:6n3
Cherry	15,552.89 ± 268.82 c	15.56 ± 0.29 cd	115,106.67 ± 1845.13 e	48.37 ± 1.64 f	6.08 ± 0.35 f	5.46 ± 1.76 b	23.66 ± 1.10 bc	664.41 ± 8.02 a	32.31 ± 1.38 e	20.92 ± 0.29 d
Plum	4769.94 ± 59.64 e	14.53 ± 0.49 d	35,517.38 ± 464.96 g	28.55 ± 0.23 f	17.48 ± 4.84 ef	3.00 ± 0.82 b	22.74 ± 0.16 bc	6.04 ± 0.25 f	76.97 ± 12.63 cd	24.03 ± 0.77 cd
Quince	18,947.23 ± 324.07 b	17.05 ± 0.85 c	136,179.13 ± 2355.71 d	ND	25.54 ± 0.53 de	5.35 ± 1.04 b	18.16 ± 0.86 cd	34.60 ± 6.67 d	59.57 ± 14.44 d	30.72 ± 3.14 bc
Pumpkin	24,488.10 ± 40.23 a	13.30 ± 0.42 de	181,102.07 ± 262.10 c	8.85 ± 0.29 g	2.67 ± 2.74 f	5.17 ± 1.28 b	13.56 ± 4.06 de	102.88 ± 17.02 c	27.29 ± 2.88 ef	21.34 ± 1.28 d
Peach	1248.40 ± 25.83 g	15.82 ± 0.71 cd	9234.66 ± 195.54 h	9.80 ± 3.55 g	2.24 ± 0.20 f	5.02 ± 1.17 b	16.86 ± 0.39 cd	1.83 ± 0.10 f	14.27 ± 0.50 f	20.51 ± 0.18 d
Melon	42,887.93 ± 424.35 a	14.23 ± 0.38 d	313,475.37 ± 312.83 b	0.88 ± 0.08 g	7.34 ± 2.36 f	4.86 ± 0.95 b	24.22 ± 0.64 bc	175.06 ± 2.57 b	148.18 ± 2.71 b	21.12 ± 0.30 d
Grape	95.89 ± 3.58 h	2.93 ± 0.05 f	641.02 ± 4.48 i	1.38 ± 0.04 g	2.55 ± 0.55 f	5.61 ± 0.06 b	27.01 ± 0.06 b	3.76 ± 0.19 f	23.05 ± 0.01 ef	40.37 ± 0.08 b
Watermelon	4030.26 ± 88.74 e	15.74 ± 0.12 cd	2149.72 ± 123.66 i	26,241.21 ± 579.99 a	ND	2.13 ± 0.64 b	11.55 ± 3.42 e	66.72 ± 12.21 cd	10.07 ± 2.99 f	20.27 ± 0.44 d
Apricot	11.89 ± 2.31 h	1.71 ± 0.04 f	731.85 ± 3.23 i	37.43 ± 0.39 f	1.49 ± 0.04 f	2.03 ± 0.60 b	15.53 ± 3.89 de	1.35 ± 0.40 f	12.40 ± 3.10 f	19.78 ± 0.07 d
Lemon	2921.05 ± 107.47 f	18.41 ± 0.40 c	224,738.00 ± 125.20 c	13,310.98 ± 589.01 c	1.05 ± 0.56 f	7.80 ± 0.50 b	25.69 ± 0.43 b	20.42 ± 4.52 e	20.75 ± 0.09 f	42.77 ± 2.33 b
Avocado	344.30 ± 17.31 h	16.79 ± 0.38 c	27,739.90 ± 238.33 g	1868.39 ± 5.12 e	266.96 ± 3.88 a	2882.83 ± 285.47 a	2370.34 ± 29.15 a	10.43 ± 3.31 ef	269.75 ± 1.93 a	29.05 ± 6.01 bc
Apple	10,904.87 ± 97.71 d	31.55 ± 0.19 b	508,488.33 ± 554.41 a	20,548.58 ± 671.51 b	70.57 ± 2.64 b	36.80 ± 5.77 b	101.78 ± 1.27 b	18.88 ± 0.29 e	68.73 ± 0.59 cd	91.14 ± 0.09 a
Pear	187.11 ± 1.72 h	27.14 ± 0.19 b	2153.35 ± 133.84 i	156.00 ± 10.07 f	30.81 ± 2.10 cd	5.12 ± 0.58 b	ND	3.00 ± 0.35 f	31.69 ± 0.10 e	50.13 ± 0.05 b
Pepper	65.82 ± 1.86 h	12.19 ± 0.36 e	1384.74 ± 44.11 i	93.05 ± 5.60 f	2.62 ± 0.57 f	2.64 ± 0.01 b	15.96 ± 0.35 de	1.49 ± 0.04 f	12.53 ± 0.10 f	19.88 ± 0.11 d
Sweet cherry	164.87 ± 3.78 h	1095.44 ± 44.40 a	3467.61 ± 82.24 i	12,931.00 ± 258.56 c	2.04 ± 0.07 f	13.65 ± 2.47 b	15.98 ± 0.59 de	31.25 ± 0.37 de	12.36 ± 0.12 f	19.79 ± 0.29 d
Orange	173.65 ± 4.41 h	14.38 ± 0.23 d	3968.63 ± 106.55 i	280.84 ± 9.30 f	1.04 ± 0.32 f	2.90 ± 0.49 b	15.75 ± 0.45 de	1.85 ± 0.09 f	12.53 ± 0.08 f	19.26 ± 0.05 d

ND, not detected.

Among the saturated fatty acids, palmitic acid (C16:0) was the predominant component (Table 4), reaching the highest concentrations in melon (6.71 mg g^{-1}dw), lemon (4.46 mg g^{-1}dw), quince (4.06 mg g^{-1}dw), and watermelon (4.00 mg g^{-1}dw) seeds. Stearic acid (C18:0) constituted the second most abundant SFA, particularly in pumpkin (977.26 μg g^{-1}dw) and melon (933.57 μg g^{-1}dw) seeds.

Additionally, unusually high concentrations of heptadecanoic acid (C17:0) were detected in watermelon (17.89 mg g^{-1}dw) and lemon (25.12 mg g^{-1}dw) seeds, representing a distinctive feature of the lipid profiles of these materials. Although increased SFA content generally enhances the cetane number of biodiesel, it may simultaneously deteriorate low-temperature properties by increasing the cloud point [26]. Overall, however, the SFA content in most analyzed seeds was lower than that of MUFAs and PUFAs, indicating a favorable fatty acid composition for biodiesel applications.

Additionally, quantitative analysis demonstrated a clear predominance of unsaturated fatty acids (MUFAs and PUFAs) over saturated fatty acids (SFAs) in all analyzed samples. The MUFA content ranged from 9.84% in melon seeds to 72.19% in grape seeds, while the PUFA fraction varied from 11.40% in grape seeds to 87.65% in melon seeds (Figure 1). In contrast, the SFA content was relatively low, ranging from 0.67% in apple seeds to 29.32% in pear seeds.

Table 4. The content of saturated fatty acids (SFA) (mean ± SD, n = 4) in fruit and vegetable waste seeds. Means with the same letters are not significantly different ($p \geq 0.05$) according to Tukey's post hoc test.

Fruit and Vegetable Waste Seeds	[μg g^{-1}dw]														
	C8:0	C10:0	C11:0	C12:0	C13:0	C14:0	C15:0	C16:0	C17:0	C18:0	C20:0	C21:0	C22:0	C23:0	C24:0
Cherry	97.80 ± 1.99 c	26.10 ± 0.27cd	11.90 ± 0.10 fg	23.93 ± 0.21 de	9.79 ± 0.09 c	37.57 ± 0.45 ef	11.53 ± 0.24 c	3041.21 ± 51.72 e	131.95 ± 2.51 f	821.02 ± 13.71 c	300.53 ± 4.17 e	16.38 ± 0.17 cd	77.86 ± 0.96 b	35.49 ± 0.49 b	473.49 ± 5.41 a
Plum	ND	25.23 ± 0.04 de	11.13 ± 0.03 g	22.27 ± 0.06 e	9.59 ± 0.03 c	28.35 ± 0.18 f	4.53 ± 0.08 e	1428.20 ± 16.58 g	44.70 ± 1.15 h	312.77 ± 3.49 e	54.57 ± 0.26 h	18.33 ± 0.35 bc	18.81 ± 0.11 de	6.91 ± 0.90 de	5.41 ± 1.75 f
Quince	ND	24.47 ± 0.09 e	10.94 ± 0.04 g	21.88 ± 0.08 e	9.44 ± 0.01 c	39.88 ± 0.86 e	10.40 ± 0.46 cd	4064.16 ± 562.21 cd	97.72 ± 4.59 g	301.33 ± 15.59 e	984.55 ± 15.12 d	ND	34.02 ± 3.50 c	2.16 ± 0.01 f	1.39 ± 1.23 f
Pumpkin	2.67 ± 0.11 d	25.97 ± 0.05 cd	13.68 ± 0.02 ef	27.37 ± 0.04 cd	9.58 ± 0.04 c	101.27 ± 0.86 b	23.02 ± 0.10 b	2218.74 ± 26.73 f	35.82 ± 2.88 h	977.26 ± 35.58 b	1274.71 ± 3.61 c	11.89 ± 3.46 e	23.51 ± 1.96 d	62.00 ± 2.52 a	95.24 ± 4.30 c
Peach	64.61 ± 1.61 c	25.39 ± 0.06 de	15.11 ± 0.08 e	30.22 ± 0.17 c	9.56 ± 0.04 c	32.26 ± 0.29 ef	9.43 ± 0.20 d	1584.46 ± 201.80 g	58.00 ± 0.45 h	368.43 ± 3.50 e	97.35 ± 1.35 h	16.58 ± 0.29 cd	12.91 ± 0.19 e	1.51 ± 0.08 f	23.46 ± 0.82 e
Melon	32.66 ± 0.36 cd	24.59 ± 0.25 e	12.10 ± 0.12 fg	24.20 ± 0.24 de	9.45 ± 0.09 c	59.90 ± 0.65 d	1.27 ± 0.04 gh	6711.92 ± 71.55 a	32.67 ± 0.35 h	933.57 ± 26.71 b	2151.38 ± 208.66 b	15.86 ± 0.60 cd	18.23 ± 2.37 de	5.50 ± 0.30 e	150.13 ± 0.65 b
Grape	ND	42.92 ± 0.07 b	19.09 ± 0.04 d	38.18 ± 0.08 b	16.47 ± 0.04 b	44.76 ± 0.10 e	7.79 ± 0.94 de	681.77 ± 4.44 h	47.29 ± 0.63 h	175.57 ± 0.99 f	63.54 ± 0.10 h	27.16 ± 0.07 a	22.93 ± 0.90 d	4.15 ± 0.06 ef	23.35 ± 0.80 e
Watermelon	ND	25.49 ± 0.03 de	12.93 ± 0.05 f	25.85 ± 0.10 d	9.58 ± 0.02 c	69.94 ± 7.92 c	2.23 ± 0.05 fg	4000.04 ± 111.63 d	17,885.03 ± 542.38 b	4.83 ± 1.11 g	2363.15 ± 197.35 b	126.85 ± 8.44 a	1.73 ± 0.54 f	1.42 ± 0.46 f	8.02 ± 1.56 f
Apricot	ND	24.48 ± 0.04 e	10.37 ± 0.01 g	20.74 ± 0.02 e	7.11 ± 2.06 d	19.09 ± 0.03 f	0.03 ± 0.01 h	6.44 ± 3.22 i	54.54 ± 15.08 h	ND	35.25 ± 0.18 h	15.46 ± 0.03 cd	6.64 ± 0.01 f	0.90 ± 0.02 f	3.70 ± 0.14 f
Lemon	80.94 ± 2.39 c	42.50 ± 0.13 b	21.51 ± 0.12 c	43.01 ± 0.23 b	15.61 ± 1.21 b	101.06 ± 1.64 b	14.86 ± 0.21 c	4460.98 ± 306.21 c	25,116.34 ± 407.64 a	5.52 ± 0.11 g	265.94 ± 38.48 e	300.50 ± 6.72 a	12.28 ± 0.05 e	6.68 ± 0.66 de	23.20 ± 0.85 e
Avocado	ND	26.35 ± 1.76c	11.19 ± 0.06 g	22.37 ± 0.13 e	11.79 ± 0.71 bc	38.20 ± 0.17 ef	1.51 ± 0.07 gh	249.07 ± 26.63 hi	1111.28 ± 6.37 e	2.07 ± 0.03 g	73.52 ± 0.42 h	17.46 ± 1.59 cd	7.33 ± 0.22 f	0.67 ± 0.02 f	12.90 ± 3.95 f
Apple	162.75 ± 1.79 a	120.71 ± 0.09 a	52.49 ± 0.38 a	104.98 ± 0.76 a	44.79 ± 0.08 a	211.68 ± 0.94 a	14.64 ± 0.04 c	60.87 ± 3.37 i	471.96 ± 13.06 f	36.20 ± 0.37 g	2175.28 ± 44.86 b	249.32 ± 9.72 b	704.86 ± 33.46 a	28.98 ± 0.11 c	21.63 ± 0.58 e
Pear	ND	61.69 ± 5.28 b	27.99 ± 0.09 b	55.98 ± 0.17 b	24.60 ± 0.17 b	49.19 ± 2.68 e	2.35 ± 0.16 fg	2.95 ± 0.35 i	1721.97 ± 73.10 d	15.78 ± 0.69 g	128.09 ± 4.27 g	51.97 ± 2.20 c	17.13 ± 0.07 de	2.42 ± 0.02 f	61.30 ± 4.46 d
Pepper	ND	ND	12.67 ± 0.65 f	25.34 ± 1.31 d	12.56 ± 1.38 bc	31.17 ± 0.46 ef	16.83 ± 0.57 bc	4.78 ± 0.66 i	950.28 ± 35.24 e	5.36 ± 0.60 g	42.69 ± 0.31 h	21.75 ± 1.66 c	18.69 ± 4.06 de	1.19 ± 0.40 f	5.25 ± 0.88 f
Sweet cherry	22.29 ± 0.34 d	25.18 ± 0.42 de	13.16 ± 0.92 f	26.32 ± 1.84 d	17.53 ± 1.81 b	31.78 ± 10.68 ef	133.16 ± 29.84 a	6.71 ± 2.23 i	2238.83 ± 96.41 c	47.66 ± 4.27 g	1094.59 ± 28.04 d	205.92 ± 0.93 b	10.14 ± 2.80 ef	1.68 ± 0.22 f	17.70 ± 0.27 ef
Orange	ND	25.61 ± 1.27 de	18.91 ± 7.72 d	20.73 ± 0.30 e	9.43 ± 0.16 c	19.41 ± 0.41 f	0.28 ± 0.02 h	6.42 ± 0.17 i	656.57 ± 21.76 f	3.86 ± 0.08 g	190.66 ± 3.83 f	31.12 ± 0.45 c	6.62 ± 1.22 f	2.65 ± 0.35 f	6.15 ± 0.78 f

ND, not detected.

https://doi.org/10.3390/en19071685

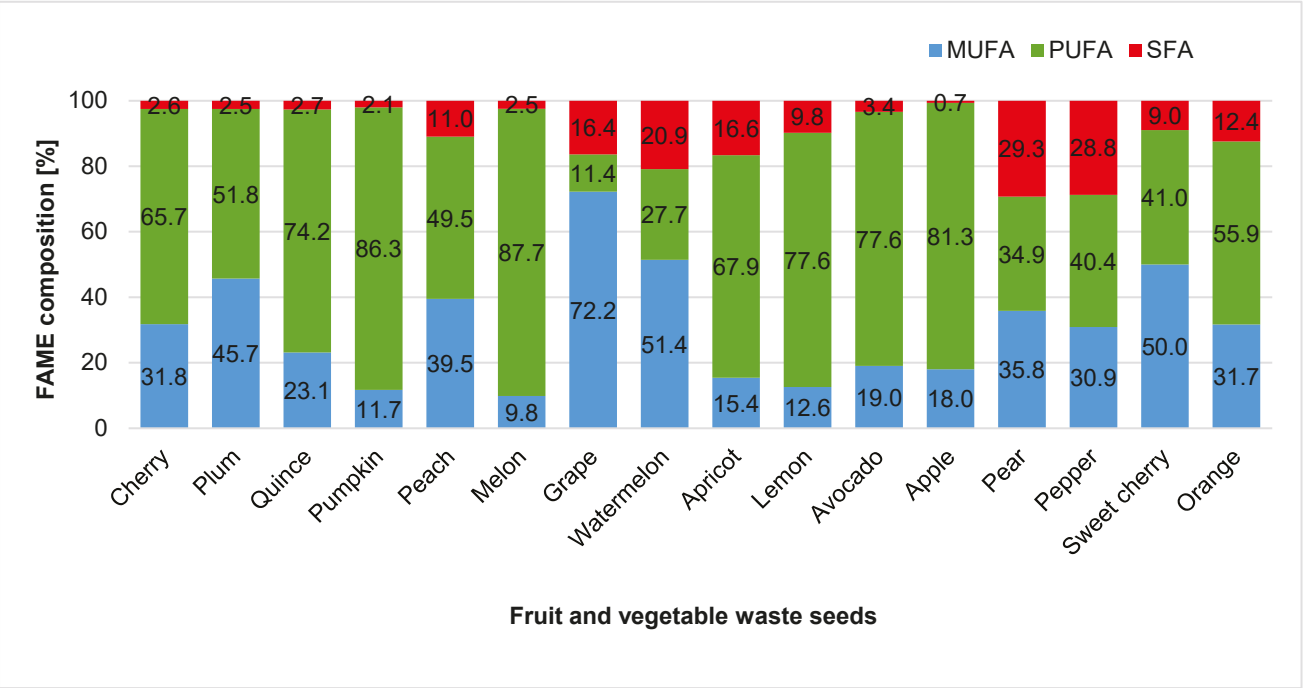


Figure 1. Fatty acid methyl ester composition of the fruit and vegetable waste seeds.

From the perspective of biodiesel quality, as defined by the BS EN 14214 standard [13], key parameters such as oxidative stability, cetane number, and low-temperature properties are directly influenced by the fatty acid profile of the methyl esters. A high content of monounsaturated fatty acids (MUFAs), particularly C18:1, contributes to enhanced oxidative stability and an increased cetane number, both crucial for optimal biodiesel performance. For example, grape seeds, with their high MUFA content (72.19%), are expected to produce biodiesel with superior oxidative stability and a higher cetane number, making them an ideal feedstock for high-quality biodiesel production. Conversely, a high polyunsaturated fatty acid (PUFA) content, such as that found in melon seeds (87.65%), improves low-temperature fluidity but reduces oxidative stability, making these feedstocks more susceptible to degradation over time. While melon and other high-PUFA seeds may enhance biodiesel's cold-weather performance, their use may require antioxidant additives or blending with more stable feedstocks, such as those rich in MUFAs, to improve oxidative stability and overall fuel performance. The low saturated fatty acid (SFA) content in most of the seeds analyzed, particularly in apple seeds (0.67%), is consistent with biodiesel standards, as lower SFA content typically correlates with improved fuel properties, such as reduced cloud points and enhanced fuel flow characteristics. However, higher SFA levels, as seen in pear seeds (29.32%), could negatively affect biodiesel performance by increasing the cloud point and decreasing fuel flowability at lower temperatures.

Górnaś and Rudzińska [23] analyzed the fatty acid and phytosterol profiles of oils obtained from the seeds of nine species constituting by-products of the fruit and vegetable processing industry, including watermelon, melon, sea buckthorn, red currant, pomegranate, Japanese quince, grape, gooseberry, and apple. The oil yield varied markedly, ranging from 11.8% in sea buckthorn seeds to 28.5% in watermelon seeds, indicating substantial diversity in the potential of these raw materials. In all analyzed oils, β-sitosterol was the dominant phytosterol, with concentrations ranging from 0.5 to 3.1 mg g^{-1} of oil. Fatty acid profiles were species-specific, with linoleic acid predominating in most samples (38.0–70.7%). A distinctive feature of pomegranate seed oil was its exceptionally high punicic acid content (86.2%), which confers particularly high biological activity. Oil obtained

from Japanese quince seeds was identified as the most promising for biodiesel production due to a favourable balance of mono- and polyunsaturated fatty acids, supporting the formation of methyl esters with good oxidative stability. In contrast, pomegranate seed oil, owing to its unique bioactive lipid composition, was considered more suitable for cosmetic and pharmaceutical applications.

According to Muthai et al. [27], baobab seed oil contains 17–22% saturated fatty acids (SFAs), 32–38% monounsaturated fatty acids (MUFAs), and 22–26% polyunsaturated fatty acids (PUFAs). Palmitic acid (C16:0) was reported as the predominant SFA, while oleic acid (C18:1) and linoleic acid (C18:2) were the dominant MUFA and PUFA, respectively.

Ferreira et al. [28] identified grape pomace (72.7% PUFA), grape stems (42.5% PUFA), grape bunches (54.3% PUFA), and brewer's spent grain (59.0% PUFA) as the most promising agri-food by-products due to their high polyunsaturated fatty acid content. In contrast, white wine lees (74.1% SFA), red wine lees (50.8% SFA), and potato peels (77.2% SFA) were considered less favourable feedstocks because of the predominance of saturated fatty acids.

Table 5 presents the total contents of monounsaturated and polyunsaturated fatty acids, as well as the overall content of fatty acid methyl esters (FAMEs), in seeds derived from fruit and vegetable by-products. Considerable variability in lipid content was observed among the analyzed raw materials. The highest fat contents, expressed as FAME, were recorded for apple (664.57 mg g^{-1}dw), melon (407.02 mg g^{-1}dw), lemon (310.68 mg g^{-1}dw), and pumpkin (238.53 mg g^{-1}dw) seeds, whereas the lowest values were observed for apricot (1.23 mg g^{-1}dw) and pepper (3.99 mg g^{-1}dw) seeds, indicating limited oil potential for these by-products.

Table 5. Sum of mean FAMEs content ± standard deviation (SD) in fruit and vegetable waste seeds both with and without distinction for MUFAs, PUFAs, and SFAs.

Fruit and Vegetable Waste Seeds	∑MUFAs ± SD	∑PUFAs ± SD	∑SFAs ± SD	∑FAMEs ± SD
	[μg g^{-1}dw]			
Cherry	63,564.56 ± 12,743.95	131,476.33 ± 34,297.60	5116.55 ± 754.09	200,157.44 ± 51,634.37
Plum	35,700.10 ± 7842.85	40,480.64 ± 10,584.78	1990.80 ± 364.73	78,171.55 ± 17,129.05
Quince	48,397.54 ± 12,158.91	155,317.34 ± 40,609.62	5602.33 ± 1047.08	209,317.21 ± 62,961.94
Pumpkin	27,846.78 ± 4859.25	205,785.26 ± 54,002.67	4902.70 ± 628.63	238,534.77 ± 89,778.94
Peach	8437.88 ± 1504.01	10,569.41 ± 2750.77	2349.27 ± 391.52	21,356.56 ± 3483.06
Melon	40,078.41 ± 7297.40	356,759.20 ± 93,476.48	10,183.41 ± 1706.20	407,021.03 ± 156,806.75
Grape	5343.89 ± 905.56	843.56 ± 187.59	1214.97 ± 165.60	7402.43 ± 2039.58
Watermelon	60,329.60 ± 15,592.36	32,547.67 ± 7768.76	24,537.09 ± 4482.14	117,414.36 ± 15,337.35
Apricot	189.55 ± 37.89	835.46 ± 216.37	204.74 ± 14.86	1229.75 ± 300.97
Lemon	39,061.96 ± 5176.62	241,106.93 ± 66,992.26	30,510.95 ± 6265.53	310,679.84 ± 97,323.03
Avocado	8776.63 ± 1165.96	35,798.73 ± 8118.07	1585.70 ± 275.46	46,161.07 ± 14,728.79
Apple	119,743.56 ± 30,254.52	540,361.24 ± 151,625.38	4461.13 ± 535.10	664,565.94 ± 230,313.36
Pear	2714.91 ± 479.39	2644.41 ± 632.63	2223.41 ± 421.88	7582.72 ± 217.00
Pepper	1232.07 ± 200.85	1610.92 ± 408.90	1148.55 ± 233.81	3991.55 ± 201.19
Sweet cherry	21,632.42 ± 4978.58	17,753.98 ± 3859.32	3892.66 ± 592.54	43,279.06 ± 7614.88
Orange	2541.91 ± 430.38	4490.81 ± 1176.57	998.40 ± 164.11	8031.12 ± 1428.97

In most samples, polyunsaturated fatty acids constituted the dominant fraction, particularly in apple, melon, lemon, and pumpkin seeds, reflecting a high degree of lipid unsaturation and potentially elevated iodine values for oils derived from these materials. The MUFA content was generally lower; high MUFA proportions were observed in watermelon and grape seeds, while cherry seeds exhibited a moderate share. In contrast, melon and lemon seeds were characterised by low MUFA proportions. Notably, in watermelon and grape seeds, the MUFA fraction was comparable to or higher than the PUFA fraction, indicating a more oleic character of the lipids and potentially enhanced oxidative stability.

The FAME profile of cherry seed by-products was characterised by a high ratio of unsaturated to saturated fatty acids [29]. A similar pattern has been reported for by-products derived from herbal plants, in which the content of unsaturated fatty acid methyl esters exceeded that of saturated ones; linoleic acid was identified as the dominant PUFA, while palmitic acid remained the main SFA [17].

Cluster analysis based on the fatty acid methyl ester (FAME) composition of seeds derived from fruit and vegetable processing waste enabled the identification of four distinct clusters (A–D) (Figure 2). Cluster A, represented exclusively by avocado seeds, is characterised by a moderate proportion of monounsaturated fatty acids (MUFAs), a high content of polyunsaturated fatty acids (PUFAs), and a low share of saturated fatty acids (SFAs). The predominance of PUFAs in this cluster may positively influence fuel fluidity and calorific value; however, the oxidative stability of the resulting biodiesel may be limited due to the high degree of unsaturation.

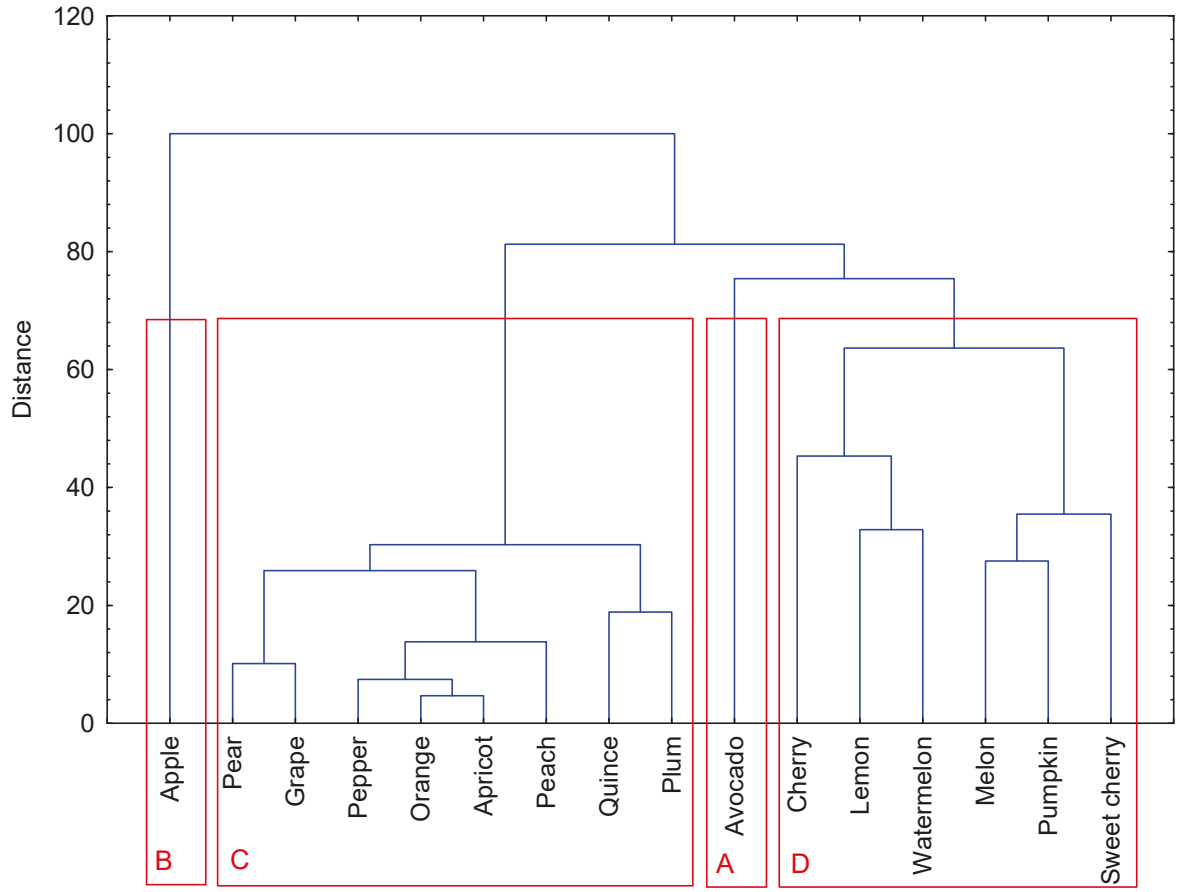


Figure 2. Dendrogram of the hierarchical cluster analysis of sixteen types of fruit and vegetable waste seeds showing four distinct clusters (A–D).

Cluster B, comprising apple seeds, is likewise dominated by polyunsaturated fatty acids. The MUFA fraction remains at a moderate level, whereas saturated fatty acids are nearly absent. This lipid profile ensures excellent cold-flow properties and a high energy value. Nevertheless, the very high PUFA content (>80%) indicates that biodiesel produced solely from these seeds would be highly susceptible to rapid oxidation. Therefore, blending with MUFA-rich oils is recommended to enhance oxidative stability and improve overall fuel performance.

Cluster C includes pear, grape, pepper, orange, apricot, peach, quince, and plum seeds and exhibits a more diversified fatty acid composition. The MUFA content in this group

ranges from 23.12% in quince seeds to 45.67% in plum seeds, while the PUFA content varies between 49.49% in peach seeds and 74.20% in quince seeds. The proportion of saturated fatty acids spans from a low level (2.55% in plum seeds) to a relatively high value (29.32% in pear seeds). The balanced fatty acid profile observed in this cluster provides a favourable compromise between oxidative stability, fluidity, and energy value, indicating that seeds within this group represent the most promising biocomponents for biodiesel production.

Cluster D, comprising cherry, lemon, watermelon, melon, pumpkin, and sweet cherry seeds, is characterised by a high proportion of polyunsaturated fatty acids, particularly in pumpkin (86.27%), melon (87.65%), and lemon (77.61%) seeds. The MUFA fraction is relatively low (e.g., 11.67% in pumpkin seeds and 9.85% in melon seeds), while saturated fatty acids account for only a minor share of the total composition, confirming the dominance of PUFAs in this cluster. Such a lipid profile favours the production of biodiesel with excellent cold-flow properties and low cloud and pour points. However, the high PUFA content is associated with reduced oxidative stability. Consequently, seeds from Cluster D are best utilised in blends with MUFA-rich oils to obtain a more oxidation-resistant and technologically stable biofuel component.

Cluster analysis, complemented by visualisation in the form of a heat map (Figure 3), enabled the grouping of seeds derived from the analyzed fruit and vegetable processing waste according to the contents of individual fatty acid methyl esters (FAMEs). The heat map revealed four principal clusters of samples, reflecting distinct fatty acid distribution patterns.

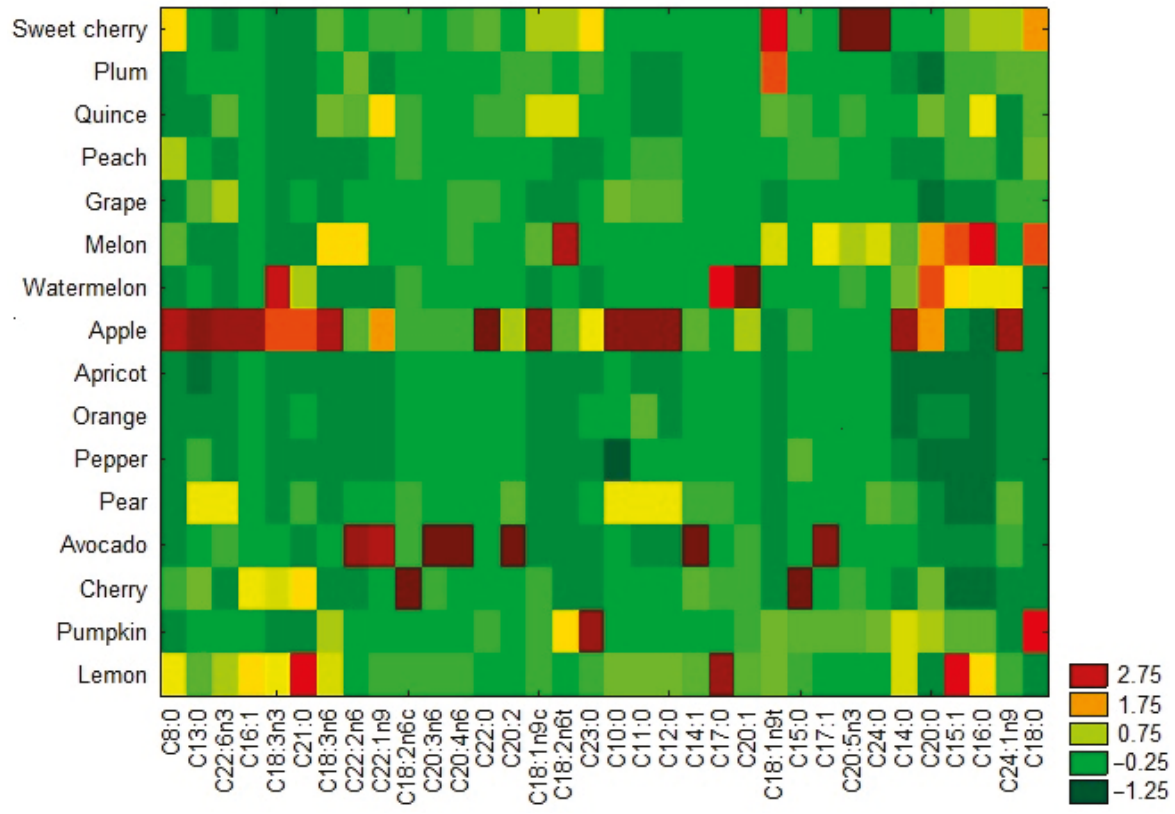


Figure 3. Graphical result of the simultaneous grouping of objects (tested fruit and vegetable waste seeds) and features (fatty acid methyl ester content). This plot shows how the samples group based on their fatty acid profiles, with clusters representing different seed types.

Avocado seeds formed a separate cluster owing to their highest concentrations of unsaturated fatty acids (indicated by red coloration), including cis-13,16-docosadienoic acid (C22:2n6), dihomo-γ-linolenic acid (C20:3n6), arachidonic acid (C20:4n6), and eicosadienoic

acid (C20:2), accompanied by relatively low levels of short-chain saturated fatty acids (C8:0–C12:0) (green coloration). This distinctive fatty acid profile explains their isolated position in the hierarchical structure.

Apple seeds constituted another distinct group, characterised by the predominance of unsaturated fatty acids, particularly oleic acid (C18:1n9c) and nervonic acid (C24:1n9), together with a low contribution of short-chain saturated fatty acids. The dominance of long-chain unsaturated compounds clearly differentiates this cluster from the remaining groups.

The third cluster comprised pear, grape, pepper, orange, apricot, peach, quince, and plum seeds, which exhibited moderate concentrations of saturated and monounsaturated fatty acids. A notable feature within this group was the pronounced presence of caprylic acid (C8:0) in peach seeds, alongside moderate levels of polyunsaturated fatty acids, such as linoleic acid (C18:2n6c) and linolenic acid (C18:3n3). The relatively balanced fatty acid distribution observed in this cluster supports its previously identified suitability for biodiesel production.

The fourth cluster included cherry, lemon, watermelon, melon, pumpkin, and sweet cherry seeds. These samples were characterised by relatively high contents of polyunsaturated fatty acids, particularly linoleic acid (C18:2n6c) and linolenic acid (C18:3n3), combined with low concentrations of saturated and monounsaturated fatty acids. The strong predominance of PUFAs explains their grouping and suggests favourable cold-flow properties of the derived biodiesel, albeit with potentially limited oxidative stability.

Overall, the heat map analysis confirms the differentiation observed in the cluster analysis and provides a comprehensive visualisation of the variability in FAME composition among seed fractions derived from fruit and vegetable processing residues.

Principal component analysis indicated that the first two principal axes jointly explained 52.86% of the total variability in the dataset (Factor 1: 33.06%; Factor 2: 19.80%) (Figure 4). Factor 1 represents the primary gradient in fatty acid composition, ranging from PUFA-dominated profiles to those relatively enriched in SFAs and MUFAs. Negative loadings along Factor 1 are therefore associated with a high degree of polyunsaturation, whereas positive loadings reflect a greater contribution of saturated and monounsaturated fatty acids. Factor 2 differentiates the samples according to the contribution of long-chain MUFAs and selected less abundant fractions (vectors located in the upper half-plane), in contrast to profiles more strongly associated with lower-carbon-number saturated fractions and/or n-6 and n-3 PUFAs (lower half-plane).

The spatial distribution of individual samples is consistent with this interpretation. Apple seeds are positioned on the negative side of Factor 1, reflecting their high PUFA content and low SFA contribution. Avocado seeds are distinctly shifted towards positive values of Factor 2, indicating a relatively higher contribution of long-chain MUFAs. Most of the remaining seeds, including pear, grape, pepper, orange, apricot, peach, quince, and plum, cluster near the origin of the coordinate system, suggesting a balanced distribution of SFAs, MUFAs, and PUFAs without a single dominant fraction.

In contrast, pumpkin, melon, watermelon, cherry, and sweet cherry seeds are located in the lower-right quadrant of the plot, indicating a moderate SFA contribution combined with a lower share of long-chain MUFAs along the Factor 2 dimension. From the perspective of their application as liquid biofuel components, the distribution of samples along Factor 1 confirms that PUFA-rich profiles (left side of the plot) favour improved fluidity and enhanced low-temperature properties, but may compromise oxidative stability. Conversely, profiles with higher MUFA and SFA contributions (right side of the plot) ensure greater oxidative resistance, albeit with slightly reduced fluidity.

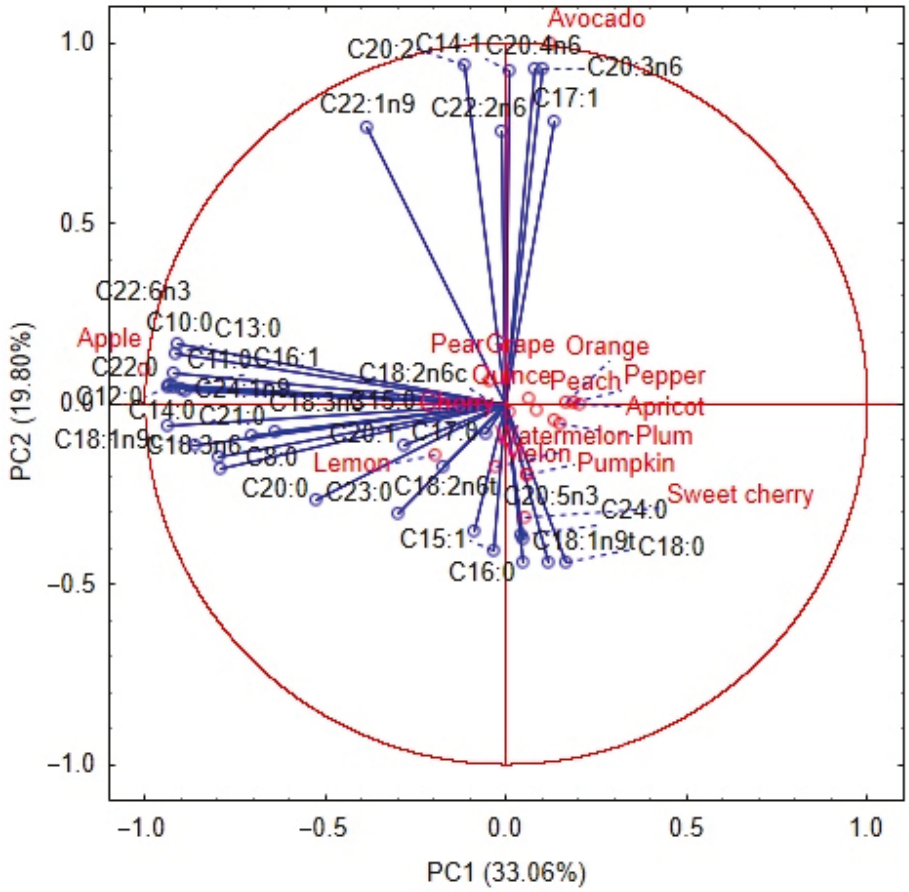


Figure 4. Biplot of fatty acid methyl ester (FAME) content for each repetition (n = 4) in sixteen types of fruit and vegetable waste seeds, showing the first two principal components (PC1 and PC2) of the PCA model that together explain 52.86% of the total variance, i.e., 33.06% and 19.80% for PC1 and PC2, respectively. Blue biplot vectors indicate the strength and direction of factor loadings for all analyzed FAME variables.

The position of avocado seeds along the positive direction of Factor 2 suggests their potential suitability as blending components due to their contribution of long-chain MUFAs. Meanwhile, the clustering of numerous seed types near the centre of the plot confirms their intermediate and balanced fatty acid composition, which is advantageous for the formulation of biodiesel fuels combining adequate stability with favourable performance characteristics.

Based on the calculated cetane number (CN) and its comparison with the requirements of ASTM D6751 (CN $\geq$ 47) [14] and BS EN 14214 (CN $\geq$ 51) [13], all analyzed feedstocks—except for cherry and watermelon seeds—may be considered suitable biocomponents for biodiesel production (Figure 5). The watermelon sample meets the standard requirements only at its nominal CN value; however, when model uncertainty is taken into account (CN_min), the value falls below the threshold of 51, classifying it as a borderline feedstock. Cherry seeds exhibit the lowest CN and do not meet the quality requirements for biodiesel.

Among the analyzed materials, grape seeds appear to be the most promising biodiesel biocomponent. They combine a favourable cetane number (CN $\approx$ 59.91) with a particularly advantageous fatty acid distribution, characterised by a very high MUFA content (72.19%), low PUFA content (11.40%), and a moderate SFA share (16.41%). Such proportions are beneficial for both ignition quality and oxidative stability, making this waste stream a highly promising candidate for fuel applications.

https://doi.org/10.3390/en19071685

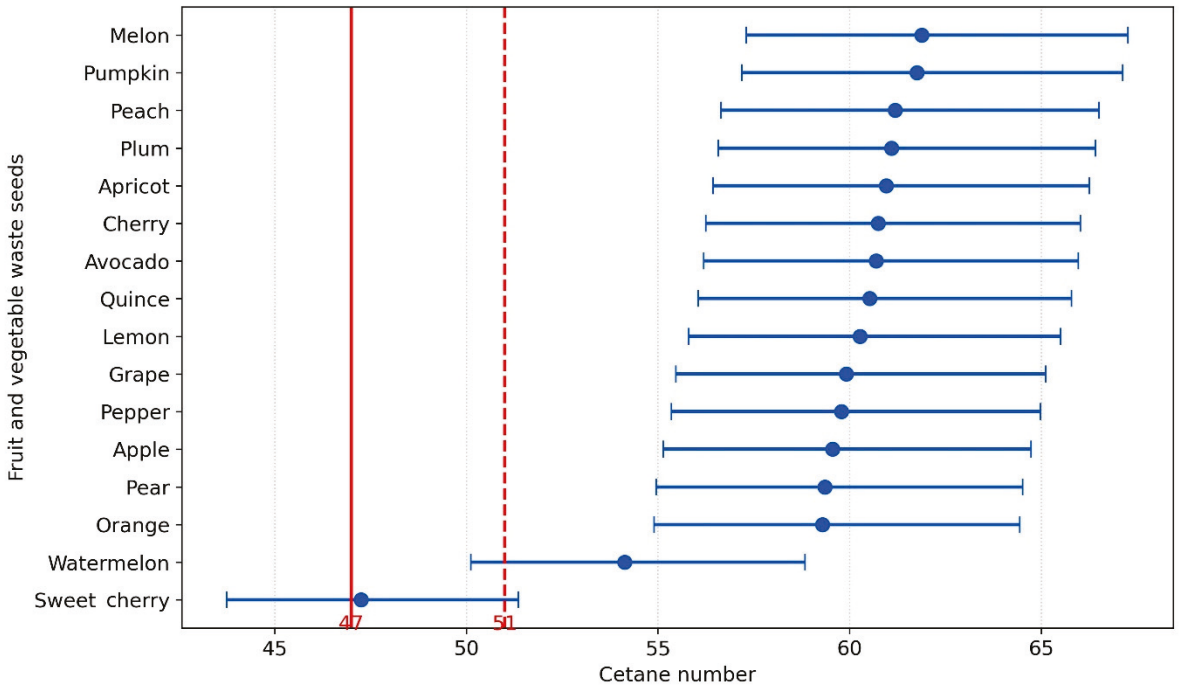


Figure 5. Predicted cetane number (CN) of fruit and vegetable waste seeds with minimum and maximum error ranges, for an assumed estimation error of 8%. The solid vertical line indicates CN = 47 (ASTM D6751 [14]), while the dashed line represents CN = 51 (BS EN 14214 standard [13]).

Plum and peach seeds also demonstrate considerable potential owing to their favourable CN values (61.10 and 61.18, respectively). However, their applicability may be constrained by a markedly higher PUFA content (51.78% and 49.49%, respectively). This elevated degree of polyunsaturation may reduce the oxidative stability of the resulting biodiesel, necessitating the use of stabilising additives or blending with MUFA-rich fractions to obtain a fuel that fully complies with quality standards.

4. Conclusions

This study demonstrates that seeds derived from fruit and vegetable processing waste possess fatty acid profiles suitable for biodiesel production. The wide variation in the content of monounsaturated fatty acids (MUFAs), polyunsaturated fatty acids (PUFAs), and saturated fatty acids (SFAs) indicates that these raw materials offer diverse feedstock options for biodiesel production. Specifically, the study identifies both monounsaturated-rich materials, similar to rapeseed oil, and polyunsaturated materials, comparable to sunflower oil, which can be strategically utilized depending on the desired biodiesel properties. The generally low SFA content in most seeds further enhances the low-temperature properties of the resulting methyl esters.

The physicochemical analysis of fruit seed oils highlighted grape seeds as the most promising raw material for biodiesel production, owing to their favorable cetane number and beneficial fatty acid composition, which ensures good ignition quality and oxidative stability. Other seeds, such as those from plum and peach, also show potential, but their higher PUFA content suggests that antioxidant additives or blending with MUFA-rich feedstocks may be necessary to mitigate potential oxidative stability issues.

The broader significance of these findings lies in their potential for contributing to the development of more sustainable and diverse feedstocks for biodiesel production. By utilizing food industry waste, this approach not only helps reduce environmental impact but also supports the circular economy by turning waste into a valuable resource.

Future research should focus on a comprehensive characterization of the physicochemical properties of FAME mixtures derived from these feedstocks, including acid value, carbon residue, cloud point, density, flash point, viscosity, and methanol content, and on their comparison with conventional petroleum diesel. Additionally, efforts should be directed toward developing efficient and scalable extraction methods that can be implemented at an industrial scale. This includes optimizing processes to reduce energy consumption, minimize waste, and lower production costs, which are crucial for the economic feasibility of using waste-derived feedstocks in biodiesel production. Furthermore, long-term stability studies are needed to evaluate the oxidative stability and storage conditions of biodiesel produced from these alternative feedstocks. It will also be important to understand how seasonal variations in raw material composition affect biodiesel performance, ensuring consistent fuel quality year-round. Lastly, future research should explore the potential for blending these FAME mixtures with conventional diesel to enhance fuel properties, particularly in terms of cold-weather performance and oxidative stability, thus broadening their practical applications in the transportation and energy sectors. Addressing these challenges will be pivotal for the large-scale adoption of biodiesel produced from fruit-vegetable food industry waste, contributing to a more sustainable and circular biofuels industry.

Author Contributions: Conceptualization, A.S.; data curation, A.S., A.P.-N., P.C. and M.K.-S.; formal analysis, A.S. and A.B.; investigation, M.K.-S., P.C. and M.K.; methodology, S.O., P.C., A.S. and A.P.-N.; resources, M.K. and A.B.; supervision, S.O. and A.S.; validation, S.O., A.P.-N., A.S., M.K.-S. and A.B.; visualization, A.S., M.K.-S. and P.C.; writing—original draft, M.K.-S., M.K. and P.C.; writing—review and editing, M.K.-S. and A.S. All authors have read and agreed to the published version of the manuscript.

Funding: The work was carried out as part of a team project no. WZ/WB-IIS/4/2026 and was financed by the Ministry of Science and Higher Education as part of a grant for maintaining research potential awarded to the Faculty of Civil Engineering and Environmental Sciences, Bialystok University of Technology.

Data Availability Statement: Data are contained within the article.

Conflicts of Interest: The authors declare no conflicts of interest.

References

1. Wang, W.; Liu, H.; Li, F.; Wang, H.; Ma, X.; Li, J.; Zhou, L.; Xiao, Q. Effects of Unsaturated Fatty Acid Methyl Esters on the Oxidation Stability of Biodiesel Determined by Gas Chromatography-Mass Spectrometry and Information Entropy Methods. *Renew. Energy* **2021**, *175*, 880–886. [CrossRef]
2. Atabani, A.E.; Silitonga, A.S.; Badruddin, I.A.; Mahlia, T.M.I.; Masjuki, H.H.; Mekhilef, S. A Comprehensive Review on Biodiesel as an Alternative Energy Resource and Its Characteristics. *Renew. Sustain. Energy Rev.* **2012**, *16*, 2070–2093. [CrossRef]
3. Karmee, S.K.; Lin, C.S.K. Valorisation of Food Waste to Biofuel: Current Trends and Technological Challenges. *Sustain. Chem. Process* **2014**, *2*, 22. [CrossRef]
4. Caldeira, C.; De Laurentiis, V.; Corrado, S.; van Holsteijn, F.; Sala, S. Quantification of Food Waste per Product Group along the Food Supply Chain in the European Union: A Mass Flow Analysis. *Resour. Conserv. Recycl.* **2019**, *149*, 479–488. [CrossRef]
5. Karmee, S.K.; Linardi, D.; Lee, J.; Lin, C.S.K. Conversion of Lipid from Food Waste to Biodiesel. *Waste Manag.* **2015**, *41*, 169–173. [CrossRef]
6. Sahar; Sadaf, S.; Iqbal, J.; Ullah, I.; Bhatti, H.N.; Nouren, S.; Rehman, H.U.; Nisar, J.; Iqbal, M. Biodiesel Production from Waste Cooking Oil: An Efficient Technique to Convert Waste into Biodiesel. *Sustain. Cities Soc.* **2018**, *41*, 220–226. [CrossRef]
7. Ruiz-Méndez, M.V.; Marmesat, S.; Liotta, A.; Dobarganes, M.C. Analysis of Used Frying Fats for Biodiesel Production. *Grasas Y Aceites* **2008**, *59*, 45–50. [CrossRef]
8. Abreu-Jaureguí, C.; Reynel-Ávila, H.E.; Bonilla-Petriciolet, A. Biodiesel Production from Wastewater Scum of Dairy Industry: Lipid Extraction Studies and Reaction Routes. *Fuel* **2023**, *342*, 127868. [CrossRef]
9. D'Ambrosio, V.; di Bitonto, L.; Angelini, A.; Gallipoli, A.; Braguglia, C.M.; Pastore, C. Lipid Extraction from Sewage Sludge Using Green Biosolvent for Sustainable Biodiesel Production. *J. Clean. Prod.* **2021**, *329*, 129643. [CrossRef]

10. Villalobos-Delgado, F.d.J.; Reynel-Avila, H.E.; Mendoza-Castillo, D.I.; Bonilla-Petriciolet, A. Lipid Extraction in the Primary Sludge Generated from Urban Wastewater Treatment: Characteristics and Seasonal Composition Analysis. *Water Sci. Technol.* **2023**, *87*, 2930–2943. [CrossRef]
11. Al Shehhi, A.; Souissi, Y.; Nair, A.S.; Usmani, Z.; Sharma, M.; Sivakumar, N. Microbial Lipid-Based Biodiesel Production Using Wastewater: Opportunities and Challenges. *Bioresour. Bioprocess.* **2025**, *12*, 70. [CrossRef]
12. Chen, N.; Xie, Y.; Liang, Z.; Shim, H. Biodiesel Production and Properties Estimation from Food Waste and Domestic Wastewater by *Rhodosporidium toruloides*. *J. Environ. Manag.* **2023**, *348*, 119368. [CrossRef] [PubMed]
13. *BS EN 14214:2012+A2:2019*; Liquid Petroleum Products—Fatty Acid Methyl Esters (FAME) for Use in Diesel Engines and Heating Applications—Requirements and Test Methods. BSI Group: London, UK, 2019.
14. *ASTM D6751–20*; Standard Specification for Biodiesel Fuel Blend Stock (B100) for Middle Distillate Fuels. ASTM International: West Conshohocken, PA, USA, 2020.
15. Vasistha, S.; Balakrishnan, D.; Manivannan, A.; Rai, M.P. Microalgae on Distillery Wastewater Treatment for Improved Biodiesel Production and Cellulose Nanofiber Synthesis: A Sustainable Biorefinery Approach. *Chemosphere* **2023**, *315*, 137666. [CrossRef] [PubMed]
16. Ghaly, A.; Dave, D.; Brooks, M.; Budge, S. Production of Biodiesel by Enzymatic Transesterification: Review. *Am. J. Biochem. Biotechnol.* **2010**, *6*, 54–76. [CrossRef]
17. Sienkiewicz, A.; Piotrowska-Niczyporuk, A.; Bajguz, A. Fatty Acid Methyl Esters from the Herbal Industry Wastes as a Potential Feedstock for Biodiesel Production. *Energies* **2020**, *13*, 3702. [CrossRef]
18. Mukherjee, J.; Gupta, M.N. Biocatalysis for Biomass Valorization. *Sustain. Chem. Process* **2015**, *3*, 7. [CrossRef]
19. Dhiman, S.; Mukherjee, G. Utilization of Food Waste for Biofuel Production: A Biorefining Perspective. *Mater. Today Proc.* 2022, *in press*. [CrossRef]
20. Zielińska, M.; Bułkowska, K. Agricultural Wastes and Their By-Products for the Energy Market. *Energies* **2024**, *17*, 2099. [CrossRef]
21. Palm, M.O.; Pavani, L.Y.; Senff, L.; Duarte, D.A.; Catapan, R.C. A Novel Liquid-Phase Plasma Discharge Process for Single-Step Emulsification and Continuous Biodiesel Production. *Fuel* **2025**, *400*, 135686. [CrossRef]
22. Salam, R.; Bibi, T.; Lal, T. Biodiesel production from Citrullus lanatus and Cucumis melo seed oil blends: A sustainable alternative feedstock. *Spectr. Eng. Sci.* **2025**, *3*, 981–991.
23. Górnaś, P.; Rudzińska, M. Seeds Recovered from Industry By-Products of Nine Fruit Species with a High Potential Utility as a Source of Unconventional Oil for Biodiesel and Cosmetic and Pharmaceutical Sectors. *Ind. Crops Prod.* **2016**, *83*, 329–338. [CrossRef]
24. Gopinath, A.; Puhan, S.; Nagarajan, G. Relating the Cetane Number of Biodiesel Fuels to Their Fatty Acid Composition: A Critical Study. *Proc. Inst. Mech. Eng. Part. D J. Automob. Eng.* **2009**, *223*, 565–583. [CrossRef]
25. Sacha, D. Wpływ dodatków antyoksydacyjnych na stabilność paliw do silników ZS poddanych działaniu miedzi. *Naft.-Gaz* **2020**, *nr 6*, 419–426. [CrossRef]
26. Pobłocki, K.; Walczak, J.; Drzeżdżon, J.; Jacewicz, D. Katalizatory Wykorzystywane w Syntezie Biodiesla. *Wiadomości Chem.* **2022**, *76*, 129–144. [CrossRef]
27. Muthai, U.K.; Indieka, A.S.; Muchugi, A.; Karori, S.M.; Mng'omba, S.; Ky-Dembele, C.; Jamnadass, R. Quantitative Variation of Fatty Acid Composition in Seed Oil from Baobab (*Adansonia digitata* L.) Wild Populations in Sub-Sahara Africa. *S. Afr. J. Bot.* **2019**, *123*, 1–8. [CrossRef]
28. Ferreira, R.; Lourenço, S.; Lopes, A.; Andrade, C.; Câmara, J.S.; Castilho, P.; Perestrelo, R. Evaluation of Fatty Acids Profile as a Useful Tool towards Valorization of By-Products of Agri-Food Industry. *Foods* **2021**, *10*, 2867. [CrossRef]
29. Kniepkamp, K.; Errico, M.; Yu, M.; Roda-Serrat, M.C.; Eilers, J.-G.; Wark, M.; van Haren, R. Lipid Extraction of High-Moisture Sour Cherry (*Prunus cerasus* L.) Stones by Supercritical Carbon Dioxide. *J. Chem. Technol. Biotechnol.* **2024**, *99*, 810–819. [CrossRef]

Disclaimer/Publisher's Note: The statements, opinions and data contained in all publications are solely those of the individual author(s) and contributor(s) and not of MDPI and/or the editor(s). MDPI and/or the editor(s) disclaim responsibility for any injury to people or property resulting from any ideas, methods, instructions or products referred to in the content.

energies

MDPI

Article

The Effect of Cherry Stone Addition to Sawdust on the Pelletization Process and Fuel Pellet Quality

Sławomir Obidziński [1], Paweł Cwalina [1], Małgorzata Kowczyk-Sadowy [1,*], Aneta Sienkiewicz [1], Jacek Mazur [2] and Paweł Braun [3]

[1] Department of Agri-Food Engineering and Environmental Management, Bialystok University of Technology, Wiejska 45E, 15-351 Białystok, Poland; s.obidzinski@pb.edu.pl (S.O.); p.cwalina@pb.edu.pl (P.C.); a.sienkiewicz@pb.edu.pl (A.S.)
[2] Department of Food Engineering and Machines, University of Life Sciences in Lublin, Głębocka 28, 20-612 Lublin, Poland; jacek.mazur@up.lublin.pl
[3] DAK-POL Sp. z o.o., Tartaczna 7, 16-020 Czarna Białostocka, Poland; dak-pol@dak-pol.pl
* Correspondence: m.kowczyk@pb.edu.pl

Abstract

This study presents the results of research on the pelleting process of pine sawdust with the addition of cherry stone waste, which was carried out using a flat-die pellet press in the context of fuel pellet production. The findings indicate that increasing the proportion of crushed cherry stones in the sawdust mixture from 10% to 20% reduced the pelletizer's power demand by approximately 14% (from 3.35 to 2.86 kW) and by around 24% (from 3.79 to 2.86 kW), compared with the compaction of sawdust alone. The incorporation of 10% crushed cherry stone waste into pine sawdust slightly improved the kinetic strength of the pellets, increasing it by about 2% (from 94.6 to 96.60%). However, raising the cherry stone content further to 20% resulted in a moderate decrease in kinetic strength, by approximately 5% (from 96.60 to 91.37%). A similar trend was observed for pellet density: the addition of cherry stones (10–20%) slightly reduced the density by about 5.5% (from 1312.02 to 1241.65 kg·m^{-3}), accompanied by a small decrease in bulk density. This study also confirmed the high calorific potential of crushed cherry stones, with a heat of combustion of 24.418 MJ·kg^{-1} (dry basis) and a net calorific value of 22.326 MJ·kg^{-1}. Their incorporation at levels of 10–20% into sawdust mixtures increased the heat of combustion of the pellets by 0.42–0.84% (from 19.959 MJ·kg^{-1} for sawdust alone at 15% moisture content to 20.042 MJ·kg^{-1} with a 10% addition and 20.126 MJ·kg^{-1} with a 20% addition). Moreover, the inclusion of cherry stone waste in the mixture had a beneficial effect on combustion performance, lowering emissions of harmful compounds such as CO, NO, and SO_2, due to the higher combustion temperature achieved. Consequently, the use of cherry stone waste as an additive to sawdust not only enhances the energetic and environmental performance of pellets but also provides an effective pathway for the management of large quantities of fruit industry residues.

Keywords: fuel pellets; sawdust; waste; cherry stones

1. Introduction

The obligation to support the development of renewable energy sources results from the provisions of EU directives, including Directive 2023/2413 (RED III) on the promotion of electricity produced from renewable sources in the internal electricity market [1]. Pursuant to the Directive, Member States are required to increase the share of renewable energy

sources in final energy consumption to at least 42.5% by 2030, with an additional indicative target of 45%. This Directive also introduces new targets for individual economic sectors in terms of obtaining energy from renewable sources. In Poland, the use of waste for the production of energy from renewable sources is regulated primarily by the Act of 20 February 2015 on renewable energy sources (Journal of Laws 2024, item 1361) [2], which defines plant and animal waste from all industrial sectors, including the agri-food industry, as biomass, which can be used as fuel for the production of electricity, heat or biogas/biomethane.

According to Bioenergy Europe, domestic pellet production in the European Union (EU27) increased from 19.83 million tons in 2021 to over 20.5 million tons in 2022 [3]. Despite numerous challenges, including a reduction in heating demand due to climate change, Europe remains the world's largest region producing and using wood pellets. Currently, over 80% of the raw materials used in European pellets are sawmill residues, including sawdust and shavings. It is becoming necessary to use other plant materials to maintain the economic attractiveness of this fuel and meet the growing demand. In addition to wood waste, other waste materials are increasingly being used in pellet production, including fruit and vegetable industry waste, which, according to Żary-Sikorska [4], is generated in Poland annually at approximately 10 million tons. These wastes come mainly from the processing of potatoes, apples, and sugar beets. Flejszman et al. [5] assumed that at least 20% to 50% of the plant raw material entering production processes becomes waste, which should then be managed. Waste from the fruit and vegetable industry is used, among others, to produce biogas and high-quality biofertilizers, compost, biopolymers, biodegradable packaging, and bioactive compounds [6–9].

One method of managing waste is to process it through pressure agglomeration (pelletization, densification) into pellets or briquettes [10–13]. Waste pelletization facilitates transport and storage of the material by increasing its bulk density. This process also allows for the use of the obtained fuel in installations with an automatic feeding system. Furthermore, densification enables the development of a product composed of two or more components, providing considerable flexibility in shaping the properties of the final fuel [14].

Arulprakasajothi et al. [10] conducted research on the production of pellets from biomass derived from fruit and vegetable market waste. The obtained pellets meet ecological fuel standards in terms of both physicochemical properties and energy suitability. Additionally, lower pellet production costs provide a potential and environmentally friendly fuel for energy generation. In a study conducted by Gholami Banadkoki et al. [15], pelletization of leaves from six vegetable crops, including tomatoes, eggplants, zucchini, cucumbers, corn, and soybeans, was investigated to assess their potential as bioenergy raw materials. The physicochemical properties of these biomasses, such as particle size and shape, lignin content, and elemental composition, were examined to assess their effect on pellet density and strength [15]. Obidziński et al. [14] assessed the effect of adding potato pulp to pine sawdust on the pelletization process and the properties of the obtained fuel pellets, taking into account both laboratory and industrial tests. It was found that potato pulp acts as a natural binder, improving the pelletization process (lower energy, higher strength). Chojnacki et al. [16], producing pellets from post-industrial waste generated during the production of apple, carrot, and beetroot juice, noted the effect of these wastes on the pellet mass density, pellet hardness, ash content and calorific value. Additionally, they found that higher proportions of additives and higher moisture content in the raw materials influenced the hardness and density of the obtained pellet. Hejft et al. [17] presented the results of research on the pelletization process of oat bran and apple pomace. The study determined a significant effect of the apple pomace content (10%, 15%, and 20%)

in the mixture with oat bran and the effect of the pomace type on the energy consumption of the device and the kinetic stability of the obtained pellets. In turn, Kraiem et al. [18] conducted experiments on the densification and combustion of pellets from sawdust with the addition of tomato and grape marl production residues (in a 1:1 ratio). They observed a high calorific value of this fuel and increased NO_x and SO_x emissions for the combustion technology used. Kang et al. [19] investigated characteristics of spent coffee ground as a fuel and combustion characteristics in a small boiler system, such as CO, NO_x, O_2 and heating characteristics of heating boiler. The high quality of coffee grounds as a fuel is also confirmed by Allesina et al. [20], giving a high heating value.

Poland is a leading cherry producer in the European Union. According to Nowicka et al. [21], on average 70% of the domestic cherry harvest goes to processing plants, where it is used to produce frozen foods, concentrates, juices, nectars, jams, preserves, and alcoholic beverages. Considering that cherry stones constitute from 8% to 15% of the total fruit weight, depending on the variety [22], tens of thousands of tons of this type of waste are generated worldwide each year, which is currently used to a small extent. Cherry stones are extensively studied, among other things, as a raw material for construction materials [23] and filtration materials [24,25], as well as an antioxidant product that can be used in healthcare, cosmetics, and packaging applications [26]. Kniepkamp et al. [27] showed that cherry stone waste could also serve as feedstock for lipid extraction. This paper presents the results of an assessment of the potential of agri-food waste, specifically cherry stones, as raw material for the production of high-quality wood pellets. The aim of the study was to assess the impact of varying the proportion of cherry stones on the pressure agglomeration process of pine sawdust and on the quality of the resulting pellets. This work is innovative because, for the first time, it allows for the determination of the optimal cherry stones content in solid biofuels produced from wood waste, taking into account the preservation of their physical (mechanical) and energy properties, while also potentially reducing the costs of electricity generation.

2. Materials and Methods

2.1. Materials

The primary raw material used in this study consisted of former production residues (sawdust, shavings, and cuttings) obtained from the "DAK-POL" plant company and crushed cherry stones supplied by C.K. Frost Sp. z o.o. (Śmiłowice, Poland) (Figure 1).



(**a**) (**b**)

Figure 1. *Cont.*



(**c**) (**d**)

Figure 1. Raw material: (**a**) sawdust sample, (**b**) bag of sawdust, (**c**) uncrushed cherry stones and (**d**) crushed cheery stones.

2.2. Moisture of the Tested Raw Materials

The moisture content of the raw materials—sawdust and mixtures of sawdust with crushed cherry stones—was determined prior to the densification process in accordance with the PN-EN ISO 18134-3:2023-12 standard [28]. Measurements were carried out using an AXIS ASG laboratory moisture analyzer (AXIS, Gdańsk, Poland).

2.3. Granulometric Distribution of Tested Raw Materials

The granulometric distribution of the raw materials (sawdust and crushed cherry stones) was analyzed using a Multiserv Morek LPz-2e programmable sieve shaker equipped with a set of sieves (Multiserv Morek, Marcyporęba, Poland), in accordance with the PN-R-64798:2009 standard [29]. A series of nine sieves with square mesh sizes of 8.0, 4.0, 2.0, 1.0, 0.5, 0.25, 0.125, and 0.063 mm was employed.

2.4. Elementary Composition Analysis of Raw Materials

The elemental composition of the waste materials was determined using a CHN628 analyzer (St. Joseph, MI, USA). The carbon and hydrogen contents in dry biomass were measured by high-temperature combustion with infrared (IR) detection, while nitrogen was quantified using the katharometric method, in accordance with PN-EN ISO 16948:2015-07 standard [30], based on a 0.1 g sample. Sulfur content was determined by high-temperature combustion with IR detection according to PN-EN ISO 16994:2016-10 standard [31], using a 0.3 g sample. The instrument operates on a combustion principle and reports results in weight percent or parts per million (ppm).

2.5. Density and Bulk Density of the Tested Raw Materials and Pellets

The density of the pellets was determined 24 h after removal from the compaction chamber. For this purpose, the height and diameter of 15 randomly selected pellets were measured using a caliper with an accuracy of ± 0.02 mm, while their mass was determined with an OHAUS AX324M laboratory balance (OHAUS Europe GmbH, Nanikon, Switzerland) with an accuracy of ± 0.0001 g. Pellet density was calculated as the ratio of mass to volume.

The bulk density of sawdust, crushed cherry stones, and pellets was determined using a metal cylinder with a volume of 407.5 cm^3, a laboratory balance (AX324M, OHAUS Europe GmbH, Nanikon, Switzerland), and a steel scraper. The procedure was carried out in accordance with the PN-EN ISO 17830:2016-07 standard [32].

2.6. Pelleting Process of Sawdust and Crushed Cherry Stones

Following the determination of the physicochemical properties, mixtures of sawdust and crushed cherry stones were prepared, containing 10%, 15%, and 20% cherry stone content. After adjusting the moisture content to 16%, the mixtures were placed in sealed containers and stored for 24 h to prevent water evaporation.

Pelletization was carried out using an SS-4 system with a P-300 pelletizer (Protechnika, Łuków, Poland), equipped with a Y132M electric motor (7.5 kW, 1440 rpm) and roller compactors, according to the methodology described in previous authors study [33].

The pelleting system was fitted with a flat die with 6 mm diameter holes and a working gap of 0.4 mm between the rollers and the die socket. The pellets obtained were cooled under ambient conditions for 24 h before further testing. The tests were carried out at a rotational speed of the compaction roller system of 270 rpm and a mass flow rate of the raw material through the working system of 50 $kg \cdot h^{-1}$.

2.7. Kinetic Strength of Pellets

Twenty-four hours after exiting the pelletizing system, the kinetic strength (durability) of the pellets was determined using a Holmen tester. The tests were carried out in accordance with PN-EN ISO 17831-1:2016-02 standard [34] and following the methodology described in previous study [33]. In the Holmen method, a 100 g pellet sample is introduced into the test chamber, where it is set in motion by an air stream, causing circulation within the chamber and repeated collisions with the perforated metal walls of the tester. The pellets remained in the test chamber for 60 s. After this period, the remaining material was collected, sieved, and weighed. The kinetic durability was calculated as the ratio of pellet mass after the test to the initial sample mass.

2.8. Calorific Value and Heat of Combustion

The calorific value and heat of combustion of the raw materials were determined in accordance with PN–EN ISO 1928:2002 standard [35] and following the methodology described in previous authors work [33], using a KL–12M calorimeter (PRECYZJA-BIT, Bydgoszcz, Poland). The calorific value (Q^a_s), taking into account the contents of volatile matter, moisture, ash, and sulfur entered into the calorimeter's software.

2.9. Combustion Tests of Produced Pellets

Combustion tests were performed using a 10 kW automatic-feed boiler designed for wood pellets and equipped with a refractory steel retort burner with multi-level air inlets to improve combustion efficiency. The fuel was transported from the hopper to the burner by a screw feeder, while the flue gases passed through a heat exchanger to the chimney, assisted by a fan supplying combustion air. The boiler controller automatically adjusted the fuel and air supply based on oxygen concentration measurements obtained from a lambda probe.

The tests were conducted under nominal operating conditions following a one-hour preheating period. The flue gas composition at the boiler outlet was measured using a SIEMENS analyzer system: ULTRAMAT 23 (for CO, CO_2, SO_2, NO, NO_2, and HCl, by the IR reference method) and OXYMAT 5 (for O_2, paramagnetic reference method, 0–25% range). Continuous sampling was performed using a heated probe with a ceramic filter, a heated hose, and a gas conditioning unit.

Additional tests were carried out in a 5th-class retort grate boiler under manual control, where both pellets and cherry stones were combusted. The fuel feed rate was maintained at 2.0 $kg \cdot h^{-1}$, with constant airflow to the combustion chamber. The boiler water temperature

was kept within the range of 65–70 °C, in accordance with standard biomass combustion testing procedures.

The concentrations of the analyzed flue gas components (CO_2, CO, NO, SO_2, and HCl) were normalized to 10% oxygen (O_2) content using Equation (1) [33]:

$$Z_{s2} = \frac{21 - O_2'}{(21 - O_2'')} \cdot Z_{s1} \ [\%, \ \mathrm{mg \cdot m^{-3}}] \quad (1)$$

where

Z_{s1}—actual content of the chemical compound in the exhaust gas [%, mg·m^{-3}],

Z_{s2}—content of the chemical compound in the exhaust gas for a given oxygen content [%, mg·m^{-3}],

O_2'—set oxygen content in the exhaust gas [%],

O_2''—actual oxygen content in the exhaust gas [%].

2.10. Statistical Analysis

The results of the raw material tests are presented as mean values with standard deviations, calculated from five replicates. The Shapiro–Wilk test was applied to verify the normality of data distribution, and all analyzed variables met the assumption of normality. Pearson correlation coefficients were then calculated for the entire dataset to identify relationships among the analyzed variables. Statistical significance was assumed at $p < 0.05$. The results are presented in the form of a correlation matrix and a principal component analysis (PCA) plot. Correlation coefficients greater than 0.8 or lower than −0.8 were considered strong correlations.

Additionally, the sum of the absolute values of the correlation coefficients was calculated to provide an aggregated measure of the overall influence of each variable on the others in the dataset. PCA was performed to model the relationships among variables, and the final biplot was constructed based on two principal components (PC1 and PC2), which together explained 99.0% of the total variance. All statistical analyses and visualizations were carried out using Statistica 13.3 software (TIBCO Software Inc., Palo Alto, CA, USA).

3. Results and Discussion

3.1. Moisture of the Tested Raw Materials

Table 1 presents the moisture content of pine sawdust and cherry stones, determined using an AXIS ASG laboratory moisture analyzer.

Table 1. Results of moisture determination for raw materials designated for pelleting process.

Raw Material	Moisture ± SD [%]
Cherry stones	4.32 ± 0.09
Pine sawdust	8.35 ± 0.10

The average moisture content of cherry stones was approximately 4.3%, while pine sawdust exhibited an average moisture content of about 8.4%. From the perspective of the pelletization process, the moisture content of sawdust was too low. Therefore, additional water or another moisture-enhancing component is required when processing sawdust of such low humidity. The inclusion of crushed cherry stones did not increase the overall moisture content of the mixture, indicating the necessity of external supplementation with water or another component that raises the moisture level.

According to Serrano et al. [36], the optimal initial moisture content for pellet production from barley straw should be in the range of 19–23%, while the recommended value after pelletization is 6–8%.

Jiang et al. [37] investigated the effect of moisture content on pellet formation and properties using three different biomass types (pine sawdust, corn straw, and peanut shell). They found optimal values of 12% for both pine sawdust and corn straw, and 14% for peanut shells.

Similarly, Matkowski et al. [38], studying pelletization of wheat straw and its mixtures with cassava starch or calcium carbonate (using a flat die with an open chamber and 8 mm opening diameter), reported that the highest single-pellet density was achieved at a mixture moisture content of 23% (w.b.).

3.2. Granulometric Distribution of Tested Raw Materials

The granulometric distribution of sawdust and cherry stones particles obtained from sieve analysis is presented in Figure 2. The dominant fraction in the sawdust was 0.50 mm, accounting for 30.64% of the total. Slightly lower proportions were observed for the 1.00 mm (26.47%), 0.25 mm (17.35%), and 2.00 mm (11.11%) fractions. The smallest proportion, 0.09%, corresponded to the undersized fraction below 0.063 mm.

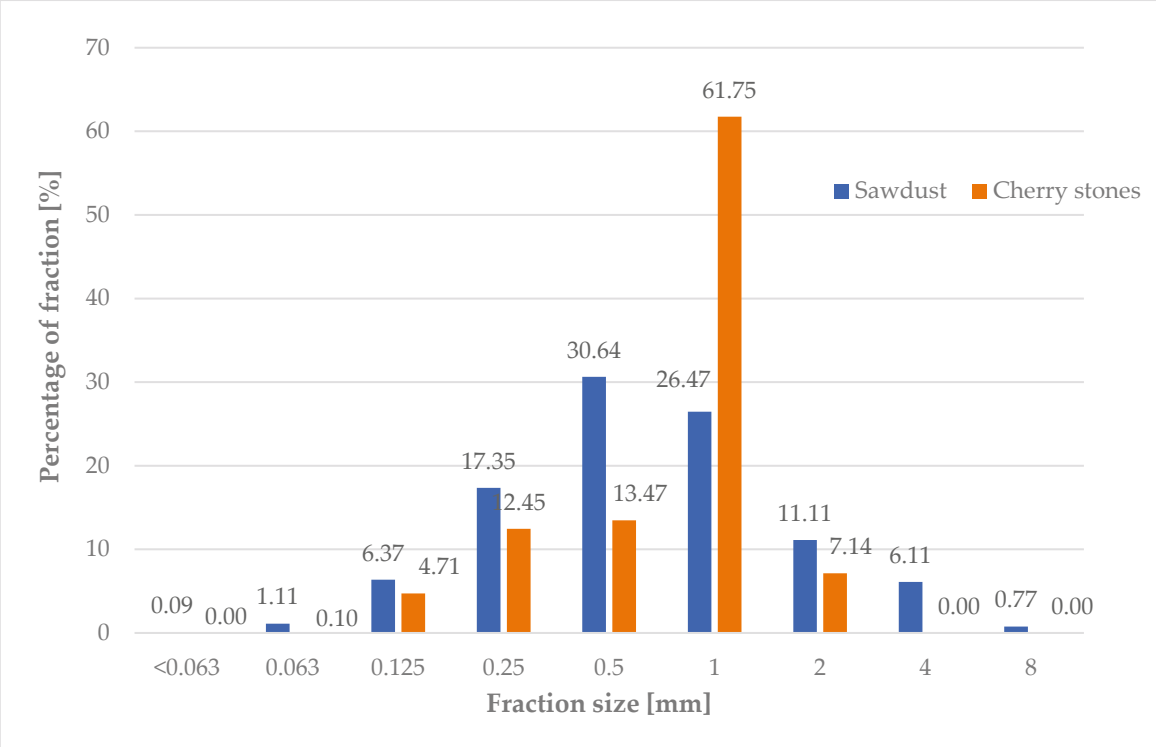


Figure 2. Granulometric distribution of sawdust and cherry stones particles subjected to sieve analysis.

The predominant fraction in the cherry stones was 1.00 mm, which represented 61.75%. Smaller contributions were recorded for the 0.50 mm (13.47%), 0.25 mm (12.45%), 2.00 mm (7.14%), and 0.125 mm (4.71%) fractions. The smallest fraction, 0.1%, was observed at 0.063 mm. Owing to the oil content of cherry stones, clogging of the analyzer sieves was observed, which prevented the detection of undersized particles smaller than 0.063 mm. Figure 3 illustrates the morphology of the individual sawdust fractions, while Figure 4 presents the morphology of the respective crushed cherry stone fractions after sieve analysis.

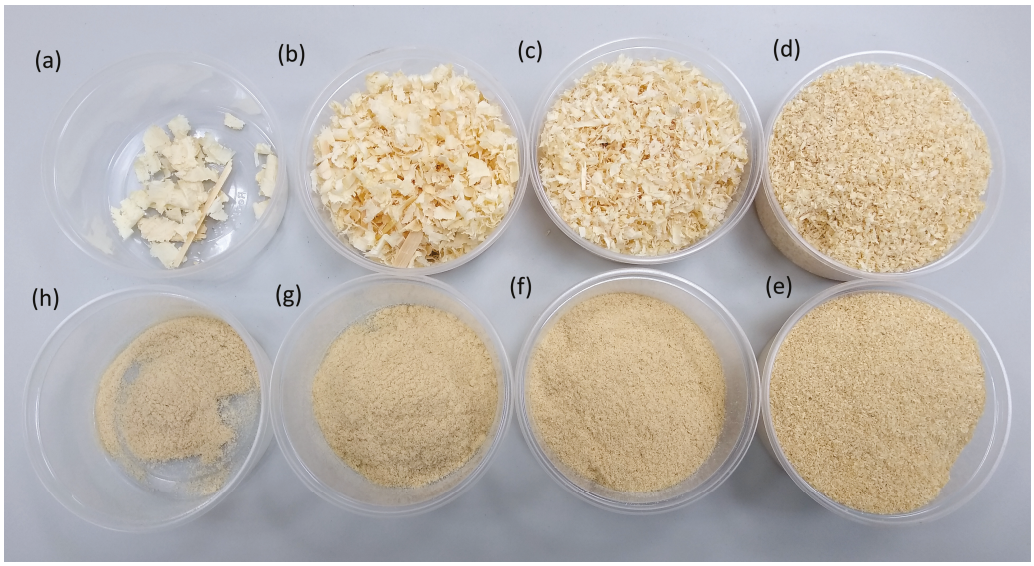


Figure 3. Individual sawdust fractions subjected to sieve analysis (**a**) >8 mm, (**b**) 4 mm, (**c**) 2 mm, (**d**) 1 mm, (**e**) 0.500 mm, (**f**) 0.250 mm, (**g**) 0.125 mm, (**h**) 0.063 mm.

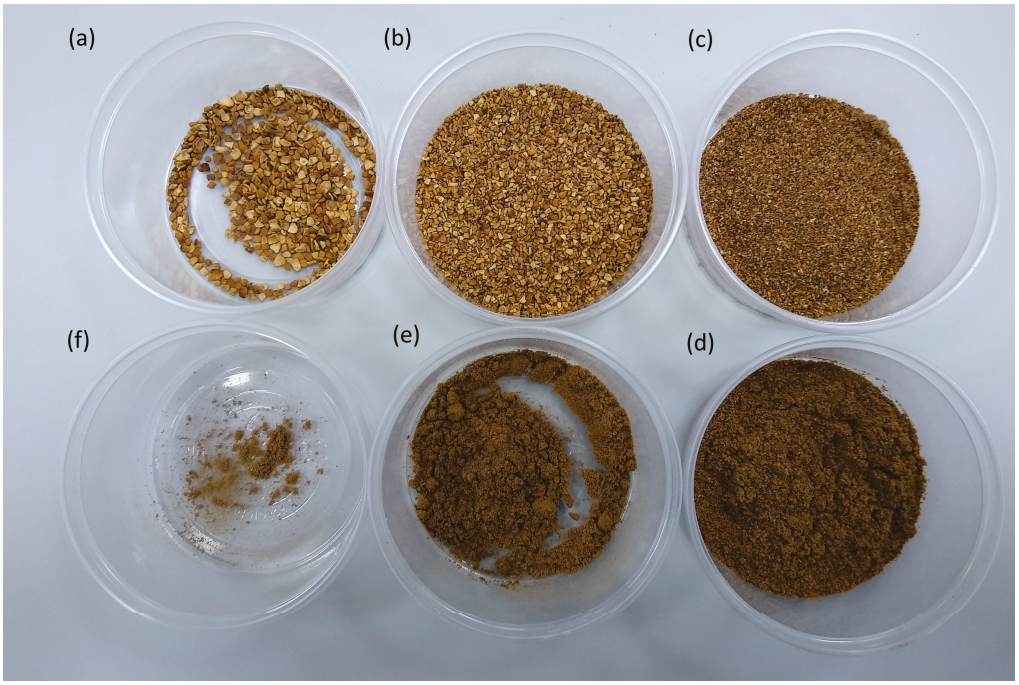


Figure 4. Individual fractions of crushed cherry stones subjected to sieve analysis (**a**) 2 mm, (**b**) 1 mm, (**c**) 0.500 mm, (**d**) 0.250 mm, (**e**) 0.125 mm, (**f**) 0.063 mm.

3.3. Elementary Composition Analysis of Raw Materials

The results of the elemental composition analysis of sawdust and crushed cherry stones are summarized in Table 2.

Table 2. Elementary composition of raw materials.

Raw Material	C ± SD [%]	H ± SD [%]	N ± SD [%]	S ± SD [%]	O* [%]	Cl [%]	Ash [%]
Cherry stones	52.51 ± 0.05	6.48 ± 0.02	1.31 ± 0.001	0.105 ± 0.001	38.20	0.001	1.40 ± 0.001
Pine sawdust	48.86 ± 0.05	6.65 ± 0.01	0.135 ± 0.001	0.024 ± 0.001	44.24	0.004	0.89 ± 0.02

O*—calculated by difference.

The conducted research revealed that sawdust contains 48.86% carbon, while crushed cherry stones contain a slightly higher amount—52.51%. Cherry stones, on the other hand, have a slightly lower hydrogen content (6.48%) compared to sawdust—6.65%. In terms of nitrogen content, sawdust contains 0.135% nitrogen, while crushed cherry stones contain a slightly higher amount—1.31%.

According to Piskowska-Wasiak [39], nitrogen in biomass is primarily associated with proteins, DNA, RNA, chlorophyll, alkaloids, and porphyrins. Its presence in thermally processed biomass is undesirable due to the potential formation of nitrogen oxides (NO_x).

Most standards for wood pellets [40,41] require pellets to contain less than 0.3% nitrogen. The EN Plus A2 certificate (PN-EN ISO 17225-2:2021-10 standard [42]) allows for a maximum of 0.5%, whereas the EN Plus B certificate permits up to 1.0%. Therefore, pellets produced with up to 20% cherry stones comply with the EN Plus B requirements. Sulfur content was also higher in cherry stones (0.105%) than in sawdust (0.024%). According to the ÖNORM M7135 standard [40], the sulfur content in wood pellets should not exceed 0.04%. As noted by Obernberger [43], a sulfur content exceeding 0.2% may significantly increase SO_x emissions. Nevertheless, sulfur in biomass can have a positive effect by mitigating the risk of chloride-induced corrosion, as chloride ions in alkali chlorides (NaCl and KCl) may be converted into more stable sulfates [44]. Hardy et al. [45] report that the risk of chloride corrosion is negligible if chlorine content in biomass does not exceed 0.02%.

3.4. Bulk Density of the Tested Raw Materials

Table 3 presents the bulk density results of sawdust and cherry stones.

Table 3. Results of bulk density tests of sawdust and cherry stones.

Raw Material	Bulk Density ± SD [kg·m^{-3}]
Pine sawdust	100.08 ± 4.48
Cherry stones	561.02 ± 3.01

Sawdust exhibited a relatively low bulk density of approximately 100 kg·m^{-3}, whereas cherry stones showed a significantly higher value of about 561 kg·m^{-3}. For comparison, Stasiak et al. [46] reported a bulk density of 143 kg·m^{-3} for sawdust at 10% moisture content, while Netinger Grubeša et al. [47] recorded 472.88 kg·m^{-3} for cherry stones at 9.30% moisture content.

3.5. Pelleting Process of Sawdust and Ground Cherry Stones

Table 4 summarizes the results of the study investigating the influence of crushed cherry stones content in mixtures with sawdust on the pelleting process. Specifically, it presents the pelletizer's power demand during pellet production, as well as the effects on the kinetic strength, density, and bulk density of the resulting pellets.

Table 4. Effect of crushed cherry stone content in sawdust mixtures on the pelleting process (pelletizer's power demand and energy consumption), as well as on the kinetic strength, density, and bulk density of the produced pellets.

	Pellet Quality				
Cherry Stones Content [%]	Pelletizer's Power Demand [kW]	Energy Consumption [kW·h·t^{-1}]	Kinetic Strength [%]	Density [kg·m^{-3}]	Bulk Density [kg·m^{-3}]
0	3.79	75.8	94.64	1312.02	675.75
10	3.35	67.0	96.60	1255.43	604.59
15	3.05	61.0	96.20	1249.55	606.36
20	2.86	57.2	91.37	1241.65	634.36

Figure 5 presents the effect of crushed cherry stone content in sawdust mixtures on the pelleting process, expressed as the pelletizer's power demand during densification.

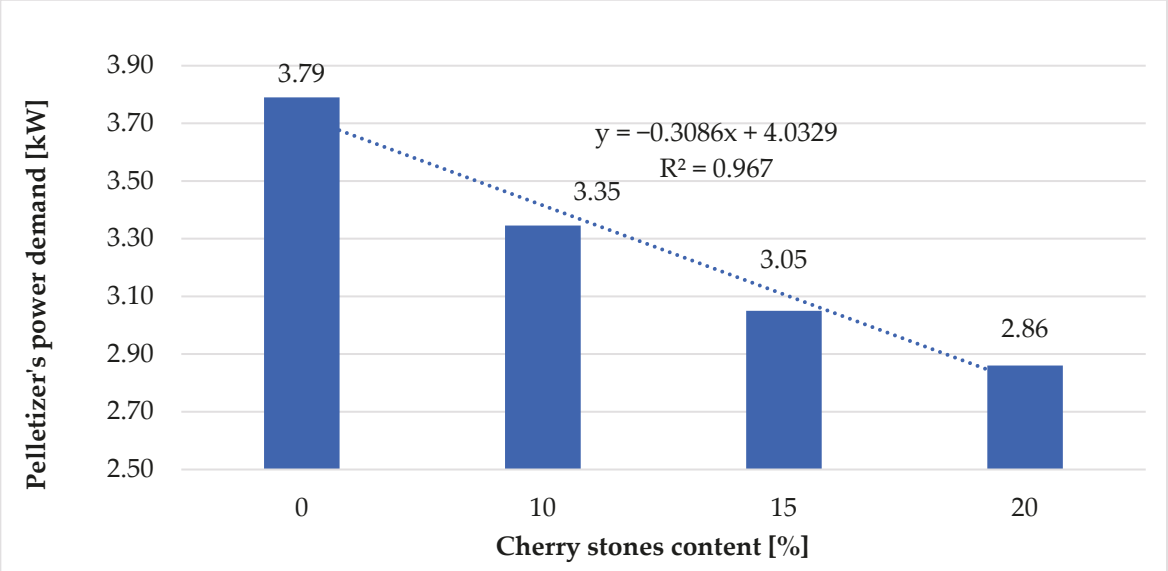


Figure 5. Dependence of the pelletizer's power demand on the content of crushed cherry stones in the mixture with sawdust.

Based on the results presented in Table 4 and Figure 5, the content of crushed cherry stones in the sawdust mixture was found to have a significant influence on the pelleting process, particularly on the pelletizer's power demand.

An increase in the proportion of crushed cherry stones from 10% to 20% (at a mixture moisture content of approximately 16%) reduced the pelletizer's power demand by about 14% (from 3.35 kW to 2.86 kW). Compared with the pelletization of pure sawdust, this reduction reached approximately 24% (from 3.79 kW to 2.86 kW).

The tests confirmed that the addition of crushed cherry stones significantly enhanced the compressibility of the mixture, as evidenced by the marked decrease in pelletizer power demand with increasing cherry stone content.

The recorded values during the compaction of the sawdust–cherry stone mixtures in a pelletizer with a flat die further confirm the beneficial effect of cherry stone addition on reducing energy consumption. Under the same moisture conditions (≈16%), the pelletizer's power demand for mixtures was substantially lower than for sawdust alone, which required 3.79 kW.

The relationship between the cherry stone content in the sawdust mixture and the pelletizer's power demand N_g is described by Equation (2):

$$N_g = -0.31 \cdot z_p + 4.03 \quad (2)$$

where

z_p—content of crushed cherry stones [%],

N_g—pelletizer's power demand [kW].

According to Obidziński et al. [48], the addition of herbaceous elderberry waste at levels ranging from 10% to 20% did not significantly affect the pelletizer's power demand, which nonetheless decreased compared to the pelletization of pure pine sawdust. The reduction relative to pure sawdust amounted to approximately 10%.

Similarly, increasing the potato pulp content in mixtures with sawdust from 10% to 25% reduced the pelletizer's power demand by about 20% (from 7.35 kW to 5.92 kW) [14].

Obidziński et al. [49] further reported that the inclusion of post-flotation dairy sludge in sawdust mixtures had a significant effect on the pelletizer's power demand. Increasing sludge content from 10% to 20% decreased the power demand by approximately 26.8% (from 3.92 kW to 2.87 kW). Compared with sawdust alone, the reduction in pelletizer's power demand for the 20% sludge mixture reached 32%.

3.6. Kinetic Strength of Pellets

Figure 6 presents the results of tests on the effect of crushed cherry stones in the mixture with sawdust on the kinetic strength of the obtained pellets.

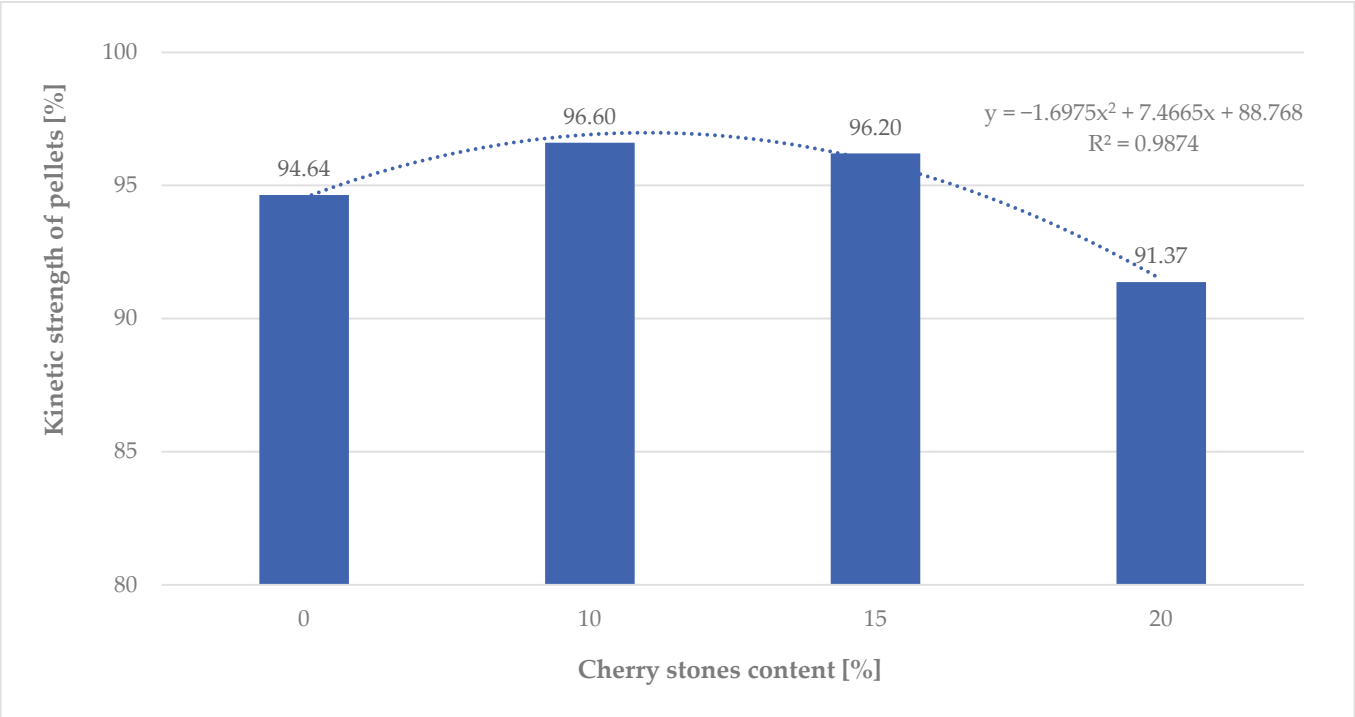


Figure 6. Dependence of the kinetic strength of the pellets on the content of crushed cherry stones in the mixture with sawdust.

Based on the conducted research (Figure 6), it was found that increasing the content of crushed cherry stones in sawdust mixtures from 10% to 20% resulted in a slight decrease in pellet kinetic strength, by approximately 5% (from 96.60% to 91.37%). The kinetic strength of pellets with a 10% addition of crushed cherry stones was slightly higher than that of pellets produced from pure sawdust under the same moisture conditions (16%), which reached 94.64%.

The addition of crushed cherry stones, combined with water (increasing the mixture moisture from approximately 8% in raw sawdust to about 16% during pelletization) or with steam supplied in the process, promotes the formation of a binder (sticky gel) at elevated temperatures. This binder enhances interparticle bonding, leading to the formation of durable agglomerates with high kinetic strength after drying.

The effect of crushed cherry stone content z_p in the sawdust mixture on pellet kinetic strength P_{dxg} is described by Equation (3):

$$P_{dxg} = -1.69 \cdot z_p{}^2 + 7.47 \cdot z_p + 88.77 \quad (3)$$

where

z_p—content of crushed cherry stones [%],

P_{dxg}—kinetic strength of pellets [%].

Research conducted by Cwalina et al. [50] showed that the kinetic strength of pellets decreased by 0.7% (from 98.21% to 97.56%). In another study [33], it was reported that pellets produced from hemp shives with a 10% addition of potato pulp exhibited a kinetic strength of 98.1%. A further increase in potato pulp content led to only a slight reduction in strength, with a minimum value of 96.42%.

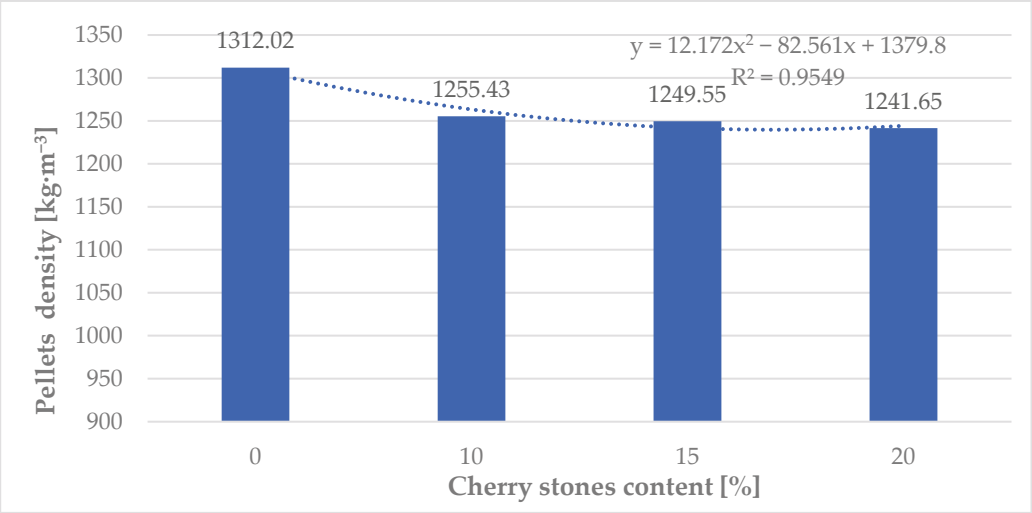
Dorokhov et al. [51] investigated pellet compositions based on wood sawdust with the addition of coal slime, peat, and a mixture of straw and rice husk. Their findings indicated that the kinetic strength coefficients were 6–32% higher compared to pellets made from pure sawdust.

3.7. Density and Bulk Density of Pellets

Figure 7 presents the effect of crushed cherry stone content in sawdust mixtures on the physical density (Figure 7a) and bulk density (Figure 7b) of the produced pellets. As shown in Figure 7a, increasing the proportion of crushed cherry stones from 10% to 20% slightly reduced pellet density, from 1255.43 kg·m^{-3} to 1241.65 kg·m^{-3}. At each level of cherry stone addition, the pellets exhibited lower density compared to those made from pure sawdust at the same moisture content (16%), which reached 1312.02 kg·m^{-3}.

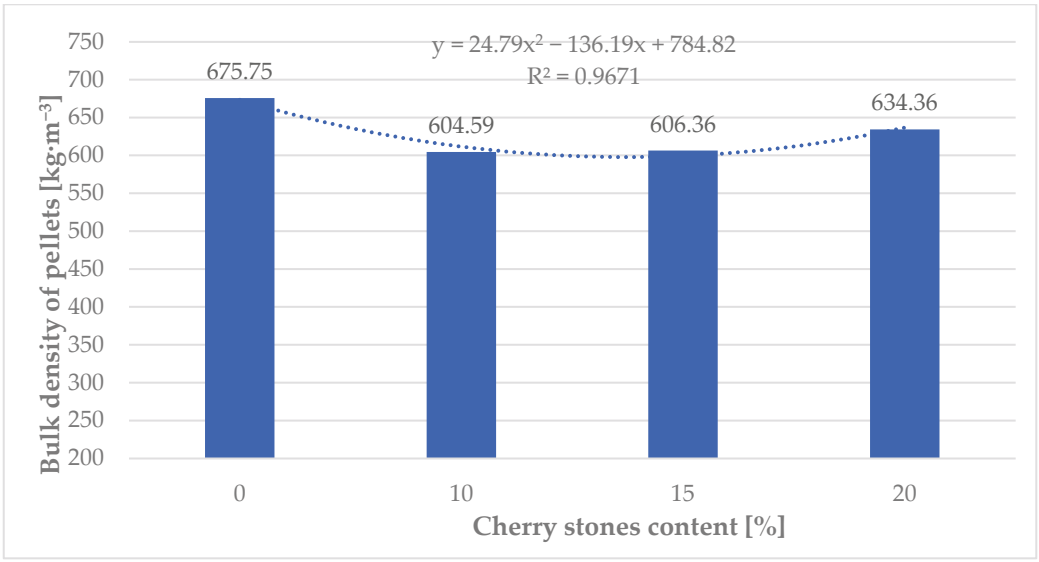
The measured pellet densities (all exceeding 1000 kg·m^{-3}) for mixtures containing 10–20% crushed cherry stones confirm that the pellets are of very high quality and can be considered a fully valuable and innovative biofuel. These values meet the requirements of the current PN-EN ISO 17225-2:2021-10 standard [42]. Consequently, the produced pellets can be used as a full-value fuel both in professional power plants equipped with high-efficiency boilers (with strict fuel quality requirements) and in individual biomass heating systems.

The relationship between the bulk density of pellets and the proportion of crushed cherry stones in the sawdust mixture is clearly evident (Figure 7b). An increase in the share of crushed cherry stones from 10% to 20% results in a rise in bulk density, from 604.59 kg·m^{-3} to 634.36 kg·m^{-3}. This increase is accompanied by a reduction in pellet length as the proportion of crushed cherry stones grows (Figure 8). The observed effect is attributed to the higher oil content of cherry stones, which promotes the formation of shorter pellets.



(**a**)

Figure 7. *Cont.*



(**b**)

Figure 7. The effect of crushed cherry stone content in the mixture with sawdust on (**a**) physical density, (**b**) bulk density of pellets.

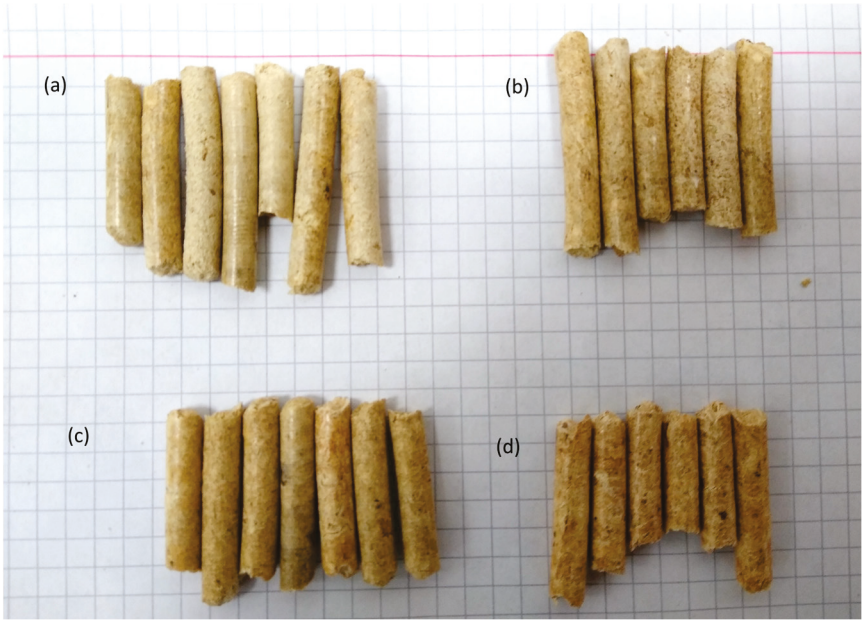


Figure 8. View of pellets obtained from a mixture of sawdust and crushed cherry stones: (**a**) 0%, (**b**) 10%, (**c**) 15%, (**d**) 20%.

The effect of crushed cherry stones z_p in the mixture with sawdust on the pellets density ρ_g and on the pellets bulk density ρ_{ug} is described by Equations (4) and (5):

$$\rho_g = -12.17 \cdot z_p{}^2 - 82.56 \cdot z_p + 1379.80 \quad (4)$$

$$\rho_{ug} = 24.79 \cdot z_p{}^2 - 136.19 \cdot z_p + 784.82 \quad (5)$$

where

z_p—content of crushed cherry stones [%],
ρ_g—pellets density [kg·m^{-3}],
ρ_{ug}—bulk density of pellets [kg·m^{-3}].

The conducted research indicates that the optimal addition of crushed cherry stones, in terms of pellet quality, ranges from 10% to 15%. Within this interval, the produced pellets exhibit favourable properties, including high kinetic strength and increased bulk density. Moreover, this level of additive reduces the energy demand of the pelleting process compared with the energy required for compacting sawdust alone. Paczkowski et al. [52] reported that increasing the proportion of black locust sawdust in the mixture to 75% decreased bulk density from 716 kg·m^{-3} to 662 kg·m^{-3}. Similarly, the incorporation of potato pulp reduced pellet density from 1290 kg·m^{-3} to 1230–1260 kg·m^{-3}, demonstrating the influence of organic additives on density. The inclusion of 10% bakery waste in the form of wholegrain bread and pumpkin bread also lowered the bulk density of pellets by approximately 11–16% [53].

3.8. Calorific Value and Heat of Combustion

Table 5 presents results of tests on the calorific value and heat of combustion of sawdust and crushed cherry stones.

Table 5. Test results of the calorific value and heat of combustion of sawdust and cherry stones.

Raw Material	Heat of Combustion [MJ·kg^{-1}]			Calorific Value [MJ·kg^{-1}]	
	Analytical Moisture ± SD [%]	Dry Matter ± SD	Analytical Moisture ± SD	Dry Matter ± SD	Analytical Moisture ± SD
Cherry stones	8.35 ± 0.09	23.499 ± 0.045	21.528 ± 0.050	22.022 ± 0.046	19.974 ± 0.046
Pine sawdust	15.00 ± 0.082	4.418 ± 0.022	20.792 ± 0.026	22.326 ± 0.087	19.004 ± 0.038

Based on tests conducted for dry sawdust (0% moisture) and for sawdust at 8.35% moisture, the effect of sawdust moisture content on the heat combustion of sawdust $Q^a{}_s$ obtained during combustion in a calorimetric bomb was determined using the following Equation (6):

$$Q^a{}_s = -0.242 \cdot w_p + 24.418 \quad (6)$$

The effect of sawdust moisture content wt on the calorific value $Q^a{}_i$ using the following Equation (7):

$$Q^a{}_s = -0.222 \cdot w_p + 22.326 \quad (7)$$

Based on the dependence of the heat of combustion and the calorific value of sawdust and crushed cherry stones on moisture content, the heat of combustion and calorific value of the tested raw material mixtures (at 15% moisture content) were determined for different proportions of cherry stones in the mixture with sawdust.

Table 6 presents the results of the study on the effect of crushed cherry stone content in the mixture with the raw material on its calorific value and heat of combustion at analytical moisture (15%).

Table 6. The effect of crushed cherry stones in the mixture with sawdust on the calorific value and combustion heat.

Cherry Stones Content [%]	Heat of Combustion [MJ·kg^{-1}]	Calorific Value [MJ·kg^{-1}]
0	19.959	18.323
5	20.001	18.357
10	20.042	18.391
15	20.084	18.425
20	20.126	18.459
25	20.167	18.493

The obtained values of the heat of combustion and calorific value indicate that the addition of crushed cherry stones enhances the energy performance of the produced pellets. For instance, incorporating 10% crushed cherry stones into sawdust increased the heat of combustion and calorific value by 0.081 MJ·kg^{-1} (approximately 0.42%), while a 20% addition resulted in an increase of 0.167 MJ·kg^{-1} (approximately 0.84%).

According to Chojnacki et al. [16], who investigated the effects of adding fruit pomace and vegetable residues to barley straw, the incorporation of pomace slightly reduced the calorific value of pellets compared with pellets produced from straw alone. A 30% pomace addition decreased the calorific value by less than 7% relative to pure barley straw pellets. Similarly, Jekayinfa et al. [54], who pelletised rice bran using a screw-type pelleting machine with starch as a binder, reported heating values in the range of 16.54–17.30 MJ·kg^{-1}. Ferreira et al. [55] characterised pellets produced from residual biomass derived from the processing of *Dinizia excelsa* and *Manilkara elata* wood, in combination with *Eucalyptus* spp. They obtained a heating value of 20.39 MJ·kg^{-1} for pellets produced from a 50:50 mixture of *Dinizia excelsa* and *Manilkara elata*.

3.9. Combustion Tests of Produced Pellets

Table 7 presents the combustion results (exhaust gas composition) obtained during the combustion of sawdust pellets and pellets made from a mixture of sawdust and crushed cherry stones.

Table 7. Exhaust gas composition from the combustion of pellets made from used sawdust and a mixture of sawdust and crushed cherry stones.

Parameters	Pellets Without Cherry Seeds		Pellets with 10% Cherry Seeds		Pellets with 15% Cherry Seeds		Pellets with 20% Cherry Seeds		Ecodesign Limit Value (at 10% O_2)
	Actual Concentration	At 10% O_2	Actual Concentration	At 10% O_2	Actual Concentration	At 10% O_2	Actual Concentration	At 10% O_2	
CO_2 [%]	6.07	7.86	6.30	7.77	6.25	7.54	7.41	7.51	-
CO [mg·Nm^{-3}]	439.38	569.27	382.51	471.83	368.66	445.14	417.54	423.31	500
NO_x [mg·Nm^{-3}]	208.24	269.81	153.29	189.04	139.95	168.99	149.81	151.88	200
SO_2 [mg·Nm^{-3}]	24.88	32.23	17.88	22.05	17.42	21.03	22.53	22.84	-
HCl [mg·Nm^{-3}]	1.98	2.56	2.22	2.74	2.19	2.64	2.76	2.79	-
O_2 [%]	12.51	-	12.08	-	11.89	-	10.15	-	-
Excess air coefficient λ	2.39		2.28		2.23		1.89		
Flue gas temperature in the boiler flue [°C]	160		170		175		190		

Analysing the combustion performance of the produced pellets, it was observed that increasing the proportion of cherry stones from 10% to 20% raised the exhaust gas temperature in the boiler flue from 160 °C (reference sawdust pellets) to 170 °C (10% cherry stone addition) and further to 190 °C (20% addition). Under identical boiler operating parameters, this increase in flue gas temperature reflects the higher calorific value of the fuel, confirming that cherry stones act as an additive enhancing the heat of combustion of the pellets. Elevated combustion temperatures contributed to a reduction in carbon monoxide and nitrogen oxide emissions, which for pellets with cherry stone additions remained within the limits set by the EU Ecodesign Directive [56], i.e., below 500 mg·Nm^{-3} for CO and 200 mg·Nm^{-3} for NO_x. Under the tested biomass combustion conditions, the main source of nitrogen oxides was fuel-bound nitrogen, as the combustion temperature did not exceed 1300 °C. Consequently, the Zeldovich mechanism was not expected to occur, and due to the high excess air coefficient (λ), so-called "Prompt NO" formation, i.e., the reaction of atmospheric N_2 with hydrocarbons in fuel-rich zones, was also negligible.

In all cases, the excess air coefficient remained at a level acceptable for the tested unit. Notably, the slight reduction in λ observed with increasing cherry stone content indicated improved contact between combustible particles and the oxidising agent (air).

During combustion, most of the chlorine present in biomass is released as hydrogen chloride (HCl), which may subsequently react with other exhaust gas components to form dioxins. As the flue gases cooled outside the combustion chamber, a considerable share of chlorine condensed as salts on heat exchanger surfaces or on fly ash particles, leading to high-temperature chloride corrosion of boiler components. Although the Ecodesign Directive does not specify maximum HCl concentrations in flue gases from small-scale boilers, German standards set a permissible limit of <5 $mg \cdot m^{-3}$. In the present study, HCl concentrations in the flue gases were comparably low, reflecting the low chlorine content of the raw materials used for pellet production.

Sulphur oxide emissions depended primarily on the sulphur content of the fuel. During combustion, biomass sulphur was oxidised mainly to sulphur dioxide (SO_2), with minor amounts of sulphur trioxide (SO_3), subsequently forming alkalis and sulphates. The significance of sulphur lies less in its emission levels and more in its role in corrosion processes. High SO_x concentrations in exhaust gases contribute to the sulphurisation of alkalis and alkali metal chlorides, reducing the flue gas dew point and promoting chlorine release. Certified wood pellets burned in the same installation generated sulphur dioxide emissions of approximately 23 $mg \cdot m^{-3}$, a level similar to that observed for the tested pellets.

For comparison, combustion tests carried out using uncrushed cherry stones in the same boiler installation showed significantly poorer emission characteristics and less favourable combustion behaviour compared with pellets. The values reported in Table 8 are expressed relative to 10% oxygen content in the exhaust gases.

Table 8. Composition of exhaust gases from the combustion of whole cherry stones.

Parameters	Value	Ecodesign Standard [56]
CO_2 [%]	7.78	-
CO [$mg \cdot Nm^{-3}$]	731.86	500
SO_2 [$mg \cdot Nm^{-3}$]	58.49	-
NO [$mg \cdot Nm^{-3}$]	381.83	200
HCl [$mg \cdot Nm^{-3}$]	9.04	-
Actual oxygen content in exhaust gases [%]	14.34	-
Excess air coefficient λ [-]	3.00	-
Flue gas temperature in the boiler flue [°C]	160	-

In summary, the incorporation of cherry stones into wood sawdust improved pellet combustion performance by reducing emissions of harmful CO, NO, and SO_2 compounds, primarily as a result of the higher combustion temperature. The observed reduction in the excess air coefficient (λ) indicated enhanced fuel–air mixing conditions within the combustion chamber, thereby decreasing heat losses through the exhaust gases. Importantly, the CO and NO emissions from the combustion of wood–sawdust pellets enriched with cherry stones in a Class 5 boiler with a retort grate complied with the requirements of the Ecodesign Directive of the European Parliament and Council [56], which has been in force since 1 January 2020.

3.10. Statistical Analysis

The proportion of cherry stones in the sawdust mixture exhibited the highest sum of absolute correlation values and was strongly associated with the physical and energy parameters of the pellets (Table S1). This factor had a significant effect ($r > 0.8$ or $r < -0.8$) on seven of the 13 variables analysed, with the strongest correlations observed for the heat of combustion and the calorific value of the pellets. In contrast, kinetic strength had

the weakest influence on pellet quality parameters, with correlation coefficients ranging from −0.8646 (CO_2 emissions) to 0.8269 (O_2 emissions). Apart from these two parameters, kinetic strength showed no strong correlations with the other variables and yielded a relatively low sum of correlation values ($\Sigma|r| = 6.0079$) (Table S1).

Principal component analysis (PCA) confirmed these results, indicating that the proportion of crushed cherry stones, heat of combustion, and calorific value were characterised by the highest negative loadings, ranging from −0.9921 (heat of combustion) to −0.9951 (cherry stone content), with respect to the first principal component (Figure 9). By contrast, kinetic strength was positively loaded (0.9303) on the second component.

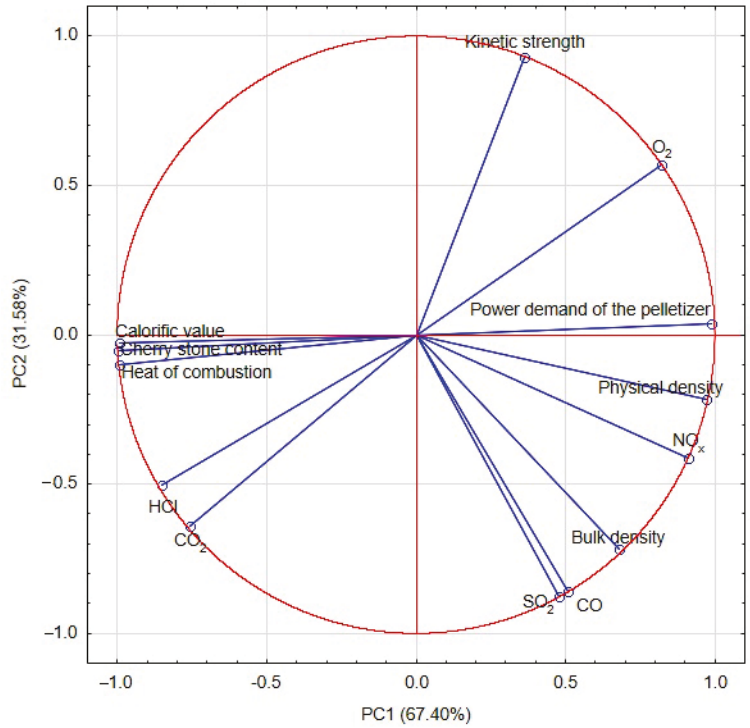


Figure 9. Two-dimensional graph of physical (mechanical), energy and exhaust emission parameters from the combustion of pellets containing crushed cherry stones, showing the two principal components (PC1 and PC2) of the PCA model, which together explain 99.0% of the total variance, i.e., 67.40% and 31.58% for PC1 and PC2, respectively. Blue two-dimensional vectors indicate the strength and direction of factor loading for all analyzed parameters.

4. Conclusions

Based on the conducted research, it was found that the sawdust was characterised by excessively low moisture content and an excessive fine fraction, which adversely affected the pelleting process and the quality of the pellets. The addition of crushed cherry stones to the mixture proved to be an effective method of improving the raw material properties. It enhanced compactibility, reduced the energy consumption of the process by more than 20%, and enabled the efficient management of the problematic fine fraction. At the same time, the incorporation of cherry stones reduced wear on the pelletizer operating system and improved overall process efficiency.

The analysis of pellet physical properties demonstrated that the addition of cherry stones caused only minor changes in strength and density while maintaining values compliant with market requirements and the PN-EN ISO 17225-2:2021-10 standard. From an energy perspective, the produced pellets exhibited higher heat of combustion and calorific values, which, combined with lower emissions of CO, NO, and SO_2, translated into improved combustion quality and reduced heat losses. The cherry stone pellets also complied

with EN Plus B, DIN-Plus, and ÖNORM M7135 requirements for nitrogen and sulphur content, and their gaseous emissions met the limits of the Ecodesign Directive.

The resulting product, with a density exceeding 1000 $kg \cdot m^{-3}$, represents a high-quality solid fuel with favourable performance parameters. Its production process can be regarded as both innovative and energy-efficient. An additional advantage lies in the utilisation of large quantities of cherry stone waste from the fruit processing industry, in line with EU waste management policies promoting prevention, recycling, and reuse. Consequently, the use of cherry stones in pellet production may be considered both technologically advantageous and environmentally sustainable within the renewable energy sector.

The proportion of cherry stones in the sawdust mixture exerted a decisive influence on pellet physical and energy parameters, particularly heat of combustion and the calorific value. By contrast, kinetic strength played only a marginal role, showing significant correlations mainly with gas emissions. Principal component analysis (PCA) confirmed the key importance of cherry stone content and energy parameters, whereas kinetic strength was associated primarily with the second component, underscoring its lesser relevance in assessing pellet quality.

Using cherry stones and sawdust for pellet production not only provides an alternative source of renewable energy but also helps reduce the burden of waste management in the agri-food sector. The valorization of these residues through pellet production enhances environmental sustainability and makes a significant contribution to the development of circular bioeconomy strategies.

Supplementary Materials: The following supporting information can be downloaded at https://www.mdpi.com/article/10.3390/en18205356/s1, Table S1: Matrix of Pearson correlation coefficients between the physical (mechanical) parameters of the obtained pellets and the energy parameters and exhaust emissions from the combustion of pellets containing crushed cherry stones.

Author Contributions: Conceptualization, P.C. and S.O.; data curation, P.C., A.S., M.K.-S., P.B. and J.M.; formal analysis, A.S., M.K.-S. and J.M.; investigation, P.C., A.S. and M.K.-S.; methodology, P.C., S.O., A.S. and P.B.; resources, P.B. and M.K.-S.; supervision, P.C. and S.O.; validation, S.O., A.S., M.K.-S., P.B. and J.M.; visualization, P.C., A.S., M.K.-S. and P.B.; writing—original draft, S.O., P.C. and M.K.-S.; writing—review and editing, A.S., M.K.-S. and P.B. All authors have read and agreed to the published version of the manuscript.

Funding: The work was carried out as part of a team project no. WZ/WB-IIS/5/2023 and was financed by the Ministry of Science and Higher Education as part of a grant for maintaining research potential awarded to the Faculty of Civil Engineering and Environmental Sciences, Bialystok University of Technology.

Institutional Review Board Statement: Not applicable.

Informed Consent Statement: Not applicable.

Data Availability Statement: The original contributions presented in this study are included in the article. Further inquiries can be directed to the corresponding author.

Conflicts of Interest: Author Paweł Braun was Co-owner of company DAK-POL Sp. z o.o. The remaining authors declare that the research was conducted in the absence of any commercial or financial relationships that could be construed as a potential conflict of interest.

References

1. Rules of Procedure of the European Parliament and of the Council (EU) 2023/2413 of 18 October 2023, Directive (EU) 2018/2001, Directive (EU) 2018/1999, Directive 98/70/EC on the Promotion of Energy from Control Sources and Repealing Council Directive (EU) 2015/652. Official Journal of the European Union. 2023. Available online: https://eur-lex.europa.eu/legal-content/EN/TXT/PDF/?uri=OJ:L_202302413 (accessed on 10 July 2025).
2. Act on Renewable Energy Sources ('RES Act', Dz.U. 2015 poz. 478) Poland (2015). Available online: https://www.prawo.egospodarka.pl/akty/dziennik-ustaw/2015/000/478 (accessed on 10 July 2025).

3. Bioenergy Europe: Internal EU Pellet Production Leapt in 2023. Available online: https://www.bioenergy-news.com/news/bioenergy-europe-internal-eu-pellet-production-leapt-in-2023/ (accessed on 21 August 2025).
4. Żary-Sikorska, E. Odpady z przetwórstwa owoców i warzyw–charakterystyka problemu. *Infrastrukt. I Ekol. Teren. Wiej.* **2024**, *19*, 93–106. [CrossRef]
5. Matuszak-Flejszman, A.; Joachimiak-Lechman, K. *Current Trends in Quality Science, Product Management—Quality, Safety and Environmental Focus*; Poznań University of Economics and Business: Poznań, Poland, 2019; ISBN 978-83-7789-588-7.
6. Chakravarty, I.; Mandavgane, S.A. Valorization of Fruit and Vegetable Waste for Biofertilizer and Biogas. *J. Food Process Eng.* **2021**, *44*, e13512. [CrossRef]
7. Zawadzińska, A.; Salachna, P.; Nowak, J.S.; Kowalczyk, W.; Piechocki, R.; Łopusiewicz, Ł.; Pietrak, A. Compost Based on Pulp and Paper Mill Sludge, Fruit-Vegetable Waste, Mushroom Spent Substrate and Rye Straw Improves Yield and Nutritional Value of Tomato. *Agronomy* **2022**, *12*, 13. [CrossRef]
8. Karimi Sani, I.; Masoudpour-Behabadi, M.; Alizadeh Sani, M.; Motalebinejad, H.; Juma, A.S.M.; Asdagh, A.; Eghbaljoo, H.; Khodaei, S.M.; Rhim, J.-W.; Mohammadi, F. Value-Added Utilization of Fruit and Vegetable Processing by-Products for the Manufacture of Biodegradable Food Packaging Films. *Food Chem.* **2023**, *405*, 134964. [CrossRef]
9. Nirmal, N.P.; Khanashyam, A.C.; Mundanat, A.S.; Shah, K.; Babu, K.S.; Thorakkattu, P.; Al-Asmari, F.; Pandiselvam, R. Valorization of Fruit Waste for Bioactive Compounds and Their Applications in the Food Industry. *Foods* **2023**, *12*, 556. [CrossRef]
10. Arulprakasajothi, M.; Beemkumar, N.; Parthipan, J.; Battu, N.R. Investigating the Physio-Chemical Properties of Densified Biomass Pellet Fuels from Fruit and Vegetable Market Waste. *Arab. J. Sci. Eng.* **2020**, *45*, 563–574. [CrossRef]
11. Rostocki, A.; Unyay, H.; Ławińska, K.; Obraniak, A. Granulates Based on Bio and Industrial Waste and Biochar in a Sustainable Economy. *Energies* **2023**, *16*, 56. [CrossRef]
12. Marreiro, H.M.P.; Peruchi, R.S.; Lopes, R.M.B.P.; Andersen, S.L.F.; Eliziário, S.A.; Rotella Junior, P. Empirical Studies on Biomass Briquette Production: A Literature Review. *Energies* **2021**, *14*, 8320. [CrossRef]
13. Kpalo, S.Y.; Zainuddin, M.F.; Manaf, L.A.; Roslan, A.M. A Review of Technical and Economic Aspects of Biomass Briquetting. *Sustainability* **2020**, *12*, 4609. [CrossRef]
14. Obidziński, S.; Cwalina, P.; Kowczyk-Sadowy, M.; Sienkiewicz, A.; Krasowska, M.; Szyszlak-Bargłowicz, J.; Zając, G.; Słowik, T.; Mazur, J.; Jankowski, M. Physical and Energy Properties of Fuel Pellets Produced from Sawdust with Potato Pulp Addition. *Energies* **2024**, *17*, 3960. [CrossRef]
15. Gholami Banadkoki, O.; Sokhansanj, S.; Lau, A.; Arunachalam, S.; Smith, D. The Physiochemical Properties of Pellets Made from the Foliage of Vegetable Crops. *Energies* **2025**, *18*, 1969. [CrossRef]
16. Chojnacki, J.; Zdanowicz, A.; Ondruška, J.; Šooš, Ľ.; Smuga-Kogut, M. The Influence of Apple, Carrot and Red Beet Pomace Content on the Properties of Pellet from Barley Straw. *Energies* **2021**, *14*, 405. [CrossRef]
17. Hejft, R.; Obidziński, S.; Jałbrzykowski, M.; Markowski, J. Production of Heating Pellets with Apple Pomace Content. *J. Res. Appl. Agric. Eng.* **2016**, *61*, 29–34.
18. Kraiem, N.; Lajili, M.; Limousy, L.; Said, R.; Jeguirim, M. Energy Recovery from Tunisian Agri-Food Wastes: Evaluation of Combustion Performance and Emissions Characteristics of Green Pellets Prepared from Tomato Residues and Grape Marc. *Energy* **2016**, *107*, 409–418. [CrossRef]
19. Kang, S.B.; Oh, H.Y.; Kim, J.J.; Choi, K.S. Characteristics of Spent Coffee Ground as a Fuel and Combustion Test in a Small Boiler (6.5 kW). *Renew. Energy* **2017**, *113*, 1208–1214. [CrossRef]
20. Allesina, G.; Pedrazzi, S.; Allegretti, F.; Tartarini, P. Spent Coffee Grounds as Heat Source for Coffee Roasting Plants: Experimental Validation and Case Study. *Appl. Therm. Eng.* **2017**, *126*, 730–736. [CrossRef]
21. Nowicka, P.; Wojdylo, A.; Oszmianski, J. Jakość produktów wiśniowych dostępnych w handlu. *Przemysł Ferment. I Owocowo-Warzywny* **2013**, *57*, 40–45.
22. Yılmaz, C.; Gökmen, V. Compositional Characteristics of Sour Cherry Kernel and Its Oil as Influenced by Different Extraction and Roasting Conditions. *Ind. Crops Prod.* **2013**, *49*, 130–135. [CrossRef]
23. Burgstaller, C.; Renner, K. Feasibility of Cherry Pit Particles as a Natural Reinforcement in Polypropylene. *Macromol* **2023**, *3*, 303–313. [CrossRef]
24. Frišták, V.; Bošanská, D.; Pipíška, M.; Ďuriška, L.; Bell, S.M.; Soja, G. Physicochemical Characterization of Cherry Pits-Derived Biochar. *Materials* **2022**, *15*, 408. [CrossRef]
25. Pollard, Z.A.; Goldfarb, J.L. Valorization of Cherry Pits: Great Lakes Agro-Industrial Waste to Mediate Great Lakes Water Quality. *Environ. Pollut.* **2021**, *270*, 116073. [CrossRef]
26. Bagheri, S.; Alinejad, M.; Nejad, M.; Aliakbarian, B. Creating Incremental Revenue from Industrial Cherry Wastes. *Chem. Eng. Trans.* **2021**, *87*, 553–558. [CrossRef]
27. Kniepkamp, K.; Errico, M.; Yu, M.; Roda-Serrat, M.C.; Eilers, J.-G.; Wark, M.; van Haren, R. Lipid Extraction of High-Moisture Sour Cherry (*Prunus cerasus* L.) Stones by Supercritical Carbon Dioxide. *J. Chem. Technol. Biotechnol.* **2024**, *99*, 810–819. [CrossRef]

28. *PN-EN ISO18134-3:2023-12*; Solid Biofuels—Determination of Moisture Content—Part 3: Moisture in the Sample for General Analysis. Polish Committee for Standardization: Warsaw, Poland, 2023.
29. *PN-R-64798:2009*; Feed—Determination of Fineness. Polish Committee for Standardization: Warsaw, Poland, 2009.
30. *PN-EN ISO 16948:2015-07*; Solid Biofuels—Determination of Total Carbon, Hydrogen and Nitrogen Content. ISO: Geneva, Switzerland, 2015.
31. *PN-EN ISO 16994:2016-10*; Solid Biofuels—Determination of Total Sulfur and Chlorine Content. ISO: Geneva, Switzerland, 2016.
32. *PN-EN ISO 17830:2016-07*; Solid Biofuels—Grain Composition of Crushed Pellets. Polish Committee for Standardization: Warsaw, Poland, 2016.
33. Obidziński, S.; Cwalina, P.; Kowczyk-Sadowy, M.; Krasowska, M.; Sienkiewicz, A.; Faszczewski, D.; Szyszlak-Bargłowicz, J. The Use of Bread Bakery Waste as a Binder Additive in the Production of Fuel Pellets from Straw. *Energies* **2023**, *16*, 7313. [CrossRef]
34. *PN-EN ISO 17831-1:2016-02*; Solid Biofuels—Determination of Mechanical Strength of Pellets and Briquettes—Part 1: Pellets. ISO: Geneva, Switzerland, 2016.
35. *PN-EN ISO 1928:2002*; Solid Mineral Fuels—Determination of Gross Calorific Value by the Bomb Calorimetric Method, and Calculation of Net Calorific Value. ISO: Geneva, Switzerland, 2002.
36. Serrano, C.; Monedero, E.; Lapuerta, M.; Portero, H. Effect of Moisture Content, Particle Size and Pine Addition on Quality Parameters of Barley Straw Pellets. *Fuel Process. Technol.* **2011**, *92*, 699–706. [CrossRef]
37. Jiang, X.; Cheng, W.; Liu, J.; Xu, H.; Zhang, D.; Zheng, Y.; Cai, H. Effect of Moisture Content during Preparation on the Physicochemical Properties of Pellets Made from Different Biomass Materials. *BioRes* **2019**, *15*, 557–573. [CrossRef]
38. Matkowski, P.; Lisowski, A.; Świętochowski, A. Pelletising Pure Wheat Straw and Blends of Straw with Calcium Carbonate or Cassava Starch at Different Moisture, Temperature, and Die Height Values: Modelling and Optimisation. *J. Clean. Prod.* **2020**, *272*, 122955. [CrossRef]
39. Piskowska-Wasiak, J. Purification and processing of gas from biomass gasification to produce SNG (Substitute Natural Gas). *Naft.-Gaz* **2011**, *67*, 347–360. Available online: https://inig.pl/magazyn/nafta-gaz/NAFTA-GAZ-2011-05-07.pdf (accessed on 18 July 2025).
40. Austrian Standards Institute. *ÖNORM M 7135: Compressed Wood and Compressed Bark in Natural State—Pellets and Briquettes—Requirements and Test Specifications*; Austrian Standards Institute: Vienna, Austria, 2000.
41. *PN-EN ISO 17225-1:2021-11*; Solid Biofuels—Fuel Specifications and Grades—Part 1: General Requirements. ISO: Geneva, Switzerland, 2021.
42. *PN-EN ISO 17225-2:2021*; Solid Biofuels—Fuel Specifications and Classes Part 2: Graded Wood Pellets. ISO: Geneva, Switzerland, 2021.
43. Obernberger, I. Physical Characteristics and Chemical Composition of Solid Biomass Fuels. In *Thermochemical Biomass Conversion*; Eindhofen University of Technology: Eindhoven, The Netherlands, 2003.
44. Król, D.; Borsukiewicz-Gozdur, A. Energy from Sawmill and Agricultural Waste Biomass. *Arch. Gospod. Odpad. I Ochr. Sr.* **2014**, *16*, 87–94.
45. Hardy, T.; Kordylewski, W.; Mościcki, K. Chlorine corrosion hazard due to firing and co-firing of biomass in boilers. *Arch. Spalania* **2009**, *9*, 181–195. Available online: https://yadda.icm.edu.pl/baztech/element/bwmeta1.element.baztech-article-BATD-0003-0006 (accessed on 18 July 2025).
46. Stasiak, M.; Molenda, M.; Bańda, M.; Wiącek, J.; Parafiniuk, P.; Lisowski, A.; Gancarz, M.; Gondek, E. Mechanical Characteristics of Pine Biomass of Different Sizes and Shapes. *Eur. J. Wood Prod.* **2019**, *77*, 593–608. [CrossRef]
47. Netinger Grubeša, I.; Šamec, D.; Juradin, S.; Hadzima-Nyarko, M. Utilizing Agro-Waste as Aggregate in Cement Composites: A Comprehensive Review of Properties, Global Trends, and Applications. *Materials* **2025**, *18*, 2195. [CrossRef]
48. Obidziński, S.; Cwalina, P.; Kowczyk-Sadowy, M.; Sienkiewicz, A.; Krasowska, M.; Szyszlak-Bargłowicz, J.; Zając, G.; Kryński, R. Effect of the Addition of Elderberry Waste to Sawdust on the Process of Pelletization and the Quality of Fuel Pellets. *Energies* **2024**, *17*, 1508. [CrossRef]
49. Obidziński, S.; Joka Yildiz, M.; Dąbrowski, S.; Jasiński, J.; Czekała, W. Application of Post-Flotation Dairy Sludge in the Production of Wood Pellets: Pelletization and Combustion Analysis. *Energies* **2022**, *15*, 9427. [CrossRef]
50. Cwalina, P.; Obidziński, S.; Sienkiewicz, A.; Kowczyk-Sadowy, M.; Piekut, J.; Bagińska, E.; Mazur, J. Production and Quality Assessment of Fertilizer Pellets from Compost with Sewage Sludge Ash (SSA) Addition. *Materials* **2025**, *18*, 1145. [CrossRef]
51. Dorokhov, V.V.; Nyashina, G.S.; Romanov, D.S.; Strizhak, P.A. Combustion and Mechanical Properties of Pellets from Biomass and Industrial Waste. *Renew. Energy* **2024**, *228*, 120625. [CrossRef]
52. Paczkowski, S.; Sauer, C.; Anetzberger, A.; Jaeger, D.; Pelz, S. Utilization of Black Locust (*Robinia pseudoacacia*) Sawdust as an Alternative Pelletization Raw Material. *Biomass Conv. Bioref.* **2024**, *14*, 25583–25597. [CrossRef]
53. Obidziński, S.; Szyszlak-Bargłowicz, J.; Zając, G.; Kowczyk-Sadowy, M.; Krasowska, M.; Sienkiewicz, A.; Cwalina, P.; Faszczewski, D.; Wasilewski, J. The Effect of Bakery Waste Addition on Pine Sawdust Pelletization and Pellet Quality. *Energies* **2024**, *17*, 523. [CrossRef]

54. Jekayinfa, S.O.; Abdulsalam, I.A.; Ola, F.A.; Akande, F.B.; Orisaleye, J.I. Effects of Binders and Die Geometry on Quality of Densified Rice Bran Using a Screw-Type Laboratory Scale Pelleting Machine. *Energy Nexus* **2024**, *13*, 100275. [CrossRef]
55. Ferreira, G.; Brito, T.M.; da Silva, J.G.M.; Minini, D.; Dias Júnior, A.F.; Arantes, M.D.C.; Batista, D.C. Wood Waste Pellets as an Alternative for Energy Generation in the Amazon Region. *Bioenerg. Res.* **2023**, *16*, 472–483. [CrossRef]
56. European Union. Commission Regulation (EU) 2015/1189 of 28 April 2015 Implementing Directive 2009/125/EC of the European Parliament and of the Council with Regard to Ecodesign Requirements for Solid Fuel Boilers (Text with EEA Relevance). Official Journal of the European Union. 2015. Available online: https://eur-lex.europa.eu/eli/reg/2015/1189/oj/eng (accessed on 18 July 2025).

Disclaimer/Publisher's Note: The statements, opinions and data contained in all publications are solely those of the individual author(s) and contributor(s) and not of MDPI and/or the editor(s). MDPI and/or the editor(s) disclaim responsibility for any injury to people or property resulting from any ideas, methods, instructions or products referred to in the content.

energies

MDPI

Article

Emission of Total Volatile Organic Compounds from the Torrefaction Process: Meadow Hay, Rye, and Oat Straw as Renewable Fuels

Justyna Czerwinska *, Szymon Szufa *, Hilal Unyay and Grzegorz Wielgosinski

Faculty of Process and Environmental Engineering, Lodz University of Technology, Wolczanska 213, 90-924 Lodz, Poland; hilal.unyay@p.lodz.pl (H.U.); grzegorz.wielgosinski@p.lodz.pl (G.W.)
* Correspondence: justyna.czerwinska@p.lodz.pl (J.C.); szymon.szufa@p.lodz.pl (S.S.)

Abstract

This study aims to quantify total VOC emissions and evaluate how torrefaction alters the heat of combustion of three agricultural residues. The work examines the amount of VOC emissions during the torrefaction process at various temperatures and investigates the changes in the heat of combustion of agri-biomass resulting from the torrefaction process. The process was carried out at the following temperatures: 225, 250, 275, and 300 °C. Total VOC emission factors were determined. The reaction kinetics analysis revealed that meadow hay exhibited the most stable thermal behavior with the lowest activation energy. At the same time, rye straw demonstrated higher thermal resistance and complex multi-step degradation characteristics. The authors analyze three types of agricultural biomass: meadow hay, rye straw, and oat straw. The research was divided into five stages: determination of moisture content in the sample, determination of ash content, thermogravimetric analysis, measurement of total VOC emissions from the biomass torrefaction process, and determination of the heat of combustion of the obtained torrefied biomass. Based on the research, it was found that torrefaction of biomass causes the emission of torgas containing VOC in the amount of 2–10 mg/g of torrefied biomass, which can be used energetically, e.g., to support the torrefaction process, and the torrefied biomass shows a higher value of the heat of combustion. Unlike prior studies focused on single feedstocks or limited temperature ranges, this work systematically compares three major crop residues across four torrefaction temperatures and directly couples VOC quantifications.

Keywords: torgas valorization; torrefaction effluent gas; VOC emissions

1. Introduction

The costs of adapting the Polish heating sector to the requirements of Fit for 55 and the Green Deal by 2050 are estimated at PLN 300 to 500 billion, which was estimated by the Polish Thermal Power Society. The Polish heating sector is the largest in Europe, and heat is the most widely consumed energy source in Poland, accounting for around 60%. This is a unique sector on a continental scale, and EU regulations are not adapted to its problems. Biomass plays a significant role in the structure of fuels used in district heating. According to data from the Energy Regulatory Office, it is used to produce over 12.5% of district heating, responsible for 97% of heat production from all renewable energy sources in heating systems.

Raw biomass has a lower heat of combustion compared to hard coal. However, subjecting it to the torrefaction process means that the obtained torrefied biomass has a

higher heat of combustion value. In the torrefaction process, which may be a stage in preparing biomass fuel for combustion or co-firing with coal, volatile organic compound (VOC)-containing torches are emitted, which can be utilized as a source of energy in the torrefaction process. Currently, there is a growing demand for energy, particularly in highly developed countries. One of the negative effects of this phenomenon is the depletion of non-renewable natural energy resources such as hard coal or lignite [1–4]. This often results in the need to import large quantities of raw materials from other countries, consequently increasing energy production costs. Therefore, other renewable energy sources have been sought. Biomass is undoubtedly an example of this renewable energy resource [5–8]. For energy purposes, the following forms of biomass are used: agricultural waste [9] (e.g., cereal straw, corn straw, and hay), waste from the wood industry, yields from energy crop plantations, organic waste, biofuels, or biogas [10–14]. Meadow hay is widely used in agriculture and animal husbandry in Poland, serving as a staple feed for cattle, horses, sheep, and goats, especially during periods when fresh feed is unavailable. Furthermore, meadow hay is used in phytobalance therapy (water therapy with herbs) in health resorts. Meadow hay is a staple food for many farm animals, including cattle, horses, sheep, and goats. Figure 1 illustrates the increasing importance of renewable energy sources in electricity production. Biomass shares account for less than 10% of all renewable energy sources in 2023, including agri-biomass. In Poland in May 2025, biomass accounted for 4.1% of total electricity production, corresponding to a 15.6% share of production from renewable energy sources, according to Forum Energy [15].

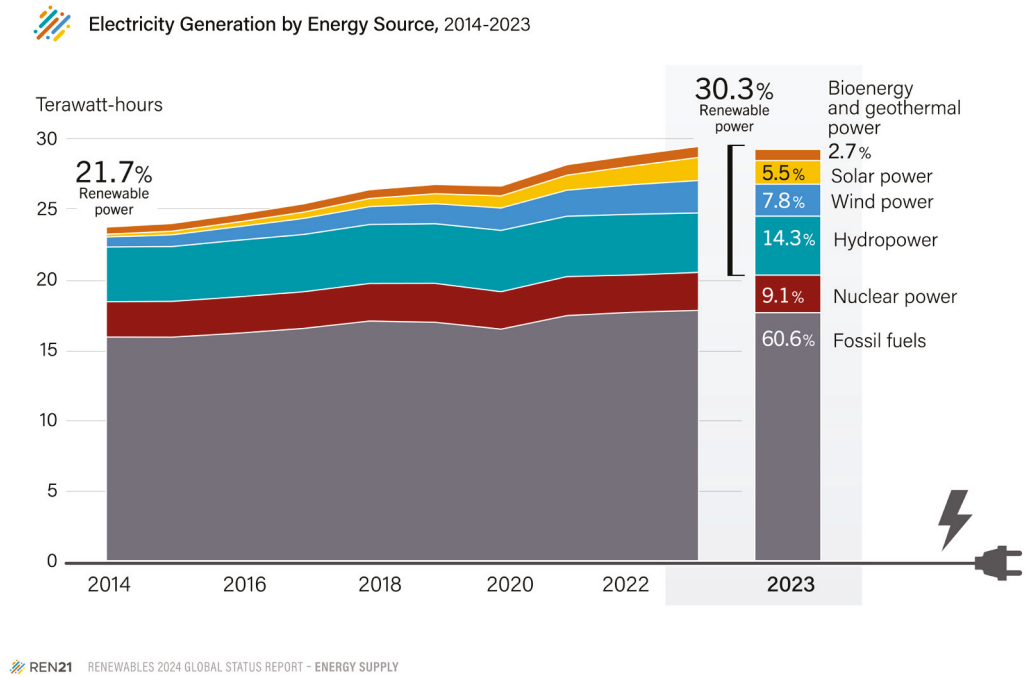


Figure 1. Electricity generation by energy source, 2014–2023 [16].

Torrefaction began to be investigated in the late 1920s and gained popularity in the last 10–20 years. A process that includes the dry, wet, and steam methods is a crucial thermal pretreatment process that enhances the properties of biomass, making it more suitable for various applications. Through torrefaction, biomass undergoes thermal decomposition at relatively low temperatures, resulting in an improved energy density, hydrophobicity, and grindability of the produced biochar.

To improve the energy properties of biomass, it is subjected to various processing techniques. Torrefaction is one of the methods of thermal treatment of biomass [17–20],

which is applied at lower temperatures (200–350 °C) than pyrolysis [21]. This process has been known for many years; however, there has been a recent growing interest in this subject. Thanks to torrefaction, a new product is obtained—a torrefied biomass, also called bio-coal [22]. It has similar properties to coal, thanks to which it is possible to co-fire it [23–26]. Torrefaction is a process of thermal conversion during which weight and part of the chemical energy contained in biomass is lost [27,28]. Conditions for the torrefaction should be selected so that the weight loss is a maximum of 30% and the energy loss is no more than 10% [29–32], which leads to a significant increase in the calorific value of the torrefied biomass obtained. The use of the torrefaction process is a solution that enables the management of substantial amounts of biomass, increases the share of co-fired biomass, and thus reduces the use of coal as a fuel. The interest in the biomass torrefaction process has been systematically growing in recent years [33].

The use of biomass for energy purposes is associated with the combustion process [34–37]. Emissions of pollutants into the environment occur both during the combustion of conventional fuels and biomass. When coal is burned, dust (including particulate matter), nitrogen dioxide, sulfur dioxide, as well as benzo(a)pyrene, dioxins, and furans, among others, are emitted into the air [38–41]. For biomass, the most commonly emitted air pollutants are nitric oxide and VOC (recorded as total organic carbon, but also ammonia) [42–49]. Biomass burning is also a source of polycyclic aromatic hydrocarbons, as well as dioxins and furans [50,51].

Given the significant differences in the elemental composition of fossil fuels, such as hard coal and biomass, as well as the variations in the content of volatile substances, moisture, and ash, co-combustion of coal and biomass presents numerous technical and technological challenges. After the torrefaction process, biomass approaches hard coal in its composition and properties, which allows us to avoid many problems during the co-burning process of these fuels [52–54].

One of the additional problems in using biomass as fuel is its storage, in particular in the form of wood chips. The presence of wood dust triggers an explosion hazard [55]. Unfortunately, torrefied biomass is also the fuel that causes this problem. During storage, VOCs are released and can easily ignite. Several papers have been devoted to the issue of VOC release from torrefied biomass during storage [56–60]. The authors of these studies found the emission of dozens of VOCs during the storage of torrefied biomass. The most extensive list of emitted compounds was recently provided by Białowiec [42–46]. The study also included VOC emissions from the torrefaction process itself [61–66]. The emissions of CO, CO_2, as well as methane, formaldehyde, furfural, formic and acetic acid, and small amounts of hydrogen, ethane, propane, ethylene, acetone, propionic acid, and water were found. Methane, carbon monoxide, and formaldehyde had the largest share of the emissions. For example, according to Hronova's [65] research, the concentrations of CO in torgas may be 0.6–1.3%, methane 1.4–2.6%, and CO_2 2.6–3.8%. The other authors of all these works gave only the concentrations of the mentioned compounds, without relating them to the mass of the tested sample.

Alternatively, biological conversion can be employed, where torrefied biomass serves as a substrate for fermentation to produce biofuels, bioenergy, and biochemicals such as ethanol, butanol, acetone, and lipids. Figure 2 highlights how biomass can be transformed into renewable energy and valuable chemicals.

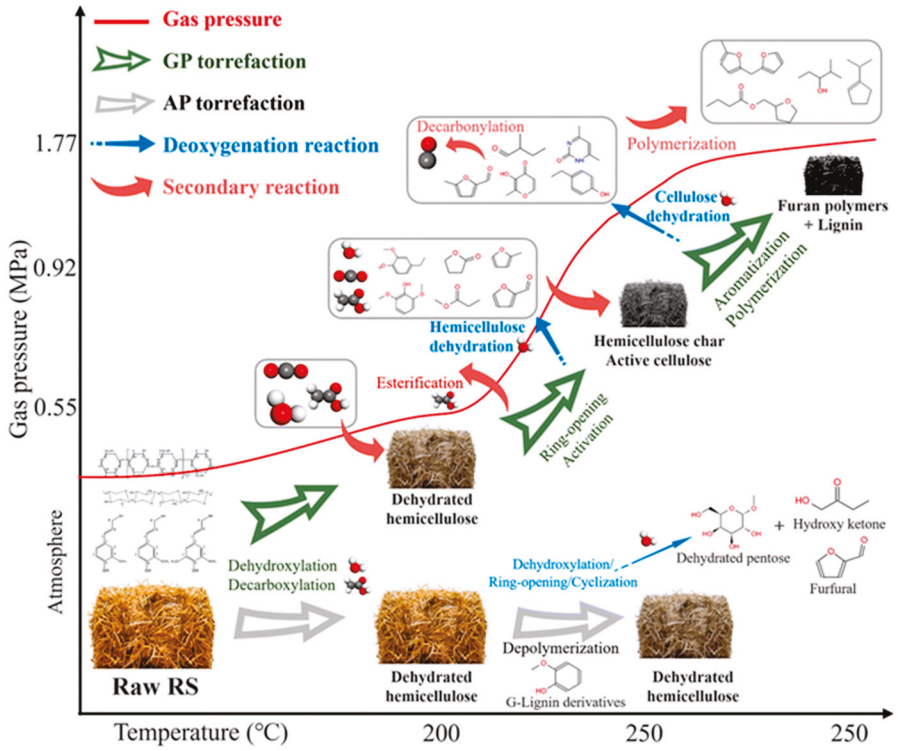


Figure 2. Chemical evolution mechanisms of biomass components during the torrefaction process [66].

The following types of agricultural biomass were tested: meadow hay, rye straw, and oat straw. The torrefaction process was carried out in a carbon dioxide atmosphere, which behaves as an inert gas under the chosen process conditions. This study's primary objective is to quantify total VOC emissions during torrefaction and assess how torrefaction at four temperatures (225, 250, 275, 300 °C) increases the heat of combustion of three agricultural residues (meadow hay, rye straw, and oat straw). Notably, it systematically compares these three feedstocks across multiple temperatures, directly coupling VOC emission measurements with changes in fuel energy content.

2. Materials and Methods

The first stage of research involved a technical analysis of the biomass, including the determination of its moisture and ash content. The biomass used in our experiments was Avena sativa (oat), Secale cereale (rye), and Sporobolus pumilus (meadow hay, also known as salt meadow hay). To determine the moisture content, 1–2 g samples were prepared and then dried at 105 °C for 24 h [67]. After this time, the samples were placed in a desiccator to cool down. This process was repeated until a constant weight of the samples was obtained. After drying, the samples were ground to a particle size of 3–5 mm. Figure 3a shows the samples placed in the dryer, and Figure 3b shows the samples placed in the desiccator after drying.

Moisture content in the biomass was calculated using the following formula [68]:

$$W = \frac{m_1 - m_2}{m_1 - m_3} \times 100 \quad (1)$$

where W—moisture content (%);
m_1—crucible weight with biomass before drying (g);
m_2—crucible weight with biomass after drying (g);
m_3—weight of the empty crucible (g).



(**a**) (**b**)

Figure 3. Samples of biomass during drying process (1—meadow hay, 2—rye straw, 3—oat straw): (**a**) placed in the dryer, (**b**) after drying.

The next stage of technical analysis involved determining ash content. For this purpose, the previously dried samples were placed in a muffle furnace LINN High Therm, (High Therm, Berlin, Germany) (1200 °C/50 Hz) at 815 °C ± 15 °C for 4 h [69]. After that time, the crucibles with ash were placed in a desiccator to cool down. Next, the samples were weighed on an analytical balance, and the results were recorded. Figure 4a shows samples placed in the muffle furnace, and Figure 4b shows samples in the desiccator after combustion.



(**a**) (**b**)

Figure 4. Samples during ash content determination (1—hay, 2—rye straw, 3—oat straw) (**a**) placed in a muffle furnace, (**b**) samples after combustion.

Ash content in the tested samples was determined using the following formula [70]:

$$A = \frac{m_5 - m_6}{m_4 - m_6} \times 100 \quad (2)$$

where A—ash content (%);
m_4—crucible weight with biomass before combustion (g);
m_5—crucible weight with biomass after combustion (g);
m_6—weight of the empty crucible (g).

At the second stage, a thermogravimetric analysis of biomass was conducted to determine the range of temperatures at which the torrefaction process would be examined and the total VOC emission would be measured. Before the thermogravimetric analysis, the samples were dried, and following, 10–20 mg samples were weighed and placed in a NETZSCH TG 209 F3 Tarsus thermogravimeter (Netzsch, Numberg, Germany). The

particle size of the material was 3–5 mm. The thermogravimetric analysis involved heating the biomass sample to 600 °C at a rate of 10 K/min, with an inert gas flow (nitrogen in this case) at a rate of 20 mL/min. In the research, the sample temperature and weight were continuously monitored and recorded using a computer program. For TGA and DTG analysis, we used NETZSCH Proteus Software (Version 7.1.0/04.02.2019, Build 7.1.19035.1). As a result of the analysis, a thermogravimetric curve was obtained. The curve was used to determine the temperature at which the weight loss of the samples was the highest [71–74].

After specifying the temperature range, the total VOC emissions were tested. To do this, a previously dried sample of 2–2.5 g was placed on quartz glass half-tubes and then inserted into an electric oven. The process was carried out at the following temperatures: 225, 250, 275, and 300 °C. Dutch researchers [64] both identify 220–300 °C as the "active torrefaction zone" for agricultural residues, where oxygen-to-carbon ratios drop rapidly and HHV increases most steeply. Broader ranges such as 200–350 °C have been studied (e.g., Libra et al., 2011 [18]), but they typically include two distinct regimes, mild torrefaction (200–230 °C) and severe carbonization (>300 °C). By concentrating at 225–300 °C, we capture the full spectrum of mild to moderate torrefaction reactions without overlapping into the pyrolysis-dominated regime, thus optimizing both yield and fuel quality [64].

Carbon dioxide gas was used as the inert gas with a flow rate of approximately 1 L/min [75]. The 1 L/min rate was chosen due to the closed system with the analyzer. At higher flow rates, the pressure in the system increased, causing the tube to spring back. At that time, the emission of total VOCs was measured using the standard [76] VOCs Total Hydrocarbon Analyzer Model 3-500 (J.U.M. Engineering Gmbh, Karlsfeld, Germany) stationary analyzer, which was connected to a computer equipped with appropriate software. The frequency of data reading was 10 s. Three replicates were performed for each type of biomass and each temperature. Typical sensitivity of J.U.M Model 3-700 FID Analyzer is 0.01 ppm CH_4. After the torrefaction process, the sample was weighed again to determine the weight loss. Figure 5a,b show a schematic of the experimental setup.

As a result of the tests, the emission of total VOC over time was determined. Based on this, the value of the emission index was calculated. The emission index determines the amount of emitted pollutants from the process. The total VOC emission index was calculated using the following formulas [77]:

$$w_{VOC} = \frac{Q_{CO_2} \cdot cm}{m} \tag{3}$$

$$\mathrm{c_m} = \frac{1}{\tau}\int_0^{\tau} \mathrm{c(t)}\cdot \mathrm{dt} \tag{4}$$

where Q_{CO_2}—carbon dioxide flow rate (m^3/s);
c_m—average VOC concentration (mg/m^3);
τ—torrefaction time (s);
m_p—weight of the sample subjected to torrefaction (g).

Figure 6 shows a sample placed on a quartz glass half tube before and after the torrefaction. Heat of combustion measurements were performed in a Parr 6400 calorimeter (PARR, Moline, IL, USA). The samples, weighing approximately 1 g, were pressed.

The reaction kinetics of oat straw, meadow hay, and rye straw were evaluated based on thermogravimetric analysis (TGA) using NETZSCH Kinetics Neo 3 software. This software enables the determination of reaction rate constants, activation energy profiles, and pre-exponential factors from non-isothermal thermal decomposition data. The kinetic analysis provided insights into the decomposition behavior of the selected biomass

types during torrefaction, allowing for the modeling of their temperature-dependent degradation mechanisms.

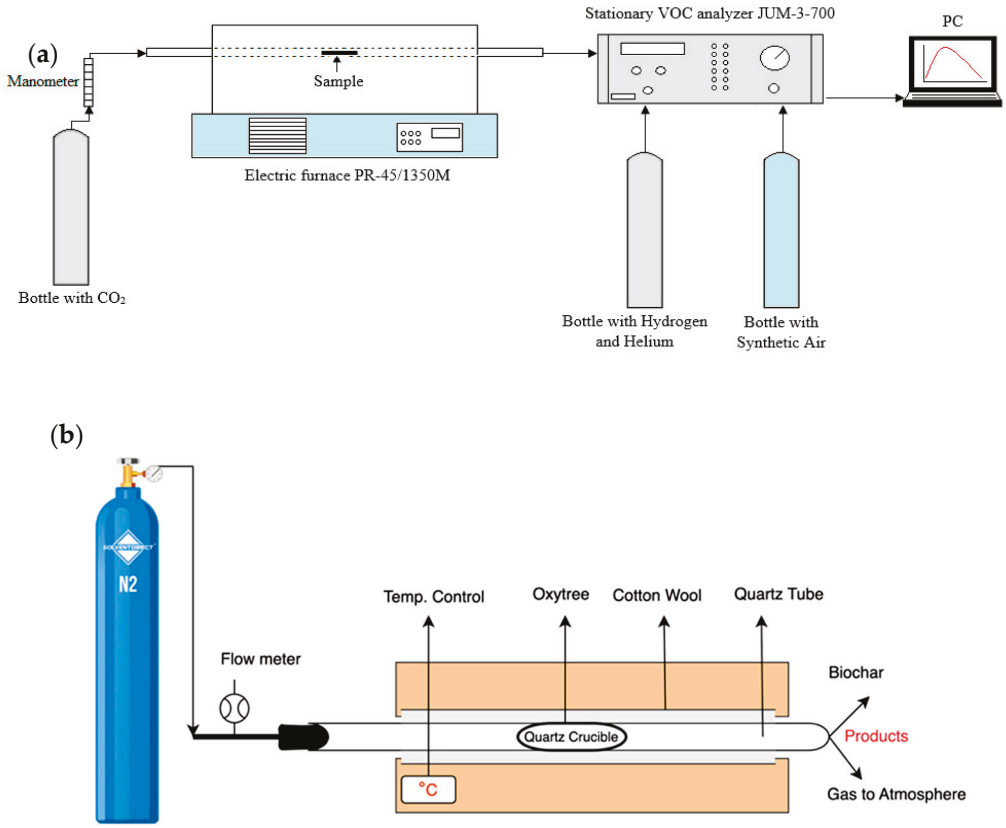


Figure 5. (**a**) Schematic of the experimental setup for total VOC emission measurement and (**b**) Electrical Furnace PR-45/135M with possible use of CO_2/N_2 gases.



Figure 6. The quartz glass half tubes with meadow hay samples before and after torrefaction.

Two model-free (isoconversional) methods were employed: the Ozawa–Flynn–Wall (OFW) method and the Vyazovkin method. The Ozawa–Flynn–Wall method, on the other hand, is an integral isoconversional method that estimates activation energy without assuming a reaction model. The Vyazovkin method further refines the model-free approach by minimizing the integral discrepancy across heating rates for each conversion level, improving the reliability of Ea determination.

In addition to these model-free methods, the model-fitting approach was applied using an nth-order reaction model, which assumes a single-step reaction mechanism and enables the estimation of the overall reaction order (n), activation energy (Ea), and pre-exponential factor (A). These kinetic parameters were obtained by fitting the experimental TGA data.

The combination of model-free and model-fitting approaches enabled a robust kinetic evaluation, facilitating the comparison of thermal stability and reactivity among the tested biomass samples.

3. Results and Discussion

As previously mentioned, the first stage of research involved determining the moisture content of the biomass samples being studied. Table 1 presents the values of moisture content.

Table 1. The content of moisture and ash in the tested biomass samples.

Biomass	Moisture Content (%)	Ash Content (%)
Meadow hay	10.88 ± 0.54	3.00 ± 0.10
Rye straw	10.81 ± 0.62	1.63 ± 0.01
Oat straw	8.82 ± 0.33	2.99 ± 0.02

Based on the above results, the highest moisture contents are characteristic of hay and rye straw, which exceed 10%, at 10.88% and 10.81%, respectively. Moisture content in oat straw was 8.82%. Both straw and hay were collected after harvest time between August and September. The samples used for the tests were seasoned for six months under shelter. Dry torrefaction has an allowance of around 10% moisture. Pyrolysis, which is applied at higher temperatures, results in higher mass loss and requires higher energy to process. HTC might be a better choice for high-humidity samples; however, 10% is acceptable for dry torrefaction and a safer process, especially in applications with lower pressures.

The next stage of the technical analysis of biomass involved determining the ash content in the samples. Results are given in Table 1. The highest ash content was reported for hay and oat straw, and was 3.00% and 2.99%, respectively. The smallest content of ash after the combustion process was documented for rye straw—1.63%. At the second stage of research, a thermogravimetric analysis was performed. Based on thermogravimetric curves, the temperature range for total VOC emissions was determined.

Figures 7 and 8 show the thermogravimetric curves for the three tested types of biomass. The maximum mass loss rate was observed at 342.4 °C for rye straw. For oat straw, this temperature was 336.6 °C, and for meadow hay, it was 326.5 °C. The most significant weight loss in the tested biomass samples occurred at temperatures higher than 320 °C. For all analyzed biomass samples, no significant changes were observed after exceeding the elevated temperatures. The weight of the samples decreased, however, at a small rate. It follows from the thermogravimetric curves that approximately 70% of the weight loss of the tested samples occurs at temperatures up to 300 °C. Accordingly, it was decided that the measurement of total VOC emissions will be carried out for four temperatures: 225 °C, 250 °C, 275 °C, and 300 °C.

The kinetic analysis was conducted using the specialized NETZSCH Kinetics Neo software, a tool designed to extract reaction kinetics from temperature-dependent experimental data. This software enables the quantitative evaluation of chemical reaction rates and the influence of various thermal conditions, providing critical insights into the mechanistic pathways of complex reactions. By incorporating multiple variables that affect reaction rates, such as activation energy, reaction order, and pre-exponential factors, Kinetics Neo facilitates the development of robust kinetic models that accurately reflect the system's behavior across a wide range of temperatures. In the context of this study, the software was utilized to model the torrefaction behavior of biomass, enabling the prediction of system responses under user-defined thermal scenarios. Such kinetic modeling is essential not

only for understanding the decomposition mechanisms of lignocellulosic materials but also for optimizing process parameters in thermochemical conversion technologies.

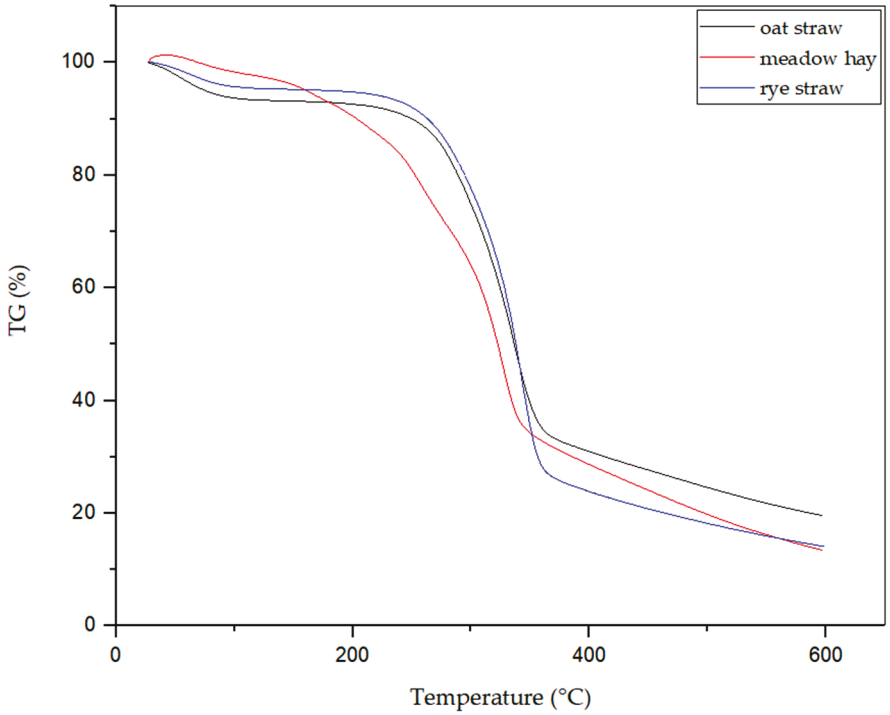


Figure 7. TGA analysis of all 3 biomasses: oat straw, meadow hay, and rye straw.

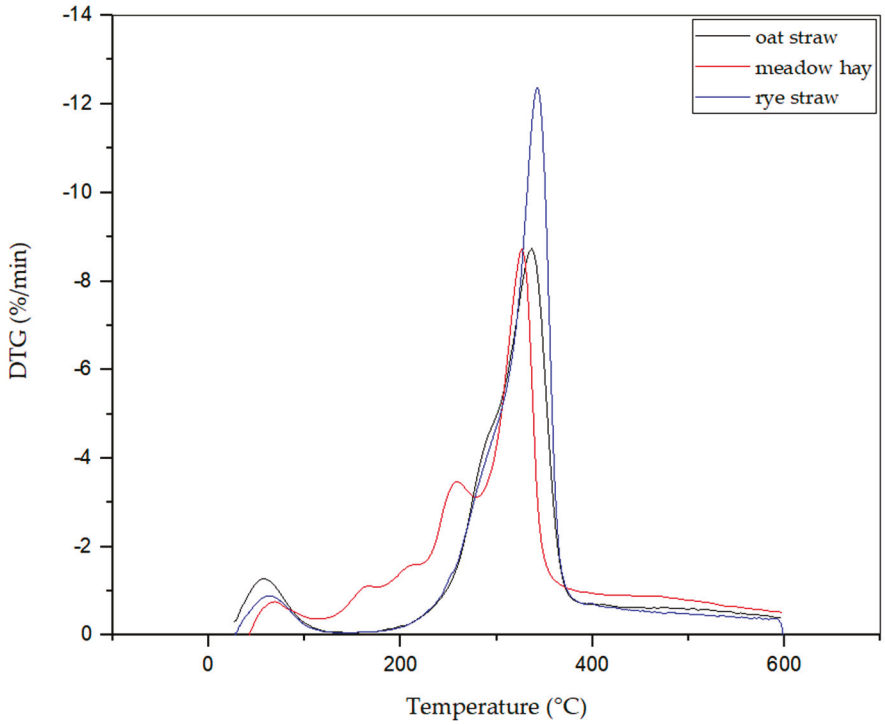


Figure 8. DTG analysis of all 3 biomasses: oat straw, meadow hay, and rye straw.

The comparison of reaction kinetics parameters derived from different biomass samples (rye straw, meadow hay, and oat straw) reveals notable variations in their thermal degradation behavior, as summarized in Table 2. Among the three, rye straw exhibited the highest activation energy (106.904 kJ/mol), suggesting greater thermal resistance and

a higher energy barrier for decomposition. In contrast, meadow hay demonstrated the lowest activation energy (63.166 kJ/mol), indicating that it decomposes more readily under thermal treatment, which may reflect differences in biochemical composition, such as lower lignin content or higher volatile fractions.

Table 2. Reaction kinetics parameters for different methods.

Parameter	Zyto	Siamo	Owies
Nth-Order Activation Energy (kJ/mol)	106.904	63.166	88.371
Nth-Order Log(PreExp)	7.575	3.807	5.946
Nth-Reaction Order (n)	5.29	3.603	3.719
R^2 (Nth Order)	0.99436	0.99548	0.99429
R^2 (Friedman)	0.98871	0.99779	0.98053
R^2 (Ozawa–Flynn–Wall)	0.99999	1	1
R^2 (Vyazovkin)	0.99045	0.99763	0.99158

The pre-exponential factor (log A) followed a similar trend, being highest for rye straw (7.575), moderate for oat straw (5.946), and lowest for meadow hay (3.807), which aligns with their respective activation energies and reflects the frequency of molecular collisions leading to the reaction. Reaction orders (n) were also distinct, with rye straw displaying a notably higher value (5.29) compared to meadow hay (3.603) and oat straw (3.719), implying a more complex reaction mechanism or multi-step degradation pathway in rye straw.

Regarding the goodness-of-fit (R^2 values), all three biomass types showed strong correlations in the nth-order model ($\geq$0.994), with meadow hay slightly outperforming others (R^2 = 0.99548). Across model-free methods, the Ozawa–Flynn–Wall approach yielded perfect or near-perfect fits for all samples (R^2 = 1.00 for meadow hay and oat straw; 0.99999 for rye straw), highlighting its robustness. The Friedman method showed the lowest R^2 for oat straw (0.98053), possibly due to higher sensitivity to noise in derivative-based data. The Vyazovkin model confirmed consistent trends, with meadow hay again showing the best fit (R^2 = 0.99763), indicating high reliability of the kinetic data.

Overall, meadow hay appears to offer a more kinetically favorable profile for thermochemical processes due to its lower activation energy and consistent model fits. In contrast, rye straw's high activation energy and complex kinetics may require more energy-intensive processing conditions. These findings provide a strong basis for selecting appropriate feedstocks and optimizing conditions in biomass torrefaction systems.

Figures 9–11 present the reaction rate profiles of oat straw, meadow hay, and rye straw, respectively, under varying heating rates (10, 20, and 30 K/min). Among the three, oat straw (Figure 9) exhibited the highest peak reaction rate (0.0028 s^{-1} at 30 K/min), followed by meadow hay (Figure 10) and rye straw (Figure 11), which showed the lowest maximum rate. Moreover, the peak degradation temperature increased with the heating rate for all samples; however, rye straw consistently required a higher temperature to reach its maximum reaction rate, indicating greater thermal stability. This is consistent with the higher activation energy values observed in rye straw.

Figures 12–14 display the variation in activation energy (Ea) with conversion (α) using the Ozawa–Flynn–Wall method. Oat straw (Figure 12) showed a decreasing trend in Ea from approximately 300 kJ/mol at low conversion to 100 kJ/mol beyond α = 0.4, reflecting the typical behavior of heterogeneous biomass decomposition. Meadow hay (Figure 13) exhibited a relatively stable Ea profile, fluctuating mildly between 50 and 200 kJ/mol across most of the conversion range, suggesting a more uniform degradation mechanism. In contrast, rye straw (Figure 14) exhibited significant fluctuations in activation energy,

including sharp peaks and negative values near $\alpha = 0.6–0.7$, which may be attributed to complex, overlapping reactions or secondary decomposition steps.

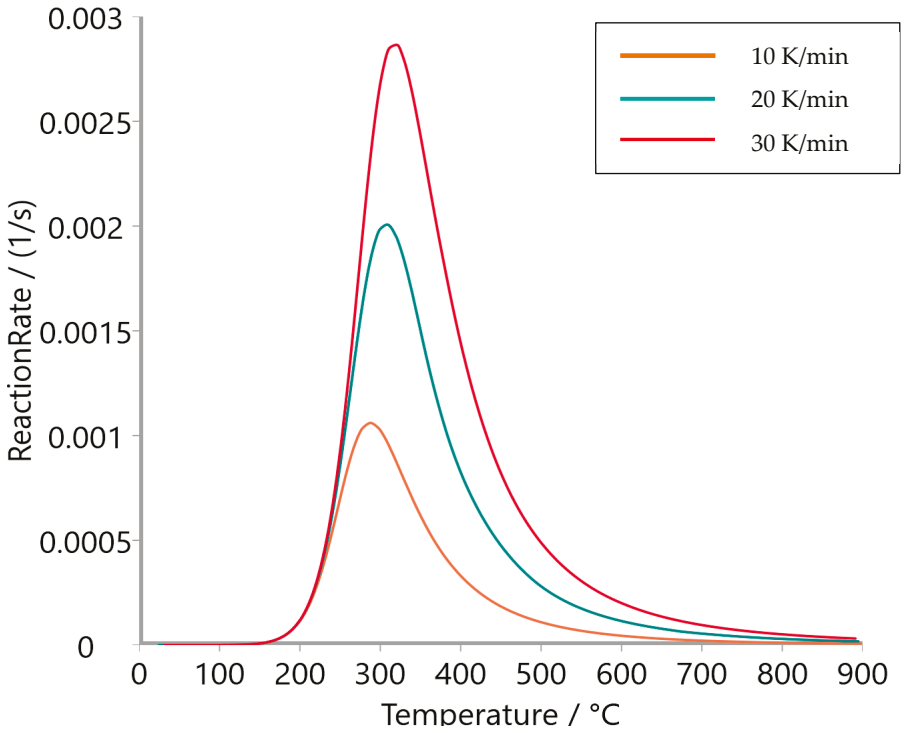


Figure 9. Reaction rate of oat straw.

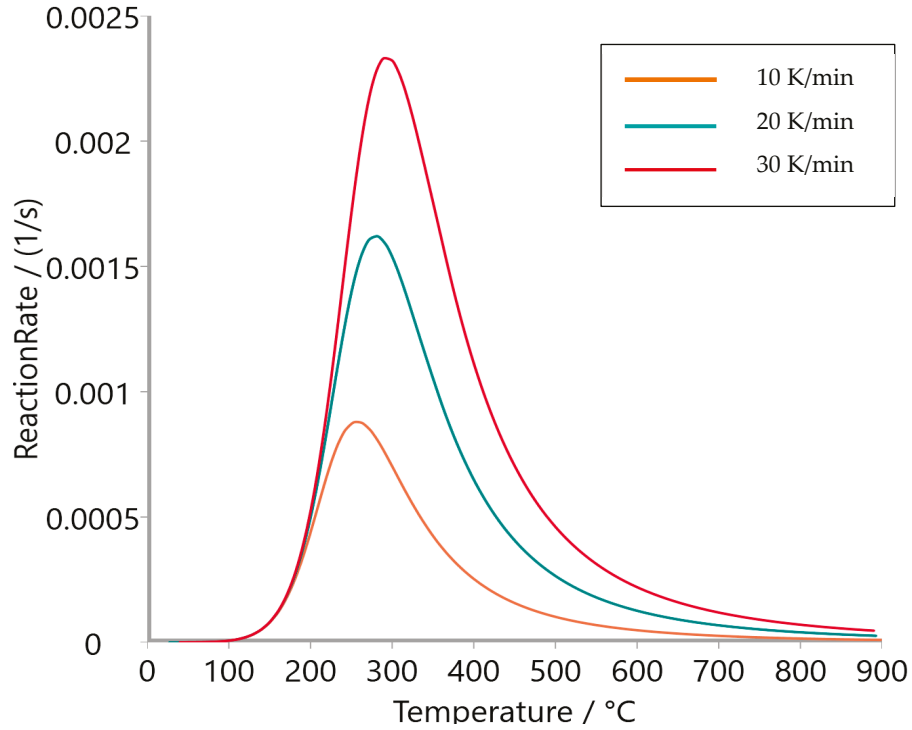


Figure 10. Reaction rate of meadow hay.

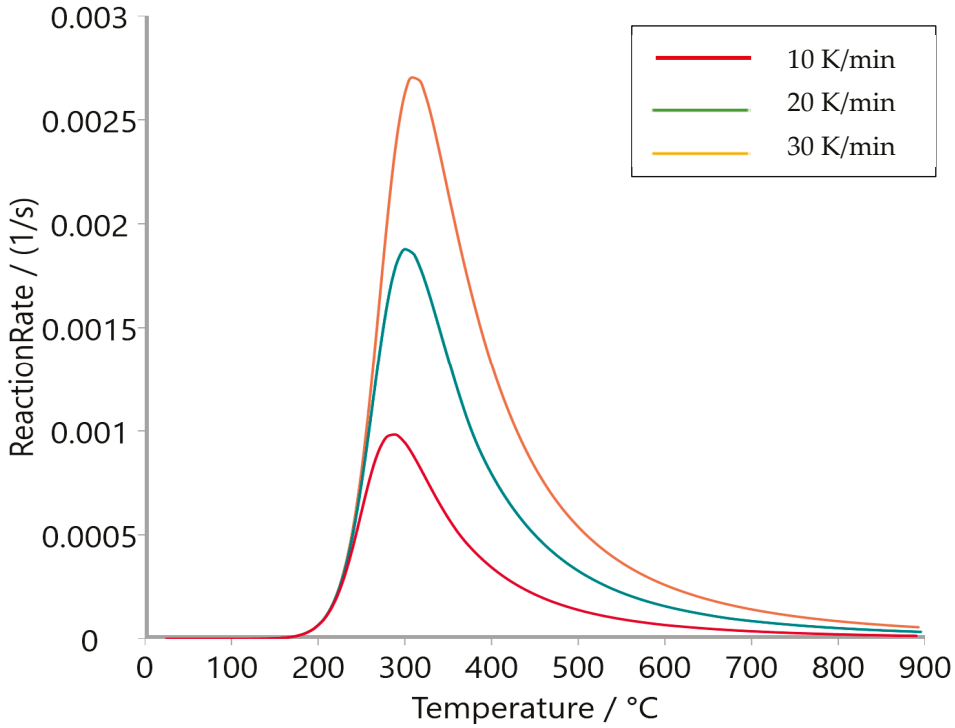


Figure 11. Reaction rate of rye straw.

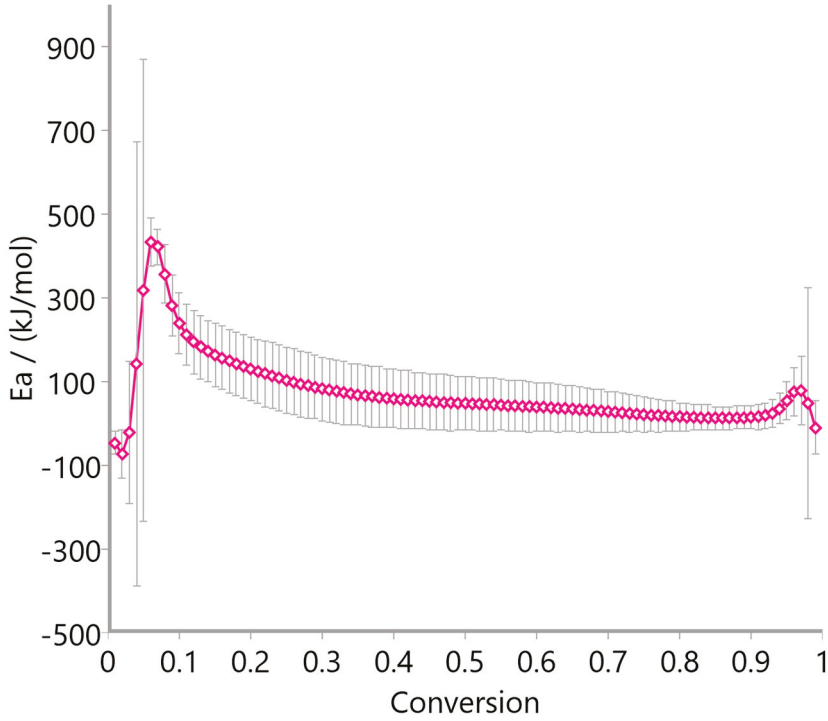


Figure 12. Activation Energy of oat straw using the Ozawa–Flynn–Wall method.

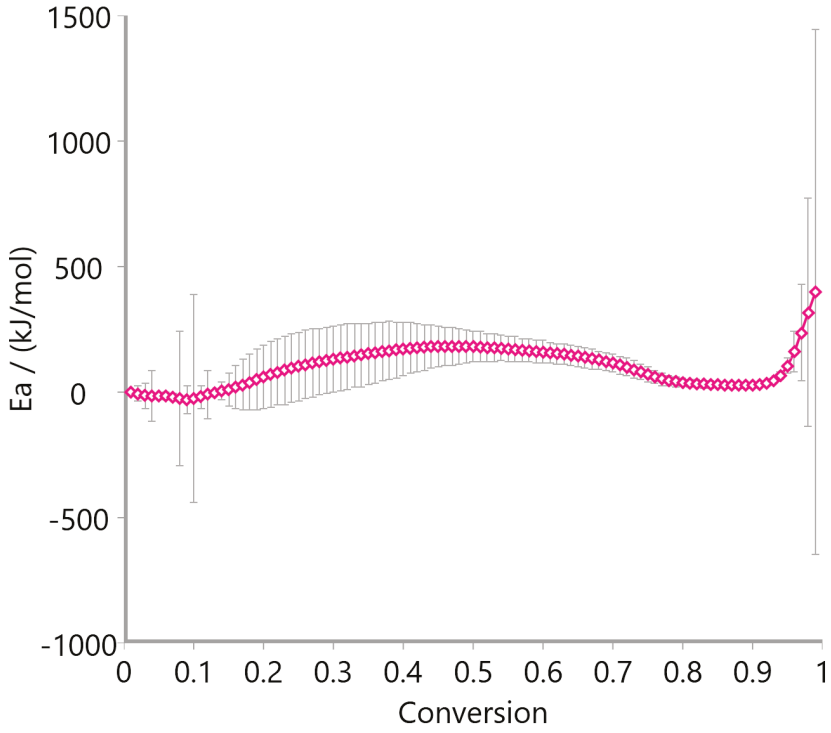


Figure 13. Activation energy of meadow hay using the Ozawa–Flynn–Wall method.

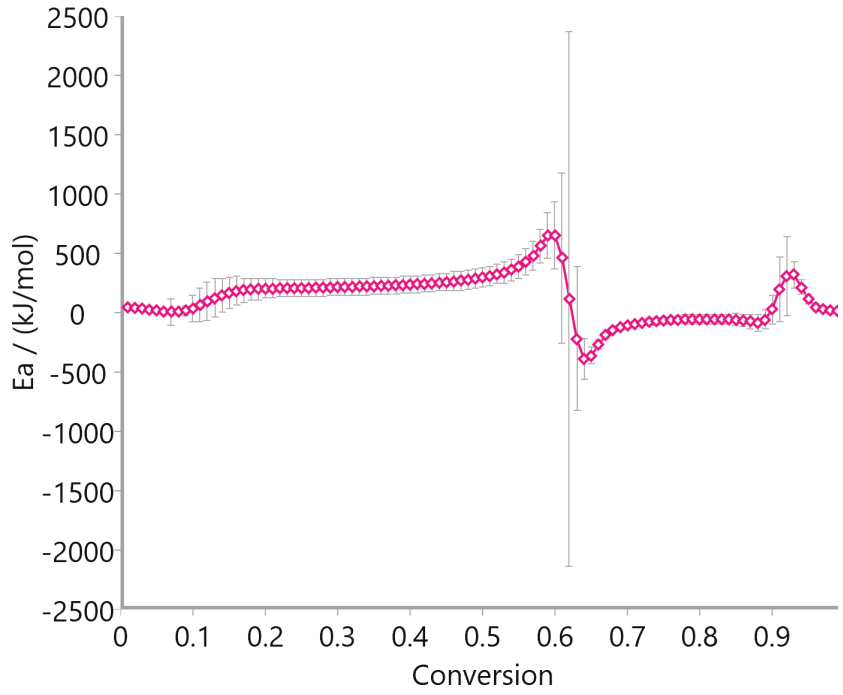


Figure 14. Activation energy of rye straw using Ozawa–Flynn–Wall method.

The pre-exponential factor (log A), calculated via the Vyazovkin method and presented in Figures 15–17, further supports the kinetic complexity of these materials. Oat straw (Figure 15) and meadow hay (Figure 16) both showed a declining trend in log A with increasing conversion, stabilizing around log A = 10–20 beyond a 0.5 conversion fraction. This trend is indicative of progressively slower molecular dynamics as the reaction proceeds. Conversely, rye straw (Figure 17) exhibited erratic behavior in log A values, with sharp deviations and a pronounced drop around $\alpha = 0.6$, mirroring the instability seen in its activation energy curve.

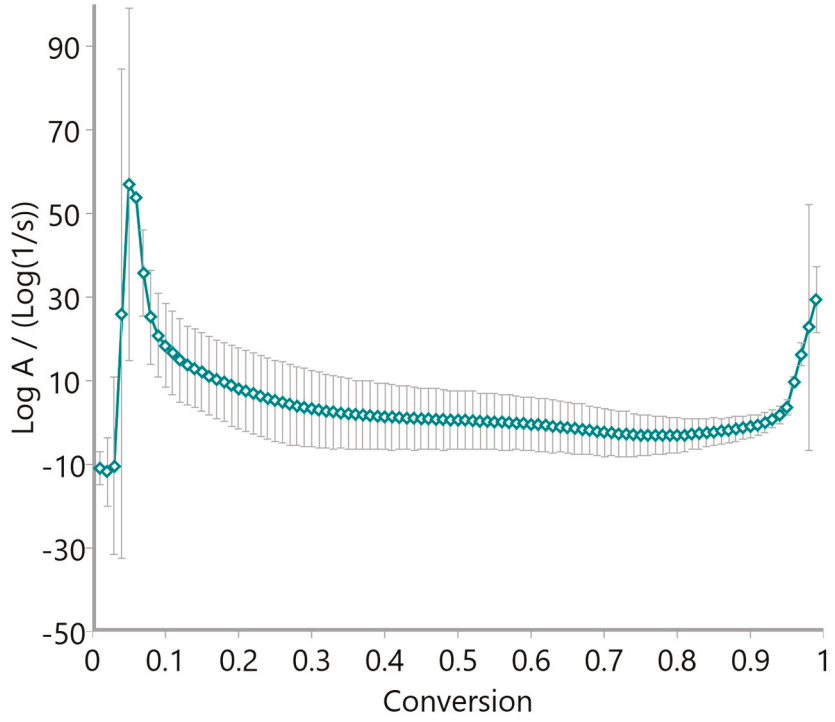


Figure 15. Pre-exponential factor of oat straw using the Vyazovkin method.

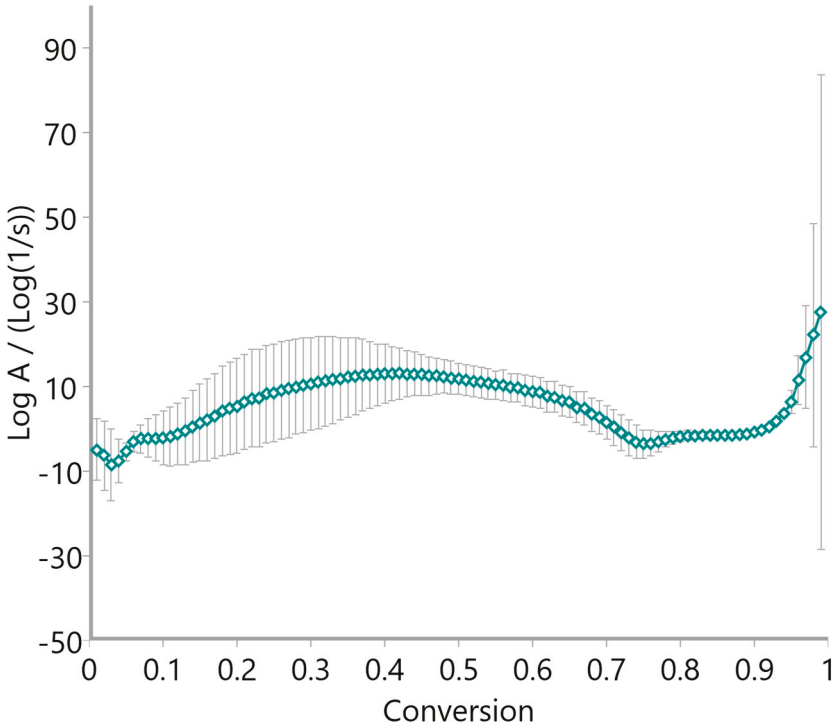


Figure 16. Pre-exponential factor of meadow hay using the Vyazovkin method.

Collectively, these figures highlight that meadow hay possesses the most kinetically consistent degradation behavior, likely due to its more homogeneous composition. Oat straw displays intermediate behavior, while rye straw is characterized by thermally resistant and kinetically complex decomposition, likely involving multiple reaction pathways and secondary processes. These differences have direct implications for the optimization of thermal conversion processes such as torrefaction or pyrolysis.

The investigation of total VOC emissions enabled the determination of emissions during the torrefaction process. The first sample that was tested was meadow hay (Figure 18).

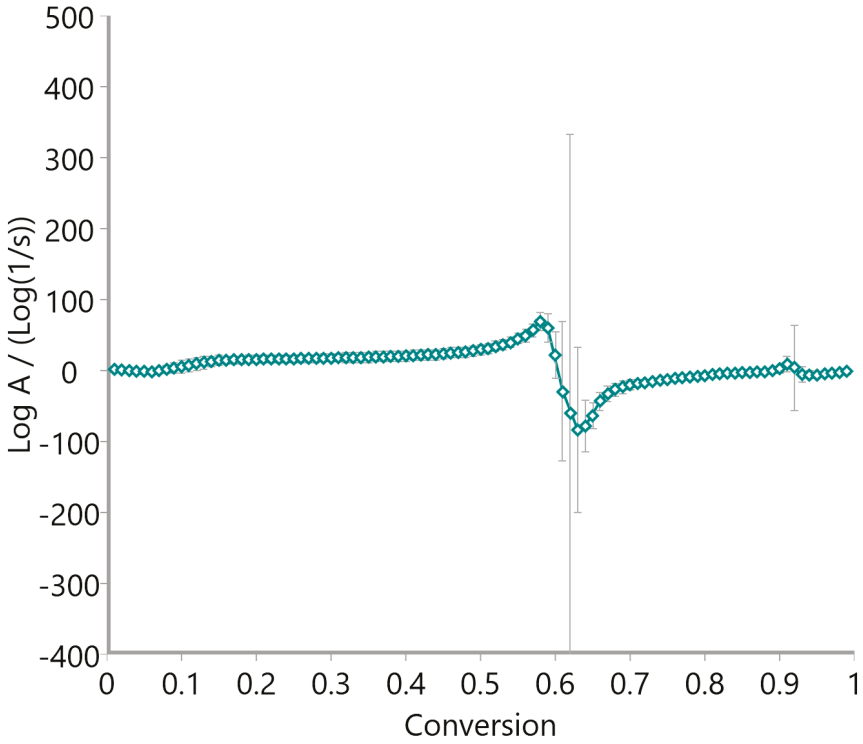


Figure 17. Pre-exponential factor of rye straw using the Vyazovkin method.

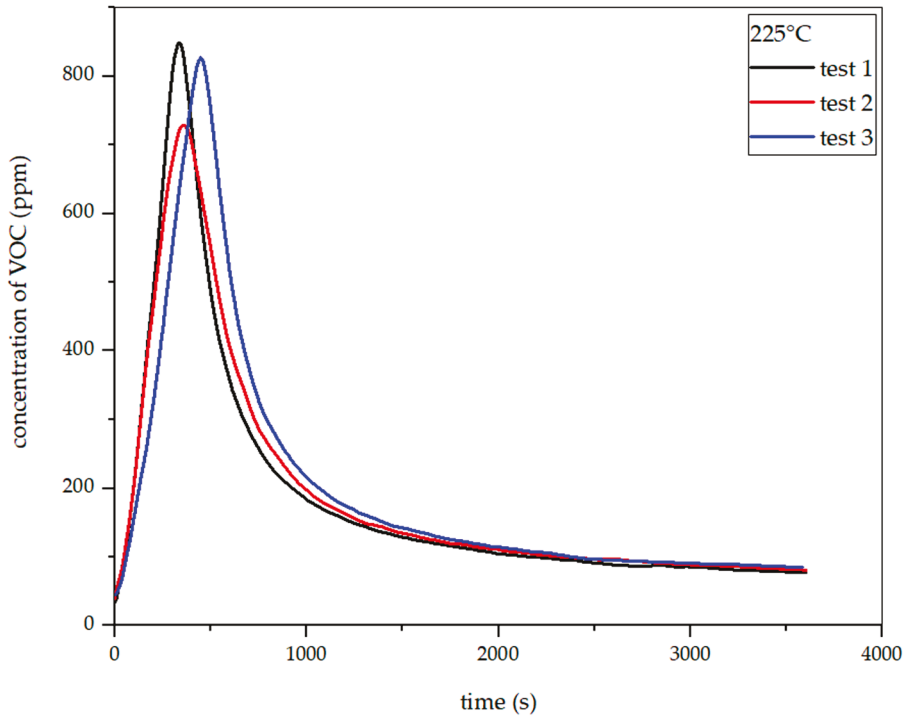


Figure 18. Dependence of total VOC emission on time for hay torrefaction at 225 °C.

Figures 19–21 show the dependence of total VOC emissions on time at subsequent temperatures for hay. The graphs show that the emissions increase with temperature. At 225 °C, the highest emission was approximately 850 ppm, occurring at the 330th second of the process. At 250 °C, the emission increased to about 1500 ppm in the 304th second.

At 275 °C, the highest emission was observed in the 283rd second and amounted to about 2050 ppm. At 300 °C in the 247th second, this value increased to about 2700 ppm.

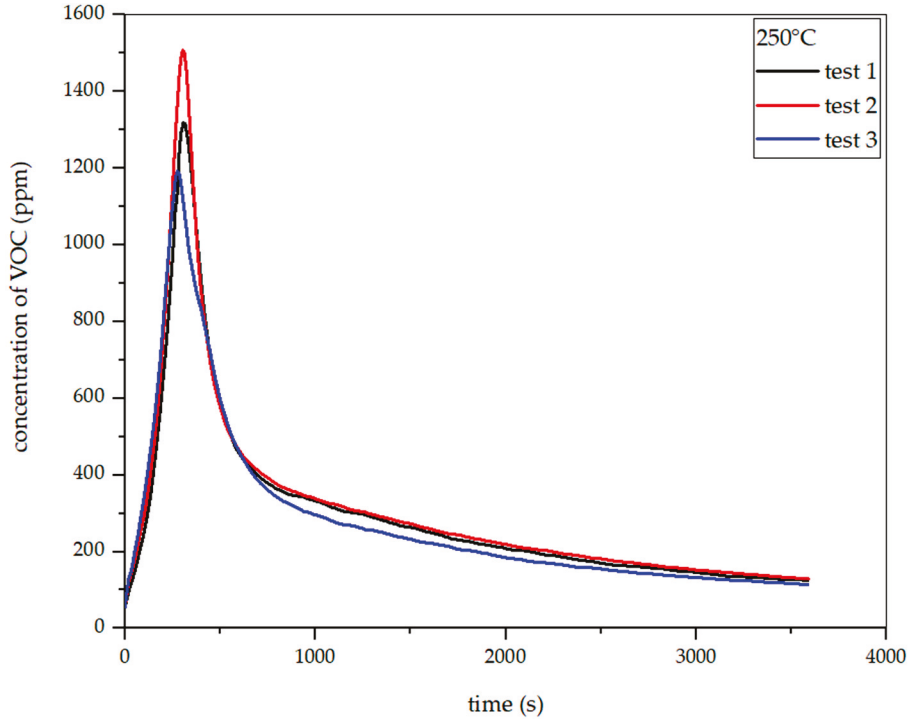


Figure 19. Dependence of total VOC emission on time for hay torrefaction at 250 °C.

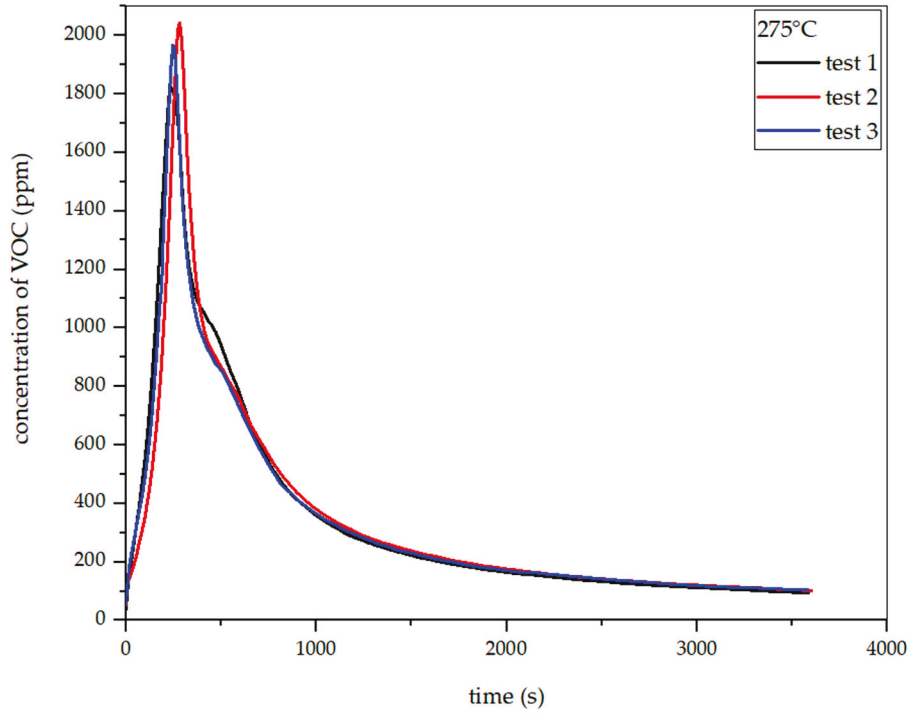


Figure 20. Dependence of total VOC emission on time for hay torrefaction at 275 °C.

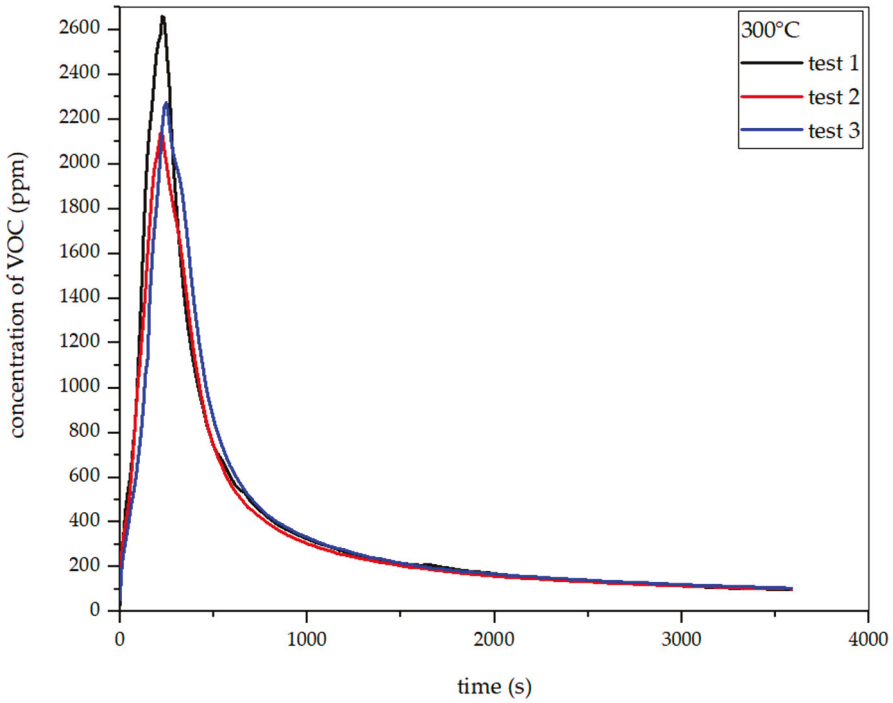


Figure 21. Dependence of total VOC emission on time for hay torrefaction at 300 °C.

Figures 22–25 show the dependence of total VOC emission on time at given temperatures for rye straw. Based on the diagrams, it can be observed that the emission increases with temperature, as in the case of hay. At 225 °C, the highest emission amounted to about 360 ppm in the 420th second of the process. At 250 °C, the emission increased to about 1000 ppm in the 330th second. At 275 °C, the highest emission was observed at the 342nd second, reaching approximately 1960 ppm. At 300 °C, in the 254th second, this value increased to about 2950 ppm. Based on the above-presented results, the total VOC emission index for rye straw was determined.

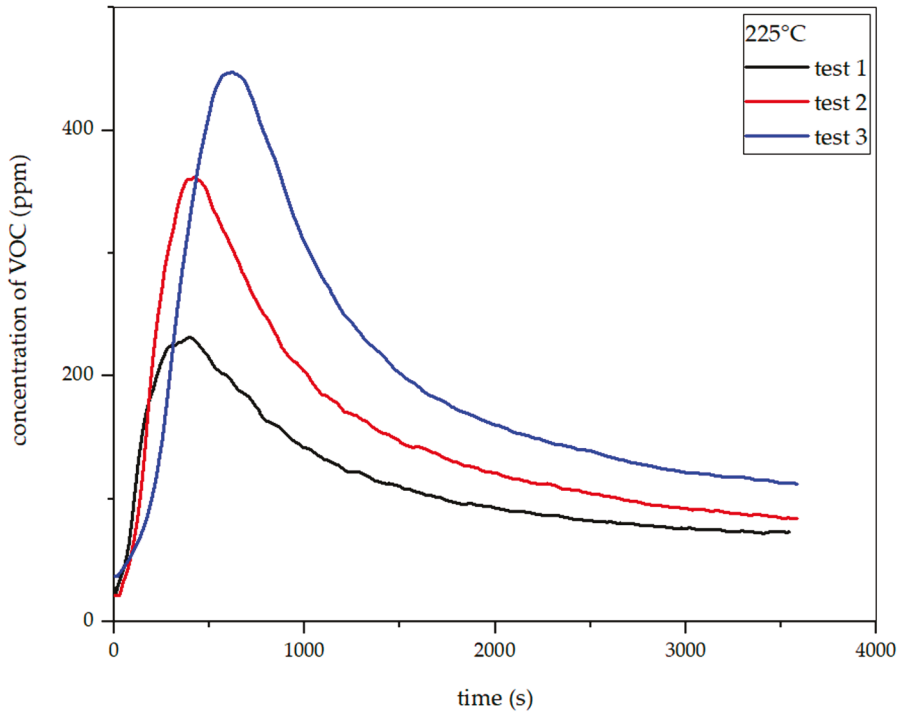


Figure 22. Dependence of total VOC emission on time for rye straw torrefaction at 225 °C.

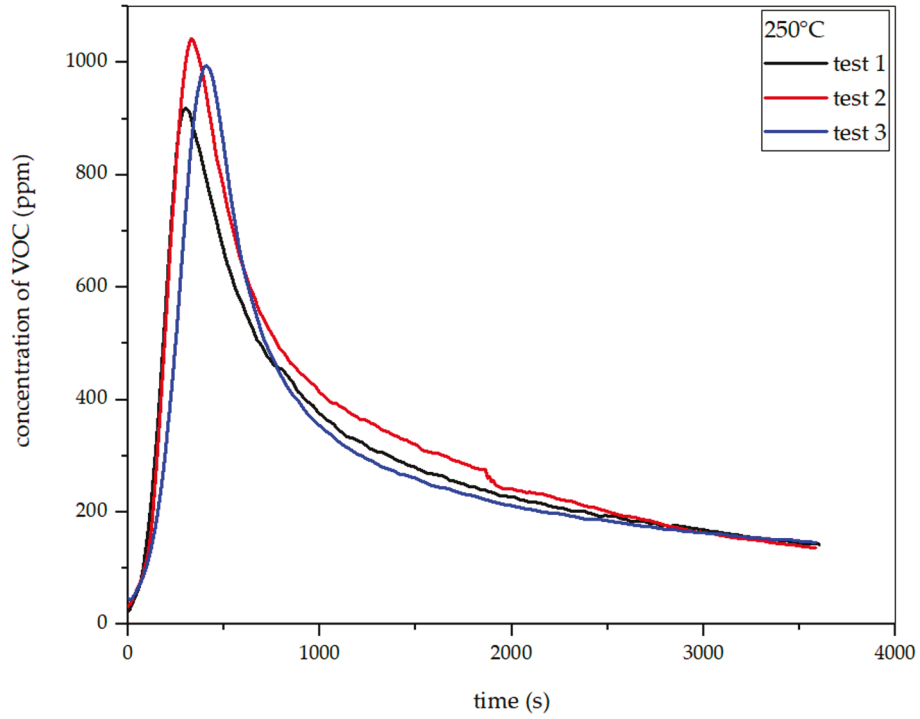


Figure 23. Dependence of total VOC emission on time for rye straw torrefaction at 250 °C.

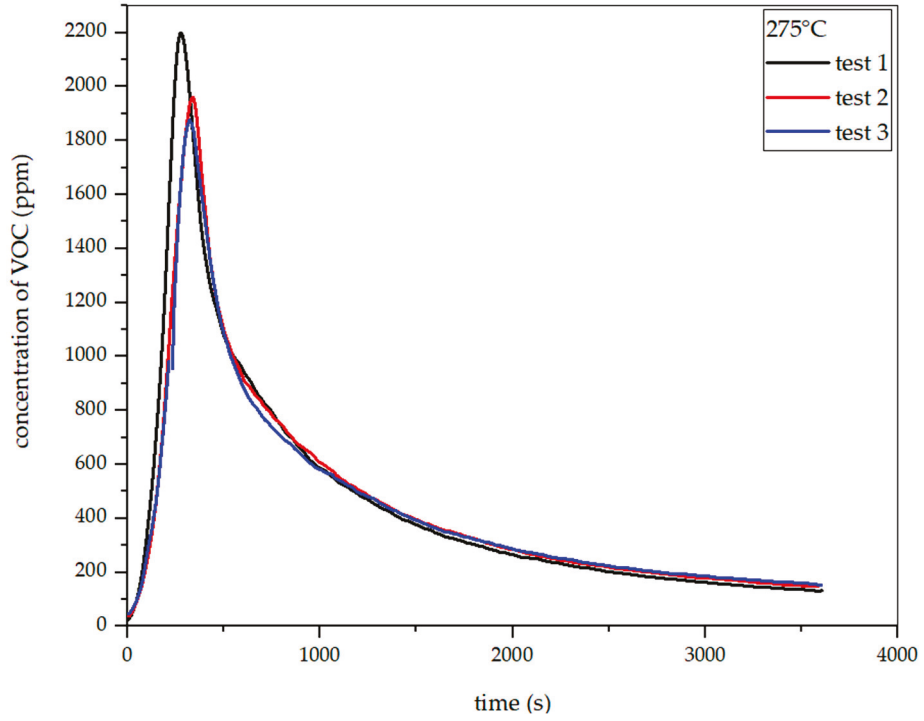


Figure 24. Dependence of total VOC emission on time for rye straw torrefaction at 275 °C.

Figures 26–29 show the dependence of total VOC emission on time at different temperatures for oat straw. It follows from these diagrams that the dependence of VOC emission on temperature is the same as in the two previous cases. At 225 °C, the highest emission was about 700 ppm in the 480th second of the process. At 250 °C, the emission increased to about 1200 ppm in the 256th second. At 275 °C, the highest emission was observed at the 245th second, with a value of around 1700 ppm. At 300 °C in the 303rd second, the emission grew to about 3700 ppm. Based on the results presented above, the total VOC emission index for oat straw was calculated.

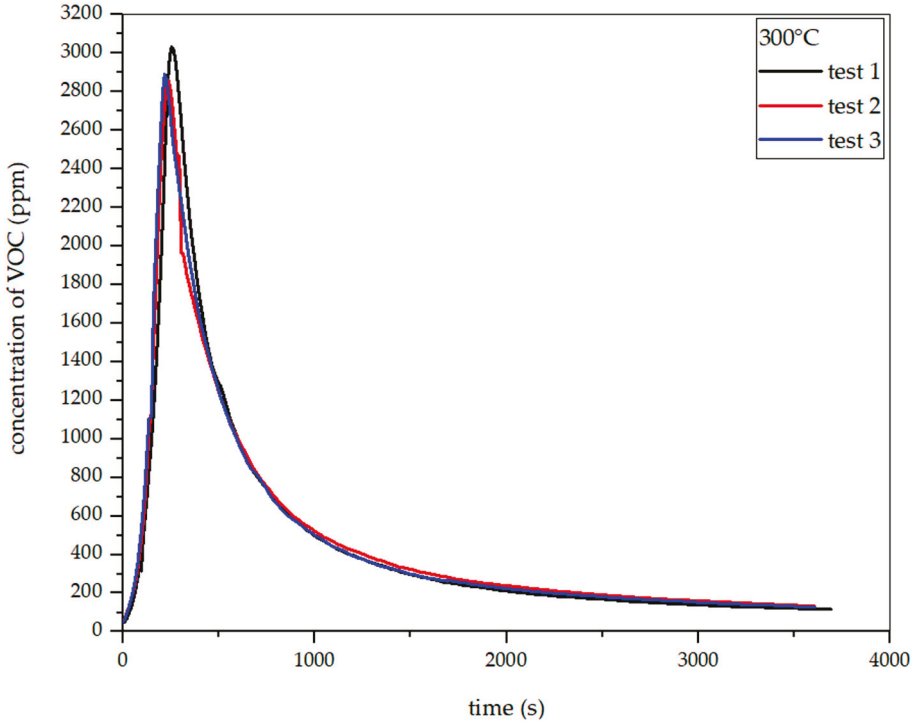


Figure 25. Dependence of total VOC emission on time for rye straw torrefaction at 300 °C.

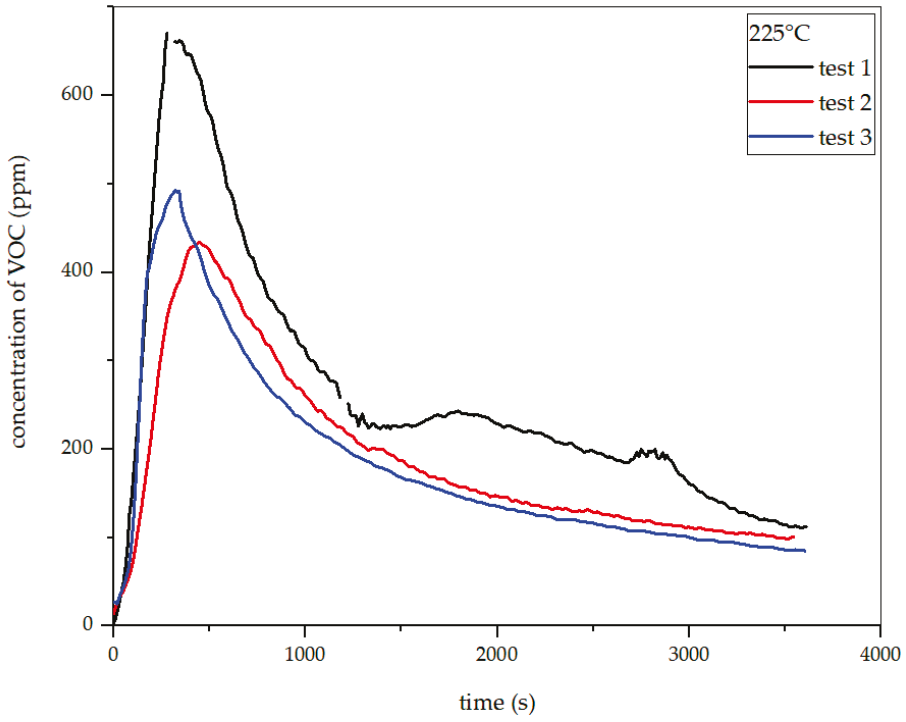


Figure 26. Dependence of total VOC emission on time for oat straw torrefaction at 225 °C.

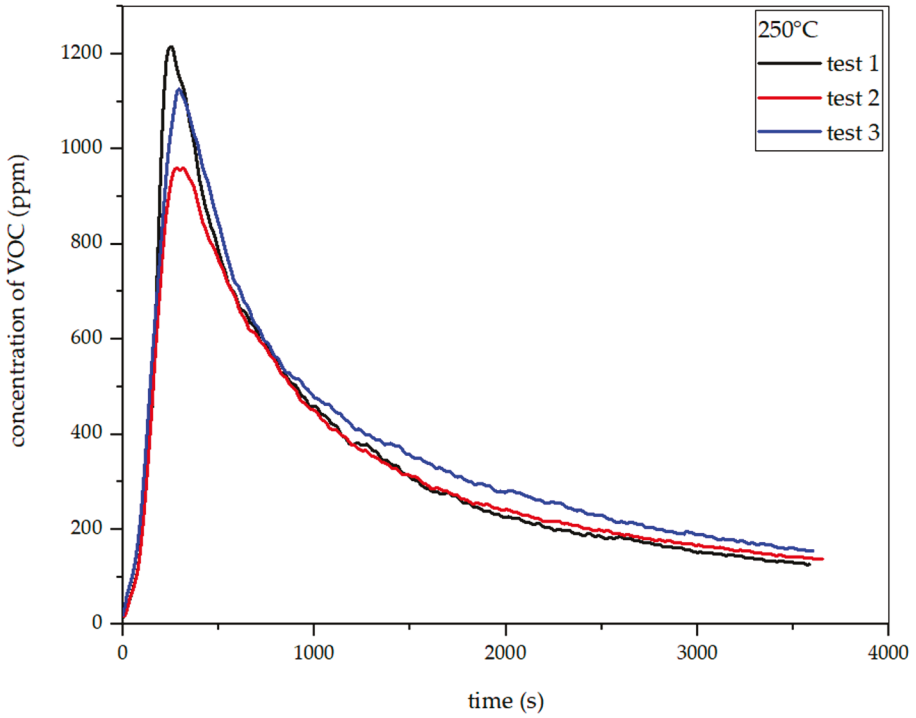


Figure 27. Dependence of total VOC emission on time for oat straw torrefaction at 250 °C.

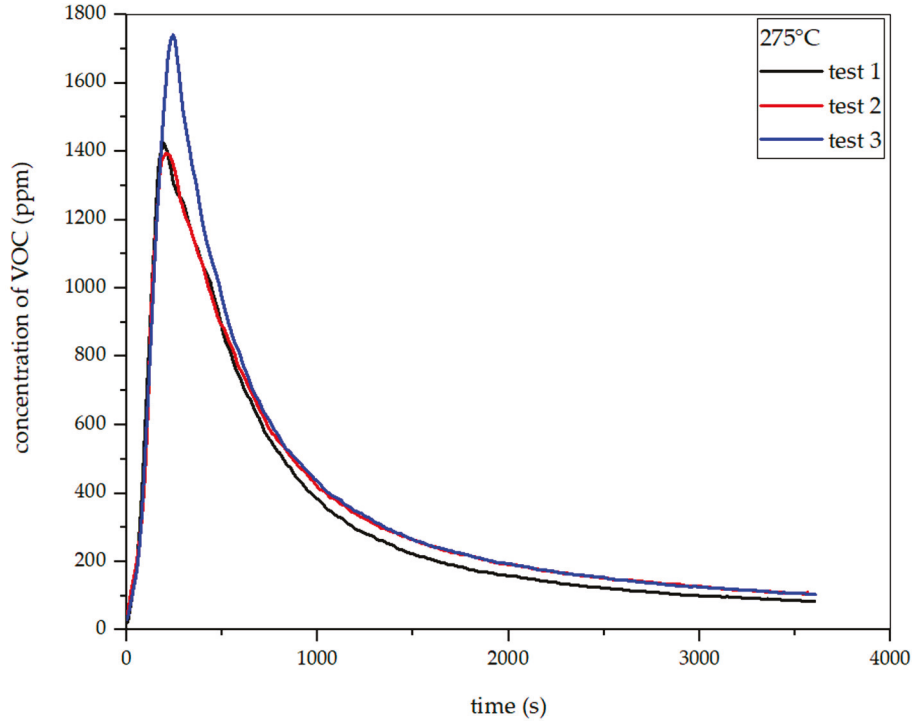


Figure 28. Dependence of total VOC emission on time for oat straw torrefaction at 275 °C.

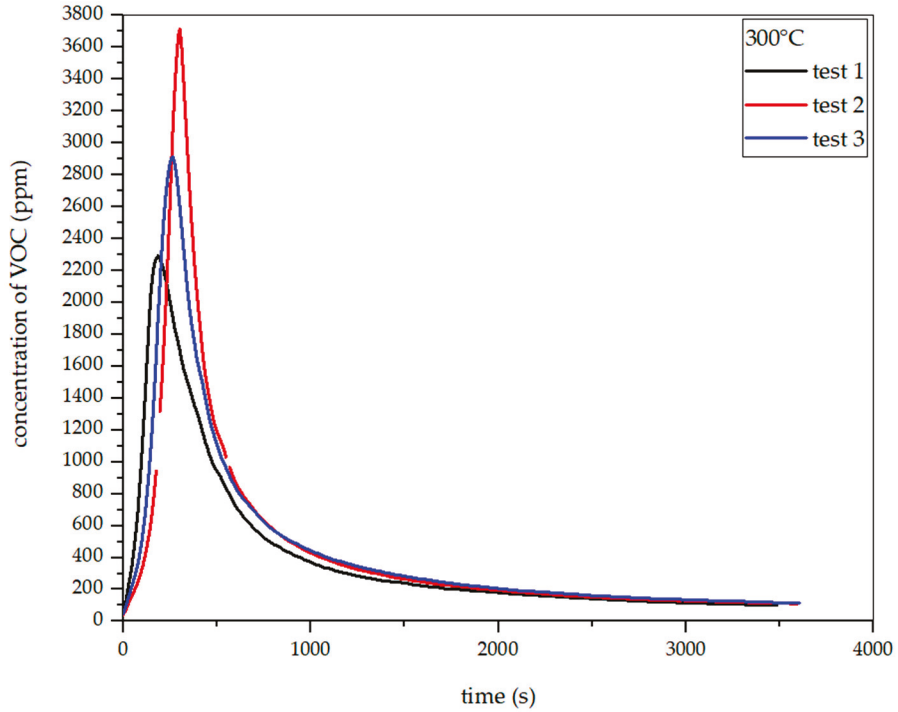


Figure 29. Dependence of total VOC emission on time for oat straw torrefaction at 300 °C.

The VOC emission factor from the torrefaction process ranged from slightly more than 2 to nearly 10 mg/g of torrefied biomass (depending on the type of biomass and temperature). Assuming, after results of Hroncova [65] and Mehrabian [66], that the main volatile components of torgas are methane and carbon monoxide, and considering the heat of combustion of methane (approx. 50 MJ/kg) [78] and carbon monoxide (approx. 10 MJ/kg), it is possible to estimate the energy emission factor contained in torgas [79]. Based on the literature, the CH_4:CO ratio can be rounded to be approximately 3:1. Hence, the average heat of combustion of torgas will be approximately 40 MJ/kg. If the emission of VOCs from the torrefaction process is 2–10 mg/g, this torgas will be a source of 80–400 kJ/kg of torrefied biomass, as shown in Table 3.

Table 3. VOC emission index for different torrefaction temperatures for 3 samples.

Temperature (°C)	Hay (Mean ± SD)	Rye Straw (Mean ± SD)	Oat Straw (Mean ± SD)
225	3.88 ± 0.12	3.03 ± 0.80	4.35 ± 0.83
250	5.49 ± 0.27	6.12 ± 0.38	6.78 ± 0.25
275	6.47 ± 0.03	8.54 ± 0.13	6.40 ± 0.60
300	7.04 ± 0.26	9.36 ± 0.06	7.84 ± 0.50

Calculated weight losses for oat straw after the torrefaction are shown in Table 4.

Table 4. Weight losses for oat straw.

Temperature (°C)	Hay (Mean ± SD)	Rye Straw (Mean ± SD)	Oat Straw (Mean ± SD)
225	39.76 ± 2.10	32.78 ± 1.46	42.12 ± 16.72
250	58.03 ± 4.69	82.63 ± 3.47	53.63 ± 12.90
275	69.09 ± 2.75	79.78 ± 5.89	72.99 ± 5.29
300	78.57 ± 5.88	84.01 ± 2.00	83.76 ± 6.39

The weight loss of oat straw ranged from 28 to 87%. The relationships between temperature and weight loss were the same as in the case of the two other types of biomass. Rye straw torrefaction resulted in weight loss ranging from 31 to 86%, depending on the process temperature. The same dependence of weight loss on temperature as for hay was observed. During the torrefaction of hay, weight loss ranged from 37 to 84% depending on temperature. The weight loss increased with temperature.

The final stage of the research involved determining the heat of combustion of the tested samples before and after the torrefaction process [54,80]. The torrefied samples are shown in Figures 30–32.

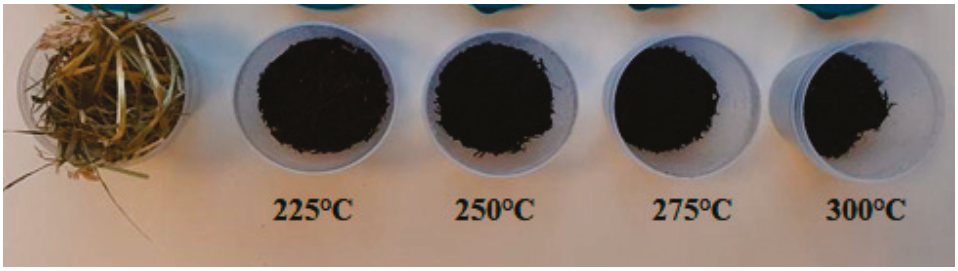


Figure 30. Hay samples before and after the torrefaction process.

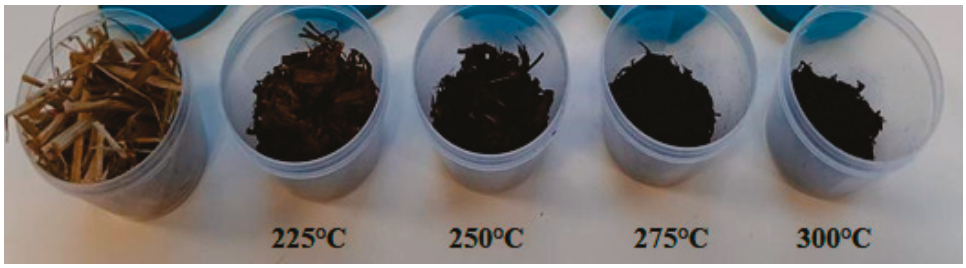


Figure 31. Rye straw samples before and after the torrefaction process.

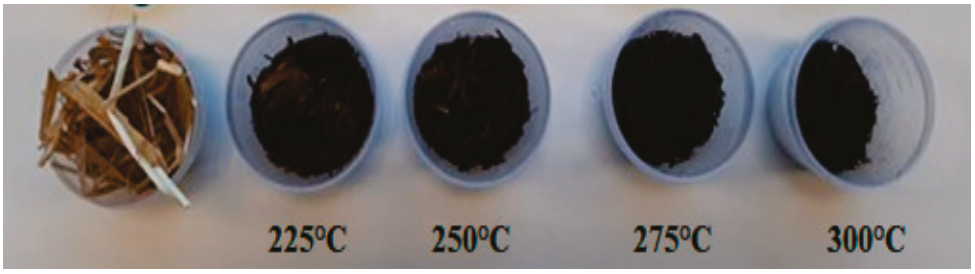


Figure 32. Oat straw samples before and after the torrefaction process.

The results of combustion heat measurements for the torrefied samples are given in Table 5.

Table 5. Heat of combustion of the tested biomass samples and their torrefied products.

Temperature (°C)	Hay	Rye Straw	Oat Straw
Raw	17.87	18.05	17.49
225	20.92	19.77	19.98
250	23.13	20.81	20.81
275	24.30	21.48	21.48
300	25.58	21.52	21.52

In the raw form, the highest heat of combustion, equal to 18.0479 MJ/kg, was measured for rye straw (Table 5). The lowest heat of combustion was observed for raw oat straw—

17.49 MJ/kg. After the torrefaction process, the highest heat of combustion was recorded for the torrefied biomass obtained from hay at 300 °C, and the lowest for rye straw and its torrefied product obtained at 225 °C—19.77 MJ/kg. Thus, it can be observed that the torrefaction process for all types of tested biomass increased the heat of combustion, thereby improving the use of biomass as a fuel. Dyjakon and Noszczyk (2020) found that torrefied at 320 °C, HHV values of forestry fruit residues ranged from 24.5 MJ·kg^{-1} to almost 27.0 MJ·kg^{-1} [81].

Therefore, it can be utilized as a heat source in a continuous torrefaction process. Research on the torrefaction process of agricultural biomass, in the form of meadow hay, rye straw, and oat straw, has shown that this process improves the combustible properties of agricultural waste biomass. Across all three agricultural residues, higher torrefaction temperatures yield both increased energy density and greater VOC release, but the rate of each response varies by feedstock. Meadow hay's HHV rises from 17.87 MJ/kg (raw) to 25.58 MJ/kg at 300 °C. At the same time, its VOC emissions climb from 3.88 mg/g at 225 °C to 7.04 mg/g at 300 °C. Rye straw shows a 30% HHV gain (18.05 to 23.39 MJ/kg) alongside the steepest VOC increase from 3.02 mg/g to 9.36 mg/g, indicating its hemicellulose and lignin fractions volatilize most aggressively. Oat straw's HHV improves by 23% (17.49 to 21.52 MJ/kg) as VOCs grow from 4.35 mg/g to 7.17 mg/g. In all cases, the bulk of the calorific upgrade occurs between 225 and 275 °C, where HHV climbs by roughly 4–6 MJ/kg, while VOC emissions double or triple. This parallel behavior confirms that devolatilization of oxygen-rich compounds both enriches the solid residue in carbon, raising HHV, and generates a torgas stream whose magnitude is feedstock- and temperature-dependent. Consequently, torrefaction parameters can be tuned to balance maximum energy densification against manageable VOC by-products for each biomass type. The overall heat of combustion increased by approximately 25–30%, which, combined with the drying of the flammable material, resulted in torrefied biomass becoming a fuel with properties similar to those of hard coal, commonly used in power generation and heating like for example Arigna Fuels Figure 33. The bulk density has decreased, which increases the energy density of the fuel and makes it easier to mix the torrefied biomass with fossil fuels for co-firing. The emission of VOCs from the torrefaction of several mg/g biomass allows us to expect that the stream of torrefied gas could be used as additional fuel, the source of energy, in the amount of 80–400 kJ/kg of torrefied biomass, supplied to the torrefaction process, improving significantly the economics of the project.

In industrial-scale installations that operate continuously, such as the one at Arigna Fuels (Ireland, Figure 24), which produces 10 t/h of torrefied biomass for renewable biofuel applications, issues related to VOC emissions are crucial due to several reasons, including energy efficiency and economic considerations.

Typically, torrefaction gas is normally de-dusted using special types of cyclones before being used as a fuel to dry incoming feedstock, such as biomass. The parts, including much heavier tars, which are inside the torrefaction gas, may condense in the ducts upstream of the burner; this can lead to hazardous operational problems. To avoid this, special torrefaction gas ducts must be insulated. Nearly all leading developers of torrefied materials reuse the torrefaction gas by combusting it in a separate combustion unit, thereby increasing the overall efficiency of the process. The additional "waste" heat from the flue gas leaving the combustion unit is then utilized in the process and circulated through the dryer to dry the wet biomass directly or indirectly, as was done by our team at Lodz University of Technology, where we use the heat from the torgas indirectly via a heat exchanger for drying the biomass in a "rolling-bed" dryer—Figure 34.



Figure 33. Biomass torrefaction plants MK1 and MK2 in Arigna, Ireland, in operation.

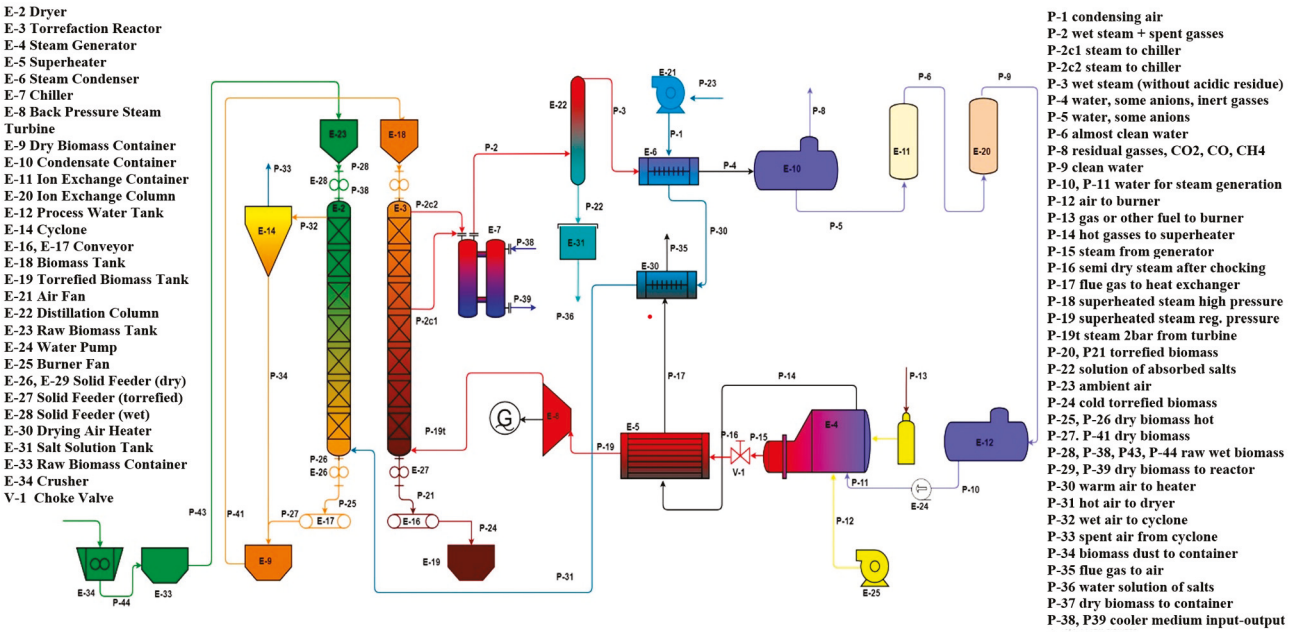


Figure 34. Installation for the torrefaction process using SHS in a counter-flow reactor and a rolling bed dryer [82].

For stable and reliable operation of the torrefaction gas burner, a sufficient residence time, adequate mixing with combustion air, and a flame temperature above 900 °C are recommended. Looking at NOx emissions, they are generally low because of the modest combustion temperature of the gas. Considering relatively high amounts of F, S, or Cl, which are typically present in the feedstock, especially in agricultural biomass such as straw, treatment of the burner flue gases using an activated carbon filter or a wet precipitator may be necessary. To clean biomass fuels, a dust filter may be sufficient. At the end, it all depends on the exact layout and the temperature profile inside the reactor, as well as on the temperature of the flue gas (to avoid the possibility of fire and explosion, which have been a big issue and danger that have already happened in many industrial-scale installations in the EU).

From a socioeconomic perspective, as mentioned, there is strong potential for the use of selected straw in Poland for energy applications. Poland ranks fourth in the European Union in terms of total available biomass potential, and third in terms of agricultural biomass potential. Using locally available straw as an energy source is a strong accelerator for creating new jobs for local people, especially in rural areas. Villages and small towns are having huge problems with high unemployment rates. Several new jobs can be created through the application of agricultural torrefaction valorization technology, which involves multiple stages of preparation of agricultural biomass before direct combustion, such as collecting from the field, cleaning, sieving, grinding, drying, and storage. Agricultural biomass is increasingly being investigated as a substrate for valorization processes, such as torrefaction [83–88], pyrolysis [89–92], or hydrothermal valorization [72,93–101].

4. Conclusions

The torrefaction of waste biomass will enable the utilization of waste biomass generated on farms in co-firing processes with coal in large and medium-sized energy facilities, such as combined heat and power plants, thereby reducing pressure on the use of fossil fuels. The use of torrefied biomass with properties similar to those of coal also has the potential to improve combustion efficiency and allow us to avoid many technical problems that arise when co-firing raw biomass with coal (e.g., fouling and slagging phenomena described in the literature). Kinetic modeling indicated that feedstock-specific differences, particularly in activation energy and pre-exponential factor profiles, significantly influence thermal conversion behavior, with meadow hay being the most reactive and rye straw the most resistant. It is very important to use volatile organic compounds rich in carbon compounds and characterized by high energy content. It is best to use the heat contained in the gases to pre-dry the biomass before its final torrefaction process. In the next step, the research team from Lodz University of Technology plans to measure the content of volatile organic compounds in installations used for the biomass torrefaction process operating in continuous mode in industry shortly. The most crucial element of further research will be to determine the most efficient and economical method of collecting heat from torgas and using it for pre-drying biomass. In future work, authors will perform a comprehensive energy balance analysis of the torrefaction gas and its chemical composition to more accurately assess its potential as a heat source for pre-drying biomass prior to the primary torrefaction step.

Author Contributions: Conceptualization, J.C. and G.W.; methodology, G.W.; software, J.C.; validation, J.C.; formal analysis, J.C., G.W. and S.S.; investigation, S.S.; resources, J.C. and S.S.; data processing, J.C.; writing—original draft preparation, J.C., H.U., G.W. and S.S.; writing—review and editing, H.U., G.W. and S.S.; visualization, J.C.; supervision, G.W.; project administration, G.W. and S.S.; funding acquisition, G.W. All authors have read and agreed to the published version of the manuscript.

Funding: The studies presented were financed by the National Science Centre (NCN), Poland, 2022/45/N/NZ9/02110. For the purpose of Open Access, the author has applied a CC-BY public copyright license to any Author Accepted Manuscript (AAM) version arising from this submission. The publication was produced as part of the NAWA Mieczysław Bekker program: "BioGainValue—Research on biomass torrefaction process using superheated steam and properties on new bio-based products" (Grant No. BPN/BEK/2021/1/00248/U/DRAFT/00001), and the Horizon Europe project: "BIOmass Valorisation via Superheated Steam Torrefaction, Pyrolisis, Gasification Amplified by Multidisciplinary Researchers TRAINing for Multiple Energy and Products' Added VALUEs" (Project No. 101086411, Horizon Europe, Maria Skłodowska-Curie Staff Exchange).

Data Availability Statement: The original contributions presented in the study are included in the article, further inquiries can be directed to the corresponding author.

Acknowledgments: This work was completed while the second author was a doctoral candidate in the Interdisciplinary Doctoral School at the Lodz University of Technology, Poland.

Conflicts of Interest: The authors declare no conflicts of interest.

References

1. Silva, S.; Soares, I.; Afonso, O. Economic and Environmental Effects under Resource Scarcity and Substitution between Renewable and Non-Renewable Resources. *Energy Policy* **2013**, *54*, 113–124. [CrossRef]
2. Allen, C.; Day, G. Depletion of Non-Renewable Resources Imported by China. *China Econ. Rev.* **2014**, *30*, 235–243. [CrossRef]
3. Hart, R. Non-Renewable Resources in the Long Run. *J. Econ. Dyn. Control* **2016**, *71*, 1–20. [CrossRef]
4. International Energy Agency Paris. World Energy Outlook 2020. Available online: https://www.iea.org/reports/world-energy-outlook-2020 (accessed on 22 May 2025).
5. Wang, Z.; Bui, Q.; Zhang, B. The Relationship between Biomass Energy Consumption and Human Development: Empirical Evidence from BRICS Countries. *Energy* **2020**, *194*, 116906. [CrossRef]
6. Unyay, H.; Perendeci, N.A.; Piersa, P.; Szufa, S.; Skwarczynska-Wojsa, A. Harnessing Switchgrass for Sustainable Energy: Bioethanol Production Processes and Pretreatment Technologies. *Energies* **2024**, *17*, 4812. [CrossRef]
7. Irfan, M.; Zhao, Z.-Y.; Panjwani, M.K.; Mangi, F.H.; Li, H.; Jan, A.; Ahmad, M.; Rehman, A. Assessing the Energy Dynamics of Pakistan: Prospects of Biomass Energy. *Energy Rep.* **2020**, *6*, 80–93. [CrossRef]
8. Schwerz, F.; Neto, D.D.; Caron, B.O.; Nardini, C.; Sgarbossa, J.; Eloy, E.; Behling, A.; Elli, E.F.; Reichardt, K. Biomass and Potential Energy Yield of Perennial Woody Energy Crops under Reduced Planting Spacing. *Renew. Energy* **2020**, *153*, 1238–1250. [CrossRef]
9. Tuğrul, K.M.; İçöz, E.; Perendeci, N.A. Determination of Soil Loss by Sugar Beet Harvesting. *Soil Tillage Res.* **2012**, *123*, 71–77. [CrossRef]
10. Schuenemann, F.; Msangi, S.; Zeller, M. Policies for a Sustainable Biomass Energy Sector in Malawi: Enhancing Energy and Food Security Simultaneously. *World Dev.* **2018**, *103*, 14–26. [CrossRef]
11. Romanowska-Duda, Z.; Piotrowski, K.; Szufa, S.; Sklodowska, M.; Naliwajski, M.; Emmanouil, C.; Kungolos, A.; Zorpas, A.A. Valorization of Spirodela Polyrrhiza Biomass for the Production of Biofuels for Distributed Energy. *Sci. Rep.* **2023**, *13*, 16533. [CrossRef]
12. Unyay, H.; Altay, H.O.; Perendeci, N.A.; Szufa, S.; Ozdemir, F.; Angelidaki, I. Valorisation potential of black tea processing wastes for bioactive compounds recovery and renewable energy production. *J. Environ. Chem. Eng.* **2025**, *13*, 117124. [CrossRef]
13. Banja, M.; Sikkema, R.; Jégard, M.; Motola, V.; Dallemand, J.-F. Biomass for Energy in the EU—The Support Framework. *Energy Policy* **2019**, *131*, 215–228. [CrossRef]
14. Başar, İ.A.; Perendeci, N.A.; Yenilmez, F.; Ünyay, H.; Yaldız, O.; Soylu, S. Characterisation and biofuel production potential assessment of eight switchgrass cultivars grown in Türkiye: Insights from principal component analysis. *Biomass Bioenergy* **2025**, *201*, 108103. [CrossRef]
15. Miesięcznik Forum Energii: Styczeń 2025–Podsumowanie. Available online: https://nowa-energia.com.pl/2025/02/10/miesiecznik-forum-energii-styczen-2025-podsumowanie/ (accessed on 22 May 2025).
16. Available online: https://www.ren21.net/gsr-2024/modules/energy_supply/01_global_trends/ (accessed on 22 May 2025).
17. Chew, J.J.; Doshi, V. Recent Advances in Biomass Pretreatment—Torrefaction Fundamentals and Technology. *Renew. Sustain. Energy Rev.* **2011**, *15*, 4212–4222. [CrossRef]
18. Libra, J.A.; Ro, K.S.; Kammann, C.; Funke, A.; Berge, N.D.; Neubauer, Y.; Titirici, M.-M.; Fühner, C.; Bens, O.; Kern, J.; et al. Hydrothermal carbonization of biomass residuals: A comparative review of the chemistry, processes and applications of wet and dry pyrolysis. *Biofuels* **2011**, *2*, 71–106. [CrossRef]
19. Tumuluru, J.S.; Sokhansanj, S.; Wright, C.T. *Boardman Biomass Torrefaction Process Review and Moving Bed Torrefaction System Model Development*; Idaho National Lab. (INL): Idaho Falls, ID, USA, 2010. [CrossRef]
20. Chen, W.H.; Lin, B.J.; Lin, Y.Y.; Chu, Y.S.; Ubando, A.T.; Show, P.L.; Ong, H.C.; Chang, J.S.; Ho, S.H.; Culaba, A.B.; et al. Progress in biomass torrefaction: Principles, applications and challenges. *Prog. Energy Combust. Sci.* **2021**, *82*, 100887. [CrossRef]
21. Kazimierski, P.; Januszewicz, K.; Godlewski, W.; Fijuk, A.; Suchocki, T.; Chaja, P.; Barczak, B.; Kardaś, D. The Course and the Effects of Agricultural Biomass Pyrolysis in the Production of High-Calorific Biochar. *Materials* **2022**, *15*, 1038. [CrossRef]
22. Unyay, H.; Piersa, P.; Perendeci, N.A.; Wielgosinski, G.; Szufa, S. Valorization of Anaerobic Digestate: Innovative Approaches for Sustainable Resource Management and Energy Production—Case Studies from Turkey and Poland. *Int. J. Green Energy* **2024**, *21*, 1928–1943. [CrossRef]
23. Mamvura, T.A.; Danha, G. Biomass Torrefaction as an Emerging Technology to Aid in Energy Production. *Heliyon* **2020**, *6*, e03531. [CrossRef]
24. Proskurina, S.; Heinimö, J.; Schipfer, F.; Vakkilainen, E. Biomass for Industrial Applications: The Role of Torrefaction. *Renew. Energy* **2017**, *111*, 265–274. [CrossRef]

25. Bridgeman, T.G.; Jones, J.M.; Shield, I.; Williams, P.T. Torrefaction of Reed Canary Grass, Wheat Straw and Willow to Enhance Solid Fuel Qualities and Combustion Properties. *Fuel* **2008**, *87*, 844–856. [CrossRef]
26. Szufa, S.; Piersa, P.; Junga, R.; Błaszczuk, A.; Modliński, N.; Sobek, S.; Marczak-Grzesik, M.; Adrian, Ł.; Dzikuć, M. Numerical Modeling of the Co-Firing Process of an in Situ Steam-Torrefied Biomass with Coal in a 230 MW Industrial-Scale Boiler. *Energy* **2023**, *263*, 125918. [CrossRef]
27. Felfli, F.; Luengo, C.; Beaton, P.; Suarez, J. Efficiency test for bench unit torrefaction and characterization of torrefied biomass. In *Biomass—A Growth Opportunity in Green Energy and Value-Added Products, Proceedings of the Fourth Biomass Conference of the Americas, Oakland, CA, USA, 29 August–2 September 1999*; Elsevier Science: Oxford, UK, 1999; pp. 1–2.
28. Jackowski, M.; Niedźwiecki, Ł.; Mościcki, K.; Arora, A.; Saeed, M.A.; Krochmalny, K.; Pawliczek, J.; Trusek, A.; Lech, M.; Skřínský, J.; et al. Synergetic Co-Production of Beer Colouring Agent and Solid Fuel from Brewers' Spent Grain in the Circular Economy Perspective. *Sustainability* **2021**, *13*, 10480. [CrossRef]
29. Szufa, S.; Wielgosiński, G.; Piersa, P.; Czerwińska, J.; Dzikuć, M.; Adrian, Ł.; Lewandowska, W.; Marczak, M. Torrefaction of Straw from Oats and Maize for Use as a Fuel and Additive to Organic Fertilizers—TGA Analysis, Kinetics as Products for Agricultural Purposes. *Energies* **2020**, *13*, 2064. [CrossRef]
30. Duranay, N.D.; Akkuş, G. Solid fuel production with torrefaction from vineyard pruning waste. *Biomass Convers Biorefinery* **2021**, *11*, 2335–2346. [CrossRef]
31. Ramos-Carmona, S.; Pérez, J.F.; Pelaez-Samaniego, M.R.; Barrera, R.; Garcia-Perez, M. Effect of torrefaction temperature on properties of Patula pine. *Maderas Cienc. Tecnol.* **2017**, *19*, 39–50. [CrossRef]
32. Marczak-Grzesik, M.; Budzyń, S.; Tora, B.; Szufa, S.; Kogut, K.; Burmistrz, P. Low-Cost Organic Adsorbents for Elemental Mercury Removal from Lignite Flue Gas. *Energies* **2021**, *14*, 2174. [CrossRef]
33. Filipe dos Santos Viana, H.; Martins Rodrigues, A.; Godina, R.; Carlos de Oliveira Matias, J.; Jorge Ribeiro Nunes, L. Evaluation of the Physical, Chemical and Thermal Properties of Portuguese Maritime Pine Biomass. *Sustainability* **2018**, *10*, 2877. [CrossRef]
34. Vandenbroek, R. Biomass Combustion for Power Generation. *Biomass Bioenergy* **1996**, *11*, 271–281. [CrossRef]
35. Saidur, R.; Abdelaziz, E.A.; Demirbas, A.; Hossain, M.S.; Mekhilef, S. A Review on Biomass as a Fuel for Boilers. *Renew. Sustain. Energy Rev.* **2011**, *15*, 2262–2289. [CrossRef]
36. da Silva, J.B.S.; Cabral, A.A.; Bezerra, G.V.P.; da Cruz, N.C.; Conconi, C.C.; Cruz, G. Buriti (*Mauritia flexuosa* L.) wastes as potential lignocellulosic feedstock for bioenergy production: Physicochemical properties, thermal behavior, and emission factors. *Ind. Crops Prod.* **2023**, *206*, 117689. [CrossRef]
37. Dyjakon, A.; Sobol, Ł.; Krotowski, M.; Mudryk, K.; Kawa, K. The Impact of Particles Comminution on Mechanical Durability of Wheat Straw Briquettes. *Energies* **2020**, *13*, 6186. [CrossRef]
38. Atienza-Martínez, M.; Fonts, I.; Ábrego, J.; Ceamanos, J.; Gea, G. Sewage sludge torrefaction in a fluidized bed reactor. *Chem. Eng.* **2013**, *222*, 534–545. [CrossRef]
39. Wielgosiński, G.; Czerwińska, J. Smog Episodes in Poland. *Atmosphere* **2020**, *11*, 277. [CrossRef]
40. Duan, Y.; Duan, L.; Wang, J.; Anthony, E.J. Observation of Simultaneously Low CO, NO_x and SO_2 Emission during Oxy-Coal Combustion in a Pressurized Fluidized Bed. *Fuel* **2019**, *242*, 374–381. [CrossRef]
41. Dmitrienko, M.A.; Nyashina, G.S.; Strizhak, P.A. Major Gas Emissions from Combustion of Slurry Fuels Based on Coal, Coal Waste, and Coal Derivatives. *J. Clean. Prod.* **2018**, *177*, 284–301. [CrossRef]
42. Danish; Wang, Z. Does Biomass Energy Consumption Help to Control Environmental Pollution? Evidence from BRICS Countries. *Sci. Total Environ.* **2019**, *670*, 1075–1083. [CrossRef] [PubMed]
43. Fais, B.; Sabio, N.; Strachan, N. The Critical Role of the Industrial Sector in Reaching Long-Term Emission Reduction, Energy Efficiency and Renewable Targets. *Appl. Energy* **2016**, *162*, 699–712. [CrossRef]
44. Zheng, S.; Yang, Y.; Li, X.; Liu, H.; Yan, W.; Sui, R.; Lu, Q. Temperature and Emissivity Measurements from Combustion of Pine Wood, Rice Husk and Fir Wood Using Flame Emission Spectrum. *Fuel Process. Technol.* **2020**, *204*, 106423. [CrossRef]
45. Alves, J.L.F.; da Silva, J.C.G.; Mumbach, G.D.; Di Domenico, M.; da Silva Filho, V.F.; de Sena, R.F.; Machado, R.A.F.; Marangoni, C. Insights into the Bioenergy Potential of Jackfruit Wastes Considering Their Physicochemical Properties, Bioenergy Indicators, Combustion Behaviors, and Emission Characteristics. *Renew. Energy* **2020**, *155*, 1328–1338. [CrossRef]
46. Guo, Z.; Wu, J.; Zhang, Y.; Wang, F.; Guo, Y.; Chen, K.; Liu, H. Characteristics of Biomass Charcoal Briquettes and Pollutant Emission Reduction for Sulfur and Nitrogen during Combustion. *Fuel* **2020**, *272*, 117632. [CrossRef]
47. Siuda, R.; Kwiatek, J.; Szufa, S.; Obraniak, A.; Piersa, P.; Adrian, Ł.; Modrzewski, R.; Ławińska, K.; Siczek, K.; Olejnik, T.P. Industrial Verification and Research Development of Lime–Gypsum Fertilizer Granulation Method. *Minerals* **2021**, *11*, 119. [CrossRef]
48. Pawlak-Kruczek, H.; Arora, A.; Mościcki, K.; Krochmalny, K.; Sharma, S.; Niedzwiecki, L. A Transition of a Domestic Boiler from Coal to Biomass—Emissions from Combustion of Raw and Torrefied Palm Kernel Shells (PKS). *Fuel* **2020**, *263*, 116718. [CrossRef]
49. Dębowski, M.; Bukowski, P.; Kobel, P.; Bieniek, J.; Romański, L.; Knutel, B. Comparison of Energy Consumption of Cereal Grain Dryer Powered by LPG and Hard Coal in Polish Conditions. *Energies* **2021**, *14*, 4340. [CrossRef]

50. Nunes, L.J.R. A Case Study about Biomass Torrefaction on an Industrial Scale: Solutions to Problems Related to Self-Heating, Difficulties in Pelletizing, and Excessive Wear of Production Equipment. *Appl. Sci.* **2020**, *10*, 2546. [CrossRef]
51. Borén, E.; Pommer, L.; Nordin, A.; Larsson, S.H. Off-Gassing from Pilot-Scale Torrefied Pine Chips: Impact of Torrefaction Severity, Cooling Technology, and Storage Times. *Fuel Process. Technol.* **2020**, *202*, 106380. [CrossRef]
52. Murayama, T. Effects of Fuel Properties in Combustion Systems. In *Advanced Combustion Science*; Springer: Tokyo, Japan, 1993; pp. 245–272.
53. Vassilev, S.V.; Vassileva, C.G.; Vassilev, V.S. Advantages and Disadvantages of Composition and Properties of Biomass in Comparison with Coal: An Overview. *Fuel* **2015**, *158*, 330–350. [CrossRef]
54. Vassilev, S.V.; Baxter, D.; Andersen, L.K.; Vassileva, C.G.; Morgan, T.J. An Overview of the Organic and Inorganic Phase Composition of Biomass. *Fuel* **2012**, *94*, 1–33. [CrossRef]
55. Kazimierski, P.; Hercel, P.; Januszewicz, K.; Kardaś, D. Pre-Treatment of Furniture Waste for Smokeless Charcoal Production. *Materials* **2020**, *13*, 3188. [CrossRef]
56. Andritz Industrial Applications. Available online: https://www.andritz.com/feed-and-biofuel-en/industries/industrial-applications (accessed on 25 May 2025).
57. Spokas, K.A.; Novak, J.M.; Stewart, C.E.; Cantrell, K.B.; Uchimiya, M.; DuSaire, M.G.; Ro, K.S. Qualitative Analysis of Volatile Organic Compounds on Biochar. *Chemosphere* **2011**, *85*, 869–882. [CrossRef]
58. Borén, E.; Larsson, S.H.; Thyrel, M.; Averheim, A.; Broström, M. VOC Off-Gassing from Pelletized Steam Exploded Softwood Bark: Emissions at Different Industrial Process Steps. *Fuel Process. Technol.* **2018**, *171*, 70–77. [CrossRef]
59. Bourgois, J.; Guyonnet, R. Characterization and Analysis of Torrefied Wood. *Wood Sci. Technol.* **1988**, *22*, 143–155. [CrossRef]
60. Białowiec, A.; Micuda, M.; Szumny, A.; Łyczko, J.; Koziel, J. Waste to Carbon: Influence of Structural Modification on VOC Emission Kinetics from Stored Carbonized Refuse-Derived Fuel. *Sustainability* **2019**, *11*, 935. [CrossRef]
61. Tumuluru, J.S.; Ghiasi, B.; Soelberg, N.R.; Sokhansanj, S. Biomass Torrefaction Process, Product Properties, Reactor Types, and Moving Bed Reactor Design Concepts. *Front. Energy Res.* **2021**, *9*, 728140. [CrossRef]
62. van der Stelt, M.J.C.; Gerhauser, H.; Kiel, J.H.A.; Ptasinski, K.J. Biomass Upgrading by Torrefaction for the Production of Biofuels: A Review. *Biomass Bioenergy* **2011**, *35*, 3748–3762. [CrossRef]
63. Nocquet, T.; Dupont, C.; Commandre, J.-M.; Grateau, M.; Thiery, S.; Salvador, S. Volatile Species Release during Torrefaction of Biomass and Its Macromolecular Constituents: Part 2—Modeling Study. *Energy* **2014**, *72*, 188–194. [CrossRef]
64. Prins, M.J.; Ptasinski, K.J.; Janssen, F.J.J.G. Torrefaction of Wood. *J. Anal. Appl. Pyrolysis* **2006**, *77*, 35–40. [CrossRef]
65. Hroncová, E.; Puskajler, J. Emission of Pollutants from Torrefaction of Wood. *Eur. J. Environ. Saf. Sci.* **2014**, *2*, 19–22.
66. Zhou, Q.; Shen, Y.; Gu, X. Progress in torrefaction pretreatment for biomass gasification. *Green Chem.* **2024**, *26*, 9652–9670. [CrossRef]
67. *PN-EN ISO 18134-1:2015-11*; Biopaliwa Stałe—Oznaczenie Zawartości Wilgoci—Metoda Suszarkowa. Część 1: Wilgoć Całkowita—Metoda Referencyjna. International Organization for Standardization: Geneva, Switzerland, 2015.
68. Lang, K.W.; Steinberg, M.P. Calculation of Moisture Content of a Formulated Food System to Any Given Water Activity. *J. Food Sci.* **1980**, *45*, 1228–1230. [CrossRef]
69. *PN-80/G-04512:1998*; Paliwa Stałe—Oznaczanie Zawartości Popiołu Metodą Wagową. Polski Komitet Normalizacyjny (PKN): Warsaw, Poland, 1998.
70. Ismail, B.P. Ash Content Determination. In *Nielsen's Food Analysis Laboratory Manual*; Springer International Publishing: Cham, Switzerland, 2017; pp. 117–119.
71. He, Q.; Ding, L.; Gong, Y.; Li, W.; Wei, J.; Yu, G. Effects of torrefaction on pinewood pyrolysis kinetics and thermal behavior using thermogravimetric analysis. *Bioresour. Technol.* **2019**, *280*, 104–111. [CrossRef]
72. Wang, S.; Wen, Y.; Shi, Z.; Niedzwiecki, L.; Baranowski, M.; Czerep, M.; Mu, W.; Kruczek, H.P.; Jönsson, P.G.; Yang, W. Effect of Hydrothermal Carbonization Pretreatment on the Pyrolysis Behavior of the Digestate of Agricultural Waste: A View on Kinetics and Thermodynamics. *Chem. Eng. J.* **2022**, *431*, 133881. [CrossRef]
73. Čespiva, J.; Niedzwiecki, L.; Wnukowski, M.; Krochmalny, K.; Mularski, J.; Ochodek, T.; Pawlak-Kruczek, H. Torrefaction and Gasification of Biomass for Polygeneration: Production of Biochar and Producer Gas at Low Load Conditions. *Energy Rep.* **2022**, *8*, 134–144. [CrossRef]
74. Luo, H.; Wang, X.; Krochmalny, K.; Niedzwiecki, L.; Czajka, K.; Pawlak-Kruczek, H.; Wu, X.; Liu, X.; Xiong, Q. Assessments and Analysis of Lumped and Detailed Pyrolysis Kinetics for Biomass Torrefaction with Particle-Scale Modeling. *Biomass Bioenergy* **2022**, *166*, 106619. [CrossRef]
75. Chen, B.; Koziel, J.A.; O'Brien, S.C.; Bialowiec, A. The Mitigation of Gaseous Emissions from Swine Manure: A Review of Biochar Application for Environmental Management. In Proceedings of the 2022 ASABE Annual International Meeting, Houston, Texas, USA, 17–20 July 2022; American Society of Agricultural and Biological Engineers: St. Joseph, MI, USA, 2022.
76. *PN-EN 12619:05*; Emisja Ze Źródeł Stacjonarnych—Metoda Ciągłego Pomiaru z Detekcją Płomieniowo-Jonizacyjną. European Committee for Standardization: Brussels, Belgium, 2013.

77. Chai, M.; Xie, L.; Yu, X.; Zhang, X.; Yang, Y.; Rahman, M.M.; Blanco, P.H.; Liu, R.; Bridgwater, A.V.; Cai, J. Poplar Wood Torrefaction: Kinetics, Thermochemistry and Implications. *Renew. Sustain. Energy Rev.* **2021**, *143*, 110962. [CrossRef]
78. Kryshtopa, S.; Kryshtopa, L.; Panchuk, M.; Smigins, R.; Dolishnii, B. Composition and Energy Value Research of Pyrolise Gases. *IOP Conf. Ser. Earth Environ. Sci.* **2021**, *628*, 012008. [CrossRef]
79. James, A.M.; Yuan, W.; Boyette, M.D.; Wang, D. The Effect of Air Flow Rate and Biomass Type on the Performance of an Updraft Biomass Gasifier. *BioResources* **2015**, *10*, 3615–3624. [CrossRef]
80. Vasileiadou, M.A.; Altiparmaki, G.; Moustakas, K.; Vakalis, S. Quality of Hydrochar from Wine Sludge under Variable Conditions of Hydrothermal Carbonization: The Case of Lesvos Island. *Energies* **2022**, *15*, 3574. [CrossRef]
81. Dyjakon, A.; Noszczyk, T. Alternative Fuels from Forestry Biomass Residue: Torrefaction Process of Horse Chestnuts, Oak Acorns, and Spruce Cones. *Energies* **2020**, *13*, 2468. [CrossRef]
82. Szufa, S.; Unyay, H.; Pakowski, Z.; Piersa, P.; Siczek, K.; Kabaciński, M.; Sobek, S.; Moj, K.; Likozar, B.; Kostyniuk, A.; et al. Batch rolling-bed dryer applicability for drying biomass prior to torrefaction. *Renew. Energy* **2025**, *239*, 122106. [CrossRef]
83. Szufa, S.; Unyay, H.; Piersa, P.; Kędzierska-Sar, A.; Romanowska-Duda, Z.; Likozar, B. Reduction of spruce phytotoxicity by superheated steam torrefaction and its use in stimulating the growth of ecological bio-products: *Lemna minor* L. *Biomass Conv. Bioref.* **2025**, *15*, 17739–17760. [CrossRef]
84. Massaro Sousa, L.; Ogura, A.P.; Anchieta, C.G.; Morin, M.; Canabarro, N.I. Biomass Torrefaction for Renewable Energy: From Physicochemical, Bulk Properties, and Flowability to Future Perspectives and Applications. *Energy Fuels* **2024**, *38*, 18367–18385. [CrossRef]
85. Ünyay, H.; Yılmaz, F.; Başar, İ.A.; Altınay Perendeci, N.; Çoban, I.; ¸Sahinkaya, E. Effects of organic loading rate on methane production from switchgrass in batch and semi-continuous stirred tank reactor system. *Biomass Bioenergy* **2022**, *156*, 106306. [CrossRef]
86. Torres Ramos, R.; Valez Salas, B.; Montero Alpírez, G.; Coronado Ortega, M.A.; Curiel Álvarez, M.A.; Tzintzun Camacho, O.; Beleño Cabarcas, M.T. Torrefaction under Different Reaction Atmospheres to Improve the Fuel Properties of Wheat Straw. *Processes* **2023**, *11*, 1971. [CrossRef]
87. Luo, H.; Niedzwiecki, L.; Arora, A.; Mościcki, K.; Pawlak-Kruczek, H.; Krochmalny, K.; Baranowski, M.; Tiwari, M.; Sharma, A.; Sharma, T.; et al. Influence of Torrefaction and Pelletizing of Sawdust on the Design Parameters of a Fixed Bed Gasifier. *Energies* **2020**, *13*, 3018. [CrossRef]
88. Szufa, S.; Adrian, Ł.; Piersa, P.; Romanowska-Duda, Z.; Grzesik, M.; Cebula, A.; Kowalczyk, S. Experimental studies on energy crops torrefaction process using batch reactor to estimate torrefaction temperature and residence time. In *Renewable Energy Sources: Engineering, Technology, Innovation*; Springer: Cham, Switzerland, 2018; pp. 365–373.
89. Kazimierski, P.; Hercel, P.; Suchocki, T.; Smoliński, J.; Pladzyk, A.; Kardaś, D.; Łuczak, J.; Januszewicz, K. Pyrolysis of Pruning Residues from Various Types of Orchards and Pretreatment for Energetic Use of Biochar. *Materials* **2021**, *14*, 2969. [CrossRef] [PubMed]
90. Głowacki, S.; Salamon, A.; Sojak, M.; Tulej, W.; Bryś, A.; Hutsol, T.; Salamon, M.; Kukharets, S.; Janaszek-Mańkowska, M. The Use of Brewer's Spent Grain after Beer Production for Energy Purposes. *Materials* **2022**, *15*, 3703. [CrossRef] [PubMed]
91. Mudryk, K.; Jewiarz, M.; Wróbel, M.; Niemiec, M.; Dyjakon, A. Evaluation of Urban Tree Leaf Biomass-Potential, Physico-Mechanical and Chemical Parameters of Raw Material and Solid Biofuel. *Energies* **2021**, *14*, 818. [CrossRef]
92. Nieścioruk, M.J.; Bandrow, P.; Szufa, S.; Woźniak, M.; Siczek, K. Biomass-Based Hydrogen Extraction and Accompanying Hazards—Review. *Molecules* **2025**, *30*, 565. [CrossRef]
93. Zhao, Y.; Lu, T.; Xu, G.; Luo, Y.; Zhang, X.; Wu, X.; Han, X.; Tester, W.J.; Wang, K. Hydrothermal co-carbonization of rice straw and acid whey for enhanced hydrochar properties and nutrient recovery. *Green Energy Resour.* **2024**, *2*, 100077. [CrossRef]
94. Wen, Y.; Wang, S.; Shi, Z.; Nuran Zaini, I.; Niedzwiecki, L.; Aragon-Briceno, C.; Tang, C.; Pawlak-Kruczek, H.; Jönsson, P.G.; Yang, W. H2-Rich Syngas Production from Pyrolysis of Agricultural Waste Digestate Coupled with the Hydrothermal Carbonization Process. *Energy Convers. Manag.* **2022**, *269*, 116101. [CrossRef]
95. Mendiara, T.; Navajas, A.; Abad, A.; Pröll, T.; Munárriz, M.; Gandía, L.M.; García-Labiano, F.; de Diego, L.F. Life Cycle Assessment of Wheat Straw Pyrolysis with Volatile Fractions Chemical Looping Combustion. *Sustainability* **2024**, *16*, 4013. [CrossRef]
96. Nizamuddin, S.; Qureshi, S.S.; Baloch, H.A.; Siddiqui, M.T.H.; Takkalkar, P.; Mubarak, N.M.; Dumbre, D.K.; Griffin, G.J.; Madapusi, S.; Tanksale, A. Microwave Hydrothermal Carbonization of Rice Straw: Optimization of Process Parameters and Upgrading of Chemical, Fuel, Structural and Thermal Properties. *Materials* **2019**, *12*, 403. [CrossRef]
97. Sobol, Ł.; Dyjakon, A.; Dlugogorski, B.Z. Dioxin-like polychlorinated biphenyls (dl-PCB) in hydrochars and biochars: Review of recent evidence, pollution levels, critical gaps, formation mechanisms and regulations. *J. Hazard. Mater.* **2025**, *486*, 136615. [CrossRef] [PubMed]
98. Jackowski, M.; Niedzwiecki, L.; Lech, M.; Wnukowski, M.; Arora, A.; Tkaczuk-Serafin, M.; Baranowski, M.; Krochmalny, K.; Veetil, V.K.; Seruga, P.; et al. HTC of Wet Residues of the Brewing Process: Comprehensive Characterization of Produced Beer, Spent Grain and Valorized Residues. *Energies* **2020**, *13*, 2058. [CrossRef]

99. Aragon-Briceño, C.; Pożarlik, A.; Bramer, E.; Brem, G.; Wang, S.; Wen, Y.; Yang, W.; Pawlak-Kruczek, H.; Niedźwiecki, Ł.; Urbanowska, A.; et al. Integration of hydrothermal carbonization treatment for water and energy recovery from organic fraction of municipal solid waste digestate. *Renew. Energy* **2022**, *184*, 577–591. [CrossRef]
100. Urbanowska, A.; Kabsch-Korbutowicz, M.; Aragon-Briceño, C.; Wnukowski, M.; Pożarlik, A.; Niedzwiecki, L.; Baranowski, M.; Czerep, M.; Seruga, P.; Pawlak-Kruczek, H.; et al. Cascade Membrane System for Separation of Water and Organics from Liquid By-Products of HTC of the Agricultural Digestate—Evaluation of Performance. *Energies* **2021**, *14*, 4752. [CrossRef]
101. Marczak-Grzesik, M.; Piersa, P.; Karczewski, M.; Szufa, S.; Ünyay, H.; Kędzierska-Sar, A.; Bochenek, P. Modified Fly Ash-Based Adsorbents (MFA) for Mercury and Carbon Dioxide Removal from Coal-Fired Flue Gases. *Energies* **2021**, *14*, 7101. [CrossRef]

Disclaimer/Publisher's Note: The statements, opinions and data contained in all publications are solely those of the individual author(s) and contributor(s) and not of MDPI and/or the editor(s). MDPI and/or the editor(s) disclaim responsibility for any injury to people or property resulting from any ideas, methods, instructions or products referred to in the content.

energies

MDPI

Article

Technology for the Production of Energy Briquettes from Bean Stalks

Krzysztof Mudryk *, Jarosław Frączek, Joanna Leszczyńska and Mateusz Krotowski

Department of Mechanical Engineering and Agrophysics, University of Agriculture in Krakow, 30-149 Kraków, Poland; jaroslaw.fraczek@urk.edu.pl (J.F.); joanna.leszczynska@urk.edu.pl (J.L.); mateusz.krotowski8@gmail.com (M.K.)
* Correspondence: krzysztof.mudryk@urk.edu.pl

Abstract

Biomass is gaining increasing importance as a renewable energy source in the global energy mix, offering a viable alternative to fossil fuels and contributing to the decarbonization of the energy sector. Among various types of biomass, agricultural residues such as bean stalks represent a promising feedstock for the production of solid biofuels. This study analyzes the impact of particle size and selected briquetting parameters (pressure and temperature) on the physical quality of briquettes made from bean stalks. The experimental procedure included milling the raw material using #8, #12, and #16 mesh screens, followed by compaction under pressures of 27, 37, and 47 MPa. Additionally, the briquetting die was heated to 90 °C to improve the mechanical durability of the briquettes. The results showed that both particle size and die temperature significantly influenced the quality of the produced briquettes. Briquettes made from the 16 mm fraction, compacted at 60 °C and 27 MPa, exhibited a durability of 55.76%, which increased to 82.02% when the die temperature was raised to 90 °C. Further improvements were achieved by removing particles smaller than 1 mm. However, these measures did not enable achieving a net calorific value above 14.5 MJ·kg^{-1}. Therefore, additional work was undertaken, involving the addition of biomass with higher calorific value to the bean stalk feedstock. In the study, maize straw and miscanthus straw were used as supplementary substrates. The results allowed for determining their minimum proportions required to exceed the 14.5 MJ·kg^{-1} threshold. In conclusion, bean stalks can serve as a viable feedstock for the production of solid biofuels, especially when combined with other biomass types possessing more favorable energy parameters. Their utilization aligns with the concept of managing local agricultural residues within decentralized energy systems and supports the development of sustainable bioenergy solutions.

Keywords: lignocellulosic biomass; solid biofuel; densification; comminution; bean straw; agglomerates

1. Introduction

Biomass, as a renewable energy source, is playing an increasingly important role in the Polish energy sector [1]. This is due both to Poland's geographical location, which is less favorable for the development of certain forms of renewable energy, and to government programs supporting renewables aimed at reducing CO_2 emissions and promoting the use of solid biofuels [2]. According to the policy of the European Commission, by 2030 Poland is expected to achieve at least a 23% share of renewable energy in total energy consumption

(KPEiK). To meet this target, it has become necessary to integrate biomass into the professional energy sector and develop its use among individual consumers. New technologies for the production of biomass fuels—such as wood chips, pellets, and briquettes—have emerged [3]. In response to growing market demand, boiler manufacturers have introduced innovative solutions based on combustion process automation, which enables better control of operational parameters and maximizes energy efficiency. Strong emphasis is placed on compliance with European regulations and directives on eco-design [4].

The sourcing of biomass for solid biofuels includes various sectors—primarily the wood industry and agriculture [5]. Initially, wood waste such as sawdust and wood shavings was used, which proved ideal for pellet and briquette production [6,7]. Over time, forestry began generating biomass in the form of wood chips, which have been used in both the professional energy sector and by individual users [8]. Agriculture, on the other hand, has provided biomass in the form of straw and grains. Straw has primarily been used in local boiler plants, while the combustion of grain—despite being economically viable—has sparked ecological and ethical concerns [9,10]. To increase biomass availability, blends of agricultural and woody residues with natural additives have also been used to improve fuel properties [11,12]. Purpose-grown energy crops such as basket willow, poplar, giant miscanthus, and switchgrass have been developed [5,13]. Research is ongoing to identify new fast-growing plants that can be processed into biofuels [14]. Numerous organic residues from agriculture, the agri-food industry, and municipal waste streams have also started to be utilized [15].

There is a growing interest in the production of biofuels in the form of briquettes and pellets from various types of plant production waste. The most widely studied raw material in this context is cereal straw [16–18]. In addition, in line with efforts to reduce waste, lower CO_2 emissions, and promote the circular economy, research has been undertaken to explore the feasibility of utilizing other types of plant-based residues. These include, among others, vine prunings [19], vegetable waste [20], coconut shells [21], sugarcane leaves [22], and bean stalks [23].

In 2021, the area under bean cultivation in Poland totaled 35,667 ha. With an average yield of 1.85 t/ha, this translated into approximately 70,000 tons of production [24]. Although this is a relatively modest figure in global terms, it is worth noting that Canada leads in yield (2.54 $t \cdot ha^{-1}$), while India has the largest area under cultivation—approximately 13 million hectares [25].

When estimating the potential amount of stalk biomass available for biofuel production, the grain-to-stalk ratio must be considered. For beans, this ratio typically ranges from 1:1.3 to 1:1.5 [26]. Even with the relatively small cultivation area and modest yields in Poland, this translates into a theoretical potential of 91,000 to 105,000 tons of post-harvest residue annually. This quantity represents a meaningful resource that should be taken into account when evaluating bio-based feedstocks for ecological fuel production—especially in the context of developing a decentralized, local, and sustainable economy aligned with circular economy principles.

The processing of biomass into briquettes or pellets aims to improve its physical properties by homogenizing and reducing particle size, which is particularly important from the perspective of logistics and boiler feed automation. The agglomeration process involves a complex sequence of operations designed to produce high-quality solid biofuels in granular form (Figure 1). The complexity of this process primarily depends on the type and quality of the biomass feedstock, while its energy demand is influenced by numerous physicochemical properties highlighted in the diagram. Nevertheless, certain stages of the technological chain are always present—such as size reduction, pelletizing or briquetting, and transport.

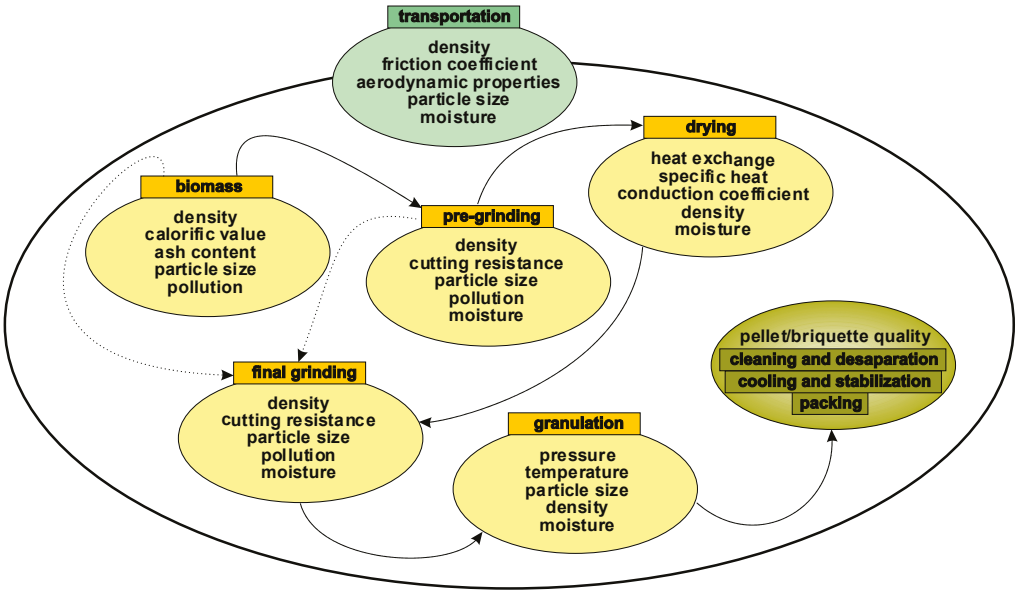


Figure 1. Diagram of the biomaterial agglomeration process.

The process begins with the acquisition and initial characterization of the biomass. At this stage, key parameters such as bulk density, calorific value, ash content, impurity levels, moisture content, and particle size distribution are assessed. These properties are critical for the downstream processing stages (e.g., the need for pre-grinding, cleaning, or drying) as well as for the final quality of the product [15].

Next, biomass with a moisture content exceeding 12% (for class A briquettes) or 15% (for class B briquettes) undergoes a drying process. During drying, intensive heat exchange takes place, where parameters such as thermal conductivity, specific heat capacity, and heat transfer rate are crucial. Optimal drying lowers the moisture content to a level that facilitates pelleting or briquetting, thereby improving both the durability and calorific value of the final product [27].

The dried biomass is then subjected to final grinding (milling), which further reduces particle size and enhances material homogeneity. This step improves technological properties, such as bulk and particle density, and contributes to better combustion performance.

The homogenized biomass is then densified under high pressure and at a controlled temperature, which is usually generated through friction between the material and the walls of the die. The increased temperature softens the cellulose and activates lignin present in the material, which serves as a natural binder, enabling the production of dense and durable briquettes—often without the need for external binding agents. This process is highly dependent on the physicochemical properties of the input material, such as moisture content, particle size, and density, all of which influence inter-particle bonding and the mechanical strength of the final product.

Studies by Frączek [11], Adam [1] and Marreiro [28] confirm that increasing compaction pressure improves briquette density and mechanical strength. Similarly, Fiszer [9] and Orisaleye [29] demonstrated that higher temperatures contribute to improved briquette density and durability.

The final stage of the technological process involves quality assessment and product preparation for distribution. The finished briquettes or pellets undergo dust and fines removal (desaparation), cooling, and stabilization before being packaged. These operations protect the product from degradation, increase its resistance to transport conditions, and reduce susceptibility to moisture and mechanical damage.

An essential element that links all stages of the process is the internal transport system. Depending on the type of conveying equipment used, biomass properties such as bulk density, moisture content, coefficient of friction, and aerodynamic characteristics become crucial. These parameters affect the efficiency of feeding mechanisms and conveyors and contribute to optimizing energy use throughout the entire process [30].

Like any other commercial product, processed biomass should meet specific quality requirements. This is particularly important from the perspective of individual consumers (who use pellets and briquettes in heating systems), whose market share is gradually increasing. A new market is emerging in which customers seek high-quality fuels compatible with fully automated boilers. These requirements are often more stringent—especially regarding moisture content, dimensional uniformity, absence of foreign matter, and mechanical durability—than those applied in the professional power sector. Consequently, there has been a growing drive to establish biofuel quality standards and standardized methods for their determination.

According to Frączek [12], such standards should do the following:

- ensure consistent fuel quality;
- define the responsibilities and obligations of market participants to guarantee legal compliance and safety for all stakeholders;
- support the harmonization of different stages along the supply chain by specifying acceptable ranges for quality indicators;
- inform end users about the characteristic properties of the product.

In the case of briquettes made from non-woody biomass, the standard "PN-EN ISO 17225-7: Solid biofuels—Fuel specifications and classes. Part 7: Graded non-woody briquettes" [31] defines the basic requirements that must be met for a briquette to be classified as A or B. In addition to origin and source, the standard also specifies recommended values for parameters such as moisture content, dimensions, ash content, particle density, additives, net calorific value, and the content of selected chemical elements. According to the research presented by Marreiro et al. [28], the most important quality parameters of solid biofuels are calorific value, moisture content, durability, ash content after combustion, and bulk density.

Raw materials for biomass briquette production should be closely aligned with local availability, and long-distance transportation and complex logistics should be minimized whenever possible [30]. In light of this, increasing attention is being given to the production of solid biofuels—briquettes and pellets—from various types of post-harvest residues. As mentioned earlier, cereal straw remains one of the most frequently studied and widely used raw materials in this category [16–18].

However, in line with objectives such as reducing waste management costs, minimizing CO_2 emissions, and promoting circular economy principles and sustainable development, research has increasingly focused on the use of alternative types of plant-based biomass. Examples include vine pruning residues [19], vegetable processing waste [20], coconut shells [21], raw sugarcane leaves [22], and the potentially large quantities of bean stalks [23].

When estimating the stalk mass available for biofuel use, the grain-to-stalk ratio should be considered, which for beans typically ranges from 1:1.3 to 1:1.5 [26]. Thus, even at the current scale of cultivation, Poland has an estimated potential of 91,000 to 105,000 tons of bean stalks annually.

This represents a biomass stream that merits consideration when identifying alternative feedstocks for ecological fuel production—particularly in the context of a decentralized and locally oriented bioenergy system that aligns with circular economy strategies.

Table 1 presents a summary of the key technological parameters reported by various researchers and compares them with the quality guidelines specified in PN-EN ISO 17225-7

for class A and B non-woody briquettes. It is worth noting that these standards focus exclusively on briquette quality and do not prescribe specific technological process parameters, which allows system designers and technologists flexibility in optimizing production methods.

Table 1. Laboratory briquetting experiments of bean stalks according to different sources and quality parameters for two classes.

Parameter	Okot et al. (2019) [32]	Obidziński et al. (2015) [33]	Jasinskas et al. (2022) [34]	Trejo_Zamudio et al. (2022) [35]	Petlickaitė et al. (2022) [36]	Krenz et al. (2024) [22]	Standard PN-EN ISO 17225-7	
							Briquette Class A	Briquette Class B
Pressure (MPa)	100–250	120–200	100–180	90–150	80–140	110–190	-	-
Temperature (°C)	20–80	70–90	50–90	60–85	60–100	70–90	-	-
Moisture content (%)	10–15	8–12	10–14	9–13	9–15	10–14	M12 $\leq$ 12	M15 $\leq$ 15
Particle size (mm)	<4	<5	<4	<4	<4	<4	-	-
Density (g·cm^{-3})	0.886–1.123	0.9–1.1	0.85–1.05	0.88–1.1	0.87–1.05	0.9–1.15	DE0.9 $\geq$ 0.9	DE0.6 $\geq$ 0.6
Durability DU (%)	>96	>90	>92	>90	>91	>93	-	-
Net calorific value (MJ·kg^{-1})	16.5–18.2	16.8–18.0	16.2–17,8	16.0–17.5	16.5–18.1	16.7–18.3	Q14.5 $\geq$ 14.5	Q14.5 $\geq$ 14.5

Moisture content is one of the most critical parameters of the input biomass. Most publications confirm that the optimal moisture content for bean stalks ranges between 8% and 15%. According to the PN-EN ISO 17225-7 standard, class A briquettes must have a moisture content of $\leq$12%, and class B $\leq$ 15%, which aligns well with the ranges reported in the literature. This allows the conclusion that briquettes produced in the reviewed studies meet the moisture-related requirements for both quality classes.

In terms of compaction pressure, reported values range widely from 80 to 250 MPa, suggesting considerable flexibility depending on the technology used and the desired briquette quality. The highest pressures (up to 250 MPa) are reported by Okot et al. (2019) [32], while the lowest pressures were used in the study by Petlickaitė et al. [36].

Briquetting temperatures also vary, typically falling within the range of 20 °C to 100 °C. Studies by Obidziński et al. [33] and Krenz et al. [22] have shown that elevated temperatures in the range of 70–90 °C support lignin activation and enhance briquette durability.

Regarding particle size, the raw material is generally ground to a size below 4 mm, indicating the need for thorough pre-treatment. Only in the study by Harun and Obidziński [33] were slightly larger fractions (<5 mm) permitted.

The density of the resulting briquettes ranged from 0.85 to 1.15 g·cm^{-3}, demonstrating good mechanical integrity of the compressed material. All cases meet the class B requirement of $\geq$0.6 g·cm^{-3}.

Mechanical durability consistently exceeded 90%, and values above 96% reported by Okot et al. [32] indicate high briquette quality and optimized processing conditions.

The net calorific value of the briquettes ranged from 16.0 to 18.3 MJ·kg^{-1}, indicating a strong energy potential for bean stalks as a feedstock. All reported values exceeded the minimum required threshold of 14.5 MJ·kg^{-1}, fulfilling the energy criteria for both class A and B biofuels.

In summary, the quality parameters of biofuels obtained from bean stalks in the reviewed studies meet the criteria defined in PN-EN ISO 17225-7, which applies to non-woody briquettes. However, since most of the reviewed data refer to pellets (with diameters below 25 mm or equivalent small dimension), their quality should be assessed according to the PN-EN ISO 17225-6 standard [37]. This standard introduces an additional requirement: mechanical durability (DU), which must be at least 97.5% for class A and 96% for class B. Among the reviewed studies, only the results reported by Okot et al. [38] met this criterion (for class B).

No specific studies on briquettes made from bean stalks were identified in the available literature. Therefore, an important research question remains:

Is it possible to produce high-quality briquettes from bean stalks, and will the appropriate selection of processing parameters—pressure, temperature, moisture, and particle size—enable the production of briquettes with sufficient durability and density to meet class A or B standards?

This question formed the basis and objective of the present research.

The scope of the work included the following: preparation of the test material, measurement of selected physical properties of the obtained particle size fractions, production of briquettes using a hydraulic briquetting press, determination of selected quality parameters of the produced briquettes, and analysis and discussion of the results.

2. Materials and Methods

The research material consisted of stalks of common bean (*Phaseolus vulgaris* L.) of the 'Igołomska' variety, cultivated for dry seed production. After combine threshing, the stalks were collected using a Roll-Bar™ 125 round baler (New Holland, Płock, Poland), forming bales with a diameter of 1.25 m, width of 1.2 m, and a weight of approximately 180 kg. This harvesting method allows for easy integration of bean stalks into the logistics chain using machinery commonly used for the collection of cereal straw.

One of the key drawbacks of this method is the increased contamination of bean stalks with mineral fractions originating from the soil. Due to the short length of the stalks, the pickup systems in the balers must operate at a very low height above ground, which directly increases the risk of mineral inclusions in the compressed biomass. The collected stalks were stored for two years under a roof, with the bales arranged in a pyramid-shaped stack. Prior to the experimental work, a visual inspection of the stored bales was conducted. As a result, the biomass in direct contact with the ground was excluded due to early signs of biological decomposition, which could have compromised the accuracy and reliability of the measurements.

This material exhibits physico-chemical properties similar to those of other agricultural residues commonly used for bioenergy purposes. The straw from dwarf bean harvesting is characterized by the following parameters, based on our own measurements and the following sources [13,39,40]:

- Working moisture content after harvest (in baled form): 20–28%;
- Ash content: 7–10%;
- Crude fiber (cellulose + hemicellulose + lignin): 35–45%;
- Carbon content (C): 45–49%;
- Hydrogen content (H): 5.5–6.4%;
- Nitrogen content (N): 0.5–1.2%;
- Sulfur content (S): <0.1%.

The research process was complex and multi-stage, aiming to ensure the reliability and comprehensiveness of the results. Each phase was conducted in a strictly defined sequence. Figure 2 presents a schematic diagram of the experimental setup used in this study. The adopted procedure enabled a detailed assessment of the impact of both biomass particle size and key briquetting process parameters on selected quality characteristics of the final product. All measurements were performed at the accredited Laboratory of Solid Biofuel Production Technology and Quality Assessment (PCA accreditation no. AB 1585).

The first step involved determining the moisture content of the material intended for testing. Measurements were conducted in accordance with the PN-EN ISO 18134-1:2015 standard [41] using a laboratory setup for analytical moisture determination, equipped with a laboratory dryer (model SLW 115, Pol-Eko, Wodzisław Śląski, Poland). The device was programmed for a 24 h drying cycle at a temperature of 105 °C.

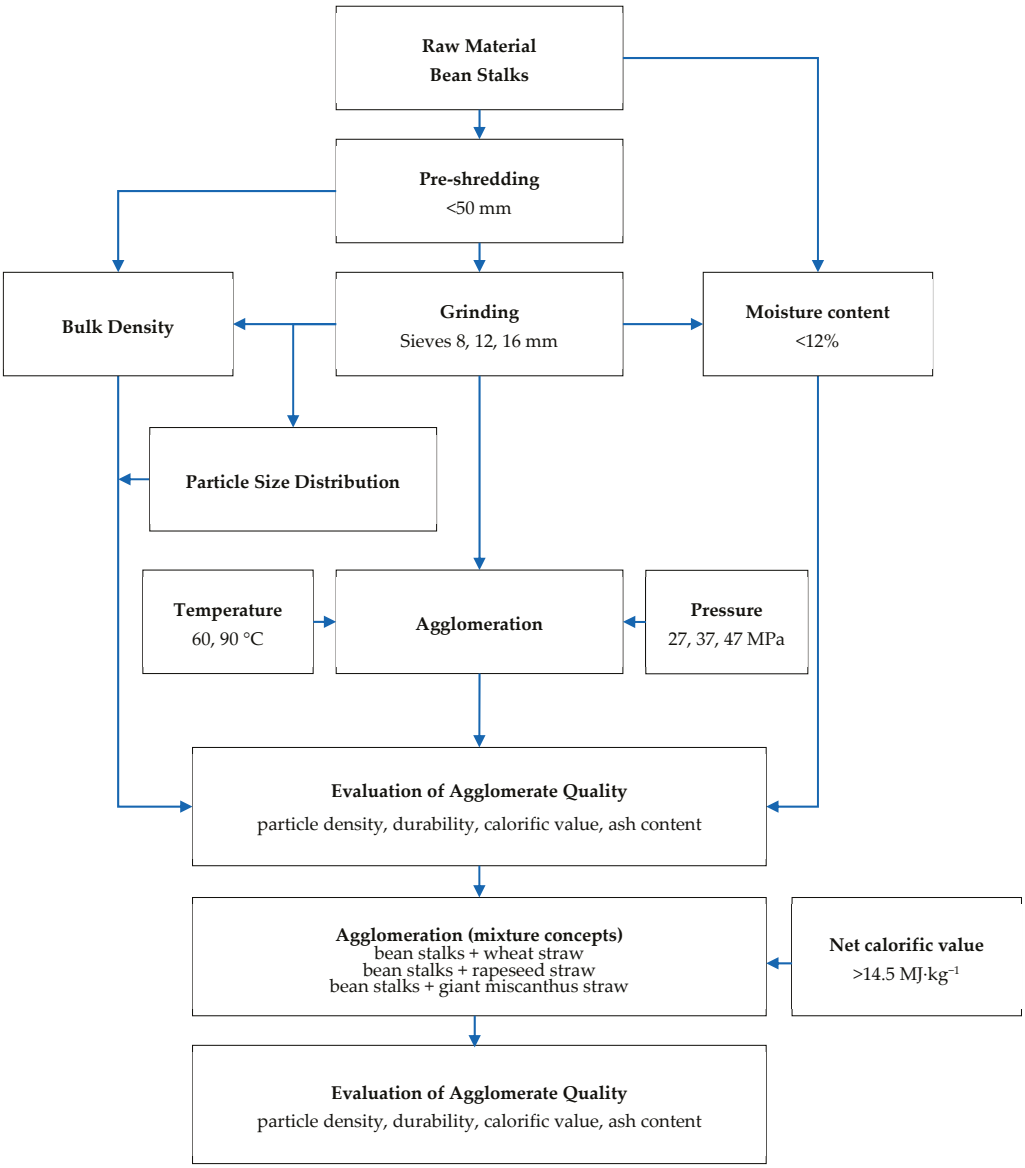


Figure 2. Schematic representation of the conducted study.

Subsequently, the material was pre-shredded into fractions shorter than 50 mm (Figure 3a) using a stationary Claas chopping machine with axe-type cutting blades (model OPTIMAT, CLAAS, Harsewinkel, Germany). The bulk density of the processed biomass was then determined in accordance with the PN-EN ISO 17828:2016 standard [42], using a cylindrical measuring container with a volume of 0.005 m^3. The sample mass was measured using a analytical laboratory balance, with an accuracy of ±0.1 g (model WLC 10/A2, RAGWAG, Radom, Poland). The measurement procedure involved filling the container with the biomass without mechanical compaction. To ensure uniform material distribution, the container was tapped twice by dropping it from a height of 10 cm.

The next stage in biomass processing was final grinding using a milling unit (model MF-4, Protechnika, Łuków, Poland). The device operated at a constant rotational speed of 650 rpm. In order to obtain three distinct particle size fractions, sieves with mesh diameters of 8 mm, 12 mm, and 16 mm were used. Photographs of the resulting fractions are shown in Figure 3b–d.

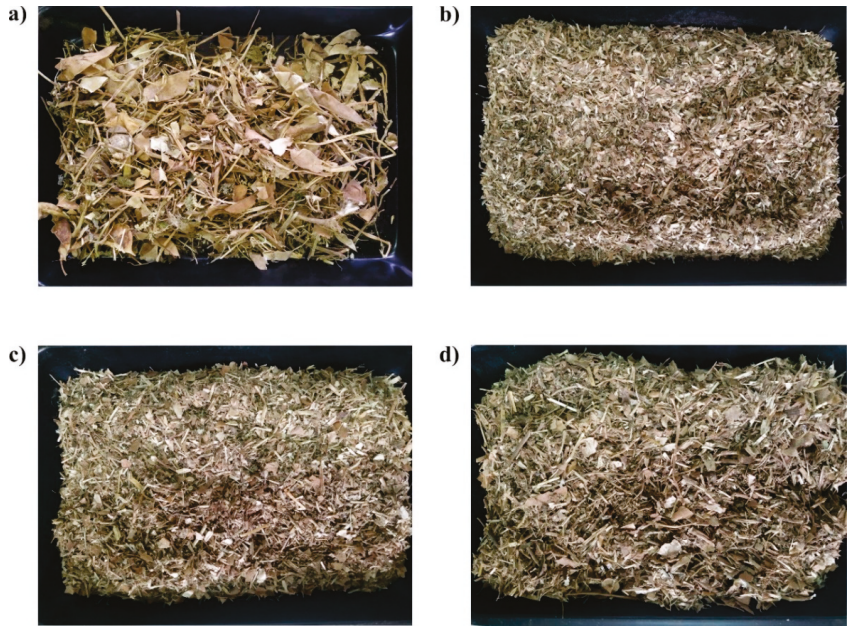


Figure 3. Ground bean stalks: (**a**) pre-shredded material, (**b**)8 mm sieve, (**c**) 12 mm sieve, (**d**) 16 mm sieve.

The prepared material was subjected to a drying process using a industrial dryer (model SLW 115, Pol-Eko, Wodzisław Śląski, Poland). Drying was conducted at a temperature of 70 °C with the airflow set at a maximum intensity of 50%, which ensured uniform moisture removal throughout the entire volume of the material. This process yielded three target moisture levels—approximately 8%, 12%, and 16%.

For the dried material, a particle size distribution analysis was performed using a laboratory shaker (model LPzE-4e, Morek Multiserw, Marcyporęba, Poland). The test employed a set of sieves with mesh sizes of 1 mm, 1.4 mm, 2 mm, 3.15 mm, 6 mm, and 12 mm. Each test lasted 5 min, and the sample mass used was 350 g. Measurements were repeated three times for each sample.

Following drying, the material was subjected to briquetting using a hydraulic briquetting press (Model Junior, Por-Ecomec, Cuveglio, Italy). The briquetting process (as illustrated in Figure 2) was conducted in two variants:

- without die heating—the temperature was determined solely by the heat generated during the operation of the compaction unit, reaching approximately 60 °C;
- with a heating sleeve—designed to maintain the inner surface of the die at 90 °C.

Each agglomeration variant was conducted in three replicates.

Figure 4 presents the key component of the heating system: a 3 mm thick aluminum clamp (2), permanently equipped with a resistance heater (1). Its main function was to heat the segmented outlet sleeve of the briquetting die to the target temperature in order to improve briquette formation quality. The clamp was mounted onto the die and tightened using a screw knob with a butterfly nut (3), ensuring stability and even heat distribution. The operation of the heating element was controlled by a programmable PLC controller from Delta, which maintained the clamp temperature at 140 °C. As a result, the inner surface of the die reached a temperature of 90 °C, confirmed by measurements at point 6 (Figure 4). The temperature control system was based on a logarithmic algorithm that continuously monitored the temperature using a type K thermocouple (point 4 in Figure 4) and dynamically regulated the heater's power accordingly.

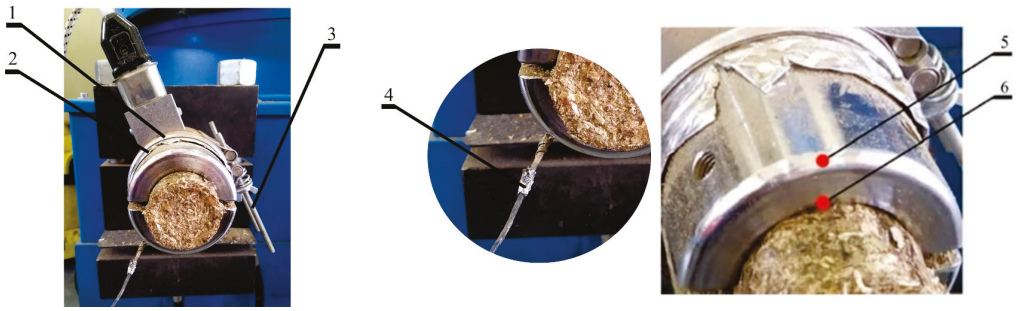


Figure 4. Structure of the die heating element: (1) heater, (2) aluminum sleeve, (3) clamping element, (4) type K thermocouple, (5) measurement point I, (6) measurement point II.

To ensure repeatability of the briquetting process parameters, preliminary heating of the briquetting press was carried out prior to the main trials. Pine sawdust with a particle size of less than 1 mm was used for this purpose, allowing for uniform heating of the die and stabilization of the machine's thermal conditions. The agglomeration of the test material was initiated only after the die had reached a stable target temperature.

Determination of Quality Parameters of Agglomerates

During the quality assessment of solid biofuels in the form of briquettes, it is essential to follow the guidelines set out in the applicable standards, which define appropriate measurement procedures. These standards encompass both basic terminology and the methodology for determining key biofuel properties, including moisture content, ash content, mechanical durability, particle density, and calorific value. Such standardization ensures comparability and interpretability of results obtained by different researchers and facilitates the evaluation of briquette quality across various production facilities.

The particle density of the briquettes was determined by measuring their mass using a analytical laboratory balance (model WLC 10/A2, RAGWAG, Radom, Poland) and calculating their volume based on the dimensions of each briquette measured with a digital caliper.

The durability analysis of the agglomerates was carried out in accordance with the requirements of the PN-EN ISO 17831-2:2016 standard [43]. A test drum with a diameter of 596 mm was used, equipped with an internal baffle of 200 mm in height. Each test cycle lasted 5 min, and the drum rotated at a speed of 21 rpm. In each trial, 2 kg of briquetted material were tested. After the cycle, the material was sieved using a 45 × 45 mm mesh. Each test was performed in triplicate. Durability was calculated using the following formula:

$$DU = \frac{m_1}{m_2} \cdot 100\% \quad (1)$$

where

DU—briquette durability, %;

m_1—mass of the sample retained on the sieve after testing, kg;

m_2—mass of the sample before testing, kg.

Ash content was determined in accordance with the PN-EN ISO 18122:2016 standard [44]. The analysis was performed in triplicate using a testing station equipped with a muffle furnace (model FCF 7SM, Czylok, Jastrzebie-Zdrój, Poland). During the procedure, 1 g of the sample was weighed into each of the three crucibles. The combustion process was carried out at a temperature of 550 °C and lasted for 5 h. The mass of the samples before and after combustion was measured using a laboratory balance (model AS 110.R2 PLUS, RAGWAG, Radom, Poland) which ensures high precision.

The calorific value was calculated based on the measured gross heat of combustion, following the requirements of the PN-EN ISO 18125:2017 standard [45]. The tests were conducted using an automatic calorimeter IKA C6000 (IKA-Werke, Staufen, Germany). The calculation of the net calorific value was performed in accordance with EN ISO 18125:2017, using the following formula:

$$Q = \left\{ q_{v.gr.d} - 212.2wH_d - 0.8[wO_d + wN_d] \right\} \cdot (1 - 0.01M) - 24.43M \quad (2)$$

where

Q—net calorific value at constant pressure and specified moisture content, $MJ \cdot kg^{-1}$;
$q_{v,gr,d}$—gross calorific value at constant volume, $MJ \cdot kg^{-1}$;
$w(H)_d$—hydrogen content, mass percent, and dry basis
(from Table C of PN-EN ISO 18125:2017: w(H)d = 6.3);
$w(O)_d$—oxygen content, mass percent, and dry basis
(from Table C of PN-EN ISO 18125:2017: $w(O)_d$ = 43);
$w(N)_d$—nitrogen content, mass percent, and dry basis
(from Table C of PN-EN ISO 18125:2017: w(N)d = 0.5);
M—moisture content and mass percent; here, M = 12.

3. Results and Discussions

3.1. Selected Physical Properties of Bean Stalks

3.1.1. Bulk Density

The bulk density of the tested samples was determined in accordance with the established methodology, and the obtained results (as the average of three replicates) are presented in Figure 5. For the pre-shredded material, the bulk density was 99.9 $kg \cdot m^{-3}$. It was observed that, as the mesh size of the milling sieve decreased, the bulk density increased systematically, reaching a value of 215 $kg \cdot m^{-3}$. This phenomenon can be explained by the fact that smaller particle sizes allow for greater packing density within a unit volume, thereby reducing the amount of void space between particles. In contrast, larger particles result in a more open structure with more empty spaces, which leads to a lower bulk density.

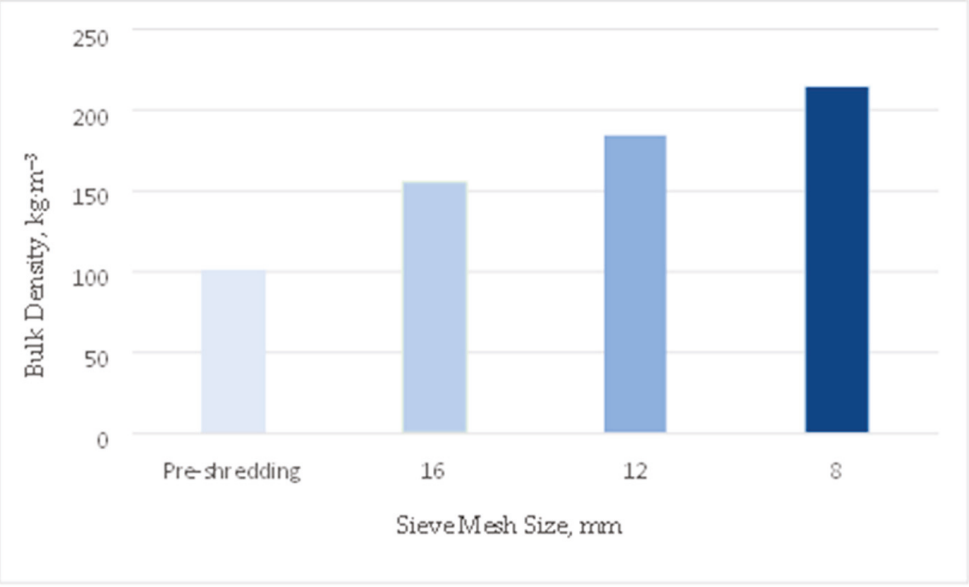


Figure 5. Bulk density of material fractions.

3.1.2. Particle Size Distribution

The particle size distribution of the three material fractions included in the study is presented in Figure 6. Analysis of the results revealed a clear trend of increasing mass share of larger particles with increasing sieve mesh size used in the milling process. The mass proportion of fine particles was highest for the 8 mm sieve, while for the 16 mm sieve, approximately 52% of the particles were larger than 3.15 mm.

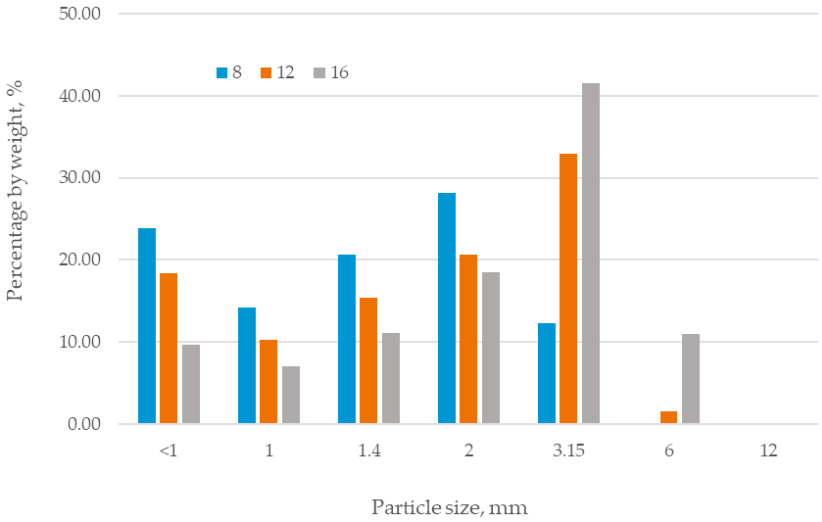


Figure 6. Particle size distribution of material processed with 8, 12, and 16 mm sieves.

To better illustrate the observed relationships, a cumulative distribution chart was created and is presented in Figure 7. Two characteristic mass share thresholds—30% and 90%—were marked on the graph to enable a detailed analysis of the dynamics of changes in the particle size distribution structure of the tested samples, depending on the sieve size used in the milling process. This was quantitatively estimated by calculating the ratios b/a and b*/a*, corresponding to the following segments:

- a and b—where a represents the difference in the position of the 30% mass share threshold between the 12 mm and 8 mm sieves and b refers to the analogous difference between the 16 mm and 12 mm sieves;
- a* and b*—where a* represents the difference in the position of the 90% mass share threshold between the 12 mm and 8 mm sieves and b* refers to the analogous difference between the 16 mm and 12 mm sieves.

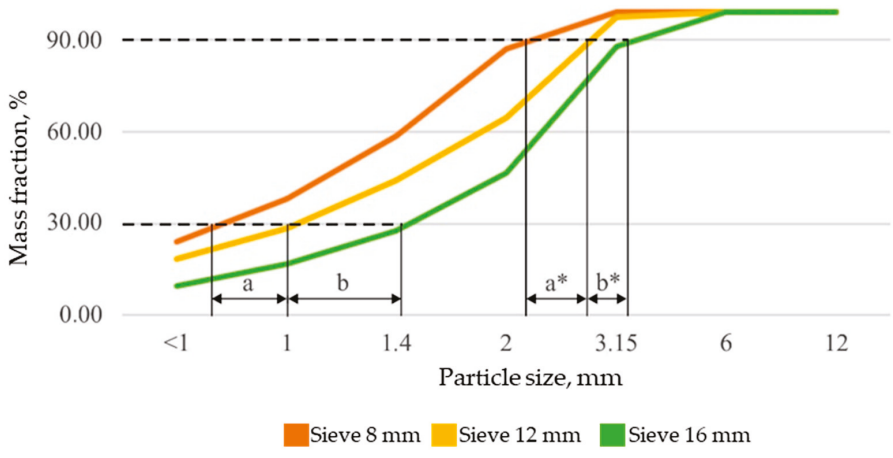


Figure 7. Cumulative curve for the mass share of 8, 12, and 16 mm sieve fractions.

The obtained b/a values clearly indicate a gradual decrease in the dynamics of mass share increase for particles passing through sieves smaller than 1.4 mm. A different trend was observed for particles retained on sieves larger than 2 mm—where the b*/a* ratio was less than one—indicating an increase in the rate of mass share growth. This suggests that the accumulation of larger particles intensifies with increasing sieve size.

3.2. Briquette Quality Parameters

3.2.1. Moisture Content

Although according to the PN-EN ISO 17225-7:2021 standard, the moisture content of briquettes should be below 12% (in this study: M_1 = 7.8% and M_2 = 12%), an additional briquetting test was performed using biomass with a higher moisture content (M_3 = 15.7%) to evaluate the effect of this parameter on the quality of the resulting biofuel. The test was conducted for the 8 mm particle size fraction at a compaction pressure of 37 MPa.

The briquetting process showed that the highest mechanical durability (DU) was achieved with biomass having a moisture content of 12%. In the case of moisture level M_1, low structural cohesion was observed (Figure 8a), while, for M_3, issues related to excessive plasticization of the biomass occurred (Figure 8b).

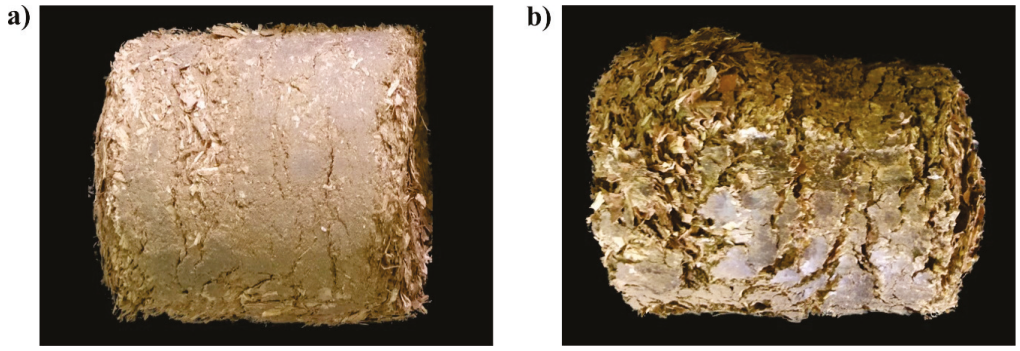


Figure 8. Appearance of briquettes produced from biomass with moisture content: (**a**) 8.7% and (**b**) 15.7%.

The temperature of the agglomeration process significantly affected the shape and properties of the briquettes. Higher temperatures promoted the plasticization of lignin, resulting in the formation of a vitrified surface. Volumetric deformation—particularly along the briquette's longitudinal axis—led to the development of microcracks on the side surface (Figure 9) and a slight increase in briquette length.

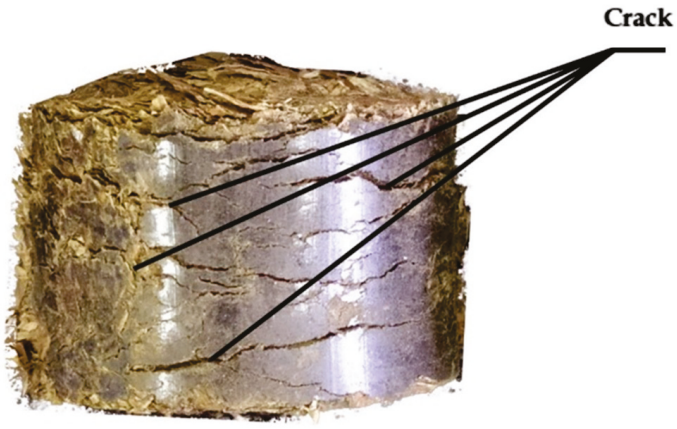


Figure 9. View of a briquette with cracks caused by internal stresses.

3.2.2. Ash Content

To assess the quality of the tested biomass, an ash content analysis was performed in accordance with applicable standards. The measurement results showed that the ash content in the material was 10.5% (Table 2). According to the requirements of the PN-EN ISO 17225-7:2021 standard, this exceeds the allowable threshold even for Class B non-woody briquettes, for which the maximum permissible ash content is 10%. As a result, the briquettes produced from the tested biomass cannot be classified within this group.

Table 2. Ash content after combustion.

Sample	Ash (%)	Ash (%) (After Sieving)
I	10.44	8.63
II	11.42	8.49
III	9.55	8.33
Average	10.5	8.5

The likely cause of this situation is the high proportion of mineral substances present in the tested material, which may be a consequence of the harvesting technology used. To verify this hypothesis, additional ash content measurements were conducted on milled bean stalks after the removal of particles smaller than 1 mm. The results are presented in Table 2. They confirmed the validity of the hypothesis—ash content in the samples without the <1 mm fraction decreased to 8.5%. Therefore, by separating out the fine dust fraction (i.e., particles < 1 mm), it is possible to produce briquettes that meet the requirements for classification in Group B with respect to ash content.

3.2.3. Particle Density (DE)

The produced briquettes were subjected to particle density (DE) measurements, as presented in Table 3. Analysis of the influence of agglomeration process parameters on briquette density showed that increasing compaction pressure led to an increase in DE. Conversely, an increase in particle size resulted in a decrease in DE.

It was observed that, for the unheated die, DE decreased as particle size increased. The opposite trend was noted for briquettes produced using a heated die. The lowest particle density was recorded for the 8 mm sieve, at a compaction pressure of 27 MPa and a die temperature of 90 °C (DE = 754.98 kg·m^{-3}), while the highest DE was obtained for the 8 mm fraction, 47 MPa pressure, and 60 °C die temperature (DE = 984.11 kg·m^{-3}).

Table 3. Particle density of agglomerates.

Temperature (°C)	Fraction (mm)	Pressure (MPa)	Particle Density (kg·m^{-3})
60	8	27	845.35
		37	925.56
		47	984.11
	12	27	854.31
		37	900.88
		47	913.82
	16	27	803.97
		37	846.36
		47	898.31

Table 3. *Cont.*

Temperature (°C)	Fraction (mm)	Pressure (MPa)	Particle Density (kg·m^{-3})
90	8	27	754.98
		37	838.71
		47	875.58
	12	27	755.78
		37	831.23
		47	882.32
	16	27	849.75
		37	868.25
		47	884.12

During the experiments, the dimensions of individual briquettes were measured after a material stabilization period. During this time, surface separation of the structure occurred (as previously mentioned), which led to an increase in the geometric dimensions of the tested briquettes. This effect may have caused an overestimation of the briquette volume and, consequently, a reduction in the calculated particle density.

3.2.4. Calorific Value

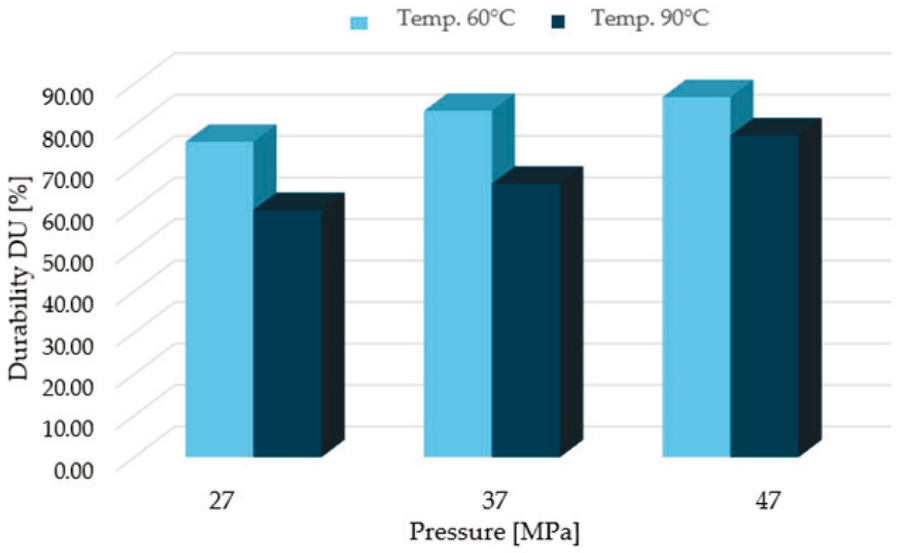
The average calorific value of the tested briquettes was 11.85 MJ·kg^{-1}. After removing dust from the input material, the calorific value increased to 12.05 MJ·kg^{-1} (Table 4). However, this increase was relatively small, and the obtained values do not meet the minimum requirement for classification even in Group B, which requires a net calorific value of at least 14.5 MJ·kg^{-1}.

Table 4. Gross and net calorific value.

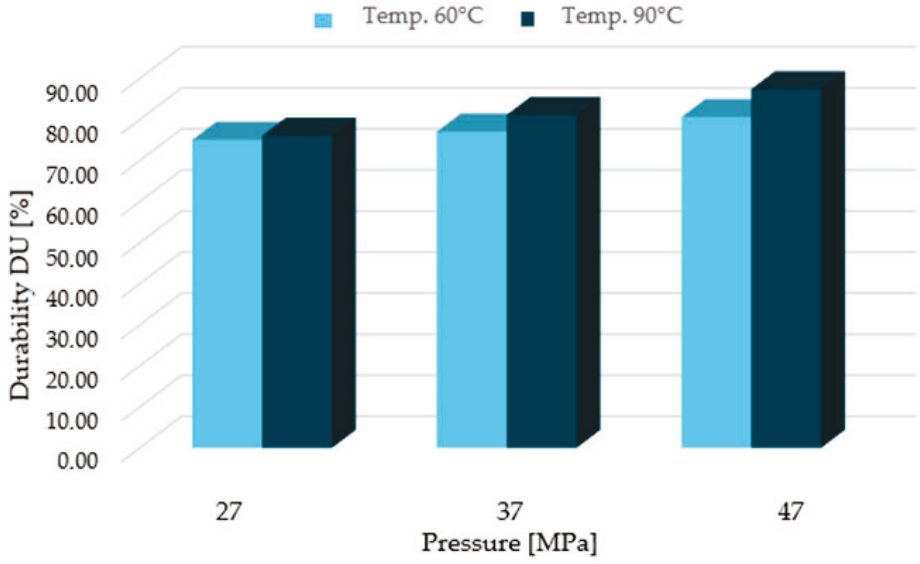
Sample	Sample with Dust		Sample Without Dust	
	Gross Calorific Value	Net Calorific Value	Gross Calorific Value	Net Calorific Value
	MJ·kg^{-1}	MJ·kg^{-1}	MJ·kg^{-1}	MJ·kg^{-1}
I	15.11	11.85	15.42	12.07
II	5.12	11.82	15.40	12.05
III	15.14	11.89	15.41	12.04
Average	15.12	11.85	15.41	12.05

3.2.5. Durability (DU)

One of the key quality parameters of briquettes is mechanical durability (DU), which indicates their resistance to stresses occurring during transport and storage. The DU measurement results for all tested samples are presented in Figure 10. From an economic perspective, considering the cost-effectiveness ratio, it can be concluded that milling the raw material using sieves smaller than 16 mm is not practically justified—due to both the increased energy demand of the process and the reduced quality parameters of the resulting product.



(**a**)



(**b**)

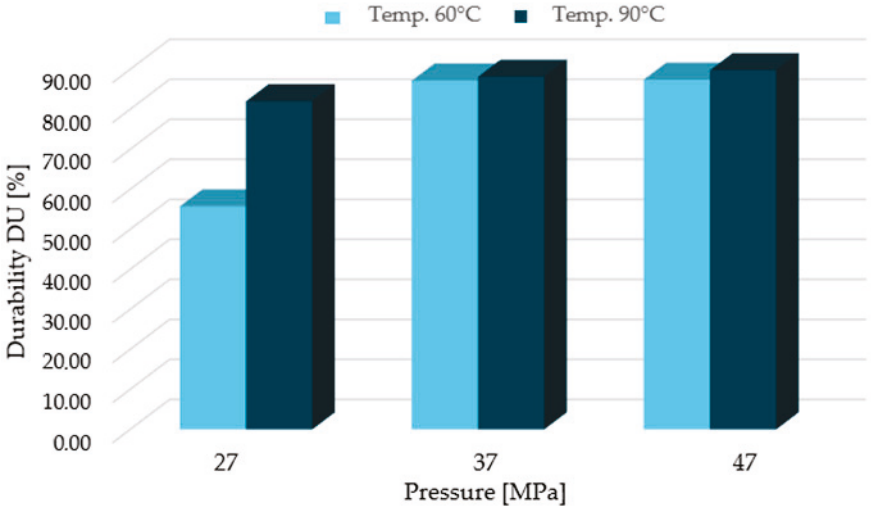


Figure 10. Mechanical durability (DU) of briquettes from sieve fractions: (**a**) 8 mm, (**b**) 12 mm, and (**c**) 16 mm.

3.2.6. Durability of Briquettes Without the <1 mm Fraction

Based on the results of the ash content analysis, which indicated a high likelihood of a significant proportion of mineral substances in the structure of the tested material, it was decided to conduct additional tests on the mechanical durability (DU) of the briquettes (Table 5). To reduce the influence of inorganic particles, the biomass was pre-screened to eliminate particles smaller than 1 mm.

Table 5. Mechanical durability (DU) of briquettes produced from biomass after removal of <1 mm fraction.

Particle Size Fraction (mm)	Mechanical Durability (DU) (%)
8	84.80
12	86.03
16	90.41

The parameters for the repeated briquetting process during DU testing were selected based on the earlier durability analysis, which showed that the most economically favorable conditions included a compaction pressure of 37 MPa and a die temperature of 90 °C.

Thanks to the removal of the fine fraction (i.e., particles smaller than 1 mm), a significant increase in mechanical durability (DU) was achieved, with the highest value recorded for briquettes produced from the 16 mm fraction. It should be emphasized that the current standard PN-EN ISO 17225-7:2021, which defines quality requirements for non-woody briquettes, does not include criteria for their mechanical durability. Nevertheless, considering that all types of briquettes—regardless of the raw material—are subjected to the same transport and storage conditions, it seems reasonable to adopt uniform durability requirements across all briquette types.

In the case of wood briquettes (according to PN-EN ISO 17225-3:2021 [46]), DU values should be $\geq$95% for Class A and $\geq$90% for Class B. Therefore, in order to classify briquettes made from bean stalks into Class B in terms of durability, the agglomeration process must be carried out using the 16 mm fraction, with particles < 1 mm removed, under a pressure of 47 MPa and at a die temperature of 90 °C.

The conducted research showed that the use of high pressure and elevated die temperature leads to partial plasticization and vitrification of lignin present in the milled bean stalks. This process results in a smoother briquette surface, which may positively influence its mechanical properties. A characteristic phenomenon observed during the tests was the difference in the degree of surface vitrification depending on the presence of the fine fraction in the biomass. Briquettes produced from biomass without the <1 mm fraction exhibited a lower degree of surface vitrification compared to those containing fine mineral and lignin particles. According to De Monte [47], bean fibers consist of 8% wax and 6% lignin. This structural content probably causes the small lignin particles present in the dust to become more intensely plasticized, leading to the sticking together of both fine mineral particles and biomass. After removing these particles, the bonding centers were partially eliminated, resulting in a reduction in the vitrified surface area of the briquettes (Figure 11).

The study revealed that the mechanical durability (DU) of briquettes containing particles smaller than 1 mm was relatively low, most likely due to the presence of mineral contaminants in the biomass. It was also demonstrated that increasing the briquetting temperature improves mechanical durability. Partial vitrification of lignin proved beneficial not only for enhancing DU, but also for increasing the hydrophobicity of the briquettes. The observed effect is comparable to that found in Pini-Kay briquettes produced using screw

presses at die temperatures exceeding 200 °C. Therefore, considering mechanical durability alone, briquettes made from bean stalks and produced at elevated temperatures and a compaction pressure of 47 MPa could be classified as Group B according to the PN-EN ISO 17225-7:2021 standard.

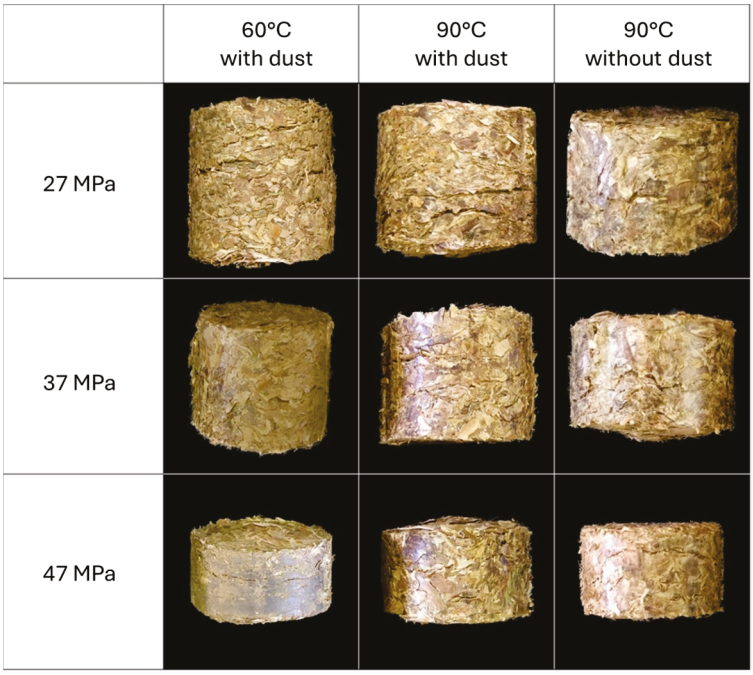


Figure 11. Comparison of briquette surface vitrification.

A summary of the quality assessment results of the tested briquettes in reference to normative requirements is presented in Table 6. It can be concluded that by implementing the proposed quality-enhancing measures (die temperature control and removal of fine dust fractions), it is feasible to produce high-quality briquettes, with most key parameters falling within the Class A1 or B range. The only exception remains the insufficient net calorific value.

Table 6. Comparison of normative values and values obtained for the briquettes.

Parameter.	Unit	Normative Value/Class	Test Result	Remarks
Moisture content, M	%	≤15/A1	12	Constant across all agglomerates
Ash content, A	%	≤10/B	8.5	After removal of <1 mm fraction
Particle density, DE	$kg \cdot m^{-3}$	≥0.6/B	≥0.85	Average across all fractions
Additives	%	<5/B	-	No additives used
Net calorific value, Q	$MJ \cdot kg^{-1}$	≥14.5/ (A1, A2, B)	12.05	For sample after removal of <1 mm fraction
Durability, DU	%	–/B	>90	For 16 mm fraction, 47 MPa pressure, 90 °C die temperature

3.3. Results of the Process of Modification of Raw Material Mixtures

The conducted research confirmed that bean stalks possess significant potential as a raw material for the production of solid biofuels in the form of briquettes. However, due to the relatively high content of mineral fractions (above 8%), which reduces the net calorific

value below 14.5 MJ·kg^{-1}, it appears necessary to introduce biomass additives with higher energy values into the briquetting process. Therefore, further steps were undertaken to produce briquettes with a minimum net calorific value of 14.5 MJ·kg^{-1}. It was proposed that the additives to the primary raw material (bean stalks) should include biomass obtainable from agricultural areas and perennial energy crops that can be harvested annually. As representatives of these two groups, maize straw (as a post-harvest agricultural residue) and miscanthus straw (from dedicated energy crop plantations) were selected. These materials have an established position in the bioenergy sector, being commonly used in both briquette and pellet production. Table 7 presents the basic properties of the substrates used in the mixing process.

Table 7. Substrate properties.

Parameter	Unit	Maize Straw	Giant Miscanthus Straw
Moisture content, M	%	12 ± 0.5	12 ± 0.5
Ash content, A	%	4.3 ± 0.1	2.2 ± 0.1
Net calorific value, Q	MJ·kg^{-1}	15.5 ± 0.2	17.6 ± 0.15

In the subsequent stage of the study, further experiments were conducted using bean stalk biomass ground with a 16 mm sieve and compacted under a pressure of 47 MPa. The maize and miscanthus straw used as additives were also comminuted, but using an 8 mm sieve due to their lower susceptibility to fragmentation. The raw materials were mixed in predetermined mass ratios using a ribbon mixer for 5 min to ensure homogeneous distribution of components in the blend. The resulting mixtures were then subjected to the briquetting process under previously defined parameters.

The produced briquettes were evaluated for their physical and mechanical quality. The bulk density of the briquettes ranged from 918 to 955 kg·m^{-3}, while the mechanical durability exceeded 91%, indicating good compaction and cohesion of the material. These results confirm the suitability of mixing bean stalks with selected agricultural residues to improve both the energetic and mechanical parameters of the briquettes.

Moreover, briquettes produced from these biomass mixtures met the quality requirements for Class A solid biofuels according to PN-EN ISO 17225-2 and 17225-7, which highlights their potential for practical use in domestic and small-scale heating systems.

Laboratory-scale tests showed that, to achieve a target net calorific value exceeding 14.5 MJ·kg^{-1}, the bean stalks should be blended with maize straw or miscanthus straw in the following proportions (Table 8):

Table 8. Calorific value of the briquettes obtained.

Mixture Bean Stalks+	Share of Bean Stalks [%]	Share of Additive [%]	Net Calorific Value [MJ·kg^{-1}]
Maize straw	29.00	71.00	14.50
Miscanthus straw	55.90	44.10	14.50

The following charts (Figure 12) present the changes in net calorific value and ash content for the analyzed biomass mixtures. The results clearly show that the addition of miscanthus biomass leads to a significantly greater increase in calorific value and a more substantial reduction in ash content compared to the variant with maize straw. These findings indicate that the effective utilization of bean stalks for the production of high-

quality briquettes is achievable through blending with other types of biomass that are readily available from agricultural areas and exhibit more favorable fuel properties.

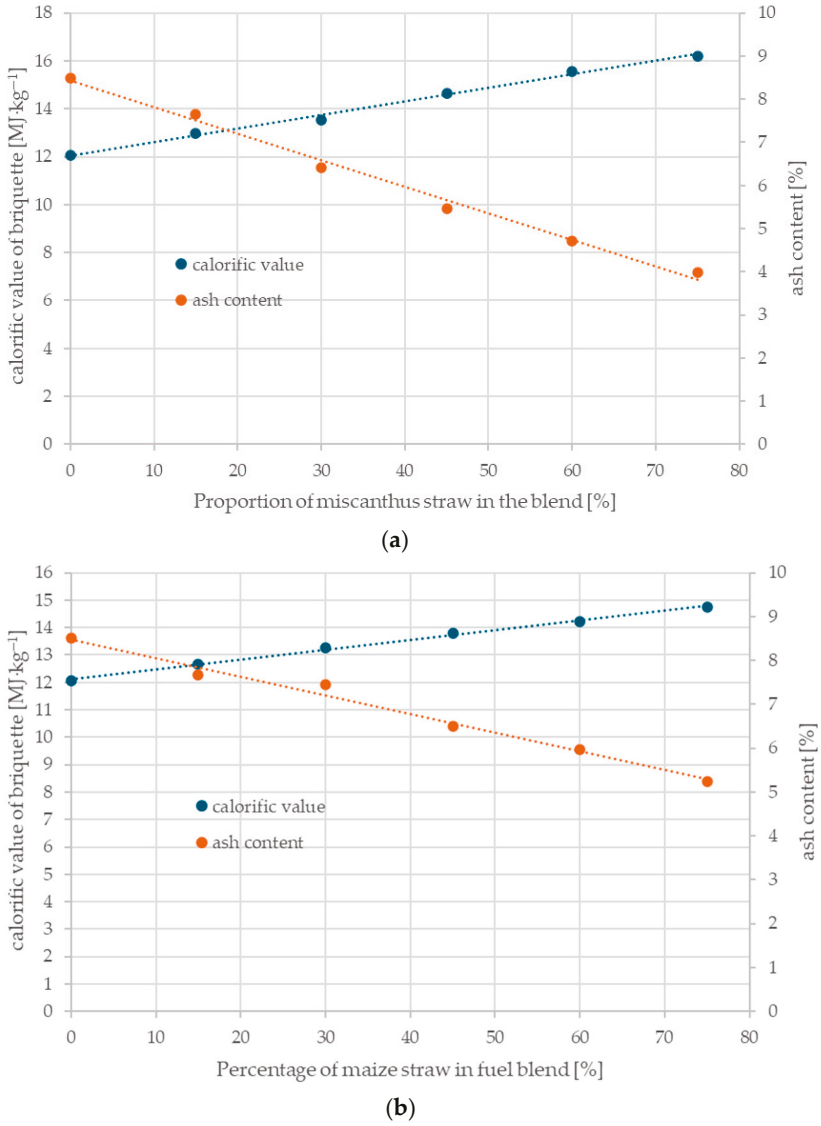


Figure 12. Variation in net calorific value and ash content in the tested biomass blends: (**a**) blend of bean stalks and miscanthus; (**b**) blend of bean stalks and maize straw.

This approach aligns with the concept of decentralized energy systems, which rely on locally sourced raw materials and minimize dependence on centralized fuel supply chains. By utilizing biomass available within the region—both as agricultural residues and from dedicated energy crops—it is possible to reduce transportation-related costs and emissions, while simultaneously promoting circular economy principles and the sustainable development of rural areas.

Moreover, the inclusion of unconventional, previously underutilized biomass such as bean stalks—combined with additives of higher calorific value—offers a practical alternative for the production of standardized, high-quality solid biofuels. This strategy enhances the flexibility of local energy systems, supports rural energy security, and stimulates the development of regional biomass supply and processing markets.

An increase in compaction pressure from 27 to 47 MPa and the use of coarser particle size (16 mm) led to a substantial improvement in both the density and mechanical durability of the briquettes, which enhances their resistance to handling and storage stresses (Table 9).

Table 9. Analysis of briquette quality improvements.

Parameter	16 mm Fraction + 27 MPa	16 mm Fraction + 47 MPa	Change (%)
Particle density	~850 kg/m^3	~955 kg/m^3	↑ +12.35%
Mechanical durability	~55.8%	~91.0%	↑ +63.1% (rel.)
Structural integrity	Low, cracked	Compact, stable	Qualitative gain

The removal of fine particles (<1 mm) had a beneficial effect on the energy and physical parameters of the briquettes, reducing ash content and improving compressibility (Table 10).

Table 10. Effect of fine fraction removal on bean biomass briquettes.

Parameter	Before Removal	After Removal	Change (%)
Ash content	10.50%	8.50%	↓ –19.0%
Net calorific value	11.85 MJ/kg	12.05 MJ/kg	↑ +1.7%
Mechanical durability	~70–74%	+3–5 pp more	↑ ~5–7% (estimated)

Although the removal of particles < 1 mm increased the calorific value to 12.05 MJ·kg^{-1}, it was still insufficient to meet the threshold for Class B fuels. To address this, high-calorific biomass additives—maize straw and miscanthus giganteus—were introduced. The experimental results showed that adding 30–45% maize straw increased the calorific value to 15.1 MJ·kg^{-1} while reducing ash content to below 6%. Even better results were obtained with miscanthus: at a 45% share, the calorific value reached 15.9 MJ·kg^{-1}, and with 60–75%, it exceeded 16.5 MJ·kg^{-1} with ash content below 4%. These values correspond to the minimum requirements for Class A2 fuels (Table 11).

Table 11. Properties of briquettes made from bean straw and high-energy biomass additives.

Additive and Share	Calorific Value	Ash Content	Classification
30% maize straw	14.6 MJ·kg^{-1}	~6.5%	B
45% maize straw	15.1 MJ·kg^{-1}	<6%	B
30% miscanthus	>15.2 MJ·kg^{-1}	<5.5%	B
45% miscanthus	15.9 MJ·kg^{-1}	~5%	B
60–75% miscanthus	>16.5 MJ·kg^{-1}	<4%	A2

These findings are consistent with those of Kaliyan and Morey [48] and Yub Harun [3] who emphasized the importance of selecting appropriate feedstocks and combining them to improve briquette calorific value and structural cohesion.

From a mechanical perspective, the presence of fibrous biomass rich in lignin (e.g., miscanthus) enhanced inter-particle bonding, improving cohesion and dimensional stability—an effect also reported by Stelte [49]. Moisture content and particle size distribution played important roles as well: while finer fractions increased bulk density, they also restricted airflow during compaction.

Transitioning from laboratory to industrial-scale briquetting (using a piston press) demonstrated the scalability of the technology. Despite limited adjustability of parameters, the produced briquettes exhibited high mechanical durability (>91%) and acceptable bulk and particle densities (918–955 kg·m^{-3}), meeting the required standards for quality solid biofuels.

From a broader perspective, utilizing bean stalks in combination with locally available high-energy biomass fits within the principles of decentralized energy systems and the circular economy. This approach supports the valorization of agricultural residues, reduces environmental impacts from burning or field decomposition, and enhances the energy autonomy of rural households and municipalities.

These results align with the findings of Obernberger and Thek [50] who highlighted the social and environmental benefits of integrated biomass utilization systems.

In conclusion, although bean stalks alone do not meet the full energy performance criteria of Class B fuels, their effective use—via blending with complementary biomass—represents a viable and sustainable strategy for producing ecological solid fuels. The findings offer practical guidance for optimizing the briquetting process and underscore the importance of raw material preparation, blend composition, and process control in achieving high-quality biofuels under local conditions.

4. Conclusions

Analysis of the obtained results led to the following conclusions:

1. The highest bulk density of shredded bean stalks was obtained for material from the 8 mm sieve fraction (215 $kg \cdot m^{-3}$), while the lowest was recorded for the 16 mm fraction (155 $kg \cdot m^{-3}$), confirming the significant influence of particle size on the technological properties of biomass.
2. The ash content in the primary raw material (bean stalks) decreased from 10.5% to 8.5% after removing the dust fraction (<1 mm), indicating the potential to improve fuel quality through simple separation of mineral particles.
3. The net calorific value of pure bean stalks was 11.85 $MJ \cdot kg^{-1}$. After the removal of the <1 mm fraction, it increased to 12.05 $MJ \cdot kg^{-1}$. Nevertheless, this value remains below the threshold required for Class B fuels according to PN-EN ISO 17225-7:2021.
4. The highest mechanical durability of briquettes was achieved at the highest compaction pressure (47 MPa) and with larger particle sizes (8–12 mm). Additionally, raising the die temperature facilitated partial lignin vitrification, resulting in improved cohesion and hydrophobicity of the briquettes.
5. Bean stalks represent a promising agricultural biomass feedstock for the production of Class B briquettes, but they require technological support in the form of additives with higher energy content.
6. Tests involving bean stalks blended with complementary biomass demonstrated that as follows:
    a. mixtures with 30% maize straw achieved a net calorific value close to 14.6 $MJ \cdot kg^{-1}$ and ash content reduced to approximately 6.5%;
    b. increasing maize straw content to 45% allowed a stable calorific value of 15.1 $MJ \cdot kg^{-1}$ with ash content below 6%;
    c. mixtures with 30% miscanthus straw yielded a calorific value above 15.2 $MJ \cdot kg^{-1}$ and ash content below 5.5%; at 45% miscanthus, the calorific value reached 15.9 $MJ \cdot kg^{-1}$ with ash around 5%;
    d. mixtures containing 60–75% miscanthus achieved calorific values exceeding 16.5 $MJ \cdot kg^{-1}$ and ash contents below 4%, placing the fuel at the boundary of Class A2.
7. The approach of blending locally available residual biomass streams aligns with the principles of the circular economy and decentralized energy systems. It offers practical opportunities for utilizing agricultural residues at the level of farms, municipalities, or small enterprises.

Author Contributions: Conceptualization, K.M.; Methodology, J.F.; Validation, J.F.; Formal analysis, J.L.; Data curation, K.M., J.F. and M.K.; Writing—original draft, J.L.; Writing—review & editing, K.M. All authors have read and agreed to the published version of the manuscript.

Funding: This research was supported by Ministry of Science and Higher Education of the Republic of Poland (Faculty of Production and Power Engineering, University of Agriculture in Krakow).

Data Availability Statement: The original contributions presented in this study are included in the article. Further inquiries can be directed to the corresponding author.

Conflicts of Interest: The authors declare no conflict of interest.

References

1. Adam, R.; Yiyang, D.; Kruggel-Emden, H.; Zeng, T.; Lenz, V. Influence of pressure and retention time on briquette volume and raw density during biomass densification with an industrial stamp briquetting machine. *Renew. Energy* **2024**, *229*, 120773. [CrossRef]
2. Akande, O.M.; Olorunnisola, A.O. Potential of Briquetting as a Waste-Management Option for Handling Market-Generated Vegetable Waste in Port Harcourt, Nigeria. *Recycling* **2018**, *3*, 11. [CrossRef]
3. Yub Harun, N.; Parvez, A.M.; Afzal, M.T. Process and Energy Analysis of Pelleting Agricultural and Woody Biomass Blends. *Sustainability* **2018**, *10*, 1770. [CrossRef]
4. Ali, M.A.; Nasir, A.; Muneer, A.; Ali, S.; Rashid, U. Compaction characteristics of sawdust, cotton stalks, maize straw and rice straw briquettes. *J. Energy Env. Carbon Credit.* **2015**, *5*, 1–9.
5. Antar, M.; Lyu, D.; Nazari, M.; Shah, A.; Zhou, X.; Smith, D.L. Biomass for a sustainable bioeconomy: An overview of world biomass production and utilization. *Renew. Sustain. Energy Rev.* **2021**, *139*, 110691. [CrossRef]
6. Araque, O.; Arzola, N.; Gallego, L. Mechanical Behavior of Briquettes Made from a Mixture of Sawdust and Rice Husks for Commercialization. *Resources* **2022**, *11*, 32. [CrossRef]
7. Chidiebele, E.J.U.; Okoroigwe, E.; Kadivar, M.; Anye, V.C.; Bello, A.; Ezealigo, U.; Ngasoh, F.O.; Pereira, H.; Onwualu, P.A. Characterization of Wood, Leaves, Barks, and pod wastes from *Prosopis africana* biomass for biofuel production. *Waste Manag. Bull.* **2024**, *2*, 172–182. [CrossRef]
8. Demirbaş, A. Biomass resource facilities and biomass conversion processing for fuels and chemicals. *Energy Convers. Manag.* **2001**, *42*, 1357–1378. [CrossRef]
9. Fiszer, A. Influence of straw humidity and temperature of briquetting process on the quality of agglomerate. *J. Res. Appl. Agric. Eng.* **2009**, *54*, 68–70.
10. Tomei, J.; Helliwell, R. Food versus fuel? Going beyond biofuels. *Land Use Policy* **2016**, *56*, 320–326. [CrossRef]
11. Frączek, J.; Cieślikowski, B.; Francik, S.; Ślipek, Z. Wpływ stopnia rozdrobnienia pędów wierzby oraz ciśnienia aglomeracji na trwałość brykietu. *Logistyka-nauka* **2014**, *6*, 3636–3641. (In Polish)
12. Fraczek, J.; Cieślikowski, B.; Ślipek, Z. Ocena jakości biopaliw stałych kompaktowanych. Część I: Wymagania jakościowe. *Autobusy.* **2011**, *58*, 161–169. (In Polish)
13. He, H.; Wang, Y.; Sun, Y.; Sun, W.; Wu, K. From raw material powder to solid fuel pellet: A state-of-the-art review of biomass densification. *Biomass Bioenergy* **2024**, *186*, 107271. [CrossRef]
14. Tumuluru, J.S.; Rajan, K.; Hamilton, C.; Pope, C.; Rials, T.G.; McCord, J.; Labbé, N.; André, N.O. Pilot-Scale Pelleting Tests on High-Moisture Pine, Switchgrass, and Their Blends: Impact on Pellet Physical Properties, Chemical Composition, and Heating Values. *Front. Energy Res.* **2022**, *9*, 788284. [CrossRef]
15. Gil, M.V.; Oulego, P.; Casal, M.D.; Pevida, C.; Pis, J.J.; Rubiera, F. Mechanical durability and combustion characteristics of pellets from biomass blends. *Bioresour. Technol.* **2010**, *101*, 8859–8867. [CrossRef] [PubMed]
16. Ha, H.; Brown, T.R.; Quinn, R.J.; Volk, T.A.; Malmsheimer, R.W.; Fortier, M.-O.P.; Frank, J.R.; Bick, S. Economic feasibility of forest biomass feedstock supply chains: Clean and dirty chips for bioenergy applications. *Biofuels Bioprod. Bioref.* **2022**, *16*, 389–402. [CrossRef]
17. Jeguirim, M.; Khiari, B. Solid biofuels production and combustion at domestic scales. In *Advances in Biofuels Production, Optimization and Applications*; Elsevier: Amsterdam, The Netherlands, 2024; pp. 207–239. ISBN 9780323950763.
18. Jasiulewicz, M. Produkcja energii z agrobiomasy w Polsce i na tle wybranych krajów Unii Europejskiej, Stowarzyszenie Ekonomistów Rolnictwa i Agrobiznesu. *Rocz. Nauk. T.* **2015**, *17*, 94–99. (In Polish)
19. Hamid, A.; Muaddah, H.H.; Sharif Za'ba, A.S.; Afandy, M.D. Biomass briqmure: BBQ briquettes fuel source from cow manure. *Educ. Humanit. Res.* **2021**, *536*, 457–460.
20. Ivaschuk, V.P.; Atamanyuk, V.M.; Chyzhovych, R.A.; Kiiaieva, S.S.; Duleba, V.P.; Sobechko, I.B. Research of solid fuel briquettes obtaining from brewer's spent grain. *J. Chem. Technol.* **2022**, *30*, 216–221.

21. Jha, S.; Okolie, J.A.; Nanda, S.; Dalai, A.K. A Review of Biomass Resources and Thermochemical Conversion Technologies. *Chem. Eng. Technol.* **2022**, *45*, 791–799. [CrossRef]
22. Krenz, L.M.M.; Grebenteuch, S.; Zocher, K.; Rohn, S.; Pleissner, D. Valorization of faba bean (Vicia faba) by-products. *Biomass Convers. Biorefinery* **2024**, *14*, 26663–26680. [CrossRef]
23. Kajda-Szczęśniak, M. Ocena jakości brykietów wykonanych w oparciu o słomę kukurydzy i polietylenu o niskiej gęstości. *Arch. Gospod. Odpad. I Ochr. Sr.* **2012**, *14*, 41–50. (In Polish)
24. Study "Protein crop market in Poland". Available online: https://www.agroberichtenbuitenland.nl/landeninformatie/polen/achtergrond/protein-crop-market-in-poland (accessed on 22 July 2025).
25. Hesami, M.; Yoosefzadeh-Najafabadi, M. Trends in production, consumption, trade, and research of dry beans across the globe and Canada. *Can. J. Plant Sci.* **2025**, *105*, 1–14. [CrossRef]
26. Akibode, C.S.; Maredia, M.K. Global and Regional Trends in Production, Trade and Consumption of Food Legume Crops. 2012. Available online: https://ageconsearch.umn.edu/record/136293?v=pdf (accessed on 22 July 2025). [CrossRef]
27. Stelte, W.; Holm, J.K.; Ahrenfeldt, J.; Henriksen, U.; Sanadi, A.R. Fuel pellets from biomass: The importance of the pelletizing pressure and its dependency on the processing conditions. *Fuel* **2011**, *90*, 3285–3290. [CrossRef]
28. Marreiro, H.M.P.; Peruchi, R.S.; Lopes, R.M.B.P.; Andersen, S.L.F.; Eliziário, S.A.; Rotella, P., Jr. Empirical Studies on Biomass Briquette Production: A Literature Review. *Energies* **2021**, *14*, 8320. [CrossRef]
29. Orisaleye, J.I.; Jekayinfa, S.O.; Dittrich, C.; Obi, O.F.; Pecenka, R. Effects of Feeding Speed and Temperature on Properties of Briquettes from Poplar Wood Using a Hydraulic Briquetting Press. *Resources* **2023**, *12*, 12. [CrossRef]
30. Kaliyan, N.; Morey, R.V. Factors affecting strength and durability of densified biomass products. *Biomass Bioenergy* **2009**, *33*, 337–359. [CrossRef]
31. *PN-EN ISO 17225-7*; Solid Biofuels—Fuel Specifications and Classes—Part 7: Graded Non-Woody Briquettes. Polish Standardization Committee: Warsaw, Poland, 2021.
32. Okot, D.K.; Bilsborrow, P.E.; Phan, A.N. Briquetting characteristics of bean straw-maize cob blend. *Biomass Bioenergy* **2019**, *126*, 150–158. [CrossRef]
33. Obidziński, S.; Kobyliński, M.; Dec, D.; Piekut, J. Badania procesu brykietowania mieszanin materiałów odpadowych pochodzenia roślinnego. *Postępy Tech. Przetwórstwa Spożywczego* **2015**, *1*, 126–130. (In Polish)
34. Jasinskas, A.; Minajeva, A.; Šarauskis, E.; Romaneckas, K.; Kimbirauskienė, R.; Pedišius, N. Recycling and utilisation of faba bean harvesting and threshing waste for bioenergy. *Renew. Energy* **2020**, *162*, 257–266. [CrossRef]
35. Trejo-Zamudio, D.; Gutiérrez-Antonio, C.; García-Trejo, J.F.; Feregrino-Pérez, A.A.; Toledano-Ayala, M. Production of fuel pellets from bean crop residues (*Phaseolus vulgaris*). *IET Renew. Power Gener.* **2022**, *16*, 2978–2987. [CrossRef]
36. Petlickaitė, R.; Jasinskas, A.; Mieldažys, R.; Romaneckas, K.; Praspaliauskas, M.; Balandaitė, J. Evaluation of the processing of multi-crop plants into pelletized biofuel and its use for energy conversion. *Processes* **2023**, *11*, 421. [CrossRef]
37. *PN-EN ISO 17225-6*; Solid Biofuels—Fuel Specifications and Classes—Part 6: Graded Non-Woody Pellets. Polish Standardization Committee: Warsaw, Poland, 2021.
38. Okot, D.K.; Bilsborrow, P.E.; Phan, A.N.; Manning, D.A.C. Kinetics of maize cob and bean straw pyrolysis and combustion. *Heliyon* **2023**, *9*, e17236. [CrossRef]
39. Lopez, A.; Morales, M.S. Intake and apparent digestibility of forages in llamas (*Lama glama*). II. clover hay (*Trifolium pratense*), ryegrass hay (*Lolium multiflorum*), beans straw (*Phaseolus vulgaris*) and oat straw (*Avena sativa*). *Arch. Med. Vet.* **2001**, *33*, 145–153. [CrossRef]
40. Arija, I.; Centeno, C.; Viveros, A.; Brenes, A.; Marzo, F.; Illera, J.C.; Silvan, G. Nutritional Evaluation of Raw and Extruded Kidney Bean (*Phaseolus vulgaris* L. var. Pinto) in Chicken Diets. *Poult. Sci.* **2006**, *85*, 635–644. [CrossRef]
41. *PN-EN ISO 18134-1:2015-11*; Solid Biofuels—Determination of Moisture Content—Drying Method—Part 1: Total Mois-Ture—Reference Method. ISO: Polish Standardization Committee: Warsaw, Poland, 2015.
42. *PN EN ISO 17828:2016*; Solid biofuels—Determination of Bulk Density. Polish Standardization Committee: Warsaw, Poland, 2016.
43. *PN-EN-ISO 17831-2:2016-02*; Solid Biofuels—Methods for the Determination of Mechanical Durability of Pellets and Briquettes—Part 2: Briquettes. Polish Standardization Committee: Warsaw, Poland, 2016.
44. *PN-EN ISO 18122:2016-01; Solid Biofuels—Determination of Ash Content. Polish Standardization Committee: Warsaw, Poland, 2016*.
45. *PN-EN ISO 18125:2017-07; Solid Biofuels—Determination of Calorific Value. Polish Standardization Committee: Warsaw, Poland, 2017.*
46. *PN-EN ISO 17225-3:2021-08*; Solid Biofuels—Fuel Specifications and Classes—Part 3: Graded Wood Briquettes. Polish Standardization Committee: Warsaw, Poland, 2021.
47. De Monte, C.; Arrighetti, L.; Ricci, L.; Civello, A.; Bronco, S. Agro-Waste Bean Fibers as Reinforce Materials for Polycaprolactone Composites. *Compounds* **2023**, *3*, 504–520. [CrossRef]
48. Kaliyan, N.; Morey, R.V. Densification characteristics of corn stover and switchgrass. *Trans. ASABE* **2009**, *52*, 907–920. [CrossRef]

49. Obernberger, I.; Thek, G. *The Pellet Handbook: The Production and Thermal Utilization of Biomass Pellets*; Earthscan: London, UK, 2010; ISBN 9781844076314.
50. Stelte, W.; Clemons, C.; Holm, J.K.; Sanadi, A.R.; Ahrenfeldt, J.; Shang, L.; Henriksen, U. Pelletizing properties of torrefied spruce. *Biomass Bioenergy* **2011**, *35*, 4690–4698. [CrossRef]

Disclaimer/Publisher's Note: The statements, opinions and data contained in all publications are solely those of the individual author(s) and contributor(s) and not of MDPI and/or the editor(s). MDPI and/or the editor(s) disclaim responsibility for any injury to people or property resulting from any ideas, methods, instructions or products referred to in the content.

energies

MDPI

Article

Performance and Environmental Assessment of Palm Oil–Coffee Husk Biodiesel Blends in a Dual-Fuel Diesel Engine Operating with Hydroxy

Jovanny Rafael Duque [1,2], Fabio Bermejo-Altamar [1], Jorge Duarte-Forero [3,*] and Brando Hernández-Comas [1]

[1] Departamento de Energía, Universidad de la Costa CUC, Calle 58 Número 55-66, Barranquilla 080002, Atlántico, Colombia; jduque14@cuc.edu.co or jduque@unibarranquilla.edu.co (J.R.D.); fbermejo2@cuc.edu.co (F.B.-A.); bhernand22@cuc.edu.co (B.H.-C.)
[2] Facultad de Ingeniería, Institución Universitaria de Barranquilla, Cra. 45 Número 48-31, Barranquilla 080002, Atlántico, Colombia
[3] KAI Research Unit, Department of Mechanical Engineering, Universidad del Atlántico, Carrera 30 Número 8–49, Puerto Colombia 081001, Atlántico, Colombia
* Correspondence: jorgeduarte@mail.uniatlantico.edu.co

Abstract

This research analyzes the influence of hydroxy on pure diesel and blends of palm oil and coffee husk biodiesel with percentages of 15% and 20%. The experimental tests were carried out in a stationary diesel engine, where the torque and speed varied from 3–7 Nm and 3000–3600 rpm. Hydroxy was used as a secondary fuel with a volumetric flow injection of 4 and 8 lpm. The injection of hydroxy can reduce the BSFC and increase the BTE of the engine when running on pure diesel and biodiesel blends. The results show a maximum decrease of 11.66%, 11.28%, and 10.94% in BSFC when hydroxy is injected into D100, D85P10C5, and D80P10C10 fuels. In the case of BTE, maximum increases of 13.37%, 12.84%, and 12.34% were obtained for the above fuels. The fuels D100 + 8 lpm, D85P10C5 + 8 lpm, and D80P10C10 + 8 lpm achieved maximum energy efficiencies of 28.16%, 27.58%, and 27.32%, respectively. In the case of exergy efficiency, maximum values of 26.39%, 25.83%, and 25.58% were obtained. The environmental and social costs of CO, CO_2, and HC emissions are significantly reduced with the addition of hydroxy in pure diesel and biodiesel blends from palm oil and coffee husk. The injection of a volumetric flow rate of 8 L/min results in reductions of 11.66%, 10.61%, and 10.94% in operational cost when the engine is fueled with D100, D85P10C5, and D80P10C10, respectively, complying with standards essential for safe engine operation. In general, the research conducted indicates that hydroxy injection is a viable alternative for reducing fuel consumption and improving engine efficiency when using biodiesel blends made from palm oil and coffee husk.

Keywords: engine; operational cost; efficiency; emissions; hydroxy; palm oil; coffee husk

1. Introduction

Diesel-fueled internal combustion engines are widely used in heavy transportation, agro-industrial activities, and power generation due to their adaptable operating range and high thermal efficiency [1]. Despite this, the emissions produced by diesel engines have a significant impact on the environment and human health [2]. Due to environmental concerns, emission standards for diesel engines have become increasingly stringent, motivating researchers to seek strategies for reducing emissions [3]. Among the various

alternatives studied, the use of biofuels is one of the most promising due to their renewable nature and ability to be blended with traditional diesel [4]. Biofuels can be produced from waste fats, waste hulls, vegetable seeds, and waste vegetable oil. Among the advantages of biofuels are the reduction in environmental impact and the fostering of new economic activities [5]. The blend of biofuel and diesel, known as biodiesel, is characterized by a more efficient combustion process, as well as lower emissions of smoke opacity and soot compared to conventional diesel [6]. The above allows for improving air quality, especially in urban areas [7].

Studies available in the literature indicate that biodiesel is a viable alternative for replacing conventional diesel [8]. Krishnamoorthi et al. [7] investigated the effect of a blend of delonix regia seed biodiesel in a compression ignition engine. The results obtained indicate a decrease in specific fuel consumption of 0.015–0.0425 kg/kWh and an increase in brake thermal efficiency of 1.2–3.1%. Similarly, a reduction in carbon monoxide and hydrocarbon emission levels was observed. Chen et al. [9] evaluated the performance and emission characteristics of a diesel engine fueled with five proportions of biodiesel blends (0%, 5%, 10%, 10%, 15%, and 20%). The study showed reductions of 1.20%, 2.64%, 3.88%, and 4.65% in soot emissions compared to pure diesel. Mulkan et al. [10] analyzed the characteristics of a diesel engine fueled with waste cooking oil (WCO) biodiesel blends under various engine speeds. They observed a significant reduction in CO emissions between 6.11% and 48.63% compared to pure diesel. Qenawy et al. [11] investigated biodiesel fuels composed of a mixture of castor bean and jatropha seeds. An analysis of the results showed a reduction in carbon dioxide, smoke opacity, and hydrocarbon emissions. Kesharvani et al. [12] numerically studied biodiesel fuels from microalgae with various proportions (20%, 40%, 60%, and 100%). The results show a reduction in particulate matter and smoke opacity. Mu et al. [13] investigated the performance and emission characteristics of a diesel engine with tung-oil-based biodiesel blends (B10, B20, and B50). In general, it was observed that the biodiesel blends showed a significant decrease in CO, HC, NOx, and smoke opacity emissions compared to pure diesel.

To ensure biofuel production, the use of oil-rich seeds from indigenous plants and agricultural sources is recommended [14]. Palm oil has the highest production volume among vegetable oils globally. The high production of palm oil ensures the supply of feedstock for biodiesel production [15]. Although second- and third-generation biofuels are in development to become commercially viable, the use of first-generation biofuels, such as palm oil, still represents the most practical alternative for meeting the market demand [16]. In general, the use of palm oil is considered a promising option as a feedstock for biodiesel production, making it economically viable and sustainable in the long term [17].

The use of organic waste as a raw material for producing biofuels is a current innovative strategy for addressing waste management and fossil fuel dependence issues. Furthermore, using organic waste helps to reduce CO_2 emissions. This is because waste disposal often leads to the release of pollutants. From an economic perspective, using agricultural waste promotes local development and independence from fluctuations in the crude oil market [18]. One agricultural activity that generates significant waste is coffee processing. Each year, 102 tons of coffee husks are produced, which are typically burned outdoors without any energy recovery. This contributes to substantial environmental pollution. Utilizing this waste would enhance the economic viability of the coffee industry and mitigate environmental pollution [19].

Fuel modification is another strategy used to enhance the physicochemical properties of fuels, such as biodiesel. Among these are the use of additives, water, nanoparticles, ethers, alcohols, and the use of gaseous fuels [20]. Literature studies indicate that mixtures of biodiesel with gaseous fuels have yielded positive results. In the last few years, research has

been conducted with various types of gaseous fuels, such as biogas, synthesis gas, liquefied petroleum gas (LPG), compressed natural gas (CNG), and hydrogen, as a secondary fuel in internal combustion engines [21]. The findings indicate that hydrogen is a source with high energy potential and is environmentally friendly. Hydrogen is the most abundant element in the universe and one of the most widely used fuels [22]. This resource stands out for its versatility, as it can be used independently or combined with traditional fuels such as gasoline and diesel. Recently, hydrogen has garnered significant interest as a clean and sustainable energy source. When used in combustion processes or fuel cells, it generates primarily water as a byproduct, resulting in a reduced environmental impact and virtually zero greenhouse gas emissions [23]. In the field of combustion, hydrogen has been implemented in various applications, such as internal combustion engines, gas turbines, and homogeneous charge compression ignition systems, to optimize performance and reduce polluting emissions [24]. Due to the potential of hydrogen, several investigations have been conducted in recent years to analyze its influence on performance and emission parameters when mixed with various types of biodiesels. Zhang et al. [25] investigated the use of blends of biodiesel and used cooking oil nanoparticles in a hydrogen direct ignition engine. Trends show a reduction in carbon monoxide, hydrocarbons, and carbon dioxide. Mohan and Dinesha et al. [26] analyzed the use of hydrogen peroxide with emulsions in biodiesel blends for compression ignition engines. Improved combustion is reported, resulting in reduced emissions of carbon monoxide and hydrocarbons. Shanmuganathan et al. [27] used hydrogen as a secondary fuel to improve the combustion characteristics of spirulina biodiesel. Tests indicated a higher cylinder chamber pressure and higher heat release rate in the biodiesel mixtures with hydrogen injection. Xia et al. [28] concluded that the use of hydrogen in castor oil biodiesel blends improves thermal efficiency and specific fuel consumption.

Studies in the literature suggest that biofuels could potentially replace traditional diesel fuel to varying degrees. However, engine performance parameters tend to decrease as the percentage of substitution increases. This loss of performance is an obstacle to replacing fossil fuels with renewable biofuels derived from vegetable oils and agricultural waste. For this reason, the present research seeks to minimize the reduction in biofuel performance parameters by adding hydroxy. This study evaluates the performance characteristics, thermodynamic balances, environmental impact, and operating costs of internal combustion engines fueled by biodiesel from a palm oil and coffee husk blend (D85P10C5 and D80P10C10) with different hydroxy injection rates (4 and 8 lpm). Thus, this study aims to contribute to the analysis of the impact of hydroxy on palm oil and coffee husk biofuels, a topic not yet explored in the literature. This will promote the use of agricultural waste, such as coffee husks, providing economic benefits to the sector while reducing the demand for fossil fuels and decreasing pollutant emissions.

2. Production of Biodiesel from Coffee Husks

Coffee husks have a high carbon and oxygen content, which allows them to be used as raw material for producing biofuel. The methodology used to produce biofuel from coffee husks is described in Figure 1.

The approximate composition of coffee husk is 10.38 wt% moisture, 71.08 wt% dietary fiber, 2.71 wt% protein, 0.73 wt% lipids, and 1.35 wt% ash, respectively. On the other hand, it was observed that coffee husk contains 2.54 g of oil per 100 g of dry coffee husk. The biofuel derived from coffee husks is obtained in three stages: grinding, esterification, and transesterification. In the first stage, coffee husk powder is ground using a screw press to extract the oil. In the second stage, the coffee husk oil is poured into a reactor flask and heated to 64 °C. Once the oil has reached this temperature, methanol and sulfuric acid are

added and mixed using a stirrer at a constant speed of 700 rpm. After two hours of heating and continuous stirring, the mixture is transferred to a separatory funnel. After four hours, two liquids had formed: the oil was at the top, and the diglyceride was at the bottom. In the final stage, methanol is mixed with sodium hydroxide pellets to produce a methoxide solution. This solution is then combined with the oil that was separated in the previous stage. The mixture is heated and stirred at 64 °C and 700 rpm until a homogeneous mixture is obtained. The mixture is then transferred to a separatory funnel and left to stand for three hours. The glycerol that has formed at the bottom of the funnel is then separated from the methyl ester of coffee husk oil. The excess methanol in the methyl ester was removed by heating to 70 °C.

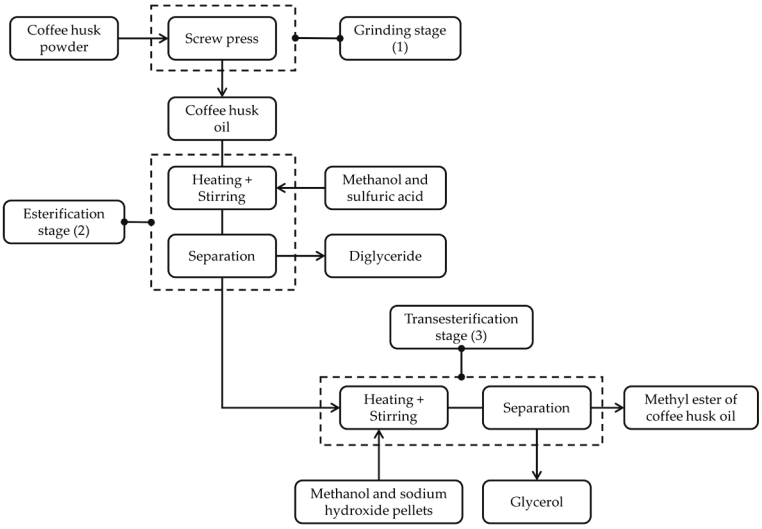


Figure 1. Production process for biofuel from coffee husks.

3. Materials and Methods

The experimental tests were conducted on a test bench consisting of a stationary diesel engine and a hydroxy gas generation system. The test bench's schematic is shown in Figure 2.



(**a**) (**b**)

Figure 2. Experimental test bench: (**a**) engine bench and (**b**) hydroxy gas generation system.

The stationary diesel engine is a single-cylinder, four-stroke, air-cooled, naturally aspirated, direct injection engine. The technical characteristics of the engine are described in Table 1.

Table 1. Technical characteristics of stationary diesel engine.

Model	**SOKAN SK-MDF300**
Manufacturer name	Shandong Kangwo Holding Co., Heze City, China
Diameter	78 mm
Stroke	63 mm
Cycle	4
Volume	300 cc
Maximum power	3.43 kW
Injection mechanisms	Direct injection
Intake mechanisms	Natural aspiration

The engine speed and torque were controlled using an alternator coupled to its output shaft. Fuel consumption was measured using a gravimetric meter (OHAUS PA313, Parsippany, NJ, USA). The combustion chamber pressure was determined utilizing a piezoelectric sensor (KISTLER 7063-A, Wien, Austria) installed in the cylinder head. The rotational speed of the engine was calculated using a rotational angle sensor (Beck Arnley 180-0420, Amherst, NY, USA). The temperature inside the combustion chamber was measured through a K-type thermocouple. The intake air mass flow was determined by a flow sensor (BOSCH 22680 7J600, Stuttgart, Germany). Engine emission measurements were calculated using two analyzers (Brain-Bee AGS-688, Parma, Italy and Bacharach® PCA 400, New Kensington, PA, USA).

The hydroxy gas injected into the engine was generated using a system based on the water electrolysis process. This system includes key components such as a dry cell, an electrolytic tank, a bubbler tank, a storage tank, and safety devices. The dry cell was fabricated from stainless steel, chosen for its excellent conductivity and resistance to extreme temperatures, voltages, and corrosion. This cell incorporates electrodes with dimensions of 0.15 cm thickness, 13.3 cm width, and 20 cm height, separated by a space of 2 mm. The electrolytic tank serves as a continuous water supply to the dry cell. In contrast, the bubbler tank catches water vapor mixed with hydroxy gas, thereby protecting the engine components against corrosion. The hydroxy gas produced is stored in 304 austenitic stainless-steel tanks. To ensure the safety of the system, a silica gel filter and two flame filters were installed to prevent flame backflow during combustion. The technical specifications of the measuring instruments installed on the test bench are detailed in Table 2.

Table 2. Measuring instruments.

Instrument	**Manufacturer**	**Range**		**Accuracy**
Gravimetric meter PA313	OHAUS, Parsippany, NJ, USA	0–310 g		1.5%
Piezoelectric transducer 7063-A	KISTLER, Wien, Austria	0–250 bar		±0.5%
Thermocouple Type K	MICC, Yancheng, China	−200–1370 °C		0.1%
Piezoresistive transducer PSA-C01	AUTONICS, Mundelein, IL, USA	−100–100 kPa		0.2%
Angle sensor 180-0420	BECK/ARNLEY, Amherst, NY, USA	5–9999 RPM		0.03%
Intake air meter 22680 7J600	BOSCH, Stuttgart, Germany	0–125 g/s		1%
Exhaust gas analyzer	Bacharach® PCA 400, New Kensington, PA, USA	NOx	0–3000 ppm	±0.5%
	Brain-Bee AGS-688, Parma, Italy	HC	0–20 ppm	±1%
		CO	0–10 vol.%	±0.1%
		CO_2	0–20 vol.%	±0.01%

4. Uncertainty Model

The literature describes two main approaches to determining sources of uncertainty. The first is the type A evaluation method, which is based on the statistical analysis of a series of measurements. The second is the type B evaluation method, which uses a

distribution derived from experience or external instrument information. Both methods are considered suitable for estimating instrument uncertainties. In the uncertainty analysis performed in this study, the Type A evaluation method was applied. Consequently, the following expression is used to calculate the best estimate (z_i) for the set of measurements $y_1, y_2, \ldots y_n$:

$$z_i = \overline{y} = \frac{\sum_{i=1}^{n} y_i}{n} \tag{1}$$

The variability in the results of the set of measurements $(y_1, y_2, \ldots y_n)$ is evaluated by calculating the standard deviation (s).

$$s = \sqrt{\frac{\sum_{i=1}^{n} (y_i - \overline{y})^2}{n-1}} \tag{2}$$

Finally, the standard uncertainty is determined using the average experimental standard deviation $u(y_i)$.

$$u(y_i) = \sqrt{\frac{\sum_{i=1}^{n} (y_i - \overline{y})^2}{n(n-1)}} \tag{3}$$

where n is the number of repetitions. For operational variables that are related to various parameters, the combined uncertainty was used [29]. Table 3 shows the procedure for determining the combined uncertainty of the main study parameter.

Table 3. Combined uncertainty for study parameters.

Variable	Nomenclature	Combined Uncertainty	Unit
Brake-specific fuel consumption	BSFC	$u_{(BSFC)} = \sqrt{\left(u_{(\omega)} \times \frac{BSFC}{\omega}\right)^2 + \left(u_{(\Gamma)} \times \frac{BSFC}{\Gamma}\right)^2 + \left(u_{(\dot{m}_{fuel})} \times \frac{BSFC}{\dot{m}_{fuel}}\right)^2}$	kg/kWh
Mechanical power	$\dot{E}_s$	$u_{(\dot{E}_s)} = \sqrt{\left(u_{(\omega)} \times \frac{\dot{E}_s}{\omega}\right)^2 + \left(u_{(\Gamma)} \times \frac{\dot{E}_s}{\Gamma}\right)^2}$	kW
Brake thermal efficiency	BTE	$u_{(BTE)} = \sqrt{\left(u_{(\omega)} \times \frac{BTE}{\omega}\right)^2 + \left(u_{(\Gamma)} \times \frac{BTE}{\Gamma}\right)^2 + \left(u_{(\dot{m}_{fuel})} \times \frac{BTE}{\dot{m}_{fuel}}\right)^2}$	%
Carbon monoxide	CO	$u_{(CO)} = \sqrt{\left(\frac{u_{(CO)}}{CO}\right)^2 + \left(\frac{u_{(\dot{E}_s)}}{\dot{E}_s}\right)^2}$	g/kWh
Carbon dioxide	CO_2	$u_{(CO_2)} = \sqrt{\left(\frac{u_{(CO_2)}}{CO_2}\right)^2 + \left(\frac{u_{(\dot{E}_s)}}{\dot{E}_s}\right)^2}$	g/kWh
Hydrocarbons	HC	$u_{(HC)} = \sqrt{\left(\frac{u_{(HC)}}{HC}\right)^2 + \left(\frac{u_{(\dot{E}_s)}}{\dot{E}_s}\right)^2}$	g/kWh
Nitrogen oxides	NO_x	$u_{(NO_x)} = \sqrt{\left(\frac{u_{(NO_x)}}{NO_x}\right)^2 + \left(\frac{u_{(\dot{E}_s)}}{\dot{E}_s}\right)^2}$	g/kWh

5. Combustion Diagnostic Model

The use of the combustion diagnostic model requires the use of the geometrical parameters of the engine. The collection of this information was performed using the investigations previously developed on the test engine [30]. Table 4 shows the geometrical characteristics collected.

Table 4. Geometric characteristics of stationary diesel engine.

Parameter	Unit	Value
Piston stroke	mm	63
Piston diameter	mm	78
Compression ratio	[-]	20
Strain constant	[-]	1.18
Connecting rod length	mm	105.85
Piston pin diameter	mm	21
Piston–piston pin mass	g	431.2
Connecting rod mass	g	353.3

To analyze the behavior of the combustion process, a combustion model was used to identify the heat release rate (HRR) curves as a function of the angle of rotation. The engine combustion chamber is considered an open-system thermodynamic model, which agrees with the literature [31]. The development of the model involved the following considerations for its formulation:

1. The pressure inside the combustion chamber is uniform. This is reasonable because the fluid propagation velocity and the flame velocity are significantly lower than the speed of sound [32].
2. The gases present in the combustion chamber behave as an ideal gas. Valencia et al. [33] validated this hypothesis for internal combustion engines.
3. The specific heat of gases depends only on their chemical composition and temperature. This assumption is based on the idea that gases act as an ideal mixture.
4. The products of combustion are calculated stoichiometrically. This assumption is valid since combustion in diesel engines occurs mainly by diffusion, which makes it possible to assume stoichiometric combustion [34].
5. The thermodynamic properties are determined using the average temperature of the combustion chamber. This is justifiable because diffusion and heat transfer processes tend to homogenize the temperature inside the chamber.
6. The heat transfer through the cylinder walls and the strains of the piston mechanism are considered in order to obtain more representative results of the phenomenon.
7. The heat transfer coefficients are calculated by applying the Woschni equations [35].
8. The combustion model cannot adequately simulate the expansion stage due to the complex interaction between liquid (diesel) and gaseous (hydroxy gas) fuels. However, since self-detonation is a process that occurs at the beginning of the compression stage, the model can be used to identify anomalies during this part of the combustion cycle.

Equation (4) presents the combustion model formulated from the first law of thermodynamics [36].

$$HRR = \frac{dQ}{d\theta} = \frac{dQ_w}{d\theta} + RT\frac{d\dot{m}_{bb}}{d\theta} + m_{cam}c_v\frac{dT}{d\theta} - (h_{f(l),iny} - u)\frac{d\dot{m}_f}{d\theta} + p\frac{dV}{d\theta} \quad (4)$$

where $dQ/d\theta$ represents the fuel's heat release rate, Q_w denotes the heat loss (combustion chamber walls), R is the constant for exhaust gases, T is the gas temperature, $\dot{m}_{bb}$ refers to the blow-by mass flow rate, m_{cam} is the mass (inside the combustion chamber), c_v is the specific heat (constant volume), u corresponds to the internal energy, p is the cylinder's instantaneous pressure, θ is the crankshaft angle, $\dot{m}_f$ is the mass flow rate (injected fuel),

$h_{f(l),iny}$ represents the enthalpy (injected fuel), and V is the cylinder's instantaneous volume. The heat loss through (Q_w) was determined using Equation (5).

$$Q_w = hA_s(T - T_w) \tag{5}$$

where A_s is the total surface area through which heat loss occurs, h represents the heat transfer coefficient, and T_w denotes the temperature of the combustion chamber walls. The total heat loss surface area (A_s) is determined using Equation (6).

$$A_s = A_{cylinder} + A_{cylinderhead} + A_{piston} = \left(\frac{\pi BV}{A_p}\right) + \left(A_p + H_{cc}\pi B\right) + \left(\frac{\pi B^2}{4}\right) \tag{6}$$

where B is the piston diameter and A_p is the piston area. The combustion chamber wall temperature (T_w) is determined by Equation (7) [36].

$$T_w = T_{ref} + \varphi_1\left(\rho_c \times v_p\right)^{0.8} + \varphi_2 \times pme \tag{7}$$

where T_{ref} is the coolant temperature, ρ_c is the density of gases in the chamber, v_p is the average piston velocity, and pme is the average effective pressure. φ_1 and φ_2 are constants that depend on each heat transfer area, as shown in Table 5.

Table 5. Coefficients φ_1 and φ_2 for the heat transfer model.

Area	$\boldsymbol{\varphi_1}$	$\boldsymbol{\varphi_2}$
Cylinder	2.3	3.0
Cylinder heat	2.7	3.5
Piston	8.6	5.5

The heat transfer coefficient (h) utilized in Equation (5) was calculated using the formula proposed by Woschni, as detailed below:

$$h = C_o d^{b-1} p^b w^b T^{0.75-1.62b} \tag{8}$$

where w is the gas velocity, and d is the inner diameter of the cylinder. The term b and C_o are constants with a value of 0.80 and 3.26 [37]. The gas velocity (w) was calculated by the following equation [38]:

$$w = C_1 v_p + C_2 \frac{V_d T_o (p - p_o)}{V_o p_o} \tag{9}$$

where v_p is the piston velocity. The subindice o refers to the beginning of the combustion phase. The piston velocity $\left(v_p\right)$ was calculated by Equation (10):

$$v_p = 2 \times N \times S \tag{10}$$

where N is the speed, and S is the piston stroke, respectively.

The blow-by flow rate $\left(\dot{m}_{bb}\right)$ was represented as a compressible flow process, as shown in Equation (11) [39,40]:

$$\dot{m}_{bb} = \left\{ \begin{array}{ll} \frac{c_{bb}A_r p}{\sqrt{RT}} k^{1/2}\left(\frac{2}{k+1}\right)^{\left(\frac{k+1}{2k-2}\right)} & , p_c/p \le (2/[k+1])^{\left(\frac{k}{k-1}\right)} \\ \left[\frac{2k}{k-1}\left(\left(\frac{p_c}{p}\right)^{(2/k)} - \left(\frac{p_c}{p}\right)^{\left(\frac{k+1}{k}\right)}\right)\right]^{1/2} & , p_c/p > (2/[k+1])^{\left(\frac{k}{k-1}\right)} \end{array} \right\} \tag{11}$$

where c_{bb} is the discharge coefficient, p is the combustion chamber pressure, k is the ratio of specific heat capacities, A_r is the gap area, and p_c is the crankcase pressure. The variable k was determined using Hoffman's correlation [41]:

$$k = 1.46 - 1.63 \times 10^{-4}\mathrm{T} + 4.14 \times 10^{-8}T^2 \tag{12}$$

The instantaneous volume of the cylinder consists of four components, as expressed in Equation (13).

$$V = V_{cc} + V_d + \Delta V_1 + \Delta V_2 \tag{13}$$

where V_{cc} is the combustion chamber volume, V_d is the instantaneous volume displaced, and ΔV is the volume variation due to strain from inertia forces and pressure (ΔV_1), and clearances (ΔV_2). The combustion chamber volume (V_{cc}) was calculated, as shown below [30,42]:

$$V_{cc} = \frac{\pi d^2}{4}\left(\frac{2l_c}{r_c - 1}\right) \tag{14}$$

where r_c is the volumetric compression ratio, and l_c is the crankshaft length. The instantaneous volume displaced (V_d) is calculated by Equation (15).

$$V_d = \frac{\pi d^2}{4}(l_c + l_b - R_p) \tag{15}$$

where R_p is the vertical position (piston), and l_b is the length of the connecting rod. The volume variation (ΔV_1) is calculated by Equation (16).

$$\Delta V_1 = \frac{\pi d^2}{4}\frac{k_d l_b (pA_p + m_i a_p)}{E_s} \tag{16}$$

where E_s is the elastic modulus (steel), A_p is the piston area, a_p is the piston acceleration, m_i is the inertial mass, and k_d is the mechanical deformation, respectively. The joints of the engine mechanism cause a volume variation in the combustion chamber due to the clearances (ΔV_2). This volume variation is calculated by Equation (17) [30].

$$\Delta V_2 = \frac{\pi d^2}{4} \times \sum_{m=1}^{n} \{-e_m \times \sin(\gamma_m) \times \cos(\beta_m)\} \tag{17}$$

where e_m is the eccentricity between the journal and bearing, and β_m is the angle between the connecting rod and the piston displacement axis, respectively. The average temperature in the combustion chamber is determined by Equation (18).

$$T = \frac{pV}{m_{cam}R} \tag{18}$$

where m_{cam} is the confined mass in the combustion chamber, which is determined by the following balance:

$$m_{cam} = m_{fuel} + m_{aire} - m_{bb} \tag{19}$$

To determine the specific heats at constant pressure (C_p) and volume (C_v), the polynomial equations shown below were used:

Specific heat at constant volume:

$$C_{v,a} = -10.4199 \times T^{0.5} + 2522.88 - 67227.1 \times T^{-0.5} + 917124.4 \times T^{-1} - 4174853.6 \times T^{-1.5} \tag{20}$$

$$C_{v,f} = -256.4 + 6.95372 \times \mathrm{T} - 4.04715 \times 10^{-3}T^2 + 9.10259 \times 10^{-7}T^3 + 1458487 \times T^{-2} \tag{21}$$

$$C_{v,g} = 641.154 + 0.43045 \times \mathrm{T} - 0.0001125 \times T^2 + 8.979 \times 10^{-9}T^3 \tag{22}$$

Specific heat at constant pressure:

$$C_{p,a} = C_{v,a} + R_a \tag{23}$$

$$C_{p,f} = C_{v,f} + R_f \tag{24}$$

$$C_{p,q} = C_{v,q} + R_q \tag{25}$$

where the subscripts a, f, and g refer to the specific heats of air, fuels, and combustion gases, respectively. R is the ideal gas constant of air, which was calculated using the following equations:

$$R_a = \frac{R}{M_a} \tag{26}$$

$$R_f = \frac{R}{M_f} \tag{27}$$

$$R_g = \frac{R}{M_g} \tag{28}$$

where M_a, M_f, and M_g are the molar mass of the air, fuel, and combustion gases.

6. Analysis of the Maximum Injection Flow Rate of Hydroxy

To analyze the limit of hydroxy gas that can be injected, a series of experimental tests were performed on the diesel engine. During the experimental tests, the engine was fueled with pure diesel and five volumetric flows of hydroxy gas. The engine was run at maximum power, with a torque of 9 Nm, and a rotational speed of 3600 rpm. The conditions of each experimental run are shown in Table 6.

Table 6. Experimental runs to determine the hydroxy injection limit.

Test N°	Torque [Nm]	Speed [rpm]	Hydroxy Volumetric Flow Rate [lpm]
1	9	3600	0
2			4
3			8
4			10
5			12

For each experimental run, the behavior of the pressure curve during the intake and compression stages of the engine was recorded. These results are subsequently used in the combustion diagnostic model as input data to obtain the heat release rate. The combustion model described in Section 5 is used to analyze the behavior of the heat release rate curves in the intake and compression stages of the engine. The procedure for using the model is shown in Figure 3.

The use of the model consists of three main stages: (1) data input, (2) data processing, and (3) the export of results. In the first stage, all the data required by the model are supplied, which include pressure curves, operational variables, environmental conditions, and geometric parameters. During the second stage, the input data is processed to solve all sub-models of the combustion diagnostics. This process is carried out using MATLAB R2025a software. In the third stage, the model exports as output the heat release rate curve, which will be used for the analysis of auto-ignition indications. The heat release rate curves for each of the diesel–hydroxy mixtures are shown in Figure 4.

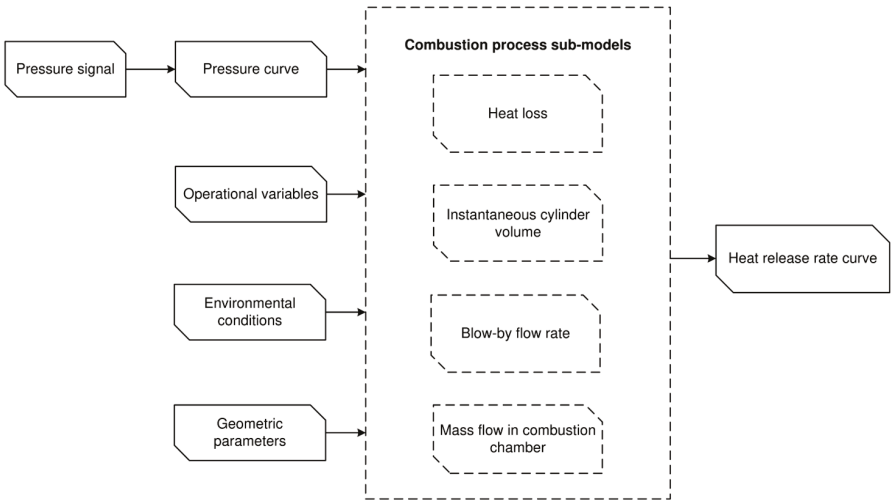


Figure 3. Calculation procedure of the combustion diagnostic model.

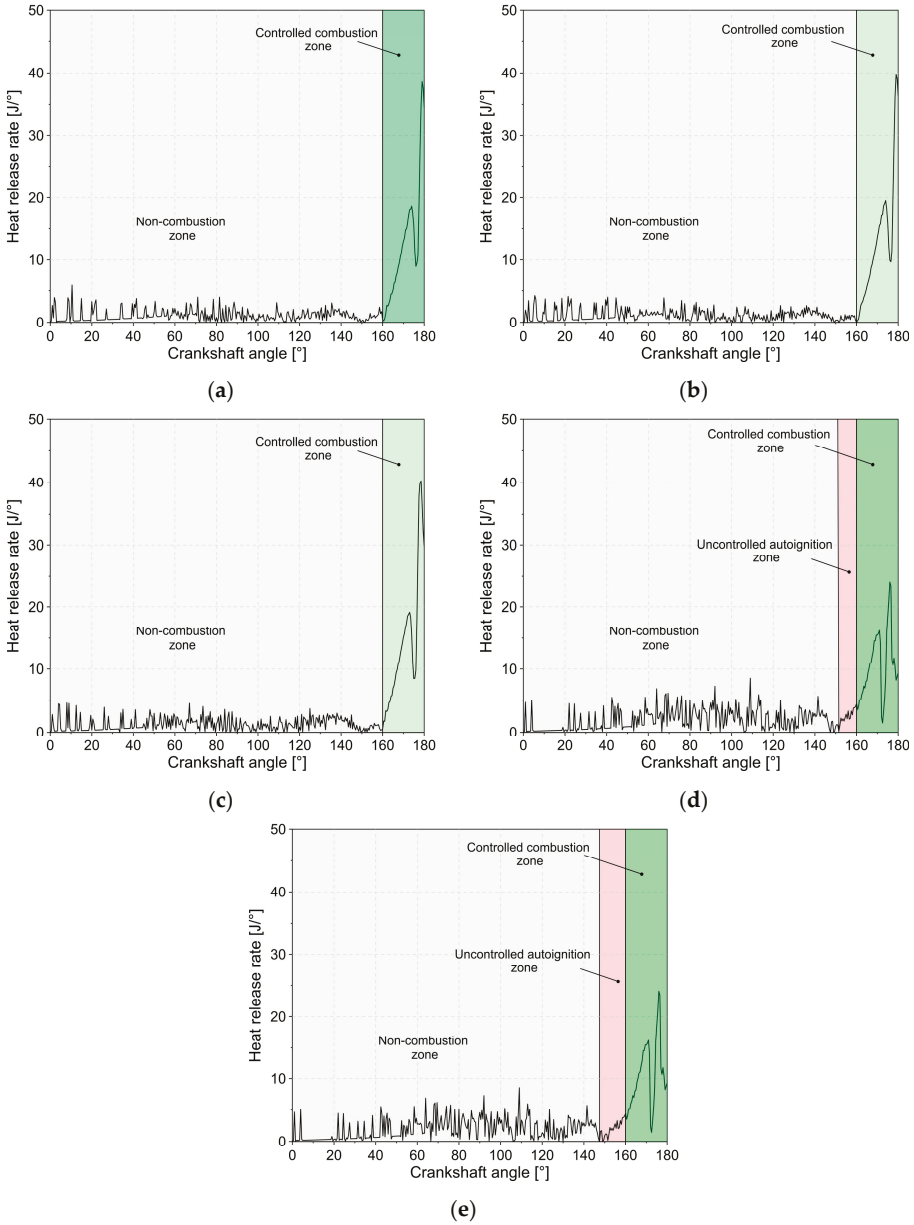


Figure 4. Heat release rate (HRR) curves for the different diesel–hydroxy gas mixtures: (**a**) D100 + 0 lpm, (**b**) D100 + 4 lpm, (**c**) D100 + 8 lpm, (**d**) D100 + 10 lpm, and (**e**) D100 + 12 lpm.

Figure 4 shows the trend of the heat release rate inside the combustion chamber for a crankshaft angle range of 0°–180°. This range encompasses the intake stage and compression stage of the engine. The 0° angular position represents the start of the intake, and the 180° angular position represents the condition where the piston has reached the top dead center (TDC). The figures show a degree of variability in the curves; however, this is natural behavior because of the high sensitivity of the model to noise in the input signals.

From the results, two types of zones can be identified in the mixtures D100 + 0 lpm, D100 + 4 lpm, and D100 + 8 lpm. The first zone (gray area) corresponds to the non-combustion zone, where the heat release rate values are zero. This implies that the combustion process has not started. The second zone (green area) is the location where combustion is expected to start. In the case of the first three mixtures, it is observed that the heat release curve begins to grow continuously from an angle of approximately 160°. This is because the fuel injection point in the test engine occurs 20° before the piston reaches the top dead center (20° BTDC). Therefore, in these three diesel–hydroxy mixtures, a natural behavior is evident in the combustion process of the engine.

In the case of the mixtures D100 + 10 lpm and D100 + 12 lpm, it is observed that the heat release rate curve tends to grow continuously before the angular position of 160°. This behavior becomes more evident as the volumetric flow rate of hydroxy gas is increased. For the D100 + 10 lpm mixture, a continuous growth in the curve is observed starting at an angle of 151.5 °C, and, for the D100 + 12 lpm mixture, the development begins with an angular position of 147.5 °C. Since the diesel fuel is injected at the angular position of 160°, the above behaviors correspond to an uncontrolled combustion start. This phenomenon is known as auto-ignition and is a consequence of the wide range of hydrogen flammability, which is one of the main dangers and limitations of its use in internal combustion engines since it leads to a degradation of their valuable life and essential losses of performance. Considering these results, it was established that the safe limit for the hydroxy gas addition is a volumetric flow of 8 lpm. This will be the maximum amount injected in the following experimental tests.

7. Experimental Procedure

In the present investigation, palm oil and coffee husk biofuel were mixed with pure diesel in two proportions, 15% and 20%, which were identified as D85P10C5 and D80P10C10. Additionally, two hydroxy injection rates were defined (4 and 8 lpm). The physicochemical characteristics of the fuels used in the experimental tests are shown in Table 7.

Table 7. Physicochemical characteristics of fuels.

Property	Unit	D100	D85P10C5	D80P10C10	Hydroxy
Density	kg/m^3	822.32	829.25	835.02	0.49115
Viscosity	cSt	2.64	2.93	3.02	36.6487
Flash point	°C	76	88	96	[-]
LHV	MJ/kg	44.09	42.36	41.48	21.995

The experimental tests began with the engine running on pure diesel (D-100%) for a period of 10 min to warm up and establish the operational variables. Subsequently, the fuel tank was emptied and filled with the new fuel. During the experimental tests, the torque and engine speed varied in the range of 3 to 7 Nm and 3000 to 3600 rpm, respectively. The experimental tests were carried out while maintaining constant operational parameters (steady state) for engine torque and rpm. This is because the research focuses on stationary engines for the generation of electrical energy, which maintain a constant

speed to ensure a constant electrical frequency. Table 8 shows the configuration of each of the experimental runs.

Table 8. Test engine operating conditions.

N°	Speed [rpm]	Torque [Nm]
1	3000	
2	3300	3
3	3600	
4	3000	
5	3300	5
6	3600	
7	3000	
8	3300	7
9	3600	

8. Results and Discussion

The results obtained from the analyses carried out on the engine when fueled with diesel, a blend of biodiesel (palm oil and coffee husk), and hydrogen are shown below. The analyses included an evaluation of performance parameters, the energy and exergy distribution, the impact of emissions, and the economic savings and costs.

8.1. Performance Parameter Analysis

Figure 5 shows the brake-specific fuel consumption (BSFC) of the engine under different operating conditions and fuel types.

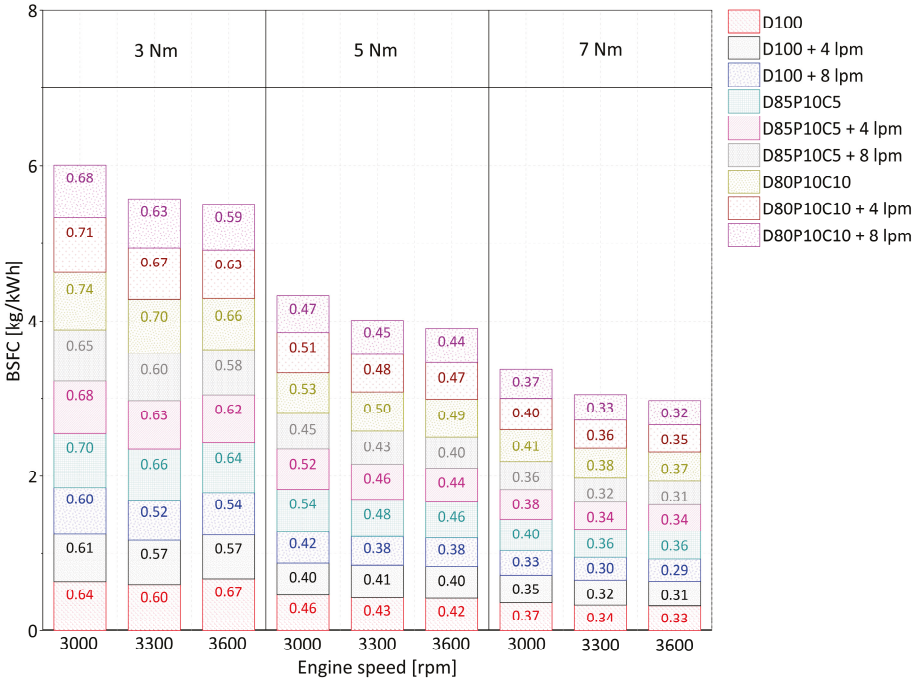


Figure 5. Brake-specific fuel consumption trends for D100, D85P10C5, and D80P10C10.

BSFC is a key performance parameter, since it allows the fuel consumption to be associated with the mechanical power output of the engine. Therefore, it is desirable for the engine to operate at low BSFC levels. The experimental findings indicate that pure diesel has the lowest BSFC values compared to the D85P10C5 and D80P10C10 biodiesel blends. In general, the lowest BSFC values were obtained with a torque of 7 Nm, regardless

of the type of fuel used. For the experimental configurations, BSFC values in the range of 0.33–0.67 kg/kWh, 0.36–0.70 kg/kWh, and 0.37–0.74 kg/kWh were obtained for the D100, D85P10C5, and D80P10C10 fuels, respectively. The results show an increase of 9.79% and 13.33% in engine BSFC with the D85P10C5 and D80P10C10 fuels compared to D100. The higher BSFC levels with the palm oil and coffee husk biodiesel blends may be a consequence of the lower calorific value of these fuels compared to pure diesel; therefore, higher fuel consumption is needed to achieve the same mechanical power output. In the case of the blends D85P10C5 and D80P10C10, it is observed that their lower calorific value is lower by 3.92% and 5.91% than D100. Similar results are reported in the literature for blends of biodiesel from vegetable seeds [43].

On the other hand, it is observed that fuels containing hydroxy consume the least amount of fuel, which is reflected in the reduction in engine BSFC. As the addition of hydroxy volumetric flow increases, a further reduction in BSFC is observed. The D100 + 4 lpm, D85P10C5 + 4 lpm, and D80P10C10 + 4 lpm fuels cause a 6.91%, 4.38%, and 4.20% reduction compared to the D100, D80P10C5, and D85P10C10 fuel, respectively. In the case of D100 + 8 lpm, D85P10C5 + 8 lpm, and D80P10C10 + 8 lpm fuels, a reduction of 11.66%, 11.28%, and 10.94% was observed. A high calorific value characterizes hydroxy compared to pure diesel and biodiesel blends. This implies a greater availability of energy in the combustion process, which favors fuel reduction. Additionally, hydroxy injection allows a higher oxygen concentration, favoring the quality of the air–fuel mixture. Reports in the literature show that the injection of hydrogen into the engine tends to reduce fuel consumption [44].

Figure 6 shows the engine brake thermal efficiency (BTE) trends for the D100, D85P10C5, and D80P10C10 fuels.

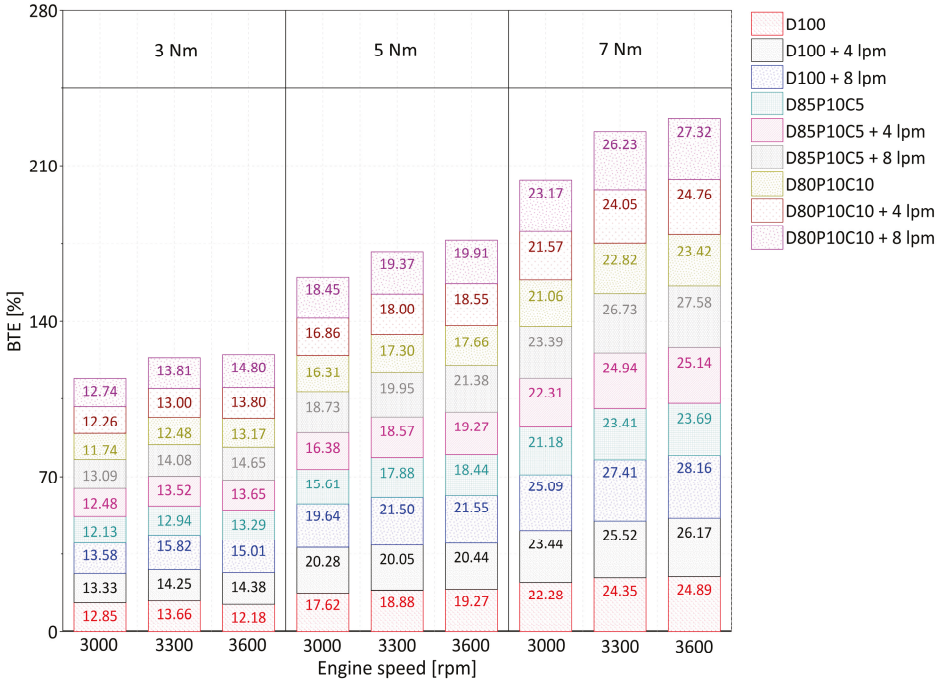


Figure 6. Brake thermal efficiency trends for D100, D85P10C5, and D80P10C10.

BTE is a performance parameter that relates mechanical power to the energy supplied to the engine. This parameter allows determining the efficiency of the conversion of chemical energy from fuel to mechanical power. In general, it was observed that engine BTE increases with increasing torque and speed. This behavior was evident in all the fuels tested. For the D100, D85P10C5, and D80P10C10 fuels, a range of BTE values of 12.18–24.89%, 12.13–23.69%, and 11.74–23.42% were obtained, respectively. Compared to

pure diesel, palm oil and coffee husk biodiesel blends lead to a reduction in engine BTE. This reduction becomes more noticeable as the percentage of biofuel in the blend increases. In the case of D85P10C5 and D80P10C10 fuels, a 6.08% and 7.47% decrease in engine BTE was observed compared to D100. The density of the D85P10C5 and D80P10C10 biodiesel blends is 0.84% and 1.54% higher compared to pure diesel. This increase in density causes problems in the combustion process and its quality due to the poor atomization of the fuel droplets. On the other hand, the lower calorific value of palm oil and coffee husk biodiesel also favors the reduction in BTE due to the increase in fuel consumption. Similar trends are reported in the literature for blends of biodiesel from other feedstocks [44].

The injection of hydroxy in all fuels tested causes an increase in engine BTE. For D100 + 4 lpm, D85P10C5 + 4 lpm, and D80P10C10 + 4 lpm, an increase of 7.64%, 4.59%, and 4.39% is reported compared to the D100, D85P10C5, and D80P10C10 fuels, respectively. In the case of the D100 + 8 lpm, D85P10C5 + 8 lpm, and D80P10C10 + 8 lpm fuels, the trends indicate an increase of 13.37%, 12.84%, and 12.34%. Hydroxy has a wide flammability range as well as a high flame speed. These two characteristics enable a proper air–fuel mixture and improve fuel combustion in the combustion chamber. Previous studies in the literature indicate that the properties of hydroxy tend to increase the BTE of internal combustion engines [45].

8.2. Energy Distribution Analysis

To analyze the influence of hydroxy injection on the engine fueled with pure diesel, palm oil, and coffee husk biodiesel blends, an energy analysis was performed for D100, D85P10C5, and D80P10C10 fuels, with hydroxy injection rates of 4 and 8 lpm. The engine energy distributions are shown in Figures 7–9.

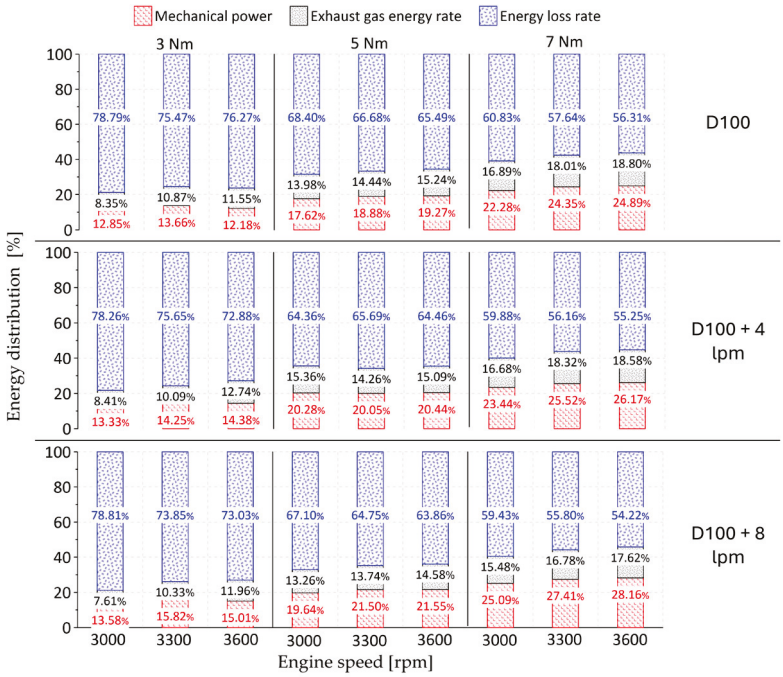


Figure 7. Energy distribution for D100, D100 + 4 lpm, and D100 + 8 lpm.

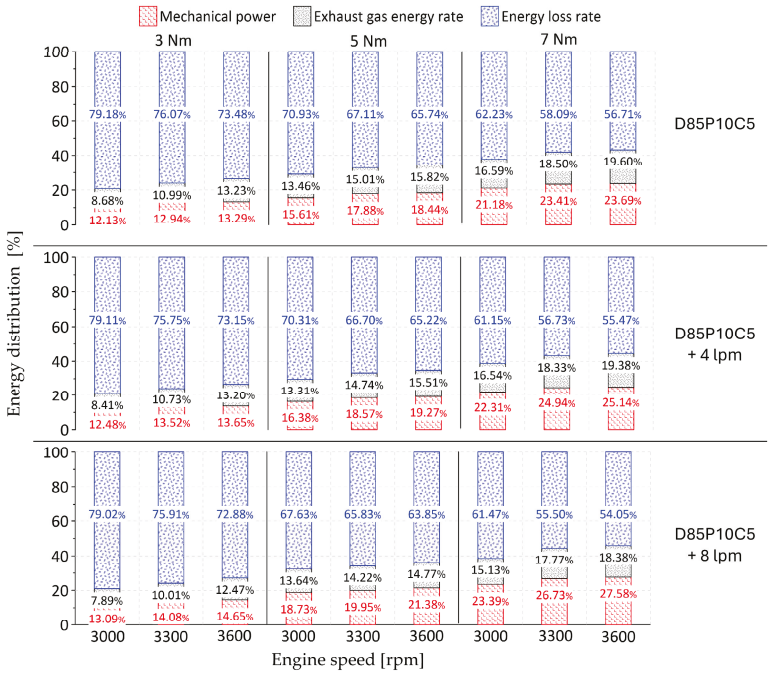


Figure 8. Energy distribution for D85P10C5, D85P10C5 + 4 lpm, and D85P10C5 + 8 lpm.

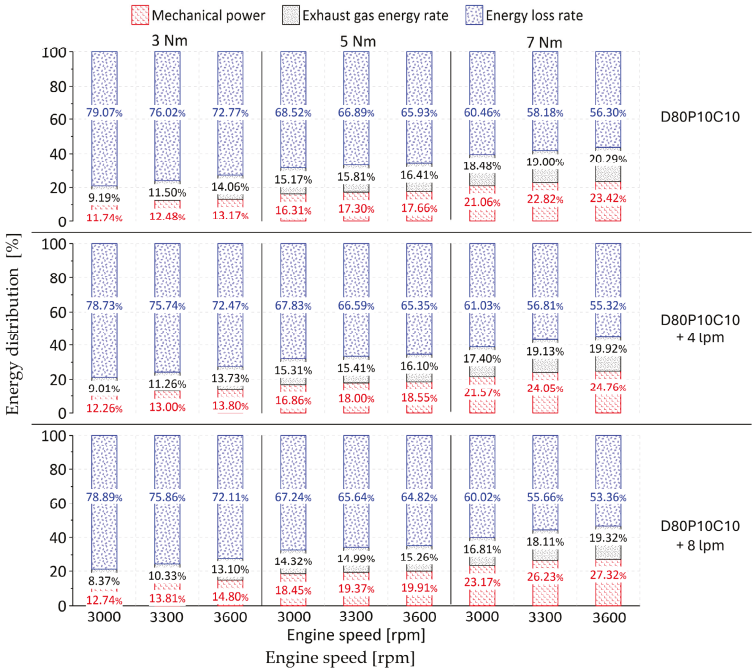


Figure 9. Energy distribution for D80P10C10, D80P10C10 + 4 lpm, and D80P10C10 + 8 lpm.

The chemical energy of the fuel is converted to mechanical power, and the energy is lost in the form of heat and through exhaust gases. On average, the D100, D85P10C5, and D80P10C10 fuels were observed to produce a fuel chemical energy to mechanical power conversion of 18.44%, 17.62%, and 17.33%. The lower conversion rate in the biodiesel blends is a consequence of the lower efficiency compared to pure diesel. In the case of the exhaust gas energy rate, an average percentage distribution of 14.24%, 14.65%, and 15.55% is shown for the D100, D85P10C5, and D80P10C10 fuels. The higher exhaust gas energy rates in the D85P10C5 and D80P10C10 blends are a consequence of their higher oxygen content, which tends to increase the temperature during the combustion process. For the D100, D85P10C5, and D80P10C10 fuels, an average loss energy rate of 67.32%, 67.73%, and

67.13% was obtained, respectively. This loss energy rate is associated with heat loss to the environment, friction, and the quality of the combustion process.

Hydroxy injection achieves a reduction in the loss energy rate for all fuels. The fuels D100 + 4 lpm and D100 + 8 lpm produce a 2.26% and 2.55% reduction in the loss energy rate compared to D100. For the fuel D85P10C5 + 4 lpm and D85P10C5 + 8 lpm, a decrease of 1.06% and 2.34% was obtained. In the case of D80P10C10 + 4 lpm and D80P10C10 + 8 lpm, a reduction of 0.95% and 1.89% was observed, respectively. The addition of hydroxy favors the conversion of chemical energy from fuel to mechanical power for pure diesel and biodiesel blends. For D100, D85P10C5, and D80P10C10, a maximum percentage conversion of fuel chemical energy to mechanical power of 24.89%, 23.69%, and 23.42% was obtained. However, with the injection of a volumetric flow rate of 4 lpm, the maximum conversion percentage was 26.17%, 25.14%, and 24.76%. In the case of the mixtures D100 + 8 lpm, D85P10C5 + 8 lpm, and D80P10C10 + 8 lpm, a maximum conversion of 28.16%, 27.58%, and 27.32% was obtained. These results are a consequence of the lower amount of fuel consumption and the higher combustion efficiency achieved by the fuels when mixed with hydroxy.

8.3. Exergy Distribution Analysis

To analyze the loss of energy in the engine, an exergy analysis was performed, considering mechanical power, exhaust gas exergy rate, exergy loss rate, and exergy destruction rate. Figures 10–12 show the exergy distributions of D100, D85P10C5, and D80P10C10.

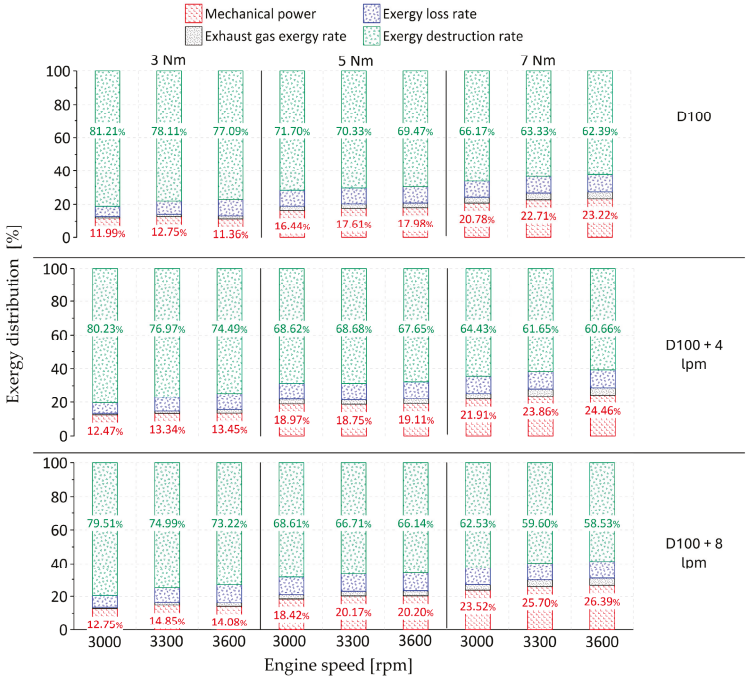


Figure 10. Exergy distribution for D100, D100 + 4 lpm, and D100 + 8 lpm.

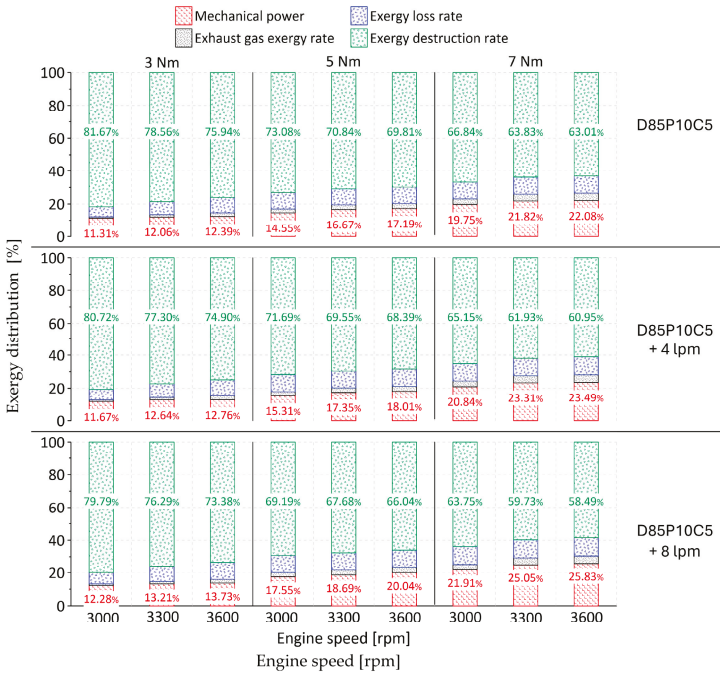


Figure 11. Exergy distribution for D85P10C5, D85P10C5 + 4 lpm, and D85P10C5 + 8 lpm.

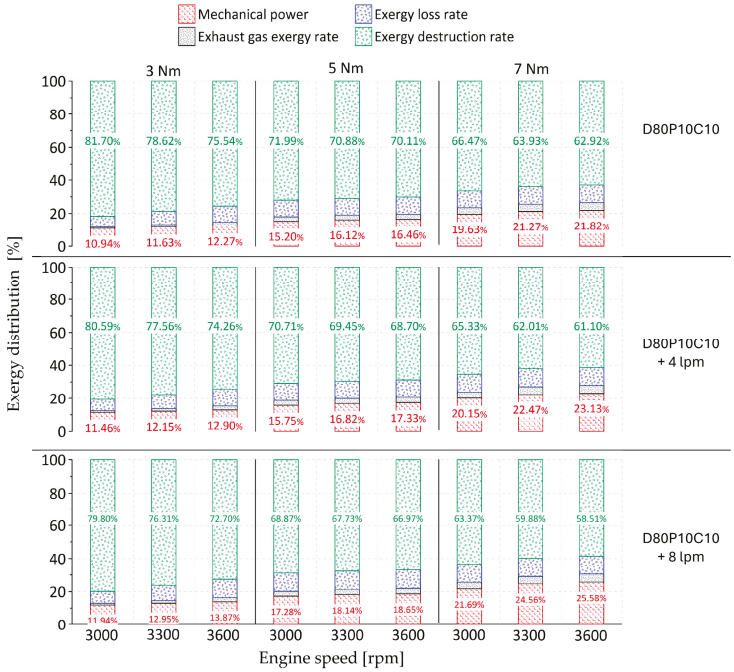


Figure 12. Exergy distribution for D80P10C10, D80P10C10 + 4 lpm, and D80P10C10 + 8 lpm.

The experimental results show that, for the D100 fuel, only 11.36–23.22% of the input exergy is transformed into useful work, exhaust gases lose 0.82–4.22% of the fuel exergy, 5.98–10.17% is eliminated by heat transfer, and irreversible processes in the engine lose 62.39–81.21% of the input exergy. In the case of the D85P10C5 fuel, 11.31–22.08% of the input exergy is transformed into useful work, 0.87–4.48% is lost through exhaust gases, 6.14–10.44% is lost through heat transfer, and 63.01–81.67% is lost through irreversibility. Finally, in the D80P10C10 fuel, 10.94–21.82% is transformed into useful work, 0.96–4.71% and 6.40–10.55% is lost through exhaust gases and heat transfer, and 62.92–81.70% due to irreversible processes. In general, D85P10C5 and D80P10C10 biodiesel blends tend to

increase exergy losses due to exhaust gas, heat transfer, and irreversibility compared to pure diesel.

The increase in hydroxy injection has a positive impact on the exergy distributions for the D100, D85P10C5, and D80P10C10 fuels. The results obtained show that the D100 + 4 lpm and D100 + 8 lpm fuels cause a 2.59% and 4.77% reduction in the exergy destruction rate compared to D100. For the fuels D85P10C5 + 4 lpm and D85P10C5 + 8 lpm, decreases of 2.07% and 4.66% were obtained. In the case of the fuels D80P10C10 + 4 lpm and D80P10C10 + 8 lpm, a reduction of 1.98% and 4.47% was observed when compared to D80P10C10, respectively. The use of hydroxy as a secondary fuel allows for increasing the exergy efficiency of the engine for all fuels. The maximum exergy efficiency of D100 was 23.22%. However, for the D100 + 4 lpm and D100 + 8 lpm fuels, a maximum exergy efficiency of 24.46% and 26.39% was obtained, respectively. In the case of the D85P10C5 + 4 lpm and D85P10C5 + 8 lpm fuels, a maximum exergy efficiency of 23.49% and 25.83% was obtained, which is an improvement compared to the efficiency achieved with D85P10C5. The fuels D80P10C10 + 4 lpm and D80P10C10 + 8 lpm allow reaching a maximum exergy efficiency of 23.13% and 25.58%, respectively.

8.4. Analysis of the Environmental and Social Costs of Emissions

Figure 13 shows the environmental and social cost of carbon monoxide (CO) emissions for pure diesel and palm oil and coffee husk bio iesel blends.

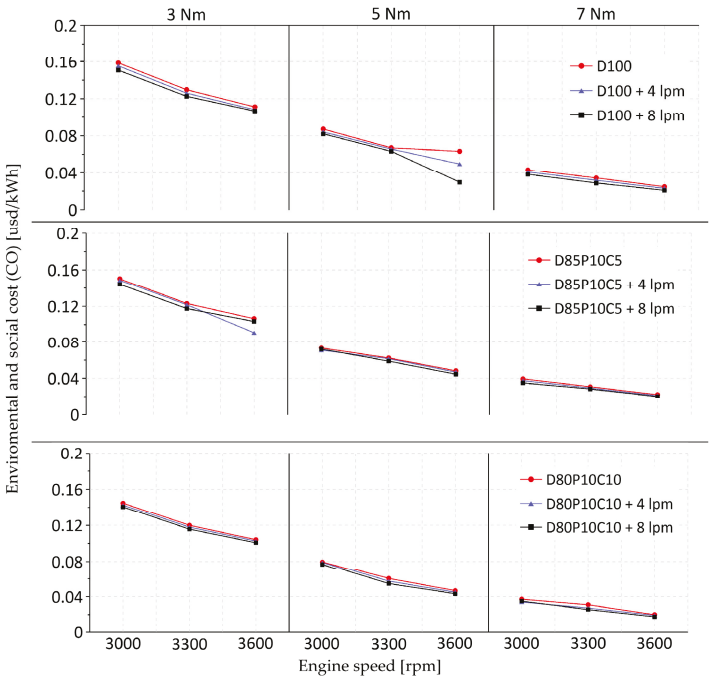


Figure 13. Environmental and social cost of carbon monoxide for D100, D85P10C5, and D80P10C10.

CO emission levels are associated with oxygen deficiency in the combustion chamber and poor combustion quality [46]. The highest environmental and social cost of CO emissions occurs at a torque of 3 Nm for all fuels. The blends of biodiesel D85P10C5 and D80P10C10 achieve a decrease in the environmental and social cost of CO emissions. For the experimental tests carried out, a reduction of 10.50% and 13.69% was observed in comparison with pure diesel. This remarkable reduction is the result of the oxygen content in the D85P10C5 and D80P10C10 fuels. Similar results have been reported in the literature for various types of biodiesels [47].

Hydroxy injection has resulted in a reduction in the environmental and social cost of CO emissions for pure diesel (D100), and biodiesel blends (D85P10C5, and D80P10C10). The fuels D100 + 4 lpm and D100 + 8 lpm produce a reduction of 6.11% and 13.63% compared to pure diesel. For D85P10C5 + 4 lpm and D85P10C5 + 8 lpm, a decrease of 4.33% and 6.16% was obtained in D85P10C5. Finally, in the fuel D80P10C10 + 4 lpm and D80P10C10 + 8 lpm, a reduction of 4.31% and 7.28% was observed in comparison with D80P10C10, respectively. The leading cause of this behavior is the formation of hydroxide (OH) molecules with hydroxy injection, which leads to an improvement in combustion quality and a reduction in CO formation [48].

Figure 14 shows the environmental and social cost of carbon dioxide (CO_2) emissions for the D100, D85P10C5, and D80P10C10 fuels.

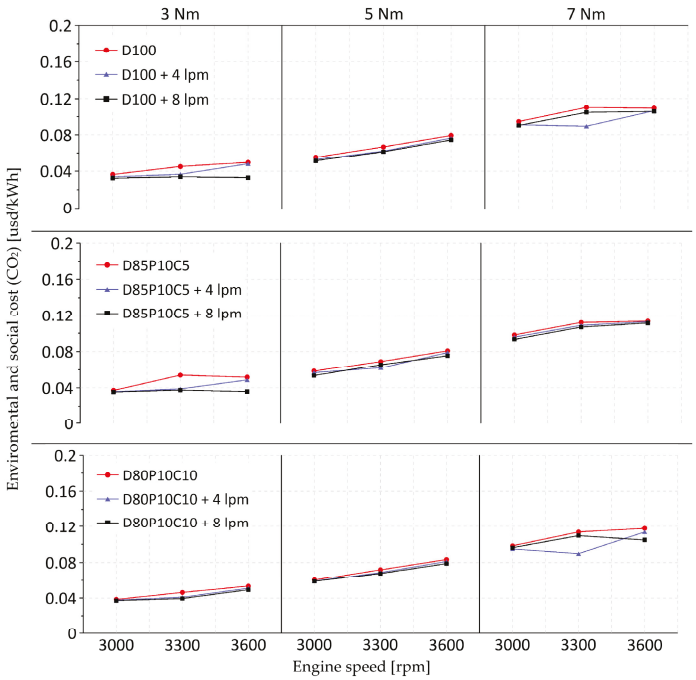


Figure 14. Environmental and social cost of carbon dioxide for D100, D85P10C5, and D80P10C10.

Carbon dioxide emissions are products of the complete combustion of the fuel. Figure 14 analyzes the environmental and social costs of CO_2 emissions for diesel, biodiesel, and their mixtures with hydroxy injection. In general, the engine tends to produce higher CO_2 emissions with increasing torque and engine speed. The D85P10C5 and D80P10C10 biodiesel blends result in a 5.07% and 5.96% increase in the environmental and social cost of CO_2 emissions compared to D100. This implies higher CO_2 levels with the biodiesel blends. This result is associated with the high oxygen content of D85P10C5 and D80P10C10 fuels, which promotes complete combustion [49].

All fuel types tested decrease the environmental and social cost of CO_2 emissions with hydroxy injection. By adding a volumetric flow of 4 and 8 lpm, a reduction of 7.74% and 11.49% was obtained in the D100 fuel. In the case of the D85P10C5 blend, a decrease of 6.53% and 10.80% was obtained when the engine is operated with fuel D85P10C5 + 4 lpm and D85P10C5 + 8 lpm, respectively. The use of the fuels D80P10C10 + 4 lpm and D80P10C10 + 8 lpm allows a reduction of 6.11% and 6.28% in the environmental and social cost of CO_2 emissions. Since hydroxy has a high energy content, less fuel is required, and, thus, a decrease in carbon molecules inside the combustion chamber. As the volumetric flow of hydroxy increases, the environmental and social cost of CO_2 emissions decreases.

Figure 15 shows the environmental and social cost trends of hydrocarbon (HC) emissions for D100, D85P10C5, and D80P10C10 fuels.

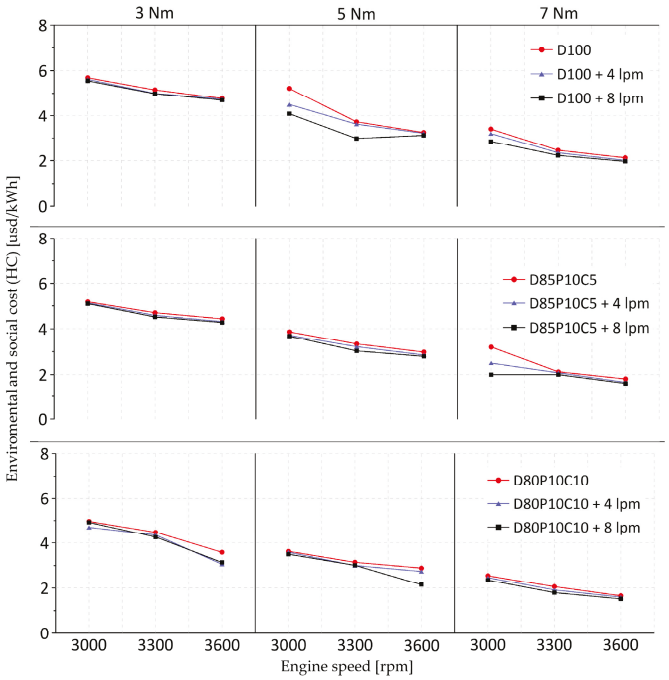


Figure 15. Environmental and social costs of hydrocarbon for D100, D85P10C5, and D80P10C10.

Hydrocarbons are caused by inadequate combustion in the combustion chamber. The results obtained show that the environmental and social costs of HC emissions are reduced with the increase in engine torque and speed, which may be related to the lower fuel consumption and better efficiency in these operational conditions. Under low engine load conditions, excess fuel injection and a poor air–fuel ratio occur, thus resulting in higher levels of environmental and social costs of HC emissions. The D85P10C5 and D80P10C10 biodiesel blends allow a reduction of 11.52% and 19.04% compared to D100.

This reduction in the environmental and social cost of HC emissions is a consequence of the oxygen available in the palm oil and coffee husk biodiesel blends, which results in better combustion quality. Hydroxy injections can significantly reduce the environmental and social cost of HC emissions. The wide flammability range of hydroxy and the better homogeneity allow a reduction in unburned hydrocarbons during combustion [50]. With the addition of a volumetric flow of 4 lpm, a decrease of 4.24%, 5.56%, and 5.30% in the environmental and social cost of HC emissions was obtained for the D100, D85P10C5, and D80P10C10 fuels. In the case of a volumetric flow of 8 lpm, a decrease of 9.56%, 9.30%, and 8.93% was observed for fuels D100, D85P10C5, and D80P10C10, respectively.

Figure 16 shows the environmental and social costs of nitrogen oxide emissions for fuels.

NOx emissions are mainly caused by high temperatures during the combustion process. These high temperatures favor the reaction of nitrogen and oxygen. Another factor that influences NOx formation is the availability of oxygen in the combustion chamber. This explains the higher environmental and social cost of NOx emissions in palm oil and coffee husk biodiesel blends. The results show that D85P10C5 and D80P10C10 fuels cause an increase of 2.20% and 7.40% compared to D100.

Although hydroxy injections improve efficiency and reduce CO, CO_2, and HC emissions from the engine, the trends obtained show an increase in NOx emissions when using this type of fuel. For D100 + 4 lpm and D100 + 8 lpm fuels, there is an increase of 9.25% and 20.97% in the environmental and social cost of NOx emissions compared to D100. In the case of D85P10C5 + 4 lpm and D85P10C5 + 8 lpm fuel, an increase of 9.61% and 10.73% was obtained when compared to D85P10C5. Finally, for the fuel D80P10C10 + 4 lpm

and D80P10C10 + 8 lpm, the results show an increase of 14.13% and 15.61%. Due to this behavior, it is necessary that we implement strategies to mitigate NOx emissions. This is especially important in transportation and power generation applications, due to NOx emission regulations.

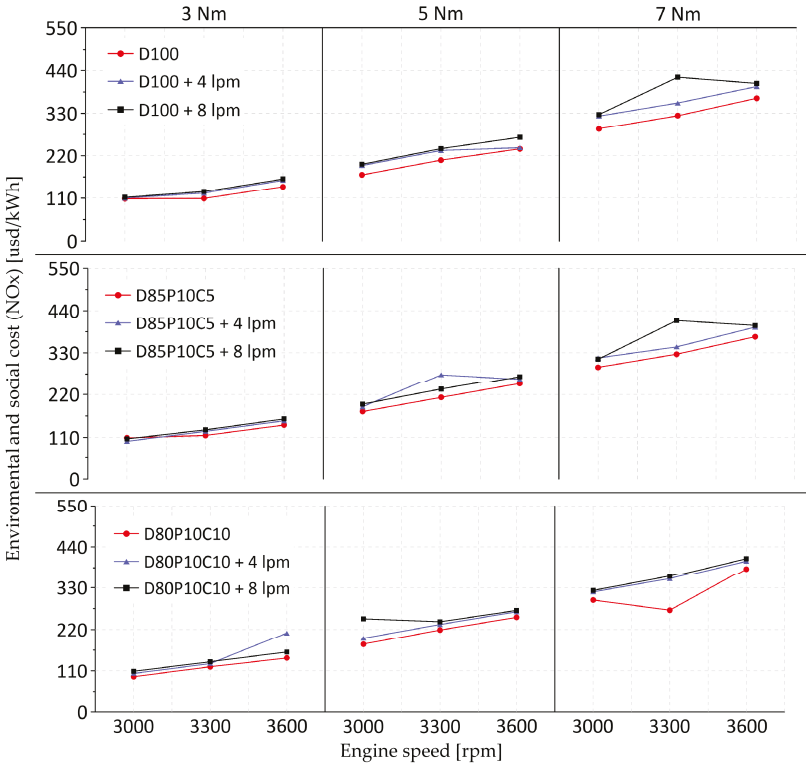


Figure 16. Environmental and social cost of nitrogen oxide for D100, D85P10C5, and D80P10C10.

The increase in NOx emissions caused by using biodiesel and hydroxy can be minimized through various strategies such as fuel treatment (emulsification, fuel additives, and blending), engine parameter modification (combustion modification, dual injection, and combustion type), and exhaust gas aftertreatment technologies (EGR and SCR) [51]. Table 9 shows a comparison of the NOx emission mitigation capacity for various strategies.

Table 9. Technologies for mitigating NOx emissions.

Ref.	Technology	Biodiesel	Engine Type	Maximum NOx Reduction
[52]	Emulsification	Waste cooking oil	Direct injection	60.6%
[53]	Additives fuel	Coconut	Indirect injection	7.78%
[54]	Water injection	Rapeseed biodiesel	Direct injection	50%
[55]	SCR	Soybean	Direct injection	68%
[56]	SCR	Neem	Direct injection	82%

Among the most notable options is selective catalytic reduction (SCR) due to its high efficiency in mitigating NOx emissions [57]. Studies in the literature indicate that NOx emissions in biodiesel blends with an SCR application are reduced by 68% to 82% [55,56]. This favors the viability of using biodiesel and hydroxy mixtures to take advantage of their lower carbon content without causing a significant increase in NOx emissions.

8.5. Cost Savings Analysis

Figure 17 shows the engine operating cost for pure diesel, biodiesel, and their mixtures with hydroxy for the different operating conditions.

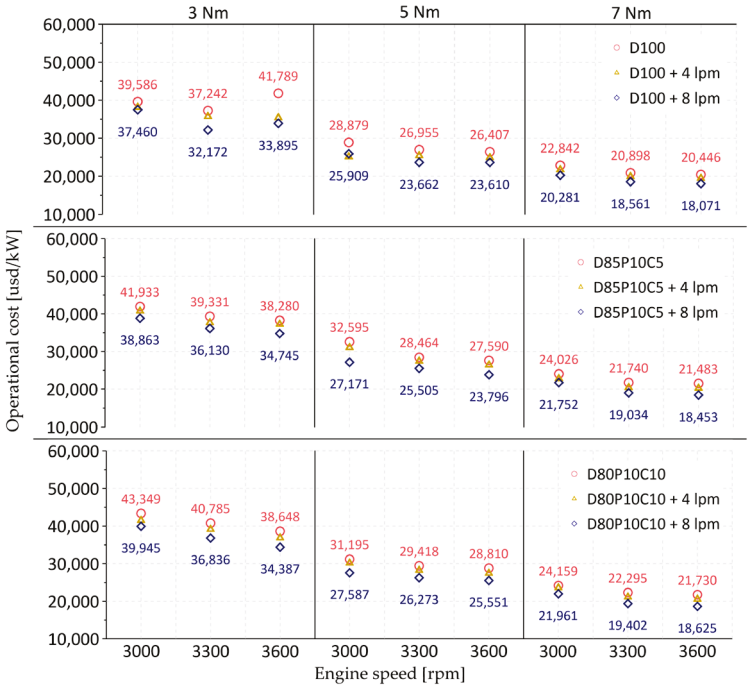


Figure 17. Operational cost for D100, D85P10C5, and D80P10C10.

The engine operating cost shown is associated with fuel consumption. The trends indicate a reduction in operating cost with increasing torque and speed levels. The operating cost intervals for D100, D85P10C5, and D80P10C10 fuels were 20,446–41,789 usd/kWh, 21,483–41,933 usd/kWh, and 21,730–43,349 usd/kWh, respectively. In general, the D85P10C5 and D80P10C10 biodiesel blends produce an increase of 5.13% and 8.01% in engine operating cost, compared to pure diesel. These trends are a consequence of the higher fuel consumption when the engine is fueled with palm oil and coffee husk biodiesel blends. The injection of hydroxy can reduce the operational cost in pure diesel and biodiesel blends. For the experimental tests carried out, it was observed that the D100 + 4 lpm and D100 + 8 lpm fuels achieve a reduction of 6.91% and 11.66% compared to pure diesel. In the case of the D85P10C5 + 4 lpm and D85P10C5 + 8 lpm fuels, a decrease of 4.34% and 10.61% was obtained. Finally, in the blends D80P10C10 + 4 lpm and D80P10C10 + 8 lpm, there is a reduction of 4.20% and 10.94% compared to D80P10C10, respectively.

9. Conclusions

In the present research, an analysis of the influence of hydroxy on pure diesel and blends of palm oil and coffee husk biodiesel with a percentage of 15% and 20% was carried out. The experimental tests were carried out in a stationary diesel engine, in which the torque and speed varied from 3–7 Nm and 3000–3600 rpm. Hydroxy was used as a secondary fuel with a volumetric flow injection of 4 and 8 lpm.

The results show that palm oil and coffee husk biodiesel blends tend to increase the BSFC of the engine compared to pure diesel. This implies an increase in injected fuel consumption. In general, D85P10C5 and D80P10C10 fuels produce a rise of 9.79% and 13.33% compared to D100. The use of palm oil and coffee husk biodiesel blends also results in a reduction of engine BTE, which implies a less efficient combustion process. The D85P10C5 and D80P10C10 fuels reduce BTE by 6.08% and 7.47%, respectively. The injection of hydroxy can reduce BSFC and increase engine BTE when running on pure diesel and biodiesel blends. On average, a maximum decrease of 11.66%, 11.28%, and 10.94% in BSFC was observed when hydroxy is injected into the D100, D85P10C5, and D80P10C10 fuels. In

the case of BTE, a maximum increase of 13.37%, 12.84%, and 12.34% was obtained for the above fuels.

The energy and exergy analysis shows that the use of hydroxy as a secondary fuel causes an improvement in the energy and exergy efficiency of the engine. For fuels D100 + 8 lpm, D85P10C5 + 8 lpm, and D80P10C10 + 8 lpm, a maximum energy efficiency of 28.16%, 27.58%, and 27.32% was observed. In the case of exergy efficiency, a maximum value of 26.39%, 25.83%, and 25.58% was obtained for the above fuels. Additionally, hydroxy causes a maximum reduction of 4.77%, 4.66%, and 4.47% in the exergy destruction rate for fuels D100, D85P10C5, and D80P10C10.

The environmental and social costs of CO, CO_2, and HC emissions are significantly reduced with the addition of hydroxy in pure diesel, and palm oil and coffee husk biodiesel blends. For D100, a maximum decrease of 13.63%, 11.49%, and 9.56% in the environmental and social cost of CO, CO_2, and HC emissions was obtained when mixed with hydroxy (8 lpm). In the D85P10C5 case, a reduction of 6.16%, 10.80%, and 9.30% was observed. Finally, for the D80P10C10 fuel, a decrease of 7.28%, 6.28%, and 8.93% was reported.

The improvement in combustion quality due to hydroxy is reflected in a decrease in engine operating costs. The injection of a volumetric flow rate of 8 lpm allows a reduction of 11.66%, 10.61%, and 10.94% in operational cost when the engine is fueled with D100, D85P10C5, and D80P10C10.

The present research proposes the use of biodiesel derived from agricultural waste materials such as coffee husks. Unlike other common feedstocks used for biodiesel production, such as vegetable oils, the use of coffee husks promotes a circular economy by enabling better resource utilization. Additionally, it results in a significant reduction in raw material costs, as coffee husks are considered a waste product. Moreover, the partial substitution of diesel with biodiesel and hydroxy allows for the use of existing engine technology without requiring significant modifications. This alternative offers greater feasibility compared to options such as the complete replacement of diesel with hydrogen. Although the latter presents high environmental sustainability, it still poses a technological challenge that limits its large-scale implementation.

In general, the research conducted shows that hydroxy injection is a viable alternative for reducing fuel consumption and improving engine efficiency when fed with palm oil and coffee husk biodiesel blends. In this way, the environmental and social cost of emissions associated with internal combustion engines can be minimized while maintaining performance characteristics like those of pure diesel.

Author Contributions: Conceptualization: J.R.D. and J.D.-F.; methodology: J.R.D., F.B.-A. and J.D.-F.; software: J.R.D., F.B.-A. and B.H.-C.; validation: J.R.D., J.D.-F. and B.H.-C.; formal analysis: J.R.D., F.B.-A., and J.D.-F.; investigation: J.R.D.; resources: J.R.D.; writing—original draft preparation: J.R.D.; writing—review and editing: F.B.-A., J.D.-F. and B.H.-C.; funding acquisition: J.R.D. All authors have read and agreed to the published version of the manuscript.

Funding: This research received no external funding.

Data Availability Statement: The original contributions presented in this study are included in the article. Further inquiries can be directed to the corresponding author.

Acknowledgments: The authors acknowledge the Universidad de la Costa CUC, Institución Universitaria de Barranquilla, and Universidad del Atlántico for the support received.

Conflicts of Interest: The authors declare no conflicts of interest.

Abbreviations

The following abbreviations are used in this manuscript:

Nomenclature

Abbreviation	
WCO	Waste cooking oil
LPG	Liquefied petroleum gas
CNG	Compressed natural gas
BSFC	Brake-specific fuel consumption
BTE	Brake thermal efficiency
HRR	Heat release rate
EGR	Exhaust gas recirculation
SCR	Selective catalytic reduction
Symbols list	
CO	Carbon monoxide
HC	Hydrocarbons
NOx	Nitrogen oxides
CO_2	Carbon dioxide
S	Standard deviation
u	Uncertainty
$\dot{E}_s$	Mechanical power
R	Exhaust gas constant
T	Temperature
$\dot{m}_{bb}$	Blow-by flow rate
c_v	Specific heat at constant volume
u	Internal energy
p	Instantaneous cylinder pressure
V	Instantaneous cylinder volume
h	Heat transfer coefficient
B	Piston diameter
v_p	Piston velocity
k_d	Mechanical deformation
Greek letters	
$\boldsymbol{\theta}$	Crankshaft angle
Subscripts	
cam	Combustion chamber
$\boldsymbol{p}$	Piston
$\boldsymbol{v}$	Volume

References

1. Zhang, Z.; Liu, H.; Li, Y.; Ye, Y.; Tian, J.; Li, J.; Xu, Y.; Lv, J. Research and Optimization of Hydrogen Addition and EGR on the Combustion, Performance, and Emission of the Biodiesel-Hydrogen Dual-Fuel Engine with Different Loads Based on the RSM. *Heliyon* **2024**, *10*, e23389. [CrossRef] [PubMed]
2. Estrada, L.; Moreno, E.; Gonzalez-Quiroga, A.; Bula, A.; Duarte-Forero, J. Experimental Assessment of Performance and Emissions for Hydrogen-Diesel Dual Fuel Operation in a Low Displacement Compression Ignition Engine. *Heliyon* **2022**, *8*, e09285–e09295. [CrossRef]
3. Umar, M.; Ji, X.; Kirikkaleli, D.; Alola, A.A. The Imperativeness of Environmental Quality in the United States Transportation Sector amidst Biomass-Fossil Energy Consumption and Growth. *J. Clean. Prod.* **2021**, *285*, 124863. [CrossRef]
4. Duarte, N.; Arango, D.; Polanco, G.; Valencia, G.; Duarte-Forero, J. Experimental Evaluation of Low-Displacement Compression Ignited Engines Operating with Hydroxy Gas as a Supplementary Gaseous Fuel. *Heliyon* **2022**, *8*, e11545. [CrossRef]
5. Eldiehy, K.S.H.; Daimary, N.; Borah, D.; Sarmah, D.; Bora, U.; Mandal, M.; Deka, D. Towards Biodiesel Sustainability: Waste Sweet Potato Leaves as a Green Heterogeneous Catalyst for Biodiesel Production Using Microalgal Oil and Waste Cooking Oil. *Ind. Crops Prod.* **2022**, *187*, 115467. [CrossRef]
6. Winangun, K.; Setiyawan, A.; Sudarmanta, B. The Combustion Characteristics and Performance of a Diesel Dual-Fuel (DDF) Engine Fueled by Palm Oil Biodiesel and Hydrogen Gas. *Case Stud. Therm. Eng.* **2023**, *42*, 102755–102765. [CrossRef]

7. Krishnamoorthi, T.; Sudalaimuthu, G.; Dillikannan, D.; Jayabal, R. Influence of Thermal Barrier Coating on Performance and Emission Characteristics of a Compression Ignition Engine Fueled with Delonix Regia Seed Biodiesel. *J. Clean. Prod.* **2023**, *420*, 138413. [CrossRef]
8. Subramanian, K.; Paramasivam, S.A.; Dillikannan, D.; Jayabal, R. Effect of Pilot Fuel Injection Strategies and EGR on a CRDI Diesel Engine Powered by Simmondsia Chinensis Seed Biodiesel-Methyl Acetate Blend. *Sustain. Energy Technol. Assess.* **2023**, *58*, 103345. [CrossRef]
9. Chen, Y.; Zhang, J.; Zhang, Z.; Zhong, W.; Zhao, Z.; Hu, J. Utilization of Renewable Biodiesel Blends with Different Proportions for the Improvements of Performance and Emission Characteristics of a Diesel Engine. *Heliyon* **2023**, *9*, e19196. [CrossRef] [PubMed]
10. Mulkan, A.; Zulkifli, N.W.M.; Husin, H.; Dahlan, I. Performance and Emissions Assessment under Full Load Operation of an Unmodified Diesel Engine Running on Biodiesel-Based Waste Cooking Oil Synthesized Using JPW Solid Catalyst. *Renew. Energy* **2024**, *224*, 120145. [CrossRef]
11. Qenawy, M.; Khalaf, M.; Wang, J.; Tian, J.; Zuo, L.; Mustafa, H.M.M.; Esmail, M.F.C. Performance and Emission of Extracted Biodiesel from Mixed Jatropha-Castor Seeds. *Fuel* **2024**, *357*, 130060. [CrossRef]
12. Kesharvani, S.; Verma, T.N.; Dwivedi, G. Computational Analysis of Chlorella Protothecoides Biofuels on Engine Combustion, Performance and Emission. *Sustain. Energy Technol. Assess.* **2023**, *55*, 102972. [CrossRef]
13. Mu, Z.; Fu, J.; Zhou, F.; Yuan, K.; Yu, J.; Huang, D.; Cui, Z.; Duan, X.; Liu, J. A Comparatively Experimental Study on the Performance and Emission Characteristics of a Diesel Engine Fueled with Tung Oil-Based Biodiesel Blends (B10, B20, B50). *Energies* **2023**, *16*, 5577. [CrossRef]
14. Klymchuk, O.; Khodakivska, O.; Kovalov, B.; Brusina, A.; Benetyte, R.; Momotenko, I. World Trends in Bioethanol and Biodiesel Production in the Context of Sustainable Energy Development. *Int. J. Glob. Environ. Issues* **2020**, *19*, 90–108. [CrossRef]
15. Mahlia, T.M.I.; Ismail, N.; Hossain, N.; Silitonga, A.S.; Shamsuddin, A.H. Palm Oil and Its Wastes as Bioenergy Sources: A Comprehensive Review. *Environ. Sci. Pollut. Res.* **2019**, *26*, 14849–14866. [CrossRef] [PubMed]
16. Zahan, K.; Kano, M. Biodiesel Production from Palm Oil, Its By-Products, and Mill Effluent: A Review. *Energies* **2018**, *11*, 2132. [CrossRef]
17. Suhara, A.; Karyadi; Herawan, S.G.; Tirta, A.; Idris, M.; Roslan, M.F.; Putra, N.R.; Hananto, A.L.; Veza, I. Biodiesel Sustainability: Review of Progress and Challenges of Biodiesel as Sustainable Biofuel. *Clean Technol.* **2024**, *6*, 886–906. [CrossRef]
18. Stephen, J.L.; Periyasamy, B. Innovative Developments in Biofuels Production from Organic Waste Materials: A Review. *Fuel* **2018**, *214*, 623–633. [CrossRef]
19. Merete, W.; Haddis, A.; Alemayehu, E.; Ambelu, A. The Potential of Coffee Husk and Pulp as an Alternative Source of Environmentally Friendly Energy. *East Afr. J. Sci.* **2014**, *8*, 29–36.
20. Gurusamy, M.; Subramaniyan, M.; Subramaniyan, B. Assessment of Hydrogen and Diethyl Ether Enrichment on CI Engine Operating with Binary Blend of Jatropha and Camphor Oil Using Response Surface Methodology. *Energy* **2024**, *289*, 129919. [CrossRef]
21. Vasan, V.; Sridharan, N.V.; Feroskhan, M.; Vaithiyanathan, S.; Subramanian, B.; Tsai, P.-C.; Lin, Y.-C.; Lay, C.-H.; Wang, C.-T.; Ponnusamy, V.K. Biogas Production and Its Utilization in Internal Combustion Engines-a Review. *Process Saf. Environ. Prot.* **2024**, *186*, 518–539. [CrossRef]
22. Algayyim, S.J.M.; Saleh, K.; Wandel, A.P.; Fattah, I.M.R.; Yusaf, T.; Alrazen, H.A. Influence of Natural Gas and Hydrogen Properties on Internal Combustion Engine Performance, Combustion, and Emissions: A Review. *Fuel* **2024**, *362*, 130844. [CrossRef]
23. Akinyele, D.; Olabode, E.; Amole, A. Review of Fuel Cell Technologies and Applications for Sustainable Microgrid Systems. *Inventions* **2020**, *5*, 42. [CrossRef]
24. Azad, A.K.; Rasul, M.G.; Khan, M.M.K.; Sharma, S.C.; Bhuiya, M.M.K. Recent Development of Biodiesel Combustion Strategies and Modelling for Compression Ignition Engines. *Renew. Sustain. Energy Rev.* **2016**, *56*, 1068–1086. [CrossRef]
25. Zhang, X.; Yang, R.; Anburajan, P.; Van Le, Q.; Alsehli, M.; Xia, C.; Brindhadevi, K. Assessment of Hydrogen and Nanoparticles Blended Biodiesel on the Diesel Engine Performance and Emission Characteristics. *Fuel* **2022**, *307*, 121780. [CrossRef]
26. Mohan, S.; Dinesha, P. Performance and Emissions of Biodiesel Engine with Hydrogen Peroxide Emulsification and Cerium Oxide (CeO_2) Nanoparticle Additives. *Fuel* **2022**, *319*, 123872. [CrossRef]
27. Shanmuganathan, R.; Chi, N.T.L.; Chinnathambi, A.; Salmen, S.H.; Jhanani, G.K.; Gavurová, B.; Sekar, M.; Pugazhendhi, A.; Praveenkumar, T.R. Spirulina Microalgae Blend with Biohydrogen and Nanocatalyst TiO_2 and Ce_2O_3 as Step towards Emission Reduction: Promoter or Inhibitor. *Fuel* **2023**, *334*, 126791. [CrossRef]
28. Xia, C.; Brindhadevi, K.; Elfasakhany, A.; Alsehli, M.; Tola, S. Performance, Combustion and Emission Analysis of Castor Oil Biodiesel Blends Enriched with Nanoadditives and Hydrogen Fuel Using CI Engine. *Fuel* **2021**, *306*, 121541. [CrossRef]
29. Yesilyurt, M.K. A Detailed Investigation on the Performance, Combustion, and Exhaust Emission Characteristics of a Diesel Engine Running on the Blend of Diesel Fuel, Biodiesel, and 1-Heptanol (C7 Alcohol) as a Next-Generation Higher Alcohol. *Fuel* **2020**, *275*, 117893. [CrossRef]

30. Consuegra, F.; Bula, A.; Guillín, W.; Sánchez, J.; Duarte Forero, J. Instantaneous In-Cylinder Volume Considering Deformation and Clearance Due to Lubricating Film in Reciprocating Internal Combustion Engines. *Energies* **2019**, *12*, 1437. [CrossRef]
31. Valencia, G.; Núñez, J.; Duarte, J. Multiobjective Optimization of a Plate Heat Exchanger in a Waste Heat Recovery Organic Rankine Cycle System for Natural Gas Engines. *Entropy* **2019**, *21*, 655–675. [CrossRef]
32. Ochoa, G.V.; Isaza-Roldan, C.; Forero, J.D. A Phenomenological Base Semi-Physical Thermodynamic Model for the Cylinder and Exhaust Manifold of a Natural Gas 2-Megawatt Four-Stroke Internal Combustion Engine. *Heliyon* **2019**, *5*, e02700. [CrossRef] [PubMed]
33. Valencia Ochoa, G.; Acevedo Peñaloza, C.; Duarte Forero, J. Thermoeconomic Optimization with PSO Algorithm of Waste Heat Recovery Systems Based on Organic Rankine Cycle System for a Natural Gas Engine. *Energies* **2019**, *12*, 4165. [CrossRef]
34. Cundy, V.A. Combustion, 2nd Edition by Irvin Glassman, Academic Press, Inc., Orlando, FL, 501pages [ISBN No.: 0-12-285851-4] U.S. List Price: $49.50 (1987). *Environ. Prog.* **1993**, *12*, M6–M7. [CrossRef]
35. Woschni, G. A Universally Applicable Equation for the Instantaneous Heat Transfer Coefficient in the Internal Combustion Engine. *SAE Trans.* **1968**, *670931*, 3065–3083.
36. Duarte Forero, J.E. Aportación Al Estudio y Modelado Termodinámico En Motores de Combustión Interna. Ph.D. Thesis, Universidad del Norte, Puerto Colombia, Colombia, 2016. Available online: https://manglar.uninorte.edu.co/handle/10584/10167 (accessed on 1 July 2025).
37. Sanli, A.; Ozsezen, A.N.; Kilicaslan, I.; Canakci, M. The Influence of Engine Speed and Load on the Heat Transfer Between Gases and In-Cylinder Walls at Fired and Motored Conditions of an IDI Diesel Engine. *Appl. Therm. Eng.* **2008**, *28*, 1395–1404. [CrossRef]
38. Serrano, J.; Jiménez-Espadafor, F.J.; López, A. Analysis of the Effect of the Hydrogen as Main Fuel on the Performance of a Modified Compression Ignition Engine with Water Injection. *Energy* **2019**, *173*, 911–925. [CrossRef]
39. Lyubarskyy, P.; Bartel, D. 2D CFD-Model of the Piston Assembly in a Diesel Engine for the Analysis of Piston Ring Dynamics, Mass Transport and Friction. *Tribol. Int.* **2016**, *104*, 352–368. [CrossRef]
40. Diaz, J.M. Aportación Al Diagnóstico de La Combustión En Motores Diésel de Inyección Directa. Ph.D. Thesis, Universitat Politècnica de València, Valencia, Spain, 2007. Available online: https://riunet.upv.es/bitstream/10251/135955/2/Tesis.pdf (accessed on 1 July 2025).
41. Zucrow, M.J.; Hoffman, J.D. Gas Dynamics. In *Fundamental Fluid Mechanics for the Practicing Engineer*; CRC Press: Boca Raton, FL, USA, 2018; pp. 198–297.
42. Duarte Forero, J.; Guillín Estrada, W.; Sánchez Guerrero, J. Desarrollo de Una Metodología Para La Predicción Del Volumen Real En La Cámara de Combustión de Motores Diésel Utilizando Elementos Finitos. *Inge Cuc* **2018**, *14*, 122–132. [CrossRef]
43. Chetia, B.; Debbarma, S.; Das, B. Enhancing Engine Performance, Combustion, and Emissions Characteristics through CeO_2-Modified Cottonseed Biodiesel with Hydrogen Enrichment: A Comprehensive Investigation. *Int. J. Hydrogen Energy* **2024**, *89*, 1149–1165. [CrossRef]
44. Suhel, A.; Rahim, N.A.; Rahman, M.R.A.; Ahmad, K.A. Bin Engine's Behaviour on Magnetite Nanoparticles as Additive and Hydrogen Addition of Chicken Fat Methyl Ester Fuelled DICI Engine: A Dual Fuel Approach. *Int. J. Hydrogen Energy* **2021**, *46*, 14824–14843. [CrossRef]
45. Şanlı, B.; Uludamar, E. Effect of Hydrogen Addition in a Diesel Engine Fuelled with Diesel and Canola Biodiesel Fuel: Energetic-Exergetic, Sustainability Analyses. *Int. J. Hydrogen Energy* **2024**, *49*, 1148–1159. [CrossRef]
46. Patel, C.; Hwang, J.; Chandra, K.; Agarwal, R.A.; Bae, C.; Gupta, T.; Agarwal, A.K. In-Cylinder Spray and Combustion Investigations in a Heavy-Duty Optical Engine Fueled with Waste Cooking Oil, Jatropha, and Karanja Biodiesels. *J. Energy Resour. Technol.* **2019**, *141*, 12201. [CrossRef]
47. Leo, G.M.L.; Jayabal, R.; Kathapillai, A.; Sekar, S. Performance and Emissions Optimization of a Dual-Fuel Diesel Engine Powered by Cashew Nut Shell Oil Biodiesel/Hydrogen Gas Using Response Surface Methodology. *Fuel* **2025**, *384*, 133960.
48. Raju, P.; Masimalai, S.K.; Ganesan, N.; Karthic, S. V Engine's Behavior on Hydrogen Addition of Waste Cooking Oil Fueled Light Duty Diesel Engine-A Dual Fuel Approach. *Energy* **2020**, *194*, 116844. [CrossRef]
49. Rathinavelu, V.; Kulandaivel, A.; Pandey, A.K.; Bhatt, R.; De Poures, M.V.; Hossain, I.; Seikh, A.H.; Iqbal, A.; Murugan, P. Production of Green Hydrogen from Sewage Sludge/Algae in Agriculture Diesel Engine: Performance Evaluation. *Heliyon* **2024**, *10*, e23988. [CrossRef]
50. Khandal, S.V.; Razak, A.; Veza, I.; Afzal, A.; Alwetaishi, M.; Shaik, S.; Ağbulut, Ü.; Rashedi, A. Hydrogen and Dual Fuel Mode Performing in Engine with Different Combustion Chamber Shapes: Modelling and Analysis Using RSM-ANN Technique. *Int. J. Hydrogen Energy* **2024**, *52*, 973–1005. [CrossRef]
51. Masera, K.; Hossain, A.K. Advancement of Biodiesel Fuel Quality and NOx Emission Control Techniques. *Renew. Sustain. Energy Rev.* **2023**, *178*, 113235. [CrossRef]
52. Annamalai, M.; Dhinesh, B.; Nanthagopal, K.; SivaramaKrishnan, P.; Lalvani, J.I.J.; Parthasarathy, M.; Annamalai, K. An Assessment on Performance, Combustion and Emission Behavior of a Diesel Engine Powered by Ceria Nanoparticle Blended Emulsified Biofuel. *Energy Convers. Manag.* **2016**, *123*, 372–380. [CrossRef]

53. Fattah, I.M.R.; Hassan, M.H.; Kalam, M.A.; Atabani, A.E.; Abedin, M.J. Synthetic Phenolic Antioxidants to Biodiesel: Path toward NOx Reduction of an Unmodified Indirect Injection Diesel Engine. *J. Clean. Prod.* **2014**, *79*, 82–90. [CrossRef]
54. Tesfa, B.; Mishra, R.; Gu, F.; Ball, A.D. Water Injection Effects on the Performance and Emission Characteristics of a CI Engine Operating with Biodiesel. *Renew. Energy* **2012**, *37*, 333–344. [CrossRef]
55. Tadano, Y.S.; Borillo, G.C.; Godoi, A.F.L.; Cichon, A.; Silva, T.O.B.; Valebona, F.B.; Errera, M.R.; Neto, R.A.P.; Rempel, D.; Martin, L.; et al. Gaseous Emissions from a Heavy-Duty Engine Equipped with SCR Aftertreatment System and Fuelled with Diesel and Biodiesel: Assessment of Pollutant Dispersion and Health Risk. *Sci. Total Environ.* **2014**, *500*, 64–71. [CrossRef]
56. Sachuthananthan, B.; Balaji, G.; Krupakaran, R.L. Experimental Exploration on NO_x Diminution by the Combined Effect of Antioxidant Additives with SCR in a Diesel Engine Powered by Neem Biodiesel. *Int. J. Ambient. Energy* **2020**, *41*, 889–900. [CrossRef]
57. Zhang, Y.; Lou, D.; Tan, P.; Hu, Z. Experimental Study on the Durability of Biodiesel-Powered Engine Equipped with a Diesel Oxidation Catalyst and a Selective Catalytic Reduction System. *Energy* **2018**, *159*, 1024–1034. [CrossRef]

Disclaimer/Publisher's Note: The statements, opinions and data contained in all publications are solely those of the individual author(s) and contributor(s) and not of MDPI and/or the editor(s). MDPI and/or the editor(s) disclaim responsibility for any injury to people or property resulting from any ideas, methods, instructions or products referred to in the content.

energies

MDPI

Article

Turning Construction, Renovation, and Demolition (CRD) Wood Waste into Biochar: A Scalable and Sustainable Solution for Energy and Environmental Applications

Aravind Ganesan [1,2,*], Simon Barnabé [1,*], Younès Bareha [1], Simon Langlois [2], Olivier Rezazgui [2] and Cyrine Boussabbeh [2]

[1] Institut d'Innovations en Écomatériaux, Écoproduits et Écoénergies, Pavillon CIPP, Université du Québec à Trois-Rivières, Boul. des Forges, Trois-Rivières, QC G8Z 4M3, Canada
[2] Innofibre—Centre d'Innovation des Produits Cellulosiques, 3351, Boul. des Forges C.P.97, Trois-Rivières, QC G9A 5E6, Canada
* Correspondence: aravind.ganesan@uqtr.ca (A.G.); simon.barnabe@uqtr.ca (S.B.)

Abstract

This study investigates the pyrolysis of construction, renovation, and demolition (CRD) wood waste to produce biochar, with a focus on its robustness, scalability, and characterization for energy and environmental applications. Pyrolysis conditions, including the temperature, biomass residence time (BRT), and feedstock mass, were varied to evaluate their effects on biochar properties. High-temperature biochars (B800) showed the highest fixed carbon (FC) (87%) and thermostable fraction (TSF) (96%) and the lowest volatile carbon (VC) (9%), with a high carbon content (92%), a large BET surface area (300 m^2/g), and a high micropore volume (0.146 cm^3/g). However, the hydrogen (0.9%) and oxygen (2.2%) content, Van-Krevelen parameters (H/C: 0.1; O/C: 0.02), and biochar yield (21%) decreased with increasing temperature. Moderate-temperature biochars (B600) have balanced physicochemical properties and yields, making them suitable for adsorption applications. Methyl orange dye removal exceeded 90% under the optimal conditions, with B600 fitting well with the Freundlich isotherm model (R^2 = 0.97; 1/n = 0.5) and pseudo-second-order kinetic model (R^2 = 1). The study highlights biochar's suitability for varied applications, emphasizing the need for scalability in CRD wood pyrolysis.

Keywords: biomass; pyrolysis; biochar; adsorption; environment; metallurgy; carbon

1. Introduction

Discarded construction, renovation, and demolition (CRD) wood waste presents environmental risks due to its heterogeneous composition and metal contamination [1]. Disposal practices vary with construction trends, legislation, and location, while traditional methods, like landfilling and incineration, raise issues of space scarcity, leachate pollution, odor, and greenhouse gas emissions. Pyrolysis, a thermal decomposition process that takes place in low-oxygen environments, offers a feasible alternative for CRD wood waste management, yielding a multifaceted energy-dense product stream encompassing bio-oil, pyrolysis gas, and biochar. Moreover, pyrolysis can also be optimized by varying process conditions as slow, fast, and flash stages depending upon the aforementioned product of interest [2]. This valorization technique reduces the waste volume and immobilizes pollutants in biochar, supporting circular and sustainable waste management [3].

Biochar, a carbon-rich solid derived from pyrolysis, finds utility in soil remediation, carbon sequestration, wastewater treatment, metallurgy, and construction as a partial coal/coke substitute [4]. Emerging applications include sustainable agriculture [5], biopolymer fillers [6], and supercapacitor components [7]. Its properties are governed by feedstock and process parameters, like temperature, biomass residence time (BRT), heating rate, feedstock mass, and particle size [8,9]. Feedstocks, like CRD wood, differ from residues, like agricultural manure or municipal waste, in their biochemical and inorganic makeup. High-ash biomass (e.g., agri-waste) introduces alkaline and alkaline earth metals (AAEMs), such as Na, K, Ca, Mg, and Ba, which promote CO_2 release, lower carbon retention, and reduce biochar yields [10]. Above 600 °C, biochar becomes stable, aromatic, and graphitized, ideal for carbon sequestration [10], while milder temperatures produce surface-charge-rich reactive biochar suited for adsorption and soil remediation. However, key surface functionalities decline beyond 500 °C due to decarbonylation, decarboxylation, and other de-functionalization reactions [11]. Activation via acids, alkalis, steam, or CO_2 may alter the surface area, pore volume, and reactivity for adsorption [12], but many biochars perform well without such treatment methods [13].

Methyl orange, a synthetic anionic azo dye, is common in the textile, pulp and paper, and chemical industries [14]. The pulp and paper demonstration plant involved in this study uses methyl orange dye as one of the key pH indicators and for adjusting the acidity–basicity of hydrolysis and pulp solutions within the paper-manufacturing unit's operations, so its wastewater contains notable levels of the dye. Due to its carcinogenic and ecotoxic effects, persistent methyl orange in effluents raises environmental concerns [15]. Therefore, this dye has been chosen as the model compound for adsorption studies. Although activated carbon is the benchmark adsorbent, its high emissions from its fossil coke substrate, activation requirements, and transport from remote locations drive the search for sustainable alternatives [16]. While biochar has previously been studied for dye removal [17], CRD wood biochar remains largely underexplored. Adjustable porosity, surface area, surface functional groups, and carbon stability are four important properties necessary for biochar to be an effective adsorbent in water treatment to remove organic/inorganic pollutants [18]. The nature of the biomass feedstock, the pyrolysis parameters, and any chemical, thermal, or physical activation techniques govern these properties [19]. Activated biochars, though effective, are less feasible for single-use applications due to the cost of regeneration. Hence, using raw industrial residues, like CRD wood, is promising [20]. The adsorption efficiency also depends on the pollutant concentration, adsorbent dose, temperature, pH, co-ions, and contact time, influencing mechanisms such as electrostatic interactions, π-π bonding, hydrogen bonding, and pore filling [19,21,22]. If all these conditions are satisfied, adsorption is thermodynamically spontaneous and endothermic [23].

This study investigates raw CRD wood biochar for methyl orange adsorption without chemical or physical activation. Given CRD wood's end-of-life and low-cost nature, the spent biochar may be immobilized in concrete or asphalt for long-term pollutant containment and the elimination of desorption risks. Soil use, however, would require attention to leaching risks. Avoiding chemicals, reactive gases, or energy-intensive steps, this approach enables on-site production, use, and disposal with minimal cost and impact. Adsorption tests determine the best-performing biochar, selected solely from pyrolysis experimental outcomes.

The novelty of this work lies in applying a design of experiments (DOE) framework to study the influence of temperature, BRT, and feed mass on CRD-wood-derived biochar via slow pyrolysis in a laboratory horizontal tube furnace reactor—an underrepresented area in the current literature—building on our prior work [24]. The same CRD wood was later processed under chosen identical conditions in a semi-pilot horizontal rotary retort-furnace

reactor to assess scalability potential. Unique to this study is the combined evaluation of CRD wood biochar for its physicochemical suitability in carbon sequestration, soil amendment, and metallurgy (as a reductant), alongside its performance in non-activated dye adsorption. Kinetic, isotherm, and thermodynamic modeling add depth, offering critical insights into its practical environmental and industrial applications.

2. Materials and Methods

2.1. Sample Preparation

CRD wood residues sourced from BRQ Fibre et Broyure, Trois-Rivières, Quebec, Canada, with an initial moisture content of 18%, were received in cartons (Figure 1A) and oven-dried overnight at 105 °C until moisture content fell below 1 wt% (0.18 wt% in this case). This low moisture level facilitates faster pyrolysis, enhances heat transfer, and reduces reactor energy demand. A known mass of dried wood was subjected to vibrational sieving (LABTECH unit) for $\geq$5 min to determine particle size distribution. Non-wood contaminants of varying sizes were manually removed throughout. The mass retained on each sieve was recorded to calculate the average particle size. Biomass with particle size >2.5 cm was milled using a Thomas Wiley mill model 4 to achieve a manageable size range of 3 mm–2.5 cm (Figure 1B) for pyrolysis in both reactors. For characterization, the same mill (Figure 1C) with a screen for the smallest pore size was used to generate fines of both biomass (Figure 1D) and pyrolytic biochar (Figure 1E).

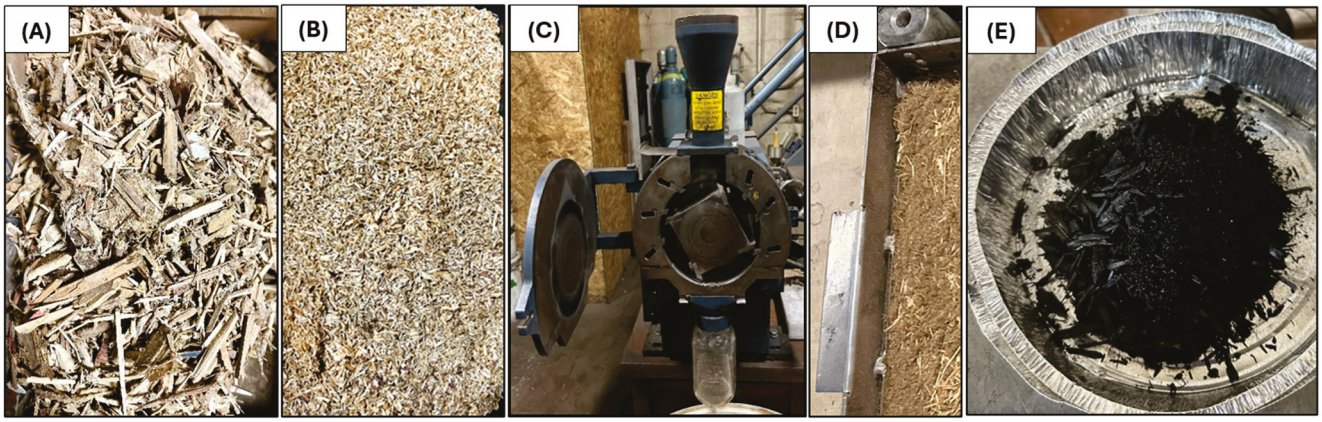


Figure 1. Sample preparation for pyrolysis and characterization. (**A**) CRD wood as received from source site; (**B**) size separation and selection of suitable particle size (3 mm to 2.5 cm); (**C**) Thomas Wiley mill model 4; (**D**) CRD wood fines; and (**E**) biochar fines.

2.2. Slow Pyrolysis Setup and Design of Experiments

Response Surface Methodology (RSM) was chosen to optimize CRD wood pyrolysis due to its effectiveness in modeling systems with few variables (temperature, BRT, feedstock mass, as in the current study), providing dependable polynomial equations and robust statistical validation (R^2, ANOVA, *p*-values) for easy interpretation. Its low experimental demand makes it a practical, cost/time-efficient option for resource-intensive processes like pyrolysis. RSM also ensures reproducibility, replicability, and transparency in process optimization studies—a vast understanding has already been established. In this work, slow pyrolysis followed a DOE framework using Stat-Ease's Design Expert v25.0 RSM tool with central composite design (CCD), varying the three aforesaid variables across multiple runs to assess their individual and interactive effects on key biochar properties. The conditions are summarized in Table 1, with model rationale and validation outlined in Supplementary Figure S1 and Supplementary Table S1. Performance was evaluated using

statistical tools, regression coefficients, and multiple plot types (surface, contour, predicted versus actual, and perturbation plots), serving as key performance indicators (KPIs).

Table 1. Experimental conditions chosen for pyrolysis.

Coded Independent Variable	Actual Independent Variable	Coded and Actual Values for the Five Levels				
		$-\alpha$ (Lowest)	−1 (Low)	0 (Mid-Point)	1 (High)	α (Highest)
A	Pyrolysis temperature (°C)	400	500	600	700	800
B	BRT (min)	30	45	60	75	90
C	Mass of feedstock (g)	50	100	150	200	250

Two reactors were used for pyrolysis. The first, a horizontal tube furnace reactor ("Thermo Scientific Lindberg Blue M™ 1100 °C", Waltham, MA, USA) (Figure 2, left), followed the design in [24]. A 2.5-inch-diameter, 69-inch-long steel tube reactor (5.55 L) holding up to 400 g CRD wood was inserted into the furnace cavity. The system reached set pyrolysis temperatures within 15 min, with three K-type thermocouples for zone monitoring and one in the reaction zone. Nitrogen with a flow rate of 1–5 L/min and a high-suction vacuum pump maintained inert conditions. The drawn-out gases are fed directly to a combustion chamber of the in-house pilot pyrolyzer to meet a small portion of its energy demand in tandem with natural gas and pilot pyrolysis gas. To prevent the carry-over of dust and other particulates from the reaction zone, a steel mesh filter is used.

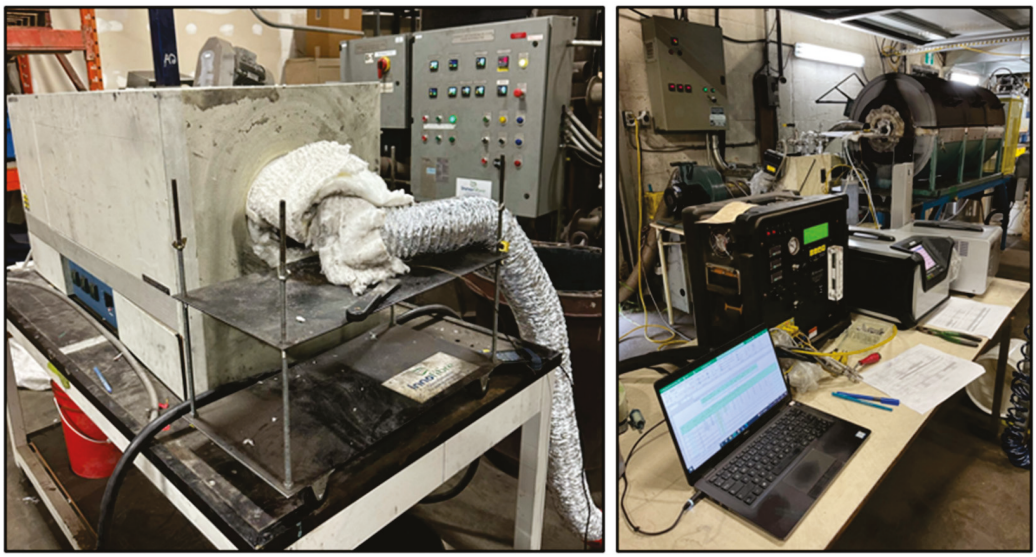


Figure 2. (**Left**)—horizontal tube furnace reactor; (**Right**)—horizontal rotary retort-furnace reactor.

The second, a horizontal rotary retort-furnace reactor (Figure 2, right), used the same thermocouple configuration, including one inside the retort to track thermal inertia. Thermal inertia can be defined as the reactor's resistance to an increase in temperature caused by non-uniform heating patterns and loss of heat via the reactor walls due to inefficient insulation. As a result, the refractory bricks of the furnace heat up to the set-point temperature, but this heat is not transferred adequately to the retort, and thus, the biomass inside experiences delayed heat transfer. Adequate heat transfer is essential to minimize unconverted biomass percentage as inferred from [25]. In fact, the influence of thermal inertia on material energy balance during pyrolytic thermal decomposition in both these reactor configurations is also addressed in Supplementary Tables S4 and S5. Quartz

wool insulated the retort ends, and the same nitrogen flow and vacuum system enabled volatile removal. The retort processed ~3 kg of CRD wood per batch, with rotational mixing promoting uniform heating and minimizing secondary reactions from volatile condensation.

2.3. Physicochemical and Morphological Characterization of Biochar

All characterizations were performed by the same technician using the same CRD wood and instrumentation as in [24]. This section outlines the equipment used to assess biochar's carbon structure, degree of aromatization, thermal and oxidative stability, and permeance. Selected analyses were also conducted on the original CRD wood biomass.

Proximate analysis was performed using 1 g of dried biochar fines in a muffle furnace, heated at 5 °C/min from room temperature to 550 °C and held for 2 h to measure ash content. Volatile carbon (VC) was determined per ISO 562 by heating 1 g of dried biochar fines in a lidded quartz crucible at 900 °C for 7 min. Fixed carbon (FC) was calculated by the difference [VC + FC + ash = 100]—all values are reported as weight percentage dry basis (wt% DB). Elemental analysis used an Elementar Vario Macro Cube (Langenselbold, Germany) with a helium carrier and oxygen combustion at 1200 °C; oxygen was calculated as [O = 100 − (C + H + N + S + ash)]. Thermogravimetric analysis (TGA) was performed on 8 mg of undried biochar using a PerkinElmer TGA 8000 (Waltham, MA, USA) ramped at 10 °C/min to 900 °C under air to assess thermal and oxidative decomposition. Correcting the thermograms for moisture and ash is key to calculating the TGA R50 recalcitrance index, i.e., the ratio of temperatures at which 50% weight loss in a biochar material happens to that of a reference graphite material. Surface functionalities were identified by Fourier Transform Infrared (FTIR) spectroscopy (Agilent Cary 630 spectrometer, Santa Clara, CA, USA) using diamond/germanium crystal and transmittance spectra (500–4000 cm^{-1}) processed in ORIGIN. A Raman spectrometer (ThermoScientific DXR3) with a 532 nm laser, 7 mW power, and 60 s exposure time was used over a scan range of 800–1800 cm^{-1} to quantify the I_D/I_G ratio for assessing carbon structural disorder or the degree of amorphous-to-crystalline carbon transitions in biochar. The Brunauer–Emmett–Teller (BET) surface area and micropore volume were measured on a Micromeritics Tristar II (Norcross, GA, USA) using helium/nitrogen as a carrier gas. Metal content was analyzed via a Microwave Plasma–Atomic Emission Spectrometer (MP-AES) (Agilent 4210) after acid digestion and nitrogen plasma nebulization of biochar. The pH was determined by mixing biochar (1:10 w/v) with demineralized water, shaking, resting for 30 min, and measuring with a bench-top pH analyzer. Bulk density was calculated from the mass-to-volume ratio in a leveled, pre-weighed steel container. Biochar yield from pyrolysis was expressed as the mass percentage relative to the initial biomass feed taken. The higher heating value (HHV) was estimated using elemental data from [26,27]. Scanning Electron Microscopy–Energy-Dispersive X-ray spectroscopy (SEM-EDX) (Hitachi SU-70, 15 kV, vacuum, Tokyo, Japan) was used to image dry biochar fines at 100×, 250×, 500×, and 1000× to detect surface elements—primarily C, O, Fe, and AAEMs—and the porous morphologies of biochar.

3. Results and Discussion

3.1. CRD Wood Pyrolysis in Horizontal Tube Furnace Reactor

Five biochar samples produced between 400 and 800 °C were randomly selected (B400–B800) for characterization and scalability tests to better assess the influence of pyrolysis parameters. Nonetheless, all data from Table 2 were incorporated into the DOE model for statistical analysis.

Table 2. Results of slow pyrolysis runs from the DOE model. Bulk density and HHV are discussed separately as plots (Figure 3E,F). Five biochars at five different pyrolysis temperatures of 400, 500, 600, 700, and 800 °C with mixed BRT/mass of feedstock conditions are considered for future characterizations. These are labeled as B400, B500, B600, B700, and B800 (highlighted in gray).

Run	Independent Variables for RSM			Elemental Parameters					Porosity		Biochar Output	Proximate Parameters			Thermal and Chemical Stability Indices			
															TGA	Van-Krevelen		Carbon Strength
	A: Temperature (°C)	B: BRT (min)	C: Mass of Feedstock (g)	N (wt%)	C (wt%)	H (wt%)	S (wt%)	O (wt%)	BET Surface Area (m^2/g)	Micropore Volume (cm^3/g)	Yield (%)	VC (wt%DB)	FC (wt%DB)	Ash (wt%DB)	R50	H/C	O/C	TSF (%)
CRD wood	**N.A**	**N.A**	**N.A**	**0.990**	**49.880**	**6.123**	**0.101**	**41.736**	**N.A**	**N.A**	**N.A**	**83.480**	**15.350**	**1.170**	**0.391**	**1.473**	**0.628**	**15.534**
1 (B400)	**400**	**60**	**100**	**0.780**	**65.320**	**4.293**	**0.442**	**26.145**	**4.238**	**0.002**	**57.800**	**26.384**	**70.596**	**3.020**	**0.513**	**0.789**	**0.300**	**73.271**
2	600	90	200	0.670	86.180	2.193	0.210	7.417	308.703	0.139	21.800	15.748	80.922	3.330	0.570	0.305	0.065	86.061
3	600	30	200	1.070	83.660	2.329	0.213	6.288	309.032	0.132	20.700	17.427	76.133	6.440	0.568	0.334	0.056	80.501
4 (B500)	**500**	**75**	**200**	**0.630**	**79.430**	**2.933**	**0.177**	**13.110**	**195.278**	**0.095**	**26.900**	**25.837**	**70.443**	**3.720**	**0.544**	**0.443**	**0.124**	**73.169**
5	600	60	100	0.910	82.370	2.391	0.241	8.578	255.854	0.123	21.300	18.473	76.017	5.510	0.603	0.348	0.078	80.132
6	500	75	150	0.870	78.340	2.910	0.180	13.840	179.077	0.090	26.400	24.312	71.828	3.860	0.561	0.446	0.132	74.783
7	500	90	150	0.720	77.600	2.746	0.218	12.546	260.562	0.114	26.500	24.247	69.583	6.170	0.545	0.425	0.121	72.452
8	600	45	50	0.700	86.720	2.034	0.123	5.613	334.887	0.149	19.200	14.132	81.058	4.810	0.632	0.281	0.049	86.794
9	700	90	200	0.940	88.760	1.379	0.205	4.026	315.809	0.148	23.300	12.151	83.159	4.690	0.587	0.186	0.034	90.002
10 (B800)	**800**	**75**	**200**	**0.890**	**91.740**	**0.870**	**0.168**	**2.232**	**299.554**	**0.146**	**21.100**	**9.169**	**86.731**	**4.100**	**0.647**	**0.114**	**0.018**	**96.191**
11 (B700)	**700**	**75**	**200**	**0.950**	**88.340**	**1.413**	**0.253**	**2.914**	**293.195**	**0.138**	**23.600**	**11.640**	**82.230**	**6.130**	**0.588**	**0.192**	**0.025**	**89.295**
12	500	90	250	0.510	82.000	2.825	0.151	11.344	229.033	0.108	26.600	23.857	72.973	3.170	0.546	0.413	0.104	76.032
13 (B600)	**600**	**90**	**250**	**0.430**	**87.510**	**2.209**	**0.123**	**6.168**	**323.776**	**0.145**	**21.900**	**15.037**	**81.403**	**3.560**	**0.577**	**0.303**	**0.053**	**86.817**
14	700	45	150	1.630	85.880	1.352	0.332	2.136	217.947	0.118	25.200	13.903	77.427	8.670	0.638	0.189	0.019	82.996
15	400	90	200	1.000	73.770	3.351	0.151	17.598	4.034	0.002	31.200	32.542	63.328	4.130	0.534	0.545	0.179	65.274
16	600	60	150	1.140	72.180	1.786	0.215	2.649	247.457	0.112	25.600	22.723	55.247	22.030	0.647	0.297	0.028	57.678

N.A: Not analyzed.

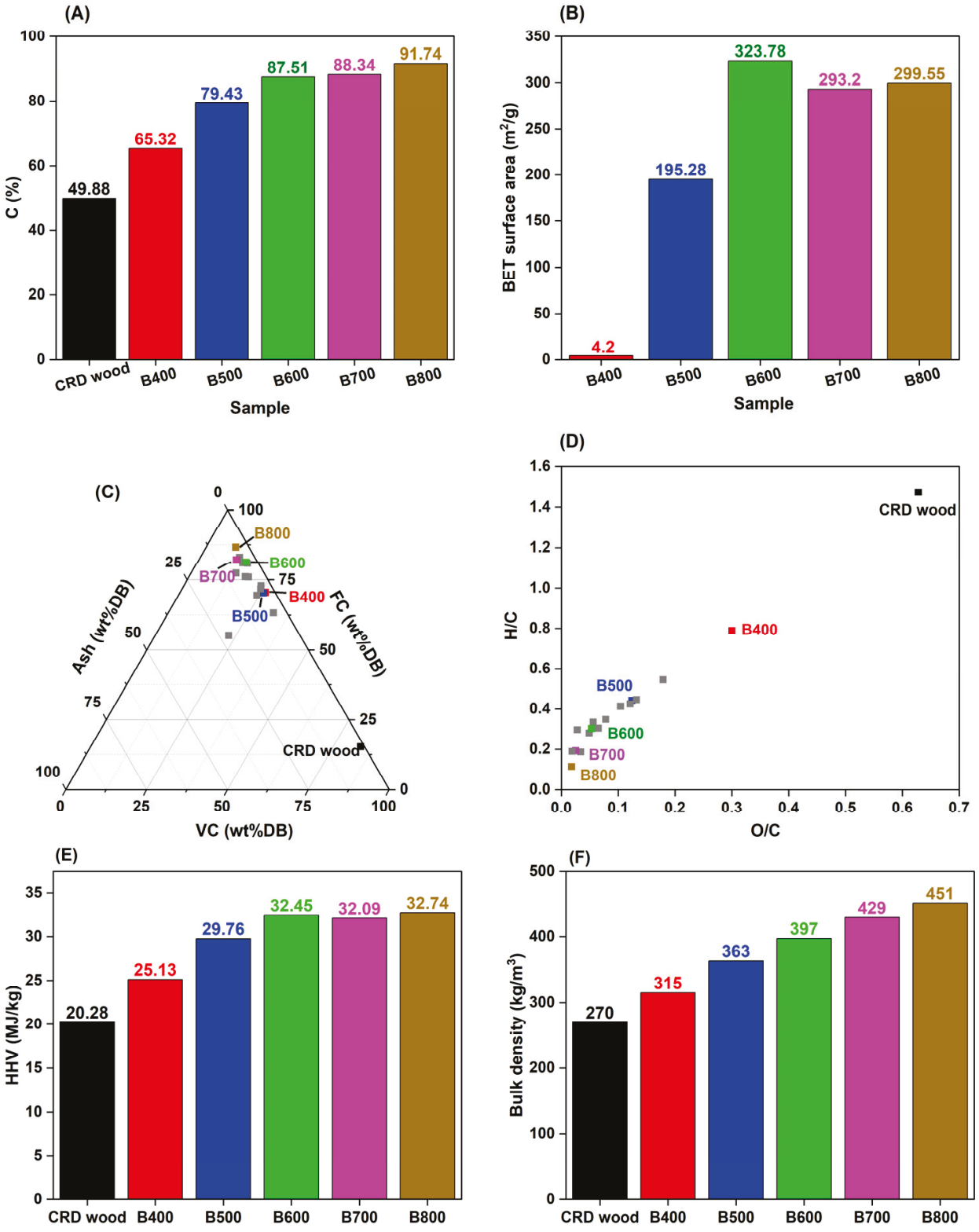


Figure 3. (**A**) Carbon content, (**B**) BET surface area, (**C**) proximate analysis, (**D**) Van-Krevelen plot, (**E**) HHV, and (**F**) bulk density for B400-B800.

3.1.1. Physicochemical Characterization

CRD wood shares some similar physicochemical properties with hardwoods like poplar and beech, including comparable carbon, oxygen, hydrogen, and ash content. However, it contains slightly higher sulfur, likely from gypsum residues in drywall fractions

present in the initial heterogeneous feedstock. CRD wood also differs from lignin-rich softwoods like pine, which have higher carbon and lower oxygen due to their inherent structural aromaticity. This is implicit from CRD wood's higher O/C, which confirms its holocellulose richness—characteristic of hardwoods with oxygen-based functional groups such as hydroxyls and carboxyls.

The results from all 16 slow pyrolysis runs in the horizontal tube furnace reactor are presented in Table 2. Pearson's coefficient of correlation (r) and model *p*-value were used as statistical indicators to analyze the influence of key process variables. The carbon content rose by 40–41% from B400 to B800, strongly correlated with pyrolysis temperature (r = 0.92; *p*-value = 0.0002). Concurrent declines in oxygen and hydrogen yielded lower O/C (r = −0.88; *p*-value < 0.0001) and H/C ratios (r = −0.95; *p*-value < 0.0001), indicating aromatic stability and biochar maturity. For soil amendment, especially in acidic or metal-contaminated soils, biochars like B400 and B500 are preferable due to their higher O/C, associated with increased surface negativity and CEC [28,29]. The BET surface area peaked at 600 °C before falling below 300 m^2/g (r = 0.83; *p*-value = 0.001), likely from micropore wall collapse and mesopore formation. This aligns with [30], where a higher pyrolysis temperature and a longer BRT enlarged the pore size. Biochars at 600 °C exhibited a high surface area (320–340 m^2/g) and micropore volume (0.112–0.149 cm^3/g), supporting adsorption. Such porous structures also enhance soil fertility and water retention in arid zones [31]. FC increased by 360% from raw CRD wood to B400, demonstrating the positive role of even the slightest of carbonization. From B400 to B800, FC rose further to 86.73% (r = 0.95; *p*-value = 0.0099), driven by the decomposition of volatile organics, as confirmed by a 65% drop in VC (r = −0.96; *p*-value < 0.0001).

Other biochar properties were also significantly affected by the pyrolysis temperature. The ash content in CRD wood biochar was comparable to that in other woody biomass types, specifically pinewood (0.40–1.80 wt%), poplar (3.45 wt%), and softwood pellets (0.61 wt%), classifying CRD wood as a low-ash feedstock [32]. B700 showed the highest ash content (6.13%), which declined to 4.10% in B800, likely due to the volatilization of unstable inorganics. The biochar yield decreased from 57.8% (B400) to 21.1% (B800) (r = −0.78). At 400 °C, incomplete pyrolysis left behind unconverted woody material, inflating the yield; a 53% drop at 500 °C confirmed B400 overestimation. The HHV rose from 20.28 MJ/kg (CRD wood) to 32.74 MJ/kg (B800), reflecting increased carbon and reduced volatiles (r = 0.87). This enhances energy density, benefiting combustion and high-temperature applications. The bulk density increased from 270 to 451 kg/m^3 from B400 to B800 (r = 0.99), aligning with [31]. Higher heat exposure induced compaction, crystallite ordering, and volume shrinkage [33], although [34] reported the opposite. They also noted declining ion exchange and reactivity at higher temperatures, possibly due to surface charge loss and carbon localization. The resulting structured FC improves thermal and electrical conductivity, supporting its use in metallurgy and charge storage.

As noted in [35], polyaromatic hydrocarbon (PAH) content in high-temperature biochars may decline if the carrier gas flow is sufficient to prevent volatile condensation and uncontrolled polymerization. Rather than adjusting the nitrogen flow, this study used a high-suction vacuum pump to minimize the gas residence time. According to [36], low-temperature biochars prioritize yield and contain fewer PAHs, lowering ecotoxicity risks. However, higher pollutant desorption can elevate ecotoxicity. Future work will assess priority PAHs such as Phenanthrene, Naphthalene, Pyrenes, and their benzo-derivatives [37].

Effect of Particle Size on Biomass Thermal Decomposition and Biochar Properties

The biomass particle size in pyrolysis affects conversion, reactivity, surface area, and composition. In this study, CRD wood particles ranged from >3 mm to <2.5 cm in the

horizontal tube furnace reactor. This range enabled thorough volatilization under slow heating, ensuring uniform heat penetration from the boundary layer towards the core of each particle. As [38] reported, small to intermediate particles with low moisture favor efficient heat transfer and yield. The observed 20–30% average biochar yield aligns with biomass pyrolysis studies at similar temperatures, confirming the suitability of the particle size. Successful conversion was evident from the crisp texture and uniformity of biochar, supporting micro- and mesopore development [39]. According to [40], densified, small-particle biochar may serve as a metallurgical reductant, enhancing strength, density, and controlled reactivity under high temperatures. Some biochar particles showed reduced surface area due to micro- to mesoporous structures, which can benefit wastewater treatment and nutrient recovery [41]. Larger pores may aid in heavy metal entrapment. For carbon sequestration, porosity is less critical than FC, VC, carbon content, and stability indices. High-temperature CRD wood biochars exhibited both high stability and enhanced surface characteristics. Their large surface area, balanced by low H/C, O/C, and hydrophobicity, balances reactivity towards ambient reactive species, moisture, or air. Conversely, larger particles may offer structural integrity for shear-intensive industrial processes [41].

Visual descriptions of these data are provided in Figure 3A–D.

3.1.2. Evaluating the Robustness of the RSM Model—Statistical Analysis, Contour/3-D Plots, and Predicted Versus Actual Value Distribution

To evaluate DOE robustness, four biochar properties—surface area, micropore volume, H/C, and O/C—were selected. After 16 runs, interdependence between pyrolysis parameters and these properties was modeled using a polynomial equation, with coefficients, ANOVA (p-value < 0.05 indicating model significance), and model fit indicating significance. Statistical results are summarized in Table 3, with detailed data provided in Supplementary Tables S2 and S3. Next, surface and contour plots of two response variables—BET surface area and Van-Krevelen H/C index—are also described as examples with reference to the influence of independent pyrolysis variables. Finally, for all four aforesaid response or dependent variables, a comparison of theoretical and actual experimental results was performed to validate the predictability of the model.

RSM's CCD tool recommended quadratic models for BET surface area and micropore volume and two-factor interaction models for H/C and O/C. In all cases, synergistic effects of pyrolysis variables were evident. The pyrolysis temperature was significant for all responses, identifying it as the most influential parameter. The BRT significantly affected only the BET surface area and micropore volume; an excessive BRT reduced both, likely due to pore rupture and coalescence. The feedstock mass alone showed no significant effect (p-value > 0.05) but influenced the BET surface area and micropore volume through interactions and squared terms (Figure 4iv). A higher feed mass requires an extended BRT to ensure complete pyrolysis and maintain yield. For H/C and O/C, feed mass and temperature governed volatilization and surface group rearrangement (Figure 4xii). Smaller samples at higher temperatures facilitated uniform heating and promoted oxygen/hydrogen elimination, favoring carbon retention. In contrast, a higher feed mass restricted heat/mass transfer, extending volatile residence time and causing condensation on biochar surfaces, forming C–O–C and C=O groups [42], which increase uncontrolled reactivity and reduce suitability for carbon sequestration and metallurgical use. Secondary cracking reactions may also cause carbon loss as light gases [43]. To mitigate these effects, a higher inert gas flow, an extended BRT, and elevated temperatures are necessary.

Table 3. Statistical significance results—equation coefficients, significance of each independent variable (*p*-values) on the nature of the chosen response variables, and model-fit data are shown. Cells shaded in the color gray are not accounted for due to the type of applicable model.

Response Variable	A	B	C	AB	AC	BC	A^2	B^2	C^2	Intercept	Model Type	Fit (R^2)	Lack of Fit
BET surface area (m^2/g)	84.6827	57.4696	−23.4390	4.2486	−12.0859	−125.5880	−46.6398	10.6473	209.0550	230.5000	Quadratic	0.9724	Insignificant
p-value	0.0010	0.0194	0.3150	0.8474	0.7916	0.0230	0.0034	0.2764	0.0119				
Micropore volume (cm^3/g)	0.0425	0.0240	−0.0086	−0.0006	−0.0061	−0.0478	−0.0203	0.0016	0.0806	0.1130	Quadratic	0.9753	Insignificant
p-value	0.0004	0.0214	0.3844	0.9532	0.7546	0.0358	0.0031	0.6873	0.0184				
H/C	−0.2017	−0.0224	0.0303	−0.0075	0.1497	0.0153				0.3136	Two-factor interaction	0.9769	Insignificant
p-value	<0.0001	0.1099	0.1850	0.7145	0.0038	0.4522							
O/C	−0.0829	−0.0040	0.0121	−0.0162	0.1069	0.0112				0.0613	Two-factor interaction	0.9326	Insignificant
p-value	<0.0001	0.6894	0.4763	0.3198	0.0059	0.4779							

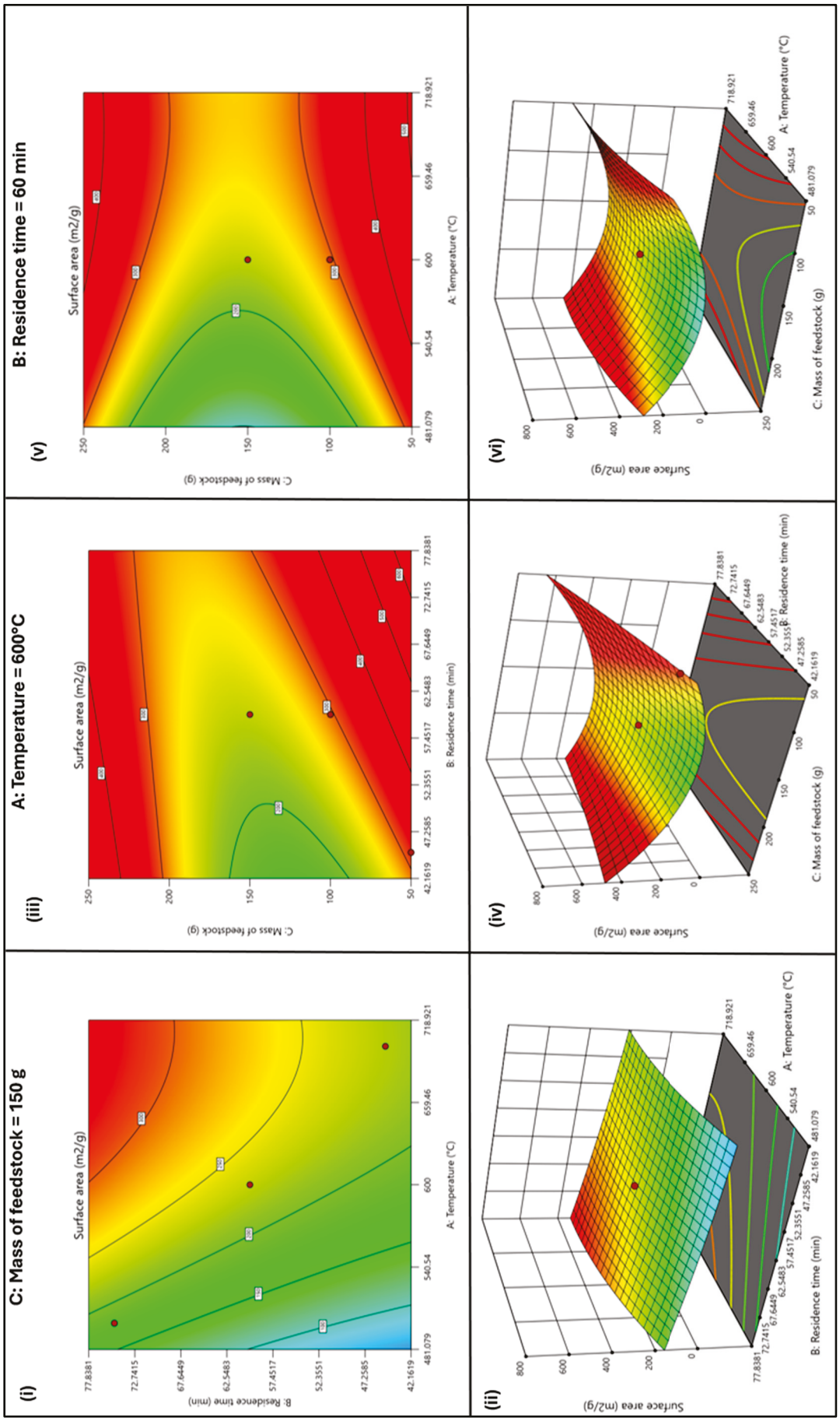


Figure 4. *Cont.*

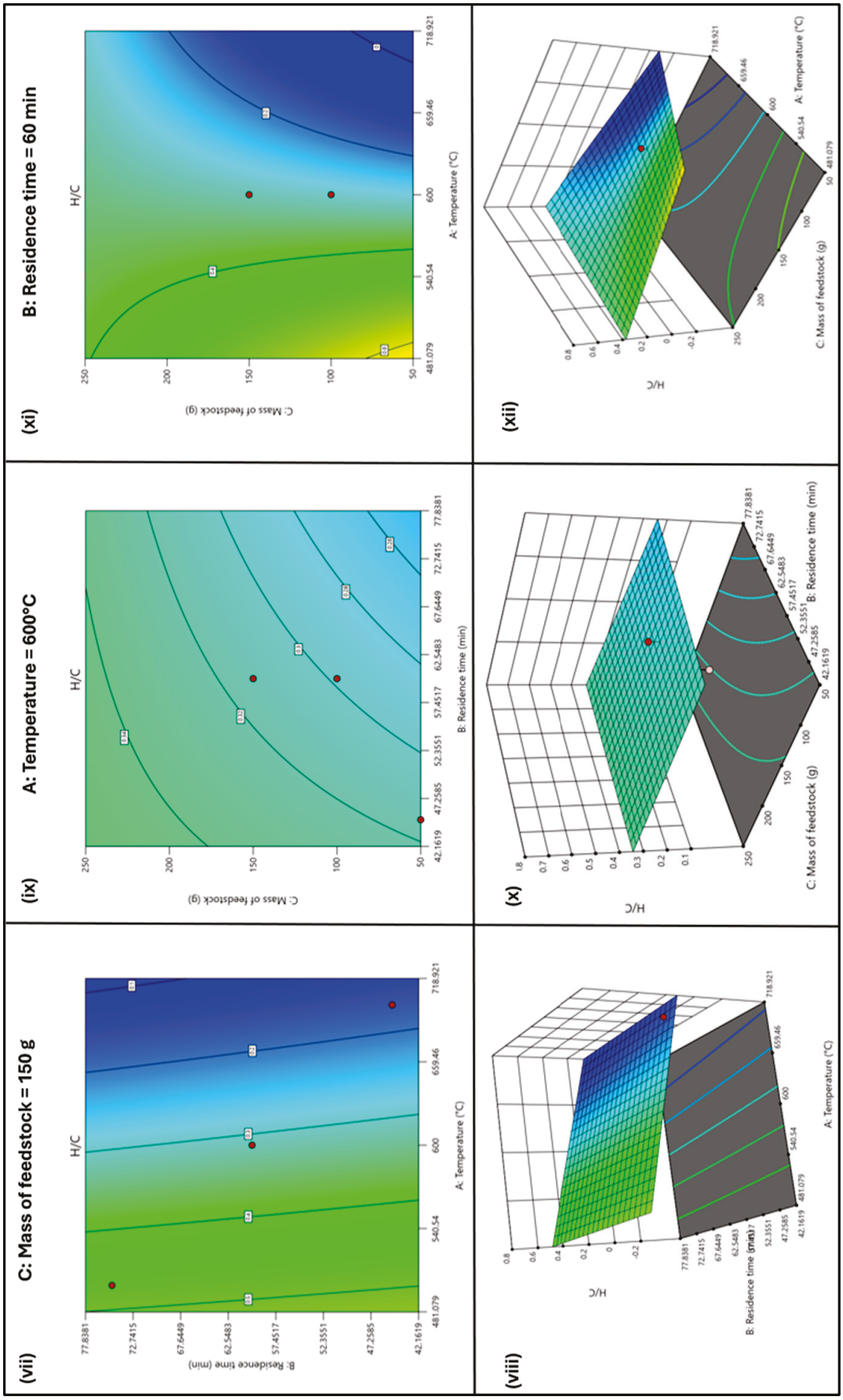


Figure 4. Surface and contour plots delineating the effects of temperature, residence time (BRT), and mass of feedstock on biochar properties. BET surface area (**i–vi**) and H/C (**vii–xii**). The 'red dots' represent experimental data points. The lowest to highest values are indicated by the color blue to the color red, respectively.

The model fit ($R^2 > 0.90$ for all responses) confirmed a strong correlation and high predictive accuracy. This is evident in the predicted-versus-actual plots in Figure 5, where points cluster near the origin line, validating model selection. In the following DOE equations, (−) indicates antagonistic, and (+) indicates synergistic effects.

$$\begin{aligned}\textbf{BET surface area} \\ &= 84.6827A + 57.4696B - 23.4390C + 4.2486AB - 12.0859AC - 125.5880BC \\ &- 46.6398A^2 + 10.6473B^2 + 209.0550C^2 + 230.5000\end{aligned} \quad (1)$$

Slow pyrolysis DOE model Equation (1)

$$\begin{aligned}\textbf{Micropore volume} \\ &= 0.0425A + 0.0240B - 0.0086C - 0.0006AB - 0.0061AC - 0.0478BC - 0.0203A^2 \\ &+ 0.0016B^2 + 0.0806C^2 + 0.1130\end{aligned} \quad (2)$$

Slow-pyrolysis DOE model Equation (2)

$$\frac{\mathbf{H}}{\mathbf{C}} = -0.2017A - 0.0224B + 0.0303C - 0.0075AB + 0.1497AC + 0.0153BC + 0.3136 \quad (3)$$

Slow-pyrolysis DOE model Equation (3)

$$\frac{\mathbf{O}}{\mathbf{C}} = -0.0829A - 0.0040B + 0.0121C - 0.0162AB + 0.1069AC + 0.0112BC + 0.0613 \quad (4)$$

Slow-pyrolysis DOE model Equation (4)

Choosing the best or optimal biochar production conditions is ultimately dependent upon the application under focus. Based on our findings, temperature can be underscored as the deciding pyrolysis parameter with the most drastic influence on biochar properties. This can be confirmed by the r, *p*-value, and perturbation analysis (relatively steeper slopes observed for pyrolysis temperature) obtained from the DOE model.

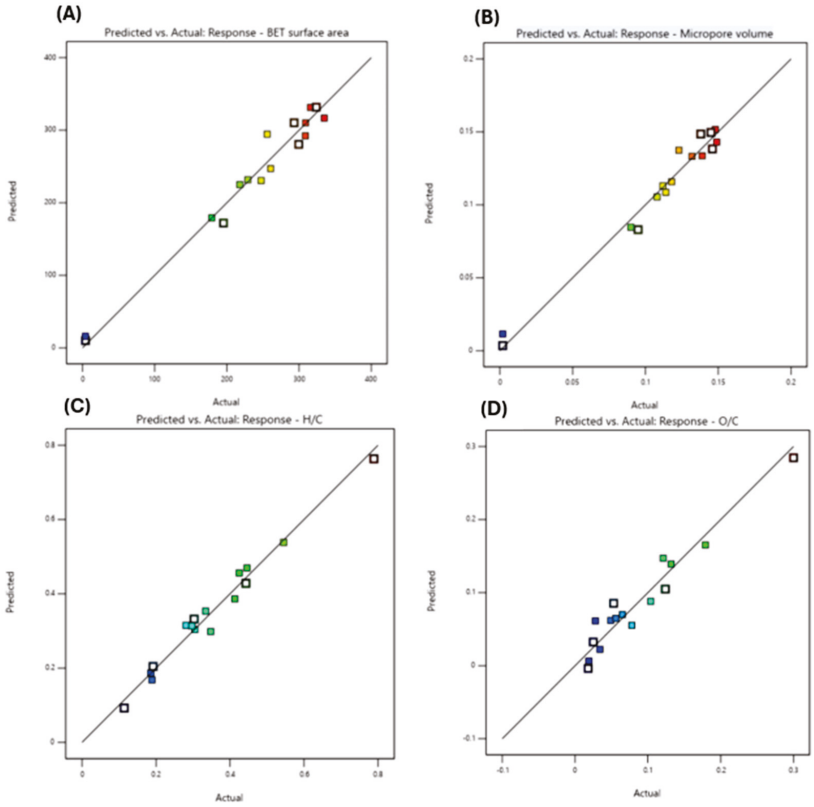


Figure 5. Predicted (y-axis) versus experimental/actual (x-axis) values for (**A**) BET surface area; (**B**) micropore volume; (**C**) H/C; and (**D**) O/C. Squares outlined in dark black represent B400–B800, spread along the reference line. All colored points represent the different DOE points.

3.1.3. Other Characterizations

Thermogravimetric Analysis (TGA)

The TGA and DTG curves (Figure 6A,B) show the weight loss patterns for CRD wood and its biochars, influenced by pyrolysis conditions and feedstock composition. CRD wood (~70–75% holocellulose, 20–30% lignin) exhibited three distinct degradation phases [44]. In Phase I (0–150 °C), dehydration and extractive removal caused 2.38% weight loss in CRD wood, and 1.29–1.64% for B400–B800. Perturbations in B600–B800 likely resulted from moisture/labile species adsorption during cooling/storage. Phase II (200–400 °C) showed a major mass loss in raw wood (66.95%) due to cellulose and hemicellulose breakdown, releasing CO, CO_2, CH_4, and volatiles. The release of these species in particular was observed when the internal reactor temperature was between 200–325 °C and 325–400 °C. Key intermediates like carboxylic acids, furfural, oxygenates, levoglucosan, and aldehydes formed pyrolysis oil. CRD wood's first peak occurred at 344.28 °C. Biochar weight loss in this phase decreased from 27.53% (B400) to 1.87% (B800), indicating reduced volatile content and higher charring with increased heat treatment severity. B400 displayed a minor peak at 337.44 °C, and graphitized biochars showed a shift in decomposition to higher temperatures, consistent with [45].

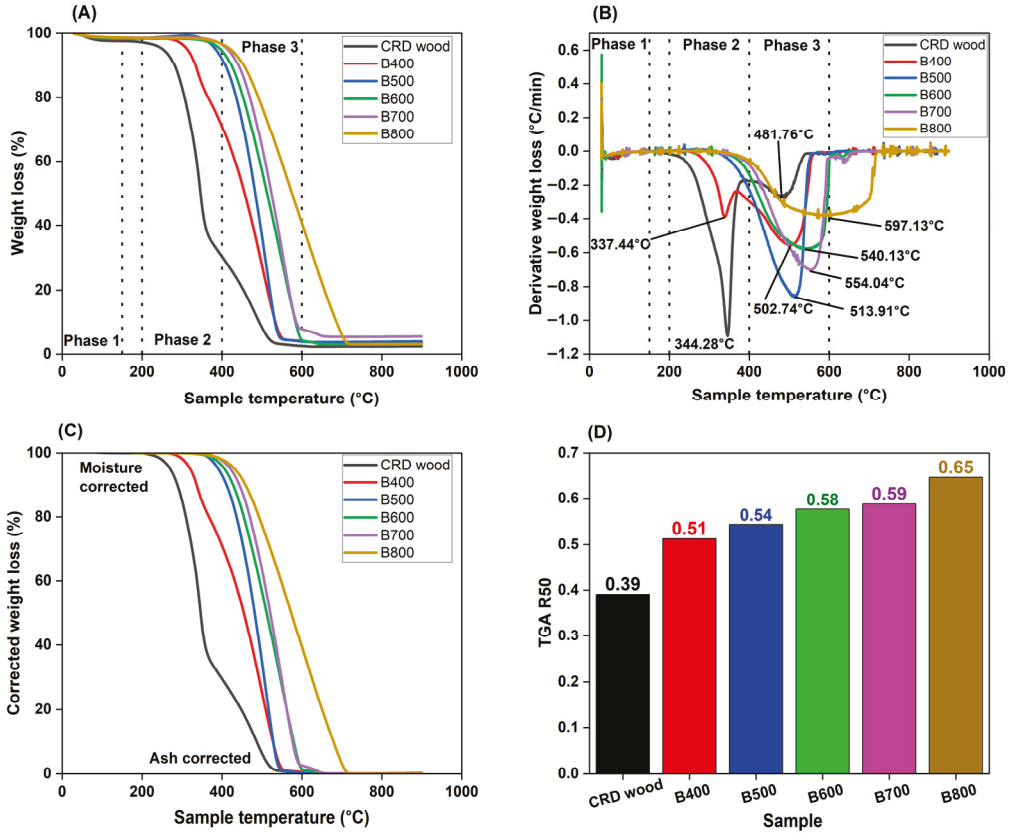


Figure 6. (**A**) TGA and (**B**) DTG curves, (**C**) moisture- and ash-corrected TGA curves, and (**D**) TGA R50 index variation with pyrolysis temperature for B400-B800.

Phase III (400–600 °C) involved lignin breakdown into phenolics and aromatics. CRD wood had a second peak at 481.76 °C (27.80% loss), while B400 peaked at 502.74 °C (66.81% loss). For B500–B800, decomposition occurred between 513.91 and 597.13 °C, indicating greater aromatic condensation. B500–B700 lost 88.17–90.39% mass; B800 lost only 56.10% due to stable C–C, C=C, and C≡C bonds from dehydrogenation, cyclization, and aromatization. Between 600 and 900 °C, B800 showed 37.46% additional loss from the breaking of these bonds, requiring higher activation energy [46,47]. This reflects the

turbostratic transformation of amorphous carbon to hyper-stable graphitized forms. Other biochars showed <2.5% loss in this range, indicating prior conversion. Residual mass at 900 °C corresponds to recalcitrant ash/inorganics. TGA confirms that high-temperature biochars possess traits ideal for carbon sequestration and metallurgical use.

TGA R50

Before calculating the R50 recalcitrance index, TGA curves were corrected for moisture and ash, as shown in Figure 6C. The R50 index increased with pyrolysis temperature, from 0.39 (CRD wood) and 0.51 (B400) to 0.65 (B800), as shown in Figure 6D. This highlights its direct relationship with temperature and Van-Krevelen ratios. B800 showed the highest thermal stability due to high carbonization, FC, and low VC, consistent with [48]. Based on [49], B400–B800 fall into the minimally degradable biochar category ($0.5 \leq R50 < 0.70$), suitable for long-term soil carbon sequestration. Such stability also benefits metallurgical use, where high resistance to stress and breakage is crucial. As noted in [50], higher pyrolysis temperatures can form stable organo-metal complexes (e.g., Al_2O_3–O–C), enhancing durability—likely in CRD wood biochars as they contain Al. However, high R50 also suggests low reactivity, making these biochars less ideal for soil amendments, where surface interaction matters. Ultimately, while R50 indicates overall degradation resistance, it does not reveal the structural arrangement of organic carbon (amorphous-to-graphitic transformations in particular).

FTIR Spectroscopy

FTIR analysis of CRD wood and B400–B800 assessed chemical changes via functional group presence and transformation under varying pyrolysis conditions. Shifts in functional group intensity reflected structural evolution and its impact on biochar properties. Peaks in the 500–4000 cm^{-1} range (Figure 7) were analyzed using spectral databases from [51,52].

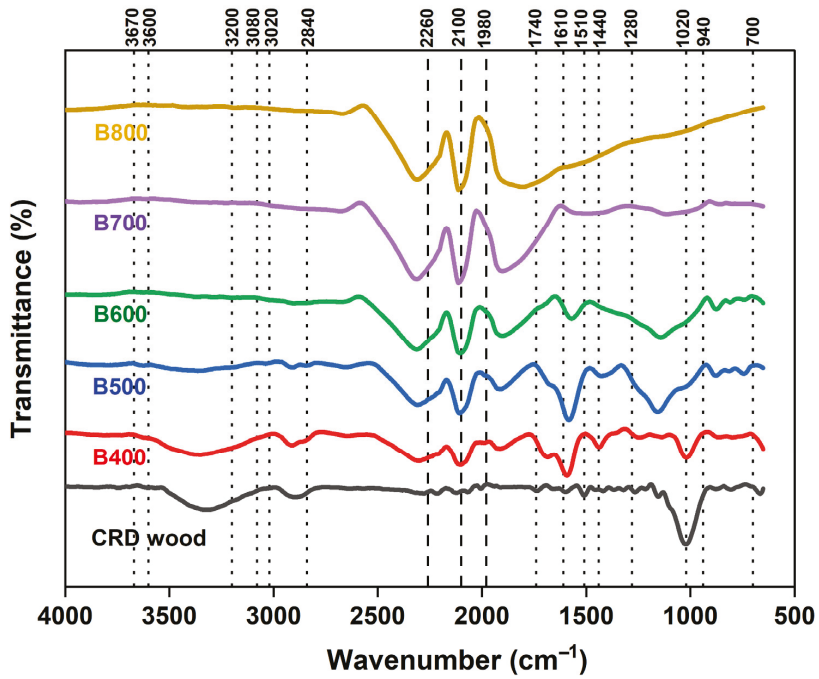


Figure 7. FTIR spectra for B400-B800.

Hydrogen-bonded –OH vibrations (3200–3600 cm^{-1}) indicated moisture in CRD wood, with decreasing intensity from CRD wood to B800 due to thermal dehydration. Similar diminishing perturbations in the 3020–3080 cm^{-1} band, linked to aromatic C–H vibrations,

were most pronounced in CRD wood, reflecting high amorphous carbon undergoing aromatic transformation. Minor ramps in B400–B600 suggest gradual cyclization, which disappears at higher temperatures as aromatization stabilizes. However, ref. [53] noted that these vibrations alone do not define graphitization. In the 2840–3020 cm^{-1} region, aliphatic C–H vibrations diminished progressively from CRD wood to B800 due to dehydration, demethylation, and condensation of terminal $–CH_3$ and $–CH_2$ groups from depolymerizing holocellulose [54], aligning with [52]. This implies incomplete decomposition in B400 and B500, consistent with their high VC, O/C, and H/C ratios.

In the 2100–2260 cm^{-1} region, C≡C alkyne stretching associated with condensed polyaromatics increased from B400 to B800, correlating positively with the pyrolysis temperature [51]. C≡N stretching (~2250 cm^{-1}) also intensified, indicating growing nitrile group presence and enhanced structural rigidity. Between 1740 and 2100 cm^{-1}, increasing C=C=C allene stretches from B400 to B800 signaled strain propagation during graphitization due to adjacent dienes, as reported in [51]. C=O stretches, linked to lignin breakdown, became more pronounced at higher temperatures. Lignin-derived carbonyls (1610–1740 cm^{-1}) diminished from B400 to B800 due to degradation under thermal severity [53]. These carbonyls are products of aldehydes, acids, ketones, and esters [51,52].

C=C ring stretching (1510–1610 cm^{-1}) was most intense in B400–B600, marking holocellulose breakdown and structural deprotonation, which increased biochar hydrophobicity. The 1440–1510 cm^{-1} band reflected early-stage aromatic skeletal vibrations with oxygen and hydrogen loss. C–OH stretching and O–H bending (1280–1440 cm^{-1}) contributed to aromatic backbone formation. A decline in 1020–1280 cm^{-1} peaks from CRD wood to B800 indicated decomposition of hemicellulose and cellulose, as seen through weakening C–O, C–OH, C–H, and C–O–C skeletal vibrations [54,55]. These labile groups in B400 and B500 contribute to higher CEC [56]. Finally, peaks in 700–840 cm^{-1}, related to surface acidic functionalities, were eliminated at higher pyrolysis temperatures.

SEM-EDX Spectroscopy

SEM analysis of B400 [Figure 8A–C], B600 [Figure 8D–F], and B800 [Figure 8G–I] at 250×, 500×, and 1000× magnifications, respectively, was conducted without gold sputtering. Higher pyrolysis temperatures yielded partly smooth surfaces, while lower temperatures resulted in pronounced roughness with residual cell walls and fibers. B400 micrographs revealed minimal porosity, as only hemicellulose and partial cellulose decomposition occurred, with lignin largely intact. This led to sporadic macropores, as noted in [38], making B400 suitable for soil amendments due to its water retention, aeration, and microbial compatibility [57]. Low-temperature chars like B400 have also been used as additives to boost methane yields in anaerobic digestion [58]. Surface oxidative residues contribute to reactivity, supporting their use as solid fuels for energy purposes [59].

At intermediate pyrolysis temperature, B600 developed more defined pores [Figure 8F], following lignin softening, melting, and breakdown after holocellulose decomposition [60]. Depolymerization and monomer cross-linking increased solid char yield [61]. Rapid volatile release and collapsing cell walls expanded ordered porosities, causing shrinkage and growth of FC-rich layers, particularly with a longer BRT [59]. As the temperature approached 600 °C, the pore sizes diminished [62]. Its surface area and thermal maturity support carbon sequestration, metallurgical use, and the adsorption of dyes and heavy metals. The loss of surface acidic groups renders B600 alkaline, enabling acidic soil remediation [59]. At higher temperatures, B800 exhibited smooth, honeycomb-like structures [Figure 8A–I], indicating complete carbonization and surface volatile removal. High carbon content, TSF (low VC/FC ratio), and low H/C and O/C ratios promote the formation of stable graphitic sheets ideal for energy materials (e.g., supercapacitors, electrodes) and

carbon sequestration. This trend with rising temperature was confirmed by [63]. From [64], pore expansion likely arises from micropore wall cracking and mesopore coalescence, reducing surface area and micropore volume in B700 and B800—a finding already discussed under the Physicochemical Characterization Section.

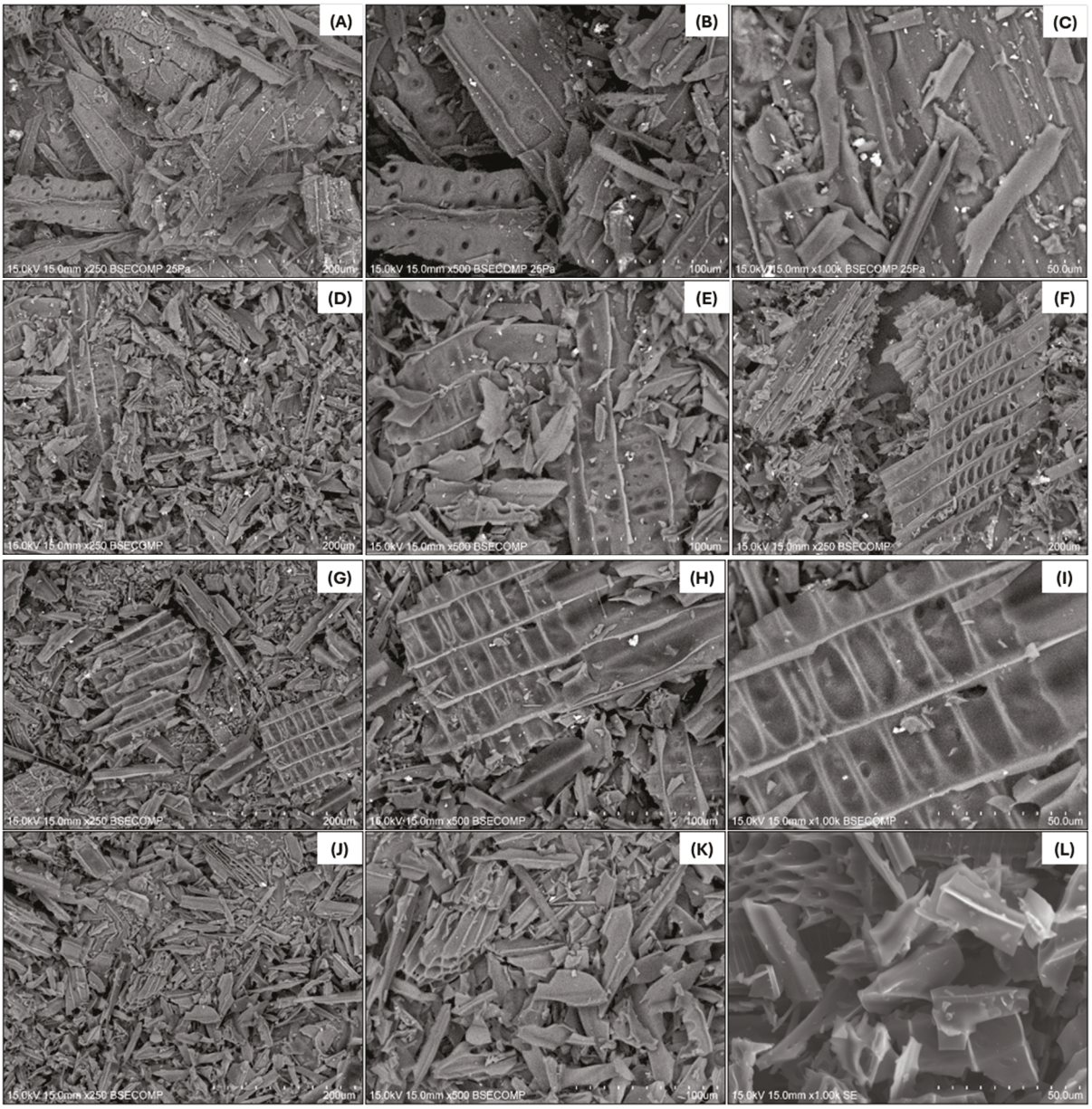


Figure 8. SEM micrographs of B400 (**A**–**C**), B600 (**D**–**F**), B800 (**G**–**I**), and B600 in dye adsorption application (**J**–**L**) at 250×, 500×, and 1000× magnifications.

Pore blockage may occur due to increasing ash and AAEM concentrations, which reduce active surface sites up to a certain temperature. Beyond this, less stable monovalent AAEMs like Na and K volatilize at higher temperatures, aiding pore reaming. SEM-EDX spectra [Figure 9] confirm the presence of AAEMs on biochar surfaces. As shown in Figure 9A–C, surface carbon increased from 81.6% (B400) to 95.3% (B600) and 96.2% (B800), as also noted in [63]. Conversely, surface oxygen content dropped by ~80%, revealing an inverse relation with pyrolysis temperature. EDX peaks indicated trace levels (0.2–0.4%) of AAEMs (Ca, K, Na), which may form salts (carbonates, oxides, chlorides), elevate pH, and enhance CEC for electrostatic interactions [65]. These elements were dispersed across

the biochar, including near or within pores [66]. Sulfur (probably from gypsum drywall in CRD wood residues) appeared at 0.1% in B400 but volatilized at higher temperatures as SOx. Overall, biochar morphology is highly tunable based on feedstock composition (with or without pretreatment) and pyrolysis conditions—directly influencing its applicability in the environmental, energy, and agricultural sectors.

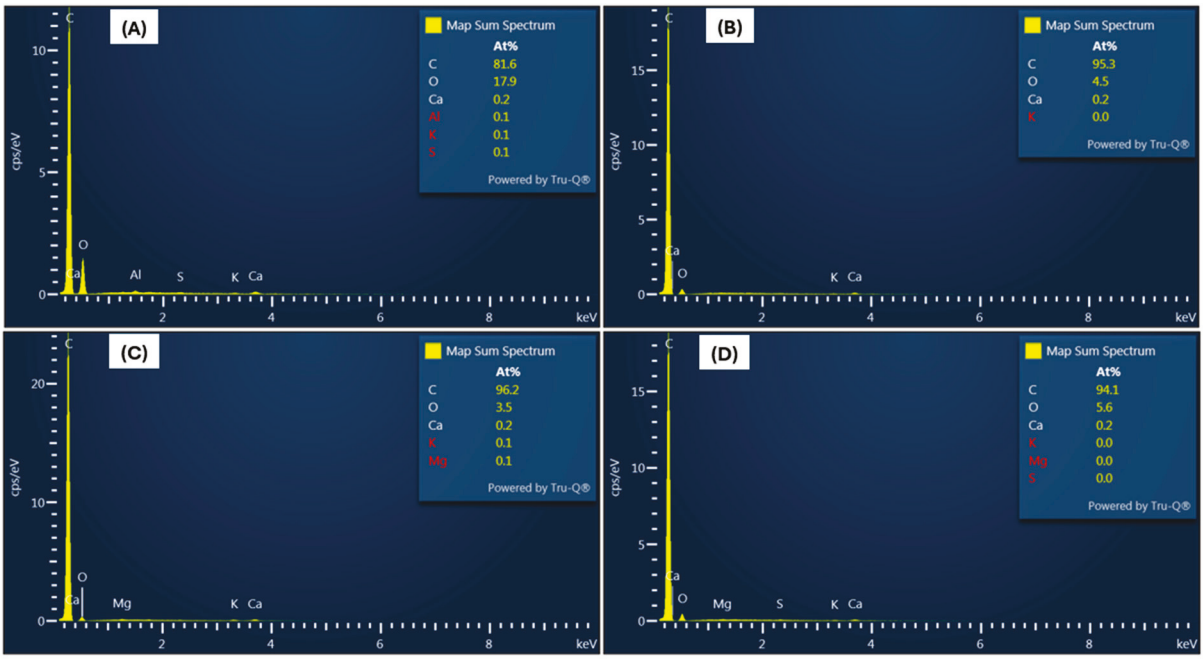


Figure 9. SEM-EDX surface elemental analysis: (**A**) B400; (**B**) B600; (**C**) B800; and (**D**) B600 in dye adsorption application.

Raman Spectroscopy

Raman spectroscopy was employed to detect structural transitions from amorphous to crystalline carbon in biochars produced at pyrolysis temperatures ranging from 400 to 800 °C. Figure 10 illustrates the spectral bands, with the I_D/I_G index—i.e., the ratio of the intensity of deformations or disorderliness in amorphous carbon (D-band) to that of the quantity of graphitic carbon structures (G-band)—used as a quantitative measure of graphitization. A higher I_D/I_G ratio implies greater structural disorder or deformation in amorphous carbon, indicating a progressive transformation toward turbostratic carbon arrangements under thermal stress [67]. In contrast, highly crystalline carbonaceous materials like graphite or graphene exhibit low I_D/I_G values, reflecting minimal lattice defects [68].

For biochars B400-B800, the I_D/I_G index ranged from 0.78 to 0.97, supporting the conclusion that increasing heat treatment intensifies defects arising from incomplete graphitization. This observation is consistent with [68], confirming that pyrolysis induces restructuring in disordered carbon domains. As noted by [69], these defect-rich zones, particularly in low-temperature biochars, harbor functional groups such as hydroxyls and carboxylic acids, which contribute beneficially to adsorption tendencies. Notably, the I_D/I_G ratio tends to rise with the temperature until most disordered carbon reorganizes into sp^2-bonded graphitic layers. At this stage, the trend may plateau or reverse, signaling nearly complete graphitization. The authors of [67] also showed that incorporating chemical activators like sulfur and boron into biochar can facilitate this transition by reducing the activation energy required for lattice rearrangement, enabling graphitization even at sub-1000 °C temperature ranges, significantly below the 2000 °C typically required for full transformation.

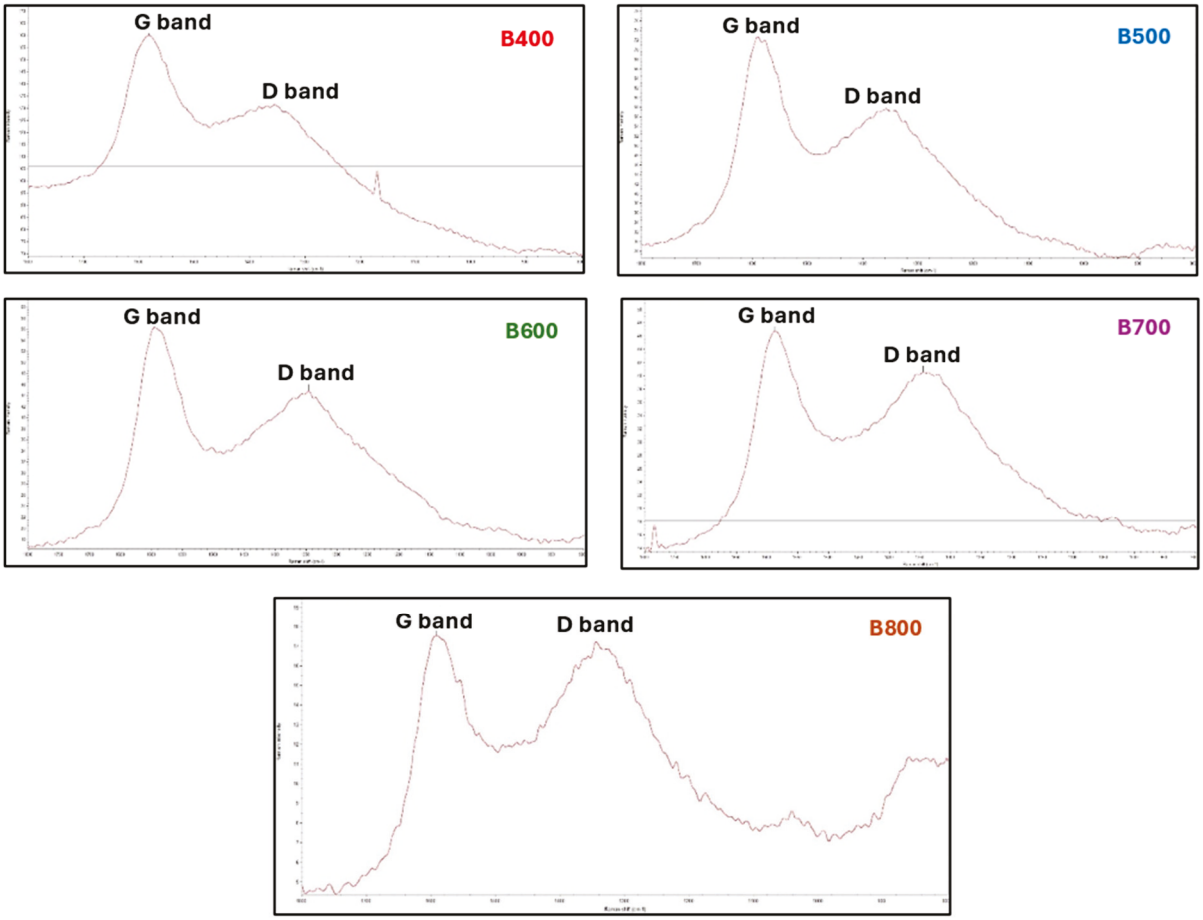


Figure 10. Raman spectra for B400-B800. Peak positioning from right to left on x-axis (800–1800 cm^{-1}): B400—D-band: 1355.63 cm^{-1}; G-band: 1581.92 cm^{-1}. B500—D-band: 1358.55 cm^{-1}; G-band: 1590.43 cm^{-1}. B600—D-band: 1345.67 cm^{-1}; G-band: 1595.96 cm^{-1}. B700—D-band: 1345.52 cm^{-1}; G-band: 1587.93 cm^{-1}. B800—D-band: 1344.82 cm^{-1}; G-band: 1592.10 cm^{-1}.

Once graphitization reaches a maximum, biochar becomes ideal for carbon sequestration, even in sensitive biotic or abiotic environments. Such thermally stable materials are also promising candidates for catalytic applications due to enhanced electron transfer capabilities [45]. Furthermore, their low oxygen content and high mechanical strength render them suitable as partial coke substitutes in high-temperature metallurgical operations, such as blast furnaces, where it is advised that premature reactivity be avoided. Under these elevated conditions, labile inorganic impurities gradually volatilize, reducing ash and volatile matter. In fact, as reported in [50], coal-derived gangue has been co-pyrolyzed with lignocellulosic biomass to improve I_D/I_G values (0.5–0.8), showing enhanced structural evolution with temperature.

Metal Content

AAEMs in biochars were concentrated up to 600 °C at 92.28%, after which they may have decreased due to volatilization. Relative to CRD wood, AAEM content is higher in all biochars due to shrinkage in biomass volume (loss of volatiles) and the breakdown of organo-metallic linkages with increasing temperatures [70]. Non-volatile trace metals like Fe, Cu, Cr, Zn, Ni, Pb, Co, and Cd are present in varying percentages, which could be explained by advanced treatments that these CRD wood residues were subjected to initially (e.g., chromated copper arsenates or ACC) during their applications in regional construction projects, such as houses, electricity poles, piers, and bridge components. That

is why treated wood, as in CRD wood waste, if openly burnt for energy purposes, will be classified as hazardous in nature according to the United States Environment Protection Agency (USEPA) [1]. From [71], the upper and lower (permissible) limits of some metallic constituents in biochar are very important to consider. In B400–B800 evaluated here, it is conclusive that hazardous metal content is within the prescribed range and meets the stipulations set forth by renowned biochar standards like those of the International Biochar Initiative (IBI), European Biochar Certificate (EBC), Australia New Zealand Biochar Industry Group (ANZBIG), Biochar Quality Mandate (BQM), and Singapore standard SGS). Metals below the detection limits in CRD wood and its biochars were Hg, As, and Se. Also, Fe was the most abundant metal (non-AAEM entity) in CRD wood (16,086 mg/kg) and its biochars (from 15,546 mg/kg in B400 to 16,699 mg/kg in B800) due to the presence of embedded remnants of nuts, bolts, nails, and joints, once part of the feedstock before disassembly or demolition. The metal analysis of all tested biochars has been tabulated below in Table 4.

3.1.4. Choosing a Potential Adsorbent Material for Dye Removal Tests from Contaminated Water—B600

B600 was selected as the optimal adsorbent for the removal of methyl orange from aqueous solutions. Although another biochar produced at the same temperature range (Run 8) exhibits slightly higher surface area and micropore volume, B600 surpasses it in elemental composition (carbon, hydrogen, oxygen), FC, and molar ratios (H/C, O/C), all of which are critical indicators of a biochar's adsorption potential. These parameters influence not only hydrophilicity and chemical/thermal stability but also the ability to form electrostatic, covalent, and hydrogen bonds through surface functional groups, making B600 more suitable for adsorption of pollutants in water across variable temperature and pH conditions. This aligns with findings from [72], which emphasize that surface area alone does not dictate adsorption performance. Since methyl orange is a polar dye that readily dissolves in polar solvents like water, it is essential that the adsorbent's surface possesses adequate polarity to interact favorably. B600's relatively high H/C ratio suggests a moderate positive surface charge, which may reduce electrostatic repulsion between negatively charged functional groups on the biochar and the anionic dye, enhancing the overall adsorption efficiency.

In contrast, biochars like B700 and B800, though more thermally mature, have lower H/C and O/C ratios, indicating increased hydrophobicity. These may be better suited for adsorbing non-polar or hydrophobic contaminants in wastewater. However, for a polar molecule like methyl orange, B600 offers a balanced profile of surface chemistry and porosity. Additionally, B600 retained a significant surface area (323.78 m^2/g)—the second highest across the entire DOE and impressively achieved without any post-pyrolysis activation (chemical, thermal, physical, or mechanical). While it is still lower than surface areas seen in activated carbons, this value is considerable for raw biochar. Given the molecular size of methyl orange (<10 nm), adsorption via dense micro- to mesoporous channels is feasible, similar to mechanisms seen in mineral-based adsorbents [73]. There is a possibility that if a pore-filling mechanism takes place during adsorption, and if the porosity of biochar is too high, desorption of the dye molecules may occur!

Table 4. Metal content in B400–B800 and the permissible limit set by the IBI.

Sample	Al	Ba	Ca	Cd	Co	Cr	Cu	Fe	K	Mg	Mn	Mo	Na	Ni	Pb	V	Zn	Total	AAEM	AAEM
	mg/kg	mg/kg	mg/kg	mg/kg	mg/kg	mg/kg	mg/kg	mg/kg	mg/kg	mg/kg	mg/kg	mg/kg	mg/kg	mg/kg	mg/kg	mg/kg	mg/kg	mg/kg	mg/kg	%
CRD wood	12,043	1165	149,284	2	69	86	613	16,086	38,043	17,566	5587	24	37,685	5	561	21	1389	280,229	243,742	86.98
B400	7707	1949	163,961	2	58	79	5777	15,546	49,507	17,794	6799	21	37,901	41	381	17	1484	309,026	271,113	87.73
B500	4273	1554	143,017	4	57	112	300	8861	36,641	15,503	7649	<2	44,478	17	450	11	1924	264,852	241,194	91.07
B600	3505	1834	165,480	11	51	179	237	11,898	68,529	20,299	7576	<2	41,471	92	296	13	1038	322,507	297,612	92.28
B700	8856	1900	161,627	9	39	179	231	10,387	38,942	15,529	3883	11	23,800	104	210	24	1316	268,940	241,797	89.91
B800	9680	3889	167,379	14	60	318	2297	16,699	44,660	20,019	8303	19	26,990	82	225	27	76	300,738	262,938	87.43
IBI (low)				0.3		15	40					10		10	10		150			
IBI (high)				39		1200	6000					75		600	500		7400			

3.2. CRD Wood Pyrolysis in Horizontal Rotary Retort-Furnace Reactor—Scale-Up from Horizontal Tube Furnace Reactor

The same batch of contaminant-separated, dried, and size-reduced CRD wood (3 mm–2.5 cm) was subjected to scaled-up pyrolysis in a horizontal rotary retort-furnace reactor. The exact temperature and BRT conditions listed in the DOE for B400–B800 were replicated to enable an approximate comparison with the horizontal tube furnace reactor experiments. These samples were selected to represent a broad pyrolysis temperature range, which critically influences biochar properties. The results are tabulated in Table 5.

Table 5. Yield, proximate, and elemental analysis results for B400-B800 in the horizontal rotary retort-furnace reactor.

Sample	N (wt%)	C (wt%)	H (wt%)	S (wt%)	Ash (wt%DB)	O (wt%)	H/C	O/C	VC (wt%DB)	FC (wt%DB)	TSF (%)	Yield (%)
B400	0.650	78.380	2.887	0.184	2.640	15.259	0.442	0.146	26.739	70.621	72.536	37.700
B500	0.380	80.580	2.489	0.089	4.120	12.342	0.371	0.115	23.451	72.429	75.541	32.100
B600	1.150	81.690	2.410	0.372	4.050	10.328	0.354	0.095	17.992	77.958	81.249	29.500
B700	0.580	83.790	2.149	0.114	5.970	7.397	0.308	0.066	14.858	79.172	84.199	27.900
B800	0.740	85.610	2.042	0.133	5.820	5.655	0.286	0.050	12.613	81.567	86.608	26.200

Note: Only proximate and elemental analyses were conducted for scaled-up biochars. All advanced characterizations were reserved only for samples produced in the horizontal tube furnace reactor, as in the former case.

Compared to the previous experiments, yields were more reliable this time, particularly for B400, which underwent complete pyrolysis. Similar yields for 400 °C (B400: 37.7%) and 600 °C (B600: 29.5%) were also reported in [74]. However, the carbon content in B600–B800 was 5–7% lower, despite a strong positive correlation with temperature ($r = 0.99$). This is likely due to the larger feedstock mass (3 kg) used in the rotary retort, compared to 50–250 g in the horizontal tube furnace reactor, indicating heat transfer limitations despite rotation. Additional factors could include (a) carbon loss from the secondary cracking of volatiles due to low inert gas flow and (b) ambient air infiltration causing mild combustion. Still, ash levels remained consistent with tube furnace tests. Slightly elevated H/C and O/C ratios for B600–B800 suggest some residual surface volatiles, yet both indices remain well within accepted limits, indicating good carbonization and aromaticity with negative correlations with temperature (O/C: $r = -0.99$; H/C: $r = -0.98$).

As noted in [71], CRD wood biochars produced at higher pyrolysis temperatures meet superior-grade criteria, with O/C < 0.2 and H/C < 0.4, indicating low VC, high FC, strong aromatization, and long-term stability for soil and carbon sequestration. Their possible resistance to oxidation, hydrophilic interactions, and microbial degradation also aligns with Van-Krevelen parameters. The IBI states that it is now better to use the index H/C_{org} in place of H/C since carbon content as a whole will also include inorganics like carbonates in the ash fraction and not be selectively describing the organic carbon aromatics of interest in biochar, which is the baseline condition for any thermochemical conversions to have taken place relative to the original biomass feedstock [37]. Proximate values showed FC increasing by 15% and VC decreasing by 53% from B400 to B800, with $r = 0.98$ and -0.99, respectively. TSF rose by 19% ($r = 0.99$), indicating enhanced thermal stability. HHV values (29–32 MJ/kg) aligned with those in earlier tests, confirming suitability for energy and metallurgical applications.

Overall, scalability experiments showed good relatability in terms of proximate values, elemental properties, and a similar dominant effect of pyrolysis temperature. Future studies entailing pilot-scale conversions can thus be recommended, where at least 15–20 kg of CRD wood can be treated at once via batch pyrolysis.

3.3. The Effect of Feedstock Composition and Pyrolysis Process Parameters on Biochar Properties—Comparison to Similar Works

Biochar's physicochemical properties depend heavily on biomass composition and pyrolysis conditions, both of which must be optimized for applications like carbon sequestration, metallurgy, and pollutant adsorption. Lignocellulosic biomass, such as forest residues, CRD wood, and crop waste, yields stable, carbon-rich biochars due to its lignin, cellulose, and hemicellulose content, which decompose over a broad temperature range [75]. Lignin-rich feedstocks can exceed 80% carbon, while cellulose-rich ones yield more volatiles [76]. In contrast, algae-derived biochars are typically unstable, with low carbon and surface area due to high N, P, S, and inorganic contents [77]. Co-pyrolysis, combining weak feedstocks like biosolids with lignocellulosic materials, improves the elemental balance, porosity, and surface area (up to 300–400 m^2/g) while preserving minerals [78].

Among process variables, temperature is critical. Above 500 °C, the biochar yield drops, but carbon content, aromaticity, hydrophobicity, and surface area improve [79], as seen in B600–B800. Around 700 °C, structural ruptures from surface treatments increase porosity for gas adsorption [80]. Lower temperatures (<400 °C) preserve nutrients and functional groups, enhancing water retention [81,82]. The surface area can rise from 150 m^2/g at 300 °C to over 500 m^2/g at 700 °C [83,84]. Micropores predominate at 450–600 °C, while mesopores form at temperatures >600 °C due to bulk volatile release, aligning with our surface area trends and favoring water filtration or catalysis applications [85]. Despite the reduced surface area at 700–800 °C, high FC, low VC, and thermal stability make such biochars suitable for metallurgical use. BRT also plays a key role. An extended BRT promotes uniform heat transfer, deeper carbonization, and stable aromatization [86], reducing H/C ratios to <0.3 [80] and O/C to <0.2 at 700 °C [80,87]. High carbon yields (>85%) and surface areas (~500 m^2/g) are also reported under these conditions. A long BRT enhances FC while reducing volatiles, improving stability [88,89]. In contrast, a short BRT (<30 min) yields reactive but less stable chars. Higher pyrolysis temperatures also induce alkaline pH, aiding acidic soil remediation [81]. Long BRTs in slow-heating fluidized reactors further improve gas–solid interaction and morphology and subdue premature volatile condensation [90]. The feedstock mass impacts heat transfer and carbonization. Smaller masses, especially under low heating rates, moderate temperatures, and long BRTs, enhance porosity and moisture retention, benefiting adsorption and soil applications [91–94]. Larger masses risk uneven heating, incomplete devolatilization, and inferior structure. Therefore, understanding the interplay between feedstock traits and pyrolysis conditions is key to tailoring biochar for targeted outcomes.

3.4. Methyl Orange Batch Adsorption Experiments—An Application for CRD Wood Biochar (B600) from the DOE

As a practical application derived from the DOE runs, adsorption experiments were conducted to assess the removal of the industrial dye methyl orange from contaminated water. Among the produced biochars, B600 was selected as the adsorbent due to its optimal combination of morphological features, surface chemistry, and thermal stability. These attributes made B600 a suitable candidate for water treatment, and it was tested across varying dosage levels of the pollutant dye during the adsorption trials.

3.4.1. Adsorption Standard Determination

To begin with, the methyl orange indicator with a concentration of 0.05 w/v (i.e., 0.05 g per 100 mL or 0.5 g/L) was sourced from the institute's pulp and paper analytical laboratory. Using its molar mass of 327.33 g/mol, the molarity of the stock solution was calculated as 1.5 mM. Reference solutions of 10 mL total volume were then prepared at varying concentrations—0.001, 0.01, 0.0175, 0.025, and 0.0375 mM—by applying the dilution

formula $C_1V_1 = C_2V_2$, where C_1 is the original concentration (1.5 mM), V_1 is the volume of stock to be used, C_2 is the target concentration, and V_2 is the final volume (10 mL). The absorbance values of each solution were measured using a UV–visible spectrophotometer (HACH—DR 6000) at 464 nm under alkaline conditions (pH $\geq$ 4.4, orange color) and at 506 nm under acidic conditions (pH $\leq$ 3.2, pink color). The absorbance data were fitted to Beer–Lambert's law, yielding the intercept, molar absorptivity coefficient, and an excellent linear correlation, with $R^2 = 0.9995$.

3.4.2. Batch Adsorption Experiments

For the adsorption experiments (key steps shown in Figure 11), 50 mL test solutions with varying initial concentrations of methyl orange were prepared using deionized water to eliminate interference from competing ions. All tests were conducted in 250 mL reaction flasks placed on a magnetic stirrer (300 rpm) with temperature control. Two concentrations, 0.025 mM (8 ppm) and 0.5 mM (164 ppm), were selected based on prior studies (Supplementary Table S7). Other process parameters were varied to evaluate dye removal efficiency: pH (1–9, adjusted using 0.1 M H_2SO_4 and 0.1 M NaOH), temperature (20–50 °C or 293–323 K), contact time (up to 24 h), and B600 biochar dosage (1–10 mg/mL). At set intervals, solutions were filtered using 0.45 µm syringe filters to separate B600 particles; vacuum filtration with papers of similar porosity was also applied. UV-vis absorbance readings were then compared against the standard calibration curve to determine residual methyl orange concentrations, removal percentages, and adsorption capacity (q_e). Each experiment was repeated three times, and average values are reported.

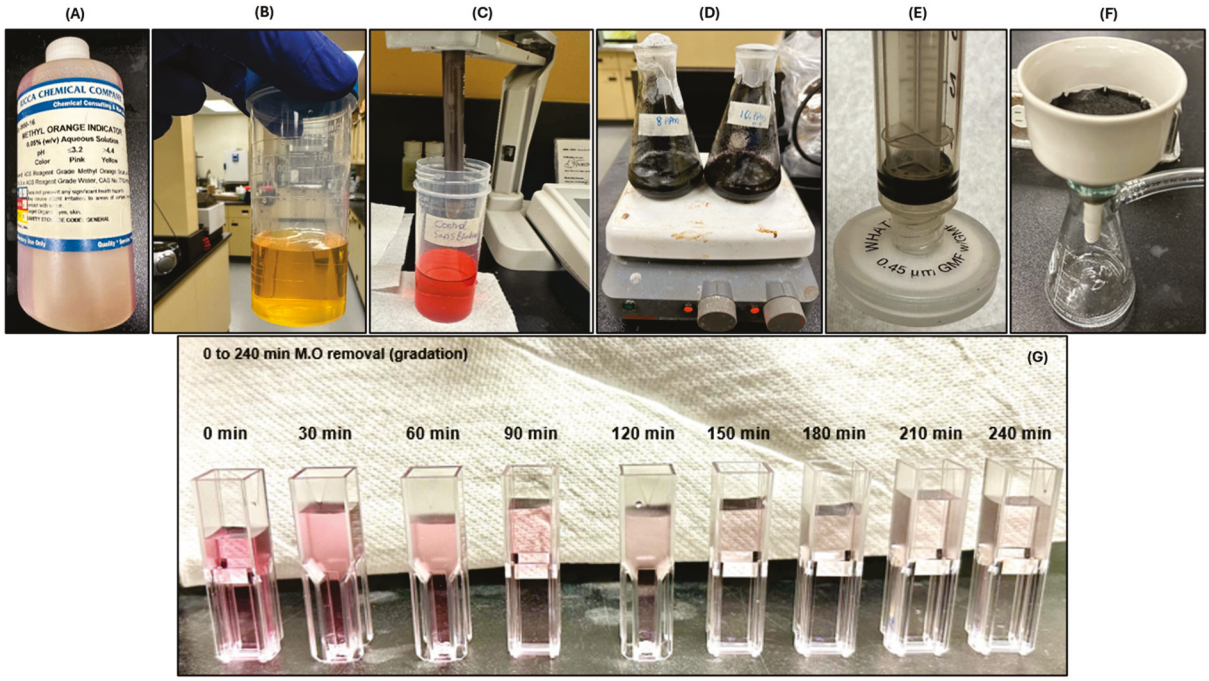


Figure 11. Methyl orange batch adsorption experiments with B600. (**A**) Methyl orange dye, (**B**) yellowish-orange color before changing pH, (**C**) pink color after pH alteration, (**D**) adsorption tests on temperature-controlled magnetic stirrer plate, (**E**) 0.45 µm syringe filter, and (**F**) vacuum filtration setup—for separation of B600 from treated water during kinetic and isotherm tests. (**G**) Effect of B600 on test solution with increase in duration (0–240 min). Here, M.O represents methyl orange.

The fundamental equations governing dye adsorption estimation methods, particularly removal percentage, q_e, and kinetic/equilibrium/thermodynamic models, can be referred to in Supplementary Equations (S13)–(S34).

3.4.3. Optimization of Adsorption Parameters and Results

Before conducting adsorption isotherm and kinetic studies, two parameters—pH and B600 dosage—were optimized. Based on Supplementary Table S7, the initial methyl orange concentration tested was approximately 150 ppm, consistent with values reported in [95]. Accordingly, 164 ppm was selected for the test solution due to its close range. Similarly, the maximum temperature (50 °C or 323 K) and contact time (24 h) were chosen after reviewing comparable studies involving biochar adsorbents derived from pyrolyzed biomass for methyl orange removal (Supplementary Table S7). The 24 h duration was intentionally selected to extend the observation window and capture potential saturation behavior, if any.

(A) Effect of pH

The pH range of 1–9 (values: 1, 3, 5, 7, 9) was tested to assess dye removal based on methyl orange's affinity to biochar. Since biochars produced at higher pyrolysis temperatures tend to have alkaline pH and negatively charged surfaces, they are less favorable for adsorbing anionic dyes like methyl orange unless surface protonation occurs. A high AAEM content in CRD wood, as per [96], likely contributed to B600's alkaline pH (9.7) through the presence of Ca, Mg, K, and Na salts, carbonates, and oxides and the loss of acidic surface groups with increasing temperature. B600's surface area, micropore volume, Van-Krevelen molar ratios, FC, and thermal stability further supported its selection for adsorption tests, especially under acidic conditions and elevated temperatures. A low pH enhances the protonation and anion exchange capacity (AEC) of the biochar surface, promoting adsorption [97]. Alternatively, acid activation can also be used to shift surface charges positively [98]. The electrostatic attraction mechanism is further explained by the pHpzc of B600, measured at 9.02 (Figure 12A); below this pH, B600's surface carries positive charges that attract negatively charged dye molecules. Above pHpzc, the surface becomes negative and repels methyl orange. Despite the high pHpzc, maximum dye removal occurred at solution pH 1–3.

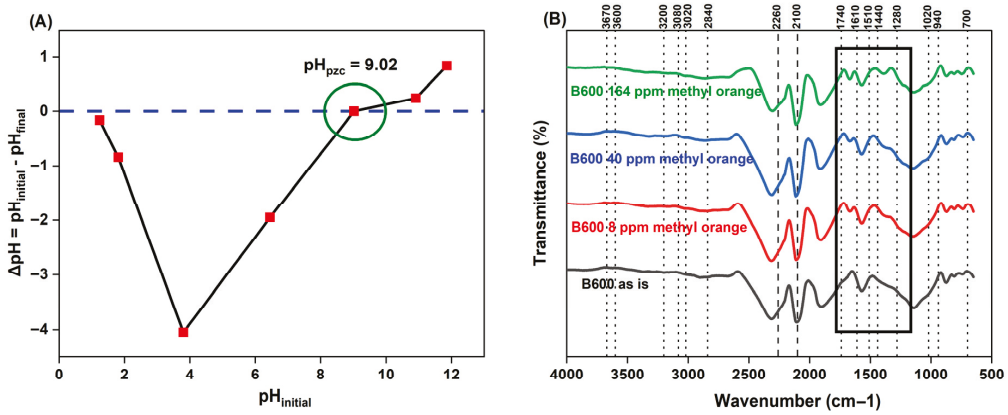


Figure 12. (**A**) B600 pH_{PZC} and (**B**) FTIR spectra of B600 with varying concentrations of methyl orange (8–164 ppm) to detect spectral differences before and after adsorption.

Confirming Changes to B600 Surface Chemical Composition Post-pH Modification

To confirm surface-level adsorption after pH modification across methyl orange concentrations (8–164 ppm), FTIR spectra of B600 post-adsorption were analyzed (Figure 12B). Most spectral features of native B600 remained unchanged, though three subtle differences were observed: (a) a mild drop in peak intensity between 1020 and 1280 cm^{-1} suggests the masking of oxygenated groups (C–O, C–O–C), possibly due to interaction with positively charged sulfonic acid groups of methyl orange under acidic conditions; (b) slight peak-

ing between 1280 and 1440 cm^{-1} at higher dye concentrations may reflect O–H bending from alcohols and phenols formed via heteroatom abstraction by methyl orange; and (c) the emergence of peaks in the 1610–1740 cm^{-1} range indicates C=C and amide C=O stretching, pointing to π–π interactions between biochar aromatics and methyl orange's benzene rings—absent in native B600. As noted in [99,100], acidic media can also promote hydrogen bonding and π–π interactions beyond electrostatics. Conversely, at higher pH, hydroxyl groups dominate the B600 surface, potentially competing with methyl orange and increasing repulsion on the now negatively charged surface [101].

The concept of electrostatic attraction is evident from Figure 13A, where methyl orange removal peaked at pH 1 (93.53%) and declined progressively at higher pH levels: 88.64% (pH 3), 60.56% (pH 5), 48.09% (pH 7), and 33.72% (pH 9). Similar behavior was observed in [102], indicating that mass transfer and equilibrium uptake (q_e) are enhanced in acidic media. Methyl orange's structure supports this: at low pH, it can carry a Na^+-derived positive charge and an additional HSO_3^+ charge (in contrast to its sulfonate SO_3^- form at higher pH) [16]. This facilitates a charge transfer mechanism with B600, where surface protonation at low pH promotes effective adsorption of the anionic dye. However, since pH 1 is too harsh for practical use, pH 3, where dye removal was still high, was selected for subsequent adsorption experiments.

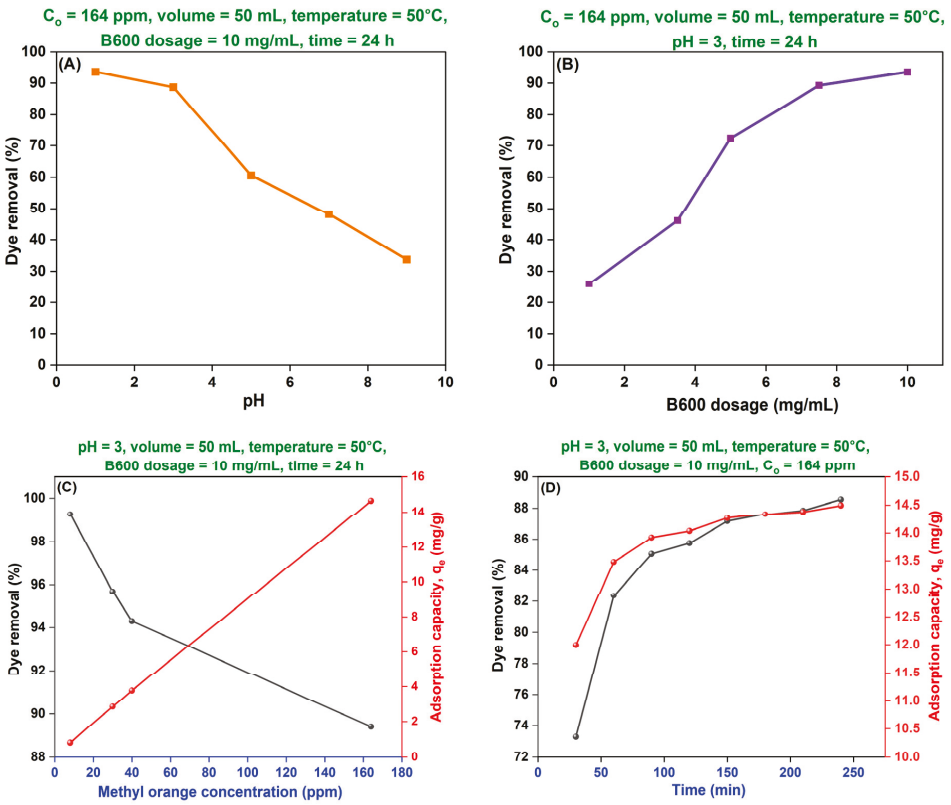


Figure 13. Optimization of adsorption parameters with respect to dye removal percentage and q_e of B600: (**A**) pH; (**B**) adsorbent dosage; (**C**) initial dye concentration; and (**D**) duration.

(B) Effect of Adsorbent Dosage

Methyl orange removal was studied at B600 dosages of 1, 3.5, 5, 7.5, and 10 mg/mL. Maximum dye removal (93.48%) occurred at 10 mg/mL due to abundant adsorption sites, with a decreasing trend observed at lower dosages: 89.24% (7.5 mg/mL), 72.33% (5 mg/mL), 46.04% (3.5 mg/mL), and 25.89% (1 mg/mL), as shown in Figure 13B. Similar behavior was noted with Congo red dye in [101]. However, despite higher removal efficiency, q_e decreased at higher dosages due to a diminished concentration gradient and less driving

force for diffusion. With excessive binding sites and limited dye per unit mass, many sites remain unutilized or overlap, reducing accessibility and the surface area [103–105]. Compared to other studies, as shown in Supplementary Table S7, this work used a 100-fold higher biochar loading, leading to significantly lower q_e. For instance, at 10 g/L (10 mg/mL) and 164 ppm dye, q_e is low. However, reducing the dosage to 1 g/L could yield qe ≈ 146 mg/g, and at 0.5 g/L, qe ≈ 293 mg/g—making the results comparable to others. Hence, the adsorbent dosage is inversely related to q_e but directly related to dye removal efficiency. Increasing the adsorbate–adsorbent ratio or using lower, optimized dosages with high-binding-energy sites can enhance performance.

(C) Effect of Initial Dye Concentration—Adsorption Isotherms

As the methyl orange concentration increased from 8 to 164 ppm, its removal dropped from >99% to 89% (Figure 13C), consistent with the findings from [106], which employed another azo dye called 'Acid Orange 7'. This suggests that at higher concentrations, not all B600 sites have a strong affinity, leading to weaker interactions and dye aggregation. As noted in [107,108], adsorption plateaus beyond the optimal concentration since only high-energy sites remain effective. At low concentrations, strong driving forces ensure rapid adsorption, but these weaken with saturation. Similar trends were observed in [109]. High dye and adsorbent levels can also cause mass transfer resistance and fewer collisions, limiting efficiency despite increased q_e. Lowering the B600 dosage at high dye concentrations may improve q_e and adsorption kinetics, as seen in [110].

Adsorption isotherms using Langmuir, Freundlich, and Temkin models were applied to describe dye-adsorbent equilibrium interactions, similar to [111–113]. Freundlich and Langmuir showed strong fits with R^2 = 0.97 and 0.94, respectively (Figure 14A,B; Table 6).

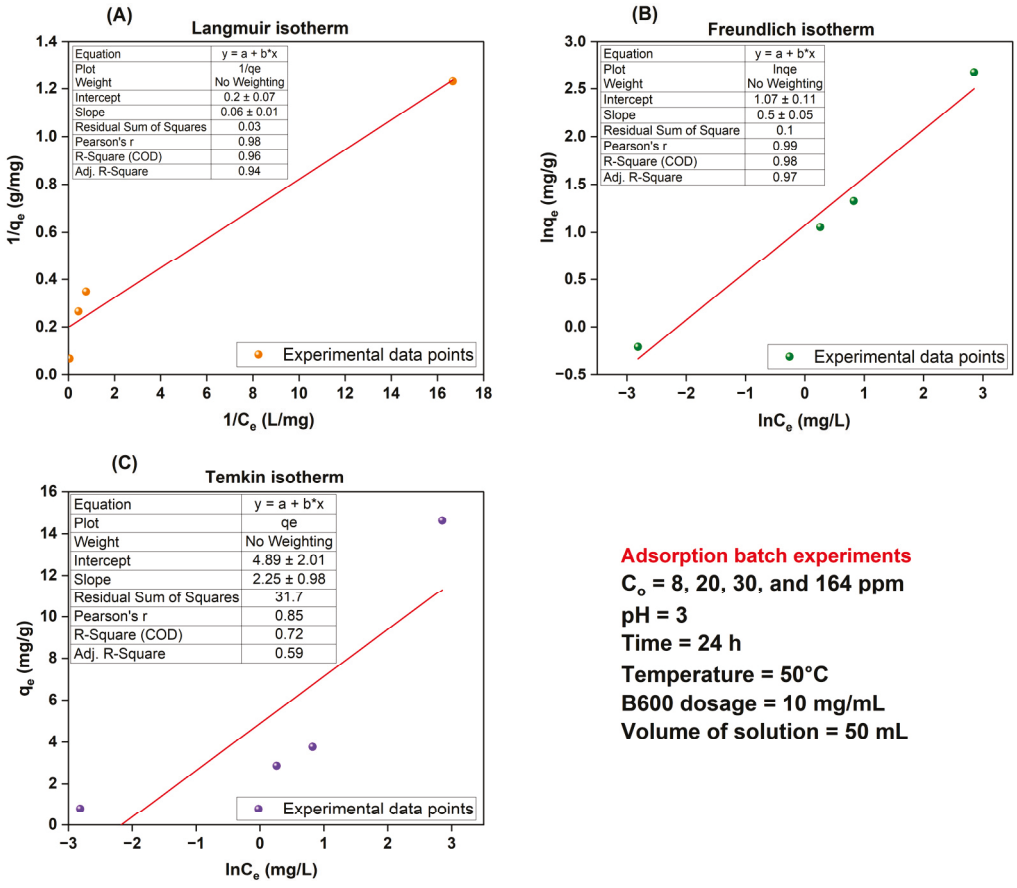


Figure 14. Adsorption isotherm models: (**A**) Langmuir isotherm, (**B**) Freundlich isotherm, and (**C**) Temkin isotherm, with conditions for experimentation.

Table 6. Adsorption isotherm parameters.

Average	Langmuir Isotherm					Freundlich Isotherm				Temkin Isotherm			
$q_{e,exp}$ (mg/g)	q_m (mg/g)	$q_{e,cal}$ (mg/g)	K_L (L/mg)	R_L	R^2	K_F [(mg/g)(L/mg)$^{1/n}$]	1/n	$q_{e,cal}$ (mg/g)	R^2	B (J/mol)	K_T (L/mg)	$q_{e,cal}$ (mg/g)	R^2
5.52	5.00	3.56	3.33	0.002–0.036 from 164–8 mg/L	0.94	2.92	0.50	5.15	0.97	2.25	8.79	5.52	0.59

The Freundlich model indicates multilayer adsorption on heterogeneous B600 sites, supported by 1/n = 0.5 (favorable, since $0 < 1/n < 1$) and K_F = 2.92, with reference to [114–117]. The low q_e and K_F are due to the high dosage (10 g/L) and increasing dye concentration. Nevertheless, model reliability is high (RMSE = 0.216, χ^2 = 0.03), with $q_{e,cal} \approx q_{e,exp}$, indicating both physisorption and chemisorption may occur [16,109,110]. The Langmuir model also suggests favorable adsorption ($0 < R_L < 1$) as explained conceptually in [118–120], likely as a monolayer, with minimal dye aggregation and homogeneous active sites (K_L = 3.33) [69,107,108,121]. Though it has slightly higher errors than Freundlich (RMSE = 1.133, χ^2 = 1.08), the fit remains good. The lower q_m than $q_{e,exp}$ may stem from site competition or experimental factors. The Temkin fit (Figure 14C) was weaker (R^2 = 0.59), though errors were minimal (RMSE = 0.002, χ^2 = 0), implying some degree of applicability. The low B value (2.25 J/mol) hints at low adsorption heat and physisorption dominance at higher dye levels. As the concentration rose from 8 to 164 ppm, q_e increased linearly, but with decreasing heat of adsorption as fewer high-energy sites remained [122]. Thus, Temkin supports a weaker interaction model, ranking behind Freundlich and Langmuir in overall reliability [123].

To summarize, the Freundlich model followed by the Langmuir isotherm model indicates favorable methyl orange adsorption over B600, where both monolayer and multilayer interactions can be deduced. Despite being less contrary to the theory, the Temkin isotherm is ranked last here only due to the low model correlation factor.

(D) Effect of Adsorption Duration—Adsorption Kinetics

As the contact time increased from 0 to 240 min, complete equilibrium was not yet reached (Figure 13D). However, both q_t and removal efficiency steadily increased: from 0.64 to 0.73 mg/g (77–89%) for 8 ppm and from 11.99 to 14.49 mg/g (73–89%) for 164 ppm. Over 50% of dye removal occurred within the first 30 min, indicating a rapid initial adsorption phase [111]. Despite the higher dye concentration, the curve shape suggests removal rates were not significantly impacted, likely due to a limited mass transfer gradient and increased competition for active sites. By 24 h (used in isotherm experiments), maximum q_e (14.63 mg/g) and removal (89.39%) were recorded, which were only slightly higher than those at 240 min (by 0.14 mg/g and 0.85%, respectively), indicating near-saturation. Beyond this, minimal change suggests that most B600 sites were occupied. Any further adsorption was likely limited by electrostatic repulsion, site saturation, and slow intra-particle diffusion.

As for the kinetics involving initial methyl orange concentrations of 8 ppm and 164 ppm, pseudo-first-order, pseudo-second-order, and intra-particle diffusion models were used to calculate adsorption parameters (Table 7), like in [99,124–128]. Both linear (Figure 15A–C) and non-linear (Figure 15D,E) fitting plus regression methods were evaluated and compared, as in [97]. All error estimations for analyzing the closeness between $q_{e,exp}$ and $q_{e,cal}$ for both linear and non-linear kinetic modeling are computed separately in Table 8.

Table 7. Adsorption kinetic parameters.

Dye Concentration	Pseudo-First-Order Kinetics			Pseudo-Second-Order Kinetics			Intra-Particle Diffusion Kinetics		
	q_e (mg/g)	k_1 (min^{-1})	R^2	q_e (mg/g)	k_2 (g/mg.min)	R^2	k_3 ($mg/g.min^{1/2}$)	C (mg/g)	R^2
Linear fitting with linear regression									
8 ppm	0.194	0.004	0.978	0.748	0.158	1.000	0.010	0.583	0.983
164 ppm	2.752	0.012	0.951	14.872	0.010	1.000	0.214	11.473	0.772
Non-linear fitting with non-linear regression									
8 ppm	0.700	0.059	0.495	0.726	0.254	0.879	0.010	0.583	0.983
164 ppm	14.107	0.056	0.517	14.716	0.011	0.890	0.214	11.473	0.772

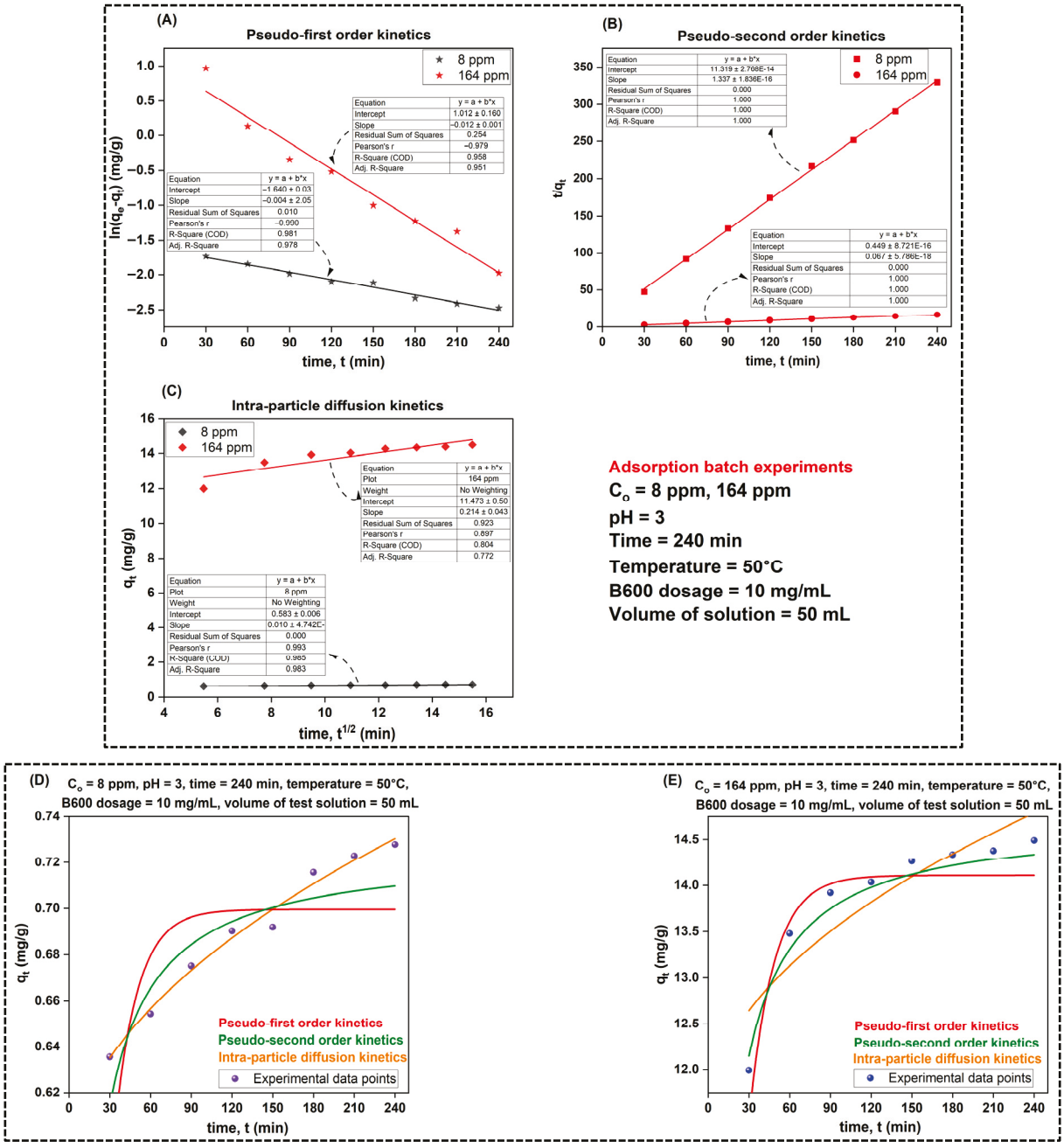


Figure 15. Adsorption kinetic models: linear (**A**–**C**) and non-linear (**D**,**E**) fitting methods.

Table 8. RMSEs derived from comparison of $q_{e,exp}$ and $q_{e,cal}$ for two initial methyl orange concentrations (Co: 8 ppm and 164 ppm) during adsorption kinetic model evaluation.

Kinetic Model	C_o (ppm)	Average $q_{e,exp}$ (mg/g)	$q_{e,cal}$ (mg/g)	RMSE
Linear fitting with linear regression				
Pseudo-first-order	8	0.812	0.194	0.234
Pseudo-first-order	164	14.630	2.752	4.489
Pseudo-second-order	8	0.812	0.748	0.024
Pseudo-second-order	164	14.630	14.872	0.091
Intra-particle diffusion	8	0.812	0.583	0.087
Intra-particle diffusion	164	14.630	11.473	1.193
Non-linear fitting with non-linear regression				
Pseudo-first-order	8	0.812	0.700	0.042
Pseudo-first-order	164	14.630	14.107	0.198
Pseudo-second-order	8	0.812	0.726	0.033
Pseudo-second-order	164	14.630	14.716	0.033
Intra-particle diffusion	8	0.812	0.583	0.087
Intra-particle diffusion	164	14.630	11.473	1.193

The pseudo-second-order model showed excellent linearity ($R^2 = 1$) for both 8 ppm and 164 ppm methyl orange concentrations, indicating chemisorption as the primary mechanism [129]. This suggests strong, slow-forming chemical bonds between B600 and methyl orange, consistent with systems like Zn-activated sawdust biochar [130]. Functional groups on B600, particularly oxygen- and hydrogen-containing moieties, likely interact with methyl orange's sulfonic acid groups via electron sharing and diffusion-driven processes [131]. A high B600 dosage ensures abundant active sites, making site availability and dye concentration the key limiting factors. The $q_{e,cal}$ values (0.75 mg/g for 8 ppm and 14.87 mg/g for 164 ppm) closely matched $q_{e,exp}$, with RMSEs of 0.02–0.09. Non-linear fits confirmed the trend ($q_{e,cal}$ = 0.73 and 14.72 mg/g for 8ppm and 164 ppm; RMSE = 0.03), though R^2 decreased slightly to 0.88 and 0.89. This validates the pseudo-second-order model, particularly at lower concentrations, where $k_2 > k_1$, reinforcing chemisorption's role.

For the pseudo-first-order model, linear regression yielded high R^2 values of 0.98 (8 ppm) and 0.95 (164 ppm), suggesting a role for physisorption, particularly influenced by methyl orange diffusion at the solid–liquid interface. At 8 ppm, dye molecules interact uniformly with available B600 sites, while at 164 ppm, site saturation and competitive interactions reduce efficiency. This is reflected in the large gap between $q_{e,cal}$ (2.75 mg/g) and $q_{e,exp}$ (14.63 mg/g) at 164 ppm, with a high RMSE of 4.49, compared to just 0.23 at 8 ppm. This implies that pseudo-first-order kinetics better describe adsorption at low dye concentrations. In contrast, non-linear fitting produced very low R^2 values (0.50 and 0.52), questioning its reliability despite close matches between $q_{e,cal}$ and $q_{e,exp}$ at 164 ppm (14.11 versus 14.63 mg/g; RMSE = 0.20). Across both methods, $k_1 < 0.1$ min^{-1}, indicating that weak forces and diffusion limitations govern the process, consistent with physisorption behavior.

For the intra-particle diffusion model, linear and non-linear fits showed a strong R^2 of 0.98 at 8 ppm, but only 0.77 at 164 ppm. This drop suggests that higher dye concentrations cause diffusion barriers, limited pore access due to B600 agglomeration, and the exhaustion of high-energy binding sites. The $q_{e,cal}$ rose from 0.58 mg/g (8 ppm) to 11.47 mg/g (164 ppm), with RMSE increasing from 0.09 to 1.19. At 8 ppm, $k_3 > k_1$, highlighting intra-

particle diffusion's dominance over pseudo-first-order kinetics. At 164 ppm, k_3 exceeds both k_1 and k_2, indicating that once surface sites are saturated, the dye continues diffusing into pores until mass transfer resistance and full saturation limit further uptake. Thus, adsorbate transport, active site binding, and B600 porosity are key to the adsorption process.

To sum up, physisorption, chemisorption, and molecular diffusion within the pores of the adsorbent are the key adsorption mechanisms identified, each of which harbors one or multiple rate-limiting steps with respect to the concentration of the adsorbate, adsorption sites, binding interactions, and finally, pore diffusion.

(E) Effect of Temperature—Adsorption Thermodynamics

The theory behind adsorption thermodynamics were similar to [132,133] and the calculated thermodynamic parameters for the adsorption process are presented in Table 9. As the temperature increased from 20 °C to 50 °C (293–323 K), q_e rose from 0.20 to 0.81 mg/g and removal efficiency improved from 24 to 99% for an initial methyl orange concentration of 8 ppm, aligning with observations in [134]. This temperature dependence necessitates thermodynamic evaluation. From the $\ln K_d$-versus-1/T plot, a ΔH value of 144.15 kJ/mol was calculated, indicating a strongly endothermic process characteristic of chemisorption, likely involving covalent, hydrogen, and π–π bonding. The high-energy input facilitates increased dye molecule mobility, leading to more frequent and forceful collisions with B600 surfaces [102]. A positive ΔS (0.46 kJ/mol·K) points to increased disorder as dye molecules move from the bulk solution to the adsorbent interface, allowing for interfacial diffusion and eventual attachment. However, entropy decreases once adsorption completes and molecular motion becomes restricted. The calculated ΔG values ranged from +8.38 kJ/mol at 20 °C to –6.21 kJ/mol at 50 °C, indicating that adsorption becomes increasingly spontaneous at higher temperatures, as external energy requirements decline and system favorability rises [135].

Table 9. Adsorption thermodynamic parameters and the influence of temperature.

Enthalpy	**Entropy**	**Gibbs Free Energy**		
ΔH (KJ/mol)	**ΔS (KJ/mol.K)**	**Temperature (K)**	**ΔG (KJ/mol) = ΔH-TΔS**	**ΔG (KJ/mol) = $-RT\ln k_d$**
144.153	0.460	293	9.419	8.376
		303	4.823	5.437
		313	0.227	2.488
		323	−4.369	−6.207

3.4.4. Adsorption Mechanism and Theory

Being a surface-driven process, methyl orange molecules migrated from the bulk solution to B600's surface, where adsorption was influenced by factors like surface charge, functional groups, pore structure (micro- to mesopores), and energy-diverse binding sites. Ambient pH, temperature, contact time, adsorbent dosage, and dye concentration also played crucial roles. Under acidic conditions, B600's surface became positively charged, promoting electrostatic attraction with the anionic azo dye and minimizing repulsion [136]. FTIR analysis revealed hydroxyl, carboxyl, and amide groups on B600, which facilitated covalent and hydrogen bonding with methyl orange's sulfonate group at low pH.

As observed in Figure 9D, the adsorption of methyl orange affected the surface elemental composition of B600, which is evident from a drop in surface carbon from 95.3% to 94.1% and an increase in surface oxygen from 4.5% to 5.6% after adsorption. Such strong chemical interactions resulted in chemisorption, which was affirmed by the pseudo-second-order kinetic model, where adsorption efficiency increased and showed signs of irreversibility.

This may be evident from the Langmuir isotherm parameter R_L, which was close to 0 (still > 0 and favorable). The Langmuir isotherm's monolayer adsorption with a fixed number of active binding sites with high energies and the Freundlich isotherm's heterogeneous multilayer interactions ($0 < 1/n < 1$) are both explainable. Pseudo-first-order kinetics also fit well as a supportive mechanism, with the adsorption data showing the dominance of weak physical forces via physisorption, as discussed in [137].

FTIR also indicated C=C and C≡C linkages, suggesting π–π stacking interactions with methyl orange's aromatic rings [138]. π–π electron donor–acceptor (EDA) mechanisms may also be involved, as reported in [139]. The BET surface area (~323 m^2/g) and strong intra-particle diffusion model fit at low dye concentrations point to pore filling and molecular diffusion. As shown in Figure 8J–L, dye adsorption visibly altered B600's porosity (disappearance) and surface morphology (growth of clusters).

4. Conclusions

Sustainable management of CRD wood waste remains challenging due to its non-recyclable status and degradation from demolition and surface treatments, but this study shows that pyrolysis offers a scalable and sustainable valorization pathway with industrial and environmental benefits. Using a statistically validated DOE approach, the effects of pyrolysis temperature, BRT, and feedstock mass were assessed across lab-scale (horizontal tube furnace) and semi-pilot (rotary retort-furnace) reactors. High-temperature biochars like B800 showed peak properties—FC (87%), TSF (96%), carbon content (92%), BET surface area (300 m^2/g), and micropore volume (0.146 cm^3/g)—alongside declines in VC (9%), hydrogen (0.9%), oxygen (2.2%), and Van-Krevelen ratios (H/C: 0.1; O/C: 0.02), with a low yield of 21%, supporting their use in metallurgical reduction or as coke blends. The moderate-temperature biochar B600 balanced reactivity and stability—FC (81%), TSF (87%), H/C: 0.3, O/C: 0.1, surface area (324 m^2/g), and micropore volume (0.145 cm^3/g)—enabling >90% methyl orange removal under low pH, a high dose, and a long contact time. Its adsorption followed the Freundlich isotherm ($R^2 = 0.97$, $1/n = 0.5$) and pseudo-second-order kinetics ($R^2 = 1$ for linear fitting and regression; 0.87–0.89 for non-linear fitting and regression), confirming dominant multilayer chemisorption. Notably, no chemical or physical activation was applied, avoiding environmental burdens. Cross-scale comparisons confirmed consistent B400–B800 properties, with the pyrolysis temperature being most influential, raising FC by 15% and TSF by 19% and reducing VC by 53%. The HHV ranged from 25 to 33 MJ/kg, supporting energy applications. Despite its demonstrated feasibility, challenges remain: securing CRD wood supply, managing inherent contaminants, utilizing co-products (bio-oil, syngas), and designing cost-effective, scalable systems. Future work will address pilot-scale trials with an even higher mass of CRD wood feed, post-pyrolysis thermal activation of biochar, and self-ignition risks to support safe deployment.

Supplementary Materials: The following supporting information can be downloaded at https://www.mdpi.com/article/10.3390/en18153902/s1: Supplementary Figure S1: RSM's CCD design points. Supplementary Table S1: Run order with coded and actual values for pyrolysis independent variables. Supplementary Table S2: Coefficients table for DOE independent variables to evaluate their influence on the different response variables. The *p*-values for pyrolysis temperature (A) are <0.05 for all response variables suggesting that it has the most dominant influence on biochar properties. Supplementary Table S3: Fit statistics for DOE response variables. Supplementary Table S4: Material energy balance and pyrolyzer efficiency during biomass thermal decomposition. Case 1: 0.18% internal moisture. Supplementary Table S5: Material energy balance and pyrolyzer efficiency during biomass thermal decomposition. Case 2: 18% internal moisture. Supplementary Table S6: Non-linear

and linear fitting equations for adsorption kinetic models. Supplementary Table S7: Comparison of methyl orange removal by biochars from relevant studies.

Author Contributions: Conceptualization, A.G.; data curation, A.G.; formal analysis, A.G.; investigation, A.G.; methodology, A.G.; project administration, S.B. and C.B.; resources, S.B.; software, A.G.; supervision, S.B., Y.B., S.L. and O.R.; validation, A.G.; visualization, A.G.; writing—original draft, A.G.; writing—review and editing, A.G., S.B., Y.B., S.L., O.R. and C.B. All authors have read and agreed to the published version of the manuscript.

Funding: This research was funded by MITACS (IT40901), through Escouade Energie, Citeq, and supported by Innofibre and I^2E^3—UQTR, Québec, Canada. The work was conducted at Innofibre—Centre d'Innovation des Produits Cellulosiques, Trois-Rivières, and at the Institute for Innovation in Ecomaterials, Ecoproducts, and Ecoenergies (I^2E^3), University of Québec Trois-Rivières (UQTR), Québec, Canada.

Data Availability Statement: Data will be shared upon request. Since it is an industry-associated project result, data will be shared upon request with careful consideration.

Conflicts of Interest: The authors declare no conflicts of interest. The funders had no role in the design of the study; in the collection, analyses, or interpretation of data; in the writing of the manuscript; or in the decision to publish the results.

References

1. Robey, N.M.; Solo-Gabriele, H.M.; Jones, A.S.; Marini, J.; Townsend, T.G. Metals content of recycled construction and demolition wood before and after implementation of best management practices. *Environ. Pollut.* **2018**, *242*, 1198–1205. [CrossRef] [PubMed]
2. Al-Rumaihi, A.; Shahbaz, M.; Mckay, G.; Mackey, H.; Al-Ansari, T. A review of pyrolysis technologies and feedstock: A blending approach for plastic and biomass towards optimum biochar yield. *Renew. Sustain. Energy Rev.* **2022**, *167*, 112715. [CrossRef]
3. Li, W.; Dang, Q.; Brown, R.C.; Laird, D.; Wright, M.M. The impacts of biomass properties on pyrolysis yields, economic and environmental performance of the pyrolysis-bioenergy-biochar platform to carbon negative energy. *Bioresour. Technol.* **2017**, *241*, 959–968. [CrossRef] [PubMed]
4. Sivaranjanee, R.; Kumar, P.S.; Chitra, B.; Rangasamy, G. A critical review on biochar for the removal of toxic pollutants from water environment. *Chemosphere* **2024**, *360*, 142382. [CrossRef] [PubMed]
5. Ayaz, M.; Feizienė, D.; Tilvikienė, V.; Akhtar, K.; Stulpinaitė, U.; Iqbal, R. Biochar role in the sustainability of agriculture and environment. *Sustainability* **2021**, *13*, 1330. [CrossRef]
6. Malińska, K.; Dróżdż, D.; Postawa, P.; Stachowiak, T. Biochar—A Filler in "Bioplastics" for Horticultural Applications. *Materials* **2024**, *17*, 6208. [CrossRef] [PubMed]
7. Ahuja, V.; Palai, A.K.; Kumar, A.; Patel, A.K.; Farooque, A.A.; Yang, Y.-H.; Bhatia, S.K. Biochar: Empowering the future of energy production and storage. *J. Anal. Appl. Pyrolysis* **2024**, *177*, 106370. [CrossRef]
8. Anand, A.; Gautam, S.; Ram, L.C. Feedstock and pyrolysis conditions affect suitability of biochar for various sustainable energy and environmental applications. *J. Anal. Appl. Pyrolysis* **2023**, *170*, 105881. [CrossRef]
9. Ghorbani, M.; Amirahmadi, E.; Neugschwandtner, R.W.; Konvalina, P.; Kopecký, M.; Moudrý, J.; Perná, K.; Murindangabo, Y.T. The impact of pyrolysis temperature on biochar properties and its effects on soil hydrological properties. *Sustainability* **2022**, *14*, 14722. [CrossRef]
10. Nan, H.; Yin, J.; Yang, F.; Luo, Y.; Zhao, L.; Cao, X. Pyrolysis temperature-dependent carbon retention and stability of biochar with participation of calcium: Implications to carbon sequestration. *Environ. Pollut.* **2021**, *287*, 117566. [CrossRef] [PubMed]
11. Bolan, S.; Hou, D.; Wang, L.; Hale, L.; Egamberdieva, D.; Tammeorg, P.; Li, R.; Wang, B.; Xu, J.; Wang, T.; et al. The potential of biochar as a microbial carrier for agricultural and environmental applications. *Sci. Total Environ.* **2023**, *886*, 163968. [CrossRef] [PubMed]
12. Beljin, J.; Đukanović, N.; Anojčić, J.; Simetić, T.; Apostolović, T.; Mutić, S.; Maletić, S. Biochar in the Remediation of Organic Pollutants in Water: A Review of Polycyclic Aromatic Hydrocarbon and Pesticide Removal. *Nanomaterials* **2024**, *15*, 26. [CrossRef] [PubMed]
13. Buffi, M.; Hurtig, O.; Prussi, M.; Scarlat, N.; Chiaramonti, D. Energy and GHG emissions assessment for biochar-enhanced advanced biofuels value chains. *Energy Convers. Manag.* **2024**, *309*, 118450. [CrossRef]
14. Iwuozor, K.O.; Ighalo, J.O.; Emenike, E.C.; Ogunfowora, L.A.; Igwegbe, C.A. Adsorption of methyl orange: A review on adsorbent performance. *Curr. Res. Green. Sustain. Chem.* **2021**, *4*, 100179. [CrossRef]

15. Serban, G.V.; Iancu, V.I.; Dinu, C.; Tenea, A.; Vasilache, N.; Cristea, I.; Niculescu, M.; Ionescu, I.; Chiriac, F.L. Removal efficiency and adsorption kinetics of methyl orange from wastewater by commercial activated carbon. *Sustainability* **2023**, *15*, 12939. [CrossRef]
16. Lee, H.; Fiore, S.; Berruti, F. Adsorption of methyl orange and methylene blue on activated biocarbon derived from birchwood pellets. *Biomass Bioenergy* **2024**, *191*, 107446. [CrossRef]
17. Jian, X.; Zhuang, X.; Li, B.; Xu, X.; Wei, Z.; Song, Y.; Jiang, E. Comparison of characterization and adsorption of biochars produced from hydrothermal carbonization and pyrolysis. *Environ. Technol. Innov.* **2018**, *10*, 27–35. [CrossRef]
18. Cano, F.J.; Reyes-Vallejo, O.; Sánchez-Albores, R.M.; Sebastian, P.J.; Cruz-Salomón, A.; Hernández-Cruz, M.d.C.; Montejo-López, W.; Reyes, M.G.; Ramirez, R.d.P.S.; Torres-Ventura, H.H. Activated Biochar from Pineapple Crown Biomass: A High-Efficiency Adsorbent for Organic Dye Removal. *Sustainability* **2025**, *17*, 99. [CrossRef]
19. Aziz, K.H.H.; Fatah, N.M.; Muhammad, K.T. Advancements in application of modified biochar as a green and low-cost adsorbent for wastewater remediation from organic dyes. *R. Soc. Open Sci.* **2024**, *11*, 232033. [CrossRef] [PubMed]
20. Ramath, R.; Sukumaran, A.M.; Ramachandran, A.; Basheer, S.B. Methyl orange dye adsorption and degradation at low temperature using iron oxide-incorporated biochar derived from industrial by-products. *Bioresour. Technol. Rep.* **2023**, *22*, 101470. [CrossRef]
21. Issaka, E.; Fapohunda, F.O.; Amu-Darko, J.N.O.; Yeboah, L.; Yakubu, S.; Varjani, S.; Ali, N.; Bilal, M. Biochar-based composites for remediation of polluted wastewater and soil environments: Challenges and prospects. *Chemosphere* **2022**, *297*, 134163. [CrossRef] [PubMed]
22. Zhao, X.; Wang, J.; Zhu, G.; Zhang, S.; Wei, C.; Liu, C.; Cao, L.; Zhao, S.; Zhang, S. Efficient removal of high concentration dyes from water by functionalized in-situ N-doped porous biochar derived from waste antibiotic fermentation residue. *Chemosphere* **2024**, *364*, 143215. [CrossRef] [PubMed]
23. Behera, A.K.; Shadangi, K.P.; Sarangi, P.K. Efficient removal of Rhodamine B dye using biochar as an adsorbent: Study the performance, kinetics, thermodynamics, adsorption isotherms and its reusability. *Chemosphere* **2024**, *354*, 141702. [CrossRef] [PubMed]
24. Ganesan, A.; Rezazgui, O.; Langlois, S.; Boussabbeh, C.; Barnabé, S. Pyrolytic conversion of construction, renovation, and demolition (CRD) wood wastes in Québec to biochar: Production, characterization, and identifying relevant stability indices for carbon sequestration. *Sci. Total Environ.* **2025**, *965*, 178650. [CrossRef] [PubMed]
25. Sangsuk, S.; Suebsiri, S.; Puakhom, P. The metal kiln with heat distribution pipes for high quality charcoal and wood vinegar production. *Energy Sustain. Dev.* **2018**, *47*, 149–157. [CrossRef]
26. Channiwala, S.A.; Parikh, P.P. A unified correlation for estimating HHV of solid, liquid and gaseous fuels. *Fuel* **2002**, *81*, 1051–1063. [CrossRef]
27. Khatibi, M.; Nahil, M.A.; Williams, P.T. Improving the Quality of Bio-oil Using the Interaction of Plastics and Biomass through Copyrolysis Coupled with Nonthermal Plasma Processing. *Energy Fuels* **2023**, *38*, 1240–1257. [CrossRef] [PubMed]
28. Huff, M.D.; Marshall, S.; Saeed, H.A.; Lee, J.W. Surface oxygenation of biochar through ozonization for dramatically enhancing cation exchange capacity. *Bioresour. Bioprocess.* **2018**, *5*, 1–9. [CrossRef]
29. Lehmann, J.; Rillig, M.C.; Thies, J.; Masiello, C.A.; Hockaday, W.C.; Crowley, D. Biochar effects on soil biota—A review. *Soil. Biol. Biochem.* **2011**, *43*, 1812–1836. [CrossRef]
30. Nartey, O.D.; Zhao, B. Biochar preparation, characterization, and adsorptive capacity and its effect on bioavailability of contaminants: An overview. *Adv. Mater. Sci. Eng.* **2014**, *2014*, 715398. [CrossRef]
31. Khater, E.-S.; Bahnasawy, A.; Hamouda, R.; Sabahy, A.; Abbas, W.; Morsy, O.M. Biochar production under different pyrolysis temperatures with different types of agricultural wastes. *Sci. Rep.* **2024**, *14*, 2625. [CrossRef] [PubMed]
32. Li, J.; Sun, W.; Lichtfouse, E.; Maurer, C.; Liu, H. Life cycle assessment of biochar for sustainable agricultural application: A review. *Sci. Total Environ.* **2024**, *951*, 175448. [CrossRef] [PubMed]
33. Dufourny, A.; Van De Steene, L.; Humbert, G.; Guibal, D.; Martin, L.; Blin, J. Influence of pyrolysis conditions and the nature of the wood on the quality of charcoal as a reducing agent. *J. Anal. Appl. Pyrolysis* **2019**, *137*, 1–13. [CrossRef]
34. He, D.; Luo, Y.; Zhu, B. Feedstock and pyrolysis temperature influence biochar properties and its interactions with soil substances: Insights from a DFT calculation. *Sci. Total Environ.* **2024**, *922*, 171259. [CrossRef] [PubMed]
35. Greco, G.; Videgain, M.; Di Stasi, C.; Pires, E.; Manyà, J.J. Importance of pyrolysis temperature and pressure in the concentration of polycyclic aromatic hydrocarbons in wood waste-derived biochars. *J. Anal. Appl. Pyrolysis* **2021**, *159*, 105337. [CrossRef]
36. Alharbi, H.A.; Alotaibi, K.D.; El-Saeid, M.H.; Giesy, J.P. Polycyclic aromatic hydrocarbons (PAHs) and metals in diverse biochar products: Effect of feedstock type and pyrolysis temperature. *Toxics* **2023**, *11*, 96. [CrossRef] [PubMed]
37. International Biochar Initiative. *Standardized Product Definition and Product Testing Guidelines for Biochar That Is Used in Soil*; International Biochar Initiative, 2015.
38. Patel, M.R.; Panwar, N.L. Development, process optimization and assessment of sustainable mobile biochar kiln for agricultural use. *J. Clean. Prod.* **2024**, *477*, 143866. [CrossRef]

39. Maziarka, P.; Kienzl, N.; Dieguez-Alonso, A.; Fierro, V.; Celzard, A.; Arauzo, P.J.; Hedin, N.; Prins, W.; Anca-Couce, A.; Manyà, J.J.; et al. Part 1– Impact of pyrolysis temperature and wood particle length on vapor cracking and char porous texture in relation to the tailoring of char properties. *Energy Fuels* **2024**, *38*, 9751–9771. [CrossRef]
40. Xu, C.; Wei, K.; Du, Z.; Ma, W. Effect of particle size on the properties of biomass gasification residue pellets used as a metallurgical-grade silicon reducing agent. *Powder Technol.* **2024**, *435*, 119406. [CrossRef]
41. Bian, H.; Wang, M.; Huang, J.; Liang, R.; Du, J.; Fang, C.; Shen, C.; Man, Y.B.; Wong, M.H.; Shan, S.; et al. Large particle size boosting the engineering application potential of functional biochar in ammonia nitrogen and phosphorus removal from biogas slurry. *J. Water Process Eng.* **2024**, *57*, 104640. [CrossRef]
42. Hu, R.; Li, C.; Hu, X.; Qiao, Y. Varied impacts of volatiles from pyrolysis of poplar wood, bark and leaves on property of coal char. *J. Anal. Appl. Pyrolysis* **2024**, *178*, 106389. [CrossRef]
43. Saleem, M.; Baig, N. Production of bio-oil and bio-char from different biomass wastes. In *IOP Conference Series: Materials Science and Engineering*; IOP Publishing: Bristol, UK, 2018; Volume 458, p. 12021.
44. Panizio, R.; Castro, C.; Pacheco, N.; Assis, A.C.; Longo, A.; Vilarinho, C.; Teixeira, J.C.; Brito, P.; Gonçalves, M.; Nobre, C. Investigation of biochars derived from waste lignocellulosic biomass and insulation electric cables: A comprehensive TGA and Macro-TGA analysis. *Heliyon* **2024**, *10*, e37882. [CrossRef] [PubMed]
45. Pei, S.; Zhao, Y.; Li, W.; Qu, C.; Ren, Y.; Yang, Y.; Liu, J.; Wu, C. Critical impact of pyrolysis temperatures on biochars for peroxymonosulfate activation: Structural characteristics, degradation performance and mechanism. *Chem. Eng. J.* **2023**, *477*, 147274. [CrossRef]
46. Kim, D.; Hadigheh, S.A.; Wei, Y. Unlocking biosolid pyrolysis: Towards tailored biochar with different surface properties. *Mater. Today Sustain.* **2024**, *27*, 100868. [CrossRef]
47. Gonnella, G.; Ischia, G.; Fambri, L.; Fiori, L. Thermal analysis and kinetic modeling of pyrolysis and oxidation of hydrochars. *Energies* **2022**, *15*, 950. [CrossRef]
48. Babu, K.K.B.S.; Nataraj, M.; Tayappa, M.; Vyas, Y.; Mishra, R.K.; Acharya, B. Production of biochar from waste biomass using slow pyrolysis: Studies of the effect of pyrolysis temperature and holding time on biochar yield and properties. *Mater. Sci. Energy Technol.* **2024**, *7*, 318–334. [CrossRef]
49. Windeatt, J.H.; Ross, A.B.; Williams, P.T.; Forster, P.M.; Nahil, M.A.; Singh, S. Characteristics of biochars from crop residues: Potential for carbon sequestration and soil amendment. *J. Environ. Manag.* **2014**, *146*, 189–197. [CrossRef] [PubMed]
50. Chen, M.; Sun, Y.; Peng, Y.; Han, Z.; Chen, G.; Chen, X.; Lu, S. Effect of low-carbon coal gangue on the stability and dissolved organic matter characteristics of co-pyrolysis biochar: Insights on pyrolysis temperatures and minerals. *Carbon Res.* **2025**, *4*, 19. [CrossRef]
51. Handiso, B.; Pääkkönen, T.; Wilson, B.P. Effect of pyrolysis temperature on the physical and chemical characteristics of pine wood biochar. *Waste Manag. Bull.* **2024**, *2*, 281–287. [CrossRef]
52. Nicholas, H.L.; Mabbett, I.; Apsey, H.; Robertson, I. Physico-chemical properties of waste derived biochar from community scale faecal sludge treatment plants. *Gates Open Res.* **2022**, *6*, 96. [CrossRef] [PubMed]
53. McCall, M.A.; Watson, J.S.; Sephton, M.A. Predicting Stability of Barley Straw-Derived Biochars Using Fourier Transform Infrared Spectroscopy. *ACS Sustain. Resour. Manag.* **2024**, *1*, 1975–1983. [CrossRef] [PubMed]
54. Matin, N.H.; Aydin, E. Reviewing the effect of pyrolysis temperature on the fourier-transform infrared spectra of biochars. *Acta Hortic. Regiotect.* **2022**, *25*, 160–173. [CrossRef]
55. Zou, X.; Debiagi, P.; Amjed, M.A.; Zhai, M.; Faravelli, T. Impact of high-temperature biomass pyrolysis on biochar formation and composition. *J. Anal. Appl. Pyrolysis* **2024**, *179*, 106463. [CrossRef]
56. Roshan, A.; Ghosh, D.; Maiti, S.K. How temperature affects biochar properties for application in coal mine spoils? A meta-analysis. *Carbon Res.* **2023**, *2*, 3. [CrossRef]
57. Shaaban, A.; Se, S.-M.; Dimin, M.; Juoi, J.M.; Husin, M.H.M.; Mitan, N.M.M. Influence of heating temperature and holding time on biochars derived from rubber wood sawdust via slow pyrolysis. *J. Anal. Appl. Pyrolysis* **2014**, *107*, 31–39. [CrossRef]
58. Świechowski, K.; Matyjewicz, B.; Telega, P.; Białowiec, A. The influence of low-temperature food waste biochars on anaerobic digestion of food waste. *Materials* **2022**, *15*, 945. [CrossRef] [PubMed]
59. Dhar, S.A.; Sakib, T.U.; Hilary, L.N. Effects of pyrolysis temperature on production and physicochemical characterization of biochar derived from coconut fiber biomass through slow pyrolysis process. *Biomass Conv. Bioref.* **2022**, *12*, 2631–2647. [CrossRef]
60. Salinas-Farran, L.; Mosonik, M.C.A.; Jervis, R.; Marathe, S.; Rau, C.; Volpe, R. Tracked evolution of single biochar particle's morphology during pyrolysis in operando x-ray micro-computed tomography. *Biochar* **2024**, *6*, 86. [CrossRef]
61. Das, O.; Mensah, R.A.; George, G.; Jiang, L.; Xu, Q.; Neisiany, R.E.; Umeki, K.; Tomal Jose, E.; Phounglamcheik, A.; Hedenqvist, M.S.; et al. Flammability and mechanical properties of biochars made in different pyrolysis reactors. *Biomass Bioenergy* **2021**, *152*, 106197. [CrossRef]
62. Clarke, J.; Olea, M. The effect of temperature and treatment regime on the physical, chemical, and biological properties of poultry litter biochar. *Reactions* **2024**, *5*, 379–418. [CrossRef]

63. Ma, X.; Zhou, B.; Budai, A.; Jeng, A.; Hao, X.; Wei, D.; Zhang, Y.; Rasse, D. Study of biochar properties by scanning electron microscope—Energy dispersive X-ray spectroscopy (SEM-EDX). *Commun. Soil Sci. Plant Anal.* **2016**, *47*, 593–601. [CrossRef]
64. Nkomo, N.; Odindo, A.O.; Musazura, W.; Missengue, R. Optimising pyrolysis conditions for high-quality biochar production using black soldier fly larvae faecal-derived residue as feedstock. *Heliyon* **2021**, *7*, e07025. [CrossRef] [PubMed]
65. Suárez-Hernández, L.; Ardila-A., A.N.; Barrera-Zapata, R. Morphological and physicochemical characterization of biochar produced by gasification of selected forestry species. *Rev. Fac. Ing.* **2017**, *26*, 123–130. [CrossRef]
66. Sharma, T.; Ratner, A. Analysis and characterization of metallic nodules on biochar from single-stage downdraft gasification. *Processes* **2021**, *9*, 533. [CrossRef]
67. Grimm, A.; Conrad, S.; Gentili, F.G.; Mikkola, J.-P.; Hu, T.; Lassi, U.; Silva, L.F.; Lima, E.C.; dos Reis, G.S. Highly efficient boron/sulfur-modified activated biochar for removal of reactive dyes from water: Kinetics, isotherms, thermodynamics, and regeneration studies. *Colloids Surf. A Physicochem. Eng. Asp.* **2025**, *713*, 136486. [CrossRef]
68. Makowska, M.; Dziosa, K. Influence of different pyrolysis temperatures on chemical composition and graphite-like structure of biochar produced from biomass of green microalgae Chlorella sp. *Environ. Technol. Innov.* **2024**, *35*, 103667. [CrossRef]
69. Senapati, S.; Giri, J.; Mallick, L.; Singha, D.; Bastia, T.K.; Rath, P.; Rana, M.K.; Panda, A.K. Rapid adsorption of industrial cationic dye pollutant using base-activated rice straw biochar: Performance, isotherm, kinetic and thermodynamic evaluation. *Discov. Sustain.* **2025**, *6*, 46. [CrossRef]
70. Marmiroli, M.; Bonas, U.; Imperiale, D.; Lencioni, G.; Mussi, F.; Marmiroli, N.; Maestri, E. Structural and functional features of chars from different biomasses as potential plant amendments. *Front. Plant Sci.* **2018**, *9*, 1119. [CrossRef] [PubMed]
71. Lin, G.; Wang, Y.; Wu, X.; Meng, J.; Ok, Y.S.; Wang, C.-H. Enhancing agricultural productivity with biochar: Evaluating feedstock and quality standards. *Bioresour. Technol. Rep.* **2025**, *29*, 102059. [CrossRef]
72. Teweldebrihan, M.D.; Dinka, M.O. Methyl red adsorption from aqueous solution using Rumex Abyssinicus-derived biochar: Studies of kinetics and isotherm. *Water* **2024**, *16*, 2237. [CrossRef]
73. Wu, L.; Liu, X.; Lv, G.; Zhu, R.; Tian, L.; Liu, M.; Li, Y.; Rao, W.; Liu, T.; Liao, L. Study on the adsorption properties of methyl orange by natural one-dimensional nano-mineral materials with different structures. *Sci. Rep.* **2021**, *11*, 10640. [CrossRef] [PubMed]
74. Altıkat, A.; Alma, M.H.; Altıkat, A.; Bilgili, M.E.; Altıkat, S. A comprehensive study of biochar yield and quality concerning pyrolysis conditions: A multifaceted approach. *Sustainability* **2024**, *16*, 937. [CrossRef]
75. Conz, R.F.; Abbruzzini, T.F.; de Andrade, C.A.; Milori, D.M.B.P.; Cerri, C.E.P. Effect of pyrolysis temperature and feedstock type on agricultural properties and stability of biochars. *Agric. Sci.* **2017**, *8*, 914–933. [CrossRef]
76. Choudhary, T.K.; Khan, K.S.; Hussain, Q.; Ahmad, M.; Ashfaq, M. Feedstock-induced changes in composition and stability of biochar derived from different agricultural wastes. *Arab. J. Geosci.* **2019**, *12*, 1–13. [CrossRef]
77. Yu, K.L.; Lau, B.F.; Show, P.L.; Ong, H.C.; Ling, T.C.; Chen, W.-H.; Ng, E.P.; Chang, J.-S. Recent developments on algal biochar production and characterization. *Bioresour. Technol.* **2017**, *246*, 2–11. [CrossRef] [PubMed]
78. Rathnayake, N.; Patel, S.; Hakeem, I.G.; Pazferreiro, J.; Sharma, A.; Gupta, R.; Rees, C.; Bergmann, D.; Blackbeard, J.; Surapaneni, A.; et al. Co-pyrolysis of biosolids with lignocellulosic biomass: Effect of feedstock on product yield and composition. *Process Saf. Environ. Prot.* **2023**, *173*, 75–87. [CrossRef]
79. Crombie, K.; Mašek, O.; Sohi, S.P.; Brownsort, P.; Cross, A. The effect of pyrolysis conditions on biochar stability as determined by three methods. *GCB Bioenergy* **2013**, *5*, 122–131. [CrossRef]
80. Chatterjee, R.; Sajjadi, B.; Chen, W.-Y.; Mattern, D.L.; Hammer, N.; Raman, V.; Dorris, A. Effect of pyrolysis temperature on physicochemical properties and acoustic-based amination of biochar for efficient CO2 adsorption. *Front. Energy Res.* **2020**, *8*, 85. [CrossRef]
81. Antonangelo, J.A.; Zhang, H.; Sun, X.; Kumar, A. Physicochemical properties and morphology of biochars as affected by feedstock sources and pyrolysis temperatures. *Biochar* **2019**, *1*, 325–336. [CrossRef]
82. Ferraro, G.; Pecori, G.; Rosi, L.; Bettucci, L.; Fratini, E.; Casini, D.; Rizzo, A.M.; Chiaramonti, D. Biochar from lab-scale pyrolysis: Influence of feedstock and operational temperature. *Biomass Conv. Bioref.* **2024**, *14*, 5901–5911. [CrossRef]
83. Tomczyk, A.; Sokołowska, Z.; Boguta, P. Biochar physicochemical properties: Pyrolysis temperature and feedstock kind effects. *Rev. Environ. Sci. Bio/Technol.* **2020**, *19*, 191–215. [CrossRef]
84. Mukherjee, A.; Patra, B.R.; Podder, J.; Dalai, A.K. Synthesis of biochar from lignocellulosic biomass for diverse industrial applications and energy harvesting: Effects of pyrolysis conditions on the physicochemical properties of biochar. *Front. Mater.* **2022**, *9*, 870184. [CrossRef]
85. Venkatesh, G.; Gopinath, K.A.; Reddy, K.S.; Reddy, B.S.; Prabhakar, M.; Srinivasarao, C.; Kumari, V.V.; Singh, V.K. Characterization of biochar derived from crop residues for soil amendment, carbon sequestration and energy use. *Sustainability* **2022**, *14*, 2295. [CrossRef]
86. Cimò, G.; Kucerik, J.; Berns, A.E.; Schaumann, G.E.; Alonzo, G.; Conte, P. Effect of heating time and temperature on the chemical characteristics of biochar from poultry manure. *J. Agric. Food Chem.* **2014**, *62*, 1912–1918. [CrossRef] [PubMed]

87. Kumar, N.V.; Sawargaonkar, G.; Rani, C.S.; Pasumarthi, R.; Kale, S.; Prakash, T.R.; Triveni, S.; Singh, A.; Davala, M.S.; Khopade, R.; et al. Harnessing the potential of pigeonpea and maize feedstock biochar for carbon sequestration, energy generation, and environmental sustainability. *Bioresour. Bioprocess.* **2024**, *11*, 5. [CrossRef] [PubMed]
88. Mariyam, S.; Alherbawi, M.; Pradhan, S.; Al-Ansari, T.; McKay, G. Biochar yield prediction using response surface methodology: Effect of fixed carbon and pyrolysis operating conditions. *Biomass Conv. Bioref.* **2024**, *14*, 28879–28892. [CrossRef]
89. Ronsse, F.; Van Hecke, S.; Dickinson, D.; Prins, W. Production and characterization of slow pyrolysis biochar: Influence of feedstock type and pyrolysis conditions. *GCB Bioenergy* **2013**, *5*, 104–115. [CrossRef]
90. Patel, S.; Kundu, S.; Halder, P.; Veluswamy, G.; Pramanik, B.; Paz-Ferreiro, J.; Surapaneni, A.; Shah, K. Slow pyrolysis of biosolids in a bubbling fluidised bed reactor using biochar, activated char and lime. *J. Anal. Appl. Pyrolysis* **2019**, *144*, 104697. [CrossRef]
91. Nair, R.R.; Kißling, P.A.; Schaate, A.; Marchanka, A.; Shamsuyeva, M.; Behrens, P.; Weichgrebe, D. The influence of sample mass (scaling effect) on the synthesis and structure of non-graphitizing carbon (biochar) during the analytical pyrolysis of biomass. *RSC Adv.* **2023**, *13*, 13526–13539. [CrossRef] [PubMed]
92. Zhang, K.; Zhang, K.; Li, Y.; Kang, Q.; Wang, Y.; Wang, J.; Yang, K.; Mao, J. Easily Pyrolyzable Biomass Components Significantly Affect the Physicochemical Properties and Water-Holding Capacity of the Pyrolyzed Biochar. *Agriculture* **2023**, *13*, 2053. [CrossRef]
93. Xiong, Z.; Huanhuan, Z.; Jing, W.; Wei, C.; Yingquan, C.; Gao, X.; Haiping, Y.; Hanping, C. Physicochemical and adsorption properties of biochar from biomass-based pyrolytic polygeneration: Effects of biomass species and temperature. *Biochar* **2021**, *3*, 657–670. [CrossRef]
94. Kalina, M.; Sovova, S.; Svec, J.; Trudicova, M.; Hajzler, J.; Kubikova, L.; Enev, V. The effect of pyrolysis temperature and the source biomass on the properties of biochar produced for the agronomical applications as the soil conditioner. *Materials* **2022**, *15*, 8855. [CrossRef] [PubMed]
95. Aichour, A.; Zaghouane-Boudiaf, H.; Khodja, H.D. Highly removal of anionic dye from aqueous medium using a promising biochar derived from date palm petioles: Characterization, adsorption properties and reuse studies. *Arab. J. Chem.* **2022**, *15*, 103542. [CrossRef]
96. Muema, F.M.; Richardson, Y.; Keita, A.; Sawadogo, M. An interdisciplinary overview on biochar production engineering and its agronomic applications. *Biomass Bioenergy* **2024**, *190*, 107416. [CrossRef]
97. Ghani, U.; Jiang, W.; Hina, K.; Idrees, A.; Iqbal, M.; Ibrahim, M.; Saeed, R.; Irshad, M.K.; Aslam, I. Adsorption of methyl orange and Cr (VI) onto poultry manure-derived biochar from aqueous solution. *Front. Environ. Sci.* **2022**, *10*, 887425. [CrossRef]
98. Islam, M.S.; Roy, H.; Afrose, S. Phosphoric acid surface modified Moringa oleifera leaves biochar for the sequestration of methyl orange from aqueous solution: Characterizations, isotherm, and kinetics analysis. *Remediat. J.* **2022**, *32*, 281–298. [CrossRef]
99. Loc, N.X.; Tuyen, P.T.T.; Mai, L.C.; Phuong, D.T.M. Chitosan-modified biochar and unmodified biochar for methyl orange: Adsorption characteristics and mechanism exploration. *Toxics* **2022**, *10*, 500. [CrossRef] [PubMed]
100. Chen, G.; Yin, Y.; Zhang, X.; Qian, A.; Pan, X.; Liu, F.; Li, R. Enhanced Adsorption of Methyl Orange from Aqueous Phase Using Chitosan–Palmer Amaranth Biochar Composite Microspheres. *Molecules* **2024**, *29*, 1836. [CrossRef] [PubMed]
101. Akl, M.A.; Serage, A.A. Chitosan impregnated sugarcane bagasse biochar for removal of anionic dyes from wastewater. *Sci. Rep.* **2024**, *14*, 27097. [CrossRef] [PubMed]
102. Lu, Y.; Chen, J.; Bai, Y.; Gao, J.; Peng, M. Adsorption properties of methyl orange in water by sheep manure biochar. *Pol. J. Environ. Stud.* **2019**, *28*, 3791–3797. [CrossRef]
103. Nizam, N.U.M.; Hanafiah, M.M.; Mahmoudi, E.; Halim, A.A.; Mohammad, A.W. The removal of anionic and cationic dyes from an aqueous solution using biomass-based activated carbon. *Sci. Rep.* **2021**, *11*, 1–17. [CrossRef] [PubMed]
104. Praveen, S.; Jegan, J.; Pushpa, T.B.; Gokulan, R.; Bulgariu, L. Biochar for removal of dyes in contaminated water: An overview. *Biochar* **2022**, *4*, 10. [CrossRef]
105. Bassareh, H.; Karamzadeh, M.; Movahedirad, S. Synthesis and characterization of cost-effective and high-efficiency biochar for the adsorption of Pb2+ from wastewater. *Sci. Rep.* **2023**, *13*, 15608. [CrossRef] [PubMed]
106. Jameel, R.; Lashari, S.; Sharif, M.N.; Javaid, S.; Alam, K.; Mahmood, F.; Ahmad, W.; Kokab, A. Effective Sequestration of Acid Orange-7 Dye from Wastewater by using Ricinus Communis Biochar along with Zinc Oxide Nanocomposites. *Indus J. Biosci. Res.* **2024**, *2*, 1214–1222. [CrossRef]
107. Eleryan, A.; Güner, E.K.; Hassaan, M.; El-Nemr, M.A.; Ragab, S.; El Nemr, A. Mandarin biochar-CO-TETA was utilized for Acid Red 73 dye adsorption from water, and its isotherm and kinetic studies were investigated. *Sci. Rep.* **2024**, *14*, 13021. [CrossRef] [PubMed]
108. Eleryan, A.; Hassaan, M.; Nazir, M.A.; Shah, S.S.A.; Ragab, S.; El Nemr, A. Isothermal and kinetic screening of methyl red and methyl orange dyes adsorption from water by Delonix regia biochar-sulfur oxide (DRB-SO). *Sci. Rep.* **2024**, *14*, 13585. [CrossRef] [PubMed]
109. Nirmaladevi, S.; Palanisamy, N. A comparative study of the removal of cationic and anionic dyes from aqueous solutions using biochar as an adsorbent. *Desalination Water Treat.* **2020**, *175*, 282–292. [CrossRef]

110. Kaya, N.; Uzun, Z.Y.; Altuncan, C.; Uzun, H. Adsorption of Congo red from aqueous solution onto KOH-activated biochar produced via pyrolysis of pine cone and modeling of the process using artificial neural network. *Biomass Conv. Bioref.* **2022**, *12*, 5293–5315. [CrossRef]
111. Priyanka; Vashisht, D.; Ibhadon, A.O.; Mehta, S.K.; Taylor, M.J. Enhanced wastewater remediation using mesoporous activated wheat straw biochars: A dye removal perspective. *ACS Sustain. Resour. Manag.* **2024**, *1*, 355–367. [CrossRef]
112. Jadhav, S.K.; Thorat, S.R. Adsorption of azo dyes using biochar prepared from regional crop waste material. *Biosci. Biotechnol. Res. Asia* **2022**, *19*, 141–151. [CrossRef]
113. Güleç, F.; Williams, O.; Kostas, E.T.; Samson, A.; Stevens, L.A.; Lester, E. A comprehensive comparative study on methylene blue removal from aqueous solution using biochars produced from rapeseed, whitewood, and seaweed via different thermal conversion technologies. *Fuel* **2022**, *330*, 125428. [CrossRef]
114. Agboola, O.D.; Benson, N.U. Physisorption and chemisorption mechanisms influencing micro (nano) plastics-organic chemical contaminants interactions: A review. *Front. Environ. Sci.* **2021**, *9*, 678574. [CrossRef]
115. Wang, J.; Guo, X. Adsorption isotherm models: Classification, physical meaning, application and solving method. *Chemosphere* **2020**, *258*, 127279. [CrossRef] [PubMed]
116. Mahajan, T.; Paikaray, S.; Mahajan, P. Applicability of the equilibrium adsorption isotherms and the statistical tools on to them: A case study for the adsorption of fluoride onto Mg-Fe-CO3 LDH. *J. Phys. Conf. Ser.* **2023**, *2603*, 12056. [CrossRef]
117. Acharya, A.; Jeppu, G.; Girish, C.R.; Prabhu, B.; Murty, V.R.; Martis, A.S.; Ramesh, S. Adsorption of arsenic and fluoride: Modeling of single and competitive adsorption systems. *Heliyon* **2024**, *10*, e31967. [CrossRef] [PubMed]
118. Hou, Y.; Liang, Y.; Hu, H.; Tao, Y.; Zhou, J.; Cai, J. Facile preparation of multi-porous biochar from lotus biomass for methyl orange removal: Kinetics, isotherms, and regeneration studies. *Bioresour. Technol.* **2021**, *329*, 124877. [CrossRef] [PubMed]
119. Meroufel, B.; Benali, O.; Benyahia, M.; Benmoussa, Y.; Zenasni, M.A. Adsorptive removal of anionic dye from aqueous solutions by Algerian kaolin: Characteristics, isotherm, kinetic and thermodynamic studies. *J. Mater. Environ. Sci.* **2013**, *4*, 482–491.
120. Raza, A.; Mahmoud, M.; Alafnan, S.; Arif, M.; Kirmani, F.U.D.; Kamal, M.S.; Murtaza, M.; Rana, A. Role of high-density brines in reservoir development stages: A review. *Energy Geosci.* **2024**, *5*, 100304. [CrossRef]
121. Tcheka, C.; Conradie, M.M.; Assinale, V.A.; Conradie, J. Mesoporous biochar derived from Egyptian doum palm (Hyphaene thebaica) shells as low-cost and biodegradable adsorbent for the removal of methyl orange dye: Characterization, kinetic and adsorption mechanism. *Chem. Phys. Impact* **2024**, *8*, 100446. [CrossRef]
122. Hassaan, M.A.; Yılmaz, M.; Helal, M.; El-Nemr, M.A.; Ragab, S.; El Nemr, A. Isotherm and kinetic investigations of sawdust-based biochar modified by ammonia to remove methylene blue from water. *Sci. Rep.* **2023**, *13*, 12724. [CrossRef] [PubMed]
123. Wei, X.; Miao, J.; Lv, Z.; Wan, X.; Zhang, N.; Zhang, R.; Peng, S. Phosphate adsorption onto an Al-Ti bimetal oxide composite in neutral aqueous solution: Performance and thermodynamics. *Appl. Sci.* **2022**, *12*, 2309. [CrossRef]
124. Guo, X.; Liu, A.; Lu, J.; Niu, X.; Jiang, M.; Ma, Y.; Liu, X.; Li, M. Adsorption mechanism of hexavalent chromium on biochar: Kinetic, thermodynamic, and characterization studies. *ACS Omega* **2020**, *5*, 27323–27331. [CrossRef] [PubMed]
125. Abdu, M.; Babaee, S.; Worku, A.; Msagati, T.A.M.; Nure, J.F. The development of Giant reed biochar for adsorption of Basic Blue 41 and Eriochrome Black T. azo dyes from wastewater. *Sci. Rep.* **2024**, *14*, 18320. [CrossRef] [PubMed]
126. Van Hien, N.; Valsami-Jones, E.; Vinh, N.C.; Phu, T.T.; Tam, N.T.T.; Lynch, I. Effectiveness of different biochar in aqueous zinc removal: Correlation with physicochemical characteristics. *Bioresour. Technol. Rep.* **2020**, *11*, 100466. [CrossRef]
127. Shafiq, M.; Alazba, A.A.; Amin, M.T. Kinetic and isotherm studies of Ni2+ and Pb2+ adsorption from synthetic wastewater using Eucalyptus camdulensis—Derived biochar. *Sustainability* **2021**, *13*, 3785. [CrossRef]
128. Daffalla, S.; Da'na, E.; Taha, A.; El-Aassar, M.R. Synthesis of a Novel Magnetic Biochar from Lemon Peels via Impregnation-Pyrolysis for the Removal of Methyl Orange from Wastewater. *Magnetochemistry* **2024**, *10*, 95. [CrossRef]
129. Wang, Z.; Li, J.; Liu, G.; Li, C. Biochar obtained from alkaline earth metal-treated mushroom residue: Thermal behavior and methyl orange adsorption capability. *J. Environ. Manag.* **2024**, *351*, 119669. [CrossRef] [PubMed]
130. Maiti, P.; Mangsatabam, M.; Chatterjee, A.; Siddiqi, H.; Mishra, A.; Meikap, B.C. In-situ synthesis of efficient ZnCl2 doped pyrolyzed biochar for adsorptive remediation of organic dyes: Performance evaluation, mass transfer and mechanism. *Sep. Purif. Technol.* **2024**, *329*, 125096. [CrossRef]
131. Diaz-Uribe, C.; Ortiz, J.; Duran, F.; Vallejo, W.; Fals, J. Methyl Orange Adsorption on Biochar Obtained from Prosopis juliflora Waste: Thermodynamic and Kinetic Study. *ChemEngineering* **2023**, *7*, 114. [CrossRef]
132. Lingamdinne, L.P.; Angaru, G.K.R.; Pal, C.A.; Koduru, J.R.; Karri, R.R.; Mubarak, N.M.; Chang, Y.-Y. Insights into kinetics, thermodynamics, and mechanisms of chemically activated sunflower stem biochar for removal of phenol and bisphenol-A from wastewater. *Sci. Rep.* **2024**, *14*, 4267. [CrossRef] [PubMed]
133. Jain, M.; Khan, S.A.; Sahoo, A.; Dubey, P.; Pant, K.K.; Ziora, Z.M.; Blaskovich, M.A. Statistical evaluation of cow-dung derived activated biochar for phenol adsorption: Adsorption isotherms, kinetics, and thermodynamic studies. *Bioresour. Technol.* **2022**, *352*, 127030. [CrossRef] [PubMed]

134. Hanoon, M.A.; Ahmed, M.J. Adsorption of methyl orange from wastewater by using biochar. *Iraqi J. Chem. Pet. Eng.* **2019**, *20*, 23–29. [CrossRef]
135. Azim, E.A.; Samy, M.; Hanafy, M.; Mahanna, H. Novel mint-stalks derived biochar for the adsorption of methylene blue dye: Effect of operating parameters, adsorption mechanism, kinetics, isotherms, and thermodynamics. *J. Environ. Manag.* **2024**, *357*, 120738. [CrossRef] [PubMed]
136. Ding, W.; Habineza, A.; Zeng, X.; Yan, Z.; Yan, J.; Yang, G. Adsorption of Methylene blue and Methyl orange on nano zero-valent iron (nZVI) coated biochar: Column adsorption experiments. *Desalination Water Treat.* **2022**, *260*, 169–178. [CrossRef]
137. Shi, Y.-Y.; Shan, R.; Yuan, H.-R. Effects and mechanisms of methyl orange removal from aqueous solutions by modified rice shell biochar. *Huan Jing Ke Xue Huanjing Kexue* **2019**, *40*, 2783–2792. [PubMed]
138. Zubair, M.; Mu'azu, N.D.; Jarrah, N.; Blaisi, N.I.; Aziz, H.A.; Al-Harthi, M.A. Adsorption behavior and mechanism of methylene blue, crystal violet, eriochrome black T, and methyl orange dyes onto biochar-derived date palm fronds waste produced at different pyrolysis conditions. *Water Air Soil Pollut.* **2020**, *231*, 1–19. [CrossRef]
139. Aladeokin, O.; Fletcher, A. A novel activated carbon material from peanut shells for the removal of methyl orange and methylene blue dyes from wastewater: Kinetics, isotherms and mechanism. *Adsorpt. Sci. Technol.* **2024**, *42*, 02636174241256843. [CrossRef]

Disclaimer/Publisher's Note: The statements, opinions and data contained in all publications are solely those of the individual author(s) and contributor(s) and not of MDPI and/or the editor(s). MDPI and/or the editor(s) disclaim responsibility for any injury to people or property resulting from any ideas, methods, instructions or products referred to in the content.

energies

MDPI

Article

Thermogravimetric Assessment and Kinetic Analysis of Forestry Residues Combustion

João Pedro Silva [1,2,*], Senhorinha Teixeira [2] and José Carlos Teixeira [1]

[1] MEtRICs Research Centre, University of Minho, 4800-058 Guimarães, Portugal; jt@dem.uminho.pt
[2] ALGORITMI Research Centre, LASI (Laboratório Associado de Sistemas Inteligentes), University of Minho, 4800-058 Guimarães, Portugal; st@dps.uminho.pt
* Correspondence: js@dem.uminho.pt

Abstract

The development of combustion experiments in a controlled environment is essential for comparing different fuels and quantifying the influence of different key parameters. It is fundamental to understand the transport phenomena at the particle level to obtain reliable results and information for further proper biomass combustion modeling of large-scale equipment. Hence, this paper presents a comprehensive analysis of the thermal decomposition and kinetic of eight samples of forest biomass fuels in terms of combustion behavior by using the thermogravimetric analysis (TGA) technique. The tests were carried out in an oxidizing atmosphere at a heating rate between 5 and 100 °C/min up to 900 °C. It was observed that, for all samples, fuel conversion follows a sequence of drying, devolatilization, and char combustion. Furthermore, differences in chemical and physical composition, as well as in structures and their thermal stability, justify the differences observed between the mass-loss curves of the different fuels. For this, the complexity of kinetic study is addressed in this paper by using different approaches: isoconversional and model-fitting methods. However, the use of isoconversional methods proved ineffective for determining reliable kinetic parameters, due to their sensitivity to particle conversion. A significant variation in activation energy was observed during the devolatilization stage, ranging from 47.92 to 101.30 kJ/mol. For the char oxidation stage, it ranged from 14.97 to 35.48 kJ/mol. These results highlight Eucalyptus as the most reactive species among those studied.

Keywords: biomass; combustion; forestry residues; kinetic; thermogravimetric analysis

1. Introduction

The energy sector faces regulatory pressure, higher competition, and a demand to provide greater flexibility and environmentally friendly solutions. Due to this, at this time, it is necessary to respond effectively and rapidly to the fast-changing context of the electricity market. Motivated by its availability, widespread abundance, and environmental concerns, solid biomass has become a competitive option to diversify electricity production and direct heat among renewable energy resources [1]. However, although biomass is considered a sustainable, renewable, and CO_2-neutral energy source [1], this characterization has been the subject of significant debate in recent years [2–6]. It is crucial to ensure that only residues from biomass, rather than whole harvested trees, are utilized. Promoting the use of biomass in the industrial sector can help reduce the amount of combustible material in woodlands, thereby lowering the risk of forest fires. This approach offers additional benefits for society, the environment, and the economy [7,8].

According to the last set of data for Portugal [9], in 2023 the contribution of biomass to renewable-energy production was approximately 42%. However, 60% of biomass has been converted into other forms of energy, specifically in cogeneration and dedicated power plants. Thus, biomass represents one of the main vectors contributing to the decarbonization of the primary energy demand and final energy consumption. Regarding these two parameters, biomass contribution is 40% and 36%, respectively, being the main renewable-energy source.

Combustion, the most usual conversion process of solid biomass, still requires further research since it is related to low efficiency and pollutants emissions [10,11]. This is particularly true if low-value fuels are used. Low-value fuels refer to biomass fuels with a high moisture content, high ash or inert content, and a significant proportion of non-wood components, such as bark and leaves. A need for the expansion of knowledge about alternative solid biomass fuels drives the need for the determination of the characteristics of such new energy sources. In recent decades, a lot of research has focused on TGA to study the thermal conversion of solid biomass, particularly considering pyrolysis among the different conversion technologies [12]. Thermogravimetric analysis is particularly suitable for studying biomass combustion as it enables accurate monitoring of mass loss during thermal decomposition, providing essential data to characterize reaction mechanisms and establishing reliable kinetic parameters for modeling combustion behavior.

The environmental atmosphere and the heating program are two crucial parameters influencing TGA. Non-isothermal experiments are generally adopted as they are considered more reliable for further studies and less time-consuming than isothermal experiments [5]. These experiments include information on the temperature dependence of the reaction rate, and it is commonly believed that it would be sufficient to derive the Arrhenius parameters and the reaction model of a process [6]. Consequently, the heating rate is one of the most relevant parameters in TGA as it affects thermal decomposition. Usually, experiments must be performed with several heating rates to solve possible compensation effects [7]. This is an important parameter as it greatly affects the volatiles' release rate due to the thermal inertia of the particles, and, in this way, different heating rates should be applied in order to study its influence [8].

Regarding the ambient atmosphere, an oxidative atmosphere greatly affects the devolatilization behavior [9]. There are some works in the literature reporting the effect of this parameter [10–12]. For instance, according to Anca-Couce et al. [11] and Shen et al. [12], the presence of oxygen enhances biomass decomposition and promotes char combustion.

In the literature, TGA is not only the most usual thermoanalytical technique used for solid-phase thermal degradation studies but also for assessing the kinetics of the different reactions [13,14]. However, the determination of the kinetic parameters for biomass thermal degradation is particularly complicated considering the presence of complex components and their consecutive and/or parallel reactions. There are two main mathematical approaches to obtaining the kinetics data from the thermogravimetric analysis: (1) model-free methods (isoconversional) and (2) model-based methods [7]. In order to avoid modeling complex reactions, model-free methods can be preferable since the chemical parameters are determined without using any specific reaction model [15]. The model-free method generates unique kinetic parameters as a function of the conversion rate since they are based on the principle for each constant conversion; the reaction rate is a function only of the temperature [16].

Hence, reaction kinetics is based on the evaluation of the dependence of the effective activation energy (E), one of the Arrhenius parameters, on the conversion rate according to the TGA data at multiple heating rates, such as suggested by the International Confederation for Thermal Analysis and Calorimetry (ICTAC) [17]. The effective term is applied

to emphasize a consequence of this dependency. Since, in solid-state reactions, the kinetic parameters may vary during the reaction, it is highly recommended to verify if E remains constant to rule out the multi-step kinetic mechanism [18]. If E varies significantly, it means that the reaction process has more than one dominant reaction, and a model-free type cannot be used for kinetic analysis. To overcome this problem, the CR method, a model-based method, is frequently applied by different researchers and yields values of E similar to those calculated by model-free methods, depending on the selected reaction model [7].

Nevertheless, although the complexity and instability of the biomass combustion process is a well-known feature, there are still some recent investigations applying model-free methods [19–24]. Thus, it remains unclear which kinetic method is more effective when analyzing solid biomass combustion. Consequently, the purpose of this study is to analyze the thermal conversion of different forest biomass fuels and their different parts in an oxidative environment and to evaluate their reaction kinetics. The knowledge derived from this work is essential for subsequent modeling and simulation of combustion facilities where the different fuels are important resources.

2. Materials and Methods

2.1. Biomass Feedstock

The selection of biomass was framed by the range of resources and the different parts of the fuels often used in a typical solid biomass power plant [25] and by considering the main forest species in Portugal [26]. Pine, eucalyptus, and acacia are extensively used in Portugal as fuel for power generation. Since Portugal is a reference in modern olive production (it is expected that during the next decade it will be the third largest producer of olive oil in the world [27]) olive-tree pruning should be a very interesting alternative for power generation. According to Nunes et al. [27], Portugal has 361 thousand hectares of olive groves. Hence, residues from olive-grove maintenance or from the olive-oil production process can become an important energy resource. For instance, it was estimated that approximately 50% of the biomass potential in the Mediterranean regions where this residue is available derives from olive-grove maintenance [7].

Therefore, to study their combustion behavior, these four distinct solid fuels were collected in a forest in the northern region of Portugal. As mentioned before, different parts are being used in power plants. To also understand their differences, it was decided to divide each fuel by the different zones of the tree. Thus, all parts of the eucalyptus tree were collected, including the trunk (ET), branches (EB), and bark (EBA). For pine and acacia trees, both the branches (PB for pine and AB for acacia) and the trunk (PT for pine and AT for acacia) were considered. From olive trees, only the branches (OB), excluding leaves and olives, were harvested.

Then, the raw materials were milled in a knife mill into powdered samples until they achieved a size lower than 0.5 mm. After the milling process, the samples were sieved in a vibratory sieve shaker to collect only particles with a size between 0.125 and 0.250 mm. Subsequently, before each thermogravimetric experiment, small samples were stored in a desiccator. During this process, a transition in the color of the lighter trunk samples (inner part) to the darker bark and branches (outer part) was observed. This is commonly associated with increased extractive content in the outer part of the tree [23].

Table 1 presents the elemental and proximate composition, and the calorific value of all solid biomass fuels analyzed in this study. More details about the experimental procedure and the different standards for solid fuel characterization can be found in Silva et al. [28].

Table 1. Physicochemical properties and calorific value of the different biomass fuels [28].

Property	Parameter	Acacia		Eucalyptus			Pine	Olive
		Trunk	Branches	Bark	Trunk *	Branches	Trunk *	Branches
Proximate Analysis (%, db)	Moisture	5.0	6.2	3.4	2.1	6.7	11.5	11.2
	Volatile matter	81.8	77.8	89.6	88.9	82.9	83.7	81.5
	Ashes	1.1	0.7	4.2	1.0	3.2	0.8	1.8
	Fixed Carbon	17.1	21.5	6.2	10.1	13.9	15.5	16.7
Ultimate Analysis (%, db)	Carbon	45.40	52.40	43.10	47.20	55.90	47.30	49.40
	Hydrogen	6.88	7.38	6.46	7.03	7.55	6.40	6.95
	Nitrogen	0.77	3.21	0.25	0.11	1.44	0.13	0.24
	Sulfur	0.01	0.04	0.01	0.01	0.01	0.99	0.88
	Oxygen	46.94	36.97	50.18	45.65	35.10	45.18	42.53
Air–Fuel Ratio (stoichiometric—g_{air}/g_{sample})		5.54	6.94	5.00	5.85	7.48	5.69	6.23
Calorific Value (db)	HHV (MJ/kg)	17.14	20.41	15.20	17.56	22.30	19.10	17.71
	LHV (MJ/kg)	15.66	18.81	13.81	16.05	20.67	18.60	16.22

* without bark, db—dry basis.

2.2. Experimental Conditions

The thermal-conversion behavior of solid biomass fuels was analyzed using a piece of equipment from TA Instruments, model SDT 2960, in non-isothermal conditions up to a maximum temperature of 900 °C within three different regions. The first period of in-situ drying was performed to ensure the complete dehydration of the samples. For this, a heating ramp at 10 °C/min from the ambient temperature up to 105 °C was applied, followed by an isothermal stabilization period of 20 min. Then, a dynamic heating run was carried out with a steady heating rate from 105 to 900 °C.

Nevertheless, preliminary experiments were developed to guarantee that biomass combustion is only temperature-dependent, neglecting transport effects, and, therefore, the experiments were performed according to a pure kinetic regime [10,29]. Achieving this requires careful control of parameters such as particle size, initial mass, and airflow rate. Hence, a parametric analysis was initially developed to understand the influence of the atmosphere, its flow rate, the particle size, and also to evaluate the heating rate [10,29].

These were essential experiments to specify the proper conditions for the development of further thermogravimetric experiments. Furthermore, a strategy was implemented to avoid the differences in the conversion process due to the different moisture contents of the samples, by introducing an initial drying stage. Moreover, blank experiments were carried out to understand the effect of the gas-density variation in the weight measurement, commonly denominated as the buoyancy effect. Although the variation of the weight measurement can be reduced, it is essential to quantify it since the experiments are performed with a small amount of biomass.

Thus, based on the previous experiments, the TGA experiments were developed with particles with a size between 0.125 and 0.25 mm, an initial weight of 10 mg, and an air flow rate of 100 mL/min. (oxidant atmosphere). Additionally, heating rates of 5, 10, 20, and 100 °C/min up to 900 °C were considered after the drying stage. Before each

experiment, the samples were measured on a high-accuracy scale (precision of 0.0001 g) and spread adequately in a 90 µL Alumina crucible used in the TG equipment to avoid diffusion problems.

2.3. Kinetic Study

The kinetic parameters for the eight fuels were determined based on the data generated from the TGA with the low heating rates, 5, 10, and 20 °C/min. This range of low heating rates was selected to balance experimental feasibility with practical relevance, enabling the resolution of overlapping thermal events and, consequently, improving the accuracy of kinetic-parameter estimation.

The fundamental basis of the kinetic models assumes that the solid-state transformation rate from biomass to volatile products, is generally described by Equation (1):

$$\frac{d\alpha}{dt} = k f(\alpha) \tag{1}$$

where t is the time, $f(\alpha)$ is a function called the reaction model which describes the dependence of the reaction model with the conversion rate (α), and k is the thermal dependence term that can be defined by the following Arrhenius Equation (2):

$$k = A \ \exp\left(-\frac{E}{R\,T}\right) \tag{2}$$

Here E is the activation energy (J/mol), T is the absolute temperature (K), R is the universal gas constant (J/mol·K), and A is the pre-exponential factor (s^{-1}). The former parameter is the minimum energy barrier required to break the bonds and change the chemical structure to another, while A is based on the collision theory and represents the number of collisions per unit of time occurring in the reaction.

Regarding the conversion rate, this term can be defined as a relation between the initial (m_0), final (m_f), and instantaneous (m_t) sample mass. It can be obtained from each thermogravimetric experiment, and it is defined by Equation (3):

$$\alpha = \frac{m_0 - m_t}{m_0 - m_f} \tag{3}$$

For non-isothermal experiments, at a constant heating rate ($\beta = dT/dt$), Equation (1) can be expressed as a function of temperature at a constant heating rate, yielding Equation (4):

$$\frac{d\alpha}{dT} = k f(\alpha)\frac{1}{\beta} \tag{4}$$

The experimental conditions and the reaction stage are considered to influence the reaction model. Generally, it is considered to be a first-order reaction, and this function can be expressed as $(1-\alpha)$ [15,30]. Other functions commonly used are presented by White et al. [14]. After all these considerations, Equation (4) can be simplified as

$$\frac{d\alpha}{(1-\alpha)} = \frac{A}{\beta} \ \exp\left(-\frac{E}{R\,T}\right) dT \tag{5}$$

The left side of Equation (5) is a function of the conversion rate, and the right side is a function of the temperature. Integrating both sides of Equation (5), the following equation is obtained:

$$g(\alpha) = \int_0^{\alpha} \frac{d\alpha}{(1-\alpha)} = \frac{A}{\beta} \cdot \int_{T_0}^{T} \exp\left(\frac{-E}{RT}\right) \cdot dT \tag{6}$$

Equation (6) has no exact solution, and it is necessary to use one of the two main mathematical approaches to solve this equation: (1) model-free methods (isoconversional) and (2) model-based methods [7]. Both methods are considered to provide a comprehensive kinetic analysis of the biomass combustion process and to obtain a better understanding of the complex and multi-step nature of biomass thermal degradation.

There are many isoconversional kinetic methods, and in this study, Friedman (FR) [31], Ozawa-Flynn-Wall (OFW) [32,33], Kissinger-Akahira-Sunose (KAS) [34–36], and Starink [37] are considered.

In model-fitting, Coats-Redfern (CR) [38], the most common model, was selected. This model can be fitted to experimental data, resulting in different reaction models that give the best statistical fit to evaluate the kinetic parameters. The CR model uses the asymptotic series expansion for approximating the exponential integral in Equation (6). According to this model, the kinetic parameters can be determined by the equation presented in Table 2 and by neglecting the term *2RT/E*, which can be considered much lower than one. The value of A is then determined from the interception of the plot indicated in Table 2 [10], with the possibility of making this analysis at different stages of the conversion process. Otherwise, to complete the determination of the kinetic parameters A and $f(\alpha)$, usually, the Kissinger or compensation factor methods and master plots methods have been used to obtain both parameters, respectively [39]. The corresponding equations for each model and the advantages and disadvantages of their application can be found in Table 2.

Table 2. Different kinetics methods used in literature—equation and advantages and disadvantages. Adapted from [4,40].

Method	Equation	$E\alpha$ Determination (Slope of the Plots)	Advantages and Disadvantages
FR	$\ln\left[\beta_i\left(\frac{d\alpha}{dT}\right)_{\alpha,i}\right] = \ln[A_\alpha f(\alpha)] - \frac{E_\alpha}{RT_{\alpha,i}}$	$\ln\left[\beta_i\left(\frac{d\alpha}{dT}\right)_{\alpha,i}\right]$ vs $\frac{-1}{RT_{\alpha,i}}$	Simple and accurate; numerically unstable and sensitive to data noise
OFW	$\ln\beta_i = \ln\left[\frac{A_\alpha E_\alpha}{R\, g(\alpha)}\right] - 5.331 - 1.052\frac{E_\alpha}{RT_{\alpha,i}}$	$\ln\beta_i$ vs $\frac{-1.052}{RT_{\alpha,i}}$	Oversimplified temperature integral
KAS	$\ln\left(\frac{\beta_i}{T_{\alpha,i}^2}\right) = \ln\left[\frac{A_\alpha R}{E_\alpha\, g(\alpha)}\right] - \frac{E_\alpha}{RT_{\alpha,i}}$	$\ln\left(\frac{\beta_i}{T_{\alpha,i}^2}\right)vs$ $\frac{-1}{RT_{\alpha,i}}$	More accurate than OFW; oversimplified temperature integral
Starink	$\ln\left(\frac{\beta_i}{T_{\alpha,i}^{1.92}}\right) = \text{Constant} - 1.008\frac{E_\alpha}{RT_{\alpha,i}}$	$\ln\left(\frac{\beta_i}{T_{\alpha,i}^{1.92}}\right)$ vs $\frac{-1.0008}{RT_{\alpha,i}}$	More accurate temperature integral approximation
CR	$\ln\left[\frac{g(\alpha)}{T^2}\right] = \ln\left[\left(\frac{A\,R}{\beta\,E}\right)\left(1-\frac{2\,RT}{E}\right)\right] - \frac{E}{RT}$	$\ln\left[\frac{g(\alpha)}{T_\alpha^2}\right]vs$ $\frac{-1}{RT_\alpha}$	Forcible fitting to reaction mechanism; single values of E are obtained

2.4. Data Analysis

There is a significant amount of data either generated during the experiments or derived from their results. The TG and DTG curves from the TGA experiments allow the identification of different key parameters and indexes. On this basis, the analysis consists of identifying the ignition, peak, and burnout temperature and the maximum, average, and mass-loss rate in the different stages of biomass conversion, as well as the characteristic times when the biomass is ignited and completely oxidized. Furthermore, to assess the combustion performance of the different biomass samples, considering the previous parameters, four indexes can be calculated according to formulas presented by Yu et al. [41]. Hence, indexes for each stage of the biomass conversion, i.e., for ignition, volatile matter release, burnout, and an overall index, were calculated. All this information

enables the thermal decomposition characterization of the different fuels. Table 3 presents all the parameters considered for the characterization of the TGA experiments and a brief description of the meaning of each one.

Table 3. Characteristic parameters considered for thermal-analysis evaluation and comparison.

Property	Parameter	Description
Temperature	T_{ig}	Ignition temperature (°C). Corresponds to the beginning of the weight loss and is defined as the temperature at which the rate of weight loss reaches 1%/min after the initial moisture loss peak in the DTG profile.
	T_b	Burnout temperature (°C). It is identified when the last peak comes to the end and is the temperature at which the sample is completely oxidized. It is taken as the point immediately before the reaction ceases when the rate of weight loss is down to 1%/min.
	T_1	Peak temperature in devolatilization (°C). It is the point at which the maximum reaction rate occurs during devolatilization.
	T_2	Peak temperature in char combustion (°C). It is the point at which the maximum reaction rate occurs during char combustion.
	$T_{\max}$	Temperature at the maximum weight loss (°C). It is the point at which the maximum reaction rate occurs.
Mass Loss	DTG_{mean}	Average weight loss rate, wt.%/min
	$DTG_{\max}$	Maximum weight loss rate, wt.%/min
	R_1	Weight loss during devolatilization, wt.%
	R_2	Weight loss during char combustion, wt.%
	m_b	Residual weight, mg
Time	t_{ig}	Ignition time, min.
	t_b	Burnout time, min.
Indexes	$I = \frac{DTG_{\max}}{t_b \cdot t_{ig}}$	It indicates the ignition performance. This means how fast or slow the fuel is ignited. wt.%/min^3
	$V = \frac{DTG_{\max}}{T_P \cdot T_{ig} \cdot \Delta T_{1/2}}$	Reflects the volatile matter release performance. wt.%/min.T^3
	$B = \frac{\Delta T_b}{\Delta T_{1/2}}$	Expresses the burnout performance. It is inversely proportional to how fast the char burn. (-)
	$C = \frac{DTG_{\max} \cdot DTG_{mean}}{T_b \cdot T_{ig}^2}$	Presents the comprehensive characteristics. The higher the value, the more significantly the samples are burned. wt.%/min^2.T^3

The kinetic parameters were directly obtained from the TGA experiments. Computational tools to derive this information are convenient, more accessible, and faster to handle, which is better for the large number of data acquired during the experiments. In the present study, a code using MATLAB 2020b was developed with mathematical and inbuilt functions to effortlessly smooth, filter, and fit the data. Figure 1 presents the main steps involved in determining the kinetic triplet parameters using different isoconversional methods and the CR equation.

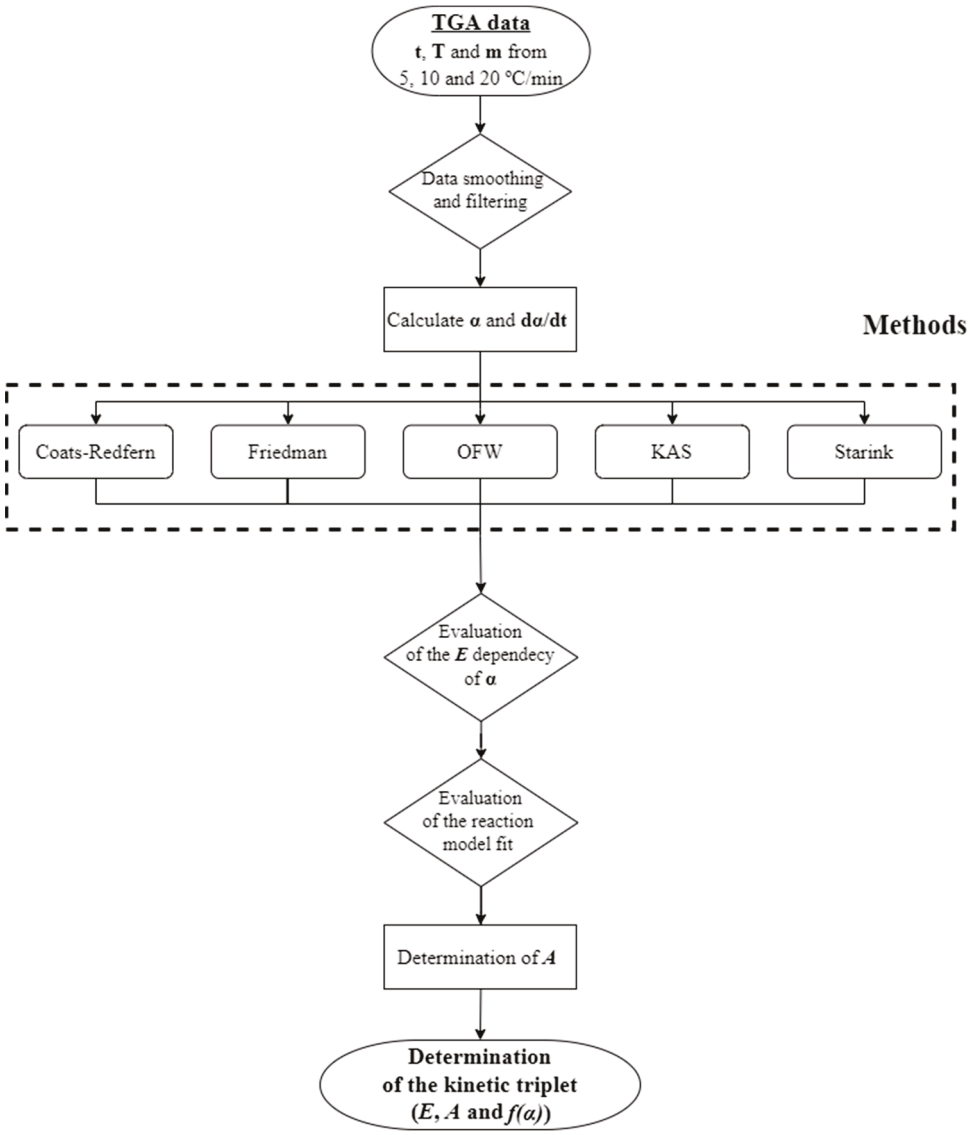


Figure 1. Flowchart of the different stages considered in kinetic analysis.

This set of stages is fundamental to obtaining the effective kinetic parameters for the combustion of the selected fuels [42]. After each experiment, there were more than 3000 data points, and due to the sensitivity of the devices, it is expected that some noise is present in the data. The noise causes a discontinuity in the normal trend of the data and, consequently, leads to mathematical problems in the differentiation. Additionally, during the heating of the biomass sample, there was an amount of water and volatiles that were released, and a decrease in mass with time was expected. Hence, these points were removed, as well as the initial mass loss due to the drying of the fuel, where the weight loss data before 150 °C was not considered. The noise problem was resolved using a local regression applying a weighted linear least square method that smooths the data points and avoids inflection points in the mass-loss curve. Subsequently, the conversion values and their numerical differentiation were easily computed in MATLAB, and the number of data points was reduced according to the ICTAC recommendations [17]. Then, the kinetic parameters were determined by the slope of the numerical plots, which were obtained by the different methods through an inbuilt function for linear fitting.

The particular importance for post-processing TGA data is also highlighted by the utilization of the FR method. This method is different from the other isoconversional methods since it is based on the differential form of the Arrhenius equation, Equation (5),

for the kinetic analysis. In this way, since no approximations or assumptions are used to solve the equation, it is considered more accurate than the other isoconversional methods which are known as integral methods [40]. However, Mishra et al. [43] compared the E values from different isoconversional methods, and it was observed that there were higher values at the end of the conversion from the FR method. This means that the FR method is more dependent on the instantaneous conversion rate and more prone to experimental noise. This statement is in line with the findings reported by Starink [44].

3. Results and Discussion

3.1. Thermal Decomposition

The evaluation of combustion performance at the particle scale is important for understanding the phenomena and acquiring accurate data to determine the kinetics of the different reactions. Since the heating rate is one of the significant factors in thermal decomposition, its influence was firstly analyzed. Then, the differences between each type of fuel and their different parts were analyzed to further understand the conversion of these types of solid fuels. During each thermogravimetric experiment, the values of the temperature (°C) and weight of the sample (mg) were registered at a 1 Hz rate.

3.1.1. Influence of the Heating Rate

Figure 2 presents, for each fuel, the influence of the heating rate on the variation of the normalized weight loss by the thermogravimetric (TG) curve and shows the first derivative of the TG curve—known as the derivative thermogravimetric (DTG) curve—representing the rate of the weight-loss profile. The dashed lines represent the DTG curves while the solid lines correspond to the TG profiles. Looking at the different TG and DTG profiles, the conversion of all biomass fuels takes place over a wide range of temperatures and can be divided into three different zones. The first one is related to the drying stage, which during the experiments was performed at 105 °C for 20 min, mainly to ensure that a large amount of moisture was removed from the sample.

The present results are in agreement with previous studies reported in the literature [5,39,45–48]. However, some of these studies address biomass conversion in an inert atmosphere, and differ particularly in the last conversion stage due to the presence of oxygen that enhances the conversion of the solid residue by at least 15% [10]. Mishra et al. [5] also described an effect of an increase of the peak temperature of around 30 °C for pine, and more than 1% of volatile matter was released when the heating rates of 5 and 20 °C/min were compared. Siddiqi et al. [39] also described the same findings for waste biomass pyrolysis. Moreover, Álvarez et al. [46] studied the combustion of twenty-eight biomass samples using four different heating rates, and it was found that the temperature at maximum DTG of the second stage can occur at lower values, while the last stage can occur up to 627 °C.

Thus, the different characteristic parameters like T_{ig}, T_b, T_1, and T_2, or m_b are a function of the heating rate at which the particle is exposed. Considering the results from the present work, for instance, T_{ig} was seen to have increased from 4 °C up to around 90 °C when the TG results from lower and higher heating rates were compared. t_b was also substantially reduced as the heating rate was increased, achieving values three times lower than those at 5 °C/min. Figure 3 presents an example of the variation of these characteristic parameters, which are not directly observed in the TG and DTG curves T_{max}, T_1, and T_2, for the different parts of eucalyptus fuel. Through these data, it is possible to observe that T_{ig}, t_{ig}, and t_b decreased as the heating rate increased, while the opposite effect was observed for T_b. These findings support the previously mentioned findings, where the higher heating rates were responsible for shifting the TG and DTG profile towards higher combustion temperatures.

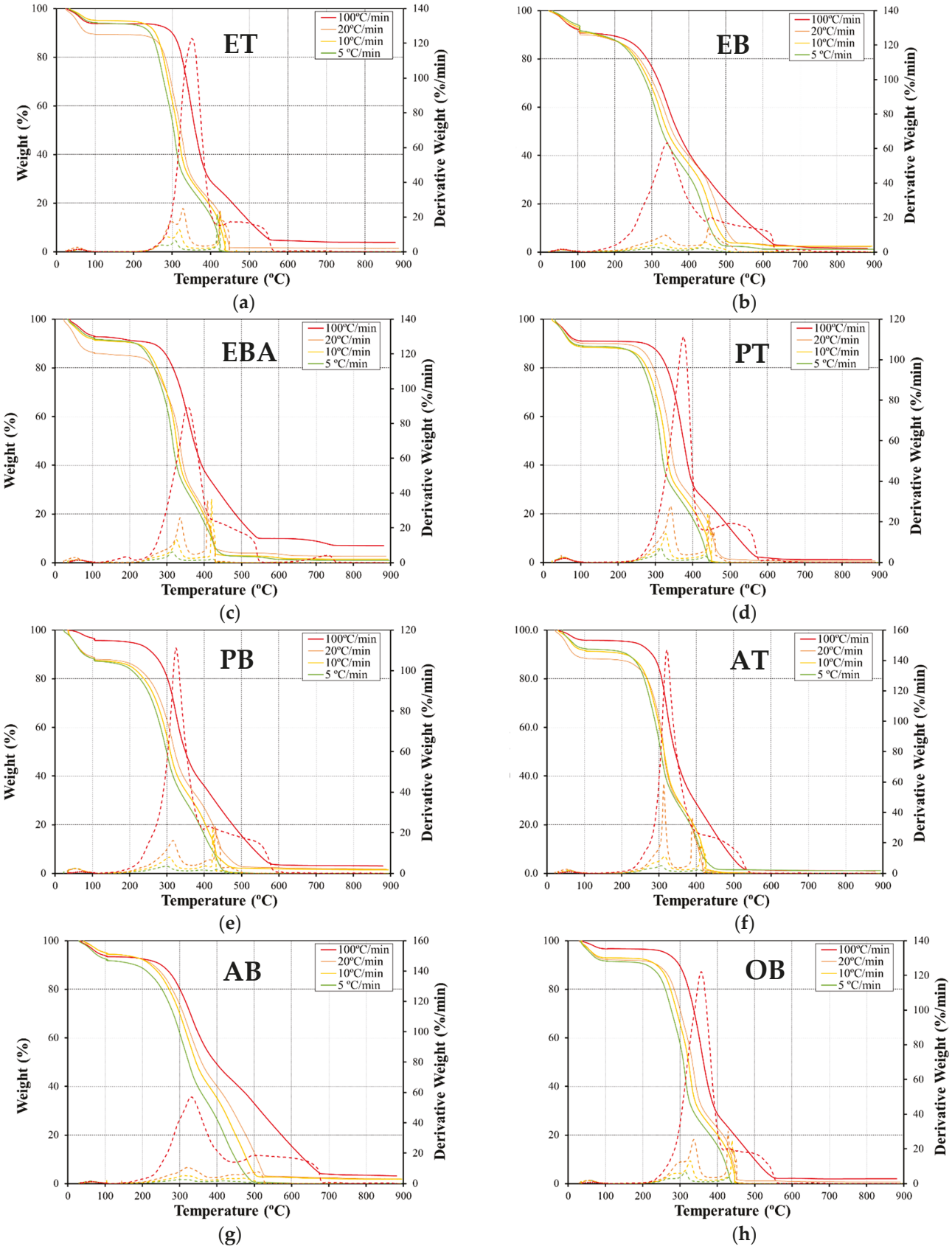


Figure 2. TG and DTG curves of (**a**) ET, (**b**) EB, (**c**) EBA, (**d**) PT, (**e**) PB, (**f**) AT, (**g**) AB, and (**h**) OB.

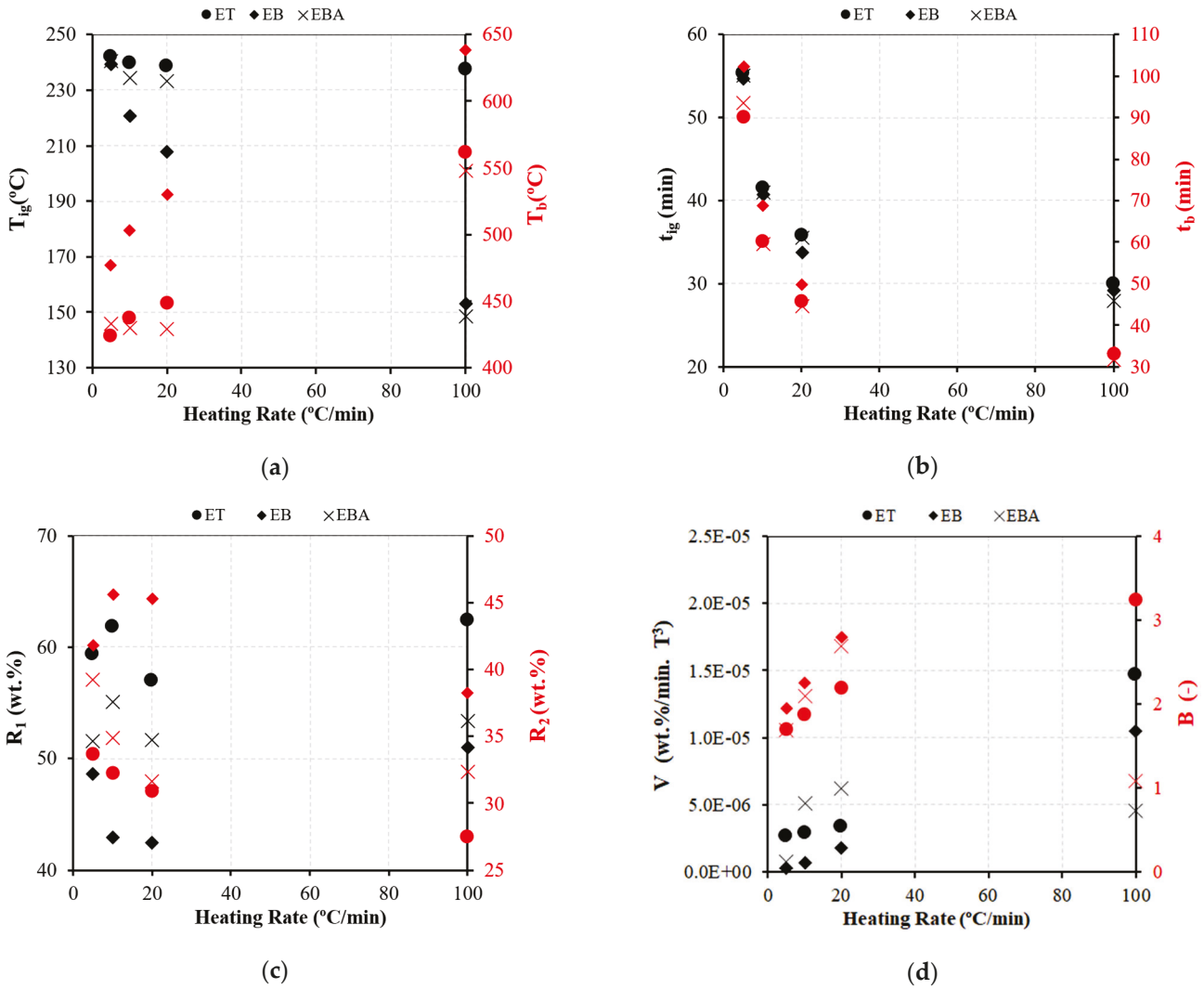


Figure 3. Comparison of the different parts of eucalyptus fuel in terms of characteristic parameters: (**a**) ignition and burnout temperature, (**b**) ignition and burnout time, (**c**) weight loss during devolatilization and char combustion, and (**d**) indexes of volatile-matter release and burnout performance.

However, R_1 and R_2 do not present a clear influence on the heating rate. Nonetheless, if the small fluctuations observed at intermediate heating rates are neglected, the heating rate has an inverse effect on both parameters. As already verified, the weight loss during devolatilization, R_1, tends to increase up to 3%, while the weight loss during the char conversion, R_2, tends to decrease, in particular for EBA, which showed a reduction of 7%. Regarding the volatile matter release (V) and burnout (B) performance indexes, they present a strong correlation with the heating rate since the second and third stages were substantially affected by this parameter. All characteristic parameters for every fuel, at different heating rates, are summarized in Table A1 in Appendix A.

Looking at the patterns of the TG and DTG curves for the different fuels, and their characteristic parameters, there are significant differences between the three samples of eucalyptus. For the inner part of the eucalyptus, the trunk sample, a higher mass loss was observed, as well as a more effective conversion of the second reaction.

Consequently, the combustion of ET is more reactive. According to Vega et al. [23], the thermal conversion of the inner part of biomass fuels is more evident due to their rich cellulosic structure, whereas the outer part is rich in lignin. This is why EBA and EB fuels present a higher conversion of char. EBA conversion in the last region still differs from the other fuels' conversion as it presents a small peak at lower and higher temperatures,

around 180 °C and 725 °C, respectively. A reduced amount of other constituents, like extractives, may be responsible for these variations [14,48].

3.1.2. Comparative Analysis of Various Fuel Types

As previously referred to, there are significant differences in the thermal conversion behavior of all different fuels considered in this work. Also, differences are observed between their different parts. It is evident that the discrepancies are related to the intrinsic variability in the chemical and physical composition as well as in the structures and their thermal stability. The different contents of hemicellulose, cellulose, and lignin are important to justify the differences observed with the TG and DTG curves. For instance, the differences in residual weight at the end of the TGA experiments could be justified by the various contents of lignin, which are also dependent on the fixed carbon content of the samples. Figure 4 presents the conversion of the biomass samples from the trunk part of the different fuels (ET, PT, and AT), for the lowest and highest heating rates. As demonstrated in [28], AT has the highest fixed carbon content and at lower heating rates this was the fuel with the highest residual weight. However, at higher heating rates AT presented the lower m_b since the char conversion increased, as opposed to the behavior presented by the other fuels. Furthermore, it is important to point out that the ET conversion in the third stage presents a high reactivity since there is a higher mass-loss rate identified by a slender peak in the DTG thermogram. This feature is observed for lower heating rates, although the differences between the fuels in this region are not significant at a higher heating rate.

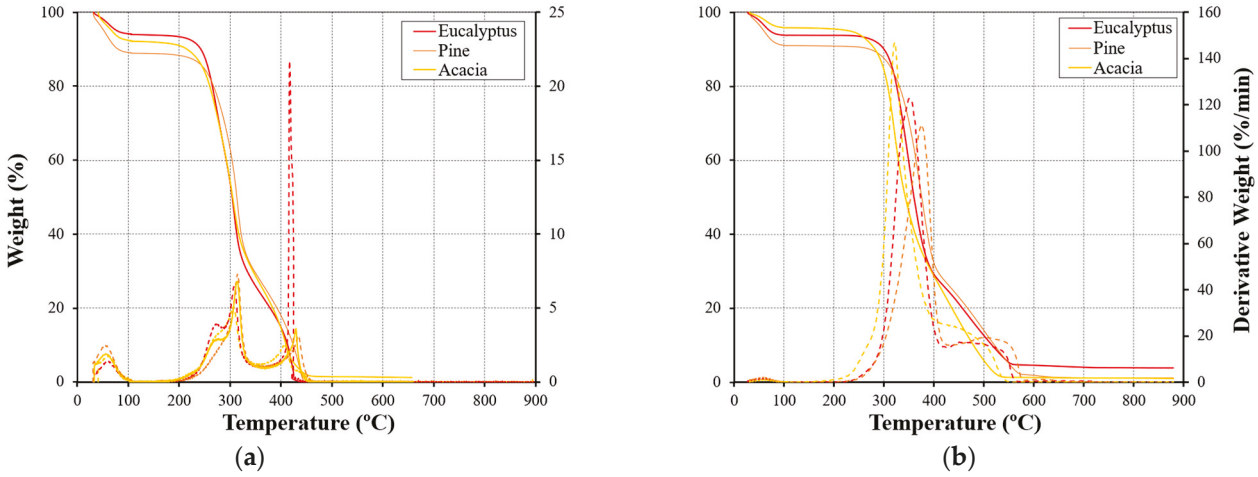


Figure 4. TG and DTG curves for the trunk part of the different samples at: (**a**) lower heating rate—5 °C/min, and (**b**) higher heating rate—100 °C/min.

In contrast, differences in the second stage can be observed. This is another important aspect that should be mentioned as DTG thermograms present large variations. At 5 °C/min the hemicellulose and cellulose, which should be converted in the range of temperatures of the second zone, are converted at different temperatures, while for higher heating rates their degradation overlaps and only one peak is visible. The results presented in Figure 4a suggest that hemicellulose reacts at lower temperatures, and the cellulose conversion occurs at a slightly higher temperature [14]. Moreover, the differences between the three fuels could be explained by looking at the volatile matter, although the cellulose content in these samples is another important factor that affects the maximum weight-loss rate. Figure 5 compares the weight loss from the branch part (EB, PB, AB, and OB) of the four biomass samples.

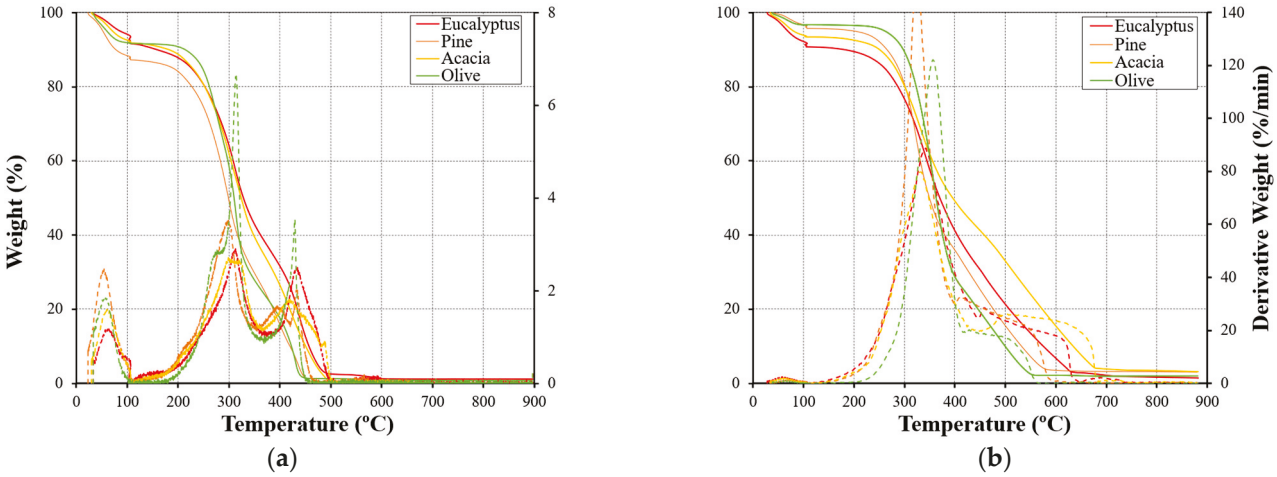


Figure 5. TG and DTG curves for the branch part of the different samples at: (**a**) lower heating rate—5 °C/min, and (**b**) higher heating rate—100 °C/min.

For these fuels, there is no separation of the hemicellulose and cellulose conversion in the second stage and the reactivity is lower than in the trunk samples. However, in the third zone, a higher mass-loss rate was observed as well as a degradation over a wider range of temperatures. Figure 6 presents a comparison of the characteristic parameters for the different fuels. In agreement with the previous discussion, there are differences between the fuels. The OB fuel shows a higher Tig but has the highest value of V since it is the fuel with higher R1. Regarding the performance in the last stage, EB presents higher R2 and B for lower heating rates, while at 100 °C/min PB degradation presented higher values. As demonstrated before for the eucalyptus samples, tig and tb present the same trend but the differences are reduced when the four fuels are compared, in particular at higher heating rates. This indicates that thermal conversion is more dependent on the heating rate than the fuel type.

3.2. Kinetic Parameters

E was calculated using four different isoconversional methods, OFW, FR, KAS, and the Starink method. Although the overall reaction mechanism with a single first-order reaction model is simpler to implement in a Computational Fluid Dynamics (CFD) model, biomass conversion has distinct reactions that need to be considered. The thermal oxidation of biomass is a complex process involving a set of physical processes and chemical reactions and a single reaction cannot correctly determine the kinetic parameters of biomass combustion. Consequently, the kinetic analysis relies on a two-step consecutive reaction model, which is composed of the two essential single reactions that more realistic describe the biomass combustion. The reaction scheme is hypothesized by Equations (7) and (8):

$$\text{Biomass} \xrightarrow{k_1} \text{Gases} + \text{Char} \quad (7)$$

$$\text{Char} \xrightarrow{k_2} \text{Gases} + \text{Residue} \quad (8)$$

Hence, the two main conversion processes, dealing with the devolatilization and char oxidation, are modeled.

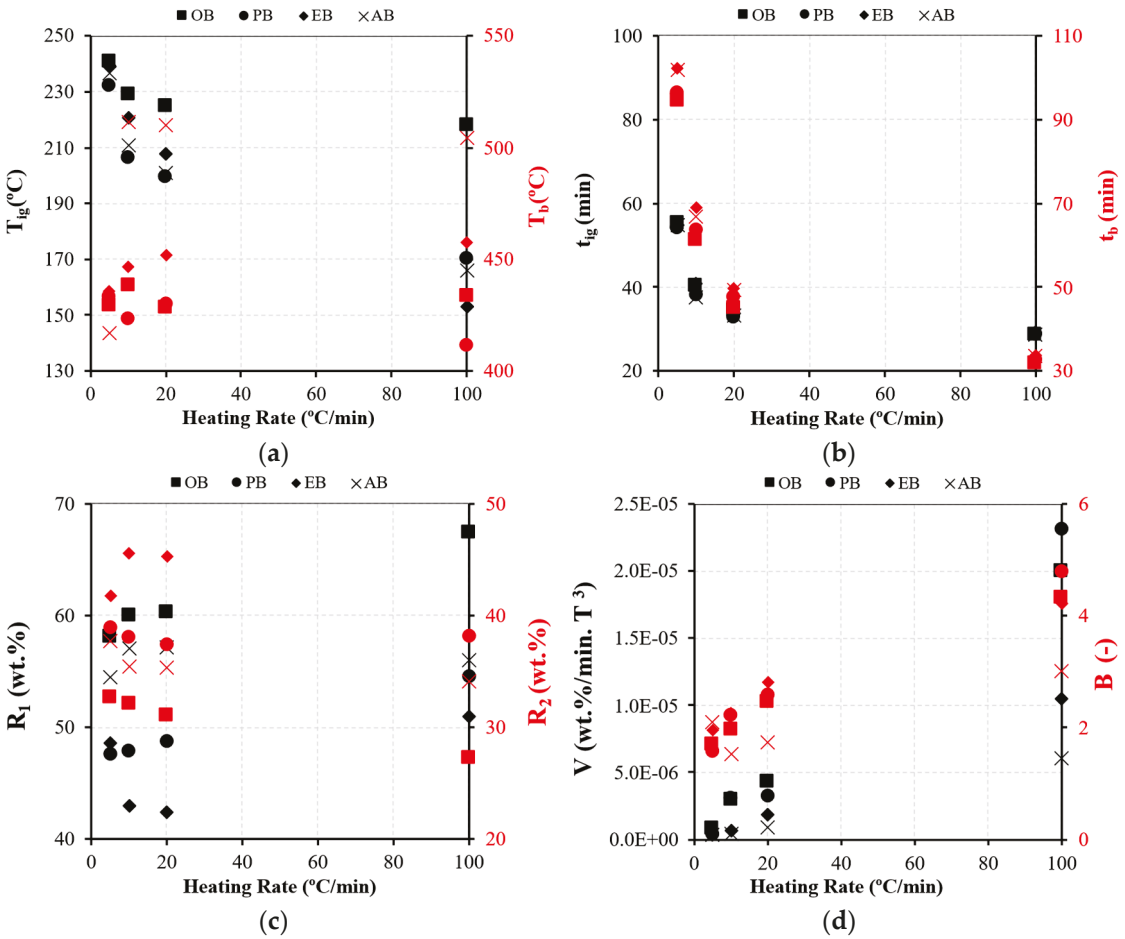


Figure 6. Comparison of the different biomass fuels (from the same part of the tree—branches) in terms of characteristic parameters: (**a**) ignition and burnout temperature, (**b**) ignition and burnout time, (**c**) weight loss during devolatilization and char combustion, and (**d**) indexes of volatile matter release and burnout performance.

3.2.1. Evaluation of the Kinetic Method

The *E* calculated for all isoconversional methods considered in this work was obtained by linear regression, as indicated in Table 2. The plot of different terms enabled the determination of *E* for a conversion range between 5% and 95%, using a step size of 5%, as recommended by ICTAC [17]. Figure 7 presents the plots using the different specifications of the four kinetic methods, and the corresponding *E* was determined for each conversion by the linear equation [17].

Figure 8 presents an example of the results for *E* as a function of the conversion for the ET sample. It can be observed that the OFW, KAS, and Starink methods yield similar results, while, when using the FR method, the results are distinct. The first three methods are based on an integral form and, although there are some approximations associated with the temperature function, the results are similar. However, the FR method is based on the differential form of the conversion equation, without assumptions to assess the temperature function. Consequently, this method is sensitive to the experimental results with noise and zones where the reaction starts spontaneously, and it is known to be more susceptible to inconsistent results [40]. However, the plot for *E* is useful for understanding the nature of the decomposition reaction and for defining zones where the different reaction takes place. Table 4 presents the average *E* values considering the two main reactions during biomass combustion.

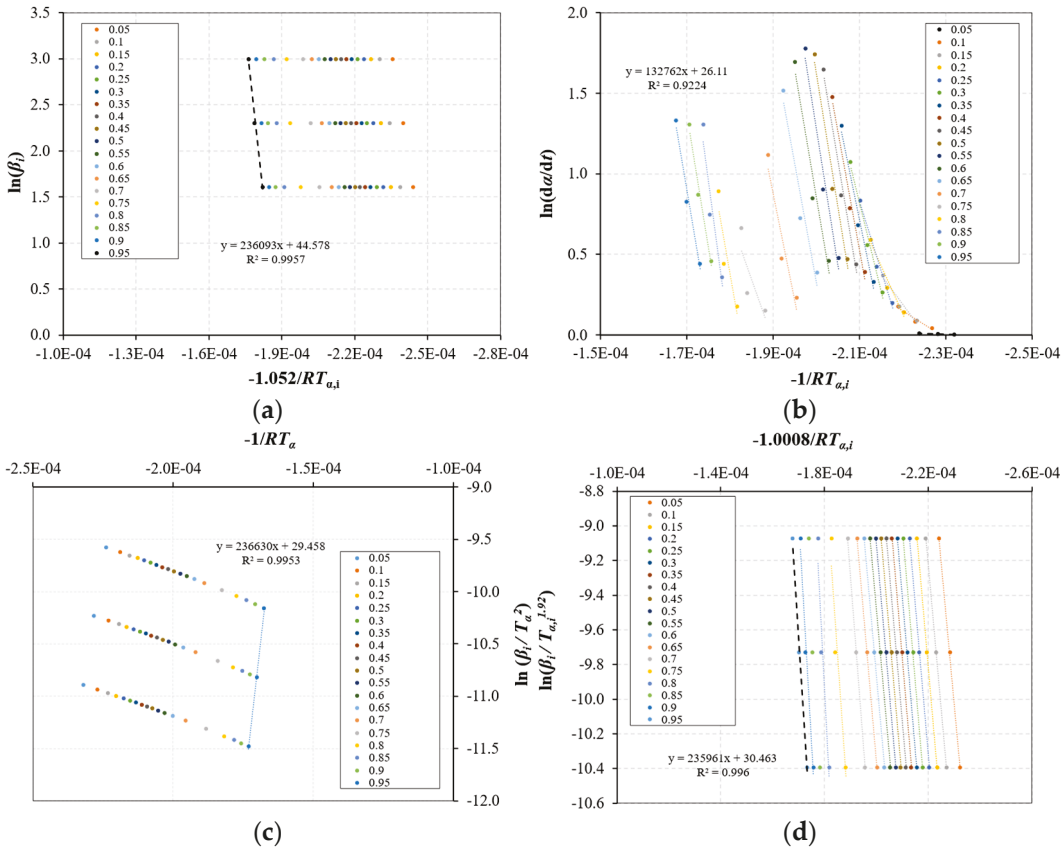


Figure 7. Curves obtained for the different methods: (**a**) OFW, (**b**) FR, (**c**) KAS, and (**d**) Starink for ET sample.

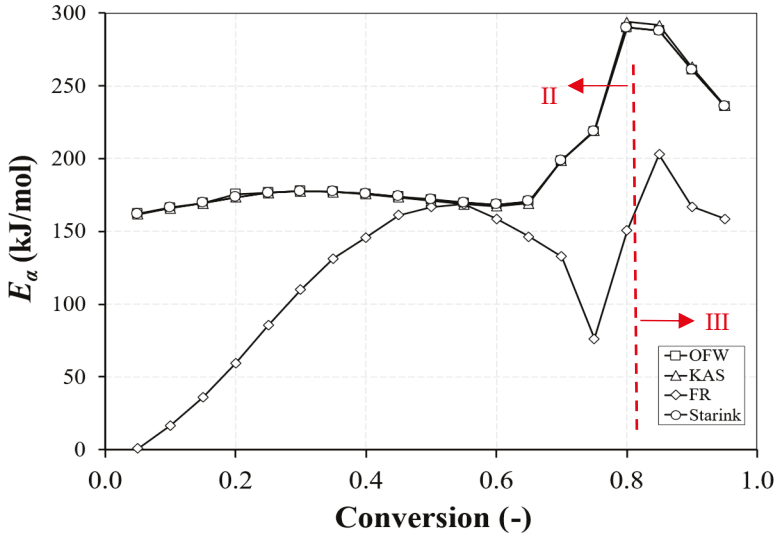


Figure 8. *E* value as a function of the conversion for ET. The red dashed line symbolizes the transition from the devolatilization (II) to the char oxidation (III) reaction during the combustion of biomass.

Nevertheless, the dependence of *E* on conversion is an indication that this is made up of independent and consecutive reactions. This is expected since biomass is composed of different components that decompose in different temperature ranges. Hence, since *E* varies significantly with conversion, isoconversional methods are not recommended [17]. This is because isoconversional methods assume that *E* remains constant throughout the entire biomass conversion process, which can lead to systematic errors [14]. To overcome this limitation, the CR method has been successfully applied to determine the kinetic

parameters [12,15,20,46,49–52]. Hence, subsequently, the fitting of the CR method was evaluated using four types of simple reaction models, the 1st and 2nd order reaction models and the 1D and 2D diffusion models. Figure 9 presents an example of the linear regression curves, applying the separation based on the two different conversion stages of biomass combustion, which present 65% of conversion. In Table 2 (Appendix A), it is possible to verify the reaction mechanism selected to fit the conversion of each fuel and the corresponding kinetic parameters obtained through the linear regression equations. The linear correlation coefficient was higher than 0.906, representing a reasonable and acceptable data fit for all biomass fuels considered in this study.

Table 4. Average *E* values (kJ/mol) obtained by the different kinetic methods for ET, PT, and AT.

	ET	PT	AT
OFW			
Devolatilization	172.01	161.41	177.00
Char Combustion	248.78	211.84	258.46
KAS			
Devolatilization	171.27	160.40	176.68
Char Combustion	250.55	219.37	260.69
FR			
Devolatilization	106.67	87.64	103.09
Char Combustion	148.02	129.16	236.85
Starink			
Devolatilization	171.13	166.35	176.92
Char Combustion	248.69	215.53	260.93

3.2.2. Influence of the Type of Fuel

Taking into account that *E* means the minimum quantity of energy required to initiate chemical reactions, lower values correspond to higher reactivity. According to the kinetic data presented in Table 2 (Appendix A), the biomass fuels can be ranked by their reactivity in the devolatilization conversion process as EB > AB > PB > EBA > AT > OB > PT > ET. The values vary between 47.92 and 101.30 kJ/mol while, for char oxidation, *E* ranges from 14.97 to 35.48 kJ/mol. The devolatilization conversion was best characterized by reaction kinetics, using a second-order reaction model, and the char oxidation was successfully described by a diffusion-controlled mechanism. The diffusion of oxygen to char affects the combustion process and should be considered the main mechanism of thermal conversion of biomass in the last stage. The significant difference between *E* for the two stages is due to the lower values of *E* for lignin conversion when compared to cellulose degradation [46]; less energy is required to break the chemical bonds in lignin. Additionally, as there are different thermal conversion behaviors in the last stage of biomass combustion, the reactivity for this stage is defined as: ET > OB > PT > PB > AB> AT > EB > EBA.

Hence, the fuel type presented a significant influence on the activation energy during biomass combustion. Regarding the effect of the heating rate, the dependence of *E* with the heating rate was less evident and not all fuels presented a consistent trend with the heating rate. According to the literature, Magalhães et al. [15] analyzed the effect of the heating rate on the kinetic behavior, and a marginal difference was also reported. Álvarez et al. [46] studied the kinetic behavior of different biomass fuels including eucalyptus, olive, and pine, and similar results were observed. In this study, olive fuel also presented a lower reactivity. Fang et al. [49] and Shen et al. [51] determined *E* for pine combustion using a two-stage mechanism and CR method. Both studies presented lower energy requirements for char oxidation. Thus, the results from the present study are in the range of the reported

results in the literature, although a small variation was detected, which can be attributed to the different physiochemical compositions of the biomass fuels.

Regarding the pre-exponential factor, another observation should be highlighted since the *A* parameter presented a dependence on the heating rate. As the heating rate increased, *A* also increased. As suggested by Siddiqi et al. [39] this behavior represents the increase in frequency and intensity of collisions among the molecules.

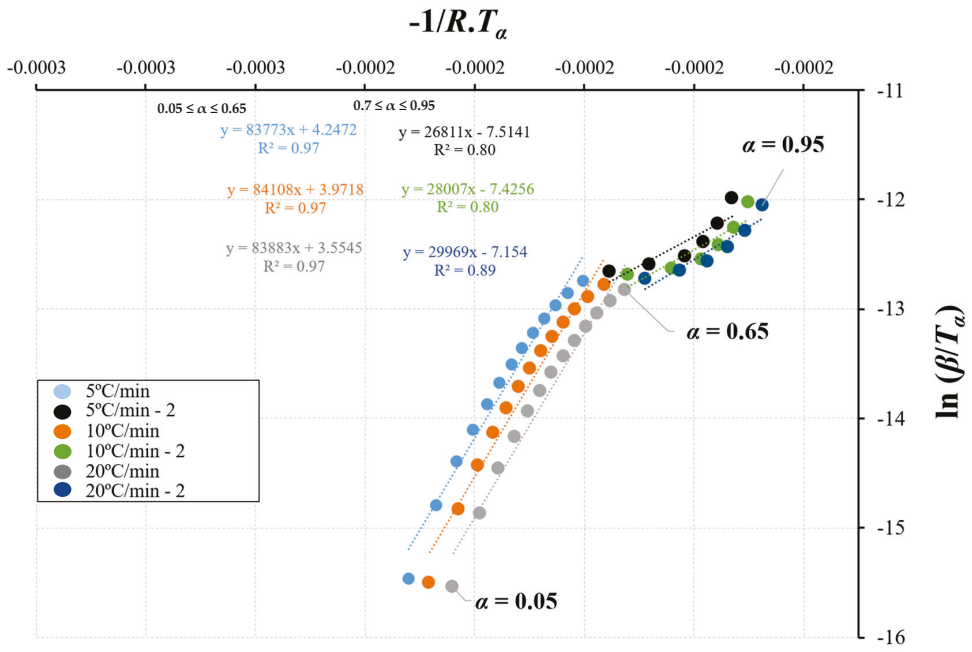


Figure 9. Curves obtained for CR method considering a first-order reaction and for ET sample.

3.3. Reconstruction and Modeling

Based on the *E* and *A* data determined for the second and third stage, the conversion rate α can be predicted based on Equations (9) and (10) or (11), respectively.

$$\text{Biomass} \xrightarrow{k_1} \text{Gases} + \text{Char} \quad \frac{d\alpha_1}{dt} = \frac{1}{\beta} A_1 \cdot \exp\left(\frac{-E_1}{RT}\right) \cdot (1-\alpha)^2 \tag{9}$$

$$\text{Char} \xrightarrow{k_2} \text{Gases} + \text{Residue} \quad \frac{d\alpha_2}{dt} = \frac{1}{\beta} A_2 \cdot \exp\left(\frac{-E_2}{RT}\right) \cdot \frac{1}{2\alpha} \tag{10}$$

$$\text{Char} \xrightarrow{k_2} \text{Gases} + \text{Residue} \quad \frac{d\alpha_2}{dt} = \frac{1}{\beta} A_2 \cdot \exp\left(\frac{-E_2}{RT}\right) \cdot [-\ln(1-\alpha)]^{-1} \tag{11}$$

Two possibilities were considered for the third reaction stage since the best fit to predict the conversion of EBA fuel differs from the other fuels. Hence, the char conversion was computed considering the 2D diffusion mechanism for EBA fuel (Equation (11)), while for the other fuels the conversion was predicted by using the 1D diffusion mechanism (Equation (10)).

Figure 10 illustrates the reconstruction and modeling of conversion as a function of temperature for the heating rates 5, 10, and 20 °C/min using parameters derived from the CR method. There are differences, in particular, at the initial stages of the conversion, and mainly for trunk samples (ET, PT, and AT). The differences are due to the hemicellulose and cellulose degradation at different temperatures in the second stage, and the average *E* for the second stage had some difficulties with reproducing the experimental behavior. The difference between the experimental and computed curves is a measure of the applicability of the derived kinetic parameters. To facilitate the comparison of the data, the square of the

Pearson product moment correlation coefficient through the experimental and calculated values was determined for each fuel and heating rate. This value is interpreted as the proportion of the variance in the experimental results attributable to the variance in the results. A value above 0.95 was obtained, which corresponds to a good correlation between the experimental and numerical results. Therefore, the differences may be considered acceptable from the perspective of engineering calculations and predictions.

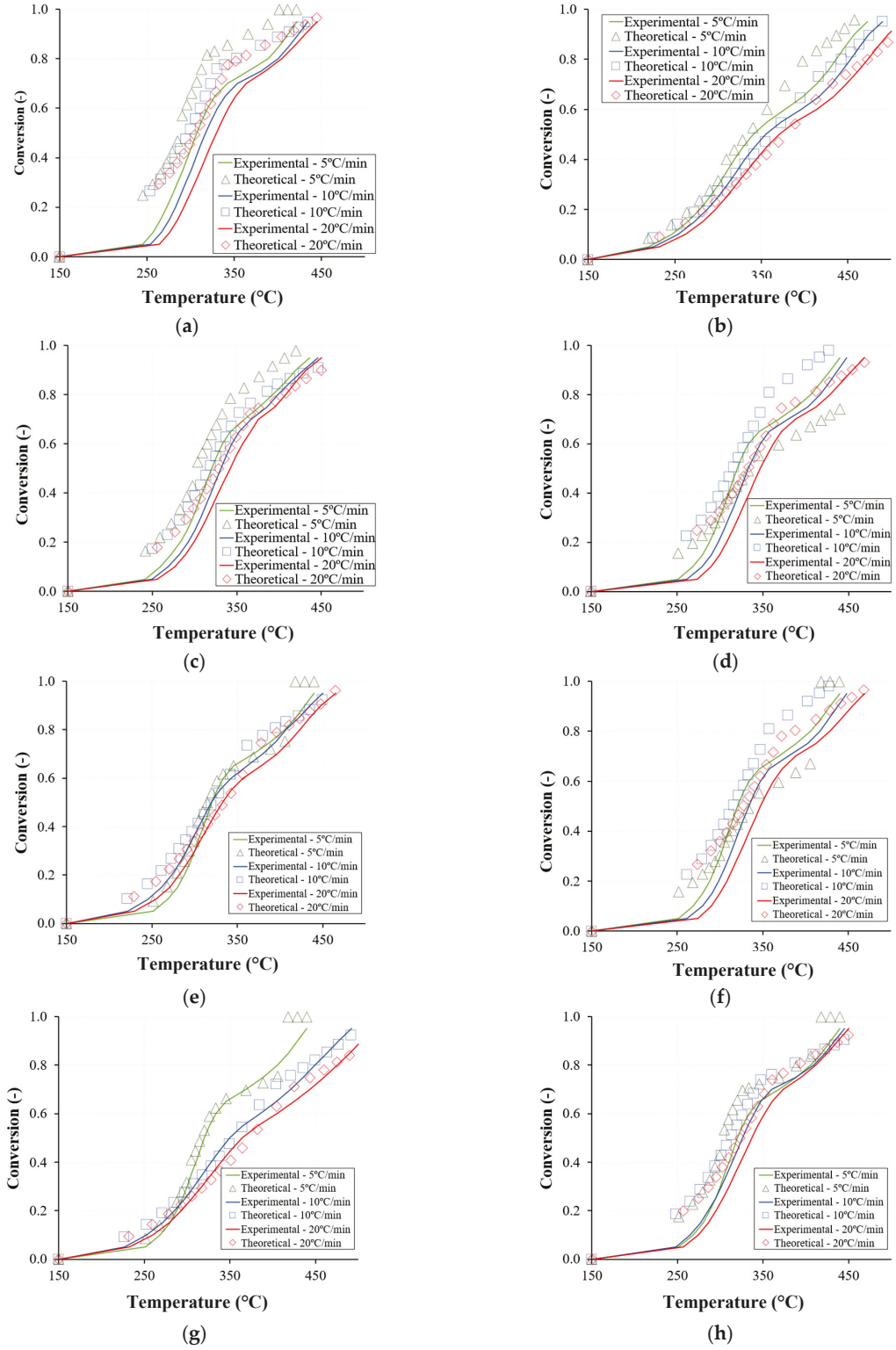


Figure 10. Comparison between experimental and modeled conversion results for the different samples: (**a**) ET, (**b**) EB, (**c**) EBA, (**d**) PT, (**e**) PB, (**f**) AT, (**g**) AB, and (**h**) OB.

4. Conclusions

This paper presents a comprehensive analysis of the thermal decomposition and kinetics of various forest biomass fuels. The combustion behavior for the scales and conditions relevant to the operation in an industrial environment was analyzed, while a two-step reaction mechanism was used to describe the reaction kinetics. The main conclusions can be summarized as follows:

- The evaluation of combustion performance at a particle scale by TGA showed that the conversion of all biomass fuels takes place over a wide range of temperatures, which can be divided into three different zones: drying, devolatilization, and char combustion;
- Regarding the differences between the combustion behavior of the different fuels, a higher mass was observed for the inner part of the fuels, and there was a more effective conversion of the second-stage reaction. In its turn, the outer part of the eucalyptus presents a higher conversion of char, which may be associated with the higher lignin content of this fuel. Thus, variations in the chemical and physical composition, as well as in the structures and their thermal stability, justify the differences between the TG and DTG curves;
- Based on the TGA data, a kinetic analysis was performed, which relied on a two-step consecutive reaction model. The utilization of isoconversional methods proved ineffective in determining the kinetic parameters since E is not constant throughout the particle conversion. The CR method was successfully applied to determine the kinetic parameters to overcome this limitation;
- The devolatilization conversion was best characterized by the reaction kinetics model, using a second-order model, and the char oxidation was successfully described by a diffusion-controlled mechanism. The oxygen diffusion to the char affects the combustion process and should be considered the main mechanism of thermal conversion of biomass in the last stage;
- The kinetic parameters during biomass combustion are strongly dependent on the type of fuel, while the effect of the heating rate was less evident, and not all fuels presented a consistent trend with the heating rate. According to the results, during the main conversion stage, devolatilization, the branch part of the fuels presented a lower energy of activation, while eucalyptus was the most reactive fuel.

Although the experiments were conducted on a laboratory scale, they provided valuable insights into transport phenomena at the particle level. The comparative analysis of kinetic modeling methods offers a novel contribution to the field. These findings can significantly support the scientific community by informing the development of more accurate CFD models, where the derived kinetic parameters enable the detailed prediction of particle mass loss and its integration with gas-phase reactions. Future work should explore the application of these parameters in larger-scale equipment and validate the models under real combustion conditions.

Author Contributions: Conceptualization, J.P.S., S.T. and J.C.T.; Methodology, J.P.S., S.T. and J.C.T.; Investigation, J.P.S.; Writing—Original Draft Preparation, J.P.S., J.C.T. and S.T.; Writing—Review and Editing, J.P.S., J.C.T. and S.T.; Supervision, J.C.T. and S.T. All authors have read and agreed to the published version of the manuscript.

Funding: This research was funded by Portuguese Foundation for Science and Technology (FCT) grant number SFRH/BD/130588/2017.

Data Availability Statement: Data is contained within the article.

Acknowledgments: The first author would like to express his acknowledgment for the support given by the Portuguese Foundation for Science and Technology (FCT) through the PhD grant SFRH/BD/130588/2017. FCT has supported this work within the R&D Units Project Scope UIDB/00319/2020 (ALGORITMI) and R&D Units Project Scope UIDP/04077/2020 (MEtRICs).

Conflicts of Interest: The authors declare no conflicts of interest.

Nomenclature

Latin symbols

A	Pre-exponential factor, s^{-1}
B	Burnout performance, -
C	Comprehensive index, $\%/min^2T^3$
E	Activation energy, J/mol
I	Ignition performance index, $\%/min^3$
k	Rate constant, s^{-1}
m	Mass, kg
R	Universal Gas Contant, J/mol·K/Weight loss, %
t	Time, s
T	Temperature, °C
V	Volatile matter release performance, $\%/T^3$

Greek symbols

α	Extent of reaction, -
$f(\alpha)$	Reaction model, -
$g(\alpha)$	Integral form of the reaction model, -
β	Heating rate, K/min

Subscripts and superscripts

0	Initial
i	Instantaneous
b	Burnout

List of Acronyms

AB	Acacia Branch
AT	Acacia Trunk
CR	Coats-Redfern
DTG	Derivative thermogravimetry
EB	Eucalyptus Branch
EBA	Eucalyptus Bark
ET	Eucalyptus Trunk
FR	Friedman method
ICTAC	International Confederation for Thermal Analysis and Calorimetry
KAS	Kissinger-Akahira-Sunose linear integral method
OB	Olive Branch
PB	Pine Branch
PT	Pine Trunk
OFW	Ozawa-Flynn-Wall linear integral method

Appendix A

Table A1. Characteristic parameters obtained for different experiments.

Fuel	β (°C/min)	Temperatures					Mass Loss				Time			Indexes			
		T_{ig}	T_b	T_1	T_2	T_{max}	DTG_{mean}	DTG_{max}	R_1	R_2	m_b	t_{ig}	t_b	I	V	B	C
ET	5	241.78	423.96	309.02	416.42	416.42	21.20	0.58	59.41	33.64	0.155	55.28	90.01	4.26×10^{-3}	2.64×10^{-6}	1.70	4.97×10^{-7}
	10	239.78	436.98	318.90	423.89	423.89	23.01	1.17	61.80	32.25	0.145	41.44	60.03	9.25×10^{-3}	2.87×10^{-6}	1.88	1.07×10^{-6}
	20	238.42	448.47	328.18	423.93	328.18	24.93	2.14	56.98	30.92	0.184	35.75	45.59	1.53×10^{-2}	3.33×10^{-6}	2.19	2.09×10^{-6}
	100	237.36	561.91	350.87	451.07	350.87	122.71	9.98	62.45	27.48	0.481	29.95	32.93	1.24×10^{-1}	1.47×10^{-5}	3.24	3.87×10^{-5}
EB	5	239.47	476.82	313.68	435.70	313.68	2.90	0.57	48.66	41.82	0.448	54.68	102.18	5.19×10^{-4}	3.16×10^{-7}	1.95	5.99×10^{-8}
	10	220.59	503.16	321.57	446.47	446.47	5.64	1.10	42.97	45.59	0.453	40.65	68.84	2.02×10^{-3}	6.36×10^{-7}	2.26	2.53×10^{-7}
	20	207.92	530.03	336.67	451.63	451.63	14.57	2.15	42.48	45.30	0.391	33.71	49.72	8.69×10^{-3}	1.81×10^{-6}	2.80	1.37×10^{-6}
	100	152.94	638.04	342.43	457.31	342.43	63.39	9.94	51.04	38.28	0.296	29.11	33.57	6.49×10^{-2}	1.05×10^{-5}	4.22	4.22×10^{-5}
EBA	5	240.55	432.91	315.18	428.77	315.18	6.21	0.57	51.62	39.23	0.490	55.06	93.41	1.21×10^{-3}	7.21×10^{-7}	1.69	1.41×10^{-7}
	10	234.19	429.65	326.22	419.17	419.17	36.34	1.12	55.07	34.86	0.318	40.90	59.40	1.50×10^{-2}	5.12×10^{-6}	2.10	1.72×10^{-6}
	20	233.37	428.77	335.65	408.17	408.17	35.47	2.05	51.71	31.66	0.536	35.54	44.62	2.24×10^{-2}	6.25×10^{-6}	2.69	3.11×10^{-6}
	100	148.60	547.86	356.69	726.63	356.69	89.77	9.52	53.41	32.40	0.914	27.95	31.54	1.02×10^{-1}	4.58×10^{-6}	1.08	7.06×10^{-5}
PT	5	251.92	445.11	316.35	436.46	316.35	7.14	0.55	51.85	36.78	0.007	57.25	95.76	1.30×10^{-3}	7.46×10^{-7}	1.61	1.39×10^{-7}
	10	247.39	450.12	328.17	440.06	440.06	24.05	1.09	54.60	33.21	0.102	43.28	62.54	8.89×10^{-3}	2.65×10^{-6}	1.81	9.52×10^{-7}
	20	242.06	484.53	339.58	444.82	339.58	27.88	2.19	57.14	32.38	0.175	35.15	47.19	1.68×10^{-2}	3.22×10^{-6}	2.30	2.16×10^{-6}
	100	240.67	579.16	374.80	505.04	374.80	111.47	9.98	61.99	27.83	0.192	29.62	32.74	1.15×10^{-1}	9.49×10^{-6}	2.60	3.32×10^{-5}
PB	5	232.17	443.93	298.05	433.13	298.05	3.46	0.54	47.61	38.96	0.24	54.09	96.29	6.64×10^{-4}	3.70×10^{-7}	1.57	7.60×10^{-8}
	10	206.23	461.45	307.79	423.42	423.42	22.61	1.08	47.94	38.07	0.36	37.99	63.45	9.38×10^{-3}	3.08×10^{-6}	2.21	1.06×10^{-6}
	20	199.27	494.73	315.32	430.09	430.09	23.03	2.11	48.77	37.45	0.27	32.70	47.49	1.48×10^{-2}	3.19×10^{-6}	2.57	1.69×10^{-6}
	100	170.05	589.39	323.58	411.21	323.58	111.16	10.31	54.54	38.18	0.31	28.72	32.57	1.19×10^{-1}	2.31×10^{-5}	4.79	1.75×10^{-5}
AT	5	238.62	421.24	308.75	404.83	308.75	5.08	0.57	54.83	36.22	0.56	54.46	90.78	1.03×10^{-3}	7.18×10^{-7}	1.90	1.20×10^{-7}
	10	225.80	424.92	316.04	411.38	411.38	20.68	1.13	54.07	36.95	0.25	40.46	59.00	8.66×10^{-3}	3.04×10^{-6}	2.09	1.08×10^{-6}
	20	217.41	417.51	312.98	389.47	312.98	58.08	2.11	51.09	36.14	0.15	34.93	44.18	3.76×10^{-2}	1.12×10^{-5}	2.62	6.22×10^{-6}
	100	196.59	539.53	321.96	457.54	321.96	146.91	10.50	58.49	36.33	0.10	29.23	32.35	1.55×10^{-1}	1.71×10^{-5}	2.53	7.40×10^{-5}
AB	5	236.71	471.81	304.35	417.05	304.35	2.71	0.57	54.50	37.74	0.48	54.73	101.62	4.87×10^{-4}	3.34×10^{-7}	2.09	5.89×10^{-8}
	10	210.91	505.79	317.73	511.51	317.73	5.27	1.15	57.11	35.51	0.30	37.58	66.84	2.10×10^{-3}	4.06×10^{-7}	1.52	2.69×10^{-7}
	20	200.77	527.77	321.61	510.10	321.61	10.67	2.27	57.17	35.34	0.32	33.18	49.21	6.53×10^{-3}	8.77×10^{-7}	1.73	1.14×10^{-6}
	100	165.86	680.97	332.70	504.08	332.70	57.00	10.03	56.09	34.19	0.37	28.63	33.38	5.96×10^{-2}	6.03×10^{-6}	3.01	3.05×10^{-5}
OB	5	240.99	437.76	313.61	429.19	313.61	6.67	0.57	58.18	32.75	0.02	55.33	94.43	1.28×10^{-3}	7.63×10^{-7}	1.70	1.49×10^{-7}
	10	229.04	445.48	327.79	438.42	438.42	24.56	1.15	60.08	32.11	0.11	40.25	61.21	9.97×10^{-3}	2.96×10^{-6}	1.96	1.20×10^{-6}
	20	224.65	451.47	336.07	428.49	428.49	30.05	2.24	60.34	31.13	0.18	34.45	44.99	1.94×10^{-2}	4.31×10^{-6}	2.45	2.96×10^{-6}
	100	218.13	558.84	354.60	433.67	354.60	122.13	10.50	67.48	27.25	0.19	28.70	31.78	1.34×10^{-1}	2.00×10^{-5}	4.31	4.82×10^{-5}

Table A2. Reaction mechanism, linear regression, and kinetic parameters obtained through the CR method.

Fuel	Reaction and Mechanism	β (°C/min)	Equation	R^2	E (kJ/mol)	A (min^{-1})
ET	Devolatilization/2nd order	5	$y = 101295x + 8.2521$	0.992	101.30	2.34×10^8
		10	$y = 101251x + 7.8343$	0.991	101.25	3.08×10^8
		20	$y = 100489x + 7.2413$	0.990	100.49	3.37×10^8
	Char oxidation/1D diffusion	5	$y = 15839x - 10.5$	0.908	15.84	0.26
		10	$y = 16605x - 10.452$	0.906	16.61	0.58
		20	$y = 17569x - 10.335$	0.973	17.57	1.37
EB	Devolatilization/2nd order	5	$y = 51765x - 2.7084$	0.997	51.77	2.07×10^3
		10	$y = 49487x - 3.414$	0.997	49.49	1.96×10^3
		20	$y = 47922x - 3.9658$	0.996	47.92	2.18×10^3
	Char oxidation/1D diffusion	5	$y = 29083x - 8.6433$	0.982	29.08	3.08
		10	$y = 31628x - 8.387$	0.985	31.63	8.67
		20	$y = 31225x - 8.6433$	0.994	31.23	13.24
EBA	Devolatilization/2nd order	5	$y = 85654x + 4.5529$	0.998	85.65	4.89×10^6
		10	$y = 86200x + 4.327$	0.999	86.20	7.85×10^6
		20	$y = 82918x + 3.3558$	0.999	82.92	5.72×10^6
	Char oxidation/2D diffusion	5	$y = 30592x - 8.1818$	0.985	35.48	5.15
		10	$y = 30967x - 8.2068$	0.994	30.97	10.16
		20	$y = 35476x - 7.4913$	0.985	35.48	47.61
PT	Devolatilization/2nd order	5	$y = 98227x + 7.0495$	0.994	98.23	6.81×10^7
		10	$y = 97665x + 6.498$	0.996	97.67	7.80×10^7
		20	$y = 95716x + 5.6669$	0.995	95.72	6.66×10^7
	Char oxidation/1D diffusion	5	$y = 21532x - 9.6393$	0.968	21.53	0.84
		10	$y = 24184x - 9.2627$	0.947	24.18	2.76
		20	$y = 20082x - 10.082$	0.971	20.08	2.02
PB	Devolatilization/2nd order	5	$y = 62339x + 0.0238$	0.997	62.34	3.84×10^4
		10	$y = 63929x + 0.1433$	0.997	63.93	8.87×10^4
		20	$y = 62681x - 0.4084$	0.997	62.67	1.00×10^5
	Char oxidation/1D diffusion	5	$y = 20051x - 9.8785$	0.998	20.05	0.62
		10	$y = 22106x - 9.5897$	0.996	22.11	1.82
		20	$y = 24687x - 9.2734$	0.991	24.69	5.58
AT	Devolatilization/2nd order	5	$y = 85995x + 4.972$	0.996	85.99	7.46×10^6
		10	$y = 85790x + 4.5696$	0.996	85.79	9.96×10^6
		20	$y = 85606x + 4.185$	0.996	85.61	1.35×10^7
	Char oxidation/1D diffusion	5	$y = 19874x - 9.7866$	0.989	19.87	0.67
		10	$y = 24213x - 9.1003$	0.990	24.21	3.25
		20	$y = 29230x - 8.3163$	0.968	29.23	17.19

Table A2. *Cont.*

Fuel	Reaction and Mechanism	β (°C/min)	Equation	R^2	E (kJ/mol)	A (min^{-1})
AB	Devolatilization/2nd order	5	$y = 54053x - 2.1273$	0.999	54.05	3.87×10^3
		10	$y = 52172x - 2.7972$	0.998	52.17	3.83×10^3
		20	$y = 49453x - 3.5741$	0.996	49.45	3.34×10^3
AB	Char oxidation/1D diffusion	5	$y = 22176x - 9.7457$	0.994	22.18	0.78
		10	$y = 24926x - 9.4639$	0.997	24.93	2.33
		20	$y = 24551x - 9.7265$	0.995	24.55	3.52
OB	Devolatilization/2nd order	5	$y = 87737x + 5.2242$	0.999	87.74	9.80×10^6
		10	$y = 87342x + 4.7329$	0.999	87.34	1.19×10^7
		20	$y = 86760x + 4.2662$	0.998	86.76	1.49×10^7
	Char oxidation/1D diffusion	5	$y = 14977x - 10.721$	0.978	14.97	0.20
		10	$y = 15894x - 10.643$	0.906	15.89	0.46
		20	$y = 19990x - 9.9649$	0.978	19.99	2.26

References

1. Saidur, R.; Abdelaziz, E.A.; Demirbas, A.; Hossain, M.S.; Mekhilef, S. A review on biomass as a fuel for boilers. *Renew. Sustain. Energy Rev.* **2011**, *15*, 2262–2289. [CrossRef]
2. Nussbaumer, T. Combustion and Co-combustion of Biomass: Fundamentals, Technologies, and Primary Measures for Emission Reduction. *Energy Fuels* **2003**, *17*, 1510–1521. [CrossRef]
3. Jones, J.M.; Lea-Langton, A.R.; Ma, L.; Pourkashanian, M.; Williams, A. *Pollutants Generated by the Combustion of Solid Biomass Fuels*; Springer: Berlin/Heidelberg, Germany, 2015. [CrossRef]
4. Cai, J.; Xu, D.; Dong, Z.; Yu, X.; Yang, Y.; Banks, S.W.; Bridgwater, A.V. Processing thermogravimetric analysis data for isoconversional kinetic analysis of lignocellulosic biomass pyrolysis: Case study of corn stalk. *Renew. Sustain. Energy Rev.* **2018**, *82*, 2705–2715. [CrossRef]
5. Mishra, R.K.; Mohanty, K. Pyrolysis kinetics and thermal behavior of waste sawdust biomass using thermogravimetric analysis. *Bioresour. Technol.* **2018**, *251*, 63–74. [CrossRef]
6. Vyazovkin, S.; Wight, C.A. Isothermal and non-isothermal kinetics of thermally stimulated reactions of solids. *Int. Rev. Phys. Chem.* **1998**, *17*, 407–433. [CrossRef]
7. Garcia-Maraver, A.; Perez-Jimenez, J.A.; Serrano-Bernardo, F.; Zamorano, M. Determination and comparison of combustion kinetics parameters of agricultural biomass from olive trees. *Renew. Energy.* **2015**, *83*, 897–904. [CrossRef]
8. Saeed, M.A.; Andrews, G.E.; Phylaktou, H.N.; Gibbs, B.M. Global kinetics of the rate of volatile release from biomasses in comparison to coal. *Fuel* **2016**, *181*, 347–357. [CrossRef]
9. Su, Y.; Luo, Y.; Wu, W.; Zhang, Y.; Zhao, S. Characteristics of pine wood oxidative pyrolysis: Degradation behavior, carbon oxide production and heat properties. *J. Anal. Appl. Pyrolysis* **2012**, *98*, 137–143. [CrossRef]
10. Fraga, L.G.; Silva, J.; Teixeira, S.; Soares, D.; Ferreira, M.; Teixeira, J. Thermal Conversion of Pine Wood and Kinetic Analysis under Oxidative and Non-Oxidative Environments at Low Heating Rate. *Proceedings* **2020**, *58*, 23. [CrossRef]
11. Anca-Couce, A.; Zobel, N.; Berger, A.; Behrendt, F. Smouldering of pine wood: Kinetics and reaction heats. *Combust. Flame.* **2012**, *159*, 1708–1719. [CrossRef]
12. Shen, D.K.; Gu, S.; Jin, B.; Fang, M.X. Thermal degradation mechanisms of wood under inert and oxidative environments using DAEM methods. *Bioresour. Technol.* **2011**, *102*, 2047–2052. [CrossRef] [PubMed]
13. Vyazovkin, S.; Chrissafis, K.; Di Lorenzo, M.L.; Koga, N.; Pijolat, M.; Roduit, B.; Sbirrazzuoli, N.; Suñol, J.J. ICTAC Kinetics Committee recommendations for collecting experimental thermal analysis data for kinetic computations. *Thermochim. Acta* **2014**, *590*, 1–23. [CrossRef]
14. White, J.E.; Catallo, W.J.; Legendre, B.L. Biomass pyrolysis kinetics: A comparative critical review with relevant agricultural residue case studies. *J. Anal. Appl. Pyrolysis* **2011**, *91*, 1–33. [CrossRef]
15. Magalhães, D.; Kazanç, F.; Riaza, J.; Erensoy, S.; Kabaklı, Ö.; Chalmers, H. Combustion of Turkish lignites and olive residue: Experiments and kinetic modelling. *Fuel* **2017**, *203*, 868–876. [CrossRef]

16. Vyazovkin, S.; Sbirrazzuoli, N. Isoconversional Kinetic Analysis of Thermally Stimulated Processes in Polymers. *Macromol. Rapid Commun.* **2006**, *27*, 1515–1532. [CrossRef]
17. Vyazovkin, S.; Burnham, A.K.; Criado, J.M.; Pérez-Maqueda, L.A.; Popescu, C.; Sbirrazzuoli, N. ICTAC Kinetics Committee recommendations for performing kinetic computations on thermal analysis data. *Thermochim. Acta* **2011**, *520*, 1–19. [CrossRef]
18. Khawam, A.; Flanagan, D.R. Basics and Applications of Solid-State Kinetics: A Pharmaceutical Perspective. *J. Pharm. Sci.* **2006**, *95*, 472–498. [CrossRef]
19. Rico, J.J.; Pérez-Orozco, R.; Vilas, D.P.; Porteiro, J. TG/DSC and kinetic parametrization of the combustion of agricultural and forestry residues. *Biomass Bioenergy* **2022**, *162*, 106485. [CrossRef]
20. Xu, X.; Pan, R.; Chen, R. Combustion Characteristics, Kinetics, and Thermodynamics of Pine Wood Through Thermogravimetric Analysis. *Appl. Biochem. Biotechnol.* **2021**, *193*, 1427–1446. [CrossRef]
21. Chen, R.; Li, Q.; Xu, X.; Zhang, D.; Hao, R. Combustion characteristics, kinetics and thermodynamics of Pinus Sylvestris pine needle via non-isothermal thermogravimetry coupled with model-free and model-fitting methods. *Case Stud. Therm. Eng.* **2020**, *22*, 100756. [CrossRef]
22. Fu, S.; Chen, H.; Yang, J.; Yang, Z. Kinetics of thermal pyrolysis of Eucalyptus bark by using thermogravimetric-Fourier transform infrared spectrometry technique. *J. Therm. Anal. Calorim.* **2019**, *139*, 3527–3535. [CrossRef]
23. Vega, L.Y.; López, L.; Valdés, C.F.; Chejne, F. Assessment of energy potential of wood industry wastes through thermochemical conversions. *Waste Manag.* **2019**, *87*, 108–118. [CrossRef] [PubMed]
24. Cai, Z.; Ma, X.; Fang, S.; Yu, Z.; Lin, Y. Thermogravimetric analysis of the co-combustion of eucalyptus residues and paper mill sludge. *Appl. Therm. Eng.* **2016**, *106*, 938–943. [CrossRef]
25. Silva, J.P.; Teixeira, S.; Grilo, É.; Peters, B.; Teixeira, J.C. Analysis and monitoring of the combustion performance in a biomass power plant. *Clean. Eng. Technol.* **2021**, *5*, 100334. [CrossRef]
26. Ferreira, S.; Monteiro, E.; Brito, P.; Vilarinho, C. Biomass resources in Portugal: Current status and prospects. *Renew. Sustain. Energy Rev.* **2017**, *78*, 1221–1235. [CrossRef]
27. Nunes, L.J.R.; Loureiro, L.M.E.F.; Sá, L.C.R.; Silva, H.F.C. Evaluation of the potential for energy recovery from olive oil industry waste: Thermochemical conversion technologies as fuel improvement methods. *Fuel* **2020**, *279*, 118536. [CrossRef]
28. Silva, J.P.; Teixeira, S.; Teixeira, J.C. Characterization of the physicochemical and thermal properties of different forest residues. *Biomass Bioenergy* **2023**, *175*, 106870. [CrossRef]
29. Fraga, L.G.; Silva, J.; Teixeira, S.; Soares, D.; Ferreira, M.; Teixeira, J. Influence of Operating Conditions on the Thermal Behavior and Kinetics of Pine Wood Particles using Thermogravimetric Analysis. *Energies* **2020**, *13*, 2756. [CrossRef]
30. Bahng, M.-K.; Mukarakate, C.; Robichaud, D.J.; Nimlos, M.R. Current technologies for analysis of biomass thermochemical processing: A review. *Anal. Chim. Acta.* **2009**, *651*, 117–138. [CrossRef]
31. Friedman, H.L. Kinetics of thermal degradation of char-forming plastics from thermogravimetry. Application to a phenolic plastic. *J. Polym. Sci. Part C Polym. Symp.* **1964**, *6*, 183–195. [CrossRef]
32. Ozawa, T. A New Method of Analyzing Thermogravimetric Data. *Bull. Chem. Soc. Jpn.* **1965**, *38*, 1881–1886. [CrossRef]
33. Flynn, J.H.; Wall, L.A. General treatment of the thermogravimetry of polymers. *J. Res. Natl. Bur. Stand. Sect. A Phys. Chem.* **1966**, *70A*, 487. [CrossRef]
34. Kissinger, H. Variation of peak temperature with heating rate in differential thermal analysis. *J. Res. Natl. Bur. Stand.* **1956**, *57*, 217–221. [CrossRef]
35. Kissinger, H.E. Reaction Kinetics in Differential Thermal Analysis. *Anal. Chem.* **1957**, *29*, 1702–1706. [CrossRef]
36. Akahira, T.; Sunose, T. Method of determining activation deterioration constant of electrical insulating materials. *Res. Rep. Chiba Inst. Technol. (Sci. Technol.)* **1971**, *16*, 22–31.
37. Starink, M. The determination of activation energy from linear heating rate experiments: A comparison of the accuracy of isoconversion methods. *Thermochim. Acta* **2003**, *404*, 163–176. [CrossRef]
38. Coats, A.W.; Redfern, J.P. Kinetic Parameters from Thermogravimetric Data. *Nature* **1964**, *201*, 68–69. [CrossRef]
39. Siddiqi, H.; Bal, M.; Kumari, U.; Meikap, B.C. In-depth physiochemical characterization and detailed thermo-kinetic study of biomass wastes to analyze its energy potential. *Renew. Energy* **2019**, *148*, 756–771. [CrossRef]
40. Dhyani, V.; Bhaskar, T. Kinetic Analysis of Biomass Pyrolysis. In *Waste Biorefinery*; Elsevier: Amsterdam, The Netherlands, 2018; pp. 39–83. [CrossRef]
41. Yu, D.; Chen, M.; Wei, Y.; Niu, S.; Xue, F. An assessment on co-combustion characteristics of Chinese lignite and eucalyptus bark with TG–MS technique. *Powder Technol.* **2016**, *294*, 463–471. [CrossRef]
42. Conesa, J.A.; Marcilla, A.; Caballero, J.A.; Font, R. Comments on the validity and utility of the different methods for kinetic analysis of thermogravimetric data. *J. Anal. Appl. Pyrolysis* **2001**, *58–59*, 617–633. [CrossRef]
43. Mishra, G.; Kumar, J.; Bhaskar, T. Kinetic studies on the pyrolysis of pinewood. *Bioresour. Technol.* **2015**, *182*, 282–288. [CrossRef]
44. Starink, M.J. A new method for the derivation of activation energies from experiments performed at constant heating rate. *Thermochim. Acta* **1996**, *288*, 97–104. [CrossRef]

45. Vamvuka, D.; Sfakiotakis, S. Combustion behaviour of biomass fuels and their blends with lignite. *Thermochim. Acta* **2011**, *526*, 192–199. [CrossRef]
46. Álvarez, A.; Pizarro, C.; García, R.; Bueno, J.L.; Lavín, A.G. Determination of kinetic parameters for biomass combustion. *Bioresour. Technol.* **2016**, *216*, 36–43. [CrossRef]
47. Chen, Z.; Zhu, Q.; Wang, X.; Xiao, B.; Liu, S. Pyrolysis behaviors and kinetic studies on Eucalyptus residues using thermogravimetric analysis. *Energy Convers. Manag.* **2015**, *105*, 251–259. [CrossRef]
48. Sanchez-Silva, L.; López-González, D.; Villaseñor, J.; Sánchez, P.; Valverde, J.L. Thermogravimetric–mass spectrometric analysis of lignocellulosic and marine biomass pyrolysis. *Bioresour. Technol.* **2012**, *109*, 163–172. [CrossRef]
49. Fang, X.; Jia, L.; Yin, L. A weighted average global process model based on two−stage kinetic scheme for biomass combustion. *Biomass Bioenergy* **2013**, *48*, 43–50. [CrossRef]
50. Gil, M.V.; Casal, D.; Pevida, C.; Pis, J.J.; Rubiera, F. Thermal behaviour and kinetics of coal/biomass blends during co-combustion. *Bioresour. Technol.* **2010**, *101*, 5601–5608. [CrossRef]
51. Shen, D.K.; Gu, S.; Luo, K.H.; Bridgwater, A.V.; Fang, M.X. Kinetic study on thermal decomposition of woods in oxidative environment. *Fuel* **2009**, *88*, 1024–1030. [CrossRef]
52. Yorulmaz, S.Y.; Atimtay, A.T. Investigation of combustion kinetics of treated and untreated waste wood samples with thermogravimetric analysis. *Fuel Process. Technol.* **2009**, *90*, 939–946. [CrossRef]

Disclaimer/Publisher's Note: The statements, opinions and data contained in all publications are solely those of the individual author(s) and contributor(s) and not of MDPI and/or the editor(s). MDPI and/or the editor(s) disclaim responsibility for any injury to people or property resulting from any ideas, methods, instructions or products referred to in the content.

energies

MDPI

Article

Diagnosis of Socio-Economic Prospects and Constraints for Household Biogas Adoption: A Case of Lizulu Market in Ntcheu District of Malawi

Admore Samuel Chiumia [1,*], Betchani Tchereni [1], Hope Baxter Chamdimba [2], Benjamin L. Robinson [3] and Mike Clifford [3]

[1] School of Business and Economic Sciences, Malawi University of Business and Applied Sciences, Private Bag 303, Chichiri, Blantyre 3, Malawi
[2] Energy Resources Management Department, Malawi University of Science and Technology, Limbe P.O. Box 5196, Malawi
[3] Faculty of Engineering, University of Nottingham, University Park, Nottingham NG7 2RD, UK
* Correspondence: admoresc@gmail.com; Tel.: +265-999-40-18-04

Abstract: Biogas is once again emerging as a potential household cooking option that can help developing countries achieve energy targets. However, the adoption of biogas remains relatively slow, necessitating a diagnosis of the problem the review of literature identified. The review identified key factors influencing the adoption of household biogas technology, including policy and regulatory frameworks, financing mechanisms, public awareness, and socio-economic factors. Therefore, this study involved undertaking a survey where heads of 385 households were interviewed. The study found that low income of households, averaging USD 67/month, is a major constraint to biogas adoption, especially when dirty fuels cost little or nothing. In addition, a lack of awareness of the benefits of biogas over the available dirty fuels has the potential to limit its adoption. This explains why 99% of the households interviewed indicated firewood and charcoal were their first option, and 52% believed that these dirty fuels were dependable. Regardless of these bottlenecks, the study found that households are ready to try better cooking options. About 99% of households were interested in using biogas, and 94% wanted to learn more about biogas. Therefore, there is a need for increased awareness, and suppliers must adopt innovations that make biogas more accessible and competitive against traditional cooking fuels.

Keywords: biogas; cooking; adoption; household; opportunities; challenges

1. Introduction

The 2024 International Energy Agency's Energy Poverty Report indicated that renewable energy sources, including biogas, contributed the most to the overall growth in total energy supply, accounting for 38%. This was followed by natural gas (28%), coal (15%), oil (11%), and nuclear energy (8%). Globally, the use of traditional biomass for cooking has declined in many areas, but Sub-Saharan Africa remains an exception, where most households still rely on charcoal and firewood for cooking due to limited access to cleaner alternatives [1–4].

Africa holds significant potential for biogas production, yet progress in developing the sector remains limited [5]. While the continent has advanced in implementing small-scale and household biogas systems, commercial biodigesters are still at an early stage. Numerous national and regional studies have explored Africa's biogas potential, covering technical, economic, and policy aspects [6]. Research conducted in South Africa, home to

the continent's largest installed electricity generation capacity, revealed that, despite the installation of approximately 700 biogas plants, only around 300 were operational as of 2017. Among those in operation, roughly 90% were household systems [2]. In the East African region, countries such as Uganda have a largely underdeveloped policy and regulatory framework for supporting renewable energy development, including biogas. The existing policy environment includes the Energy Policy, which aims to establish a financially sustainable electricity sector without subsidies and was completed in 2012. Additionally, the Renewable Energy Policy 2007 set a target to increase the share of renewable energy sources to 61% of total energy consumption by 2017. Furthermore, Vision 2040 acknowledges the significance of technological energy choices in addressing climate change. While these targets have yet to be fully realized, efforts to promote biogas and other renewable energy technologies through subsidies, tax incentives, and public awareness campaigns continue to progress, albeit at a slow pace, toward 2030 [7,8]. Biogas technology, like other renewable energy solutions, has not gained significant traction in Malawi. However, several African nations, including Kenya, Uganda, Ethiopia, Tanzania, Rwanda, Cameroon, Burkina Faso, and Benin, have successfully leveraged the technology [9]. Some of these countries share borders with Malawi and experience similar tropical climate conditions, suggesting that biogas technology could also be a viable option for Malawi.

In Malawi, biomass in the form of firewood, charcoal, and agricultural waste accounts for more than 97% of household cooking energy [10–14], but the challenge is worse in rural areas. Currently, less than 10% of the rural population has access to electricity [15,16], and the majority of those connected to the grid do not use electricity for cooking [3,12]. Additionally, alternative cooking fuels in rural areas are almost nonexistent. Therefore, households in rural areas rely on dirty and unsustainable fuels, such as fuelwood, charcoal, and agricultural waste [6,7,10,14,17]. The country consumes about 9.2 metric tons of firewood and 1.7 metric tons of charcoal annually [15]. The unsustainable use of fuelwood and charcoal is criticized for the high rates of deforestation and land degradation being experienced in the country [3,14]. Due to high rates of deforestation, fuelwood and charcoal have become less accessible and unaffordable [10,11,14]. In addition, various studies have reported that the use of these dirty fuels (in this study, dirty fuels refer to traditional, inefficient, and highly polluting energy sources used for cooking, such as firewood, charcoal, kerosene, coal, and agricultural residues) is blamed for indoor emissions that cause respiratory diseases among women and children [7,10,15,18]. Therefore, the government and development stakeholders are increasingly promoting transitioning to clean and sustainable cooking options to reduce national overdependence on firewood and charcoal [10].

The Government of Malawi (GoM) adopted the National Energy Policy and the Sustainable Energy for All (SE4ALL) National Action Agenda, which seeks to achieve universal access to modern, affordable, and sustainable energy by the year 2030 [3,6,10,15,19]. However, with only seven years remaining, it is impractical for the country to achieve this ambitious goal by 2030. Malawi's 2018 Energy Policy, under its third broad objective, aims to ensure the availability of biogas in sufficient quantities at affordable prices for both industrial and domestic use. Additionally, the 2024 Malawi Energy Compact plans to roll out 80,000 biogas cookstoves by introducing tax incentives and duty exemptions for project developers, private sector players, cooperatives, and other stakeholders to promote the adoption of biogas solutions. Ref [9] reported that since the introduction of biogas technology in Malawi, various initiatives led by the government, individuals, and private sector players have focused on expanding access to biogas solutions, particularly for poorer communities and households. Organizations such as Malawi University of Science and Technology, Mzuzu University, EcoGen, Green Impact Technologies, the Ministry of Energy,

Intrinsic Biogas, and Community Energy Malawi have been instrumental in these efforts, installing a total of 343 community home-based biogas systems aimed at improving energy access for low-income households. The country must explore alternative pathways for achieving cooking energy objectives and goals. For instance, one of the strategies identified by the national energy policy is promoting alternative energy technologies, such as biogas and LPG, to reduce the demand for charcoal and firewood [7]. The government of Malawi, through the Malawi Energy Regulatory Authority (MERA), has been promoting the use of Liquefied Petroleum Gas (LPG) to improve access to clean cooking energy. However, this imported LPG is less affordable and not widely accessible in the country [1,7,10,15]. The costs of the imported LPG cylinders are extremely high, thus creating a major obstacle to the adoption of LPG as cooking fuel [10]. In addition, the lack of foreign currency affects the importation of adequate LPG [13].

The power outages have led to high dependency on biomass energy, especially charcoal for cooking, which is an unsustainable and unreliable source of energy in Malawi [1,7]. The average electricity tariff will be adjusted by 50.8% segmented into four annual tranches of 18%, 16%, 12%, and 9% to be implemented from 2023 to 2027 [20]. It is driving deforestation and forest degradation, with an estimated 75,000 hectares of natural forest across Malawi destroyed annually [13]. The 2018 Malawi Energy Policy's goal is to "enhance access to affordable, reliable, sustainable, efficient, and modern energy for all Malawians by 2030". It promotes the sustainable production and utilization of charcoal and firewood while promoting alternative energy sources, such as LPG, to reduce dependence on degradable biomass for cooking. LPG has the potential to deliver major health benefits as well as to reduce the adverse climate impacts associated with current cooking fuels used [3,12]. Promoting access to cleaner cooking fuels and devices would contribute to environmental and developmental goals. The main debates still revolve around the issues of sustainability, availability, affordability, perception, cost, safety, and other barriers associated with alternative cooking solutions [7]. A number of challenges remain, including cultural habits of using biomass for cooking, unfamiliarity with solutions such as LPG, briquettes, and pellets, the wider availability and affordability of biomass fuels, and the relatively high cost of alternatives and equipment [21].

Amidst the challenges concerning the adoption of modern cooking options, such as LPG and electricity [1,3,12], biogas is emerging as a viable option for addressing cooking energy poverty in urban as well as rural areas. Currently, 10.6% and 0.2% of the city population use electricity and LPG for cooking and heating, respectively [21]. Biogas is a clean and renewable fuel generated through a process called Anaerobic Digestion (AD), a process in which special microorganisms digest organic material in sealed containers to produce biogas, which is a mixture of methane, carbon dioxide, and other gases [21–23]. Biogas can be produced from any biodegradable material, such as animal manure and food waste [23–25]. Biogas produced can be used for cooking, heating, and electricity generation [23,24,26–28]. Bioslurry produced as a byproduct is rich in soil nutrients, and farmers use it for crop cultivation [18,21,25,29,30]. Smallholder farmers are already transitioning to organic manure because inorganic fertilizers have become unaffordable [31–33]. In addition, the use of organic waste as a feedstock contributes to community sanitation [21,29,30]. For markets that produce enormous amounts of vegetable waste, it becomes a natural choice to adopt the technology as it helps to solve waste management challenges. Surprisingly, the progress of biogas development has been slow, and the use of dirty fuels remains unabated, as evidenced by the inability of the country to reduce the role of firewood and charcoal in the nation's energy mix.

Malawi's heavy reliance on firewood and charcoal for cooking has led to severe environmental degradation, deforestation, and health risks from indoor air pollution. With

biomass accounting for 99% of household cooking energy and rural electricity access below 14%, there is an urgent need to explore alternative solutions such as biogas. As a renewable energy source derived from organic waste, biogas presents a viable alternative for clean cooking while also addressing waste management challenges. Therefore, the aim of this study was to examine the socio-economic factors influencing household adoption of biogas at Lizulu Market in Ntcheu District, an area with low electricity access and significant organic waste generation. The study identified barriers and opportunities for biogas uptake and will contribute to clean energy policy discussions and inform strategies for increasing accessibility, affordability, and awareness. The findings will support mostly African countries' energy transition efforts and the Sustainable Energy for All (SE4ALL) Action Agenda, which seeks universal access to modern and sustainable energy by 2030. Understanding household adoption dynamics will help shape interventions that reduce dependence on firewood and charcoal, ultimately promoting a cleaner environment and improving public health.

2. Materials and Methods

2.1. Description of the Study Area

This study was conducted in the Lizulu Market area located in Ntcheu District, which is in the central region of Malawi. The geographical coordinates of the area are 14° 31′ 0″ south and 34° 28′ 0″ east. Lizulu is a rural area that is known for agricultural activities and organic waste generation, which are carelessly dumped at the market and river streams. Careless dumping of organic waste at the market and its surroundings has created significant environmental, health, and economic consequences. Environmentally, decomposing waste releases methane, a potent greenhouse gas that contributes to climate change [25]. It also clogs drainage systems, leading to waterlogging and increased flooding risks, especially during the rainy season. Additionally, organic waste contaminates nearby water sources, reducing water quality. From a health perspective, rotting waste attracts pests such as flies, rats, and stray animals, which can spread diseases like cholera, dysentery, and respiratory infections [34].

The surrounding communities grow various fruits and vegetables, which farmers and traders sell at this market. Every day the market manages enormous quantities of these fruits and vegetables, serving consumers in major cities of Malawi, especially Lilongwe and Blantyre. Consequently, this market generates substantial amounts of organic waste. The Malawi University of Science and Technology (MUST) and Green Impact Technologies (GIT) in Malawi have piloted commercial biogas generation at Lizulu, where the plant uses organic waste to produce biogas and organic manure. A pilot study conducted by MUST and GIT at Lizulu Market, a key trading hub for small-scale farmers specializing in horticultural produce, evaluated organic waste generation through a comprehensive site assessment, waste characterization, sampling, and measurement over seven days. The findings indicated that over 90% of the market's waste consists of biodegradable vegetable matter, highlighting its potential for biogas production. The study estimated that the organic waste from Lizulu Market could support a 2000 cubic meter biogas digester, but currently the market has a 40 m^3 capacity biodigester only. In addition to organic vegetable waste, cooperatives and small-scale farmers around Lizulu Market raise livestock, providing an additional source of feedstock for biogas generation. This combination of waste streams enhances the market's potential for sustainable waste-to-energy solutions, creating opportunities to boost renewable energy production and improve waste management efficiency. Therefore, Lizulu was determined to be a suitable area for this study, and the results will help to unearth the socio-economic prospects and constraints that development stakeholders will face as they promote the adoption of biogas for cooking by households in

various locations of Malawi. Figure 1 shows the study area of Lizulu Market in Ntcheu District of Malawi.

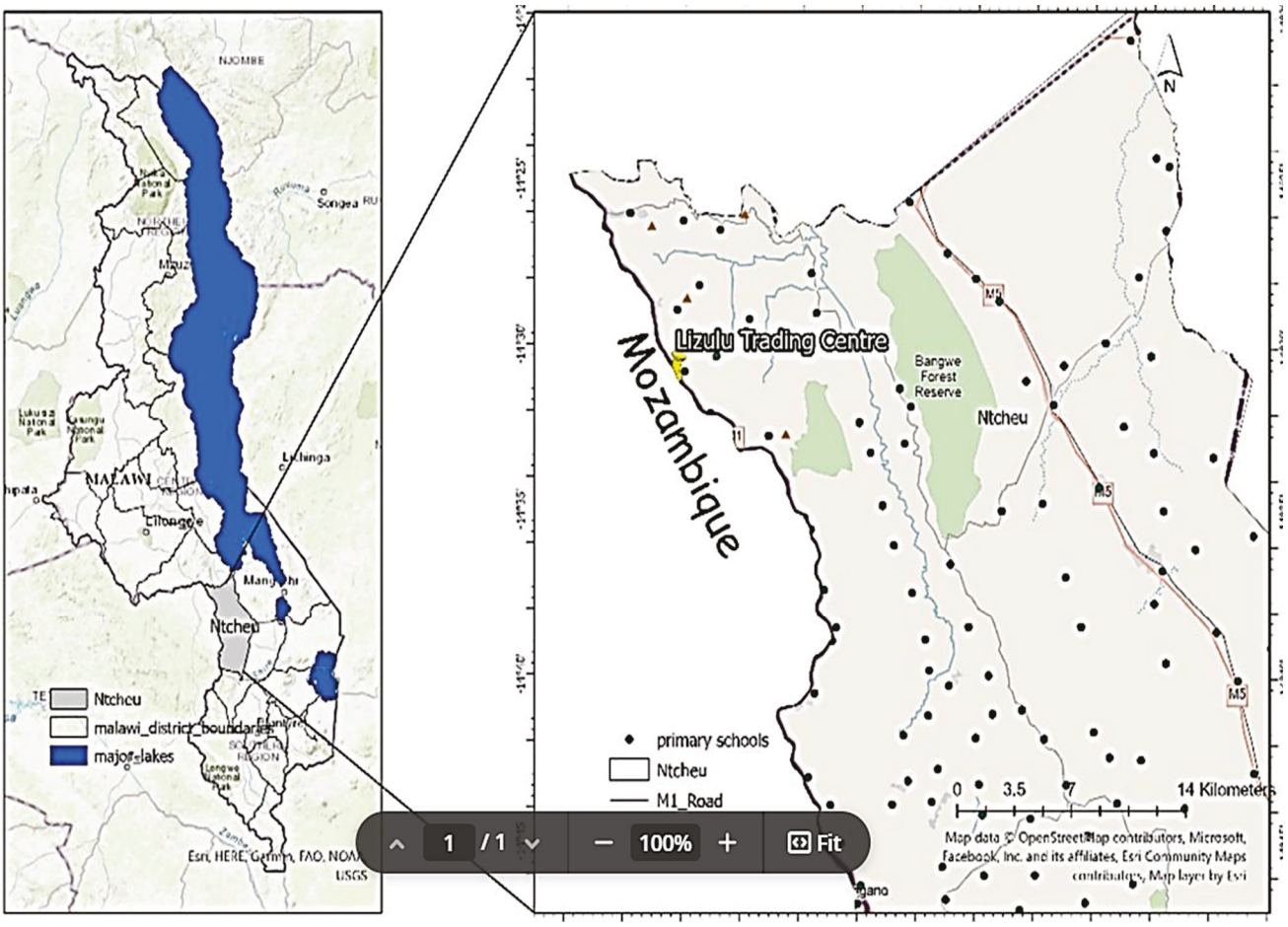


Figure 1. Lizulu Market Area and Surrounding Communities.

2.2. Research Design and Conceptual Framework

A cross-sectional research design was applied in this study design, collecting data from households in the Lizulu Market area and surrounding communities. The survey method was chosen to gather quantitative data addressing household socio-economic status and cooking fuel preferences with barriers and opportunities regarding biogas adoption as cooking fuel. This design allows the collection of data on more than one case and at a single point in time to gather a body of quantitative or quantifiable data in connection with two or more variables, which are then examined to detect patterns of association. During data collection, the participants were questioned on the available cooking fuels in their communities, with an understanding that they know the advantages and disadvantages of such cooking fuels. However, biogas is new; thus, some had already heard about this cooking fuel, but they had never used it before, which means that they were not aware of the benefits of biogas over traditional cooking fuels. On the other hand, others were completely unaware of the biogas cooking fuel. In this case, enumerators had to explain what the biogas cooking fuel is and its advantages and disadvantages without comparing it with other cooking fuels. Therefore, the respondents had adequate knowledge of various cooking options.

This study employed a cross-sectional research design to assess household socio-economic status, cooking fuel preferences, and the barriers and opportunities influencing biogas adoption in the Lizulu Market area and surrounding communities. In addition

to quantitative, the study also employed the Focus Group Discussions (FGDs), which provided in-depth insights into the perceptions, experiences, and challenges related to household biogas adoption in Lizulu Market and its surrounding communities. Four FGDs were conducted, each comprising 8–12 participants, carefully selected based on factors such as gender, age, socio-economic status, and experience with alternative cooking fuels. The discussions explored themes such as biogas awareness, energy choices, socio-cultural factors, economic considerations, and adoption barriers. The conceptual framework is anchored in Energy Transition Theory, which explains how factors such as awareness, perceived benefits, and socio-economic conditions shape the adoption of new technologies like biogas. The concept of energy transition as a key solution to climate change gained widespread recognition following the adoption of the 2030 Agenda for Sustainable Development and the establishment of the Sustainable Development Goals (SDGs) by the United Nations in 2015 [3].

The study examined two primary sets of variables: independent variables, which include household socio-economic characteristics (such as income levels, education, and household size), and dependent variables, including cooking fuel choices and willingness to adopt biogas. Additionally, intervening variables, such as awareness and access to information on biogas, play a crucial role in shaping decision-making processes. Utilizing a survey methodology, the study identified patterns of association between these variables, offering insights into how knowledge dissemination influences household energy preferences. Since biogas is relatively new in the region, the survey was administered to non-users of biogas to assess their awareness, perceptions, opportunities, and potential adoption barriers. Enumerators played a vital role in addressing the knowledge gap by explaining its benefits and limitations, ensuring that respondents had sufficient information to evaluate its potential compared to traditional cooking fuels. The study ensured the voices of women were adequately represented in the Lizulu study by implementing gender-sensitive sampling and data collection strategies. First, during household selection, efforts were made to include female-headed households and women within male-headed households to capture diverse perspectives on cooking fuel preferences and energy needs. Second, enumerators were trained to engage both men and women in discussions, creating an inclusive environment where women felt comfortable sharing their experiences. Additionally, the study considered the socio-cultural dynamics of the community by consulting local leaders and women's groups to encourage female participation.

2.3. Sample Size and Sampling Methods

This study used Cochran's formula, shown in Equation (1), to calculate the sample size of 385 participants. The formula is suitable when the population considered is deemed to be infinite. The research study also used a probability sampling technique to ensure that each member of the target population had an equal and independent chance of being selected for the sample. Simple random sampling was specifically employed to avoid any selection bias and ensure that the sample accurately represents the population.

$$\begin{aligned} n_0 &= \frac{z^2 \times pq}{e^2} \\ n_0 &= \frac{(1.96)^2 \times (0.5)(0.5)}{(0.05)^2} = 385 \text{ Sample size} \end{aligned} \quad (1)$$

where

n_0 = required sample size

Z = Z-value, which corresponds to the desired confidence level (95% confidence level, Z = 1.96)

p = estimated population proportion (if unknown, 0.5 is often used to get the maxim um sample size)

$q = 1 - p$

e = margin of error

The simple random sampling approach was conducted by first delineating the study area within Lizulu Market and its surrounding communities. Given that an official household list was unavailable, a systematic field-mapping exercise was undertaken in collaboration with local leaders to identify and approximate the number of households within the target area. To ensure randomness, a lottery method was used, where households were assigned numbers, and a random number generator was applied to select participants. Enumerators then visited the selected households to conduct interviews. The primary criteria for selection were: residence in the study area—Only households within the predefined Lizulu Market area were eligible; cooking fuel use—Households were included regardless of their current cooking fuel type to capture a diverse range of experiences; willingness to participate—Participation was voluntary, with informed consent obtained before data collection. This method ensured that every household had an equal chance of selection while maintaining representativeness despite the logistical challenges of obtaining a formal household list.

2.4. Target Population

The target population for the survey was comprised of households in the Lizulu Market zone. The household head was chosen as the primary respondent, and in this study, the household head is defined as the person who is a breadwinner regardless of their gender, whether male or female. The household head understands the socio-economic issues such as household income and expenditures and cooking energy options. However, other family members were given an opportunity to help the household heads answer the questions to obtain detailed and accurate information.

2.5. Sources of Data and Data Collection Methods

Primary data were collected directly from the respondents using a semi-structured questionnaire. Both qualitative and quantitative research techniques were applied in this study. Data were collected through focus group discussion, key informant interviews, questionnaire surveys, and personal observations. Secondary data were collected from relevant published and unpublished sources like books, journal articles, the internet, and reports from the Ministry of Energy and the district energy office.

2.5.1. Focus Group Discussion (FGD)

The focus group discussion (FGD) was employed to gather information on the shared experiences, perceptions, and opinions of community members regarding biogas utilization. To achieve this, 4 focus groups were formed, each consisting of 8–12 participants carefully selected based on their experience with alternative cooking fuels, age, gender, and socioeconomic status. A moderator facilitated the discussions using a semi-structured guide, and the sessions were audio-recorded, lasting approximately 1 h. This approach yielded rich, qualitative data on the benefits and challenges of biogas utilization in the Lizulu area, as well as suggestions for improvement along with the feasible technology that could be employed.

The participants for the Focus Group Discussions (FGDs) were selected through purposive sampling, ensuring a diverse representation based on experience with alternative cooking fuels, age, gender, and socio-economic status. This selection process allowed the study to gather a wide range of perspectives on biogas utilization, particularly from those who had firsthand experience with or knowledge of cooking alternatives. To ensure gender

inclusivity, the focus groups were split by gender, allowing for open and comfortable discussions where both men and women could freely express their thoughts without the influence of the opposite sex. This separation was critical to ensure that women, often the primary decision-makers regarding household cooking, could voice their opinions in a space where their perspectives were prioritized.

The FGDs were facilitated by trained professionals with experience in qualitative research and group facilitation. They used a semi-structured guide to ensure key topics were covered while allowing room for participants to share their personal experiences and opinions. Ethical principles were strictly adhered to throughout the process. Informed consent was obtained from each participant, and confidentiality was assured. Additionally, the facilitators ensured that no participant felt coerced, and participation was voluntary, with the right to withdraw at any time. The language of the discussions was primarily Chichewa, the local language spoken by the community, to ensure that all participants fully understood the questions and could communicate their thoughts effectively. The sessions were audio-recorded with the participants' consent, ensuring accurate data collection while respecting their privacy. This approach was designed to ensure that the FGDs were inclusive, respectful, and conducted in an ethical manner.

2.5.2. Key Informant Interviews (KIIs)

Key informant interviews (KIIs) were conducted to gather in-depth information from individuals with expertise or experience in biogas utilization. A total of 5 key informants were identified, including biogas users, local leaders, and energy experts. This approach provided detailed, qualitative insights into the opportunities and challenges of biogas utilization, as well as recommendations for future development.

The KIIs were conducted to gather in-depth information from individuals with expertise or direct experience in biogas utilization. A total of five key informants were selected for the interviews, with a diverse range of backgrounds. The informants included biogas users, local leaders, and energy experts, providing a comprehensive perspective on the subject.

The biogas users were selected from the Lizulu Biogas Plant, located approximately 47.8 km from the Lizulu area via M1 Road in Ntcheu, Malawi. These users were selected based on their direct experience with biogas as a cooking fuel, providing valuable insights into the practical challenges and benefits of using biogas in households. The biogas users included both male and female household representatives, aged between 30 and 60 years, who had been utilizing the system for an extended period.

The local leaders included community heads and representatives from the Lizulu area, aged between 35 and 60 years, who were involved in local governance or community decision-making processes. These individuals were selected for their knowledge of community dynamics, their ability to provide feedback on the adoption of biogas in the region, and their role in supporting or promoting energy solutions at the grassroots level.

The energy experts were professionals in the field of renewable energy, with specific expertise in biogas technology and its integration into local energy systems. These experts were selected from institutions (Ntcheu District Council officials, Intrinsic Biogas, EcoGen, Green Impact Technologies, etc.) or organizations that work on energy solutions in Malawi, with ages ranging from 35 to 55 years. They provided valuable technical insights into the feasibility, potential, and challenges of biogas utilization.

The key informants' age and gender varied, ensuring a broad spectrum of perspectives. This approach enabled the study to capture diverse views on biogas use and adoption, from those who are directly engaged with the technology to those who influence energy policy and development in the region. Through this mix of informants, the KIIs provided rich, qualitative data on the opportunities and challenges of biogas utilization in the Lizulu area.

2.5.3. Questionnaire Surveys

Questionnaire surveys were administered to collect quantitative data on the demographics, biogas usage patterns, willingness to pay, ability to pay, and perceptions of households in the Lizulu area. A semi-structured questionnaire was designed and pretested to ensure its effectiveness. Then, 385 households were randomly selected for the survey, and trained enumerators administered the questionnaires through face-to-face interviews. This approach yielded quantitative data on household characteristics, cooking solutions used by households in the area, biogas potential adoption rates, usage patterns, and satisfaction levels.

2.5.4. Personal Observations

Personal observations were made to gather firsthand information on the biogas infrastructure in the area, fuel stacking, usage patterns, and challenges faced by households in accessing energy for cooking, as well as their current household expenditures. The researcher conducted detailed observations in 20 households, all of which had potential feedstock sources for biogas. These households were purposively and carefully selected, as they not only generated organic waste from daily activities but also kept livestock, such as cattle and pigs, which could contribute significantly to the feedstock for biogas production. The presence of livestock, particularly cattle and pigs, provided an additional and valuable source of manure, enhancing the sustainability and efficiency of the biogas systems.

During the observations, attention was given to the suitability of biogas system designs, installation quality, and ongoing maintenance practices. The researcher noted how the livestock waste, particularly from cattle and pigs, was utilized in the area, highlighting the role of animal manure in improving the efficiency and consistency of biogas production. Observations also included how households managed their feedstock, whether it was primarily vegetable waste, livestock manure, or a combination of both. Additionally, the researcher evaluated fuel stacking practices, where households utilized a mix of traditional cooking fuels (such as firewood) alongside charcoal, and examined how this impacted overall energy consumption and expenditures.

The researcher is also exploring the potential of developing a commercial-scale biogas facility at Lizulu Market. This facility would serve as a central hub for biogas production, and households would be able to adopt a more sustainable cooking solution by using backpacks and stoves that would be refilled at the biogas facility located at the market. This model aims to not only support biogas adoption in the community but also create a reliable, localized source of clean cooking fuel, reducing reliance on traditional fuels like firewood and charcoal, while providing a sustainable waste-to-energy solution. The potential to integrate both market waste and household waste into this commercial biogas system offers an efficient approach to addressing energy needs, waste management, and environmental sustainability in the area.

Further, the surrounding environment was carefully observed for any potential health hazards, particularly related to waste management practices and the handling of organic materials for biogas production. These observations provided valuable qualitative insights into the practicalities of biogas utilization, including the complexities of system design, feedstock availability, usage patterns, and maintenance challenges. The integration of livestock waste into the biogas system played a key role in the households' ability to maintain consistent biogas production, thus improving the overall viability of the technology as a reliable cooking energy source.

2.6. Research Ethics and Approval/Ethical Considerations

Participants were assured full anonymity and privacy, with their responses used solely for study evaluation. Additionally, formal approvals were secured from the Ntcheu District Council and the Lizulu Market Committee to conduct research in their communities.

As part of the National Commission for Science and Technology (NCST) demonstration pilots for biogas commercialization, the study complied with ethical standards, including informed consent, confidentiality, data protection, voluntary participation, the right to withdraw, and cultural sensitivity. To ensure community trust and collaboration, the researcher engaged local leaders, government officials from the Department of Social Welfare and the Ministry of Gender and representatives from district council departments.

2.7. Data Analysis

The data were analyzed using the statistical packages IBM SPSS Statistics is Version 30.0.0, STATA 18, and Microsoft Excel 2021, which enable users to manipulate, analyze, and visualize substantial amounts of data very quickly and with ease. The study employed descriptive statistics (means, percentages, and frequencies) and inferential statistics (econometric output) for summarizing essential demographic and socio-economic variables such as household income and preferences for cooking energy and biogas technology awareness. The data were also cross-tabulated to examine relationships between variables, such as the association between household income and the willingness to adopt biogas as cooking fuel. This comprehensive data analysis helped to draw conclusions about the feasibility of promoting biogas adoption in Lizulu Market and its surrounding communities.

3. Results

3.1. Socio-Economic Status of the Respondents and Households at Lizulu Market

The study involved assessing the socio-economic status of the households at Lizulu Market because they play a critical role in influencing the adoption of biogas. The areas of focus were education, sources of livelihoods, and household income. The results showed that generally education levels were very low; petty trading, casual labor and farming accounted for the major sources of livelihood; and on average the households earned 67 USD. Some respondents were unable to determine their monthly income because their income varies throughout the year. Therefore, for those who are dependent on trading and piecework, their monthly income was calculated based on their average daily income. However, for those involved in farming, their monthly income was determined based on the seasonal or annual income. Table 1 shows the results on the socio-economic status of the households at Lizulu Market.

Table 1. Socio-economic information of the respondents.

Assessed Socio-Economic Factors	Results Descriptions
Gender and marital status of the Respondents	The percentages of male and female respondents were 73% and 27%, respectively. It was determined that the respondents that were married, single, widowed, and divorced accounted for 66%, 18%, 11%, and 6%, respectively.
Education Level of the Household Heads	The family heads who attained primary education, secondary school education, vocational diplomas, and university diplomas/degrees accounted for 56%, 31%, 1%, and 1%, respectively. In addition, 10% of the respondents have never been to school, and 1% of the respondents attended adult literacy education.

Table 1. *Cont.*

Assessed Socio-Economic Factors	Results Descriptions
Household Sources of Livelihoods at Lizulu Market.	The study findings showed that 37%, 22%, 22%, 12%, 6%, and 1% of the respondents were engaged in petty trading, casual labor, farming, full-time employment, business, and others, respectively.
Households Income Generation at Lizulu Market.	The average monthly income was USD 67 for households having an average occupancy rate of 4.6.

3.2. Current Household Cooking Fuel Choices and Purchase Decision Making Process

To identify the cooking energy choices of households, the study pre-identified the cooking energy sources mostly used in Lizulu. The identified cooking energy sources were charcoal, electricity, firewood, and maize cobs. Each respondent (i.e., household head) was requested to identify the first, second, third, and fourth cooking energy options for the household. The study findings show that charcoal remains the preferred cooking energy option for 75% of the sampled households in Lizulu; the high usage of charcoal and firewood is often driven by limited access to alternative energy sources. Firewood was determined to be a cooking fuel that is regarded as the first option for 24% of households. Therefore, biomass in the form of fuelwood and charcoal is regarded as the first cooking option for 99% of the households at Lizulu Market (Table 2), which is in line with the findings of many similar studies in Malawi [1,11,12]. Additionally, none of the respondents mentioned a fourth cooking energy option, regardless of agricultural waste widely being used by low-income households. Table 2 shows cooking energy choices of the households.

Table 2. Household cooking choices at Lizulu Market.

Ranking	Fuel Type	%
First	Charcoal	75%
	Electricity	1%
	Firewood	24%
	Maize Cobs	0%
Second	Charcoal	21.5%
	Electricity	2.4%
	Firewood	75.1%
	Maize Cobs	1%
Third	Briquettes	17%
	Charcoal	17%
	Electricity	50%
	Firewood	16%
Fourth	Maize Cobs	100%

This study sought to determine the responsibility of cooking fuel purchasing at the household level at Lizulu Market. The results showed that male household heads, female household heads, other male household members, and other female household members who were responsible for providing money for purchasing cooking fuel accounted for 62%, 32%, 1%, and 2%, respectively. In addition, the findings showed that female household heads, male household heads, other female household members, and male household

members that were responsible for purchasing the firewood after the money was provided accounted for 79%, 18%, 2%, and 1%, respectively.

3.3. Existing Cooking Fuel Reliability and User Satisfaction

Reliability refers to cooking fuel availability and the ease with which it can be used for cooking. It should be noted here that charcoal and firewood cooking fuels are regarded as the first cooking energy options for 99% of households. Therefore, it can be concluded that household responses address the reliability of charcoal and firewood cooking fuels. The study findings showed that 52% of households thought the cooking fuels that they currently use were the most dependable. About 25% and 13% of the households responded that the cooking fuels are moderately dependable and partially reliable, respectively. On the other hand, only 10% of them responded that the cooking fuels they use are not reliable (Figure 2).

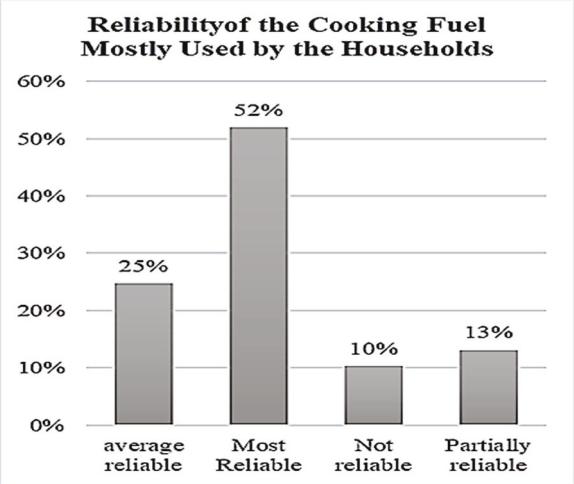


Figure 2. Cooking fuel reliability.

3.4. Prospects for Biogas Adoption

3.4.1. Household Biogas Awareness, and Willingness to Adopt

Of the 385 households interviewed, the study findings showed that only 62% of them were aware of biogas at Lizulu Market, 79% of them had never used biogas for cooking, 99% of the households were willing to try using biogas, mainly because it was a new technology, and 94% of them were interested in learning more about biogas. Occupation had no bearing on the adoption of biogas. The results of the Z-test suggest that there is no statistically significant difference in biogas awareness between males and females. The proportion of males who reported being aware of biogas was 40.2% (SD = 0.052), while for females, it was 37.3% (SD = 0.031). The computed Z-score of 0.63, with a corresponding p-value of 0.6, indicates that the observed difference is not statistically significant at conventional significance levels. These findings imply that knowledge about biogas is relatively uniform across genders in the study area, suggesting that gender may not be a key determinant of awareness. This could be attributed to similar exposure to information sources, such as community meetings, radio programs, or social interactions. However, further investigation into other socio-demographic factors, such as education level and household decision-making dynamics, could provide deeper insights into the factors influencing biogas awareness. A chi-square test of independence was conducted to assess the relationship between occupation and interest in biogas adoption. The results were not statistically significant, $\chi^2(5, N = 320) = 6.38$, $p > 0.1\backslash chi^2$ $(5, N = 320) = 6.38$, $p > 0.1$, indicating that there was no meaningful association between household willingness to adopt biogas

and the type of occupation they were engaged in. This suggests that occupation did not play a determining role in influencing household interest in biogas adoption.

3.4.2. Household Motivations and Demotivation for Transitioning to Biogas

The study findings also showed that households had other reasons for transitioning to biogas apart from socio-economic issues. For instance, most of the households (i.e., 49%) wanted just to try the new cooking technology, whereas 31% of them cited their economic status, which can allow them to buy biogas for cooking. Note that the price for biogas was USD 0.48/m^3. This amount of biogas is enough to last 2 days for a household (i.e., the household size on average is 4.6 at Lizulu), based on the study findings for Lizulu Biogas Plants. The others cited technological and environmental benefits associated with the use of biogas for cooking. Table 3 shows different reasons why respondents were interested in biogas.

Table 3. Reasons for willingness to transition to biogas.

Reasons for Willingness to Try Use Biogas for Cooking		
Reason	**No of Respondents**	**Percentage**
Just to try them	156	49%
Fuel efficient	88	28%
Current stove not fuel efficient	59	18%
Can afford to buy	98	31%
Portable	9	3%
Safe to use	23	7%
Not willing to buy	5	2%
To conserve the environment	13	4%

The study also investigated the ability to pay by the households, based on their monthly income, but also their preferred payment option. In this case, the average income was determined to be USD 67 per month. Based on this income, 66% of the households indicated their willingness to pay using cash, while the remaining 34% preferred obtaining the biogas on credit. However, this was dependent on the price of the biogas. On average, the respondents were willing to pay USD 3.5 per week. However, at the time of the study, these households were spending USD 7.6 on charcoal per month and USD 5.7 on firewood. The study also sought to determine factors that may contribute to low adoption of biogas. The results showed that inaccessibility, lack of money/high cost of biogas, cultural beliefs, and others were cited by 97%, 3%, 0%, and 0% of the respondents, respectively.

3.5. A Comparison of the Socio-Economic Factors Influencing Biogas Adoption in Regional Countries and Africa

To understand the adoption of biogas for household and cooking use in other countries, it is very crucial to understand the patterns and the socio-economic factors that drive the adoption of biogas. Therefore, a comprehensive literature review was undertaken, where various papers were reviewed. Of concern were countries located in southern and eastern Africa, but other countries in Africa were also considered. The results showed various socio-economic factors influencing the adoption of biogas in Ethiopia, Kenya, Malawi, Uganda, Rwanda, Tanzania, Mozambique, and Nigeria. However, the most common ones were lack of awareness, low income of the households, and high capital costs. These results are in line with the findings of this study, except that at Lizulu Market the majority of the households (i.e., 99%) showed willingness to try biogas on the condition that the biogas is affordable (i.e., based on their monthly income) and accessible. Table 4 shows factors that influence biogas adoption in various countries in the region and Africa.

Table 4. Socio-economic factors influencing the adoption of biogas in other countries in the region and Africa.

Biogas Adoption Status in Various Countries in Africa	Country	Author
The adoption rate has been very slow in Ethiopia; distance to firewood sources negatively affects the adoption of biogas; having access to electricity in a community negatively impacts biogas adoption; low education levels limit biogas adoption because of a lack of understanding of the socio-economic and environmental benefits of biogas; demographic compositions and social factors significantly affect biogas adoption; and the high cost of biogas technology and low income of the households.	Ethiopia	[6,29,35,36]
Regardless of the multiple benefits of using biogas, adoption in Kenya is very low. Generally, people lack a full understanding of the benefits of biogas, and the availability of cheaper sources of cooking and heating fuel, such as firewood, charcoal, and kerosene, negatively affects biogas adoption, and the high cost of biogas technology negatively affects biogas adoption.	Kenya	[37]
The negative perception of the community about biogas. Others consider biogas as not safe, while others think that biogas generated from cow dung is dirt and, as such cannot be used for cooking. The technology is less affordable for rural households that rely on low and seasonal income. Additionally, inadequate technical expertise in biogas technology is playing a key role in hindering the uptake of biogas.	Malawi	[7,9]
The factors that motivate biogas adoption are its smoke-free nature, women and children having more time to engage in other development activities, and reduced time spent on cooking. However, more awareness is needed; high costs of biogas technology, thus requiring government subsidies to increase its adoption.	Uganda	[4]
A low level of education is hampering the adoption of biogas in South Africa because of the lack of understanding of its benefits; some households are aware of biogas, but they want to learn more about technical aspects of the technology. This indicates that there is a lack of a full understanding of biogas, and due to a lack of awareness, some think that using biogas is dangerous. In addition, the high initial capital cost of biogas hinders the uptake of biogas technology, and this is exacerbated by the challenge of low income of households.	South Africa	[23,38]
Fear of change, and as a result, households are unwilling to transition to biogas from traditional cooking fuels, and a low level of literacy in the villages hinders the awareness of biogas; and capital cost remains a bottleneck to biogas adoption, and there is a need to introduce financial incentives.	Nigeria	[39]
Fear of transition from cooking the traditional way and social, cultural, and religious objections to using animal or human waste hinders biogas adoption; higher income levels contribute to increased adoption of biogas.	Rwanda and Tanzania	[40]
Households prefer cooking with a firewood stove instead of a biogas stove; social/cultural/religious/health resistance or objection to handling or using animal or human waste for biogas production; low literacy levels make the adoption of the technology more difficult, and lack of awareness about the technology and its potential benefits prevents biogas adoption; and low income of the households contribute to low adoption of biogas.	Mozambique	[18]

4. Discussion

4.1. Prospects of Biogas Cooking Adoption by Households

4.1.1. Lack of Cleaner and Alternative Cooking Fuels

Only 4% of the population in rural areas have access to electricity in Malawi, and at Lizulu Market only 1% of the households use electricity for cooking. Other alternative sources of cooking energy, such as LPG, are not accessible and used for cooking. Generally, there are limited cooking options; thus, households are forced to choose from the dirty fuels they have. This explains why 99% of the households cited biomass in the form of charcoal and firewood as their first cooking choice. It was observed that agricultural waste was only used as a last resort, mainly when households did not have money to purchase charcoal and firewood. Thus, the use of agricultural waste is not a choice but a means for survival. One participant said, "Whenever I have money, I go to Lizulu Market to purchase firewood and charcoal. However, when I do not have money, I go to my farm and collect agricultural waste for cooking and heating". Another participant during the FGD said, "These maize stalks are not efficient; you need large quantities of them to cook a meal". This confirms the narrative that says that households are forced to choose a better fuel out of the dirty cooking options at Lizulu Market. The lack of cleaner and alternative cooking fuels creates a suitable environment for stakeholders to promote the uptake of biogas.

4.1.2. The Growing Scarcity and Rising Cost of Traditional Cooking Fuels

Due to deforestation, traditional cooking fuels are becoming scarce and expensive. The respondents acknowledged the increasing difficulty in sourcing firewood and the rising cost of charcoal. During the FGDs, one woman remarked, "Every year, it gets harder to find firewood, and the price of charcoal keeps increasing. We need another option, but we don't know what else we can use". Women who do not have money are forced to walk long distances to collect firewood, where they are exposed to sexual exploitation and harassment. For example, one woman remarked, "We wake up early in the morning to collect firewood, spending more than two hours every day". Another woman during the FGD said, "In the past, maize stalks were collected from any farm here because they were not valued by the owners. Not this time; you only collect from your farm". This signifies that traditional cooking fuels in the long term will not be available due to sustainability issues. The community has been experiencing an increase in the cost of charcoal and firewood, making these fuels less affordable. One respondent said, "Look at this bundle of firewood. It used to cost USD 0.96 a week ago; now it is USD 1.34. Many are not buying now, but they will get used to this". Thus, this creates an opportunity for the adoption of biogas. However, there is a need to consider the adoption of innovative models for delivering the biogas to ensure that it is more competitive against traditional cooking fuels.

4.1.3. A Strong Desire to Embrace New Cooking Technologies Regardless of Household Income

The results showed that 94% of the respondents were interested in learning more about cooking using biogas at Lizulu Market. This did not come as a surprise because only 38 respondents reported having heard about biogas. It was observed that 99% of the respondents were willing to try biogas for cooking as long as it is affordable. During the FGD, one woman remarked, "I am ready to use biogas for cooking as long as its price is not higher than that of firewood and charcoal". During the FGDs, LPG was also mentioned as an alternative, but many found it too expensive and expressed safety concerns. Biogas was considered as a potential solution, but concerns about its availability, reliability, and initial setup costs were raised. However, inaccessibility of biogas was cited by 97% of the households as the main challenge that may contribute to low adoption of biogas. On

the other hand, only 3% of the respondents cited lack of money, and none mentioned cultural belief as an obstacle to biogas adoption. The study also investigated the ability and willingness to pay for biogas by the households. The average income was determined to be USD 67 per month, and based on this income, 66% of the households indicated their willingness to pay for biogas using cash, while the remaining 34% preferred buying the biogas on credit. However, this was dependent on the price of the biogas. On average, the respondents were willing to pay USD 3.5 per week (i.e., USD 14/month). However, at the time of the study, these households were spending USD 7.6 on charcoal per month and USD 5.7 on firewood, which were lower than what they were willing to spend on biogas per month. These results indicate that households want a cleaner cooking fuel that is accessible and affordable. However, there is a need to adopt innovative financing ways, such as Results-Based Financing (RBF), Asset-Backed Leasing, Blended Finance Models, Village Savings and Loan Associations (VSLAs) Biogas Loans, Carbon Finance Integration, and Pay-As-You-Go (PAYG), to enable households to adopt biogas systems regardless of their income.

The results of this study may reflect what is happening in many other rural areas of Malawi. For example, the results of this study are in line with findings of various studies conducted in the country, where different authors have reported that biomass remains the first cooking option for households (i.e., biomass accounting for 99% of the energy needs) [1]. This shows that limited access to clean energy sources is a common challenge, especially in rural areas. Therefore, just like in Lizulu, many households in many other rural communities do not have alternative options, thus making biomass in the form of charcoal, firewood, and agriculture their first choice by default. All they are supposed to do is choose the best out of the available dirty fuels. Additionally, the average monthly income in Lizulu (i.e., USD 67) is in line with findings of other similar studies in Malawi. For instance, the national statistics reported that 70% of the population are living on less than USD 2.15 per day (i.e., USD 64.5 per month) [41]. This means that regardless of having or not having access to clean and alternative energy, many people in the rural areas will continue to struggle due to financial limitations. However, awareness and willingness to learn and use biogas may differ depending on the geographical area because of cultural and religious beliefs. Thus, there is a need to promote biogas awareness in most rural areas, considering that the technology is not widely developed. The awareness campaigns may also address the common challenge of waste management in markets that do not have access to waste management services.

4.2. Constraints to Biogas Cooking Adoption by Households

4.2.1. Cooking Energy Decision Making Process Hindering Biogas Adoption

The decision-making process plays a key role in determining the cooking energy choices at households at Lizulu Market, which can be attributed to cultural beliefs. In total, male household members were responsible for the provision of money for cooking in 63% of the households interviewed. However, once the money was provided, female household members were responsible for purchasing the cooking fuel in the majority of the households (i.e., 81%). This shows that men played a major role in cooking energy choices regardless of women taking the responsibility of searching and buying the cooking fuel. Women, who are burdened with searching for cooking fuel and cooking, will buy a certain type of cooking fuel depending on the amount of money provided by the male household members, who do not have a better understanding of the challenges that these women face. This arrangement does not favor women and may present a major challenge to transitioning to cleaner cooking fuels, such as biogas. This explains why the majority of the respondents (i.e., 49%) wanted just to try using biogas because it was something new

and strange to them when they were asked to mention the reasons for their willingness to use biogas for cooking. Moreover, the majority of the respondents were male (73%), who happened to be the heads of the households. This meant that their motivation for trying to use biogas for cooking was not driven by the understanding of the challenges associated with dirty fuels.

4.2.2. Households Positive Perceptions Towards Dirty Fuels

The study findings show that households will choose the best cooking fuel options from what they know and what is available in their community. Currently, out of the dirty cooking fuels they have, they choose charcoal as the best option, and they consider firewood as an option that is better than agricultural waste. This is also evidenced by the study findings, where 99% of the respondents indicated that biomass in the form of charcoal and firewood was their first choice. This is in line with the findings of many similar studies that found that biomass accounts for more than 90% of the cooking fuel in rural areas of Malawi [11,13,15]. At Lizulu Market, only 1% of the households interviewed regarded electricity as the first cooking energy option, yet it is estimated that 4% of the population in rural areas have access to grid electricity [42]. Generally, the use of electricity for cooking is low by those connected to the grid in Malawi, both in rural and urban areas, because many people believe that cooking using electricity is expensive. However, between charcoal and firewood, the majority of the respondents at Lizulu (i.e., 75%) preferred using charcoal. The respondents reported that charcoal is more efficient when compared with firewood and agricultural waste. In addition, charcoal is easier to store, transport, and use than firewood and charcoal. On the other hand, firewood is considered to be much better than agricultural waste because of the same efficiency and ease of use reasons. When asked about the reliability of the cooking fuels they mostly use or prefer, only 10% indicated firewood and charcoal are unreliable. However, their responses were based on what cooking fuels they know; as such, they were unable to compare these fuels with modern cooking technologies. One participant said, "Firewood and charcoal are reliable because they are available, and cooking is done very fast, unlike agricultural waste". Another participant said, "You can access charcoal and firewood at any time here at Lizulu Market, as long as you have money". This meant that accessibility to them made the fuel reliable. However, this accessibility is affected by the price of the cooking fuel and the household's income.

4.2.3. Lack of Awareness and Understanding of Biogas

Lizulu Market has a 40 m^2 biogas plant that is operated using a social enterprise model, and the plant supplies biogas to a few households and businesses using biogas backpacks. The users are required to pay a fee for the biogas supplied. In addition, the plant produces biofertilizer that is sold to farmers. Its strategic location enables the operators to collect organic waste generated in large quantities for biogas production. In addition, locating the biogas plant at the market that is frequented by many people throughout the day helps to increase biogas awareness. Regardless of this, the study findings showed that only 38% of the respondents were aware of biogas, but it was evident that most of them did not understand the benefits of using biogas over other cooking fuels available. Moreover, it was determined that 79% of the respondents had never used biogas before. During the FGD, one woman said, "I have just heard that a biogas plant is being constructed here at Lizulu Market, but I do not know exactly how the technology works". Therefore, the study results show that biogas awareness was very low. For example, during the FGDs one participant stated, "I have heard about biogas, but I always thought it was only for big companies or schools. I never imagined it could be used in homes like ours". Cultural

cooking practices played a significant role in fuel choices. Some participants worried that biogas might not produce enough heat for certain meals, especially those requiring long cooking times, such as beans or traditional stews. One participant remarked, "We cook large meals, and some foods need a strong fire to cook well. Can biogas really handle that?" In addition, when asked about why they want to try using biogas, the majority of them (i.e., 49%) were just fascinated by a new cooking technology but not its benefits, and another 2% reported that they are not willing to use biogas for cooking. This does not come as a surprise because the majority of the respondents (73%) were males, who do not understand the challenge associated with collecting and cooking using dirty fuels. This is worsened by the fact that males are responsible for providing money for cooking fuel purchases for the majority of the households at Lizulu Market (i.e., 63% of the households).

4.2.4. Low Education Levels and Low Income

Low education levels of the family heads do not only hinder biogas adoption because of a lack of understanding of its benefits but also reduce their chances of getting formal employment in Malawi. The study findings showed that only 6% of the respondents had full employment at Lizulu Market. In addition, this challenge is exacerbated by Malawi's weak economy that generates few jobs for the growing population, where many young people compete for the few employment opportunities available. Inability to obtain employment also plays a key role in limiting the economic opportunities of households. The income of the household is one of the important factors that can affect cooking energy options. Usually, households will settle for a cooking energy source that is available for free or at an affordable price [28]. Sustainable Development Goal Seven (SDG 7), Sustainable Energy for All (SE4ALL), and the 2018 National Energy Policy focus on energy affordability as a means for improving energy access. Simply put, this means energy accessibility is incomplete without consideration for affordability. Households in Lizulu, too, are expected to settle for cooking energy options that they can afford. In this study, the average income per month for the household was USD 67.00. Lizulu is mostly rural, where the cost of living is expected to be lower when compared to urban settings. This does not come as a surprise because at the national level it is estimated that 70% of the population earn under USD 1.90 per day and another 22% under USD 0.20 [1]. However, rising costs of farm inputs, such as fertilizer, contribute to food insecurity in Malawi. Eventually, a high inflation rate affects both urban and rural areas. An average income of USD 67.00 per month for households with an average occupancy of 4.6 people is not adequate to support basic needs, such as housing, food, water, and energy. Therefore, households are expected to have limited cooking energy options. For instance, a user who seeks to transition to LPG for cooking in Malawi initially is supposed to spend about USD 60, which is almost equal to what households earn per month in Lizulu. In this case, regardless of increased awareness about the advantages of cooking with LPG, it will be difficult for most households to transition to such clean cooking fuel [1,10].

4.3. A Comparison Socio-Economic Impacts on Biogas in Regional Countries and Africa

The results of this study are in line with findings of similar studies conducted in other regional countries and Africa, such as Ethiopia, Kenya, Tanzania, Malawi, Nigeria, Mozambique, Uganda, Rwanda, and South Africa, where low adoption rates were reported. The major socio-economic challenges that contribute to low adoption of biogas were low levels of education, lack of awareness and understanding of the biogas technology and its benefits, low income of households, and negative perceptions towards biogas use because some believe that it is not safe to use. However, at Lizulu, the results showed that households had some positive perceptions towards biogas, which is contrary to the

study findings of ref [9] in Malawi, ref [40] in Rwanda and Tanzania, and ref [39] in Nigeria. Generally, the majority of the households (i.e., 99%) wanted to learn more about biogas and try to use it for cooking if given an opportunity (i.e., assuming that biogas is affordable) to try biogas for cooking. This positive response signified a mindset change after enumerators explained the technology to the households that were not familiar with the technology. This was not the case in some other countries, where it was reported that fear of change and unwillingness of the households to transition to biogas from traditional cooking fuels contributed to the adoption of biogas, which could be a result of lack of knowledge about biogas. However, lack of awareness, low household income, and the high cost of biogas technology remain the common challenges that hinder biogas adoption in all the countries, including at Lizulu Market in Malawi.

5. Conclusions

This study was undertaken to investigate the opportunities and barriers related to the socio-economic status of the households at Lizulu Market and the potential for the adoption of biogas cooking fuel. Quantitative data were collected through a household survey, where households were targeted. In addition, qualitative data were collected, where participants were asked various questions related to cooking fuel options and biogas. The study findings showed that the major opportunities for biogas adoption were scarcity and rising cost of traditional cooking fuels, the willingness of the households to try using biogas for cooking, and the willingness to learn more about this alternative cooking fuel. The constraints to biogas adoption were determined to be low awareness and lack of understanding of biogas technology, as evidenced by the study results where most of the respondents indicated that charcoal and firewood are their preferred cooking options because they are reliable. They showed willingness to try biogas only after enumerators explained the biogas technology, its benefits and disadvantages, and the low income levels of the households, which may hinder the adoption of biogas regardless of their willingness to transition from dirty cooking fuels. Low educations levels not only exacerbate the challenge of biogas awareness but also their economic opportunities because family heads are unable to secure employment. With limited income, it will be difficult for many households to transition from traditional cooking fuels to biogas and other alternative cooking fuels regardless of showing interest in biogas. These results may reflect what actually is happening in many other similar areas in Malawi because the situation in terms of lack of access to clean and modern energy and household income is not much different. However, there could be some differences in different locations partly due to cultural and religious beliefs and interventions made to increase the awareness of clean and alternative energy through various projects in targeted areas. Therefore, more studies are needed, where some areas should be targeted because of variations in cultural and religious beliefs and levels of awareness of clean cooking technologies. On the other hand, when compared with other countries in the region, the contributing factors to low biogas adoption are the same, but in Lizulu the households showed interest in trying biogas for cooking, which should be an entry point for stakeholders to promote biogas adoption.

Author Contributions: Conceptualization, A.S.C. and B.T.; methodology, A.S.C., B.T. and H.B.C.; software, A.S.C.; validation, B.T.; formal analysis, A.S.C.; investigation, A.S.C., H.B.C. and B.T.; resources, A.S.C. and B.T.; data curation, A.S.C.; writing—original draft preparation, A.S.C. and H.B.C.; writing—review and editing, A.S.C., B.L.R., M.C. and B.T.; visualization, A.S.C. and B.T.; supervision, B.T., M.C. and B.L.R.; project administration, H.B.C. and A.S.C. All authors have read and agreed to the published version of the manuscript.

Funding: This research received no external funding.

Data Availability Statement: Data are contained within the article.

Acknowledgments: The biogas pilot project at Lizulu Market in Ntcheu Malawi was funded by the United Nations Development Programme (UNDP) and implemented through a collaboration between the Malawi University of Science and Technology (MUST) and Green Impact Technologies (GIT). The contributions of co-authors Benjamin Robinson and Mike Clifford to this publication were supported by the Innovate UK Energy Catalyst project, Smart Biogas 3: Digesting Data (Project Reference No. 10046103).

Conflicts of Interest: Authors declare no conflict of interest.

Abbreviations

The following abbreviations are used in this manuscript:

AD	Anaerobic Digestion
GIT	Green Impact Technologies
GoM	Government of Malawi
LPG	Liquefied Petroleum Gas
MUST	Malawi University of Science and Technology
MECS	Modern Cooking Energy Services
MoNREM	The Ministry of Natural Resources, Energy and Mining
MERA	Malawi Energy Regulatory Authority
MoE	Ministry of Energy
USD	United States Dollar
SE4ALL	Sustainable Energy for All
SGD	Sustainable Development Goal
SEI	Stockholm Environment Institute

References

1. Coley, W.; Eales, A.; Frame, D.; Galloway, S.; Archer, L. A market assessment for modern cooking in Malawi. In Proceedings of the 2020 IEEE Global Humanitarian Technology Conference (GHTC), Seattle, WA, USA, 29 October–1 November 2020. [CrossRef]
2. Kemausuor, F.; Adaramola, M.S.; Morken, J. A Review of Commercial Biogas Systems and Lessons for Africa. *Energies* **2018**, *11*, 2984. [CrossRef]
3. Mlowa, T.K.; Chitawo, M.L.; Kasulo, V. Policy Analysis on Clean Cooking in Malawi: Case of Improved Cookstoves. In Proceedings of the 2023 7th International Conference on Renewable Energy and Environment (ICREE 2023), Eskişehir, Turkey, 22–24 September 2023; pp. 1–7.
4. Mukisa, P.J.; Ketuama, C.T.; Roubík, H. Biogas in Uganda and the Sustainable Development Goals: A Comparative Cross-Sectional Fuel Analysis of Biogas and Firewood. *Agriculture* **2022**, *12*, 1482. [CrossRef]
5. Gbadeyan, O.J.; Muthivhi, J.; Linganiso, L.Z.; Deenadayalu, N.; Alabi, O.O. Biogas production and techno—Economic feasibility studies of setting up household biogas technology in Africa: A critical review. *Energy Sci. Eng.* **2024**, *12*, 4788–4806. [CrossRef]
6. Berhe, M.; Hoag, D.; Tesfay, G.; Keske, C. Factors influencing the adoption of biogas digesters in rural Ethiopia. *Energy Sustain. Soc.* **2017**, *7*, 10. [CrossRef]
7. MoNREM. *National Energy Policy*; Ministry of Natural Resources, Energy and Mining: Lilongwe, Malawi, 2018.
8. Rhenals-Julio, J.D.; Martínez, H.A.; Oviedo, M.D.; Arango, J.F.; Fandiño, J.M.M. Economic Assessment of the Potential for Renewable Based Microgrids Generation Systems: An Application in a University Building. *Int. J. Energy Econ. Policy* **2025**, *15*, 206–212. [CrossRef]
9. Kulugomba, R.; Mapoma, H.W.T.; Gamula, G.; Blanchard, R.; Mlatho, S. Opportunities and Barriers to Biogas Adoption in Malawi. *Energies* **2024**, *17*, 2591. [CrossRef]
10. GoM. *Malawi Biomass Energy Strategy*; Malawi Government: Lilongwe, Malawi, 2009.
11. Kambewa, P.; Chiwaula, L. Biomass Energy Use in Malawi. A Background Paper Prepared for the International Institute for Environment and Development (IIED) for An International ESPA Workshop on Biomass Energy, 19–21 October 2010, Parliament House Hotel, Edinburgh. Chancellor College, Zomba, Malawi. 2010. Available online: https://www.iied.org/sites/default/files/pdfs/migrate/G03075.pdf (accessed on 13 March 2025).
12. MECS. *Modern Energy Cooking Brief: Malawi*; Modern Cooking Energy Services: New Delhi, India, 2020.

13. SEI (Stockholm Environment Institute). Energy Access and Biomass Resource Transitions in Malawi. 2013. Available online: https://mediamanager.sei.org/documents/Publications/Climate/sei-pb-2013-malawi-energy-access.pdf (accessed on 7 March 2025).
14. Tetra Tech. *Modern Cooking for Healthy Forests in Malawi: Clean Cooking Market Information Package for Urban Malawi*; Tetra Tech: St. Hialeah, FL, USA, 2020.
15. Deloitte. *Action Agenda: Support to SE4ALL Country Actions processes in Malawi*; Deloitte: Blantyre, Malawi, 2017; Available online: https://www.scotland-malawipartnership.org/assets/resources/SE4ALL_Action_Agenda.docx (accessed on 7 March 2025).
16. Taulo, J.L.; Gondwe, K.J.; Sebitosi, A.B. Energy supply in Malawi: Options and issues. *J. Energy S. Afr.* **2015**, *26*, 19–32. [CrossRef]
17. GoM. *Digest of Malawi Energy Statistics*; Ministry of Energy: Lilongwe, Malawi, 2023.
18. Mabecua, F.; Dimande, N.; Condo, A.; Klintenberg, P.; Lucas, C.; Schwede, S. Barriers to successful implementation of small-scale biogas technology in Southern Africa: What can be learned from past initiatives in Mozambique? *Energy Proc.* **2024**, *43*, 11039. [CrossRef]
19. Innovate UK & UKAID. *Energy Catalysts—Country Guide: Malawi*; Innovate UK & UKAID: Swindon, UK, 2020.
20. Mhone, K. MERA Moderates Implementation of a New Electricity Base Tariff. Malawi Energy Regulatory Authority. Available online: https://mera.mw/2023/09/04/mera-moderates-implementation-of-a-new-electricity-base-tariff/ (accessed on 7 March 2025).
21. World Biogas Association. *Global Biogas Potential*; World Biogas Association: London, UK, 2024; pp. 1–56.
22. Abdel-shafy, H.I.; Mansour, M.S.M. Solid waste issue: Sources, composition, disposal, recycling, and valorization. *Egypt. J. Pet.* **2018**, *27*, 1275–1290. [CrossRef]
23. Mukumba, P.; Makaka, G.; Mamphweli, S. Biogas Technology in South Africa, Problems, Challenges and Solutions. *Int. J. Sustain. Energy Environ. Res.* **2016**, *5*, 58–69. [CrossRef]
24. Jameel, M.K.; Mustafa, M.A.; Ahmed, H.S.; Mohammed, A.; Ghazy, H.; Shakir, M.N.; Lawas, A.M.; Mohammed, S.; Idan, A.H.; Mahmoud, Z.H.; et al. Biogas: Production, Properties, Applications, Economic and Challenges: A Review. *Results Chem.* **2024**, *7*, 101549. [CrossRef]
25. Liebetrau, J.; O'Shea, R.; Wellisch, M.; Lyng, K.A.; Bochmann, G.; McCabe, B.K.; Harris, P.W.; Lukehurst, C.; Kornatz, P.; Murphy, J.D. Potential and utilization of manure to generate biogas in seven countries. *IEA Bioenergy Task* **2021**, *37*, 6.
26. Ellacuriaga, M.; García-Cascallana, J.; Gómez, X. Biogas Production from Organic Wastes: Integrating Concepts of Circular Economy. *Fuels* **2021**, *2*, 144–167. [CrossRef]
27. Ngabala, F.J.; Emmanuel, J.K. Potential substrates for biogas production through anaerobic digestion-an alternative energy source. *Heliyon* **2024**, *10*, e40632. [CrossRef] [PubMed]
28. Practical Action Consulting. *Final Quantitative Report on the Cost and Efficiency of Cooking Fuels in Malawi*; Practical Action Consulting: Warwickshire, UK, 2017.
29. Mohammed, A.S.; Atnaw, S.M.; Desta, M. The Biogas Technology Development in Ethiopia: The Status, and the Role of Private Sectors, Academic Institutions, and Research Centers. In *Energy and Environment in the Tropics*; Lecture Notes in Energy; Springer: Singapore, 2023; Volume 92. [CrossRef]
30. Mustafa, M.Y.; Calay, R.K.; Román, E. Biogas from Organic Waste—A Case Study. *Procedia Eng.* **2016**, *146*, 310–317. [CrossRef]
31. Benson, T.; De Weerdt, J.; Duchoslav, J.; Masanjala, W. *Fertilizer Subsidies in Malawi: From Past to Present*; International Food Policy Research Institute: Washington, DC, USA, 2024.
32. Gono, H.; Takane, T. Impact of subsidized fertilizer price increase on rural livelihood: A case study in southern Malawi. *Int. J. Dev. Sustain.* **2019**, *8*, 132–140.
33. Nyondo, C.J.; Nyirenda, Z.B.; Burke, W.J.; Muyanga, M. *The Inorganic Fertilizer Price Surge in 2021: Key Drivers and Policy Options*; Mwapata Institute: Lilongwe, Malawi, 2021.
34. Amato, C.; Jerie, S.; Mutekwa, T.V.; Shabani, T.; Shabani, T.; Tafadzwa, M. Impacts of solid waste management strategies in urban high density suburbs: A case of Amaveni suburb, Kwekwe, Zimbabwe. *Discov. Environ.* **2024**, *2*, 97. [CrossRef]
35. Hadush, M.; Gebregziabher, K.; Dejen, S. Adoption of Biogas Energy Technology and Its Socio-Economic Impact: Evidence from Northern Ethiopia. *Agric. Econ. Rev.* **2024**, *25*, 74–90.
36. Shallo, L.; Ayele, M.; Sime, G. Determinants of biogas technology adoption in southern Ethiopia. *Energy Sustain. Soc.* **2020**, *10*, 1. [CrossRef]
37. Wanjohi, A.M.; Irungu, E.K.; Gicheru, H.C. Biogas Program in Kenya: History, Challenges and Milestones. *Int. J. Environ. Health Sci.* **2022**, *2*, 3. Available online: https://www.kenpro.org/biogas-program-in-kenya-history-challenges-and-milestones/ (accessed on 13 March 2025).
38. Rasimphi, T.; Kilonzo, B.; Tinarwo, D.; Nyamukondiwa, P. Challenges, Opportunities, and possible Interventions in the Biogas sector in Rural areas of Limpopo, South Africa. *Energy Strategy Rev.* **2024**, *56*, 101562. [CrossRef]
39. Akinbami, J.F.K.; Ilori, M.O.; Oyebisi, T.O.; Akinwumi, I.O.; Adeoti, O. Biogas energy use in Nigeria: Current status, future prospects and policy implications. *Renew. Sustain. Energy Rev.* **2001**, *5*, 97–112. [CrossRef]

40. Rupf, G.V.; Bahri, P.A.; De Boer, K.; McHenry, M.P. Barriers and opportunities of biogas dissemination in Sub-Saharan Africa and lessons learned from Rwanda, Tanzania, China, India, and Nepal. *Renew. Sustain. Energy Rev.* **2015**, *52*, 468–476. [CrossRef]
41. World Bank. *Poverty & Equity Brief: Africa Eastern & Southern Malawi*; World Bank: Washington, DC, USA, 2023.
42. The World Bank. *Malawi Electricity Access Project*; The World Bank: Washington, DC, USA, 2019.

Disclaimer/Publisher's Note: The statements, opinions and data contained in all publications are solely those of the individual author(s) and contributor(s) and not of MDPI and/or the editor(s). MDPI and/or the editor(s) disclaim responsibility for any injury to people or property resulting from any ideas, methods, instructions or products referred to in the content.

energies

MDPI

Article

Kinetic Analysis of Construction, Renovation, and Demolition (CRD) Wood Pyrolysis Using Model-Fitting and Model-Free Methods via Thermogravimetric Analysis

Aravind Ganesan [1,2,*], Simon Barnabé [1,*], Younès Bareha [1], Simon Langlois [2], Olivier Rezazgui [2] and Cyrine Boussabbeh [2]

[1] Institut d'Innovations en Écomatériaux, Écoproduits et Écoénergies, Pavillon CIPP, Université du Québec à Trois-Rivières, Boul. des Forges, Trois-Rivières, QC G8Z 4M3, Canada
[2] Innofibre—Centre d'Innovation des Produits Cellulosiques, 3351, Boul. des Forges C.P.97, Trois-Rivières, QC G9A 5E6, Canada
* Correspondence: aravind.ganesan@uqtr.ca (A.G.); simon.barnabe@uqtr.ca (S.B.)

Abstract: The pyrolysis of non-recyclable construction, renovation, and demolition (CRD) wood waste is a complex thermochemical process involving devolatilization, diffusion, phase transitions, and char formation. CRD wood, a low-ash biomass containing 24–32% lignin, includes both hardwood and softwood components, making it a viable heterogeneous feedstock for bioenergy production. Thermogravimetric analysis (TGA) of CRD wood residues was conducted at heating rates of 10, 20, 30, and 40 °C/min up to 900 °C, employing model-fitting (Coats–Redfern (CR)) and model-free (Ozawa–Flynn–Wall (OFW), Kissinger–Akahira–Sunose (KAS), and Friedman (FM)) approaches to determine kinetic and thermodynamic parameters. The degradation process exhibited three stages, with peak weight loss occurring at 350–400 °C. The Coats–Redfern method identified diffusion and phase interfacial models as highly correlated ($R^2 > 0.99$), with peak activation energy (E_a) at 30 °C/min reaching 114.96 kJ/mol. Model-free methods yielded E_a values between 172 and 196 kJ/mol across conversion rates (α) of 0.2–0.8. Thermodynamic parameters showed enthalpy (ΔH) of 179–192 kJ/mol, Gibbs free energy (ΔG) of 215–275 kJ/mol, and entropy (ΔS) between −60 and −130 J/mol·K, indicating an endothermic, non-spontaneous process. These results support CRD wood's potential for biochar production through controlled pyrolysis.

Keywords: biomass conversion; thermochemical; pyrolysis; biofuels; kinetics; thermodynamics

1. Introduction

Construction, renovation, and demolition (CRD) activities generate huge volumes of waste. Particularly, countries where the construction of residential, commercial, and industrial spaces utilizes substantial quantities of wood fall under this case. According to [1] over 500 million tons (Mt) of CRD waste was generated annually across Canada, the USA, and Europe. The management and disposal of CRD wood residues create numerous environmental and economic challenges. This also includes furniture parts that are organically contaminated wood fibers without a promising scope for reuse [2]. Such wood contains treated, tinted, or composite materials infused with chemicals like polyaromatic hydrocarbons (PAHs), heavy metals, paints, lubricants, and resins, making them non-recyclable and deteriorating in quality [3]. Especially, chromated copper arsenate (CCA) remnants in CRD wood waste disposal could face major hurdles in terms of disposal due to rising restrictions [4]. A common, non-advisable practice followed for their

disposal is usually landfilling, which causes problems when these toxic substances from CRD wood waste leach into the surrounding soil and groundwater, posing serious risks to human and ecosystem health. The anaerobic decomposition of organic fractions in wood waste within landfills can produce harmful greenhouse gases (GHGs) like methane and carbon dioxide, contributing to the climate crisis [5]. Inadequate monitoring, a lack of public awareness, the absence of strict regulations for landfilling, and the economic/technological burden inflicted on recycling technologies for CRD wood allow handlers to look for easy disposal methods. Even simple sorting is complicated due to the large variability in wood composition with geography and provincial sourcing practices. These externalities exacerbate an already growing strain on limited landfill spaces. Hence, alternative waste management technologies are needed to pave the way for valorizing CRD wood residues to bioenergy, biochemicals, and bioproducts.

Waste forest wood, whether sequestered directly from the forests or sourced from CRD sites, is typically a low-value feedstock with a scarce probability of being reused or recycled. The economic value of such wastes could be improved using efficient thermochemical conversion technologies such as torrefaction, gasification, or pyrolysis [6]. Pyrolysis has immense potential in serving as a recovery pathway for refused wood residues, mainly due to its distinct product stream, moderate operation conditions, and relatively simpler operation/instrumentation than gasification [7]. Upon depolymerization of biomass in low or no oxygen, the transformation yields three major products with high energy and oxygen content: solid biochar, liquid pyrolysis oil or biooil, and pyrolysis gas [8]. Depending upon the application under focus, pyrolysis can either be carried out at low or high temperatures. For instance, low-temperature pyrolysis (<500 °C) produces cyclic, stable aromatics as in biochar, whereas temperatures > 600 °C produce pyrolysis gases that are partly condensable into bio-oil [9]. Bio-oil can serve as a foundation for producing platform chemicals or can be upgraded to fuel intermediates [10]. Pyrolysis gas, commonly referred to as energy-rich syngas, made of CO, CO_2, H_2, and other light C_1–C_3, can also serve as a base for liquid synfuels or can be combusted in boilers/furnaces for energy generation, surrounding it from a resource recovery perspective [11]. Biochar may serve as a partial substitute for fossil coal and carbon black in hard-to-abate industrial sectors such as metallurgy, automobiles, construction, agriculture, soil remediation, biogas production, air and water purification [12–15]. For a complex feedstock like CRD wood, pyrolysis may even trap all inherent hazardous components and immobilize them within the biochar product. But these biochars can eventually cause toxicity concerns because they may contain original PAHs from the wood feed, as well as volatile organic compounds (VOCs), dioxins, and free radicals that are persistent [16].

For safe pyrolysis, other non-wood contaminants like nails, plastics, concrete, glass, and rubber have to be removed without fail during the pre-treatment stages to avoid complications with reactor operation and efficient biomass conversion. On this note, for smooth conversion, CRD wood biomass has to be uniformly size-treated via shredding, grinding, or milling to reduce the particle size so that heat transfer, bulk density, and energy density limitations are subdued [17]. Whenever biochar is leveraged to address environmental or industrial challenges, its stability determines the resistance toward chemical, thermal, or microbial degradation while enabling it to act as a carbon sink [18]. The nature of feedstock and pyrolysis parameters like temperature, heating rate, and biomass residence time (BRT) govern this stability factor through the physicochemical properties of biochar, as understood from research by [19]. The final quality and intended applications depend on how the biomass feedstock is pre-treated, what the process optimization steps are, and the scale of production.

Biopolymers in biomass, such as cellulose, hemicellulose (together called holocellulose), and lignin contents, have specific decomposition pathways that take place at different temperatures and different stages. Solid-gas phase reactions involving multiple reactive species make the prediction of pyrolysis reaction modeling cumbersome [20]. To understand what pyrolysis does to CRD wood biomass, getting to know the kinetics and thermodynamics is beneficial. Kinetics describes the nature and type of chemical reactions occurring during pyrolysis and the energy required to form intermediate complexes and products, whereas thermodynamics describes how energy enters and leaves a system during these chemical reactions. Usually, pyrolysis may contain single-step reactions proceeding individually or multiple competitive biomass breakdown reactions that proceed simultaneously or sequentially, underscoring the intricacies of this process [21]. Yield; ion exchange capacities; and influence of ash, pore size, volatile content, and carbon arrangement in biochar are invariably dictated by the thermal degradation profiles too. Therefore, careful consideration of the various temperatures, heating rates, conversion rates, and selecting appropriate kinetic models is very important to forecast pyrolysis behavior. Thermogravimetric analysis (TGA) is a systematic and structured method used to study the chemical kinetics of biomass pyrolysis. According to [22], for fitting experimental data, assumptions based on different theoretical models are used via model-fitting methods, whereas the biomass conversion rate with the associated temperature required for that conversion at different heating rates is applied to the experimental TGA data via model-free or isoconversional methods (used interchangeably). Kinetic parameters such as activation energy and thermodynamic parameters like enthalpy (ΔH), entropy (ΔS), and Gibbs free energy (ΔG), can be calculated at each heating rate employed to study the influence of pyrolysis process parameters on biomass decomposition [23].

To the best of our knowledge, there has not been a detailed study on the reaction kinetics and thermodynamics of CRD wood waste pyrolysis. Hence, two unique aspects are undercovered here. The first novelty element in this work surrounds the utilization of an underexplored, heterogeneous, and real-world biomass feedstock in the form of CRD wood rejects, laden with organic and inorganic contaminants, to disseminate practical findings on its thermal degradation behavior. The second novel element focuses on extracting kinetic and thermodynamic parameters from the CRD wood TGA weight loss data under multiple heating rates, comparing the results yielded from different models. So, this dual emphasis on feedstock physicochemical/biochemical composition and robust pyrolysis modeling framework could result in meaningful contributions to the field of sustainable waste material management.

To assist in answering these questions, the objectives of our study will be to (a) succinctly explain the theory behind model-fitting and model-free techniques with necessary equations along with the benefits and drawbacks of adapting to these methods; (b) investigate the physicochemical characteristics of biomass, and understand its surface chemical make-up; and (c) analyze the thermochemical degradation reactions via TGA at different heating rates and calculate kinetic and thermodynamic parameters. These measures would facilitate understanding of a robust pyrolysis processes using CRD wood as a substrate for biochar production.

To engage with the aforesaid objectives, the idea behind each model is explored initially, followed by carrying out a compositional, proximate, ultimate, and metal analysis of the CRD wood waste to understand the physicochemical properties of the feedstock. Next, the surface chemistry of CRD wood was also studied using Fourier Transform Infrared (FTIR) spectroscopy to project its composition and structural framework. Subsequently, TGA experiments using CRD wood biomass at four different heating rates—10, 20, 30, and 40 °C/min—were carried out, and the data were cleaned and curated for analysis

according to the methods under consideration. Firstly, regarding model-fitting methods, the Coats–Redfern (CR) approximation was utilized. For isoconversional methods, the Ozawa–Flynn–Wall (OFW), Kissinger–Akahira–Sunose (KAS), and Friedman (FM) models were used. Based on the computed activation energy, pre-exponential factor, and other constants, the thermodynamic parameters were calculated. Finally, a prognosis of matching suitable reaction models to specific biomass conversion rates was also attempted.

2. Theory, Materials, and Methods

All analysis were performed using the same CRD wood waste, instrumentation, methods, and by the same technician, like what was elucidated by [3]. The characterization techniques are explained here again for clarity.

2.1. Foundational Derivation

Different biomass sources exhibit different reactions due to variability in composition [24]. Therefore, an exact determination of reaction kinetics during biomass thermal decomposition is almost impossible [25]. To understand the pyrolytic conversion of CRD wood into biochar, TGA of this biomass is carried out at same or different heating rates in the presence of nitrogen as an inert carrier gas. An effective TGA test can mimick crucial process conditions such as the temperature, BRT, heating rate, and feed particle size, which are usually interdependent operational factors in a pyrolysis process that help in critically determining the composition of resulting products [26]. Through a kinetic study, the activation energy of a feedstock can be computed to evaluate its reactivity, estimate its conversion efficiency, and assist in scale-up considerations to larger pyrolyzers during the design phase [27].

Rate of reaction for biomass in an isothermal condition is given as

$$\frac{d\alpha}{dt} = k{*}f(\alpha) \tag{1}$$

Here, k is the reaction rate constant, which is temperature-dependent; $d\alpha/dt$ is the change in mass of biomass taken for the analysis with respect to time (also referred to as biomass conversion rate); and $f(\alpha)$ is a differential function representing reaction models and governed by different reaction schemes presented in Table 1.

$$k = \left(\frac{\frac{d\alpha}{dt}}{f(\alpha)}\right) \tag{2}$$

In the above equation, α, which represents a fractional change in mass of biomass reactant, can be represented as

$$\alpha = \frac{(x_o - x_t)}{(x_o - x_{f)}} \tag{3}$$

Here, x_o is the initial mass of biomass sample used for the kinetic study by TGA, x_f is the final mass of sample at the end of TGA, and x_t is the mass of sample in the TGA cycle at a given time t. Decomposition rate of biomass as a function of temperature can be construed using the Arrhenius equation as follows:

$$k = A{*}\exp\left(\frac{-E_a}{RT}\right) \tag{4}$$

In the above expression, A is the pre-exponential or frequency factor (s^{-1} or min^{-1}), which represents the extent of molecular collisions in the wake of thermal decomposition at a given time and temperature; E_a is the activation energy required to cleave the bonds between feedstock biopolymers, namely cellulose, hemicellulose, and lignin (J/mol); R is the universal gas constant (8.3145 J/mol·K); and T is the temperature at which a particular

stage of conversion proceeds (K). Upon substituting the reaction rate constant k from Equation (2) within the global one-step Arrhenius expression in Equation (4), we arrive at

$$\frac{d\alpha}{dt} = A*\exp\left(\frac{-E_a}{RT}\right)*f(\alpha) \quad (5)$$

For a specific heating rate (K/min or K/s adopted during TGA, the temperature of the system is ramped up with respect to time and is, hence, a non-isothermal process. Note: K/min is also the same as °C/min due to the same magnitude with respect to a common time frame. An increase in K by one unit is identical to an increase in °C by one unit.

$$\beta = \frac{dT}{dt} \text{ (or) } dt = \frac{dT}{\beta} \quad (6)$$

By inserting the above heat rate expression and substituting for dt in Equation (5), we arrive at

$$\beta\left(\frac{d\alpha}{dT}\right) = A*\exp\left(\frac{-E_a}{RT}\right)*f(\alpha) \quad (7)$$

Equation (7) can be re-written as

$$\left(\frac{d\alpha}{dT}\right) = \left(\frac{A}{\beta}\right)*\exp\left(\frac{-E_a}{RT}\right)*f(\alpha) \quad (8)$$

This serves as the basic expression that could be leveraged for model-fitting and model-free methods to be built further.

2.2. Model-Fitting and Model-Free TGA Methods Rooting from Foundational Equations

Generally, to perform a kinetic analysis and calculate corresponding parameters, TGA can incorporate two approaches: model-fitting and model-free methods, which can detail a thermal decomposition process [28].

2.2.1. Model-Fitting Methods

As the name suggests, model-fitting method assumes that the experimental data obtained from any thermal decomposition reaction should fit into a pre-theorized model [29]. This is where the predicted term f(α) as in the aforementioned equations comes into play: to describe the relationship between the degree of biomass conversion or α and the overall rate of reaction, where only a single heating rate is sufficient. As outlined in Table 1, various forms of f(α) can take shape according to the type of reaction mechanism chosen for analysis that provide the output values of E_a and A [25–27,30].

Chemical reactions can be classified into first, second, and third order based on how the reaction rate relates to the concentrations of reactants. First-order reactions are reliant on the concentration of a single reactant, second-order reactions involve two reactants, and third-order reactions may include combinations of three reactants or elevated powers of one reactant. In biomass pyrolysis, biopolymers such as cellulose and lignin act as reactants, enabling numerous simultaneous reactions within the biomass. This study emphasizes these three orders, as higher-order reactions are uncommon and necessitate substantial energy to surpass activation energy barriers for multiple reactants to effectively collide. Furthermore, the diffusion mechanism pertains to the rate-limiting step regarding the movement of reactants, intermediates, and products through a medium [31] which can be characterized as one-dimensional, two-dimensional, or three-dimensional diffusion. One-dimensional diffusion occurs in a singular direction, like within linear, constrained porous channels. Two-dimensional diffusion takes place at surfaces or boundaries, while three-dimensional diffusion involves movement in all spatial directions, typical of bulk

solid regions. In systems related to biomass pyrolysis, mass and heat transfer are affected by these types of diffusion, which are influenced by reaction time, residence time, and temperature. Phase interfacial reactions occur at the junctions between solids and liquids or gases, influenced by aspects such as adsorption, diffusion, and desorption processes [32]. The rate of these reactions depends on factors such as surface area, composition, particle size, residence time, temperature, and the presence of reactive atmospheres. In the process of converting biomass to biochar, heat transfer mechanisms, namely, convection from the carrier gas and conduction from the surrounding biomass, are crucial. This conversion can result in the creation of secondary char and pyrolytic volatiles through random nucleation and growth mechanisms, where surface superstructures evolve into new phases that may display isotropic or anisotropic qualities [33]. This transformation might depend on how long surface clusters remain on the biochar and the temperature conditions that facilitate repolymerization and polycondensation reactions, akin to the processes seen in hydrothermal carbonization (HTC)-derived biochar [34]. Given its carbonaceous nature, biochar remains inherently reactive and continues to undergo various phase interfacial reactions even after its production, which is evident by its tendency to self-ignite when exposed to heat or air adsorption.

Table 1. Probable reaction mechanisms exhibited (non-exhaustive) during biomass pyrolysis. Adapted from equations in [25–27,35]. Here, g(α) is the integral function of f(α).

Reaction Model	Type/Mechanism	Denotation	f(α)	g(α)
Chemical	First-order	F_1	$1-\alpha$	$-\ln(1-\alpha)$
	Second-order	F_2	$(1-\alpha)^2$	$(1-\alpha)^{-1}-1$
	Third-order	F_3	$(1-\alpha)^3$	$[(1-\alpha)^{-2}-1]/2$
Diffusion	One-dimensional	D_1	0.5α	α^2
	Two-dimensional	D_2	$[-\ln(1-\alpha)]^{-1}$	$(1-\alpha)\ln(1-\alpha)+\alpha$
	Three-dimensional Jander (J)	D_3	$1.5(1-\alpha)^{2/3}[1-(1-\alpha)^{1/3}]^{-1}$	$[1-(1-\alpha)^{1/3}]^2$
	Three-dimensional Ginstling-Brounshtein (GB)	D_4	$1.5[(1-\alpha)^{-1/3}-1]^{-1}$	$(1-2\alpha/3)-(1-\alpha)^{2/3}$
Interfacial Phase	One-dimensional	R_1	1	α
	Two-dimensional	R_2	$2(1-\alpha)^{1/2}$	$1-(1-\alpha)^{1/2}$
	Three-dimensional	R_3	$3(1-\alpha)^{2/3}$	$1-(1-\alpha)^{1/3}$
Nucleation and growth	Two-dimensional	A_2	$2(1-\alpha)[\text{-}\ln(1-\alpha)]^{1/2}$	$[-\ln(1-\alpha)]^{1/2}$
	Three-dimensional	A_3	$3(1-\alpha)[-\ln(1-\alpha)]^{2/3}$	$[-\ln(1-\alpha)]^{1/3}$

Arrhenius Model

As seen in Equation (8), it is important to note that heating rate is brought in here and matters mostly when the temperature profile, as a function of time, is combined with the Arrhenius expression during non-isothermal reactions. This can be seen in complex reaction models to theoretically simulate real-world thermal depolymerization processes like pyrolysis, gasification, or combustion, where how much time a sample is subjected to a particular temperature can alter the conversion rate. Such models also introduce the element of non-equilibrium dynamics, such as complex heat-transfer mechanisms. On the other hand, the standalone Arrhenius equation assumes a steady-state reaction where the temperature during a conversion process is held constant (isothermal) with negligible changes. Even though this model assumes a system under equilibrium, it is not used here to imply that pyrolysis by itself, is a reversible process. However, it is highlighted here just as a relative empirical approximation that could be used to discern the critical role

of heating rate as in a non-isothermal and non-equilibrium system and also to arrive at a comparison between kinetic parameters derived from the two cases. Equation (8) is simplified as

$$\frac{\left(\frac{d\alpha}{dt}\right)}{f(\alpha)} = A*\exp\left(\frac{-E_a}{RT}\right) \tag{9}$$

Here, by applying the natural logarithms on both sides, we conclude with the expression of the basic Arrhenius model:

$$\ln\left(\frac{\left(\frac{d\alpha}{dt}\right)}{f(\alpha)}\right) = \ln(A) + \frac{1}{T}\left(\frac{-E_a}{R}\right) \text{ (or) } \ln(k) = \ln(A) + \frac{1}{T}\left(\frac{-E_a}{R}\right) \tag{10}$$

Plotting $\ln\left(\frac{\left(\frac{d\alpha}{dt}\right)}{f(\alpha)}\right)$ or ln(k) versus (1/T) results in a straight line with a negative slope of $(-E_a/R)$, while the y-axis intercept can be used to directly calculate A [36]. With respect to $\ln\left(\frac{\left(\frac{d\alpha}{dt}\right)}{f(\alpha)}\right)$, different reaction models and the equations for calculating their corresponding $f(\alpha)$ are described in Table 1.

Coats-Redfern (CR) Model

The CR method is a model-fitting technique used in chemical kinetics to study thermal decomposition of solid biomass matter, irrespective of woody or non-woody nature [37]. It is widely used by researchers for analyzing the pyrolysis of lignocellulosic materials. The CR model functions as an integral of Equation (1). To understand how we land at the CR expression and for calculation clarity, [26] state that a primary model function for biomass pyrolysis kinetics can be interpreted as

$$f(\alpha) = (1-\alpha)^n \tag{11}$$

where n is the order of reaction (1, 2, 3, …, n). Also, unlike the Arrhenius model, the CR model does not assume a steady-state or isothermal model and can function effectively by following different heating rates (β). So, by substituting Equation (11) in Equation (8),

$$\left(\frac{d\alpha}{dT}\right) = \left(\frac{A}{\beta}\right)*\exp\left(\frac{-E_a}{RT}\right)*(1-\alpha)^n \tag{12}$$

Upon rearranging this equation, it can be formulated as

$$\left(\frac{d\alpha}{(1-\alpha)^n}\right) = \left(\frac{A}{\beta}\right)*\exp\left(\frac{-E_a}{RT}\right)*dT \tag{13}$$

Now, introduction of the term $g(\alpha)$, i.e., the integral conversion of $f(\alpha)$ linking the extent of reaction to temperature and time, takes precedence, which is based on a specific reaction mechanism encountered by biomass during pyrolysis. Integrating within the limits of $\alpha = 0$ and $\alpha = \alpha$ at T = 0 and T = T, respectively [35,38] generates the following:

$$g(\alpha) = \int_0^{\alpha}\left(\frac{d\alpha}{(1-\alpha)^n}\right) = \int_0^{T}\left(\frac{A}{\beta}\right)*\exp\left(\frac{-E_a}{RT}\right)*dT \tag{14}$$

After integrating Equation (14) on the LHS first,

$$\frac{1-(1-\alpha)^{1-n}}{1-n} = \left(\frac{A}{\beta}\right)\int_{T_0}^{T}\exp\left(\frac{-E_a}{RT}\right)*dT \tag{15}$$

Following the recommendations by [35], after integration on RHS, Equation (15) becomes

$$\frac{1-(1-\alpha)^{1-n}}{1-n} = \left(\frac{ART^2}{\beta E_a}\right) * \left(1-\frac{2RT}{E_a}\right) * \exp\left(\frac{-E_a}{RT}\right) \quad (16)$$

Rearranging Equation (16),

$$\frac{1-(1-\alpha)^{1-n}}{T^2(1-n)} = \left(\frac{AR}{\beta E_a}\right) * \left(1-\frac{2RT}{E_a}\right) * \exp\left(\frac{-E_a}{RT}\right) \quad (17)$$

As shown by [38], assuming that $\left(1-\frac{2RT}{E_a}\right) \ll 1$ and can be neglected, Equation (17) can be reframed as

$$\frac{1}{T^2} * \frac{1-(1-\alpha)^{1-n}}{(1-n)} = \left(\frac{AR}{\beta E_a}\right) * \exp\left(\frac{-E_a}{RT}\right) \quad (18)$$

Applying natural logarithms on both sides of Equation (18), we get

$$\ln\left(\frac{1}{T^2} * \frac{1-(1-\alpha)^{1-n}}{(1-n)}\right) = \ln\left(\frac{AR}{\beta E_a}\right) + \frac{1}{T}\left(\frac{-E_a}{R}\right) \quad (19)$$

Albeit, the above equation is valid for $n \neq 1$. According to [39], pyrolysis of lignin-based solids is a first-order reaction, where n = 1. Moreover, according to [40], CR method adopts the basis of a single-stage first-order reaction during thermochemical breakdown of a solid fuel. Thus, Equation (19) becomes

$$\ln\left(\frac{-\ln(1-\alpha)}{T^2}\right) = \ln\left(\frac{AR}{\beta E_a}\right) + \frac{1}{T}\left(\frac{-E_a}{R}\right) \quad (20)$$

By inserting the integral function once again in Equation (20), we can simplify the expression as

$$\ln\left(\frac{g(\alpha)}{T^2}\right) = \ln\left(\frac{AR}{\beta E_a}\right) + \frac{1}{T}\left(\frac{-E_a}{R}\right) \quad (21)$$

For different reaction models (chemical reaction, diffusion, phase interfacial, nucleation, and growth) and associated mechanisms, the corresponding value of $g(\alpha)$ can be used from Table 1 to calculate kinetic parameters. Plotting $\ln\left(\frac{g(\alpha)}{T^2}\right)$ versus $\left(\frac{1}{T}\right)$ gives a straight line with a negative slope equivalent to $\left(\frac{-E_a}{R}\right)$. With the known value of E_a, it is possible to calculate A using the y-axis intercept $\ln\left(\frac{AR}{\beta E_a}\right)$.

Four key shortcomings of model-fitting methods are as follows: (a) the value of E_a is subjected to heavily depend on the reaction model assumed, when in reality, there is significant possibility of a process to manifest itself via several other models; (b) secondly, if the wrong model is chosen, the reliability of the measured kinetic parameter value can be questionable; (c) thirdly, a model-fitting method like CR may function harmoniously only at one specific heating rate at a given time where different reaction mechanisms can be tested under one roof for satisfactoriness rather than several heating rates simultaneously, as in iso-conversional models; (d) fourthly, despite providing an overview of E_a under many assumed models, it is a highly time-consuming method. Henceforth, while using model-fitting methods, it is advisable to assume as many reaction models as possible to help in quantitative analysis of E_a from more than a single perspective. In fact, it may be safe to say that convoluted processes such as pyrolysis can exhibit a myriad of simultaneous (parallel), sequential or both types of reactions at once. When using this approach, it could be possible to also narrow down on the ideal model using correlation coefficient (R^2) and simple cross-comparison.

2.2.2. Model-Free or Iso-Conversional Methods

Model-free kinetic methods do not assume that a chemical reaction progresses as per a pre-selected model under only a single heating rate. It considers the possibility of addressing complex chemical reactions at multiple heating and conversion rates [41]. Here, different values of α (in the range of 0–1) are used to calculate E_a without the necessity for $g(\alpha)$ intervention, thereby offering greater flexibility for the method [42]. It is here that common slow pyrolysis heating rates are employed (10–40 °C/min in our case) in the presence of nitrogen to detect variations in E_a at each stage of α. Different values of α are obtained in different phases of pyrolysis, due to which kinetic parameters under variable heating rates need to be compared and fitted separately one after the other [39]. In other words, we will be plotting for one α value (e.g., $\alpha = 0.1$) at all four heating rates (10, 20, 30, and 40 °C/min), proceed to the next conversion value (e.g., $\alpha = 0.2$) at the four heating rates, and so on till $\alpha = 1$. Variations in extracted E_a, for instance, may indicate that biomass decomposition in a pyrolysis-like setting encompasses an interplay of many different reaction mechanisms and not just one that improves overall dependability and robustness of the derived values of E_a. Although it is not necessary to use $g(\alpha)$ to calculate E_a, model-free methods need this function to calculate A and still depend upon a specific reaction model and mechanism. This is, without a doubt, a notable drawback of model-free methods that accentuates a limitation in fully characterizing both kinetic parameters without the role of assumptions. Also, model-free methods are criticised since they are too simplistic and general in describing a complex process like pyrolysis [26].

There are different model-free methods used in practice of approximating E_a of pyrolysis reactions, like FM, KAS, OFW, Vyazovkin (VZ), and distributed activation energy model (DAEM), that offer high simplicity during calculations. Among these, FM, KAS, and OFW are used in this study as representative methods. They are able to analyze complex reactions as a function of biomass conversion value, α. Using the expressions studied by [43,44], the following Table 2 illustrates the expression for these methods, values of constants/variables, and the procedure for plotting to evaluate kinetic parameters.

Table 2. Model-free or isoconversional methods.

Model-Free Method	Equation		Procedure for Plotting
OFW	$\ln(\beta) = \ln\left(\frac{AE_a}{Rg(\alpha)}\right) - 2.315 - 0.457\frac{E_a}{RT}$	(1)	Plot $\ln(\beta)$ versus $\frac{1}{T}$ to obtain a straight line with a negative slope of $-0.457\frac{E_a}{R}$ to calculate E_a. Using this and an assumed reaction model/mechanism for $g(\alpha)$, A can be calculated from the y-axis intercept, $\ln\left(\frac{AE_a}{Rg(\alpha)}\right)$.
KAS	$\ln\left(\frac{\beta}{T^2}\right) = \ln\left(\frac{AE_a}{Rg(\alpha)}\right) - \frac{E_a}{RT}$	(2)	Plot $\ln\left(\frac{\beta}{T^2}\right)$ versus $\frac{1}{T}$ to obtain a straight line with a negative slope of $-\frac{E_a}{R}$ to calculate E_a. Using this and an assumed reaction model/mechanism for $g(\alpha)$, A can be calculated from the y-axis intercept, $\ln\left(\frac{AE_a}{Rg(\alpha)}\right)$.
FM	$\ln\beta\left(\frac{d\alpha}{dT}\right) = \ln\left[(Af(\alpha))^n\right] - \frac{E_a}{RT}$ (or) $\ln\left(\frac{d\alpha}{dt}\right) = \ln\left[(Af(\alpha))^n\right] - \frac{E_a}{RT}$	(3)	Plot $\ln\beta\left(\frac{d\alpha}{dT}\right)$ or $\ln\left(\frac{d\alpha}{dt}\right)$ versus $\frac{1}{T}$ to obtain a straight line with a negative slope of $-\frac{E_a}{R}$ to calculate E_a. Using this and an assumed reaction model/mechanism for $f(\alpha)$, A can be calculated from the y-axis intercept, $\ln\left[(Af(\alpha))^n\right]$.

2.3. Thermodynamic Study

During pyrolysis, thermodynamic parameters such as ΔH, ΔS, and ΔG are calculated using the following equations adapted from [45].

$$\Delta H = E_a - RT_m \tag{22}$$

$$\Delta G = E_a - RT_m \ln\left(\frac{K_B \times T_m}{hA}\right) \tag{23}$$

$$\Delta S = \left(\frac{\Delta H - \Delta G}{T_m}\right) \tag{24}$$

In the above equations, T_m is the maximum thermal decomposition temperature of CRD wood biomass that was obtained from DTG curves at each heating rate (10–40 °C/min). E_a is the activation energy derived using isoconversional models of OFW, KAS, and FM at each heating rate and conversion stage. Pre-exponential factor, A, was also calculated from the respective plot using the intercept. K_B is the Boltzmann constant of 1.381×10^{-23} J/K, and h is the Plank constant, 6.626×10^{-34} J/s.

Equation (25) is however, a general and simplified expression that could be used to calculate the thermodynamic parameters, and it may not cover all intricacies posed by multi-step biomass pyrolysis reactions. Rather, it conservatively represents a general overview of the wood matrix decomposition. If over-simplification of pyrolysis occurs, especially by neglecting critical energy barriers, activation energy calculations could be erroneous, inevitably influencing entropies since they are very small.

2.4. CRD Wood Biomass Sample Preparation for Characterization and Kinetic Analysis

Non-recyclable CRD wood sourced from "BRQ Fibre et Broyure" in Trois-Rivières, Québec, was delivered in pails to the Innofibre facility Figure 1A. After collecting, the CRD wood underwent mechanical sieving using a Labtech vibrational sieving unit to separate it into different particle sizes (>4.5 cm till >0.3 cm) after screening and removal of contaminants (Figure 1B). In fact, no washing was carried out due to the risk of creating contaminated wastewater from the leaching of impurities present in the CRD wood. Once the size separation was completed, the selected biomass fraction in Figure 1C was dried for an entire night at 105 °C. Given that sieving only led to particle sizes of up to 0.3 cm, it was necessary to mill the CRD wood further. A Retsch SM300 mill (3 kW motor and 100–3000 rpm), featuring a high-speed tungsten carbide rotor and screens with openings as small as 500 µm, or a Thomas Wiley mill with a similar mesh size, was utilized to produce fine particles, as shown in Figure 1D, from the biomass for subsequent analysis.

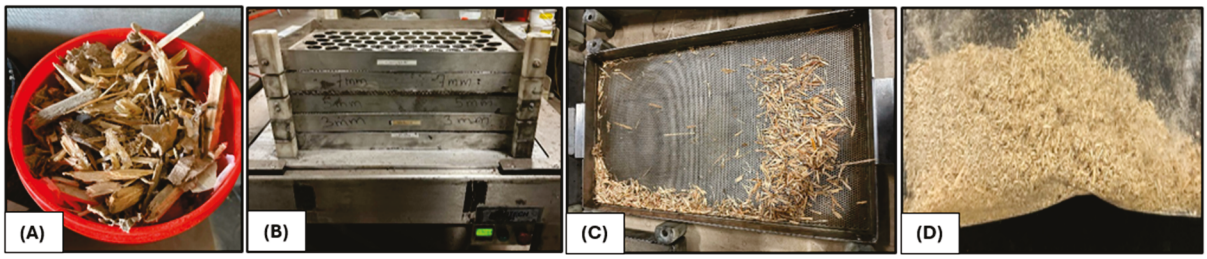


Figure 1. CRD wood sample conditioning and preparation: (**A**) CRD wood waste sourced in pails from the local provider; (**B**) vibrational sieving of CRD wood; (**C**) contaminant separated CRD wood of relevant particle size (<5mm and >3 mm); (**D**) milled CRD wood fines used for characterization and TGA experimentation.

2.5. Physicochemical Characterization

Proximate analysis was employed to evaluate ash content, volatile carbon (VC), and fixed carbon (FC) in biomass. For the ash measurement, 1 g of dry biomass fines was placed into a crucible and heated in a muffle furnace. Beginning at room temperature, the sample was heated to 106 °C at a rate of 5 °C/min and maintained at this temperature for 1 h to ensure that most residual moisture is removed. Then, the temperature was increased at the same rate from 106 °C to 550 °C to decompose labile extractives and organics under controlled heat transfer. At 550 °C, the wood sample was held for a duration of 4–6 h for further degradation of any combustible biomass components. The sample was then allowed to cool to room temperature in a desiccator to prevent any hygroscopic effects, after which the ash was weighed to ascertain the proportion of biomass remaining. For volatile carbon, 1 g of dry biomass fines was subjected to heating at 900 °C for 7 min in a sealed crucible, after which it was cooled and weighed to quantify the carbon lost. VC is utilized in certain contexts in this study to specifically refer to labile carbon, distinguishing it from other volatile components. FC was calculated using the relation FC = 100 − (VC + ash) as weight percent dry basis (wt%DB), where VC and ash are also represented as wt%DB [46].

For the ultimate analysis, an Elementar Vario Macro Cube examined 1–200 mg of dry biomass fines for elements such as carbon, hydrogen, nitrogen, and sulfur, utilizing helium (purity > 99.996%) as the carrier gas and oxygen (purity > 99.996%) for combustion up to 1200 °C. The oxygen content was determined by calculating the difference from 100%, using the percentages of all individual elements and ash, as given in [oxygen $= 100 - (\text{carbon} + \text{hydrogen} + \text{nitrogen} + \text{sulfur} + \text{ash})$]. It is derived from [47].

The higher heating value (HHV) of CRD wood biomass was determined using a similar approach outlined by [48]. This approach correlated the calorific value with elemental composition obtained from ultimate analysis of the biomass sample. For metal detection in biomass, an Agilent Technologies 4210 Microwave Plasma Atomic Emission Spectrometer (MP-AES) was utilized, which featured a nitrogen fuel source and an SPS 4 autosampler. This apparatus allowed for the simultaneous analysis of multiple elements by aerosolizing the biomass sample into a nitrogen plasma to produce monoatomic ions. The device guaranteed accurate measurements of the inorganic content by completely digesting the organic materials found in the biomass.

2.6. Composition Analysis

The presence of extractives, structural carbohydrates, and lignin in CRD wood biomass were analyzed according to National Renewable Energy Laboratory (NREL, United States of America Department of Energy) procedures as described in [49,50] respectively.

2.7. FTIR

The distribution of surface functional groups in biomass was examined using an Agilent Technologies Cary 630 spectroscope, with Microlab 5.8 and Microlab Expert 1.3 for operation. About 1 g of dry biomass fines was placed on a diamond crystal surface that was regularly cleaned with ethanol. The analysis was performed in transmittance mode over a spectral range of 500–4000 cm^{-1} to determine the chemical bonds present in the material. Baseline and peak corrections were applied to the obtained spectra, followed by signal smoothing.

2.8. TGA

In order to examine the weight loss pattern of biomass in relation to temperature, a PerkinElmer TGA 8000 analyzer was utilized. This device was also able to assess proximate analysis parameters such as moisture, VC, FC, and ash. Only 8 mg of biomass fines in

their original, non-dried state were needed per vial for the analyzer. Since TGA was leveraged to analyze the pyrolysis kinetics of CRD wood, the process gas used during heating was compressed nitrogen with a purity level exceeding 99.996%. The system was capable of accurately reaching temperatures up to 1200 °C with adjustable heating rates. For this research, 10, 20, 30, and 40 °C/min were employed, reaching a maximum temperature of 900 °C to investigate the transformation of biomass to biochar. Differential thermogravimetric (DTG) curves were generated by differentiating the weight loss features from the original thermogram in relation to time and plotting them against temperature. This led to the identification of different peaks indicating the points of maximum weight loss or melting of the sample during TGA, along with the corresponding temperatures, providing insights into biomass chemical composition and hydrocarbon structure.

3. Results and Discussion

3.1. Physicochemical Properties of CRD Wood—Comparative Analysis with Other Biomass Feedstock

The proximate and ultimate analysis parameters of CRD wood biomass were analyzed, as shown in Table 3. The elemental composition, particularly carbon content in CRD wood, resembled hardwoods like beech and poplar, reaching 49–50% despite containing softwood residues in the bale. In terms of carbon content, MSW outperformed all the feedstocks, with a carbon content of 76.26% due to a heterogeneous composition involving plastics and other hydrocarbon-rich residues. Oxygen (41.74%) and hydrogen (6.12%) were also equivalent to the ranges in hardwood species. These bolster the role of CRD wood biomass in bioenergy applications for the production of biofuels, biochemicals, and bioproducts. Low sulfur (from gypsum dust, if any) and nitrogen content in CRD wood also means that the release of NOx and SOx could be starved during pyrolysis. For proximate parameters, CRD wood is a low-ash biomass at 1.17% relative to high-ash agricultural residues like rice husk at 14.20% or medium-ash sources like MSW (8.26%).

Table 3. Physicochemical properties of CRD wood in comparison with different biomass sources. References are mentioned below the characterization results in the table.

Biomass	Pinewood	Rice Husk	Beech	Wheat Straw	Miscanthus *	Madhuca Longifolia	Poplar Sawdust *	Palm Kernel *	MSW	CRD Wood *
Proximate analysis										
Moisture (wt%)	4.01	10.10	15.20	11.63	---	5.98	---	---	2.75	**---**
Volatiles (wt%)	64.37	52.30	84.87	65.32	83.30	71.26	83.60	79.68	51.13	**82.35**
FC (wt%)	24.89	23.40	14.53	15.17	14.40	18.24	15.40	16.78	37.86	**16.48**
Ash (wt%)	6.73	14.20	0.60	7.88	2.30	4.50	1.00	3.54	8.26	**1.17**
Ultimate analysis										
C (wt%)	54.53	34.99	49.38	44.12	47.50	47.20	49.47	43.84	76.26	**49.88**
H (wt%)	6.56	4.58	6.17	6.34	6.10	5.90	5.89	6.13	6.88	**6.12**
S (wt%)	0.09	---	0.01	---	0.10	1.20	0.05	0.06	0.28	**0.10**
N (wt%)	0.94	1.95	0.28	0.63	1.00	3.60	1.40	3.11	3.32	**0.99**
O (wt%)	31.14	34.18	43.55	39.99	45.30	42.10	43.12	46.86	13.25	**41.74**
Van-Krevelen parameters										
H/C	1.44	1.57	1.50	1.72	1.54	1.50	1.43	1.68	1.07	**1.47**
O/C	0.43	0.73	0.66	0.68	0.72	0.67	0.65	0.80	0.13	**0.63**
Calorific value										
HHV (MJ/kg)	22.33	14.09	19.3	15.29	15.82	---	19.50	16.83	29.70	**20.28**
Reference	[51]	[52]	[53]	[54]	[55,56]	[57]	[58]	[59,60]	[61]	**Present study**

* Expressed in wt%DB.

However, as delineated in Figure 2, the metal content in CRD wood, mainly alkaline and alkaline earth metals (AAEM) (86–87%), was very high which may result in secondary reactions by acting as indirect catalysts, leading to excess loss of carbon or technical snags in reactor equipment through slagging, fouling, or bed agglomeration [62,63]. However, among AAEM, alkaline earth metals like Ca, Ba, and Mg constituted 59.96%, whereas alkaline metals made up just 27.03%. So, there could be a possibility where the melting of ash may be pushed toward relatively higher temperatures since the presence of divalent species dominated this AAEM fraction. On the contrary, the other possibility with high AAEM could be secondary char formation [64]. AAEM, when present with woody biomass under pyrolysis temperatures of 350–750 °C, may increase the yield of biochar through secondary reactions [65]. This holds true for an AAEM-rich feedstock like CRD wood. Additionally, CRD wood contains some heavy metallic contaminants like Cu, Cr, and mild levels of As. Other heavy metals detected were mainly Zn and Pb. All these metals are part of preservatives, paints, varnishes, roofings, and surface coatings in conditioned CRD wood that are usually part of residential buildings, electricity poles, and handrails dating back to the 1960s–1990s. The VC in CRD wood (82.35%) matches VC in poplar (83.60%) and beech (84.87%), confirming highly decomposable fractions. Also, due to high volatiles and low ash, woody biomass could produce biochar product with high FC [66]. Also, due to the lower ash content that minimizes the presence of non-combustible materials, the HHV of CRD wood biomass is relatively high, at 20.28 MJ/kg, rendering it suitable for bioenergy applications [67]. On the contrary, a high ash rice husk had a low HHV at 14.09 MJ/kg. Wheat straw with moderate ash also had a low HHV of 15.29 MJ/kg. Another pattern observed is that as volatiles increase, HHV decreases due to the non-availability of stable carbon. This was true for MSW (51.13%) and pinewood (64.37%) relative to CRD wood (82.35%), where the increase in volatiles decreased HHV from 29.70 MJ/kg, 22.33 MJ/kg, and 20.28%, respectively.

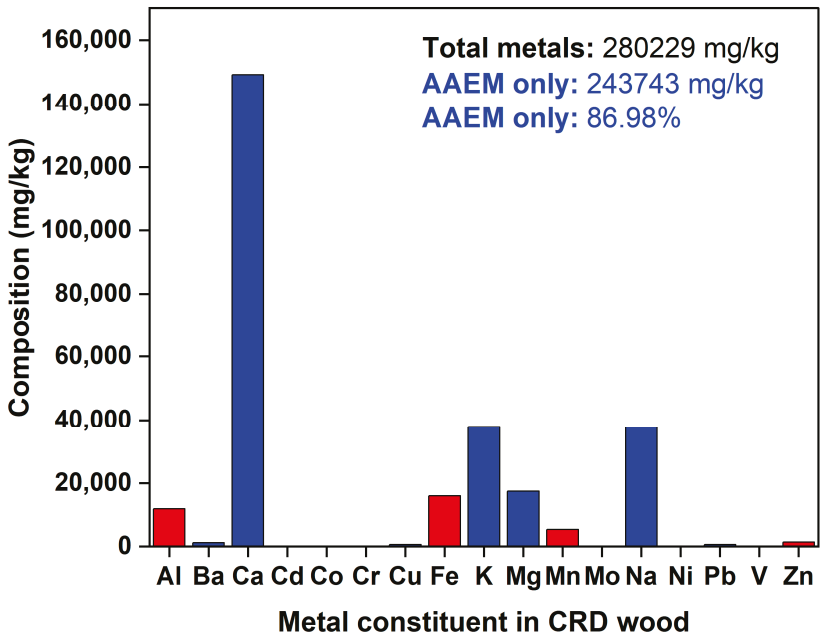


Figure 2. Metal constituents in CRD wood. Blue bars represent AAEM in CRD wood, and red bars denote other metals.

3.2. CRD Wood Compositional Analysis

To achieve a representative and robust analysis of CRD wood biomass received, samples from four different sections of the pail, post-sample preparation steps, were subjected

to compositional analysis. Percentages of extractives, holocellulose, and lignin are listed in Table 4, which may explain the nature of biomass transformation to biochar. Extractives soluble in hot water and ethanol ranged from 2 to 3.5% and 2.5 to 4%, respectively, which are usually eliminated as volatiles. Since total lignin varied from 24 to 31%, it is conclusive that CRD wood is composed of both hard and softwood and may be called "wood waste" that has a comparable lignin content, recorded at 28.9%, as shown by [68]. As shown by [69], biochar produced from agriculture wastes like buckwheat husk (holocellulose: 73.72%, lignin: 24.73%), spent coffee grounds (holocellulose: 31.58%, lignin: 23.65%), hazelnut shell (holocellulose: 62.31%, lignin: 28.30%), and waste grass biomass like hemp (holocellulose: 25.81%, lignin: 20.69%) and miscanthus (holocellulose: 63.11%. lignin: 25.48%) were also compared. The greater the lignin, the greater the structural complexity due to the presence of aromatics, and the greater the biochar yields [70]. However, the lignin content in biochar is not a solely conclusive indicator of the mechanical strength/integrity and yield of biochar [71,72]. However, in lignin, if softened and melted to form condensed aromatic structures, the overall bulk density and resistance to breakage may increase [62]. The carbon content and stability of biochar could be largely conserved as well. The total holocellulose content in CRD wood varied from 68 to 77%. With six-carbon sugars like glucose (44–54%), galactose (0.5–2.5%), and mannose (2–10%), and five-carbon sugars like xylose (8–24%) and arabinose (0–1.5%), hemicellulose decomposition in CRD wood to pyrolysis gases at lower temperatures is plausible. The overall contribution to char formation is low for hemicellulose. Cellulose decomposition could favor both condensed volatiles and intermediates (high temperatures) and some char (lower temperatures) formation. This is determined by the temperature, BRT, and heating rate employed during the process [73].

Table 4. Biochemical composition of CRD wood lots from the same bale.

Biomass Constituents	Lot 1	Lot 2	Lot 3	Lot 4
Hot Water Extractives (wt%)	3.2	2.0	3.1	2.7
Ethanol Extractives (wt%)	3.7	3.0	2.8	4.0
Total extractives (wt%)	**6.9**	**5.0**	**5.9**	**6.7**
Insoluble Lignin (wt%)	19.7	20.5	26.1	25.3
Total Lignin (wt%)	**24.9**	**26.2**	**30.2**	**29.7**
Glucan (wt%)	50.9	44.2	46.9	53.1
Xylan (wt%)	19.2	23.2	8.0	10.1
Arabinan (wt%)	0.0	0.1	0.9	1.3
Galactan (wt%)	0.6	0.8	2.5	2.4
Mannan (wt%)	2.0	2.3	9.7	10.0
Total holocellulose (wt%)	**72.7**	**70.6**	**68.0**	**76.9**

3.3. FTIR Spectroscopy Analysis

The FTIR spectral distribution of the CRD wood biomass is shown in Figure 3. A high concentration of specific functional groups in the CRD wood biomass feed is denoted by strong transmittance peaks of infrared light through the sample, which demonstrate specific vibrational patterns: stretching or bending. Spectral band assignments from [74,75] were used to match the transmittance peaks in CRD wood biomass to relevant functionalities. Firstly, the distinct peak at 3320 cm^{-1} indicates O-H stretching vibrations, as in moisture, carboxylic acids, alcohols, and phenols. Secondly, the distinct peak at 2892 cm^{-1} could signify C-H stretching in aliphatic hydrocarbons, as in alkanes that are subunits of most biomass polymers. Thirdly, the spectral band at 2003 cm^{-1} highlights stretching

vibrations in alkynes (C≡C) that may be ascribed to polyaromatics with maximal carbon condensation. Next, a carbonyl stretch (C=O) in aldehydes, ketones, esters, and carboxylic acids appears around 1730 cm^{-1}, which stems from hemicellulose in CRD wood. This contributes to the loss of biomass carbon as CO and CO_2 during the onset of pyrolysis. A subdued peak at 1503 cm^{-1} and 1265 cm^{-1} means there are faint aromatic C-C and aromatic C-O ring stretching actions, respectively, amidst the biomass carbon skeleton. Methyl, methylene, or methoxy groups of biomass lignin also exhibit these vibrations owing to the presence of dense organic residues in biomass. A sharp band at 1022 cm^{-1} may be due to C-O stretching in aliphatic ethers (C-O-R) and alcohols (C-O-H) that are key building blocks of carbohydrates/polysaccharides. The 799 cm^{-1} band could be an extractive in biomass, showcasing the C-H bend in alkynes, phenyl rings, or aromatics, followed by the band at 664 cm^{-1} stemming from C-H vibrations in alkenes.

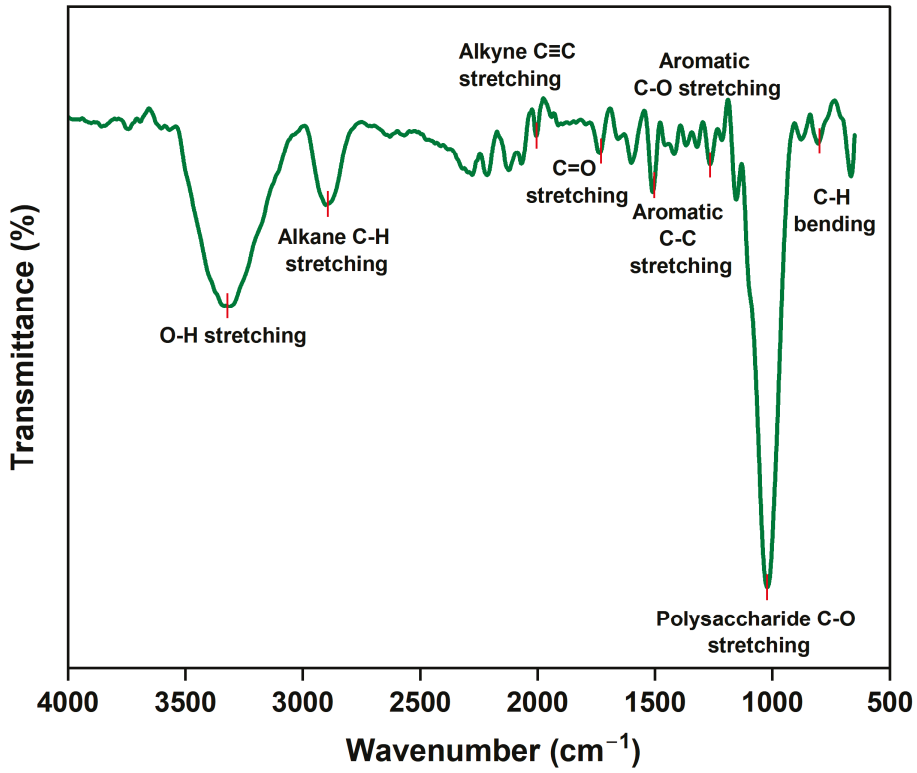


Figure 3. FTIR spectral distribution of CRD wood with functional group attributes.

3.4. TGA Analysis and Effect of Heating Rate

The thermal stability of CRD wood biomass was verified by TGA and DTG curves. The weight loss exhibited by biomass under four different heating rates, 10, 20, 30, and 40 °C/min, along with their stages of thermal degradation under an inert nitrogen atmosphere mimicking pyrolysis, were studied, as shown in Figure 4. In the TGA plot in Figure 4A, it is evident that an increase in the heating rate pushes the degradation temperature slightly higher (to the right), as reported by [76]. This is because an increase in the heating rate means that there is less time for heat to permeate from the surface to the core of the biomass particle, and that too, only non-linearly. So, the weight loss encountered is restricted as a surface effect rather than occurring throughout the particle and is hence low. At a lower heating rate, an inverse phenomenon, where there is gradual heat transfer that devolatilizes biomass constituents to fruition over an ample time frame, is clear. The biomass's outer layer and the core inside reach almost similar temperatures, allowing a linear thermal behavior. This is validated by the maximum weight loss (72.73%) between 200 and 400 °C for the heating rate of 10 °C/min, followed by 69.45%, 64.95%, and 60.85% for the heating rates of 20, 30, and 40 °C/min, respectively. However, despite an

increase in the heating rate by every 10 °C/min, the profile for degradation curves is unchanged, as concurred by [77].

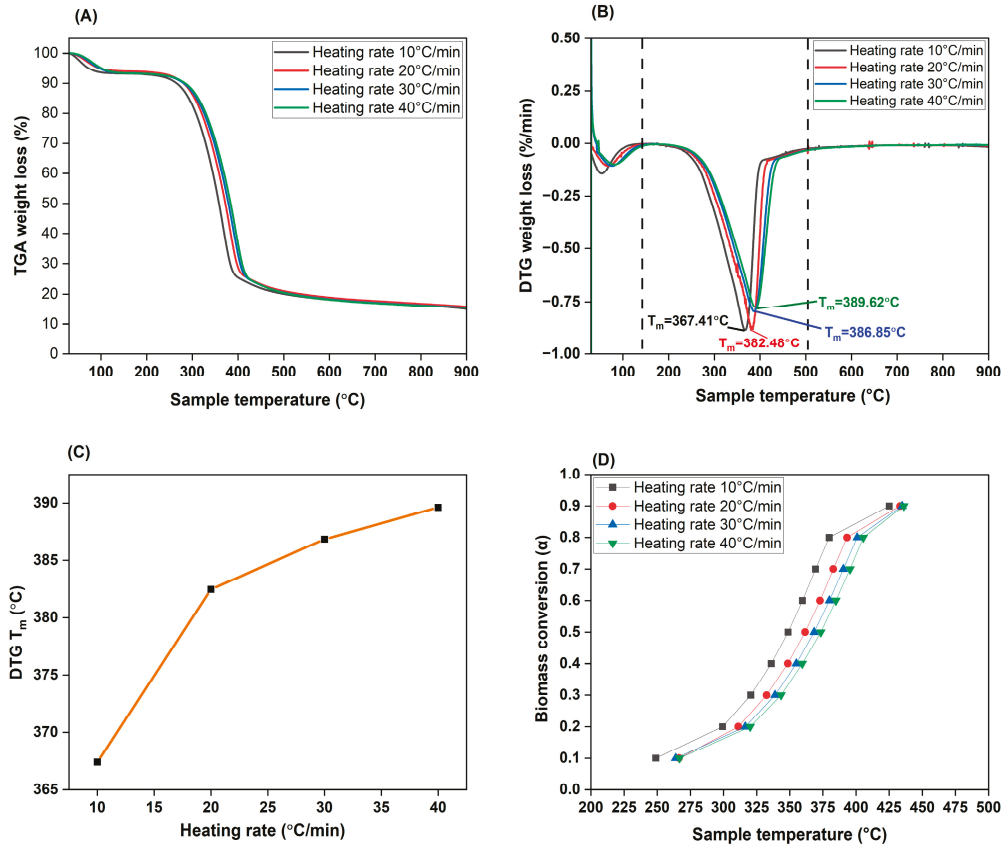


Figure 4. TGA and biomass conversion analysis. (**A**) TGA weight loss data of CRD wood for 10, 20, 30, and 40°C/min; (**B**) corresponding DTG profile; (**C**) Variation of peak melting temperature (T_m) with heating rate; (**D**) Variation of CRD wood conversion (α) with heating rate. The difference between ash measured by proximate analysis and ash in the TGA curve may be due to slower conversion due to the heating rates chosen. The ash levels in (**A**) may match the proximate analysis results if a test with heating rates < 10 °C/min is chosen to allow for sufficient depolymerization time, considering the complexity of the feedstock.

If we look more closely at the DTG peaks for these heating rates, weight loss happens in three stages. The first stage occurs < 150 °C, where evaporation of moisture and other surface-bound volatiles occurs [78]. Around 5–7% weight loss happened here. As seen in Figure 4B,C, within the second stage from 200 to 400 °C, the melting temperatures of biomass (T_m) for each heating rate was observed to increase with an increase in the heating rate (367.41 °C for 10 °C/min to 389.62 °C for 40 °C/min), validating our earlier finding that greater BRT at that specific temperature means that there is adequate time for biomass to experience loss of structural integrity by efficiently exposing its biopolymers for cleavage, signifying an ongoing pyrolysis process [79]. This region encompasses extractives, VOCs, hemicellulose, and cellulose breakdown, respectively, with peak decomposition mainly between 350 and 400 °C. Since cellulose is a straight-chain, crystalline polymer, it needs greater energy to collapse and, hence, disintegrates after relatively less stable hemicellulose degrades to a large extent. Biomass carbon (e.g., carbon loss via CO_2 and CO) and heteroatom (e.g., H_2S, SO_2, and NH_3) rejection reactions from holocellulose, followed by the simultaneous heat uptake to initiate destabilization of lignin aromatics (e.g., phenols), are key reactions that increase the yield of gas and condensible volatiles. In the conversion (α) plot in Figure 4D, we can see that 80% (α = 0.8) is completed around

400 °C. In this second stage, profound mass loss of 60–73% took place. Beyond this point, the third stage of decomposition is rather slow and proceeds well-spaced out due to complex lignin fractions and other high-molecular-weight compounds. Moreover, since CRD wood contains noticeable AAEM and other metals/inorganics in its ash fraction, it could be stable up to a certain level and delay breakdown. This is when char generation peaks due to both primary and secondary pyrolysis reactions. It is safe to say that no additional peaks were observed, which means that significant degradation of inorganic material may not be accounted for. At the end of the process, about 20% of the initial mass of CRD wood remains. All in all, there was another interesting observation. At higher heating rates of 30 and 40 °C/min, decomposition peaks appear to overlap, which indicates that the degradation of biomass polymers may not be completely separated processes and could occur sharply within a narrow temperature range and as synchronous steps. As concluded by [76,80], the thermal decomposition patterns remained fairly consistent across all the heating rates tested.

3.5. Kinetic Analysis of CRD Wood Pyrolysis

3.5.1. Model-Fitting Method

Being a model-fitting technique, the CR method fits TGA data of biomass pyrolysis to various kinetic models used for calculating the activation energies and pre-exponential factors. The calculations in Table 5 surrounded all models for the four different heating rates, i.e., 10–40 °C/min. The correlation factor (R^2) was used to judge the probability of each reaction model being interplayed. No marked increase in activation energy existed between different heating rates, although it was maximum for 30 °C/min, as shown in Figure 5.

Table 5. Activation energy (E_a), pre-exponential factor (A), and model correlation (R^2) of different pyrolysis reaction models (albeit, non-exhaustive list) evaluated using the CR method.

Reaction Model	Type/Mechanism	Heating Rate = 10 °C/min			Heating Rate = 20 °C/min			Heating Rate = 30 °C/min			Heating Rate = 40 °C/min		
		Activation Energy, E_a (kJ/mol)	Pre-Exponential Factor, A (min^{-1})	R^2 from Plot	Activation Energy, E_a (kJ/mol)	Pre-Exponential Factor, A (min^{-1})	R^2 from Plot	Activation Energy, E_a (kJ/mol)	Pre-Exponential Factor, A (min^{-1})	R^2 from Plot	Activation Energy, E_a (kJ/mol)	Pre-Exponential Factor, A (min^{-1})	R^2 from Plot
Chemical	First-order (F_1)	65.82	5.0873×10^4	0.9882	67.34	1.0329×10^5	0.9888	66.40	1.0953×10^5	0.9881	66.40	1.3118×10^5	0.9864
	Second-order (F_2)	94.62	3.0881×10^7	0.9559	94.62	6.1763×10^7	0.9563	96.89	9.7105×10^7	0.9563	95.55	6.9599×10^7	0.9524
	Third-order (F_3)	129.70	6.4717×10^{10}	0.9217	129.70	1.29434×10^{11}	0.9219	132.90	2.1212×10^{11}	0.9219	131.05	1.2162×10^{11}	0.9172
Diffusion	One-dimensional (D_1)	98.06	1.2944×10^7	0.9992	98.06	2.5889×10^7	0.9993	100.22	3.9199×10^7	0.9993	99.07	2.8758×10^7	0.9997
	Two-dimensional (D_2)	110.51	1.0282×10^8	0.9993	110.51	2.0565×10^8	0.9996	112.97	3.1433×10^8	0.9996	111.67	2.1457×10^8	0.9992
	Three-dimensional J (D_3)	125.69	6.4219×10^8	0.9958	125.69	1.2844×10^9	0.9963	128.54	1.9907×10^9	0.9963	127.04	1.2459×10^9	0.9949
	Three-dimensional GB (D_4)	115.52	6.8969×10^7	0.9986	115.52	1.3794×10^8	0.9989	118.12	2.1179×10^8	0.9989	116.75	1.4021×10^8	0.9981
Phase interfacial	One-dimensional (R_1)	43.95	3.3309×10^2	0.9990	43.95	6.6618×10^2	0.9990	44.93	9.9444×10^2	0.9990	44.26	9.6170×10^2	0.9995
	Two-dimensional (R_2)	54.03	1.7353×10^3	0.9977	54.03	3.4705×10^3	0.9977	55.25	5.2249×10^3	0.9982	54.56	4.7584×10^3	0.9970
	Three-dimensional (R_3)	57.76	2.7237×10^3	0.9953	57.76	5.4473×10^3	0.9953	59.08	8.2295×10^3	0.9958	58.24	7.3348×10^3	0.9943
Nucleation and growth	Two-dimensional (A_2)	27.83	16.139	0.9845	27.83	3.2278×10^1	0.9845	28.48	48.360	0.9853	27.92	49.806	0.9819
	Three-dimensional (A_3)	15.17	0.799	0.9784	15.17	1.5984	0.9784	15.53	2.3829	0.9795	15.14	2.6205	0.9739

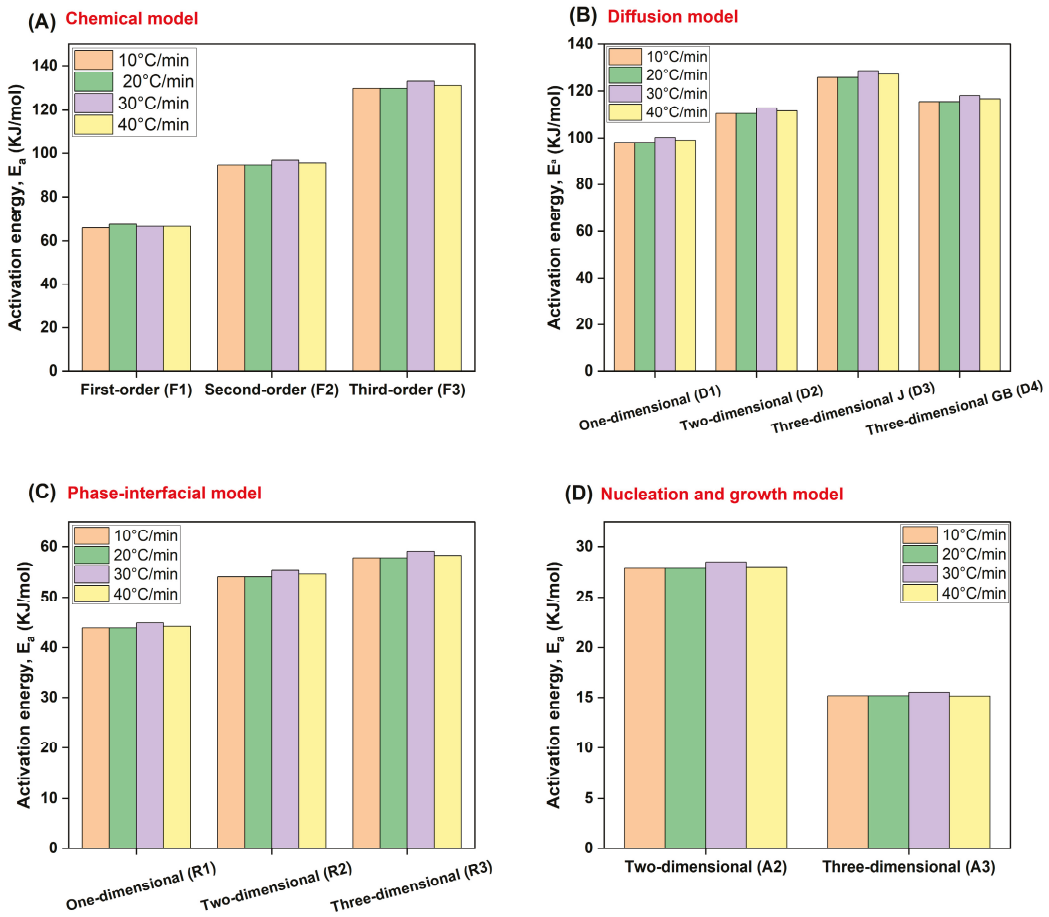


Figure 5. Dominant effect of heating rate only expressed at 30 °C/min for all reaction models assumed in the CR method: (**A**) chemical model; (**B**) diffusion model; (**C**) phase-interfacial model; and (**D**) nucleation and growth model.

For chemical reaction models (F_1, F_2, and F_3), an increase in reactants necessitated either higher temperature or reaction time because of a high activation energy demand. This is to overcome any heat or mass transfer limitations during pyrolysis, which is mainly attributed to the rampant molecular collisions within CRD wood biomass contributing to complex, overlapping reactions. It ranged from 65–68 kJ/mol for F_1 to 129–133 kJ/mol for F_3 as the heating rate increased, indicating energy-intensive heterogeneous structures competing in the reaction. This is supported by a concomitant increase in the pre-exponential factor as well. However, the average R^2 is between 0.92 and 0.98, suggesting a relatively lower correlation of these reaction models w.r.t. their counterparts. Due to the highest activation energies recorded for F_3 (more than any other reaction model tested), it may be possible to assign its role for higher conversion stages ($\alpha > 0.6$), where a thorough rearrangement of biochar's chemical structure is probable, as concluded by [81].

For the diffusion model, activation energies collectively ranged from 98 to 129 kJ/mol, with a dominant effect from linear (D_1), planar (D_2), and spherical (D_3) diffusion mechanisms. These models dominate the thermochemical data of CRD wood, as extrapolated in the findings by [82]. The average R^2 is > 0.99, highlighting their pivotal part in thermal decomposition, where the migration of volatiles and pyrolysis products could happen through porous channels and at the boundary layers. Diffusion was deemed suitable for coconut shell feedstock with a comparable activation energy of 68.9 kJ/mol, granting an appreciable bioenergy potential [83]. A high correlation factor for the diffusion model was also shown for feedstocks like wood sawdust and wheat straw [84]. In the case of any energy applications for CRD wood, D_1, D_2, and D_3 models may govern the diffusion of

ambient air/oxygen and volatile matter that initiate ignition and proceed till final combustion. This concept was also proposed by [85]. As in [86], the D_3 model showed the highest activation energy for pyrolysis of MSW, which could contain easily decomposable constituents. Meanwhile, in the CRD wood D_3 model (125–129 kJ/mol with $R^2 > 0.99$), it corresponded to a high activation energy for carrying forward diffusion within constricted spaces, especially upon clogging of porous channels with residual tar. This may also mean that surface-based diffusion has lower resistance and takes place more freely until an intermediate or product layer forms that impedes any progress. Due to high activation energies overall, F_3, D_1, D_2, and D_3 models can be attributed to the second (200–400 °C) and third (400–600 °C) stages of the TGA cycle, where the majority of disintegration reactions happen for CRD wood pyrolysis. An average activation energy of up to 84 kJ/mol was obtained by [87] for almond shell pyrolysis using the CR method, where the decomposition reactions occur in the range of 150–550 °C as well. All these results were commensurate with CRD wood.

The occurrence of phase interfacial reactions (R_1, R_2, and R_3) are also explainable due to a high correlation of >0.99. The results here are comparable to [88], where D_3 and R_3 majorly drove the biomass decomposition along with F_1, F_2, ...F_n. This means that decomposition of biomass could begin from the surface toward the less-reacted, unconverted core. As a result of constant interaction between reactants and products at an interphase, product layers are formed and sequentially shift from the outside to the inside of the biomass particle. This is why biochar production is favored at lower heating rates since it allows sufficient time for this gradual conversion. The activation energy here was lower than chemical reaction and diffusion models, at 43–60 kJ/mol. Finally, less energy (15–30 kJ/mol) was needed for secondary pyrolytic intermediates and product formation through A_2 and A_3 nucleation mechanisms (R^2 = 0.97–0.99). For this mechanism, inherent AAEM and other inorganics may have coincidentally aided in secondary charring and volatile formation by behaving as catalysts.

As depicted in Figure 5, a notable difference in activation energies existed only at a heating rate of 30 °C/min, which may signify maximum conversion at this point, unlike the ideal TGA curves, where thermal decomposition temperatures increased closely (367–390 °C) with a step-wise increase in the heating rate owing to a reduced depolymerization time, especially near the less conductive core. The same trends were observed for all other models, too. [77] reported a similar finding, where activation energies increased till a specific heating rate, after which they stabilized or dropped. However, this could be the case only till the maximum conversion is attained, after which activation energies may decrease. This was also concurred with by [35]. On the whole, since each reaction model has a different but reasonably high correlation factor ($R^2 \geq 0.92$) and variable activation energies, it is difficult to assign the most suitable pathway, mainly because the pyrolytic decomposition of biomass could be viewed as a simultaneous process rather than being assumed as an individualistic system. This was exactly proved by [37].

3.5.2. Model-Free Methods

Model-free or isoconversional methods like OFW, KAS, and FM did not rely on any pre-determined reaction models for computing the variable activation energies of biomass pyrolysis reactions [55]. Instead, the biomass conversion rate, or α, was relied upon for thermal degradation studies. However, as outlined by [89], isoconversional models have limitations wherein they assume only a single-step reaction and could neglect the role of competing reactions. On the other hand, the kinetic analysis of CRD wood using the CR method proved that competing reaction models are plausible for a thermochemical process like pyrolysis. A kinetic analysis, whether performed using model-fitting or model-free

methods, considers biomass particles that weigh between 6 and 8 mg, i.e., very small. Henceforth, the temperature on the surface can reach the center of the same particle within a short time frame, disregarding any heat transfer limitations. However, in actual pyrolysis reactors, the particle sizes of biomass can increase from a few cm to several inches, and even to logs. This is where the importance of heat conductivity is compromised, but in reality, the temperature requirements rise drastically to satiate high activation energies for biomass conversion. Thus, a TGA-based study may mostly function depending upon kinetics only and could often overlook the particle size, heating rate, composition of biomass (the percentages of holocellulose and lignin), and the externalities caused by them. In Figure 6A,B, KAS and OFW plots together seem to slightly differ from the FM plot.

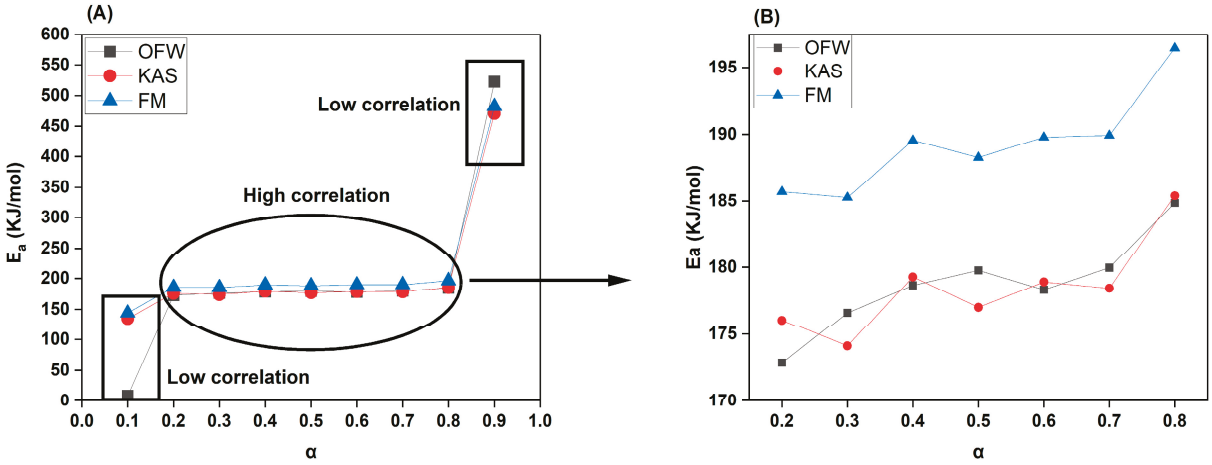


Figure 6. Variation in activation energies between OFW, KAS, and FM methods: (**A**) for α = 0.1–1.0; (**B**) for α = 0.2–0.8 only.

For reference, the calculated kinetic parameters with the model correlation for each conversion stage are listed in Table 6. For this tabulation, $\alpha > 0.8$ and $\alpha < 0.2$ were not considered due to relatively low R^2 (0.41–0.64 for α = 0.1; 0.90–0.93 for α = 0.9) and non-linearity. For other conversion rates, R^2 is >0.99, except for α = 0.2, under KAS and FM methods (R^2 = 0.98). A high correlation means that activation energies derived at these conversion rates using the three methods are accurate and dependable. The activation energies under OFW, KAS, and FM methods for α = 0.2–0.8 ranged from 172 to 185 kJ/mol, 176 to 186 kJ/mol, and 185 to 197 kJ/mol, respectively. This work discovered very minimal differences between overall activation energy requirements, along with an increase in heating and conversion rates, which may suggest fairly quick chemical reactions for the formation of activated intermediates, as stated by [90]. An α = 0.8 showed the highest activation energy since the decomposition in this phase may have occurred against highly stable aromatics in lignin and resolute inorganics/AAEM in ash.

FC in CRD wood biomass at 16–17% could also be targeted for decomposition during this stage. A significant difference in activation energy between each conversion rate was not observed since they varied very narrowly, just like the TGA curves. Moreover, there was no defined increase in activation energy, and it more or less adopted a partly sinusoidal pattern. These fluctuations could be due to complex multi-step reactions, as discussed by [27]. We may, hence, infer that 82–83% of VC in CRD wood biomass's holocellulose component could be targeted from α = 0.2–0.7. A momentary jump in E_a could indicate that the VC in biomass was either from heavier lignin bridges or was part of an organo-metallic linkage (e.g., Fe-O-C; AAEM-O-C), which demands high energy for cleavage. These are confirmed by FTIR and SEM analyses, which show the presence of a myriad of functional groups and metal content co-existing with biomass carbon and manifesting

different degradation behaviors. Since the activation energy crosses 170 kJ/mol even at an initial conversion rate of 0.2, we may conclude that the overall rate of the reaction was slow. A summary plot of all isoconversional methods for conversion rates between 0.2 and 0.8 is shown in Figure 7.

Table 6. Kinetic parameters of CRD wood pyrolysis computed using OFW, KAS, and FM isoconversional methods.

Conversion Rate, α	OFW Method			KAS Method			FM Method		
	Activation Energy, E_a (kJ/mol)	Pre-Exponential Factor, A (min^{-1})	R^2 from Plot	Activation Energy, E_a (kJ/mol)	Pre-Exponential Factor, A (min^{-1})	R^2 from Plot	Activation Energy, E_a (kJ/mol)	Pre-Exponential Factor, A (min^{-1})	R^2 from Plot
0.1	8.85	49.51005146	0.414	135.06	2.08822×10^{12}	0.599	144.09	2.9616×10^{14}	0.637
0.2	172.87	8.40043×10^{14}	0.990	176.05	1.6275×10^{15}	0.987	185.71	2.15137×10^{17}	0.988
0.3	176.61	7.47933×10^{14}	0.997	174.12	4.35321×10^{14}	0.998	185.27	8.42214×10^{16}	0.998
0.4	178.65	6.27054×10^{14}	0.996	179.28	6.85439×10^{14}	0.996	189.54	1.17277×10^{17}	0.997
0.5	179.77	4.95313×10^{14}	0.997	177.02	2.79223×10^{14}	0.999	188.26	6.43149×10^{16}	0.999
0.6	178.33	2.6664×10^{14}	0.999	178.91	2.85704×10^{14}	0.997	189.77	6.86145×10^{16}	0.998
0.7	179.97	2.79517×10^{14}	0.999	178.44	1.98226×10^{14}	0.998	189.92	6.3583×10^{16}	0.998
0.8	184.86	5.32708×10^{14}	0.999	185.41	5.66593×10^{14}	0.997	196.47	2.06678×10^{17}	0.997
0.9	522.38	7.94663×10^{39}	0.927	470.58	4.06828×10^{35}	0.901	482.38	1.04521×10^{38}	0.905

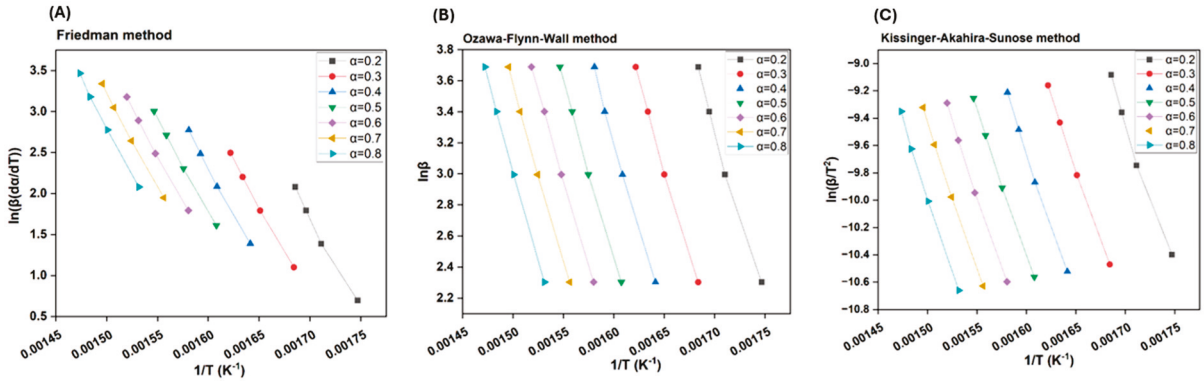


Figure 7. (**A**) Friedman (FM) method; (**B**) Ozawa–Flynn–Wall (OFW) method; (**C**) Kissinger–Akahira–Sunose (KAS) method—plots for α = 0.2–0.8.

CRD wood may, thus, be an ineffective direct fuel source because it needs a high amount of energy to start reacting. Converting it into biochar will help ease conductivity and heat transfer issues, resulting in faster reaction times.

3.6. Thermodynamic Parameters

For thermodynamic parameters, $\alpha < 0.2$ and $\alpha > 0.8$ are not considered because of low correlation factors encountered during the calculation of activation energies. As tabulated in Table 7, for OFW, KAS, and FM methods, ΔH did not vary largely with heating rates. Likewise, a lower influence of increasing conversion rates on ΔH also meant that the difference in energy requirement between reactants and the intermediates is lower, which can aid in faster formation of activated complexes. Concomitantly, positive values of ΔH indicated endothermic (exothermic if $\Delta H < 0$) reaction steps with heat absorption for biomass conversion, which is in agreement with the findings by [91]. ΔH was 179–180 kJ/mol, 179–181 kJ/mol, and 190–192 kJ/mol for OFW, KAS, and FM methods. This is in line with the findings for another woody biomass (*Ficus Nitida*), as discussed by [92]. ΔG, which describes the spontaneity of a reaction or a system, indicated a minor

increasing trend with positive values for all heating rates, conversion rates, and methods. This means that the process was not spontaneous (only if $\Delta G < 0$) and needed an external energy source to drive all parallel, sequential, and competing reactions. A ΔG of 215–230 kJ/mol was observed for both OFW and KAS methods between 0.2 and 0.8 conversion rates, which represented consistent results. However, for the FM method, ΔG ranged a bit higher, from 250 to 275 kJ/mol. This is in agreement with the studies mentioned by [93].

Table 7. ΔH, ΔG, and ΔS calculated for each heating rate according to every isoconversional method.

Conversion Rate, α	E_a and A Estimated from OFW Method											
	Heating Rate = 10 °C/min T_m = 367.41			Heating Rate = 20 °C/min T_m = 382.48			Heating Rate = 30 °C/min T_m = 386.85			Heating Rate = 40 °C/min T_m = 389.62		
	ΔH (kJ/mol)	ΔG (kJ/mol)	ΔS (J/mol·K)	ΔH (kJ/mol)	ΔG (kJ/mol)	ΔS (J/mol·K)	ΔH (kJ/mol)	ΔG (kJ/mol)	ΔS (J/mol·K)	ΔH (kJ/mol)	ΔG (kJ/mol)	ΔS (J/mol·K)
0.1	3.52	−109.52	176.48	3.40	−112.44	176.68	3.36	−113.28	176.73	3.34	−113.82	175.99
0.2	167.54	216.73	−76.79	167.42	217.64	−76.60	167.38	217.90	−76.55	167.36	218.07	−76.23
0.3	171.28	219.86	−75.83	171.16	220.75	−75.64	171.12	221.00	−75.58	171.10	221.17	−75.26
0.4	173.32	220.96	−74.36	173.20	221.82	−74.17	173.16	222.08	−74.11	173.14	222.23	−73.80
0.5	174.44	220.82	−72.40	174.32	221.66	−72.21	174.28	221.90	−72.15	174.26	222.05	−71.85
0.6	173.00	216.08	−67.25	172.88	216.85	−67.06	172.84	217.07	−67.00	172.82	217.20	−66.72
0.7	174.64	217.97	−67.65	174.52	218.74	−67.45	174.48	218.96	−67.40	174.46	219.10	−67.12
0.8	179.53	226.30	−73.01	179.40	227.14	−72.81	179.37	227.39	−72.76	179.35	227.54	−72.45
0.9	517.05	872.53	−554.95	516.93	880.64	−554.76	516.89	883.00	−554.71	516.87	884.49	−552.39
Conversion Rate, α	**E_a and A Estimated from KAS Method**											
	Heating Rate = 10 °C/min T_m = 367.41			**Heating Rate = 20 °C/min T_m = 382.48**			**Heating Rate = 30 °C/min T_m = 386.85**			**Heating Rate = 40 °C/min T_m = 389.62**		
	ΔH (kJ/mol)	**ΔG (kJ/mol)**	**ΔS (J/mol·K)**	**ΔH (kJ/mol)**	**ΔG (kJ/mol)**	**ΔS (J/mol·K)**	**ΔH (kJ/mol)**	**ΔG (kJ/mol)**	**ΔS (J/mol·K)**	**ΔH (kJ/mol)**	**ΔG (kJ/mol)**	**ΔS (J/mol·K)**
0.1	129.73	146.98	−26.93	129.61	147.14	−26.31	129.57	147.18	−26.14	129.55	147.21	−26.03
0.2	170.72	223.44	−82.29	170.60	224.43	−80.40	170.56	224.71	−79.87	170.54	224.89	−79.54
0.3	168.79	214.48	−71.33	168.66	215.30	−69.69	168.63	215.54	−69.23	168.61	215.69	−68.94
0.4	173.95	222.06	−75.10	173.83	222.94	−73.38	173.79	223.19	−72.89	173.77	223.36	−72.59
0.5	171.70	215.02	−67.64	171.57	215.79	−66.08	171.54	216.01	−65.64	171.51	216.15	−65.37
0.6	173.58	217.03	−67.83	173.46	217.80	−66.27	173.42	218.02	−65.83	173.40	218.17	−65.55
0.7	173.11	214.61	−64.79	172.98	215.33	−63.30	172.95	215.54	−62.88	172.93	215.68	−62.62
0.8	180.08	227.18	−73.52	179.96	228.03	−71.83	179.92	228.28	−71.35	179.90	228.44	−71.06
0.9	465.26	768.12	−472.81	465.13	774.99	−461.94	465.10	776.98	−458.88	465.07	778.25	−456.96
Conversion Rate, α	**E_a and A Estimated from FM Method**											
	Heating Rate = 10 °C/min T_m = 367.41			**Heating Rate = 20 °C/min T_m = 382.48**			**Heating Rate = 30 °C/min T_m = 386.85**			**Heating Rate = 40 °C/min T_m = 389.62**		
	ΔH (kJ/mol)	**ΔG (kJ/mol)**	**ΔS (J/mol·K)**	**ΔH (kJ/mol)**	**ΔG (kJ/mol)**	**ΔS (J/mol·K)**	**ΔH (kJ/mol)**	**ΔG (kJ/mol)**	**ΔS (J/mol·K)**	**ΔH (kJ/mol)**	**ΔG (kJ/mol)**	**ΔS (J/mol·K)**
0.1	138.76	182.40	−68.13	138.64	183.18	−67.93	138.60	183.40	−67.88	138.58	183.54	−67.59
0.2	180.38	259.11	−122.90	180.26	260.71	−122.71	180.22	261.17	−122.65	180.20	261.47	−122.14
0.3	179.94	253.67	−115.11	179.81	255.15	−114.91	179.78	255.58	−114.86	179.75	255.86	−114.38
0.4	184.22	259.71	−117.86	184.09	261.24	−117.67	184.06	261.68	−117.61	184.03	261.96	−117.12
0.5	182.94	255.23	−112.86	182.81	256.68	−112.67	182.77	257.10	−112.62	182.75	257.37	−112.14
0.6	184.44	257.08	−113.40	184.32	258.54	−113.21	184.28	258.96	−113.15	184.26	259.23	−112.68
0.7	184.60	256.83	−112.77	184.47	258.28	−112.58	184.44	258.70	−112.52	184.41	258.97	−112.05
0.8	191.14	269.65	−122.57	191.01	271.25	−122.38	190.98	271.71	−122.32	190.95	272.00	−121.81
0.9	477.05	809.47	−518.94	476.93	817.04	−518.75	476.89	819.23	−518.69	476.87	820.62	−516.53

A chemical reaction like pyrolysis usually supports greater disorderliness and randomness, represented by the system's entropy ($\Delta S > 0$), where a solid biomass material breaks down into volatiles, gases, and oil, which are relatively fluid and harbor greater molecular freedom. On the contrary, as shown in Table 7, the ΔS values for OFW (−60 to −80 J/mol·K), KAS (−60 to −85 J/mol·K), and FM (−110 to −130 J/mol·K) non-isothermal methods are largely negative ($\Delta S < 0$), which may mean that biomass samples

under consideration could have lower molecular freedom and need more energy to embrace further structural transformations during pyrolysis, as reflected by [2]. Low ΔS could also hint that biomass may have undergone very gradual physical/chemical transformations, consistent with [45]. On the thermodynamic forefront, negative ΔS could arise from the formation of a more ordered or stable activated complex when some decomposition reactions unfolded, as indicated by [94], who used a heterogeneous and moderate-ash biomass feedstock (wheat straw). In other words, structural rearrangements of biomass in its intermediate state could have introduced a certain degree of resistance to degradation. Given the highly heterogeneous nature of CRD wood feedstock, composed of variable lignin percentages and painted or treated surfaces laden with diverse organic and inorganic constituents, localized chemical reordering could be plausible. This could lead to a limited molecular motion and thus, negative ΔS. Interestingly, negativity in ΔS decreases with an increase in α till a certain point, signifying growing randomness in the system, before it increases yet again at higher α—possibly due to the influence of ash matter or the formation of stable metal–organic carbon complexes under high-temperature decomposition.

3.7. Summary

To summarize, the kinetic analysis of CRD wood pyrolysis utilizing model-fitting and model-free methods provided notable insights into the topic of the thermochemical decomposition of complex heterogeneous biomass. This work revealed that a reasonable lignin content and low ash content make waste CRD wood a promising feedstock for pyrolytic biochar production. The decomposition process exhibited three distinctive breakdown phases: till 150 °C, 200–400 °C, and 400–600 °C, during which where peak weight loss occurred between 350 and 400 °C. Under the four different heating rates (10–40 °C/min) tested, the model-fitting CR method derived activation energies ranging from 65 to 133 kJ/mol for the chemical reaction models (F_1, F_2, and F_3), 98 to 129 kJ/mol for the diffusion reaction models (D_1, D_2, D_3, and D_4), 43 to 60 kJ/mol for phase interfacial reaction models (R_1, R_2, and R_3), and 15 to 29 kJ/mol for random nucleation and growth reaction models (A_2, A_3). A peak in activation energy was seen, especially at 30 °C/min, for all schemes. Model-free or isoconversional OFW, KAS, and FM methods yielded activation energies between 172 and 196 kJ/mol for the conversion rates of 0.2–0.8. Thermodynamic evaluations indicated positive values of ΔH and ΔG, signifying an endothermic and non-spontaneous pyrolysis process.

Subsequent work in the domain of CRD wood pyrolysis kinetics and thermodynamics proffers understated research gaps. Firstly, CRD wood from different regions could be tested to understand the effect of feedstock variability with geography, demolition practices, and pre-processing/pre-treatment steps on thermal decomposition behavior. Secondly, different heating rates under 10 °C/min can be experimented with to discriminate TGA over significantly slower pyrolysis conditions and their role in intrinsic heat transfer for a given biomass particle size. Another interesting area of work could be to estimate the kinetic and thermodynamic behavior of CRD wood co-pyrolysis with other organic substrates. On the whole, the present manuscript is important for readers since it addresses the pressing issue of CRD wood waste management and also offers a viable valorization pathway via pyrolysis. Through the kinetic and thermodynamic analysis, this work contributes to some nascent knowledge on the interplay of pyrolysis-independent variables, like the heating rate and temperature, the biochemical composition of CRD wood, and their synergistic influence on its strucutral breakdown.

4. Conclusions

TGA was employed to assess the thermal stability and kinetic behavior of CRD wood biomass under pyrolysis conditions. Different heating rates were utilized to analyze its thermochemical decomposition, revealing that the degradation is very complex, harbors multiple reaction steps, and could be jointly influenced by the feedstock's biochemical and surface chemical composition. To calculate the kinetic parameters of pyrolysis, the weight loss data from TGA were ascribed to model-fitting and model-free/isoconversional methods, which enabled the calculation of activation energies: the former method dependent on specific assumptions pertaining to different reaction models, while the latter method without any assumptions of such reaction schemes and only functioning on the basis of biomass conversion levels (α). The CR method's perspective ranked pyrolytic transformation based on the degree of fit or correlation obtained by ascribing TGA data to each model equation. The highest R^2 (consistently >0.99) was, however, only achieved for the diffusion and phase interfacial models, thereby bolstering their criticality in biomass pyrolysis. Higher heating rates during TGA also shifted the peak melting temperatures of biomass constituents to higher temperatures, necessitating optimization toward the direction of slow pyrolysis with low heating rates and long BRT. This could make sure there is gradual yet steady heat transfer from the surface to the core of every biomass particle, aiding complete conversion. On the other hand, the model-free OFW, KAS, and FM methods offered simple and time-effective calculations of pyrolysis kinetic parameters. Simple and straightforward estimations could be drawn for most biomass conversion stages (α = 0.2–0.8), where the highest R^2 (mostly >0.99) was obtained. Extrapolating activation energies to specific energy demands across the pyrolytic transformation of CRD wood was possible and also corroborated with findings from similar works. Overall, despite a detailed outlook, experimental TGA data were well-aligned with kinetic models. Even thermodynamically speaking, these TGA tests that mimicked pyrolysis-like conditions proved that CRD wood thermal degradation is an energy-intensive process. The TGA results could be crucial for scaling up the pyrolysis of CRD wood since they offer inputs on the decomposition kinetics of a biomass material within thermochemical settings. Moreover, insights on the stability, reactivity, and disintegration of biomass polymers at specific conditions of temperature, heating rate, and BRT could be obtained, which are essential for designing pyrolysis systems.

As much as the benefits of TGA-based kinetic parameter approximations have been discussed, acknowledging their limitations also remains vital. Firstly, these tests were conducted with meagre amounts of feedstock (8–10 mg) under controlled laboratory settings that may not represent pilot, demonstration, or industrial-scale settings that are largely dynamic environments. Secondly, the particle size of biomass and the role of heat transfer within the particle differ largely between such settings. Thirdly, nuances in larger pyrolysis systems, such as the residence and eventual settling of volatiles on biomass, the cracking of volatiles and their role in carbon polymerization to PAHs, and the interplay of any vacuum/suction effects across the reactor, may not be achieved within TGA set-ups. Lastly, based on the different methods used to calculate kinetic parameters, especially model-fitting methods like CR, there could be inaccuracies posted due to the selection of wrong reaction models, assumptions, and corresponding findings derived that may fail to capture some intricacies of pyrolysis at higher scales.

Author Contributions: Conceptualization, methodology, validation, formal analysis, investigation, data curation, writing—original draft preparation, editing, and visualization—A.G. Supervision and mentorship—S.B. Supervision, review, and mentorship—S.L. Supervision, review, editing, and mentorship—O.R. Supervision, review, editing, and mentorship—Y.B. Project administration—C.B. All authors have read and agreed to the published version of the manuscript.

Funding: This research was funded by MITACS (MITACS: IT40901), through Escouade Energie, Citeq, and supported by Innofibre, and I^2E^3—UQTR, Québec, Canada. The work was conducted at Innofibre—Centre d'Innovation des Produits Cellulosiques, Trois-Rivières, and at the Institute for Innovation in Ecomaterials, Ecoproducts, and Ecoenergies (I^2E^3), the University of Québec Trois-Rivières (UQTR), Québec, Canada.

Data Availability Statement: Data will be shared upon request.

Acknowledgments: Due credit is given to the technicians, researchers, and colleagues who were a critical part of this work.

Conflicts of Interest: The authors declare no conflict of interest. The funders had no role in the design of the study; in the collection, analyses, or interpretation of data; in the writing of the manuscript; or in the decision to publish the results.

Abbreviations

AAEM	Alkaline and alkaline earth metal.
BRT	Biomass residence time.
CCA	Copper, chromium, and arsenic.
CR	Coats–Redfern.
CRD	Construction, renovation, and demolition.
DB	Dry basis.
DTG	Differential thermogram.
FC	Fixed carbon.
FM	Friedman.
FTIR	Fourier Transform Infrared.
GHGs	Greenhouse gases.
HHV	Higher heating value.
HTC	Hydrothermal carbonization.
KAS	Kissinger–Akahira–Sunose.
MP-AES	Microwave Plasma Atomic Emission Spectrometer.
Mt	Million tons.
OFW	Ozawa–Flynn–Wall.
PAH	Polyaromatic hydrocarbon.
TGA	Thermogravimetric analysis.
VC	Volatile carbon.
Wt%	Weight percent (used interchangeably with %).

References

1. Laadila, M.A.; LeBihan, Y.; Caron, R.F.; Vaneeckhaute, C. Construction, renovation and demolition (CRD) wastes contaminated by gypsum residues: Characterization, treatment and valorization. *Waste Manag.* **2021**, *120*, 125–135. [CrossRef] [PubMed]
2. Kumar, I.; Tirlangi, S.; Kathiresan, K.; Sharma, V.; Madhu, P.; Sathish, T.; Ağbulut, Ü.; Murugan, P. Co-pyrolysis of furniture wood with mixed plastics and waste tyres: Assessment of synergistic effect on biofuel yield and product characterization under different blend ratio. *Sci. Rep.* **2024**, *14*, 24584. [CrossRef] [PubMed]
3. Ganesan, A.; Rezazgui, O.; Langlois, S.; Boussabbeh, C.; Barnabé, S. Pyrolytic conversion of construction, renovation, and demolition (CRD) wood wastes in Québec to biochar: Production, characterization, and identifying relevant stability indices for carbon sequestration. *Sci. Total Environ.* **2025**, *965*, 178650. [CrossRef] [PubMed]
4. Gmar, M.; Bouafif, H.; Bouslimi, B.; Braghiroli, F.L.; Koubaa, A. Pyrolysis of chromated copper arsenate-treated wood: Investigation of temperature, granulometry, biochar yield, and metal pathways. *Energies* **2022**, *15*, 5071. [CrossRef]
5. O'Dwyer, J.; Walshe, D.; Byrne, K.A. Wood waste decomposition in landfills: An assessment of current knowledge and implications for emissions reporting. *Waste Manag.* **2018**, *73*, 181–188. [CrossRef]
6. Kizha, A.R.; Han, H.S. Processing and sorting forest residues: Cost, productivity and managerial impacts. *Biomass Bioenergy* **2016**, *93*, 97–106. [CrossRef]

7. Ganesan, A.; Rezazgui, O.; Burgos, J.B.; Mangin, P.J.; Barnabé, S. Valorization of lignocellulosic biomass forest residues in quebec via the integrated hydropyrolysis and hydroconversion (IH^2) technology: A review. *Biomass Bioenergy* **2025**, *193*, 107516. [CrossRef]
8. Rao, Y.K.; Dhanalakshmi, C.S.; Vairavel, D.K.; Surakasi, R.; Kaliappan, S.; Patil, P.P.; Socrates, S.; Lalvani, J.I.J. Investigation on forestry wood wastes: Pyrolysis and thermal characteristics of *Ficus religiosa* for energy recovery system. *Adv. Mater. Sci. Eng.* **2022**, *2022*, 3314606. [CrossRef]
9. Zhang, Y.; Liang, Y.; Li, S.; Yuan, Y.; Zhang, D.; Wu, Y.; Xie, H.; Brindhadevi, K.; Pugazhendhi, A.; Xia, C. A review of biomass pyrolysis gas: Forming mechanisms, influencing parameters, and product application upgrades. *Fuel* **2023**, *347*, 128461. [CrossRef]
10. Guedes, R.E.; Luna, A.S.; Torres, A.R. Operating parameters for bio-oil production in biomass pyrolysis: A review. *J. Anal. Appl. Pyrolysis* **2018**, *129*, 134–149. [CrossRef]
11. Mouneir, S.M.; El-Shamy, A.M. A review on harnessing the energy potential of pyrolysis gas from scrap tires: Challenges and opportunities for sustainable energy recovery. *J. Anal. Appl. Pyrolysis* **2024**, *177*, 106302. [CrossRef]
12. Peters, J.F.; Iribarren, D.; Dufour, J. Biomass pyrolysis for biochar or energy applications? A life cycle assessment. *Environ. Sci. Technol.* **2015**, *49*, 5195–5202. [CrossRef]
13. Ibitoye, S.E.; Loha, C.; Mahamood, R.M.; Jen, T.C.; Alam, M.; Sarkar, I.; Das, P.; Akinlabi, E.T. An overview of biochar production techniques and application in iron and steel industries. *Bioresour. Bioprocess.* **2024**, *11*, 65. [CrossRef]
14. Hasan, M.; Chakma, S.; Liang, X.; Sutradhar, S.; Kozinski, J.; Kang, K. Engineered Biochar for Metal Recycling and Repurposed Applications. *Energies* **2024**, *17*, 4674. [CrossRef]
15. Legan, M.; Gotvajn, A.Ž.; Zupan, K. Potential of biochar use in building materials. *J. Environ. Manag.* **2022**, *309*, 114704. [CrossRef]
16. Han, H.; Buss, W.; Zheng, Y.; Song, P.; Rafiq, M.K.; Liu, P.; Mašek, O.; Li, X. Contaminants in biochar and suggested mitigation measures–a review. *Chem. Eng. J.* **2022**, *429*, 132287. [CrossRef]
17. Mlonka-Mędrala, A.; Magdziarz, A.; Dziok, T.; Sieradzka, M.; Nowak, W. Laboratory studies on the influence of biomass particle size on pyrolysis and combustion using TG GC/MS. *Fuel* **2019**, *252*, 635–645. [CrossRef]
18. Adhikari, S.; Moon, E.; Paz-Ferreiro, J.; Timms, W. Comparative analysis of biochar carbon stability methods and implications for carbon credits. *Sci. Total Environ.* **2024**, *914*, 169607. [CrossRef]
19. Altıkat, A.; Alma, M.H.; Altıkat, A.; Bilgili, M.E.; Altıkat, S. A Comprehensive Study of Biochar Yield and Quality Concerning Pyrolysis Conditions: A Multifaceted Approach. *Sustainability* **2024**, *16*, 937. [CrossRef]
20. Ranzi, E.; Debiagi, P.E.A.; Frassoldati, A. Mathematical modeling of fast biomass pyrolysis and bio-oil formation. Note I: Kinetic mechanism of biomass pyrolysis. *ACS Sustain. Chem. Eng.* **2017**, *5*, 2867–2881. [CrossRef]
21. Silva, J.; Teixeira, S.; Teixeira, J. A review of biomass thermal analysis, kinetics and product distribution for combustion modeling: From the micro to macro perspective. *Energies* **2023**, *16*, 6705. [CrossRef]
22. Branca, C.; Galgano, A. Kinetic Modelling of Biomass Pyrolysis Processes. *Processes* **2024**, *12*, 706. [CrossRef]
23. Thejaswini, N.; Annapureddy, P.K.R.; Rammohan, D.; Kishore, N. Kinetics and thermodynamics of non-isothermal pyrolysis of *Terminalia chebula* branches at different heating rates. *Int. J. Chem. Kinet.* **2023**, *55*, 673–687. [CrossRef]
24. Zhong, Y.; Ding, Y.; Lu, K.; Mao, S.; Li, C. Kinetic parameters and reaction mechanism study of biomass pyrolysis by combined kinetics coupled with a heuristic optimization algorithm. *Fuel* **2023**, *334*, 126622. [CrossRef]
25. Rambhatla, N.; Panicker, T.F.; Mishra, R.K.; Manjeshwar, S.K.; Sharma, A. Biomass pyrolysis for biochar production: Study of kinetics parameters and effect of temperature on biochar yield and its physicochemical properties. *Results Eng.* **2024**, *25*, 103679. [CrossRef]
26. Fanezouné, C.K.; Dhahak, A.; Peixinho, J.; El Bari, H. Thermogravimetric analysis and kinetic modeling for empty fruit bunch date palm pyrolysis. *Bioresour. Technol. Rep.* **2024**, *27*, 101916. [CrossRef]
27. Patidar, K.; Singathia, A.; Vashishtha, M.; Sangal, V.K.; Upadhyaya, S. Investigation of kinetic and thermodynamic parameters approaches to non-isothermal pyrolysis of mustard stalk using model-free and master plots methods. *Mater. Sci. Energy Technol.* **2022**, *5*, 6–14. [CrossRef]
28. Zsinka, V.; Tarcsay, B.L.; Miskolczi, N. Determination of Kinetic and Thermodynamic Parameters of Biomass Gasification with TG-FTIR and Regression Model Fitting. *Energies* **2024**, *17*, 1875. [CrossRef]
29. Arenas, C.N.; Navarro, M.V.; Martínez, J.D. Pyrolysis kinetics of biomass wastes using isoconversional methods and the distributed activation energy model. *Bioresour. Technol.* **2019**, *288*, 121485. [CrossRef]
30. Postawa, K.; Fałtynowicz, H.; Szczygieł, J.; Beran, E.; Kułażyński, M. Analyzing the kinetics of waste plant biomass pyrolysis via thermogravimetry modeling and semi-statistical methods. *Bioresour. Technol.* **2022**, *344*, 126181. [CrossRef]
31. White, J.E.; Catallo, W.J.; Legendre, B.L. Biomass pyrolysis kinetics: A comparative critical review with relevant agricultural residue case studies. *J. Anal. Appl. Pyrolysis* **2011**, *91*, 1–33. [CrossRef]
32. Pecha, M.B.; Arbelaez, J.I.M.; Garcia-Perez, M.; Chejne, F.; Ciesielski, P.N. Progress in understanding the four dominant intra-particle phenomena of lignocellulose pyrolysis: Chemical reactions, heat transfer, mass transfer, and phase change. *Green Chem.* **2019**, *21*, 2868–2898. [CrossRef]
33. Zhang, X.; Chen, C.; Tang, C.; Wang, Y. Morphological control of biochar with emerging functionalities by thermodynamic and kinetic approaches. *Acc. Mater. Res.* **2022**, *3*, 525–539. [CrossRef]

34. Pfersich, J.; Arauzo, P.J.; Modugno, P.; Titirici, M.M.; Kruse, A. Evaluation of the Char Formation During the Hydrothermal Treatment of Wooden Balls. *Glob. Chall.* **2023**, *7*, 2300169. [CrossRef]
35. Mishra, R.K.; Mohanty, K. Pyrolysis kinetics and thermal behavior of waste sawdust biomass using thermogravimetric analysis. *Bioresour. Technol.* **2018**, *251*, 63–74. [CrossRef]
36. Mahmood, H.; Shakeel, A.; Abdullah, A.; Khan, M.I.; Moniruzzaman, M. A comparative study on suitability of model-free and model-fitting kinetic methods to non-isothermal degradation of lignocellulosic materials. *Polymers* **2021**, *13*, 2504. [CrossRef]
37. Mian, I.; Li, X.; Jian, Y.; Dacres, O.D.; Zhong, M.; Liu, J.; Ma, F.; Rahman, N. Kinetic study of biomass pellet pyrolysis by using distributed activation energy model and Coats Redfern methods and their comparison. *Bioresour. Technol.* **2019**, *294*, 122099. [CrossRef]
38. Wang, L.; Lei, H.; Liu, J.; Bu, Q. Thermal decomposition behavior and kinetics for pyrolysis and catalytic pyrolysis of Douglas fir. *RSC Adv.* **2018**, *8*, 2196–2202. [CrossRef]
39. Chen, L.; Hu, J.; Han, Q.; Xie, A.; Zhou, Z.; Yang, J.; Tang, Q.; Mi, B.; Wu, F. Application of distributed activation energy model and Coats-Redfern integration method in the study of industrial lignin pyrolysis kinetics. *Biomass Convers. Biorefinery* **2022**, 1–11. [CrossRef]
40. Altynbaeva, D.; Astafev, A.; Tabakaev, R. Kinetics of biomass low-temperature pyrolysis by coats–redfern method. In *MATEC Web of Conferences*; EDP Sciences: Les Ulis, France, 2018; Volume 194, p. 01058.
41. Emiola-Sadiq, T.; Zhang, L.; Dalai, A.K. Thermal and kinetic studies on biomass degradation via thermogravimetric analysis: A combination of model-fitting and model-free approach. *ACS Omega* **2021**, *6*, 22233–22247. [CrossRef]
42. Najafi, H.; Golrokh Sani, A.; Sobati, M.A. Thermogravimetric and thermo-kinetic analysis of sugarcane bagasse pith: A comparative evaluation with other sugarcane residues. *Sci. Rep.* **2024**, *14*, 2076. [CrossRef] [PubMed]
43. Mishra, R.K.; Mohanty, K.; Wang, X. Pyrolysis kinetic behavior and Py-GC–MS analysis of waste dahlia flowers into renewable fuel and value-added chemicals. *Fuel* **2020**, *260*, 116338. [CrossRef]
44. Li, J.; Shang, Y.; Wei, W.; Liu, Z.; Qiao, Y.; Qin, S.; Tian, Y. Comparative study on pyrolysis kinetics behavior and high-temperature fast pyrolysis product analysis of coastal zone and land biomasses. *ACS Omega* **2022**, *7*, 10144–10155. [CrossRef] [PubMed]
45. Singh, R.K.; Patil, T.; Pandey, D.; Sawarkar, A.N. Pyrolysis of mustard oil residue: A kinetic and thermodynamic study. *Bioresour. Technol.* **2021**, *339*, 125631.
46. Armynah, B.; Tahir, D.; Tandilayuk, M.; Djafar, Z.; Piarah, W.H. Potentials of biochars derived from bamboo leaf biomass as energy sources: Effect of temperature and time of heating. *Int. J. Biomater.* **2019**, *2019*, 3526145. [CrossRef]
47. Nzediegwu, C.; Naeth, M.A.; Chang, S.X. Elemental composition of biochars is affected by methods used for its determination. *J. Anal. Appl. Pyrolysis* **2021**, *156*, 105174. [CrossRef]
48. Channiwala, S.A.; Parikh, P.P. A unified correlation for estimating HHV of solid, liquid and gaseous fuels. *Fuel* **2002**, *81*, 1051–1063. [CrossRef]
49. Sluiter, A.; Ruiz, R.; Scarlata, C.; Sluiter, J.; Templeton, D. *Determination of Extractives in Biomass: Laboratory Analytical Procedure (LAP)*; National Renewable Energy Laboratory: Golden, CO, USA, 2008. Available online: https://docs.nrel.gov/docs/gen/fy08/42619.pdf (accessed on 1 May 2025).
50. Sluiter, A.; Hames, B.; Ruiz, R.; Scarlata, C.; Sluiter, J.; Templeton, D.; Crocker, D. *Determination of Structural Carbohydrates and Lignin in Biomass: Laboratory Analytical Procedure (LAP)*; National Renewable Energy Laboratory: Golden, CO, USA, 2008. Available online: https://docs.nrel.gov/docs/gen/fy13/42618.pdf (accessed on 1 May 2025).
51. Maaoui, A.; Trabelsi, A.B.H.; Abdallah, A.B.; Chagtmi, R.; Lopez, G.; Cortazar, M.; Olazar, M. Assessment of pine wood biomass wastes valorization by pyrolysis with focus on fast pyrolysis biochar production. *J. Energy Inst.* **2023**, *108*, 101242. [CrossRef]
52. Chakravarty, K.H.; Sadi, M.; Chakravarty, H.; Andersen, J.; Choudhury, B.; Howard, T.J.; Arabkoohsar, A. Pyrolysis kinetics and potential utilization analysis of cereal biomass by-products; an experimental analysis for cleaner energy productions in India. *Chemosphere* **2024**, *353*, 141420. [CrossRef]
53. Giglio, E.; Vitaali, G.; Lanzini, A.; Santarelli, M. Integration between biomass gasification and high-temperature electrolysis for synthetic methane production. *Biomass Bioenergy* **2021**, *148*, 106017. [CrossRef]
54. Radojević, M.; Janković, B.; Jovanović, V.; Stojiljković, D.; Manić, N. Comparative pyrolysis kinetics of various biomasses based on model-free and DAEM approaches improved with numerical optimization procedure. *PLoS ONE* **2018**, *13*, e0206657. [CrossRef] [PubMed]
55. Fischer, O.; Lemaire, R.; Bensakhria, A. Thermogravimetric analysis and kinetic modeling of the pyrolysis of different biomass types by means of model-fitting, model-free and network modeling approaches. *J. Therm. Anal. Calorim.* **2024**, *149*, 10941–10963. [CrossRef] [PubMed]
56. Szufa, S.; Piersa, P.; Adrian, Ł.; Czerwińska, J.; Lewandowski, A.; Lewandowska, W.; Sielski, J.; Dzikuć, M.; Wróbel, M.; Jewiarz, M.; et al. Sustainable drying and torrefaction processes of miscanthus for use as a pelletized solid biofuel and biocarbon-carrier for fertilizers. *Molecules* **2021**, *26*, 1014. [CrossRef]
57. Thiru, S.; Kola, R.; Thimmaraju, M.K.; Dhanalakshmi, C.S.; Sharma, V.; Sakthi, P.; Maguluri, L.P.; Ranganathan, L.; Lalvani, J.I.J. An analytical characterization study on biofuel obtained from pyrolysis of *Madhuca longifolia* residues. *Sci. Rep.* **2024**, *14*, 14745. [CrossRef]
58. Paredes, R.; Castells, B.; Tascón, A. Thermogravimetric Assessment of Biomass: Unravelling Kinetic, Chemical Composition and Combustion Profiles. *Fire* **2024**, *7*, 396. [CrossRef]

59. Punsuwan, N.; Tangsathitkulchai, C. Product Characterization and Kinetics of Biomass Pyrolysis in a Three-Zone Free-Fall Reactor. *Int. J. Chem. Eng.* **2014**, *2014*, 986719. [CrossRef]
60. Gani, A.; Desvita, H.; Munawar, E.; Mamat, R.; Nizar, M.; Darnas, Y.; Sarjono, R.E. Comparative analysis of HHV and LHV values of biocoke fuel from palm oil mill solid waste. *Case Stud. Chem. Environ. Eng.* **2024**, *9*, 100581. [CrossRef]
61. Uwaoma, R.C.; Schröer, B.J.; Strydom, C.A.; Bunt, J.R.; Matjie, R.H.; Mphahlele, K.; Meyer, J.A. Kinetics, thermodynamics, and thermal decomposition characteristics of co-pyrolysis of municipality solid waste residue hydrochar and <1.5 g/cm^3 fraction of South African discarded fine coal. *Bioresour. Technol. Rep.* **2022**, *18*, 100998.
62. Wang, W.; Lemaire, R.; Bensakhria, A.; Luart, D. Analysis of the catalytic effects induced by alkali and alkaline earth metals (AAEMs) on the pyrolysis of beech wood and corncob. *Catalysts* **2022**, *12*, 1505. [CrossRef]
63. Cao, J.; Yu, Y.; Wu, H. Primary release and transformation of inorganic and organic sodium during fast pyrolysis of sodium-loaded lignin. *Proc. Combust. Inst.* **2023**, *39*, 3439–3446. [CrossRef]
64. Liu, N.; Huang, H.; Feng, J.; Li, R.; Huang, X.; Wu, Y. Effects of alkali and alkaline earth metals in biomass on co-pyrolysis characteristics and product distribution of coal and biomass. *Fuel* **2025**, *389*, 134551. [CrossRef]
65. Grafmüller, J.; Böhm, A.; Zhuang, Y.; Spahr, S.; Müller, P.; Otto, T.N.; Bucheli, T.D.; Leifeld, J.; Giger, R.; Tobler, M.; et al. Wood ash as an additive in biomass pyrolysis: Effects on biochar yield, properties, and agricultural performance. *ACS Sustain. Chem. Eng.* **2022**, *10*, 2720–2729. [CrossRef]
66. Elhenawy, Y.; Fouad, K.; Mansi, A.; Bassyouni, M.; Gadalla, M.; Ashour, F.; Majozi, T. Experimental analysis and numerical simulation of biomass pyrolysis. *J. Therm. Anal. Calorim.* **2024**, *149*, 10369–10383. [CrossRef]
67. Nhuchhen, D.R.; Afzal, M.T. HHV predicting correlations for torrefied biomass using proximate and ultimate analyses. *Bioengineering* **2017**, *4*, 7. [CrossRef]
68. Li, J.; Sun, W.; Lichtfouse, E.; Maurer, C.; Liu, H. Life cycle assessment of biochar for sustainable agricultural application: A review. *Sci. Total Environ.* **2024**, *951*, 175448. [CrossRef]
69. Yildiz, M.J.; Wurzer, C.; Robinson, T.; Wietecha, J.; Mašek, O. Biochar from pellets: Influence of binders and pyrolysis temperature on physical properties of pyrolyzed pellets. *Sustain. Mater. Technol.* **2025**, *43*, e01327.
70. Dhyani, V.; Bhaskar, T. A comprehensive review on the pyrolysis of lignocellulosic biomass. *Renew. Energy* **2018**, *129*, 695–716. [CrossRef]
71. Gurtner, D.; Kresta, M.; Hupfauf, B.; Götz, P.; Nussbaumer, R.; Hofmann, A.; Pfeifer, C. Mechanical strength characterisation of pyrolysis biochar from woody biomass. *Energy* **2023**, *285*, 129366. [CrossRef]
72. Dufourny, A.; Van De Steene, L.; Humbert, G.; Guibal, D.; Martin, L.; Blin, J. Influence of pyrolysis conditions and the nature of the wood on the quality of charcoal as a reducing agent. *J. Anal. Appl. Pyrolysis* **2019**, *137*, 1–13. [CrossRef]
73. Xia, C.; Cai, L.; Zhang, H.; Zuo, L.; Shi, S.Q.; Lam, S.S. A review on the modeling and validation of biomass pyrolysis with a focus on product yield and composition. *Biofuel Res. J.* **2021**, *29*, 1296–1315. [CrossRef]
74. Johnston, C.T. 18 Biochar analysis by Fourier-transform infra-red spectroscopy. In *Biochar: A Guide to Analytical Methods*; CRC Press: Boca Raton, FL, USA, 2017; p. 199.
75. Nanda, S.; Mohanty, P.; Pant, K.K.; Naik, S.; Kozinski, J.A.; Dalai, A.K. Characterization of North American lignocellulosic biomass and biochars in terms of their candidacy for alternate renewable fuels. *Bioenergy Res.* **2013**, *6*, 663–677. [CrossRef]
76. Mukherjee, A.; Okolie, J.A.; Tyagi, R.; Dalai, A.K.; Niu, C. Pyrolysis kinetics and activation thermodynamic parameters of exhausted coffee residue and coffee husk using thermogravimetric analysis. *Can. J. Chem. Eng.* **2021**, *99*, 1683–1695. [CrossRef]
77. Raza, M.; Abu-Jdayil, B.; Inayat, A. Pyrolytic kinetics and thermodynamic analyses of date seeds at different heating rates using the Coats–Redfern method. *Fuel* **2023**, *342*, 127799. [CrossRef]
78. Almusafir, R.; Smith, J.D. Thermal Decomposition and Kinetic Parameters of Three Biomass Feedstocks for the Performance of the Gasification Process Using a Thermogravimetric Analyzer. *Energies* **2024**, *17*, 396. [CrossRef]
79. Apaydın Varol, E.; Mutlu, Ü. TGA-FTIR analysis of biomass samples based on the thermal decomposition behavior of hemicellulose, cellulose, and lignin. *Energies* **2023**, *16*, 3674. [CrossRef]
80. Gonzalez-Aguilar, A.M.; Cabrera-Madera, V.P.; Vera-Rozo, J.R.; Riesco-Ávila, J.M. Effects of heating rate and temperature on the thermal pyrolysis of expanded polystyrene post-industrial waste. *Polymers* **2022**, *14*, 4957. [CrossRef]
81. Călin, C.; Sîrbu, E.E.; Tănase, M.; Győrgy, R.; Popovici, D.R.; Banu, I. A Thermogravimetric Analysis of Biomass Conversion to Biochar: Experimental and Kinetic Modeling. *Appl. Sci.* **2024**, *14*, 9856. [CrossRef]
82. Dhaundiyal, A.; Singh, S.B.; Hanon, M.M.; Rawat, R. Determination of kinetic parameters for the thermal decomposition of parthenium hysterophorus. *Environ. Clim. Technol.* **2018**, *22*, 5–21. [CrossRef]
83. Monir, M.U.; Shovon, S.M.; Akash, F.A.; Habib, M.A.; Techato, K.; Abd Aziz, A.; Chowdhury, S.; Prasetya, T.A.E. Comprehensive characterization and kinetic analysis of coconut shell thermal degradation: Energy potential evaluated via the Coats-Redfern method. *Case Stud. Therm. Eng.* **2024**, *55*, 104186. [CrossRef]
84. Saleem, M.; Bahadar, A. In-Depth Study on Synergic Interactions and Thermo-Kinetic Analysis of (Wheat Straw and Woody Sawdust) Biomass Co-Pyrolysis over Mussel Shell-Derived CaO Catalyst Using Coats–Redfern Method. *Catalysts* **2024**, *14*, 655. [CrossRef]

85. Hadey, C.; Malika, A.; Mohammed, A.; Fatima, B. A study on the biomass wastes' combustion process and their biochar. *Res. Sq.* **2020**. [CrossRef]
86. Hassan, A.M.M.; Asif, M.; Hussain, T.; Sajjad, R.; Yasmin, F.; Khandaker, M.U. Pyrolysis of municipal solid waste: Kinetics and thermodynamic parameters via Coats-Redfern method. *Appl. Chem. Eng.* **2024**, *7*, 1872. [CrossRef]
87. Tariq, R.; Saeed, S.; Riaz, M.; Saeed, S. Kinetic and thermodynamic evaluation of almond shells pyrolytic behavior using Coats–Redfern and pyrolysis product distribution model. *Energy Sources Part A Recovery Util. Environ. Eff.* **2023**, *45*, 4446–4462. [CrossRef]
88. Sobek, S.; Werle, S. Kinetic modelling of waste wood devolatilization during pyrolysis based on thermogravimetric data and solar pyrolysis reactor performance. *Fuel* **2020**, *261*, 116459. [CrossRef]
89. Shrivastava, D.K.; Singh, A.K.; Chakraborty, J.P. Model-free isoconversional methods to determine the intrinsic kinetics and thermodynamic parameters during pyrolysis of boiled banana peel: Influence of inorganic species. *Bioresour. Technol. Rep.* **2023**, *24*, 101676. [CrossRef]
90. Bisen, D.; Chouhan, A.P.S.; Sarma, A.K.; Rajamohan, S.; Elumalai, P.V.; Balasubramanian, D.; Cherie, A. Thermogravimetric analysis of rice husk and low-density polyethylene co-pyrolysis: Kinetic and thermodynamic parameters. *Sci. Rep.* **2024**, *14*, 31798. [CrossRef]
91. Shagali, A.A.; Hu, S.; Li, H.; Chi, H.; Qing, H.; Xu, J.; Jiang, L.; Wang, Y.; Su, S.; Xiang, J. Thermal behavior, synergistic effect and thermodynamic parameter evaluations of biomass/plastics co–pyrolysis in a concentrating photothermal TGA. *Fuel* **2023**, *331*, 125724. [CrossRef]
92. Tabal, A.; Barakat, A.; Aboulkas, A. Pyrolysis of ficus nitida wood: Determination of kinetic and thermodynamic parameters. *Fuel* **2021**, *283*, 119253. [CrossRef]
93. Patil, Y.; Ku, X.; Vasudev, V. Pyrolysis characteristics and determination of kinetic and thermodynamic parameters of raw and torrefied Chinese fir. *ACS Omega* **2023**, *8*, 34938–34947. [CrossRef]
94. Lei, J.; Ye, X.; Wang, H.; Zhao, D. Insights into pyrolysis kinetics, thermodynamics, and the reaction mechanism of wheat straw for its resource utilization. *Sustainability* **2023**, *15*, 12536. [CrossRef]

Disclaimer/Publisher's Note: The statements, opinions and data contained in all publications are solely those of the individual author(s) and contributor(s) and not of MDPI and/or the editor(s). MDPI and/or the editor(s) disclaim responsibility for any injury to people or property resulting from any ideas, methods, instructions or products referred to in the content.

MDPI AG
Grosspeteranlage 5
4052 Basel
Switzerland
Tel.: +41 61 683 77 34

Energies Editorial Office
E-mail: energies@mdpi.com
www.mdpi.com/journal/energies



Disclaimer/Publisher's Note: The title and front matter of this reprint are at the discretion of the Guest Editors. The publisher is not responsible for their content or any associated concerns. The statements, opinions and data contained in all individual articles are solely those of the individual Editors and contributors and not of MDPI. MDPI disclaims responsibility for any injury to people or property resulting from any ideas, methods, instructions or products referred to in the content.





Academic Open
Access Publishing

mdpi.com

ISBN 978-3-7258-9262-4